Physical Metallurgy

1

Robert W. Cahn and Peter Haasen (†), editors

FOURTH, REVISED AND ENHANCED EDITION

NORTH-HOLLAND

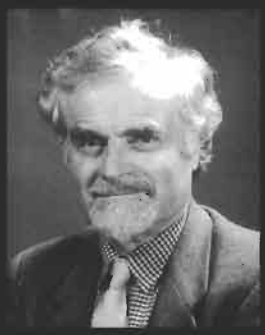

Prof. Robert W. Cahn, editor

PHYSICAL METALLURGY

VOLUME I

LIST OF CONTRIBUTORS

A. S. Argon
E. Arzt
H. K. D. H. Bhadeshia
H. Biloni
J. L Bocquet
W. J. Boettinger
G. Brebec
R. W. Cahn
G. Y. Chin†
T. W. Clyne
R. D. Doherty
H. E. Exner
R. Ferro
D. R. Gaskell
H. Gleiter
A. L. Greer
P. Haasen†
J. P. Hirth
S. Hofmann
E. D. Hondros
E. Hornbogen
G. Kostorz
C. Laird
P. Lejček
W. C. Leslie
Y. Limoge
J. D. Livingston
F. E. Luborsky
T. B. Massalski
J. R. Nicholls
A D. Pelton
D. G. Pettifor
D. P. Pope
M. Rühle
A. Saccone
S. R. J. Saunders
M. P. Seah
W. Steurer
J.-L. Strudel
R. M. Thomson
C. M. Wayman
M. Wilkens
A. H. Windle
H. J. Wollenberger

PHYSICAL METALLURGY

Fourth, revised and enhanced edition

Edited by

Robert W. CAHN
University of Cambridge

Peter HAASEN†
University of Göttingen

VOLUME I

1996

NORTH-HOLLAND
AMSTERDAM—LAUSANNE—NEW YORK—OXFORD—SHANNON—TOKYO

ELSEVIER SCIENCE B.V.
Sara Burgerhartstraat 25
P.O. Box 211, 1000 AE Amsterdam, The Netherlands

ISBN: 0 444 89875 1

This book is printed on acid-free paper.

Printed in The Netherlands

Regretfully unnoticed, in the final printing process a layout error has occurred on the original page v, due to which the authors' names of chapters 15-19 are not correctly aligned with their chapter titles. Please use this corrected page instead.

SYNOPSIS OF CONTENTS

Volume 1

Volume 2

Volume 3

SYNOPSIS OF CONTENTS

Volume 1

Volume 2

Volume 3

PREFACE TO THE FOURTH EDITION

The first, single-volume edition of this Work was published in 1965 and the second in 1970; continued demand prompted a third edition in two volumes which appeared in 1983. The first two editions were edited by myself alone, but in preparing the third, which was much longer and more complex, I had the crucial help of Peter Haasen as co-editor. The third edition came out in 1983, and sold steadily, so that the publishers were motivated to propose the preparation of yet another version of the Work; we began the joint planning for this in early 1992. We agreed on the changes and additions we wished to make: the responsibility for commissioning chapters was divided equally between us, but the many policy decisions, made during a series of face-to-face discussions, were very much a joint enterprise. Peter Haasen was able to commission all the chapters which he had agreed to handle, and this task (which involved detailed discussions with a number of authors) was completed in early 1993. Thereupon, in May 1993, my friend of many years was suddenly taken ill; the illness worsened rapidly, and in October of the same year he died, at the early age of 66. When he was already suffering the ravages of his fatal illness, he yet found the resolve and energy to revise his own chapter and to send it to me for comments, and to modify it further in the light of those comments. He was also able to examine, edit and approve the revised chapter on dislocations, which came in early. These were the very last professional tasks he performed. Peter Haasen was in every sense co-editor of this new edition, even though fate decreed that I had to complete the editing and approval of most of the chapters. I am proud to share the title-page with such an eminent physicist.

The first edition had 22 chapters and the second, 23. There were 31 chapters in the third edition and the present edition has 32. The first two editions were single volumes, the third had to be divided into two volumes, and now the further expansion of the text has made it necessary to go to three volumes. This fourth edition is nearly three times the size of the first edition thirty years ago; this is due not only to the addition of new topics, but also to the fact that the treatment of existing topics has become much more substantial than it was in 1965. There are those who express the conviction that physical metallurgy has passed its apogee and is in steady decline; the experience of editing this edition, and the problems I have encountered in holding enthusiastic authors back from even more lengthy treatments (to avoid exceeding the agreed page limits by a wholly unacceptable margin), have shown me

how mistaken this pessimistic assessment is! Physical metallurgy, the parent discipline of materials science, has maintained its central status undiminished.

The first three editions each opened with a historical overview. We decided to omit this in the fourth edition, for two main reasons: the original author had died and it would have fallen to others to revise his work, never an entirely satisfactory proceeding; it had also become plain (especially from the reaction of the translators of the earlier editions into Russian) that the overview was not well balanced between different parts of the world. I am engaged in writing a history of materials science, as a separate venture, and this will incorporate proper attention to the history of physical metallurgy as a principal constituent. — It also proved necessary to leave out the chapter on superconducting alloys: the ceramic superconductor revolution has virtually removed this whole field from the purview of physical metallurgy. — Three entirely new topics are treated in this edition: one is oxidation, hot (dry) corrosion and protection of metallic materials, another is the dislocation theory of the mechanical behavior of intermetallic compounds. The third new topic is a leap into very unfamiliar territory: it is entitled "A Metallurgist's Guide to Polymers". Many metallurgists — including Alan Windle, the author of this chapter — have converted in the course of their careers to the study of the more physical aspects of polymers (regarded by many materials scientists as *the* "materials of the future"), and have had to come to terms with novel concepts (such as "semicrystallinity") which they had not encountered in metals: Windle's chapter is devoted to analysing in some depth the conceptual differences between metallurgy and polymer science, for instance, the quite different principles which govern alloy formation in the two classes of materials. I believe that this is the first treatment of this kind.

Six of the existing chapters (now numbered 1, 4, 21, 22, 27, 30) have been entrusted to new authors, while another five chapters have been revised by the previous authors with the collaboration of additional authors (8, 13, 16, 17, 19). Chapter 19, originally entitled "Alloys rapidly quenched from the melt" has been broadened and retitled "Metastable states of alloys". A treatment of quasicrystals has been introduced in the form of an appendix to chapter 4, which is devoted to the solid-state chemistry of intermetallic compounds; this seemed appropriate since quasicrystallinity is generally found in such compounds. — Only three chapters still have the same authors they had in the first edition, written some 32 years ago.

27 of the 29 new versions of existing chapters have been substantially revised, and many have been entirely recast. Two chapters (11 and 25) have been reprinted as they were in the third edition, except for corrected cross-references to other chapters, but revision has been incorporated in the form of an Addendum to each of these chapters; this procedure was necessary on grounds of timing.

This edition has been written by a total of 44 authors, working in nine countries. It is a truly international effort.

I have prepared the subject index and am thus responsible for any inadequacies that may be found in it. I have also inserted some cross-references between chapters (internal cross-references within chapters are the responsibility of the various authors), but the function of such cross-references is better achieved by liberal use of the subject index.

As always, the editors have been well served by the exceedingly competent staff of North-Holland Physics Publishing (which is now an imprint of Elsevier Science B.V. in

Amsterdam; at the time of the first two editions, North-Holland was still an independent company). My particular thanks go to Nanning van der Hoop and Michiel Bom on the administrative side, to Ruud de Boer who is responsible for production and to Chris Ryan and Maurine Alma who are charged with marketing. Mr. de Boer's care and devotion in getting the proofs just right have been extremely impressive. My special thanks also go to Professor Colin Humphreys, head of the department of materials science and metallurgy in Cambridge University, whose warm welcome and support for me in my retirement made the creation of this edition feasible. Finally, my thanks go to all the authors, who put up with good grace with the numerous forceful, sometimes impatient, messages which I was obliged to send in order to "get the show on the road", and produced such outstanding chapters under pressure of time.

I am grateful to Dr. W.J. Boettinger, one of the authors, and his colleague Dr. James A. Warren, for kindly providing the computer-generated dendrite microstructure that features on the dust-cover.

The third edition was dedicated to the memory of Robert Franklin Mehl, the author of the historical chapter and a famed innovator in the early days of physical metallurgy in America. I would like to dedicate this fourth edition to the memory of two people: my late father-in-law, *Daniel Hanson* (1892–1953), professor of metallurgy at Birmingham University for many years, who did more than any other academic in Britain to foster the development and teaching of modern physical metallurgy; and the physical metallurgist and scientific publisher — and effective founder of Pergamon Press — *Paul Rosbaud* (1896–1963), who was retained by the then proprietor of the North-Holland Publishing Company as an adviser and in 1960, in the presence of the proprietor, eloquently urged upon me the need for a new, advanced, multiauthor text on physical metallurgy.

November 1995
Cambridge

Robert W. CAHN

PREFACE TO THE THIRD EDITION

The first edition of this book was published in 1965 and the second in 1970. The book continued to sell well during the 1970s and, once it was out of print, pressure developed for a new edition to be prepared. The subject had grown greatly during the 1970s and R. W. C. hesitated to undertake the task alone. He is immensely grateful to P. H. for converting into a pleasure what would otherwise have been an intolerable burden!

The second edition contained twenty-two chapters. In the present edition, eight of these twenty-two have been thoroughly revised by the same authors as before, while the others have been entrusted to new contributors, some being divided into pairs of chapters. In addition, seven chapters have been commissioned on new themes. The difficult decision was taken to leave out the chapter on superpure metals and to replace it by one focused on solute segregation to interfaces and surfaces — a topic which has made major strides during the past decade and which is of great practical significance. A name index has also been added.

Research in physical metallurgy has become worldwide and this is reflected in the fact that the contributors to this edition live in no fewer than seven countries. We are proud to have been able to edit a truly international text, both of us having worked in several countries ourselves. We would like here to express our thanks to all our contributors for their hard and effective work, their promptness and their angelic patience with editorial pressures!

The length of the book has inevitably increased, by 50% over the second edition, which was itself 20% longer than the first edition. Even to contain the increase within these numbers has entailed draconian limitations and difficult choices; these were unavoidable if the book was not to be priced out of its market. Everything possible has been done by the editors and the publisher to keep the price to a minimum (to enable readers to take the advice of G. CHR. LICHTENBERG [1775]: "He who has two pairs of trousers should pawn one and buy this book".).

Two kinds of chapters have been allowed priority in allocating space: those covering very active fields and those concerned with the most basic topics such as phase transformations, including solidification (a central theme of physical metallurgy), defects and diffusion. Also, this time we have devoted more space to experimental methods and their underlying principles, microscopy in particular. Since there is a plethora of texts available on the standard aspects of X-ray diffraction, the chapter on X-ray and neutron scattering has been

designed to emphasize less familiar aspects. Because of space limitations, we regretfully decided that we could not include a chapter on corrosion.

This revised and enlarged edition can properly be regarded as to all intents and purposes a new book.

Sometimes it was difficult to draw a sharp dividing line between physical metallurgy and process metallurgy, but we have done our best to observe the distinction and to restrict the book to its intended theme. Again, reference is inevitably made occasionally to nonmetallics, especially when they serve as model materials for metallic systems.

As before, the book is designed primarily for graduate students beginning research or undertaking advanced courses, and as a basis for more experienced research workers who require an overview of fields comparatively new to them, or with which they wish to renew contact after a gap of some years.

We should like to thank Ir. J. Soutberg and Drs. A. P. de Ruiter of the North-Holland Publishing Company for their major editorial and administrative contributions to the production of this edition, and in particular we acknowledge the good-humoured resolve of Drs. W. H. Wimmers, former managing director of the Company, to bring this third edition to fruition. We are grateful to Dr. Bormann for preparing the subject index. We thank the hundreds of research workers who kindly gave permission for reproduction of their published illustrations: all are acknowledged in the figure captions.

Of the authors who contributed to the first edition, one is no longer alive: Robert Franklin Mehl, who wrote the introductory historical chapter. What he wrote has been left untouched in the present edition, but one of us has written a short supplement to bring the treatment up to date, and has updated the bibliography. Robert Mehl was one of the founders of the modern science of physical metallurgy, both through his direct scientific contributions and through his leadership and encouragement of many eminent metallurgists who at one time worked with him. We dedicate this third edition to his memory.

April 1983

Robert W. CAHN, Paris
Peter HAASEN, Göttingen

PREFACE TO THE FIRST AND SECOND EDITIONS

This book sets forth in detail the present state of physical metallurgy, which is the root from which the modern saience of materials has principally sprung. That science has burgeoned to such a degree that no one author can do justice to it at an advanced level; accordingly, a number of well-known specialists have consented to write on the various principal branches, and the editor has been responsible for preserving a basic unity among the expert contributions. This book is the first general text, as distinct from research symposium, which has been conceived in this manner. While principally directed at senior undergraduates at universities and colleges of technology, the book is therefore also appropriate for postgraduates and particularly as a base for experienced research workers entering fields of physical metallurgy new to them.

Certain topics have been left to one side or treated at modest length, so as to limit the size of the book, but special stress has been placed on others which have rarely been accorded much space. For instance, a good deal of space is devoted to the history of physical metallurgy, and to point defects, structure and mechanical properties of solid solutions, theory of phase transformations, recrystallization, superpure metals, ferromagnetic properties, and mechanical properties of two-phase alloys. These are all active fields of research. Experimental techniques, in particular diffraction methods, have been omitted for lack of space; these have been ably surveyed in a number of recent texts. An exception has however been made in favour of metallographic techniques since, electron microscopy apart, recent innovations have not been sufficiently treated in texts.

Each chapter is provided with a select list of books and reviews which will enable readers to delve further into a particular subject. Internal cross-references and the general index will help to tie the various contributions together.

I should like here to acknowledge the sustained helpfulness and courtesy of the publisher's staff, and in particular of Mr. A. T. G. van der Leij, and also the help provided by Professor P. Haasen and Dr. T. B. Massalski in harmonising several contributions.

Brighton, June 1965 (and again 1970) R. W. CAHN

CONTENTS

VOLUME I

VOLUME II

VOLUME III

CHAPTER 1

CRYSTAL STRUCTURE OF THE METALLIC ELEMENTS

W. STEURER

Institute of Crystallography
ETH-Zentrum
CH-8092 Zürich, Switzerland

R. W. Cahn and P. Haasen†, eds.
Physical Metallurgy; fourth, revised and enhanced edition

1. Introduction

In the very beginning of materials "science", when men began to produce artificial materials, it was the time of trial and error, of pure empiricism. Today, we are a little closer to the realization of the old dream of designing any material with given properties owing to our improved understanding of the relationships between chemical composition, crystal structure and material properties. Though only a very few commercially and technologically important materials consist of metallic elements in their pure form (Si, Ge, Cu, Au, Ag, Pd, etc.), their crystal structures are of more than academic interest. Thus, to give an example, the crystal structure of a pure metal remains unchanged in the case of a solid solution, when one or several other components are added to tune the properties of a material. This technique has been used since time immemorial by alloying gold with copper or silver, for instance, to make jewelry or coins more resistant to wear. Especially the close packed structures and their derivatives, which are typical for pure metals, are also characteristic for numerous materials consisting of multi-component solid solutions or intermetallic alloys. Another reason for the study of "simple" element structures is that they are extremely helpful for the development and improvement of methods to understand why a given phase is adopting a particular crystal structure under certain conditions (temperature, pressure, etc.). The aim is, of course, to learn to predict the crystal structure of any given chemical compound under any ambient conditions and to model its possible phase transformations.

It is remarkable that even pure elements can have rather complicated crystal structures resulting from complex electronic interactions. Most elements are polymorphous, i.e., they occur in up to ten different crystal structures as a function of ambient conditions (temperature, pressure). The understanding of the phase transformations in these homo-atomic cases is also very helpful for understanding the more complicated phase transformations of complex intermetallic phases. Indeed, it is possible today to predict correctly most of the element structures and phase transformations by one-electron theory (SKRIVER [1985]).

2. Factors governing a crystal structure

Crystalline order, i.e., the three-dimensional (or in the case of quasicrystals or incommensurate phases, higher-dimensional) translationally periodic repetition of a particular atomic configuration, is the outstanding characteristic of condensed matter in thermodynamic equilibrium. Which crystal structure for a given chemical composition corresponds to the lowest Gibbs free energy, $G = H - TS$, depends on chemical bonding, electronic band structure and geometrical factors. Since it is not possible to solve the Schrödinger equation for a crystal and thus deduce the correct crystal structure, many approximations have been developed. Indeed, today there exist quite successful attempts to predict simpler crystal structures using one-electron approximations: the many-electron problem is reduced to a one-electron problem by the assumption that the electrons, surrounded by a mutual exclusion zone, are moving independently of each other in the

average field of all the others (local density functional theory).

Beside this rather complicated and lengthy approach to understand and predict crystal structures, there exist a number of rules based on two factors: the chemical bond factor, which also takes into account the directionality of chemical bonds, and the geometrical factor, which considers optimum space filling, symmetry and connectivity. Especially in the case of the typical metallic elements, these structural principles work very well for predicting structures. (For electron theory of structural stability, see ch. 2, § 6.1).

2.1. Chemical bond factor

The concept of chemical bonding was originally developed to understand the formation of molecules. In a crystal, a collective interaction of all atoms always exists which may approximately be considered as the sum of nearest-neighbor interactions. A further simplification comes in by the fact that only the electrons of the outer shells contribute to the chemical bonding. Traditionally, several limiting types of the chemical bond are defined: strong ionic (heteropolar), covalent (homopolar), metallic bonds, and weak van der Waals and hydrogen bonds. The strong bonds have in common that the outer atomic orbitals contribute to new collective electron states in the crystal, the electron bands. They differ mainly in the degree of localization of the valence electrons: when these are transferred from one atom to another atom, Coulomb attraction between the cation and the anion results and the bond is called *ionic*; when they remain localized between two atoms the so-called exchange interaction results from overlapping orbitals and *covalent* bonds are formed; when the valence electrons are delocalized over the whole crystal *metallic bonding* is obtained. Thus, contrary to the other bond types which also occur within molecules, the metallic bond can only exist in large arrays of atoms. Since the interaction of electron orbitals depends on their separation and mutual orientation, the bond type may change during phase transformations. Sometimes, a slight change in temperature can be sufficient, as in the transition from metallic white tin to non-metallic grey tin below 291K ("tin pest"); sometimes very high pressures are necessary, as for the transformation from molecular hydrogen to metallic hydrogen, for instance.

The type of bonding occurring in crystals of the metallic elements ranges from pure metallic in the alkali metals to increasingly covalent for zinc or cadmium, for instance. The structural implications of these two bond types, which are just two contrary limiting manifestations of electronic interactions with a continuously changing degree of electron localization, will be characterized in the following in greater detail.

2.1.1. The covalent bond

The covalent bond may be described in terms of the more qualitative VB (valence bond) theory by overlapping atomic orbitals occupied by unpaired valence electrons (fig. 1). Its strength depends on the degree of overlapping and is given by the exchange integral. In terms of the more quantitative LCAO–MO (linear combination of atomic orbitals – molecular orbitals) theory, molecular orbitals are constructed by linear combination of atomic orbitals (fig. 2). The resulting bonding, non-bonding and anti-

References: p. 45.

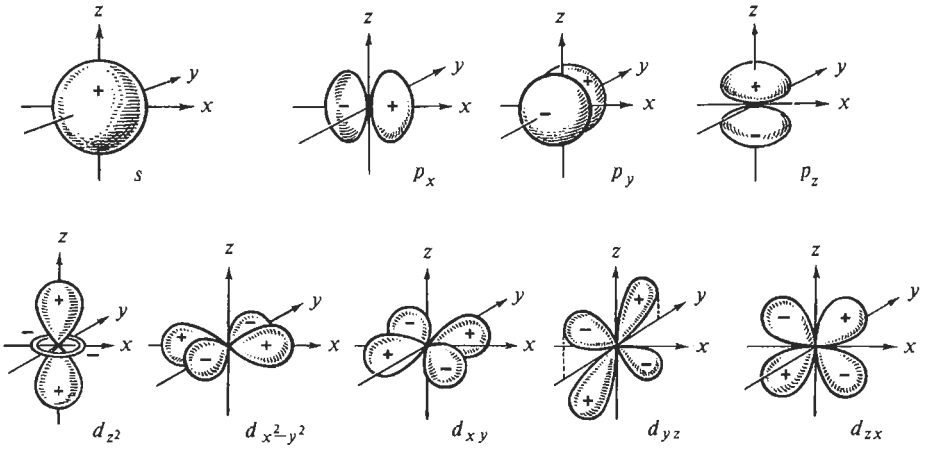

Fig. 1. Schematic structure of the atomic s-, p- and d-orbitals (from VAINSHTEIN *et al.* [1982]).

bonding molecular orbitals, filled up with valence electrons according to the Pauli exclusion principle, are localized between the bonding atoms with well defined geometry. Generally, covalent bonds can be characterized as strong, directional bonds. Increasing the number of atoms contributing to the bonds increases the number of molecular orbitals and their energy differences become smaller and smaller. Finally, the discrete energy levels of the molecular orbitals condense to quasicontinuous bands separated by energy gaps. Since in a covalent bond each atom reaches its particular stable noble gas configuration (filled shell) the energy bands are either completely filled or empty. Owing to the localization of the electrons, it needs much energy to lift them from the last filled valence band into the empty conduction band. The classic example of a crystal built from only covalently bonded atoms is diamond: all carbon atoms are bonded via tetrahedrally directed sp^3 hybrid orbitals (fig. 3). Thus the crystal structure of diamond results as a framework of tetrahedrally coordinated carbon atoms (fig. 4).

2.1.2. The metallic bond

The metallic bond can be described in a similar way as the covalent bond. The main difference between these two bond types is that the ionization energy for electrons occupying the outer orbitals of the metallic elements is much smaller. In typical metals, like the alkali metals, these outer orbitals are spherical *s*-orbitals allowing overlapping with up to 12 further *s*-orbitals of the surrounding atoms. Thus, the well-defined electron localization in bonds connecting pairs of atoms with each other loses its meaning. Quantum-mechanical calculations show that in large agglomerations of metal atoms the delocalized bonding electrons occupy lower energy levels than in the free atoms; this would not be true for isolated "metal molecules". The metallic bond in typical metals is non-directional, favoring structures corresponding to closest packings of spheres. With increasing localization of valence electrons, covalent interactions cause deviations from spherically symmetric bonding, leading to more complicated structures.

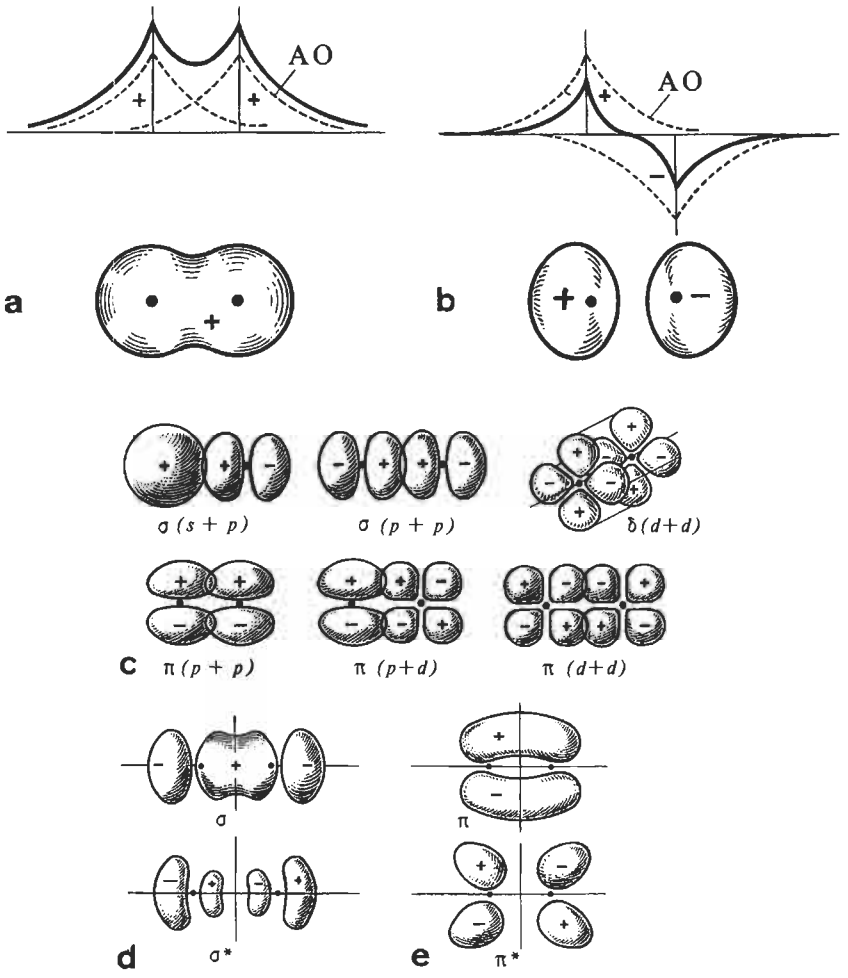

Fig. 2. (a) Bonding and (b) anti-bonding molecular orbitals of the H_2 molecule. (c) Schematic drawing of the building of the most important molecular orbitals from atomic orbitals and (d), (e) examples of molecular orbitals (bonding: σ, π and anti-bonding σ^*, π^*) (from VAINSHTEIN *et al.* [1982]).

2.2. Geometrical factors

A crystal structure type is fully defined by its general chemical composition, its space group symmetry, the equipoint (Wyckoff) positions occupied by the atoms and the coordinates of the atoms in the unit cell (fig. 5). The metrics, i.e., the dimension of the unit cell (lattice parameters), in general differ for all chemical compounds or phases occurring in one particular crystal structure type. Also, for general Wyckoff positions, the numerical values of the coordinates may vary in a range not destroying the characteris-

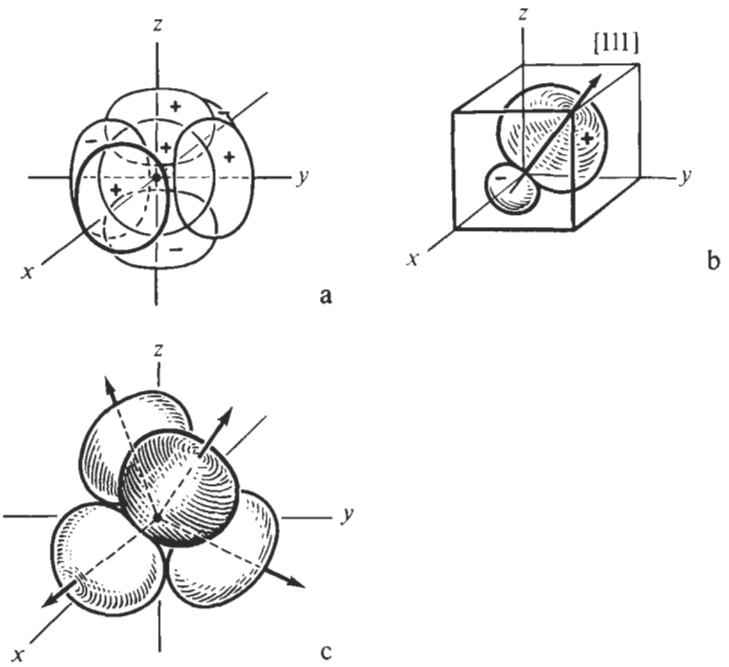

Fig. 3. Hybridization of (a) one s- and three p-orbitals to (b) sp^3–hybrid orbitals (c) which are directed along tetrahedron axes (from VAINSHTEIN *et al.* [1982]).

tics, i.e., coordination polyhedra and their linkings, of this crystal structure. With these data given it is easy to derive both the information about the global arrangement of structural units as well as the local environment of each atom (fig. 6). Besides this purely geometrical description of a structure, it is necessary to understand the characteristics of a crystal structure by identifying crystal-chemically meaningful structural units (coordination polyhedra) and their connecting principles (bonding).

For band-structure calculations, for instance, knowledge of the full crystal structure

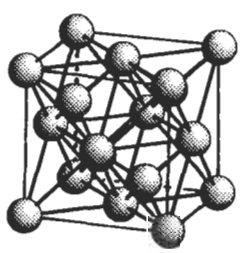

Fig. 4. The structure of diamond cF8–C, space group $Fd\bar{3}m$, No. 227, 8a: 0 0 0, ¾ ¼ ¾. All carbon atoms are tetrahedrally coordinated, they occupy the positions of a face-centered cubic lattice and one half of the centers of the eighth cubes.

is essential; for tensorial physical properties, however, the point symmetry group to which the space group belongs is the determining factor. Crystal-chemical properties are less sensitive to slight atomic shifts which may break the symmetry but do not change local environments of atoms. Thus the study of atomic coordinations may yield valuable tools in the analysis, description and comparison of crystal structures.

2.2.1. Coordination

A general technique to derive useful coordination polyhedra was suggested by BRUNNER and SCHWARZENBACH [1971]: all interatomic distances around a particular atom are calculated up to a certain limit, and all atoms within a distance defined by the first maximum gap in a histogram of distances belong to the coordination polyhedron (fig. 6). If there is no clear maximum gap observable, a second criterion may be the maximum-convex-volume rule: all coordinating atoms lying at the intersections of at least three faces should form a convex polyhedron (DAAMS *et al.* [1992]).

2.2.2. Space filling

Owing to the isotropic properties of the metallic bond the structure of typical metallic elements can often be described in terms of dense sphere packings. A sphere packing is an infinite set of non-interpenetrating spheres with the property that any pair of spheres is connected by a chain of spheres with mutual contact. A sphere packing is called homogenous if all spheres are symmetrically equivalent, otherwise it is called heterogenous (KOCH and FISCHER [1992]). In the last named case, the spheres of the different non-symmetrically equivalent subsets may have different radii and occupy the positions of different crystallographic orbits. The number of types of heterogenous sphere packings is infinite whereas it is finite for homogenous sphere packing types. There are, for instance, 199 different cubic and 394 different possible tetragonal homogenous sphere packings. The densities, i.e., the fractions of volumes occupied by the spheres, are with $q=0.7405$ highest for the well-known hexagonal closest packing (hcp) and cubic closest packing (ccp) (figs. 7 and 8, respectively). In both cases the coordination numbers (CN) are twelve and the distances to the nearest neighbors the same. The number k of contacts per sphere amounts to $3 \leq k \leq 12$. Table 1 gives some examples for sphere packings with the highest and lowest densities and contact numbers, and table 2 space filling values for a number of structure types. Very low packing densities, such as that for the cF8–C type, for instance, indicate that a hard sphere packing is no longer an adequate description of such a structure.

The crystal structures of the metallic elements adopt dense sphere packings as long as purely geometrical packing principles are dominant. Covalent bonding contributions and electronic effects give rise to more complicated structures.

2.2.3. Layer stackings, polytypism

Many crystal structures can be considered to consist of successive stackings of atomic layers. The above mentioned hexagonal closest packing (hcp) refers to a stacking of dense packed layers with periodic sequence ..AB.., the cubic closest packing (ccp) to a sequence ..ABC.. (figs. 7 and 8). The atomic layers are denoted by A, B or C depending

$Fd\bar{3}m$ O_h^7 $m\bar{3}m$ Cubic

No. 227 $F4_1/d\bar{3}2/m$ Patterson symmetry $Fm\bar{3}m$

ORIGIN CHOICE 1

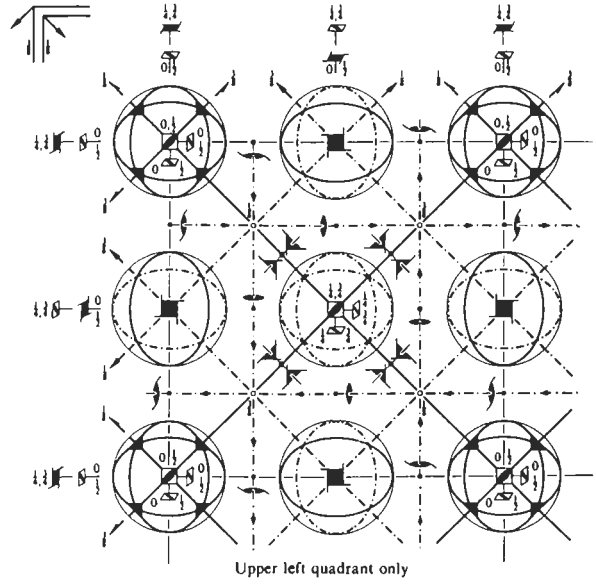

Upper left quadrant only

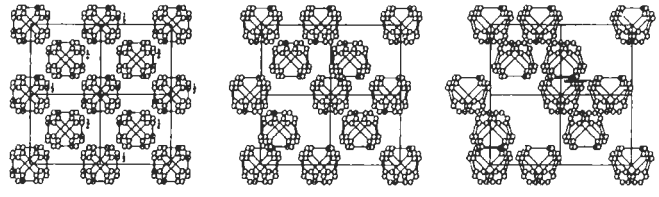

Origin at $\bar{4}3m$, at $-\frac{1}{4},-\frac{1}{4},-\frac{1}{4}$ from centre $(\bar{3}m)$

Asymmetric unit $0\le x\le\frac{1}{4}$; $0\le y\le\frac{1}{4}$; $-\frac{1}{4}\le z\le\frac{1}{4}$; $y\le\min(\frac{1}{4}-x,x)$; $-y\le z\le y$

Vertices 0,0,0 $\frac{1}{4}$,0,0 $\frac{1}{4},\frac{1}{4},\frac{1}{4}$ $\frac{1}{4},\frac{1}{4},\frac{1}{4}$ $\frac{1}{4},\frac{1}{4},-\frac{1}{4}$ $\frac{1}{4},\frac{1}{4},-\frac{1}{4}$

Symmetry operations

Fig. 5. Information given in the *International Tables for Crystallography* (HAHN [1992]) on the example of the space group Fd$\bar{3}$m of the diamond structure. Left side, top line: space group symbol in short Hermann–Mauguin and Schoenflies notation, point group (crystal class), crystal system. Second line: consecutive space group number, full space group symbol, Patterson symmetry, short space group symbol. Upper drawing: framework of symmetry elements in a unique part of one unit cell. Lower drawings: point complexes generated by the action of symmetry operations. Below: choice of origin, definition of the asymmetric unit. Right side: the Wyckoff letters a, b, c ... i denote the equipoint positions with multiplicities 8, 8, 16 ... 192. The positions of the carbon atoms in the diamond structure are given in Wyckoff position 8a.

No. 227 $Fd\bar{3}m$

Generators selected (1); $t(1,0,0)$; $t(0,1,0)$; $t(0,0,1)$; $t(0,\frac{1}{2},\frac{1}{2})$; $t(\frac{1}{2},0,\frac{1}{2})$; (2); (3); (5); (13); (25)

Positions

Multiplicity, Wyckoff letter, Site symmetry	Coordinates (0,0,0)+	$(0,\frac{1}{2},\frac{1}{2})+$	$(\frac{1}{2},0,\frac{1}{2})+$	$(\frac{1}{2},\frac{1}{2},0)+$	Reflection conditions
					h,k,l permutable
					General:
192 i 1	(1) x,y,z	(2) $\bar{x},\bar{y}+\frac{1}{2},z+\frac{1}{2}$	(3) $\bar{x}+\frac{1}{2},y+\frac{1}{2},\bar{z}$	(4) $x+\frac{1}{2},\bar{y},\bar{z}+\frac{1}{2}$	hkl : $h+k=2n$ and $h+l,k+l=2n$
	(5) z,x,y	(6) $z+\frac{1}{2},\bar{x},\bar{y}+\frac{1}{2}$	(7) $\bar{z},\bar{x}+\frac{1}{2},y+\frac{1}{2}$	(8) $\bar{z}+\frac{1}{2},x+\frac{1}{2},\bar{y}$	$0kl$: $k+l=4n$ and $k,l=2n$
	(9) y,z,x	(10) $\bar{y}+\frac{1}{2},z+\frac{1}{2},\bar{x}$	(11) $y+\frac{1}{2},\bar{z},\bar{x}+\frac{1}{2}$	(12) $\bar{y},\bar{z}+\frac{1}{2},x+\frac{1}{2}$	hhl : $h+l=2n$
	(13) $y+\frac{1}{2},x+\frac{1}{2},\bar{z}+\frac{1}{2}$	(14) $\bar{y}+\frac{1}{2},\bar{x}+\frac{1}{2},\bar{z}+\frac{1}{2}$	(15) $y+\frac{1}{2},\bar{x}+\frac{1}{2},z+\frac{1}{2}$	(16) $\bar{y}+\frac{1}{2},x+\frac{1}{2},z+\frac{1}{2}$	$h00$: $h=4n$
	(17) $x+\frac{1}{2},z+\frac{1}{2},\bar{y}+\frac{1}{2}$	(18) $\bar{x}+\frac{1}{2},z+\frac{1}{2},y+\frac{1}{2}$	(19) $\bar{x}+\frac{1}{2},\bar{z}+\frac{1}{2},\bar{y}+\frac{1}{2}$	(20) $x+\frac{1}{2},\bar{z}+\frac{1}{2},y+\frac{1}{2}$	
	(21) $z+\frac{1}{2},y+\frac{1}{2},\bar{x}+\frac{1}{2}$	(22) $z+\frac{1}{2},\bar{y}+\frac{1}{2},x+\frac{1}{2}$	(23) $\bar{z}+\frac{1}{2},y+\frac{1}{2},x+\frac{1}{2}$	(24) $\bar{z}+\frac{1}{2},\bar{y}+\frac{1}{2},\bar{x}+\frac{1}{2}$	
	(25) $\bar{x}+\frac{1}{2},\bar{y}+\frac{1}{2},\bar{z}+\frac{1}{2}$	(26) $x+\frac{1}{2},y+\frac{1}{2},\bar{z}+\frac{1}{2}$	(27) $x+\frac{1}{2},\bar{y}+\frac{1}{2},z+\frac{1}{2}$	(28) $\bar{x}+\frac{1}{2},y+\frac{1}{2},z+\frac{1}{2}$	
	(29) $\bar{z}+\frac{1}{2},\bar{x}+\frac{1}{2},\bar{y}+\frac{1}{2}$	(30) $\bar{z}+\frac{1}{2},x+\frac{1}{2},y+\frac{1}{2}$	(31) $z+\frac{1}{2},x+\frac{1}{2},\bar{y}+\frac{1}{2}$	(32) $z+\frac{1}{2},\bar{x}+\frac{1}{2},y+\frac{1}{2}$	
	(33) $\bar{y}+\frac{1}{2},\bar{z}+\frac{1}{2},\bar{x}+\frac{1}{2}$	(34) $y+\frac{1}{2},\bar{z}+\frac{1}{2},x+\frac{1}{2}$	(35) $\bar{y}+\frac{1}{2},z+\frac{1}{2},x+\frac{1}{2}$	(36) $y+\frac{1}{2},z+\frac{1}{2},\bar{x}+\frac{1}{2}$	
	(37) $\bar{y}+\frac{1}{2},\bar{x},z+\frac{1}{2}$	(38) y,x,z	(39) $\bar{y},x+\frac{1}{2},\bar{z}+\frac{1}{2}$	(40) $y+\frac{1}{2},\bar{x}+\frac{1}{2},\bar{z}$	
	(41) $\bar{x}+\frac{1}{2},\bar{z},y+\frac{1}{2}$	(42) $x+\frac{1}{2},\bar{z}+\frac{1}{2},\bar{y}$	(43) x,z,y	(44) $\bar{x},z+\frac{1}{2},\bar{y}+\frac{1}{2}$	
	(45) $\bar{z}+\frac{1}{2},\bar{y},x+\frac{1}{2}$	(46) $\bar{z},y+\frac{1}{2},\bar{x}+\frac{1}{2}$	(47) $z+\frac{1}{2},\bar{y}+\frac{1}{2},\bar{x}$	(48) z,y,x	
					Special: as above, plus
96 h ..2	$\frac{1}{8},y,\bar{y}+\frac{1}{4}$	$\frac{1}{8},\bar{y}+\frac{1}{4},\bar{y}+\frac{1}{4}$	$\frac{1}{8},y+\frac{1}{4},y+\frac{1}{4}$	$\frac{1}{8},\bar{y},y+\frac{1}{4}$	no extra conditions
	$\bar{y}+\frac{1}{4},\frac{1}{8},y$	$\bar{y}+\frac{1}{4},\frac{1}{8},\bar{y}+\frac{1}{4}$	$y+\frac{1}{4},\frac{1}{8},y+\frac{1}{4}$	$y+\frac{1}{4},\frac{1}{8},\bar{y}$	
	$y,\bar{y}+\frac{1}{4},\frac{1}{8}$	$\bar{y}+\frac{1}{4},\bar{y}+\frac{1}{4},\frac{1}{8}$	$y+\frac{1}{4},y+\frac{1}{4},\frac{1}{8}$	$\bar{y},y+\frac{1}{4},\frac{1}{8}$	
	$\frac{1}{8},\bar{y}+\frac{1}{4},y$	$\frac{1}{8},y+\frac{1}{4},y+\frac{1}{4}$	$\frac{1}{8},\bar{y}+\frac{1}{4},\bar{y}+\frac{1}{4}$	$\frac{1}{8},y+\frac{1}{4},\bar{y}$	
	$y,\frac{1}{8},\bar{y}+\frac{1}{4}$	$y+\frac{1}{4},\frac{1}{8},y+\frac{1}{4}$	$\bar{y}+\frac{1}{4},\frac{1}{8},\bar{y}+\frac{1}{4}$	$\bar{y},\frac{1}{8},y+\frac{1}{4}$	
	$\bar{y}+\frac{1}{4},y,\frac{1}{8}$	$y+\frac{1}{4},y+\frac{1}{4},\frac{1}{8}$	$\bar{y}+\frac{1}{4},\bar{y}+\frac{1}{4},\frac{1}{8}$	$y+\frac{1}{4},\bar{y},\frac{1}{8}$	
96 g ..m	x,x,z	$\bar{x},\bar{x}+\frac{1}{2},z+\frac{1}{2}$	$\bar{x}+\frac{1}{2},x+\frac{1}{2},\bar{z}$	$x+\frac{1}{2},\bar{x},\bar{z}+\frac{1}{2}$	no extra conditions
	z,x,x	$z+\frac{1}{2},\bar{x},\bar{x}+\frac{1}{2}$	$\bar{z},\bar{x}+\frac{1}{2},x+\frac{1}{2}$	$\bar{z}+\frac{1}{2},x+\frac{1}{2},\bar{x}$	
	x,z,x	$\bar{x}+\frac{1}{2},z+\frac{1}{2},\bar{x}$	$x+\frac{1}{2},\bar{z},\bar{x}+\frac{1}{2}$	$\bar{x},\bar{z}+\frac{1}{2},x+\frac{1}{2}$	
	$x+\frac{1}{2},x+\frac{1}{2},\bar{z}+\frac{1}{2}$	$\bar{x}+\frac{1}{2},\bar{x}+\frac{1}{2},\bar{z}+\frac{1}{2}$	$x+\frac{1}{2},\bar{x}+\frac{1}{2},z+\frac{1}{2}$	$\bar{x}+\frac{1}{2},x+\frac{1}{2},z+\frac{1}{2}$	
	$x+\frac{1}{2},z+\frac{1}{2},\bar{x}+\frac{1}{2}$	$\bar{x}+\frac{1}{2},z+\frac{1}{2},x+\frac{1}{2}$	$\bar{x}+\frac{1}{2},\bar{z}+\frac{1}{2},\bar{x}+\frac{1}{2}$	$x+\frac{1}{2},\bar{z}+\frac{1}{2},x+\frac{1}{2}$	
	$z+\frac{1}{2},x+\frac{1}{2},\bar{x}+\frac{1}{2}$	$z+\frac{1}{2},\bar{x}+\frac{1}{2},x+\frac{1}{2}$	$\bar{z}+\frac{1}{2},x+\frac{1}{2},x+\frac{1}{2}$	$\bar{z}+\frac{1}{2},\bar{x}+\frac{1}{2},\bar{x}+\frac{1}{2}$	
48 f 2.mm	$x,0,0$ $\frac{1}{4},x+\frac{1}{4},\frac{1}{4}$	$\bar{x},\frac{1}{4},\frac{1}{4}$ $\frac{1}{4},\bar{x}+\frac{1}{4},\frac{1}{4}$	$0,x,0$ $x+\frac{1}{4},\frac{1}{4},\frac{1}{4}$	$\frac{1}{4},\bar{x},\frac{1}{4}$ $\bar{x}+\frac{1}{4},\frac{1}{4},\frac{1}{4}$	$0,0,x$ $\frac{1}{4},\frac{1}{4},\bar{x}+\frac{1}{4}$	$\frac{1}{4},\frac{1}{4},\bar{x}$ $\frac{1}{4},\frac{1}{4},x+\frac{1}{4}$	hkl : $h=2n+1$ or $h+k+l=4n$
32 e .3m	x,x,x	$\bar{x},\bar{x}+\frac{1}{2},x+\frac{1}{2}$			no extra conditions
	$\bar{x}+\frac{1}{2},x+\frac{1}{2},\bar{x}$	$x+\frac{1}{2},\bar{x},\bar{x}+\frac{1}{2}$			
	$x+\frac{1}{2},x+\frac{1}{2},\bar{x}+\frac{1}{2}$	$\bar{x}+\frac{1}{2},\bar{x}+\frac{1}{2},\bar{x}+\frac{1}{2}$			
	$x+\frac{1}{2},\bar{x}+\frac{1}{2},x+\frac{1}{2}$	$\bar{x}+\frac{1}{2},x+\frac{1}{2},x+\frac{1}{2}$			
16 d .$\bar{3}m$	$\frac{1}{8},\frac{1}{8},\frac{1}{8}$ $\frac{1}{8},\frac{1}{8},\frac{1}{8}$	$\frac{1}{8},\frac{1}{8},\frac{1}{8}$ $\frac{1}{8},\frac{1}{8},\frac{1}{8}$			hkl : $h=2n+1$ or $h,k,l=4n+2$ or $h,k,l=4n$
16 c .$\bar{3}m$	$\frac{1}{8},\frac{1}{8},\frac{1}{8}$ $\frac{1}{8},\frac{1}{8},\frac{1}{8}$	$\frac{1}{8},\frac{1}{8},\frac{1}{8}$ $\frac{1}{8},\frac{1}{8},\frac{1}{8}$			
8 b $\bar{4}3m$	$\frac{1}{2},\frac{1}{2},\frac{1}{2}$ $\frac{1}{2},\frac{1}{2},\frac{1}{2}$				hkl : $h=2n+1$ or $h+k+l=4n$
8 a $\bar{4}3m$	$0,0,0$ $\frac{1}{2},\frac{1}{2},\frac{1}{2}$				

Symmetry of special projections

Along [001] $p4mm$
$a'=\frac{1}{2}(a-b)$ $b'=\frac{1}{2}(a+b)$
Origin at $0,0,z$

Along [111] $p6mm$
$a'=\frac{1}{2}(2a-b-c)$ $b'=\frac{1}{2}(-a+2b-c)$
Origin at x,x,x

Along [110] $c2mm$
$a'=\frac{1}{2}(-a+b)$ $b'=c$
Origin at $x,x,\frac{1}{4}$

References: p. 45.

Table 1
Examples of homogeneous sphere packings with distance d between neighboring spheres, highest and lowest contact numbers, k, and fractional packing densities, q.

k	Space Group Wyckoff position	Parameters	Distance d	Density q
12	$P6_3/mmc$ 2c $\frac{1}{3}\,\frac{2}{3}\,\frac{1}{4}$	$c/a = \frac{2}{3}\sqrt{6} = 1.633$	a	0.7405
12	$Fm\bar{3}m$ 4a 0 0 0		$\frac{1}{2}\sqrt{2}$ a	0.7405
11	C2/m 4i x 0 z	$x = \frac{1}{2}(\sqrt{2}-1)$ $z = 3\sqrt{2} - 4\ b/a = \frac{1}{3}\sqrt{3}$ $c/a = \frac{1}{6}\sqrt{6} + \frac{1}{3}\sqrt{3} = 0.986$ $\cos\beta = \frac{1}{6}\sqrt{6} - \frac{1}{3}\sqrt{3}$	b	0.7187
10	I4/mmm 2a 0 0 0	$c/a = \frac{1}{3}\sqrt{6} = 0.8165$	c	0.6981
3	$I4_132$ 24h $\frac{1}{8}$ y $\frac{1}{4}$-y	$y = \frac{1}{4}\sqrt{3} - \frac{3}{8}$	$(\frac{1}{2}\sqrt{6} - \frac{3}{4}\sqrt{2})$a	0.0555

on their relative position against each other. The packing fractions as well as the coordination numbers (CN = 12) are equal in both cases. The first shell atomic environment corresponds to a cuboctahedron for ccp and to a disheptahedron for hcp. The distribution of atomic distances becomes different not until the third and higher coordination shells (fig. 9).

These two types of layer stackings are not the only possible ones, there exist infinitely many with exactly the same coordination numbers and packing fractions. They are called *polytypes*. Examples for such layer structures occurring for metallic elements are cobalt (..ABABAB**ABC**BCBCBC..), with one ccp sequence **ABC** statistically occurring among about ten hcp sequences, ordered hP4–La (..ACAB..) or hR3–Sm (..ABABCBCAC..) (fig. 10).

2.2.4. Polymorphism

Most of the elements adopt several different (allotropic) crystal structures at different pressures, temperatures or external fields. The transitions from one modification to the other are called polymorphous transformations or phase transitions.

A phase transition is connected with a change in structural parameters and/or in the ordering of electron spins. There are two basically different types of phase transitions: first-order transitions which are correlated with a jumpwise change in the first-order

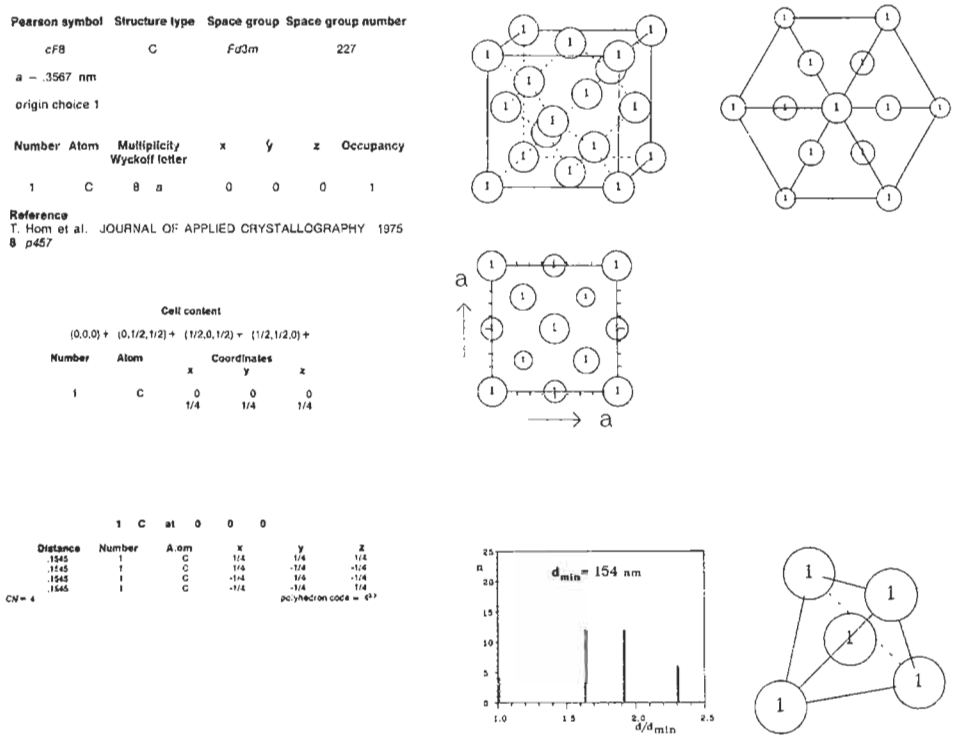

Fig. 6. Information given in the *Atlas of Crystal Structure Types for Intermetallic Phases* (DAAMS *et al.* [1991]) on the example of the diamond structure type. Beside numerical information and an atomic distances histogram, drawings of the crystal structure and characteristic coordination polyhedra in different projections are also shown.

derivatives of the Gibbs free energy G = H − TS (i.e., volume, entropy, ...), and second-order transitions which show a jump in the second derivatives of the Gibbs free energy (with respect to heat capacity, compressibility, etc.). In both types of phase transitions the crystal structure changes discontinuously at the transition point: in a first-order transition, in general no symmetry relationship exists between the two modifications; in a second-order transition, a group/subgroup relationship can always be found for the symmetry groups of the two polymorphous crystals structures.

With regard to structural changes resulting from a phase transformation of any order it is useful to distinguish between several different types: reconstructive phase transitions with essential changes in coordination numbers, atomic positions (α-Fe and γ-Fe, for instance, with coordination numbers CN = 8 and CN = 12, respectively, fig. 11) and sometimes also in chemical bonding (grey α-Sn and white β-Sn, for instance, with minimum distances changing from $d_{min}^{\alpha\text{-Sn}} = 1.54$ Å to $d_{min}^{\beta\text{-Sn}} = 3.02$ Å). These transformations are always of first order. Displacive phase transitions with small atomic shifts not changing the first coordination shells may change the lattice by small atomic displacements (martensitic diffusionless lattice rearrangement). Order/disorder transitions are related to the long-range ordered or disordered arrangement of structure elements (copper–gold system, for instance).

References: p. 45.

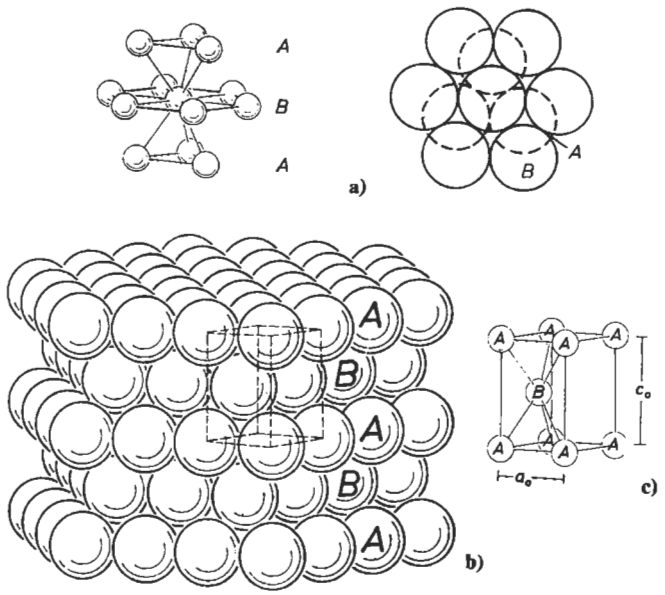

Fig. 7. Characteristics of the hexagonal closest-sphere packing. (a) The coordination polyhedron (disheptahedron) in perspective view and projected to show the packing principle, (b) the crystal structure and (c) one unit cell with atoms marked according to their belonging to layer A or B, are depicted (from BORCHARDT-OTT [1993]).

Table 2
Fractional packing densities q of elemental structures (PEARSON [1972]).

Element	Structure Type, *c/a*	Space filling value q	Element	Structure Type, *c/a*	Space filling value q
Cu	cF4	0.740	Po	cP1	0.523
Mg	hP2, 1.63	0.740	Bi	hR2, 2.60	0.446
Zn	hP2, 1.86	0.650	Sb	hR2, 2.62	0.410
Pa	tI2	0.696	As	hR2, 2.80	0.385
In	tI2	0.686	Ga	oC8	0.391
W	cI2	0.680	Te	hP3	0.364
Hg	hR1	0.609	C (diamond)	cF8	0.340
Sn	tI4	0.535	P (black)	oC8	0.285
α-U	oC4	0.534			

3. *Crystal structure of metallic elements*

In the following, the crystal structures of all metallic and semi-metallic elements (table 3) will be discussed. If it is not indicated specifically, the crystal structure data

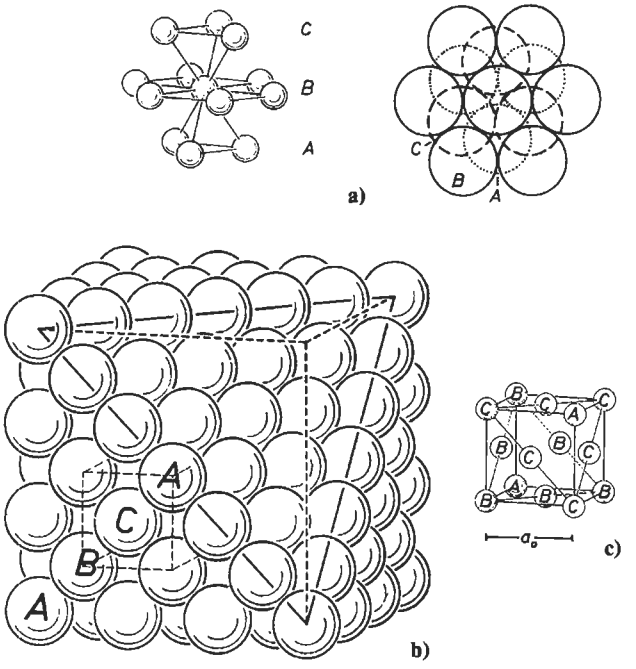

Fig. 8. Characteristics of the cubic closest-sphere packing. (a) The coordination polyhedron (cuboctahedron) in perspective view and projected to show the packing principle, (b) the crystal structure and (c) one unit cell with atoms marked according to their belonging to layer A, B or C, are depicted (from BORCHARDT–OTT [1993]).

have been taken from VILLARS and CALVERT [1991], YOUNG [1991] or MASSALSKI [1990]. In the (not so rare) cases of contradictory data, the most recent and reliable (?) ones have been used or the Pearson symbol has been replaced by a question mark. Particularly the structural information given for the high-pressure phases, which in most cases are derived from very small data sets, may be revised in future once better diffraction data become available.

3.1. Nomenclature

For the short-hand characterization of crystal structures, the Pearson notation in combination with the prototype formula defining the structure type is used throughout the paper. In accordance with the IUPAC recommendations (LEIGH [1990]) the old *Strukturbericht* designation (A3 for hP2–Mg, for instance) should not be used any longer. A comparison of the Pearson notation, prototype formula, space group and Strukturbericht designation for a large number of crystal structure types is given in MASSALSKI [1990].

The Pearson symbol consists of two letters and a number. The first (lower case letter) denotes the crystal family, the second (upper case) letter the Bravais lattice type (table 4). The symbol is completed by the number of atoms in the unit cell. The symbol cF4, for instance, classifies a structure type to be cubic (c), all-face centered (F), with 4 atoms per unit cell. In

Table 3
Periodic table of the elements. In accordance with the recommendations of the IUPAC 1988, the columns are numbered consecutively from 1 to 18. The elements whose structures are discussed in this chapter are shadowed.

1	2	3	4	5	6	7	8	9	10	11	12	13	14	15	16	17	18
1 H																	2 He
3 Li	4 Be											5 B	6 C	7 N	8 O	9 F	10 Ne
11 Na	12 Mg											13 Al	14 Si	15 P	16 S	17 Cl	18 Ar
19 K	20 Ca	21 Sc	22 Ti	23 V	24 Cr	25 Mn	26 Fe	27 Co	28 Ni	29 Cu	30 Zn	31 Ga	32 Ge	33 As	34 Se	35 Br	36 Kr
37 Rb	38 Sr	39 Y	40 Zr	41 Nb	42 Mo	43 Tc	44 Ru	45 Rh	46 Pd	47 Ag	48 Cd	49 In	50 Sn	51 Sb	52 Te	53 I	54 Xe
55 Cs	56 Ba	57* La	72 Hf	73 Ta	74 W	75 Re	76 Os	77 Ir	78 Pt	79 Au	80 Hg	81 Tl	82 Pb	83 Bi	84 Po	85 At	86 Rn
87 Fr	88 Ra	89+ Ac															

* Lanthanide metals	58 Ce	59 Pr	60 Nd	61 Pm	62 Sm	63 Eu	64 Gd	65 Tb	66 Dy	67 Ho	68 Er	69 Tm	70 Yb	71 Lu
+Actinide metals	90 Th	91 Pa	92 U	93 Np	94 Pu	95 Am	96 Cm	97 Bk	98 Cf	99 Es	100 Fm	101 Md	102 No	103 Lr

the case of rhombohedral structures, like the hR3–Sm type, the number of atoms in the unit cell in the rhombohedral setting ($a=b=c$, $\alpha=\beta=\gamma\neq 90°$) is given. The number of atoms in the corresponding hexagonal setting ($a=b\neq c$, $\alpha=\beta=90°$, $\gamma=120°$) would be three times as much.

Table 4
Meaning of the letters included in the Pearson Symbol.

Crystal family		Bravais lattice type	
a	triclinic (anorthic)	P	primitive
m	monoclinic	I	body centered
o	orthorhombic	F	all-face centered
t	tetragonal	C	side- or base-face centered
h	hexagonal, trigonal (rhombohedral)	R	rhombohedral
c	cubic		

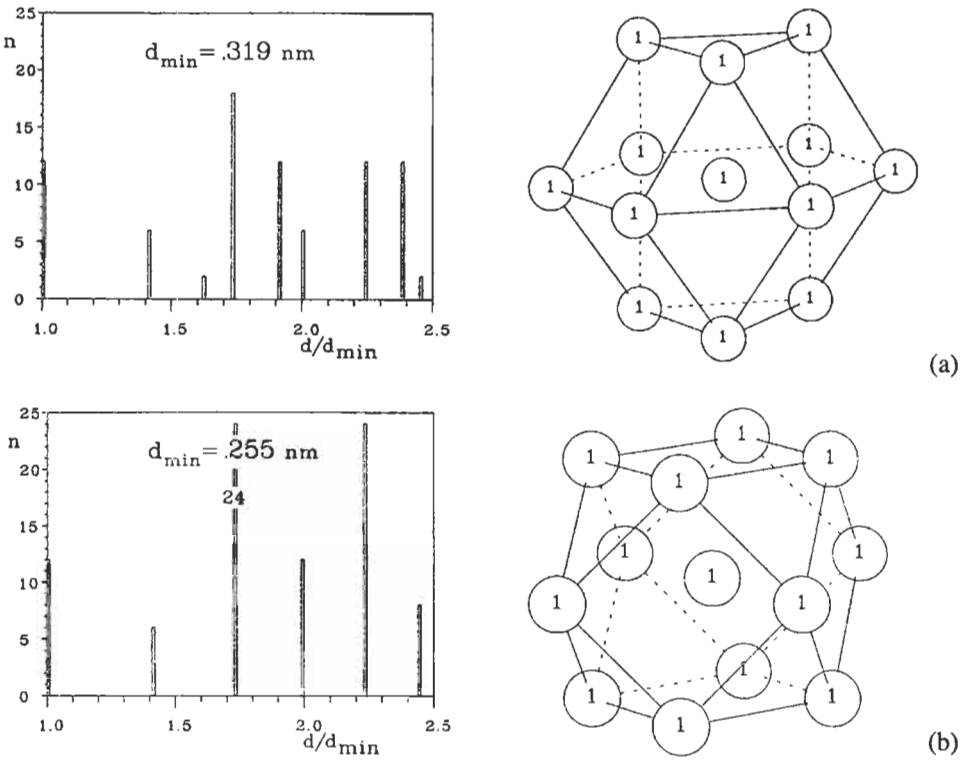

Fig. 9. Histograms of distances and coordination polyhedra of (a) hexagonal and (b) cubic closest packing (from DAAMS *et al.* [1991]).

3.2. Group 1 and 2, alkali and alkaline earth metals

The alkali and alkaline earth metals (table 5) belong to the typical metals. The outer electrons occupy the ns-orbitals, ionization removes the electrons of a whole shell, thus drastically reducing the atomic radius (Li: atomic radius 1.56 Å, ionic radius 0.60 Å, for instance). The absence of directional bonds forces close atomic (sphere) packings; the alkali metals conform most closely to the free electron gas model of metals. Under ambient conditions the alkali metals all crystallize in the simple body-centered cubic (bcc) structure cI2–W (fig. 12). The bcc structure is assumed to be more stable at higher temperature than the ccp or hcp one owing to its higher vibrational entropy. At lower temperature or higher pressure, the bcc structure is transformed martensitically to the closest-packed lattice types, hR3–Sm or cF4–Cu, respectively. Contrary to earlier studies, the hexagonal closest-packed phases are not of the hP2–Mg but of the hR3–Sm type (fig. 10) with stacking sequence ...ABABCBCAC.. (YOUNG [1991]).

The extremely strong dependence of the atomic volume on pressure, which increases with increasing atomic number due to the shielding of the outer electrons by the

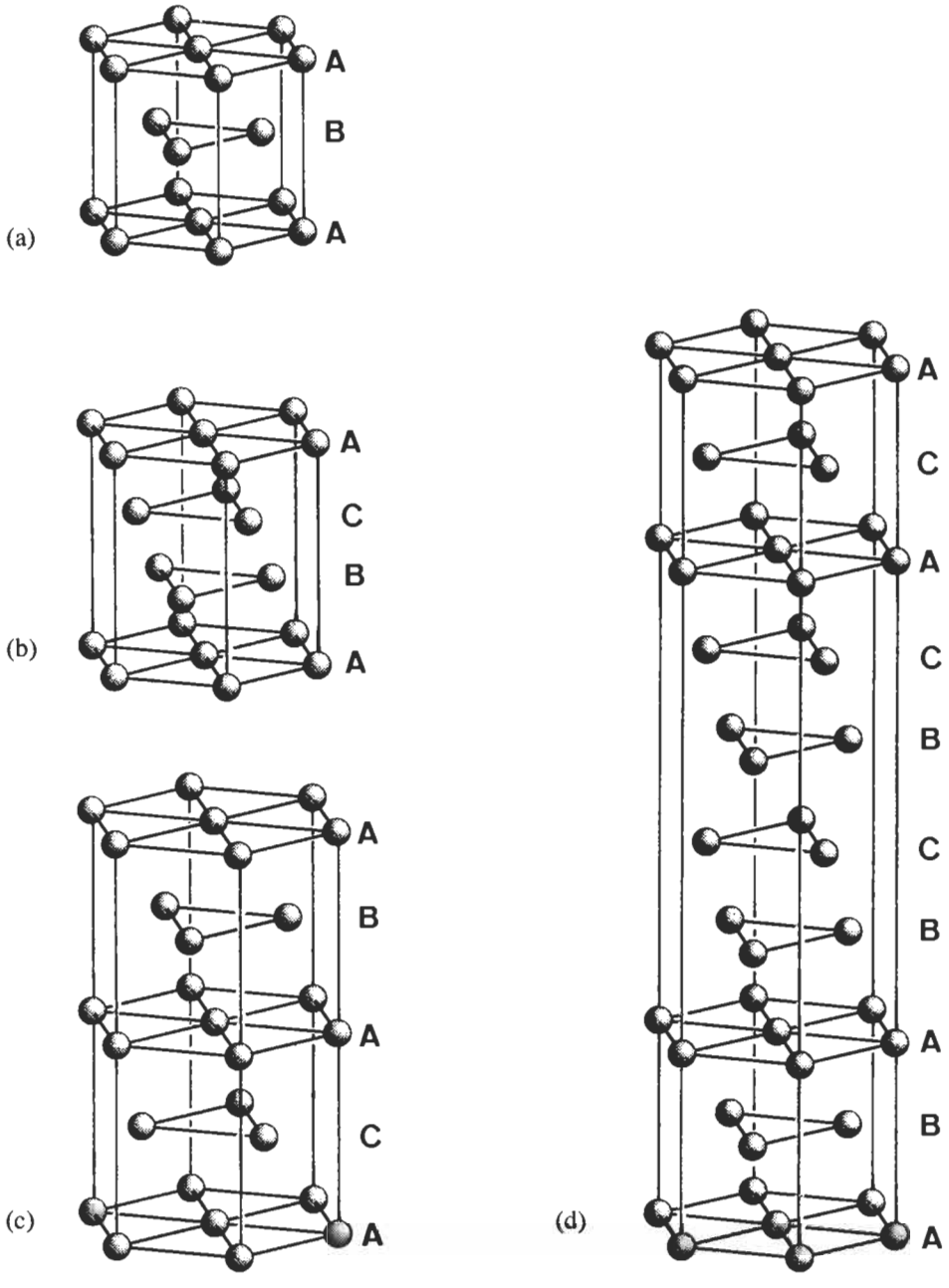

Fig. 10. Schematical representation of the stacking sequences of the closest-packed structures (a) hP2–Mg, (b) cF4–Cu, (c) hP4–La and (d) hR3–Sm.

Table 5

Structure information for the elements of group 1, alkali metals, and of group 2, alkaline earth metals. In the first line of each box the chemical symbol, atomic number Z, and the atomic volume V_{at} under ambient conditions is listed. In the second line the electronic ground state configuration is given. For each phase there is tabulated: limiting temperature T[K] and pressure P[GPa], Pearson symbol PS, prototype structure PT, and, if applicable, the lattice parameter ratio *c/a*.

	T[K]	P[GPa]	PS	PT	*c/a*
Li 3 $V_{at}=21.60$ Å^3					
$1s^2 2s^1$					
α	<70		hR3	Sm	
β			cI2	W	
γ		>6.9	cF4	Cu	
Na 11 $V_{at}=39.50$ Å^3					
$1s^2 2s^2 p^6 3s^1$					
α	<40		hR3	Sm	
β			cI2	W	
K 19 $V_{at}=75.33$ Å^3					
$1s^2 2s^2 p^6 3s^2 p^6 4s^1$					
α			cI2	W	
β		>12	cF4	Cu	
Rb 37 $V_{at}=92.59$ Å^3					
$1s^2 2s^2 p^6 3s^2 p^6 d^{10} 4s^2 p^6 5s^1$					
α			cI2	W	
β		>7.0	cF4	Cu	
γ		>14			
δ		>17			
ε		>20	tI4		
Cs 55 $V_{at}=117.79$ Å^3					
$1s^2 2s^2 p^6 3s^2 p^6 d^{10} 4s^2 p^6 d^{10} 5s^2 p^6 6s^1$					
α			cI2	W	
β		>2.37	cF4	Cu	
β'		>4.22	cF4	Cu	
γ		>4.27	tI4		
δ		>10			
ε		>72	cF4?		
Fr 87					
$1s^2 2s^2 p^6 3s^2 p^6 d^{10} 4s^2 p^6 d^{10} f^{14} 5s^2 p^6 d^{10} 6s^2 p^6 7s^1$					

	T[K]	P[GPa]	PS	PT	*c/a*
Be 4 $V_{at}=8.11$ Å^3					
$1s^2 2s^2 2$					
α			hP2	Mg	1.568
β	>1543		cI2	W	
γ		>28.3	hP8?		0.789
Mg 12 $V_{at}=23.24$ Å^3					
$1s^2 2s^2 p^6 3s^2$					
α			hP2	Mg	1.624
β		>50	cI2	W	
Ca 20 $V_{at}=43.62$ Å^3					
$1s^2 2s^2 p^6 3s^2 p^6 4s^2$					
α			cF4	Cu	
β	>728 or	>19.5	cI2	W	
γ		>32	cP1	α-Po	
Sr 38 $V_{at}=56.35$ Å^3					
$1s^2 2s^2 p^6 3s^2 p^6 d^{10} 4s^2 p^6 5s^2$					
α			cF4	Cu	
β	>504		hP2	Mg	1.636
γ	>896 or	>3.5	cI2	W	
δ		>26			
ε		>35			
Ba 56 $V_{at}=63.36$ Å^3					
$1s^2 2s^2 p^6 3s^2 p^6 d^{10} 4s^2 p^6 d^{10} 5s^2 p^6 6s^2$					
α			cI2	W	
β		>5.33	hP2	Mg	1.581
γ		>7.5			
δ		>12.6			
Ra 88 $V_{at}=68.22$ Å^3					
$1s^2 2s^2 p^6 3s^2 p^6 d^{10} 4s^2 p^6 d^{10} f^{14} 5s^2 p^6 d^{10} 6s^2 p^6 7s^2$					
α			cI2	W	

increasing number of inner electron shells, is shown by the example of Cs (fig. 13). With increasing pressure, the valence electrons change from s to d character, giving rise to a large number of pressure-induced phase transitions at ambient temperature (YOUNG [1991]):

$$\alpha\text{-Cs} \overset{2.37\ \text{GPa}}{\Leftrightarrow} \beta\text{-Cs} \overset{4.22\ \text{GPa}}{\Leftrightarrow} \beta'\text{-Cs} \overset{4.27\ \text{GPa}}{\Leftrightarrow} \gamma\text{-Cs} \overset{10\ \text{GPa}}{\Leftrightarrow} \delta\text{-Cs} \overset{72\ \text{GPa}}{\Leftrightarrow} \varepsilon\text{-Cs}$$

References: p. 45.

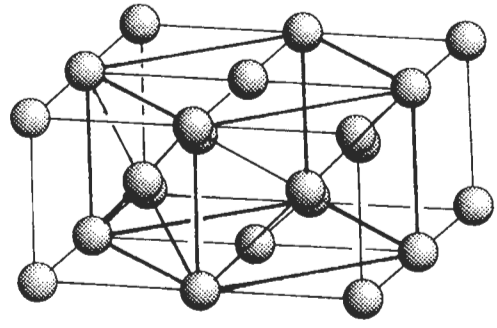

Fig. 11. Relationship between body-centered cubic (bcc) α-Fe, cI2–W type, space group $Im\bar{3}m$, No. 229, 1a: 0 0 0, and face-centered cubic (fcc) γ-Fe, cF4–Cu type, space group $Fm\bar{3}m$, No. 225, 4a: 0 0 0. The face-centered tetragonal unit cell drawn into an array of four bcc unit cells transforms by shrinking its faces to fcc.

The alkaline earth metals behave quite similarly to the alkali metals. They crystallize under ambient conditions in one of the two closest-packed structures (ccp or hcp) or in the body-centered cubic (bcc) structure type and also show several allotropic forms (fig. 14). The large deviation $c/a = 1.56$ from the ideal value of 1.633 for beryllium indicates covalent bonding contributions.

For alkali and alkaline earth metals, the pressure-induced phase transitions from cI2–W to cF4–Cu occur with increasing atomic number at decreasing pressures.

3.3. Groups 3 to 10, transition metals

The elements of groups 3 to 10 are typical metals which have in common that their d-orbitals are partially occupied. These orbitals are only slightly screened by the outer s-electrons, leading to significantly different chemical properties of the transition elements going from left to right in the periodic system. The atomic volumes decrease rapidly with increasing number of electrons in bonding d-orbitals, because of cohesion, and increase as the anti-bonding d-orbitals become filled (fig. 15). The anomalous behavior of the 3d-transition metals, Mn, Fe and Co, may be explained by the existence of non-bonding d-electrons (PEARSON [1972]).

Scandium, yttrium, lanthanum and actinium (table 6) are expected to behave quite

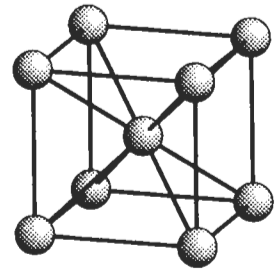

Fig. 12. Unit cell of the body-centered cubic structure type cI2–W, space group $Im\bar{3}m$, No. 229, 1a: 0 0 0.

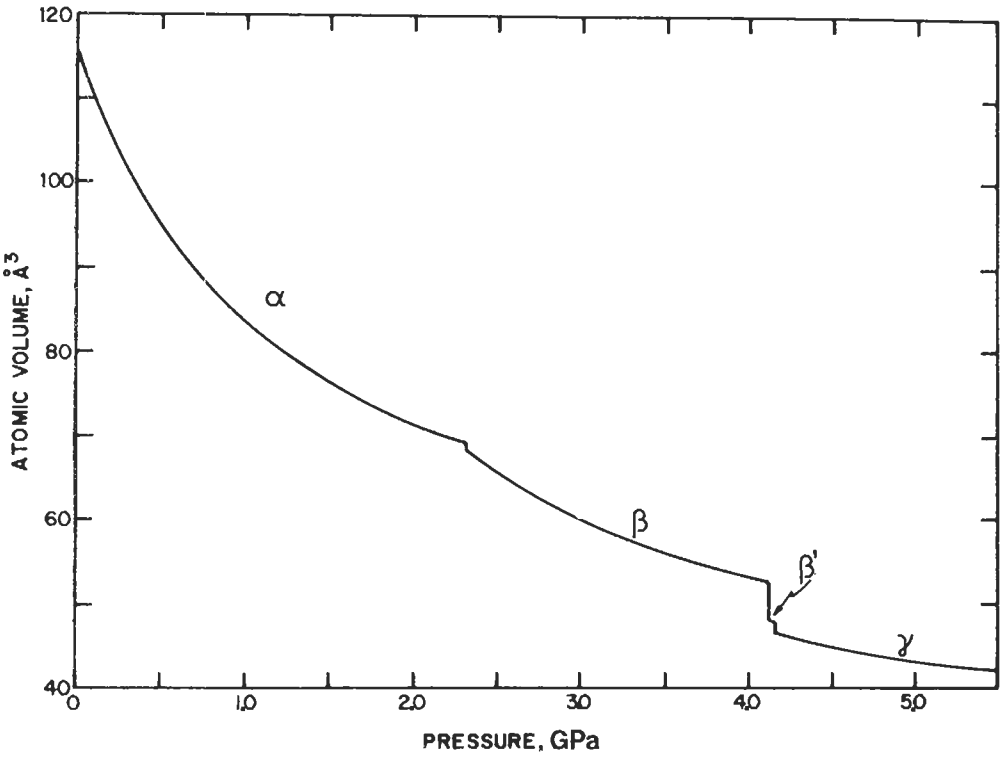

Fig. 13. The variation of the atomic volume of cesium with pressure (after DONOHUE [1974]).

similarly. Indeed they show similar phase sequences: the high-pressure phases of light elements occur as the ambient-pressure phases of the heavy homologues. The hP4 phase of lanthanum, with the sequence ..ACAB.., is one of the simpler closest-packed polytypic structures common for the lanthanides (fig. 16 and fig. 10). Another typical polytype for lanthanides is the hR3 phase of yttrium with stacking sequence ..ABABCBCAC.. (fig. 17 and fig. 10).

Titanium, zirconium and hafnium (table 6) crystallize in a slightly compressed hcp structure type and transform to bcc at higher temperatures. At higher pressures the ω-Ti phase is obtained (fig. 18). The packing density of the hP3–Ti structure with ~0.57 is slightly larger than that of the simple cubic α-Po structure (~0.52) but substantially lower than for bcc (~0.68) or ccp and hcp (~0.74) type structures. Calculations have shown that the ω-Ti phase is stable owing to covalent bonding contributions from s–d electron transfer. At even higher pressures, zirconium and hafnium transform to the cI2–W type, while titanium remains in the hp3–Ti phase up to at least 87 GPa. By theoretical considerations it is also expected that titanium performs this transformation at sufficiently high pressures (AHUJA *et al.* [1993]). A general theoretical phase diagram for Ti, Zr and Hf is shown in fig. 19.

Vanadium, niobium, tantalum, molybdenum and tungsten have only simple bcc

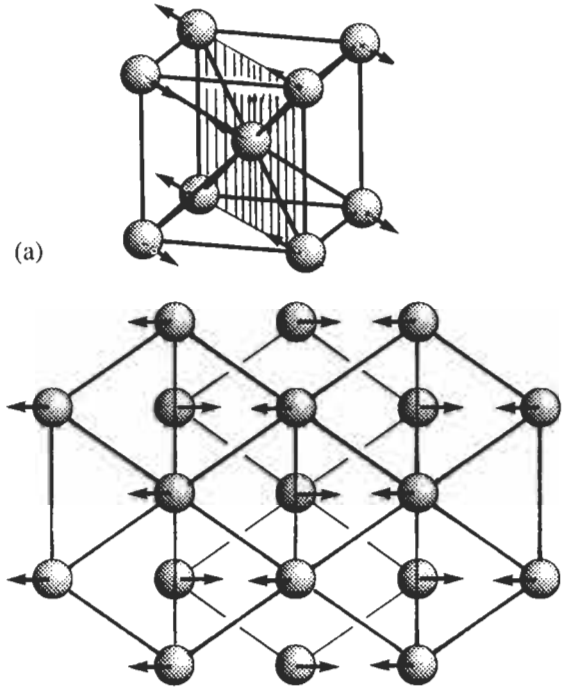

Fig. 14. Illustration of the bcc-to-hcp phase transition of Ba. (a) bcc unit cell with (110) plane marked. (b) Projection of the bcc structure upon the (110) plane. Atomic displacements necessary for the transformation are indicated by arrows.

structures (table 7). Up to pressures of 170 to 364 GPa no further allotropes could be found, in agreement with theoretical calculations. Chromium shows two antiferromagnetic phase transitions, which modify the structure only very slightly (YOUNG [1991]).

The high-temperature phases of manganese (table 8), γ-Mn, cF4–Cu type, and δ-Mn, cI2–W type, are typical metal structures, whereas α-Mn and β-Mn form very complicated structures, possibly caused by their antiferromagnetism. Thus, the α-Mn structure can be described as a $3\times3\times3$ superstructure of bcc unit cells, with 20 atoms slightly shifted and 4 atoms added resulting in 58 atoms over all (fig. 20). The structure of β-Mn (fig. 21) is also governed by the valence electron concentration ("electron compound" or Hume–Rothery-type phase). The variation of the atomic volume of manganese with temperature is illustrated in fig. 22. For technetium, rhenium, ruthenium and osmium, only simple hcp structures are known.

The technically most important element and the main constituent of the Earth's core, iron (table 8) shows five allotropic forms (fig. 23): ferromagnetic bcc α-Fe transforms to paramagnetic isostructural β-Fe with a Curie temperature of 1043 K; at 1185 K fcc γ-Fe forms while at 1667 K a bcc phase, now called δ-Fe, appears again. For the variation of

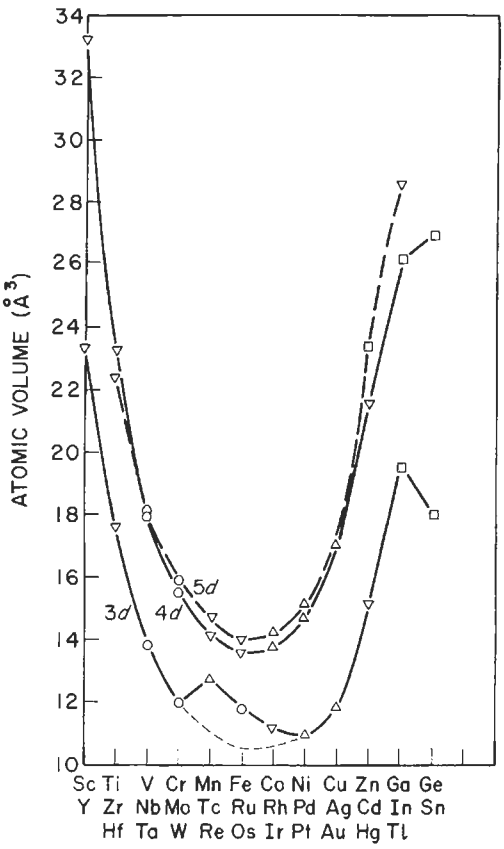

Fig. 15. Atomic volumes of the transition metals. △ means cF4–Cu type, ▽ hP2–Mg, ○ cI2–W, □ other types (after PEARSON [1972]).

the atomic volume with temperature see fig. 24. High-pressure nonmagnetic ε-Fe, existing above 13 GPa, has a slightly compressed hcp structure.

Cobalt (table 9) is dimorphous, hcp at ambient conditions and ccp at higher temperatures. By annealing it in a special way, stacking disorder can be generated: the hcp sequence ..ABAB.. is statistically disturbed by a ccp sequence ..ABCABC.. like ..ABABABABCBCBCBC.. with a frequency of about one ..ABC.. among ten ..AB... Rhodium, iridium, nickel, palladium and platinum all crystallize in simple cubic closest-packed structures.

3.4. Groups 11 and 12, copper and zinc group metals

The "mint metals", copper, silver and gold (table 10) are typical metals with ccp structure type (fig. 25). Their single ns electron is less shielded by the filled d-orbitals than the ns electron of the alkali metals by the filled noble gas shell. The d-electrons also contribute to the metallic bond. These factors are responsible for the more noble

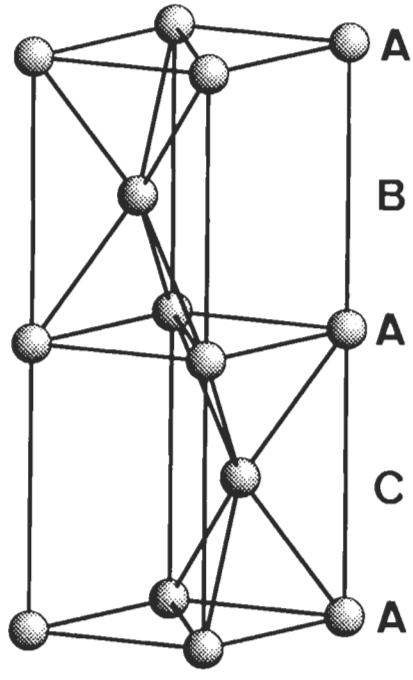

Fig. 16. One unit cell of the hP4–La structure type, space group $P6_3/mmc$, No. 194, 2a: 0 0 0, 2c: ⅓ ⅔ ¼.

character of these metals than of the alkali metals and that these elements sometimes are grouped to the transition elements.

For zinc, cadmium and mercury (table 10) covalent bonding contributions (filled d-band) lead to deviations from hexagonal closest packing (hcp), with its ideal axial ratio $c/a = 1.633$, to values of 1.856 (Zn) and 1.886 (Cd), respectively. The bonds in the hcp layers are shorter and stronger, consequently, than between the layers. With increasing pressure, c/a approximates the ideal value 1.633: for Cd $c/a = 1.68$ was observed at 30 GPa (DONOHUE [1974]), and for Hg, $c/a = 1.76$ at 46.8 GPa (SCHULTE and HOLZAPFEL [1993]).

The rhombohedral structure of α-Hg may be derived from a ccp structure by compression along the threefold axis (fig. 26). In contrast to zinc and cadmium, the ratio $c/a = 1.457$ for a hypothetical distorted hcp structure is smaller than the ideal value. There also exist several high-pressure allotropes (fig. 27).

3.5. Groups 13 to 16, metallic and semi-metallic elements

Only aluminum, thallium and lead crystallize in the closest-packed structures characteristic for typical metals (table 11). The s–d transfer effects, important for alkali- and alkaline-earth metals, do not appear for the heavier group 13 elements owing to their filled d-bands. Orthorhombic gallium forms a 6^3 network of distorted hexagons parallel to (100) at heights $x = 0$ and 1/2 (fig. 28). The bonds between the layers are considerably

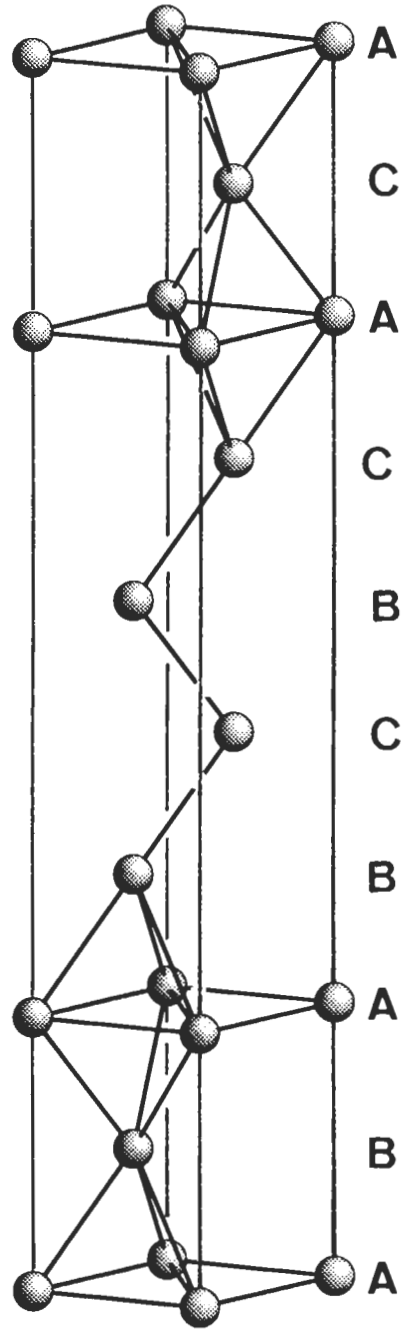

Fig. 17. One unit cell of the hR3–Sm structure type, space group $R\bar{3}m$, No. 166, 3a: 0 0 0, 6c: 0 0 0.22.

References: p. 45.

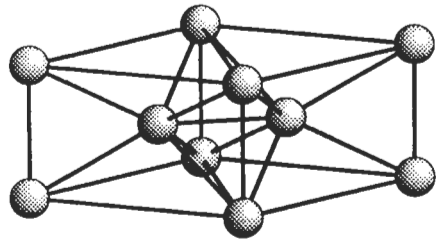

Fig. 18. The hP3–Ti structure type, space group P6/mmm, No. 191, 1a: 0 0 0, 2d: ⅓ ⅔ ½.

weaker than within. At higher pressure gallium transforms to a bcc phase, cI12–Ga, and additionally increasing the temperature leads to the tetragonal indium structure type tI2–In (fig. 29). In an alternative description based on a face-centered tetragonal unit cell with $a' = \sqrt{2}\,a$, the resemblance to a slightly distorted cubic close-packed structure with $c/a = 1.08$ becomes clear.

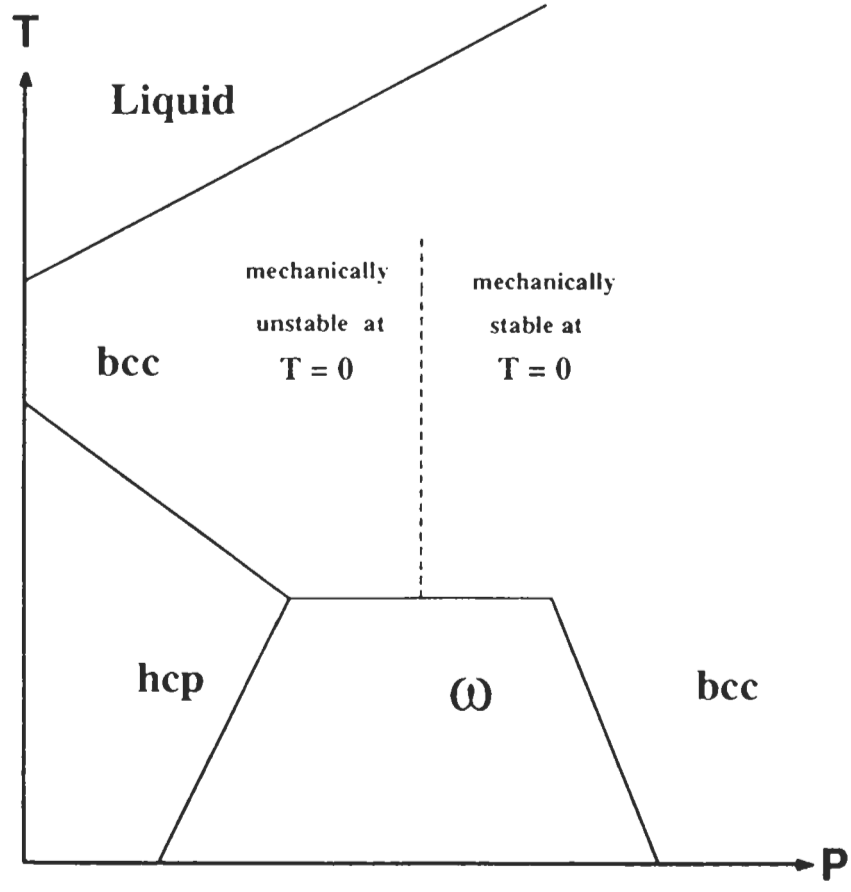

Fig. 19. Schematic calculated phase diagram for Ti, Zr and Hf (from AHUJA *et al.* [1993]).

Table 6

Structure information for the elements of groups 3 and 4. In the first line of each box the chemical symbol, atomic number Z, and the atomic volume V_{at} under ambient conditions is listed. In the second line the electronic ground state configuration is given. For each phase there is tabulated: limiting temperature T[K] and pressure P[GPa], Pearson symbol PS, prototype structure PT, and, if applicable, the lattice parameter ratio *c/a*.

	T[K]	P[GPa]	PS	PT	*c/a*
Sc 21 $V_{at}=24.97$ Å^3					
$1s^2 2s^2 p^6 3s^2 p^6 d^1 4s^2$					
α			hP2	Mg	1.592
β	>1610		cI2	W	
γ		>19	tP4?		
Y 39 $V_{at}=33.01$ Å^3					
$1s^2 2s^2 p^6 3s^2 p^6 d^{10} 4s^2 p^6 d^1 5s^2$					
α			hP2	Mg	1.571
β	>1751		cI2	W	
γ		>10	hR3	Sm	
δ		>26	hP4?		
ε		>39	cF4	Cu	
La 57 $V_{at}=37.17$ Å^3					
$1s^2 2s^2 p^6 3s^2 p^6 d^{10} 4s^2 p^6 d^{10} 5s^2 p^6 d^1 6s^2$					
α			hP4	α-La	2×1.613
β	>583 or >2.3		cF4	Cu	
γ	>1138		cI2	W	
δ		>7.0	hP6		
Ac 89 $V_{at}=37.45$ Å^3 at 293 K					
$...3s^2 p^6 d^{10} 4s^2 p^6 d^{10} f^{14} 5s^2 p^6 d^{10} 6s^2 p^6 d^1 7s^2$					
α			cF4	Cu	

	T[K]	P[GPa]	PS	PT	*c/a*
Ti 22 $V_{at}=17.65$ Å^3					
$1s^2 2s^2 p^6 3s^2 p^6 d^2 4s^2$					
α			hP2	Mg	1.587
β	>1155		cI2	W	
ω		>2	hP3	ω-Ti	
Zr 40 $V_{at}=23.28$ Å^3					
$1s^2 2s^2 p^6 3s^2 p^6 d^{10} 4s^2 p^6 d^2 5s^2$					
α			hP2	Mg	1.593
β	>1136		cI2	W	
ω		>2	hP3	ω-Ti	
ω'		>30	cI2	W	
Hf 72 $V_{at}=22.31$ Å^3					
$1s^2 2s^2 p^6 3s^2 p^6 d^{10} 4s^2 p^6 d^{10} f^{14} 5s^2 p^6 d^2 6s^2$					
α			hP2	Mg	1.581
β	>2016		cI2	W	
ω		>38	hP3	ω-Ti	
ω'		>71	cI2	W	
Ku 104					
$...3s^2 p^6 d^{10} 4s^2 p^6 d^{10} f^{14} 5s^2 p^6 d^{10} f^{14} 6s^2 p^6 d^2 7s^2$					

Silicon and germanium (table 11) under ambient conditions crystallize in the diamond structure, owing to strong covalent bonding. At higher pressures they transform to the metallic white-tin (tI4–Sn) structure. This structure type consists of a body-centered tetragonal lattice which can be regarded as being intermediate between the diamond structure of semiconducting α-Sn and ccp lead (fig. 30). For an ideal ratio of $c/a=0.528$ one atom is sixfold coordinated. The high-pressure phase hP1–BiIn has a quasi-eightfold coordination, the ideal ratio for CN = 8 would be $c/a=1$. At higher pressures, closest-packed structures with twelvefold coordinations are obtained. Thus with increasing pressure silicon runs through phases with coordination numbers 4, 6, 8 and 12.

The effective radius of tin in β-Sn and of lead in α-Pb is large compared with that of other typical metals with large atomic number due to uncomplete ionization of the single ns electron. This means that in α-Sn, for instance, the electron configuration is $...5s^1 5p^3$, allowing sp^3–hybridization and covalent tetrahedrally coordinated bonding, whereas in β-Sn with $...5s^2 5p^2$ only two p-orbitals are available for covalent and one further p-orbital for metallic bonding.

The structure of arsenic, antimony and bismuth (isotypic under ambient conditions)

References: p. 45.

Table 7

Structure information for the elements of groups 5 and 6. In the first line of each box the chemical symbol, atomic number Z, and the atomic volume V_{at} under ambient conditions is listed. In the second line the electronic ground state configuration is given. For each phase there is tabulated: limiting temperature T[K] and pressure P[GPa], Pearson symbol PS, prototype structure PT, and, if applicable, the lattice parameter ratio *c/a*.

T[K] P[GPa]	PS	PT	*c/a*	T[K] P[GPa]	PS	PT	*c/a*
V 23 $V_{at}=13.82\,Å^3$ $1s^2 2s^2 p^6 3s^2 p^6 d^3 4s^2$				**Cr** 24 $V_{at}=12.00\,Å^3$ $1s^2 2s^2 p^6 3s^2 p^6 d^5 4s^1$			
	cI2	W			cI2	W	
Nb 41 $V_{at}=17.98\,Å^3$ $1s^2 2s^2 p^6 3s^2 p^6 d^{10} 4s^2 p^6 d^4 5s^1$				**Mo** 42 $V_{at}=15.58\,Å^3$ $1s^2 2s^2 p^6 3s^2 p^6 d^{10} 4s^2 p^6 d^5 5s^1$			
	cI2	W			cI2	W	
Ta 73 $V_{at}=18.02\,Å^3$ $1s^2 2s^2 p^6 3s^2 p^6 d^{10} 4s^2 p^6 d^{10} f^{14} 5s^2 p^6 d^3 6s^2$				**W** 74 $V_{at}=15.85\,Å^3$ $1s^2 2s^2 p^6 3s^2 p^6 d^{10} 4s^2 p^6 d^{10} f^{14} 5s^2 p^6 d^4 6s^2$			
	cI2	W			cI2	W	

(table 12) consists of puckered layers of covalently bonded atoms stacked along the hexagonal axis (fig. 31). The structure can be regarded as a distorted primitive cubic structure (α-Po) in which the atomic distance d_1 in the layer equals that between the layers d_2. The metallic character of these elements increases for d_2/d_1 approximating to 1 (table 13).

The helical structures of isotypic α-Se and α-Te may also be derived from the

Table 8

Structure information for the elements of groups 7 and 8. In the first line of each box the chemical symbol, atomic number Z, and the atomic volume V_{at} under ambient conditions is listed. In the second line the electronic ground state configuration is given. For each phase there is tabulated: limiting temperature T[K] and pressure P[GPa], Pearson symbol PS, prototype structure PT, and, if applicable, the lattice parameter ratio *c/a*.

T[K] P[GPa]	PS	PT	*c/a*	T[K] P[GPa]	PS	PT	*c/a*
Mn 25 $V_{at}=12.21\,Å^3$ $1s^2 2s^2 p^6 3s^2 p^6 d^5 4s^2$				**Fe** 26 $V_{at}=11.78\,Å^3$ $1s^2 2s^2 p^6 3s^2 p^6 d^6 4s^2$			
α	cI58	α-Mn		α	cI2	W	
β >1000	cP20	β-Mn		γ >1185	cF4	Cu	
γ >1373	cF4	Cu		δ >1667	cI2	W	
δ >1411	cI2	W		ε >13	hP2	Mg	1.603
Tc 43 $V_{at}=14.26\,Å^3$ $1s^2 2s^2 p^6 3s^2 p^6 d^{10} 4s^2 p^6 d^6 5s^1$				**Ru** 44 $V_{at}=13.57\,Å^3$ $1s^2 2s^2 p^6 3s^2 p^6 d^{10} 4s^2 p^6 d^7 5s^1$			
	hP2	Mg	1.604		hP2	Mg	1.582
Re 75 $V_{at}=14.71\,Å^3$ $1s^2 2s^2 p^6 3s^2 p^6 d^{10} 4s^2 p^6 d^{10} f^{14} 5s^2 p^6 d^5 6s^2$				**Os** 76 $V_{at}=13.99\,Å^3$ $1s^2 2s^2 p^6 3s^2 p^6 d^{10} 4s^2 p^6 d^{10} f^{14} 5s^2 p^6 d^6 6s^2$			
	hP2	Mg	1.615		hP2	Mg	1.580

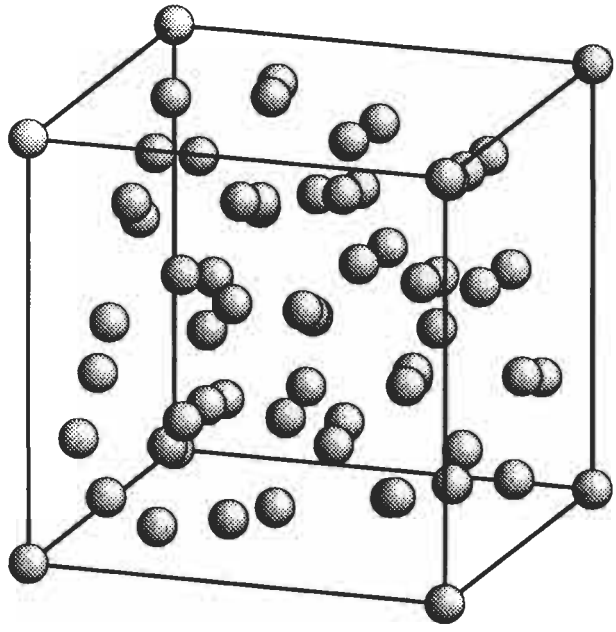

(a)

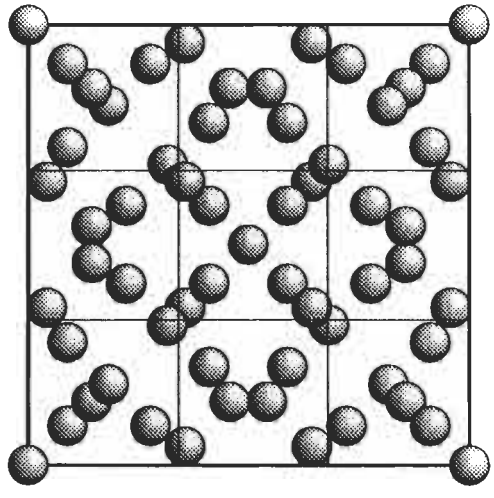

(b)

Fig. 20. One unit cell of cI58–Mn, space group $I\bar{4}3m$, No. 217, with four different types of Mn atoms in 2a: 0 0 0, 8c: 0.316 0.316 0.316, 24g: 0.356 0.356 0.034, 24g: 0.089 0.089 0.282, shown (a) in perspective view and (b) in projection. Two types of Mn atoms are coordinated by CN 16 Friauf polyhedra, one by a CN 14 Frank-Kasper polyhedron and one by an icosahedron.

primitive cubic α-Po structure (fig. 32). The infinite helices run along the trigonal axes, and have three atoms per turn. The interhelix bonding distance d_2 plays a comparable

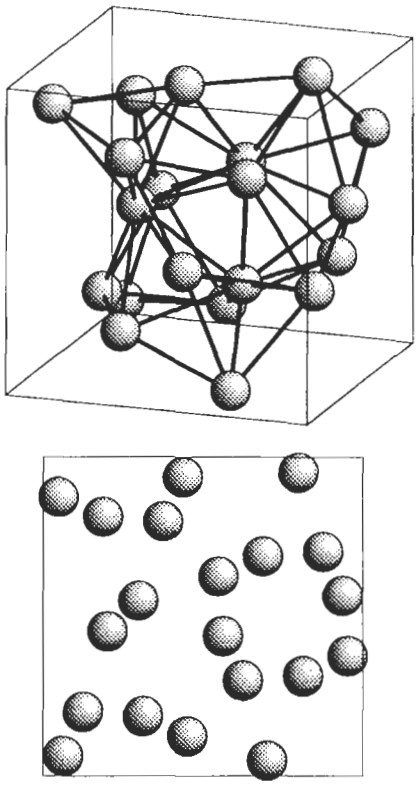

Fig. 21. One unit cell of cP20–Mn, space group $P4_132$, No 213, with two types of Mn atoms: 8c: 0.063 0.063 0.063, 12d: 0.125 0.202 0.452, shown (a) in perspective view and (b) in projection. The atoms in 8c are coordinated by 12 atoms in a distorted icosahedron, the Mn atoms in 12d by 14 atoms in a distorted Frank-Kasper CN 14 type polyhedron.

role for the metallic character of these elements as does the interlayer distance in the case of the group 15 elements. Wih increasing pressure, the transition to the metallic β–Te phase takes place.

3.6. Lanthanides and actinides

Lanthanides and actinides (table 14) are characterized by the fact that their valence electrons occupying the f-orbitals are shielded by filled outer s- and p-orbitals. The chemical properties of the lanthanides are rather uniform since the 4f-orbitals are largely screened by the 5s- and 5p-electrons. The chemical behavior of the actinides, however, is somelike in between that of the 3d transition metals and the lanthanides since the 5f-orbitals are screened to a much smaller amount by the 6s- and 6p-electrons. With the exception of Sm and Eu, all lanthanides under ambient conditions show either a simple hcp structure with the standard stacking sequence ..AB.. or a twofold superstructure with a stacking sequence ..ACAB... Samarium has, with ..ABABCBCAC.., an even more

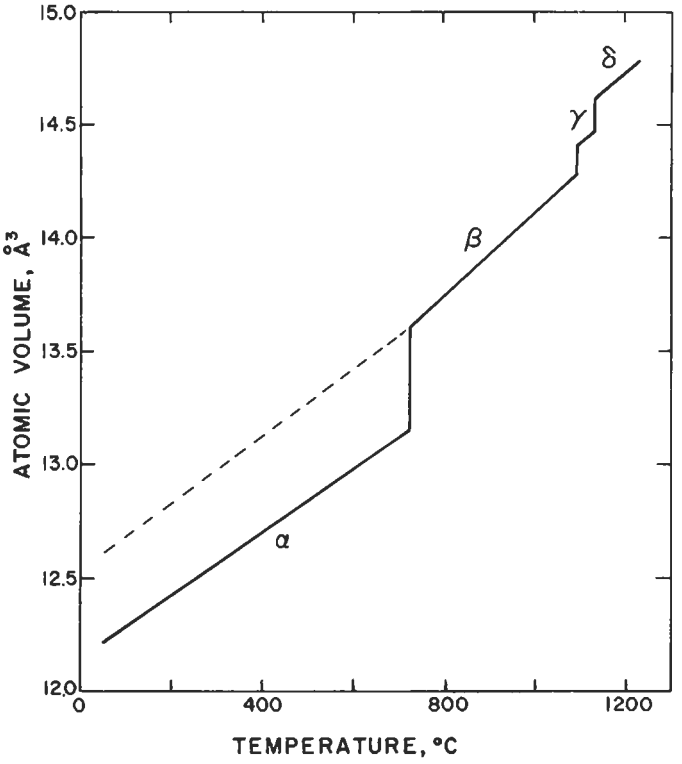

Fig. 22. The variation of the atomic volume of manganese with temperature (from DONOHUE [1974]).

Table 9

Structure information for the elements of groups 9 and 10. In the first line of each box the chemical symbol, atomic number Z, and the atomic volume V_{at} under ambient conditions is listed. In the second line the electronic ground state configuration is given. For each phase there is tabulated: limiting temperature T[K] and pressure P[GPa], Pearson symbol PS, prototype structure PT, and, if applicable, the lattice parameter ratio *c/a*.

	T[K]	P[GPa]	PS	PT	*c/a*
Co 27 $V_{at} = 11.08$ Å^3					
$1s^2 2s^2 p^6 3s^2 p^6 d^7 4s^2$					
ε			hP2	Mg	1.623
α	>695		cF4	Cu	
Rh 45 $V_{at} = 13.75$ Å^3					
$1s^2 2s^2 p^6 3s^2 p^6 d^{10} 4s^2 p^6 d^8 5s^1$					
			cF4	Cu	
Ir 77 $V_{at} = 14.15$ Å^3					
$1s^2 2s^2 p^6 3s^2 p^6 d^{10} 4s^2 p^6 d^{10} f^{14} 5s^2 p^6 d^7 6s^2$					
			cF4	Cu	

	T[K]	P[GPa]	PS	PT	*c/a*
Ni 28 $V_{at} = 10.94$ Å^3					
$1s^2 2s^2 p^6 3s^2 p^6 d^8 4s^2$					
			cF4	Cu	
Pd 46 $V_{at} = 14.72$ Å^3					
$1s^2 2s^2 p^6 3s^2 p^6 d^{10} 4s^2 p^6 d^{10}$					
			cF4	Cu	
Pt 78 $V_{at} = 15.10$ Å^3					
$1s^2 2s^2 p^6 3s^2 p^6 d^{10} 4s^2 p^6 d^{10} f^{14} 5s^2 p^6 d^9 6s^1$					
			cF4	Cu	

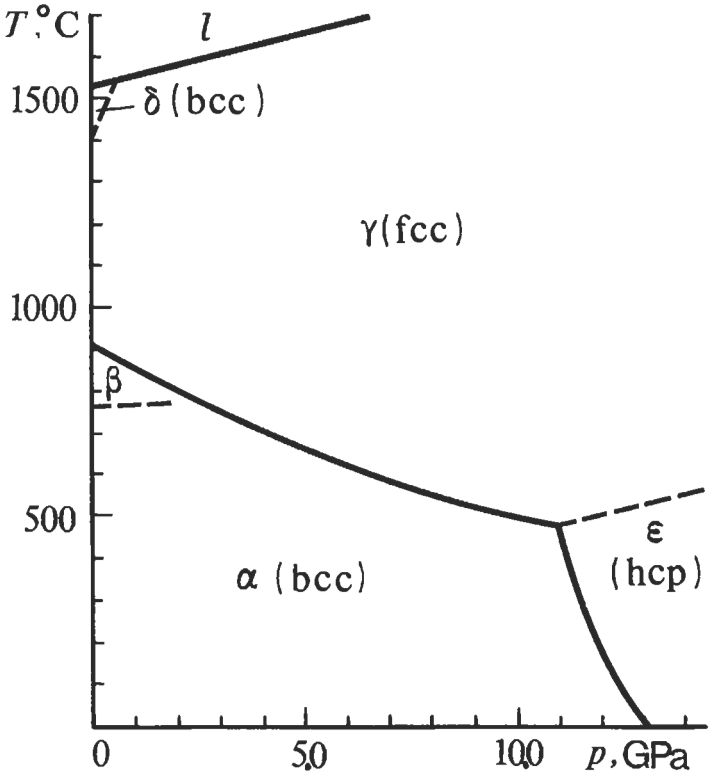

Fig. 23. Phase diagram of iron (from VAINSHTEIN *et al.* [1982]).

Table 10

Structure information for the elements of groups 11 and 12. In the first line of each box the chemical symbol, atomic number Z, and the atomic volume V_{at} under ambient conditions is listed. In the second line the electronic ground state configuration is given. For each phase there is tabulated: limiting temperature T[K] and pressure P[GPa], Pearson symbol PS, prototype structure PT, and, if applicable, the lattice parameter ratio *c/a*.

T[K]	P[GPa]	PS	PT	*c/a*
Cu 29 V_{at} = 11.81 Å^3				
$1s^2 2s^2 p^6 3s^2 p^6 d^{10} 4s^1$				
		cF4	Cu	
Ag 47 V_{at} = 17.05 Å^3				
$1s^2 2s^2 p^6 3s^2 p^6 d^{10} 4s^2 p^6 d^{10} 5s^1$				
		cF4	Cu	
Au 79 V_{at} = 16.96 Å^3				
$1s^2 2s^2 p^6 3s^2 p^6 d^{10} 4s^2 p^6 d^{10} f^{14} 5s^2 p^6 d^{10} 6s^1$				
		cF4	Cu	

T[K]	P[GPa]	PS	PT	*c/a*
Zn 30 V_{at} = 15.20 Å^3				
$1s^2 2s^2 p^6 3s^2 p^6 d^{10} 4s^2$				
		hP2	Mg	1.856
Cd 48 V_{at} = 21.60 Å^3				
$1s^2 2s^2 p^6 3s^2 p^6 d^{10} 4s^2 p^6 d^{10} 5s^2$				
		hP2	Mg	1.886
Hg 80 V_{at} = 23.13 Å^3 at 80 K				
$1s^2 2s^2 p^6 3s^2 p^6 d^{10} 4s^2 p^6 d^{10} f^{14} 5s^2 p^6 d^{10} 6s^2$				
α	< 234.3	hR1	α-Hg	
β	> 3.7	tI2	α-Pa	
γ	> 12	oP4		
δ	> 37	hP2	Mg	1.76

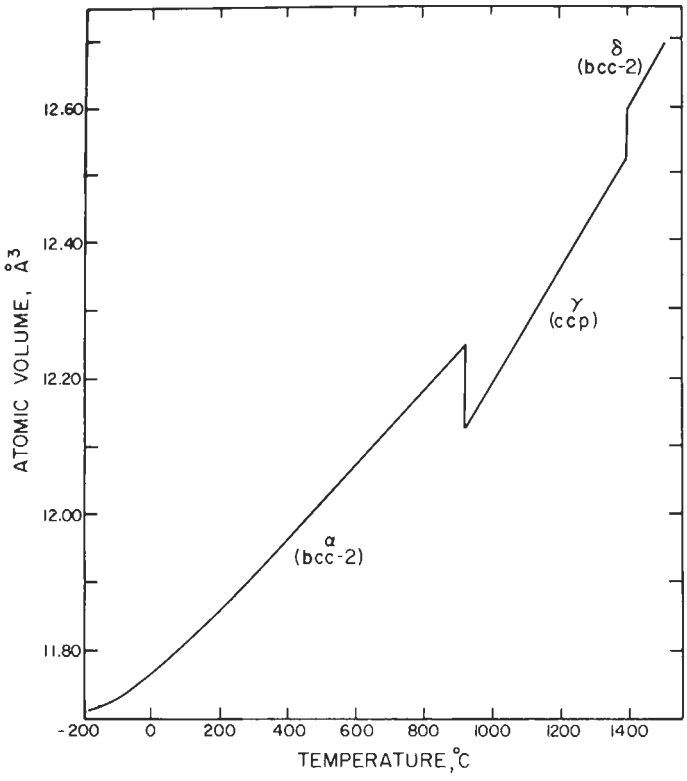

Fig. 24. The variation of atomic volume of iron with temperature (from DONOHUE [1974]).

complicated stacking order with 4.5–fold superperiod. For all lanthanides the ratio *c/a* is near the ideal value of $n \times 1.633$. It is interesting that with increasing pressure and decreasing atomic number the sequence of closest-packed phases hP2–Mg (..AB..) ⇒ hR3–Sm (..ABABCBCAC..) ⇒ hP4–La (..ACAB..) ⇒ cF4–Cu (..ABC..) ⇒ hP6–Pr appears (cf. figs. 10, 17 and 33).

Cerium undergoes a transformation from the γ to the α-phase at pressures >0.7 GPa:

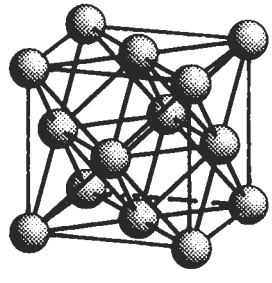

Fig. 25. The structure of cF4–Cu, space group $Fm\bar{3}m$, No. 225, 4a 0 0 0.

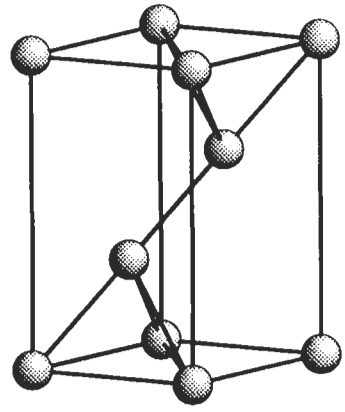

Fig. 26. The structure of hR1–Hg, space group R$\bar{3}$m, No. 166, 3a 0 0 0.

the ccp structure is preserved but the lattice constant decreases drastically from 5.14 to 4.84 Å owing to a transition of one 4f-electron to the 5d-level (fig. 34). This isostructural transition is terminated in a critical point near 550 K and 1.75 GPa (YOUNG [1991]). Further compression gives the transformation at 5.1 GPa to the α'-phase, and finally at 12.2 GPa to the ε-phase. Europium shows a completely different behavior, as do the other lanthanides, owing to the stability of its half filled 4f-orbitals. Thus, it has more similarities to the alkaline earth metals; its phase diagram is comparable to that of barium

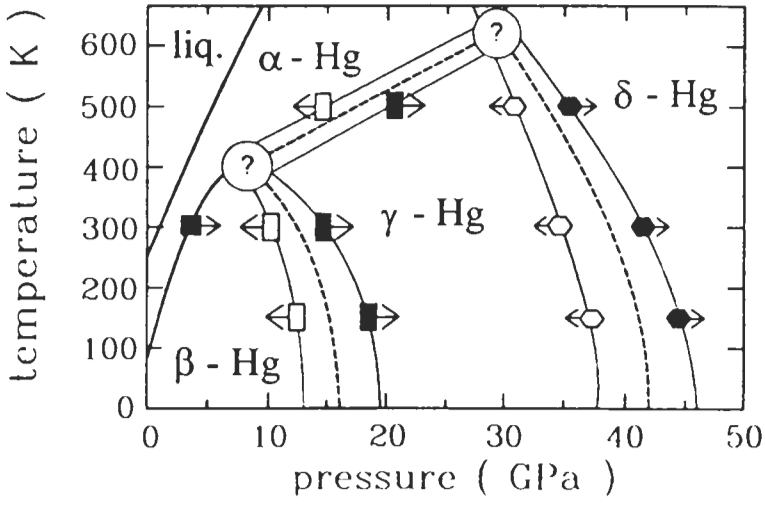

Fig. 27. Schematical phase diagram of mercury (from SCHULTE and HOLZAPFEL [1993]).

Table 11

Structure information for the elements of groups 13 and 14. In the first line of each box the chemical symbol, atomic number Z, and the atomic volume V_{at} under ambient conditions is listed. In the second line the electronic ground state configuration is given. For each phase there is tabulated: limiting temperature T[K] and pressure P[GPa], Pearson symbol PS, prototype structure PT, and, if applicable, the lattice parameter ratio *c/a*.

	T[K]	P[GPa]	PS	PT	*c/a*
Al 13 $V_{at}=16.60$ Å^3					
$1s^2 2s^2 p^6 3s^2 p^1$					
			cF4	Cu	
Ga 31 $V_{at}=19.58$ Å^3					
$1s^2 2s^2 p^6 3s^2 p^6 d^{10} 4s^2 p^1$					
α			oC8	α-Ga	
β	<330	>1.2	cI12		
γ	>330	>3.0	tI2	In	1.588
In 49 $V_{at}=26.16$ Å^3					
$1s^2 2s^2 p^6 3s^2 p^6 d^{10} 4s^2 p^6 d^{10} 5s^2 p^1$					
			tI2	In	1.521
Tl 81 $V_{at}=28.59$ Å^3					
$1s^2 2s^2 p^6 3s^2 p^6 d^{10} 4s^2 p^6 d^{10} f^{14} 5s^2 p^6 d^{10} 6s^2 p^1$					
α			hP2	Mg	1.598
β	>503		cI2	W	
γ		>3.7	cF4	Cu	

	T[K]	P[GPa]	PS	PT	*c/a*
Si 14 $V_{at}=20.02$ Å^3					
$1s^2 2s^2 p^6 3s^2 p^2$					
α			cF8	Cd	
β		>12	tI4	β-Sn	0.552
γ		>13.2	hP1	BiIn	0.92
δ		>36	o?		
ε		>43	hP2	Mg	1.699
ζ		>78	cF4	Cu	
Ge 32 $V_{at}=22.63$ Å^3					
$1s^2 2s^2 p^6 3s^2 p^6 d^{10} 4s^2 p^2$					
α			cF8	C	
β		>11	tI4	β-Sn	0.551
γ		>75	hP1	BiIn	0.92
δ		>106	hP4		
Sn 50 $V_{at}=34.16$ Å^3 at 285 K					
$1s^2 2s^2 p^6 3s^2 p^6 d^{10} 4s^2 p^6 d^{10} 5s^2 p^2$					
α	<291		cF8	C	
β	>291		tI4	β-Sn	0.546
γ		>9.2	tI2	Pa	0.91
δ		>40	cI2	W	
Pb 82 $V_{at}=30.32$ Å^3					
$1s^2 2s^2 p^6 3s^2 p^6 d^{10} 4s^2 p^6 d^{10} f^{14} 5s^2 p^6 d^{10} 6s^2 p^2$					
α			cF4	Cu	
β		>13.7	hP2	Mg	1.650
γ		>109	cI2	W	

rather than to the other lanthanides. A similar behavior is observed for ytterbium which is divalent owing to the stability of the completely filled 4f-orbitals; its phase diagram resembles that of strontium.

The *c*-lattice parameter of gadolinium exhibits an anomalous expansion when cooled below 298 K (fig. 35) due to a change in the magnetic properties of the metal. Several other lanthanides show a similar behavior.

According to their electronic properties, the actinides (table 14) can be divided into two subgroups: the elements from thorium to plutonium have itinerant 5f-electrons contributing to the metallic bond, whereas the elements from americium onwards have more localized 5f-electrons. This situation leads to superconductivity for thorium, protactinium and uranium, for instance, and to magnetic ordering for curium, berkelium and californium (DABOS-SEIGNON *et al.* [1993]). The contribution of 5f-electrons to

References: p. 45.

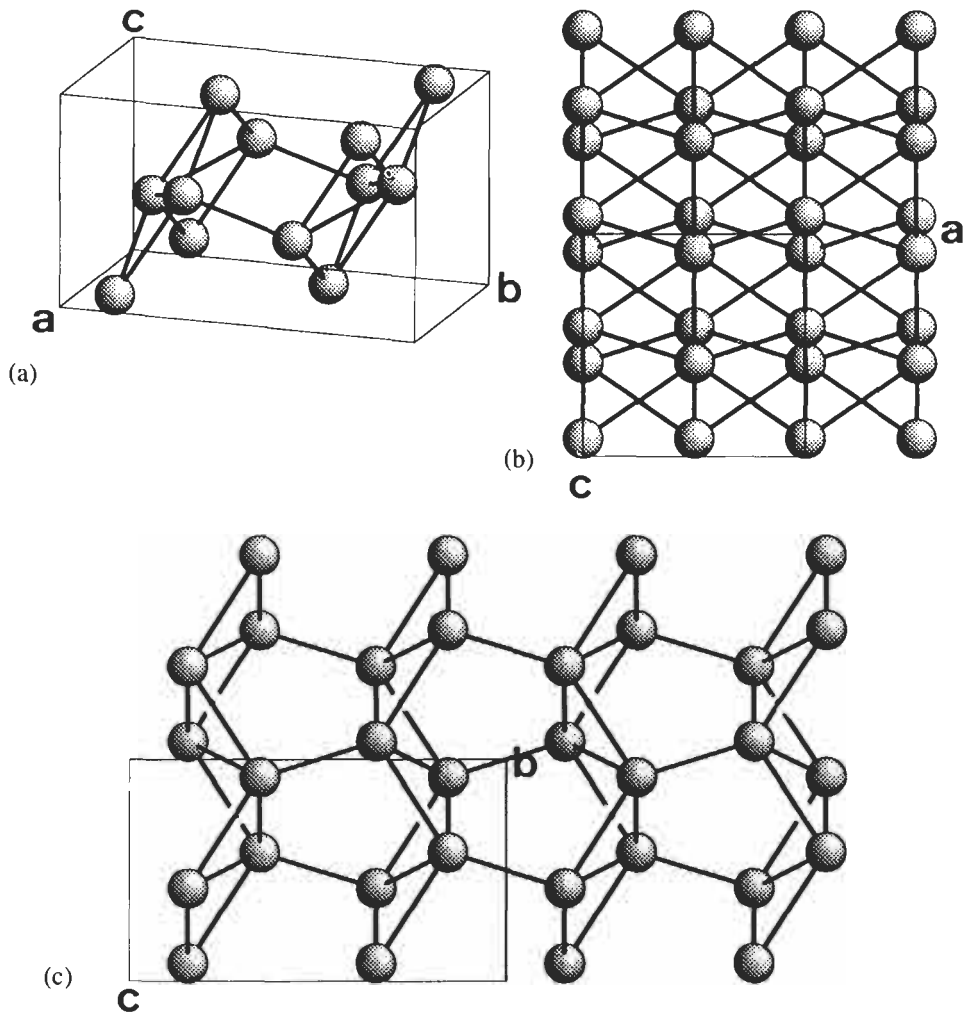

Fig. 28. The structure of oC8–Ga, Cmca, No. 64, 8f 0 0.155 0.081, (a) in a perspective view and projected upon (b) (010) and (c) (100), showing the distorted hexagonal layers.

bonding leads to low symmetry, small atomic volumes and high density in the case of the light actinides while the heavier actinides crystallize at ambient conditions in the hcp structure type. The position of plutonium at the border of itinerant and localized 5f-states causes its unusually complex phase diagram, with structures typical for both cases. Thus, monoclinic α-Pu can be considered as a distorted hcp-structure with about 20% higher packing density than cF4–Pu owing to covalent bonding contributions from 5f-electrons (fig. 36) (Ek *et al.* [1993]). This ratio is quite similar to the above-mentioned one of α–Ce and γ-Ce, which are both ccp. The phase diagram of americium is very similar to

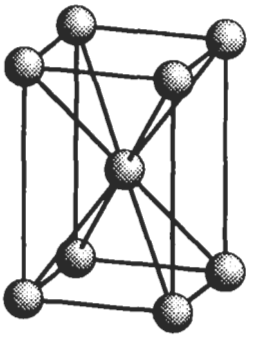

Fig. 29. The structure of tI2–In, space group I4/mmm, No. 139, 2a 0 0 0.

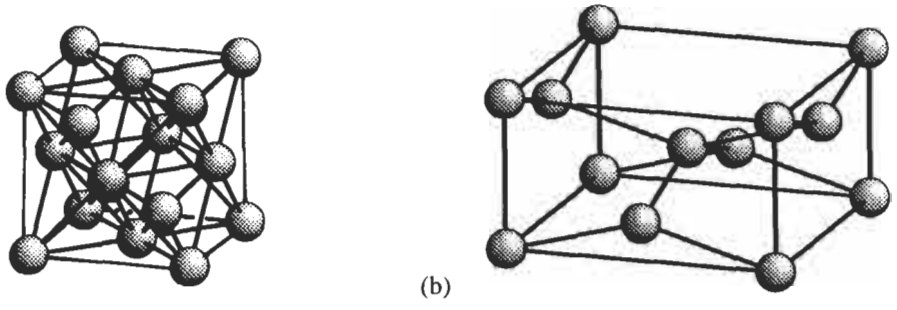

Fig. 30. Relationships between the structures of the two tin allotropes: (a) grey α-Sn, cF8–C type, space group $Fd\bar{3}m$, No. 227, 8a: 0 0 0, ¾ ¼ ¾, and (b) white β-Sn, tI4–β-Sn type, space group $I4_1/amd$, No. 141, 4a: 0 0 0. Note the large difference in the minimum distances: $d_{min}^{\alpha\text{-Sn}} = 1.54$ Å and $d_{min}^{\beta\text{-Sn}} = 3.02$ Å.

those of lanthanum, proseodymium and neodymium. Owing to the localization of 5f-electrons it is the first lanthanide-like actinide element.

Both lanthanides and actinides crystallize in a great variety of polymorphic modifications (fig. 37).

Table 12

Structure information for the more metallic elements of groups 15, pnictides, and of group 16, chalcogenides. In the first line of each box the chemical symbol, atomic number Z, and the atomic volume V_{at} under ambient conditions is listed. In the second line the electronic ground state configuration is given. For each phase there is tabulated: limiting temperature T[K] and pressure P[GPa], Pearson symbol PS, prototype structure PT, and, if applicable, the lattice parameter ratio *c/a*.

	T[K]	P[GPa]	PS	PT	*c/a*
As 33 $V_{at}=21.52$ Å^3					
$1s^2 2s^2 p^6 3s^2 p^6 d^{10} 4s^2 p^3$					
α			hR2	α-As	2.805
β		>25.0	cP1	α-Po	
Sb 51 $V_{at}=30.21$ Å^3					
$1s^2 2s^2 p^6 3s^2 p^6 d^{10} 4s^2 p^6 d^{10} 5s^2 p^3$					
α			hR2	α-As	2.617
β		>8	mP4	β-Sb	
γ		>28	cI2	W	
Bi 83 $V_{at}=35.39$ Å^3					
$1s^2 2s^2 p^6 3s^2 p^6 d^{10} 4s^2 p^6 d^{10} f^{14} 5s^2 p^6 d^{10} 6s^2 p^3$					
α			hR2	α-As	2.609
β		>2.6	mC4	β-Bi	
γ		>3.0	mP4	β-Sb	
δ		>4.3			
ε		>9.0	cI2	W	

	T[K]	P[GPa]	PS	PT	*c/a*
Se 34 $V_{at}=27.27$ Å^3					
$1s^2 2s^2 p^6 3s^2 p^6 d^{10} 4s^2 p^4$					
α			hP3	α-Se	1.135
β		>14	mP3		
γ		>28	tP4		
δ		>41	hR2		
Te 52 $V_{at}=33.98$ Å^3					
$1s^2 2s^2 p^6 3s^2 p^6 d^{10} 4s^2 p^6 d^{10} 5s^2 p^4$					
α			hP3	α-Se	1.330
β		>4.0	mP4	β-Te	
γ		>6.6	oP4		
δ		>10.6	hR1	β-Po	
ε		>27	cI2	W	
Po 84 $V_{at}=38.14$ Å^3 at 311 K					
$1s^2 2s^2 p^6 3s^2 p^6 d^{10} 4s^2 p^6 d^{10} f^{14} 5s^2 p^6 d^{10} 6s^2 p^4$					
α			cP1	α-Po	
β	>327		hR1	β-Po	

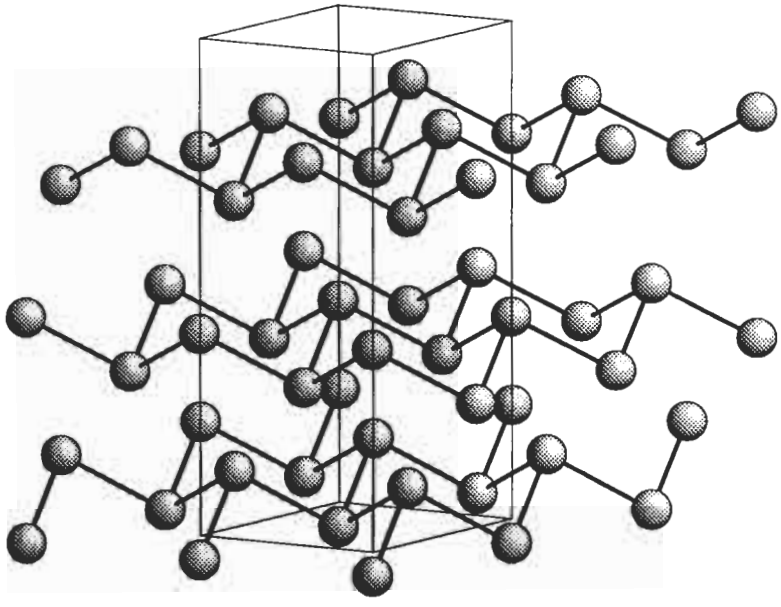

Fig. 31. The structure of hR2–As, space group $R\bar{3}m$, No. 166, 6c 0 0 0.277.

Table 13
Intralayer (d_1) and interlayer (d_2) distances in α-As-type layer structures, γ-Se-type helix structures and primitive cubic α-Po (PEARSON[1972]).

Element	Distance d_1	Distance d_2	d_2/d_1
α-As	2.51 Å	3.15 Å	1.25
α-Sb	2.87 Å	3.37 Å	1.17
α-Bi	3.10 Å	3.47 Å	1.12
γ-Se	2.32 Å	3.46 Å	1.49
γ-Te	2.86 Å	3.46 Å	1.31
α-Po	3.37 Å	3.37 Å	1.00

References: p. 45.

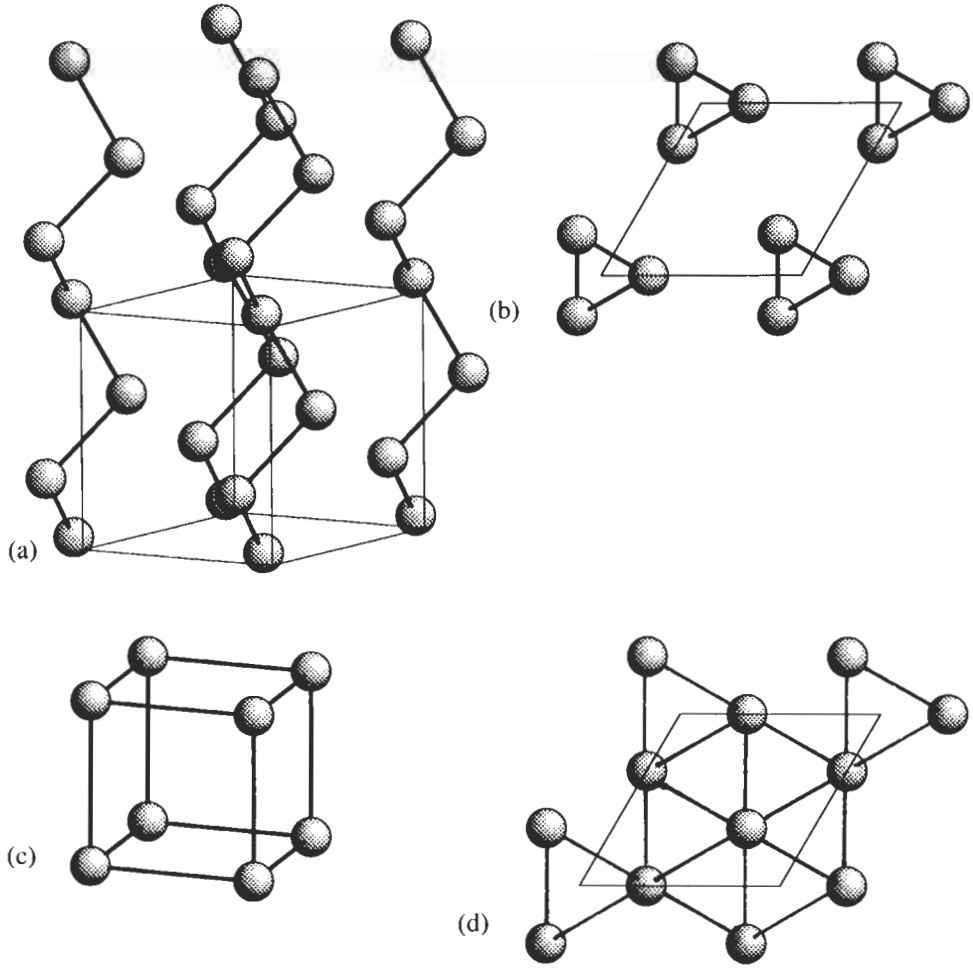

Fig. 32. (a) The structure of hP3–Se, space group $P3_121$, No. 152, 3a 0.237 0 ⅓, and (b) its projection upon (001) compared with (c) one unit cell of cP1–Po, space group $Pm\bar{3}m$, No. 221, 1a 0 0 0, and (d) its projection along [111]. The hexagonal outline of the projected cubic unit cell is drawn in.

Table 14

Structure information for the lanthanides and actinides. In the first line of each box the chemical symbol, atomic number Z, and the atomic volume V_{at} under ambient conditions is listed. In the second line the electronic ground state configuration is given. For each phase there is tabulated: limiting temperature T[K] and pressure P[GPa], Pearson symbol PS, prototype structure PT, and, if applicable, the lattice parameter ratio *c/a*.

	T[K]	P[GPa]	PS	PT	*c/a*
Ce 58 $V_{at}=34.72$ Å^3					
$1s^2 2s^2 p^6 3s^2 p^6 d^{10} 4s^2 p^6 d^{10} f^2 5s^2 p^6 6s^2$					
α	<96		cF4	Cu	
β			hP4	α-La	2×1.611
γ	>326		cF4	Cu	
δ	>999		cI2	W	
α'		>5.1	oC4	α-U?	
ε		>12.2	tI2	In	
Pr 59 $V_{at}=35.08$ Å^3					
$1s^2 2s^2 p^6 3s^2 p^6 d^{10} 4s^2 p^6 d^{10} f^3 5s^2 p^6 6s^2$					
α			hP4	α-La	2×1.611
β	>1068		cI2	W	
γ		>3.8	cF4	Cu	
δ		>6.2	hp6	Pr	3×1.622
ε		>20	oC4	α-U	
Nd 60 $V_{at}=34.17$ Å^3					
$1s^2 2s^2 p^6 3s^2 p^6 d^{10} 4s^2 p^6 d^{10} f^4 5s^2 p^6 6s^2$					
α			hP4	α-La	2×1.612
β	>1136		cI2	W	
γ		>5.8	cF4	Cu	
δ		>18	hp6	Pr	3×1.611
ε		>38	mC4	?	
Pm 61 $V_{at}=33.60$ Å^3					
$1s^2 2s^2 p^6 3s^2 p^6 d^{10} 4s^2 p^6 d^{10} f^5 5s^2 p^6 6s^2$					
α			hP4	α-La	2×1.60
β	>1163		cI2	W	
γ		>10	cF4	Cu	
δ		>18	hp6	Pr	
ε		>40	?		

	T[K]	P[GPa]	PS	PT	*c/a*
Th 90 $V_{at}=32.87$ Å^3					
$...3s^2 p^6 d^{10} 4s^2 p^6 d^{10} f^{14} 5s^2 p^6 d^{10} 6s^2 p^6 d^2 7s^2$					
α			cF4	Cu	
β	>1633		cI2	W	
Pa 91 $V_{at}=25.21$ Å^3					
$...3s^2 p^6 d^{10} 4s^2 p^6 d^{10} f^{14} 5s^2 p^6 d^{10} f^2 6s^2 p^6 d^1 7s^2$					
α			tI2	α-Pa	0.825
β	>1443		cI2	W	
U 92 $V_{at}=20.75$ Å^3					
$...3s^2 p^6 d^{10} 4s^2 p^6 d^{10} f^{14} 5s^2 p^6 d^{10} f^3 6s^2 p^6 d^1 7s^2$					
α			oC4	α-U	
β	>941		tP30	β-U	
γ	>1049		cI2	W	
Np 93 $V_{at}=19.21$ Å^3					
$...3s^2 p^6 d^{10} 4s^2 p^6 d^{10} f^{14} 5s^2 p^6 d^{10} f^5 6s^2 p^6 7s^2$					
α			oP8	α-Np	
β	>553		tP4	β-Np	0.694
γ	>849		cI2	W	

Continued on next page

Table 14—*Continued*

	T[K]	P[GPa]	PS	PT	*c/a*
Sm 62 $V_{at}=33.17$ Å^3					
$1s^2 2s^2 p^6 3s^2 p^6 d^{10} 4s^2 p^6 d^{10} f^6 5s^2 p^6 6s^2$					
α			hR3	α-Sm	4.5×1.605
β	> 1007		hP2	Mg	1.596
γ	> 1195		cI2	W	
δ		> 4.5	hP4	α-La	2×1.611
ε		> 14	cF4	Cu	
ζ		> 19	hp6	Pr	3×1.611
θ		> 33	mC4	?	
Eu 63 $V_{at}=48.10$ Å^3					
$1s^2 2s^2 p^6 3s^2 p^6 d^{10} 4s^2 p^6 d^{10} f^7 5s^2 p^6 6s^2$					
α			cI2	W	
β		> 12.5	hP2	Mg	1.553
γ		> 18	?		
Gd 64 $V_{at}=33.04$ Å^3					
$1s^2 2s^2 p^6 3s^2 p^6 d^{10} 4s^2 p^6 d^{10} f^7 5s^2 p^6 5d^1 6s^2$					
α			hP2	Mg	1.591
β	> 1508		cI2	W	
γ		> 2.0	hR3	α-Sm	4.5×1.61
δ		> 5	hP4	α-La	2×1.624
ε		> 25	cF4	Cu	
ζ		> 36	hp6	Pr	
Tb 65 $V_{at}=32.04$ Å^3					
$1s^2 2s^2 p^6 3s^2 p^6 d^{10} 4s^2 p^6 d^{10} f^9 5s^2 p^6 6s^2$					
α	< 220		oC4	α'-Dy	
α'			hP2	Mg	1.580
β	> 1562		cI2	W	
γ		> 3.0	hR3	α-Sm	4.5×1.60
δ		> 6.0	hP4	α-La	
ε		> 29	cF4	Cu	
ζ		> 32	hp6	Pr	3×1.616

	T[K]	P[GPa]	PS	PT	*c/a*
Pu 94 $V_{at}=19.88$ Å^3					
$...3s^2 p^6 d^{10} 4s^2 p^6 d^{10} f^{14} 5s^2 p^6 d^{10} f^6 6s^2 p^6 7s^2$					
α			mP16	α-Pu	
β	> 388		mC34	β-Pu	
γ	> 488		oF8	γ-Pu	
δ	> 583		cF4	Cu	
δ'	> 725		tI2	In	1.342
ε	> 756		cI2	W	
ζ		> 40.0	hP8		1.657/2
Am 95 $V_{at}=29.27$ Å^3					
$...3s^2 p^6 d^{10} 4s^2 p^6 d^{10} f^{14} 5s^2 p^6 d^{10} f^7 6s^2 p^6 7s^2$					
α			hP4	α-La	2×1.621
β	> 1042 or > 5		cF4	Cu	
γ	> 1350		cI2	W	
δ		> 12.5	mP4	δ-Am	
ε		> 15	oC4	α-U	
Cm 96 $V_{at}=29.98$ Å^3					
$...3s^2 p^6 d^{10} 4s^2 p^6 d^{10} f^{14} 5s^2 p^6 d^{10} f^7 6s^2 p^6 d^1 7s^2$					
α			hP4	α-La	2×1.621
β	> 1550 or > 23		cF4	Cu	
γ		> 43	oC4	α-U	
Bk 97 $V_{at}=27.96$ Å^3					
$...3s^2 p^6 d^{10} 4s^2 p^6 d^{10} f^{14} 5s^2 p^6 d^{10} f^8 6s^2 p^6 d^1 7s^2$					
α			hP4	α-La	2×1.620
β	> 1250 or > 8		cF4	Cu	
γ		> 25	oC4	α-U	

Continued on next page

Table 14—*Continued*

	T[K]	P[GPa]	PS	PT	*c/a*
Dy 66 $V_{at}=31.57$ Å^3					
$1s^2 2s^2 p^6 3s^2 p^6 d^{10} 4s^2 p^6 d^{10} f^{10} 5s^2 p^6 6s^2$					
α'	< 86		oC4	α'-Dy	
α			hP2	Mg	1.573
β	> 1654		cI2	W	
γ		> 5.0	hR3	α-Sm	4.5×1.606
δ		> 9.0	hP4	α-La	
ε		> 38	cF4	Cu	
Ho 67 $V_{at}=31.12$ Å^3					
$1s^2 2s^2 p^6 3s^2 p^6 d^{10} 4s^2 p^6 d^{10} f^{11} 5s^2 p^6 6s^2$					
α			hP2	Mg	1.570
β	> 1660		cI2	W	
γ		> 7.0	hR3	α-Sm	4.5×1.63
δ		> 13	hP4	α-La	
Er 68 $V_{at}=30.65$ Å^3					
$1s^2 2s^2 p^6 3s^2 p^6 d^{10} 4s^2 p^6 d^{10} f^{12} 5s^2 p^6 6s^2$					
α			hP2	Mg	1.569
β		> 7.0	hR3	α-Sm	
γ		> 13	hP4	α-La	
Tm 69 $V_{at}=30.10$ Å^3					
$1s^2 2s^2 p^6 3s^2 p^6 d^{10} 4s^2 p^6 d^{10} f^{13} 5s^2 p^6 6s^2$					
α			hP2	Mg	1.570
β	> 1800		cI2	W	
γ		> 9	hR3	α-Sm	
δ		> 13	hP4	α-La	4.5×1.57
Yb 70 $V_{at}=41.24$ Å^3					
$1s^2 2s^2 p^6 3s^2 p^6 d^{10} 4s^2 p^6 d^{10} f^{14} 5s^2 p^6 6s^2$					
α	< 270 or	> 34	hP2	Mg	1.646
β			cF4	Cu	
γ	> 1047 or	> 3.5	cI2	W	
Lu 71 $V_{at}=29.52$ Å^3					
$1s^2 2s^2 p^6 3s^2 p^6 d^{10} 4s^2 p^6 d^{10} f^{14} 5s^2 p^6 d^1 6s^2$					
			hP2	Mg	1.583
β		> 18	hR3	α-Sm	4.5×1.52
γ		> 35	hP4	α-La	

	T[K]	P[GPa]	PS	PT	*c/a*
Cf 98 $V_{at}=27.41$ Å^3					
$...3s^2 p^6 d^{10} 4s^2 p^6 d^{10} f^{14} 5s^2 p^6 d^{10} f^{10} 6s^2 p^6 7s^2$					
α			hP4	α-La	2×1.625
β	> 863 or	> 17	cF4	Cu	
γ		> 30	aP4	γ-Cf	
δ		> 41	oC4	α-U	
Es 99					
$...3s^2 p^6 d^{10} 4s^2 p^6 d^{10} f^{14} 5s^2 p^6 d^{10} f^{11} 6s^2 p^6 7s^2$					
α			hP4	α-La	
β	?		cF4	Cu	
Fm 100					
$...3s^2 p^6 d^{10} 4s^2 p^6 d^{10} f^{14} 5s^2 p^6 d^{10} f^{12} 6s^2 p^6 7s^2$					
Md 101					
$...3s^2 p^6 d^{10} 4s^2 p^6 d^{10} f^{14} 5s^2 p^6 d^{10} f^{13} 6s^2 p^6 7s^2$					
No 102					
$...3s^2 p^6 d^{10} 4s^2 p^6 d^{10} f^{14} 5s^2 p^6 d^{10} f^{14} 6s^2 p^6 7s^2$					
Lr 103					
$...3s^2 p^6 d^{10} 4s^2 p^6 d^{10} f^{14} 5s^2 p^6 d^{10} f^{14} 6s^2 p^6 d^1 7s^2$					

References: p. 45.

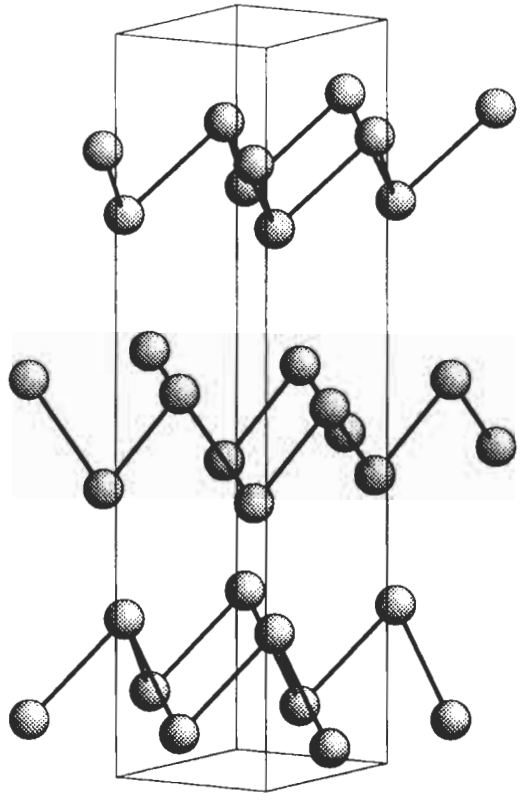

Fig. 33. The structure of hP6–Pr, space group $P3_121$, No. 152, 6c 0.28 0.28 0.772.

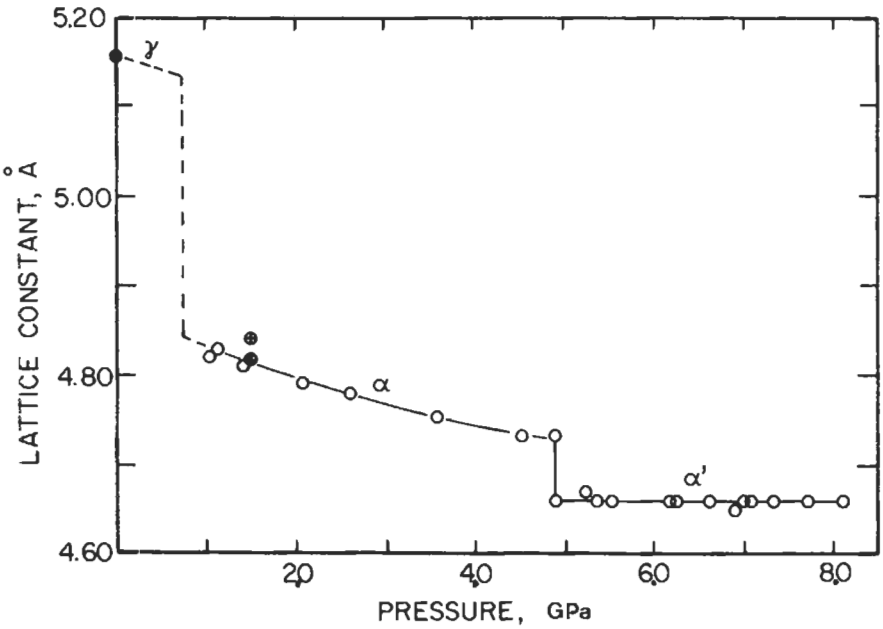

Fig. 34. Pressure dependence of the atomic volume of cerium (from DONOHUE [1974]).

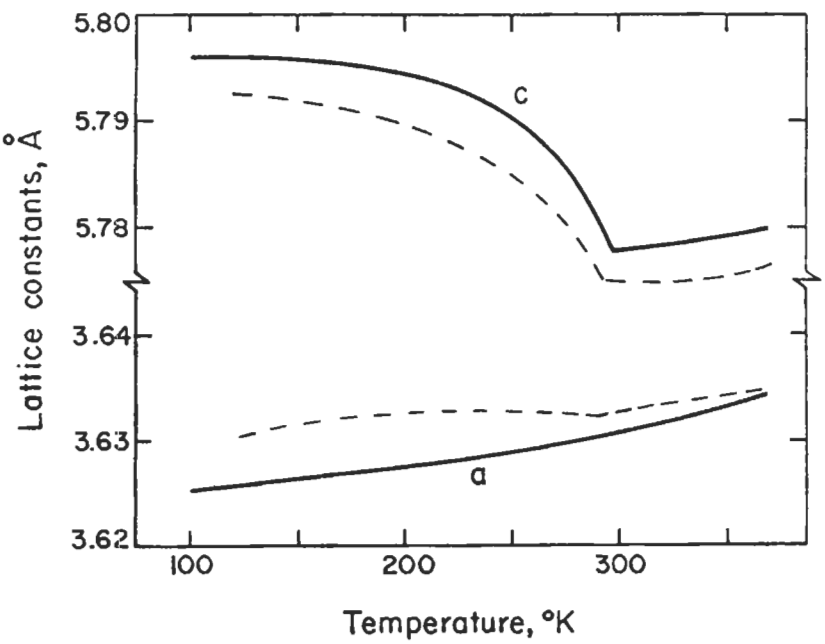

Fig. 35. Variation of the lattice parameters of gadolinium with temperature. There are no structural changes in this temperature range (from DONOHUE [1974]).

References: p. 45.

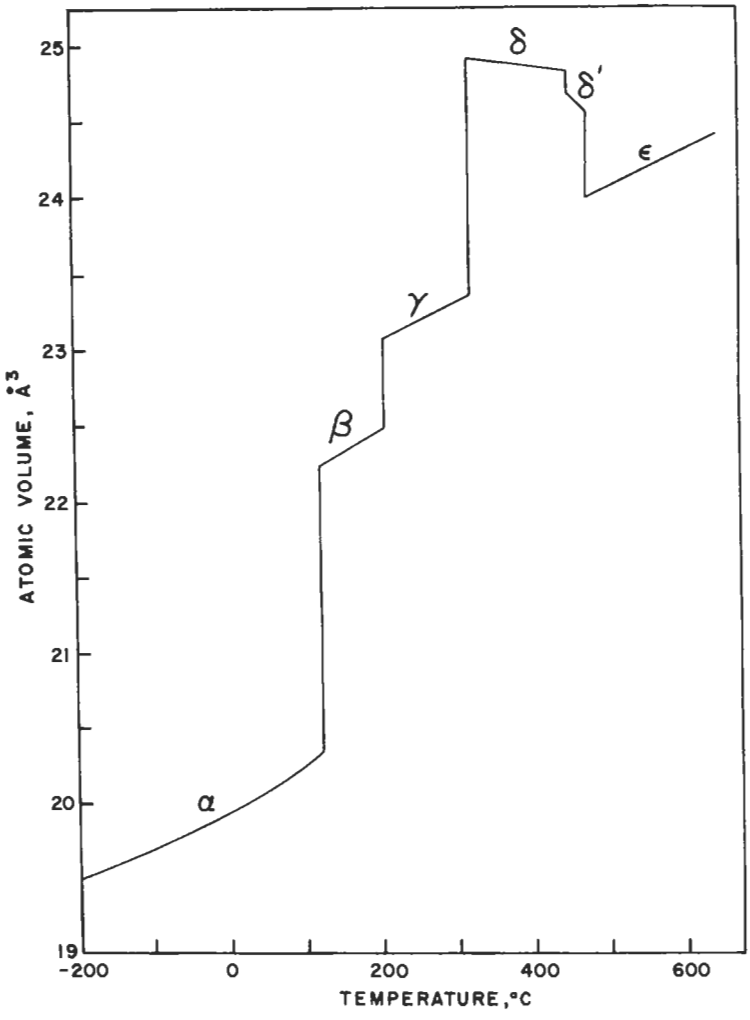

Fig. 36. The variation of the atomic volume of the various allotropes of plutonium with temperature (from DONOHUE [1974]).

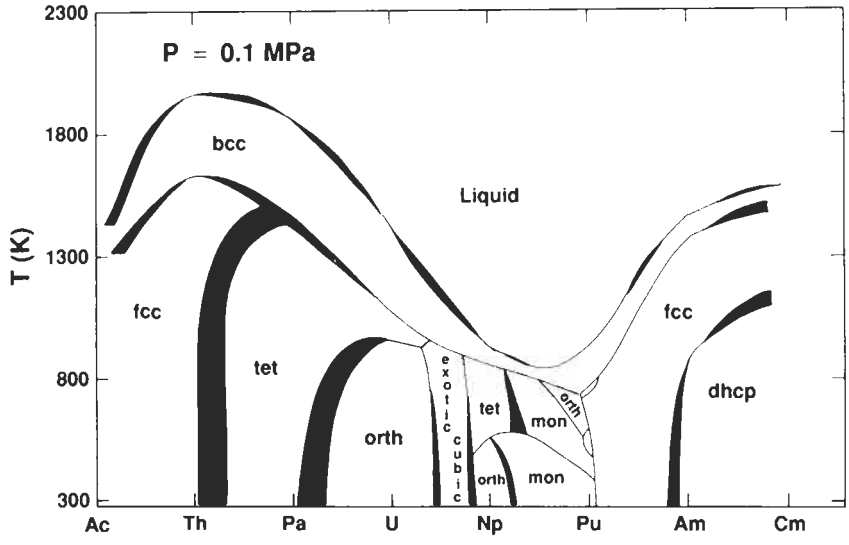

Fig. 37. Combined binary alloy phase diagrams for the light actinides (from YOUNG [1991]).

Acknowledgements

The author would like to express his sincere gratitude to Mss. M. Krichel for the preparation of the structure plots.

References

AHUJA, R., J.M. WILLS, B. JOHANSSON and O. ERIKSSON, 1993, Phys. Rev. **B48**, 16269–79.

BORCHARDT-OTT, W., 1993, Kristallographie (Springer Verlag, Berlin).

BRUNNER, G.O., and D. SCHWARZENBACH, 1971, Z. Kristallogr. **133**, 127–133.

DAAMS, J.L.C., P. VILLARS and J.H.N. VAN VUCHT, 1991, Atlas of Crystal Structure Types for Intermetallic Phases (American Society for Metals, USA), Vols. 1 to 4.

DAAMS, J.L.C., J.H.N. VAN VUCHT and P. VILLARS, 1992, J. Alloys and Compounds **182**, 1–33.

DABOS-SEIGNON, S., J.P. DANCAUSSE, E. GERING, S. HEATHMAN and U. BENEDICT, 1993, J.Alloys and Compounds **190**, 237–242.

DONOHUE, J., 1974, The structures of the elements (John Wiley & Sons, New York).

EK, J. VAN, P.A. STERNE and A. GONIS, 1993, Phys. Rev. **B48**, 16280–9.

HAHN, T. (ed.), 1992, International Tables for Crystallography, Vol. A (Kluwer Academic Publishers, Dordrecht).

KOCH, E. and W. FISCHER, 1992, Sphere packings and packings of ellipsoids. In: International Tables for Crystallography, ed. by A.J.C.Wilson (Kluwer Academic Publishers, Dordrecht).

LEIGH, G.J. (ed.), 1990, Nomenclature of Inorganic Chemistry. Recommendations 1990 (Blackwell Scientific Publications, Oxford).

MASSALSKI, T.B., 1990, Binary Alloy Phase Diagrams, Vols. 1–3, (ASM International, USA).

PEARSON, W. B., 1972, The Crystal Chemistry and Physics of Metals and Alloys (Wiley-Interscience, New-York).
SCHULTE, O., and W. B. HOLZAPFEL, 1993, Phys.Rev. **B48,** 14009–12.
SKRIVER, H. L., 1985, Phys.Rev. **B31,** 1909–23.
VAINSHTEIN, B. K., V. M. FRIDKIN and V. L. INDENBOM, 1982, Modern Crystallography II: Structure of Crystals (Springer-Verlag, Berlin).
VILLARS, P. and L. D. CALVERT, 1991, Pearson's Handbook of Crystallographic Data for Intermetallic Phases (American Society for Metals, USA), Vols. 1 to 4.
YOUNG, D. A., 1991, Phase Diagrams of the Elements (University of California Press, Berkeley).

Further reading

BARRETT, C. S., and T. B. MASSALSKI, 1980, Structure of Metals, 3rd edition (Pergamon Press, Oxford).
BOER, F. R. DE, R. BOOM, W. C. M. MATTENS, A. R. MIEDEMA and A. K. NIESSEN, 1988, Cohesion in Metals (North-Holland, Amsterdam).
HAFNER, J., F. HULLIGER, W. B. JENSEN, J. A. MAJEWSKI, K. MATHIS, P. VILLARS and P. VOGL, 1989, The Structure of Binary Compounds. (North-Holland, Amsterdam).
PETTIFOR, D. G., 1993, Electron Theory of Crystal Structure, in: Structure of Solids, ed. V. Gerold, Volume 1 of *Materials Science and Technology* (VCH, Weinheim).
VAINSHTEIN, B. K., 1994, Modern Crystallography I: Fundamentals of Crystals (Springer-Verlag, Berlin).

CHAPTER 2

ELECTRON THEORY OF METALS

D. G. PETTIFOR

Department of Materials
University of Oxford
Oxford, UK

R. W. Cahn and P. Haasen†, eds.
Physical Metallurgy; fourth, revised and enhanced edition

1. Introduction

The bulk properties of a metal depend directly on the bonding between the constituent atoms at the *microscopic* level. Thus, in order to provide a fundamental description of metals and alloys, it is necessary to understand the behaviour of the valence electrons which bind the atoms together. The theory which describes the electrons in metals is couched, however, in a conceptual framework that is very different from our everyday experience, since the microscopic world of electrons is governed by *quantum* mechanics rather than the more familiar *classical* mechanics of Newton. Rather than solving Newton's laws of motion the solid state theorist solves the Schrödinger equation,

$$\left(-\frac{\hbar^2}{2m}\nabla^2 + v(\boldsymbol{r})\right)\psi(\boldsymbol{r}) = E\psi(\boldsymbol{r}), \tag{1}$$

where $\nabla^2 = \partial^2/\partial x^2 + \partial^2/\partial y^2 + \partial^2/\partial z^2$, m is the electronic mass and $\hbar$ is the ubiquitous Planck constant (divided by 2π). $-(\hbar^2/2m)\,\nabla^2$ represents the *kinetic* energy and $v(\boldsymbol{r})$ the *potential* felt by the electron which has *total* energy E. $\psi(\boldsymbol{r})$ is the wave function of the electron where $|\psi(\boldsymbol{r})|^2$ is the probability density of finding the electron at some point $\boldsymbol{r} = (x, y, z)$. The power of the Schrödinger equation is illustrated by solving eq. (1) for the case of a single hydrogenic atom. It is found that solutions exist only if the wave function ψ is characterized by three distinct quantum numbers n, l and m whose significance has been discussed at the beginning of the preceding chapter. A fourth quantum number, m_s, representing the spin of the electron results from a relativistic extension of the Schrödinger equation. Thus, the existence of different orbital shells and hence the chemistry of the Periodic Table follows naturally from quantum mechanics through the Schrödinger equation.

WIGNER and SEITZ [1933] were the first to apply the Schrödinger equation to the problem of bonding in metals. In their classic paper they studied the formation of the bond in *monovalent* sodium and obtained the cohesive energy, equilibrium lattice constant, and bulk modulus to within 10% of the experimental values. However, it took nearly another fifty years before the same accuracy was achieved for the *polyvalent* metals. Whereas WIGNER and SEITZ [1933] could assume that the single valence electron on a sodium atom feels only the potential due to the ion core, in a polyvalent metal a given electron will also feel the strong coulomb repulsion from other valence electrons in its vicinity. Thus the problem becomes much more complex. Firstly, the potential $v(\boldsymbol{r})$ must be computed *self-consistently* in that $v(\boldsymbol{r})$ now depends on the coulomb field of valence electrons whose wave functions and hence average charge distributions themselves depend on $v(\boldsymbol{r})$ through eq. (1). Secondly, it is necessary in order to obtain bonding to go beyond the *average* self-consistent field of the Hartree approximation and to include the correlations between the electrons. Pauli's exclusion principle keeps *parallel* spin electrons apart, thereby lessening their mutual coulomb repulsion and lowering the energy by an amount called the *exchange* energy. These *statistical* correlations are described by the Hartree-Fock approximation. In addition, *dynamical* correlations also exist between the anti-parallel spin electrons, which lower the energy of the

system by an amount called the *correlation* energy.

A major breakthrough in solid-state physics occurred with the realization that these very complicated exchange and correlation effects could be accurately modeled by adding a simple local exchange correlation potential $v_{xc}(r)$ to the usual Hartree coulomb potential

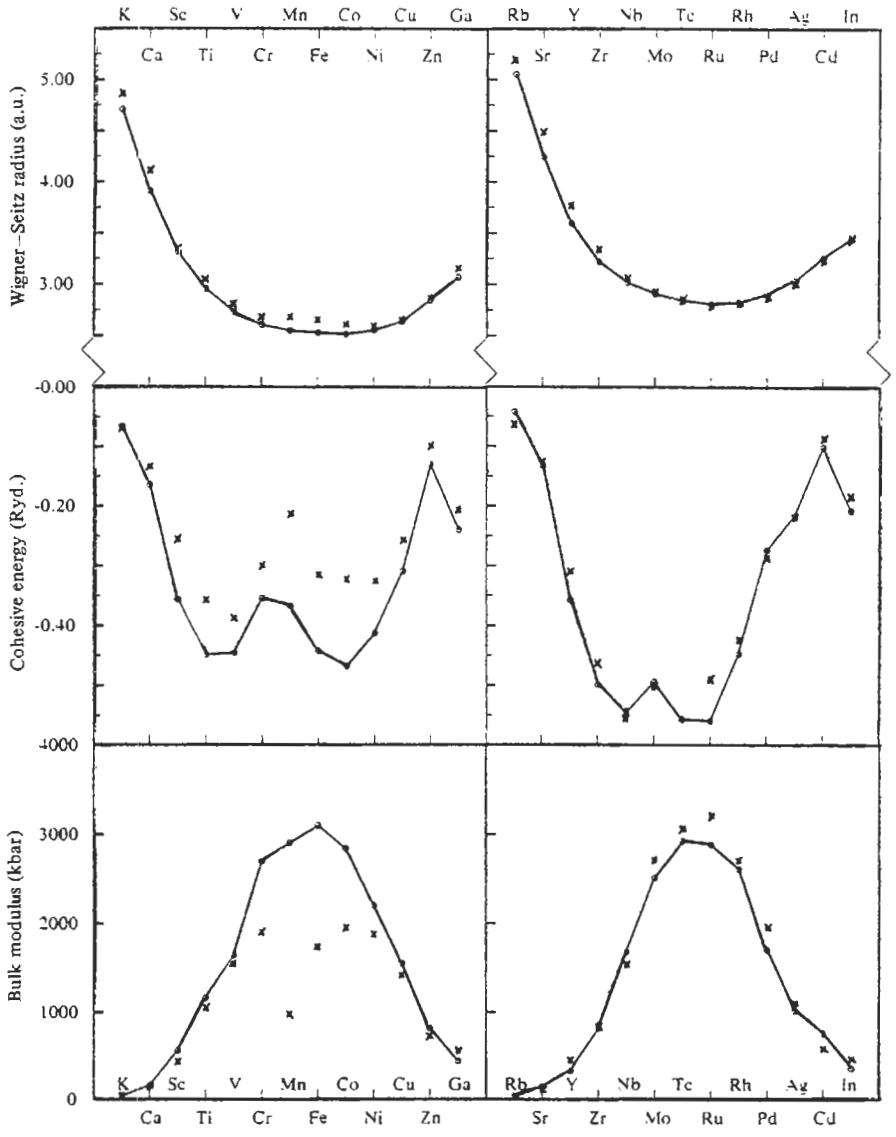

Fig. 1. The equilibrium Wigner–Seitz radii, cohesive energies, and bulk moduli of the 3d and 4d transition series. Experimental values are indicated by crosses and the computed LDF values by the connected points. (From MORUZZI *et al.* [1978].)

References: p. 129.

in eq. (1). The resulting so-called *local density functional* (LDF) equations (HOHENBERG and KOHN [1964] and KOHN and SHAM [1965]) have been shown to yield a surprisingly good description of the energetics of atoms, molecules, and solids (GUNNARSSON and LUNDQUIST [1976], HARRIS and JONES [1978], MORUZZI *et al.* [1978], JONES and GUNNARSSON [1989] and FINNIS [1992]). The success of the LDF scheme is illustrated in fig. 1 by the results of MORUZZI *et al.* [1978] for the cohesive properties of the elemental metals across the 3d and 4d transition series. We see that for the nonmagnetic 4d series the equilibrium Wigner–Seitz radius (or lattice constant), cohesive energy and bulk modulus are given to better than 10%. The large deviations in lattice constant and bulk modulus observed amongst the 3d series is due to the presence of magnetism and is removed by generalizing the LDF theory to include spin polarization (JANAK and WILLIAMS [1976]). It must be stressed that there are no arbitrary parameters in the theory, the only input being the nuclear charge and crystal structure.

This success of the LDF theory in describing the bonding between atoms allows the interpretation of the results within a *band* framework, since the motion of a given electron is governed by the *one-electron* Schrödinger equation (1). As is well-known, the energy levels, E, of the free atom broaden out into bands of states as the atoms are brought together to form the solid. In this chapter the nature of these energy bands in simple metals, transition metals and binary alloys is discussed, thereby unraveling the microscopic origin of the attractive and repulsive forces in the metallic bond. In § 2.1 we begin with a detailed description of the constituent atoms, since we will see that many bulk properties are related to the relative position of the atomic energy levels and to the size of the ionic cores. In § 2.2 the diatomic molecule is used to illustrate *bond* formation and in § 2.3 the general principle of *band* formation in solids is outlined. The nature of *simple-* and *transition*-metal bands is then discussed in §§ 3 and 4 respectively, the former being treated within the nearly-free-electron approximation, the latter within the tight-binding approximation. In § 5 the knowledge of the energy band behaviour is used to provide a microscopic picture of metallic bonding which is responsible for the cohesive properties of the elemental metals displayed in fig. 1. In § 6 *structural* stability is discussed both in the elemental metals and in binary intermetallic phases. In § 7 the ideas on metallic bonding are extended to a discussion of the *heats of formation*, ΔH, of binary alloys. Finally in § 8 the band theory of *magnetism* is presented which accounts for the antiferromagnetism of Cr and Mn and the ferromagnetism of Fe, Co, and Ni amongst the 3d transition metals.

2. *Band formation*

2.1. The constituent atoms

The hundred basic building blocks of nature, which are enshrined in the Periodic Table, lead to matter having a wide range and variety of physical properties. This diversity reflects the essential uniqueness of each element in the Periodic Table. For example, even though copper, silver and gold lie in the same noble-metal group, nobody except possibly a theoretician would be prepared to regard them as identical. In this

subsection the differences between the elements are *quantified* by discussing the behaviour of the atomic energy levels and the radii throughout the Periodic Table.

The structure of the Periodic Table results from the filling-up of different orbital shells with electrons, as outlined in the previous chapter. The chemical behaviour of a given atom is governed by both the *number* and the *angular-momentum* character of the electrons in the outer partially filled shells. (We shall refer to these electrons as *valence* in contrast to the filled shells of *core* electrons.) The angular-momentum character is determined by the orbital quantum number l, since the *magnitude* of the total orbital angular momentum $\boldsymbol{L}$ is given by quantum theory as:

$$L = \hbar\sqrt{l(l+1)}, \tag{2}$$

where l = 0, 1, 2,... A free-atom electron can, therefore, take only *discrete* values of angular momentum (i.e. 0, $\hbar\sqrt{2}$, $\hbar\sqrt{6}$,...) unlike a classical particle which would have a *continuous* spectrum. However, as in the classical case, the angular momentum is *conserved* because the electron is moving in the central spherically symmetric potential of the free atom. Electrons with l = 0, 1, 2 and 3 orbital quantum numbers are referred to as s, p, d and f electrons, respectively (after the old terminology of sharp, principal, diffuse and fine spectroscopic lines).

Angular momentum is a vector. Therefore, in addition to the *magnitude* L of the orbital angular momentum $\boldsymbol{L}$, the electronic state is also characterized by the *components* of the angular momentum. Within quantum theory the component in a given direction (say along the z-axis, specified experimentally by the direction of a very weak applied magnetic field) is quantized and given by

$$L_z = m\hbar, \tag{3}$$

where the magnetic quantum number, m, takes the $(2l+1)$ values 0, ± 1,..., ± $(l-1)$, ± l. Because the *energy* of the electron can not depend on the direction of the angular momentum in a spherically symmetric potential, these $(2l+1)$ states have the same energy and are said to be *degenerate*. Allowing for the additional *spin* quantum number, m^s, which can take two values (corresponding to an up, ↑, or down, ↓, spin electron), each l-state will be $2(2l+1)$-fold degenerate. Thus an s-shell can hold 2 electrons, a p-shell 6 electrons, a d-shell 10 electrons and an f-shell 14 electrons as discussed in ch. 2, § 1.

The state of angular momentum of the electron determines the *angular dependence* of the wave function ψ and hence the angular dependence of the probability-density $|\psi|^2$. The s-state has zero orbital angular momentum corresponding to a spherically symmetric probability density which is illustrated schematically in fig. 2a. The p-state, corresponding to $l=1$, $m=0$, has an angular variation given by $\cos\theta$, where is the polar angle. Because the Cartesian coordinates (x, y, z) can be related to the spherical polar coordinates (r, θ, ϕ), and in particular $z = r\cos\theta$, it is customary to refer to the $l=1$, $m=0$ state as the p_z *orbital*. Its probability-cloud is illustrated by the left-hand diagram in fig. 2b. We see that it has lobes pointing out along the z-axis, in which direction there is a maximum probability of finding the electron ($\cos^2\theta = 1$ for $\theta = 0, \pi$). On the other

References: p. 129.

hand, there is zero probability of finding the electron in the x–y plane ($\cos^2\theta = 0$ for $\theta = \pi/2$). Since we often deal with atoms in a *cubic* environment in which all three Cartesian axes are equivalent (e.g., fcc or bcc crystals), we form the p_x and p_y orbitals by taking linear combinations of the two remaining states corresponding to $m = +1$. They are illustrated in fig. 2b. The probability clouds of the five d orbitals corresponding to $l = 2$ are shown in fig. 2c. We might expect from fig. 2 that the nature of the bonding between atoms will be very dependent on the angular momentum character of the atomic valence electrons. This will be discussed in § 2.2.

Historically it was the discrete lines of the atomic spectra and their ordering according to Balmer's formula that led Bohr to postulate his famous model of the hydrogen atom from which he deduced that the *energy* levels were given by

$$E_n = -\left(me^4 / 32\pi^2\varepsilon_0^2\hbar^2\right) / n^2, \tag{4}$$

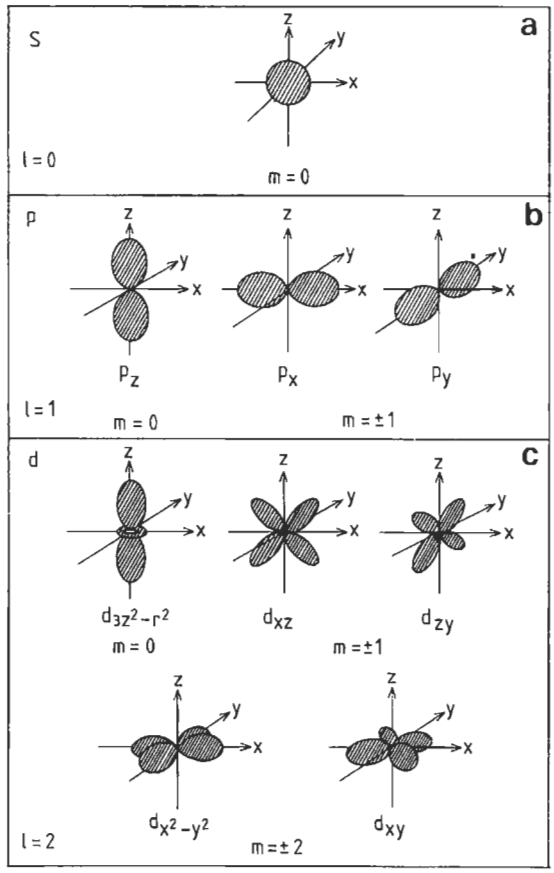

Fig. 2. The probability clouds corresponding to s, p and d orbitals are shown in (a), (b) and (c), respectively.

where e is the magnitude of the electronic charge, ε_0 is the permittivity of free space, and n is a positive integer. The corresponding radii of the so-called stationary orbits were given by

$$a_n = \left(4\pi\varepsilon_0\hbar^2 / me^2\right)n^2. \tag{5}$$

Substituting into eqs. (4) and (5) the SI values $m = 9.1096 \times 10^{-31}$ kg, $e = 1.6022 \times 10^{-19}$ C, $4\pi\varepsilon_0 c^2 = 10^7$, $c = 2.9979 \times 10^8$ m/s and $\hbar = 1.0546 \times 10^{-34}$ Js, we have:

$$E_n = 2.1799 \times 10^{-18} / n^2 \quad \text{J} \tag{6}$$

and

$$a_n = n^2 \text{ au}. \tag{7}$$

The *ground state* of the hydrogen atom, which corresponds to $n = 1$, has an energy, therefore, of 2.18×10^{-18} J and an orbital Bohr radius of 0.529×10^{-10} m or 0.529 Å. Because of the small magnitude of the energy in SI units, it is customary for solid-state physicists to work in *atomic units,* where the unit of energy is the Rydberg (Ry) and the unit of length is the atomic unit (au). The former is the ground-state energy of the hydrogen atom, the latter is the first Bohr radius. Thus, in atomic units we have

$$E_n = -n^{-2} \text{ Ry} \tag{8}$$

and

$$a_n = n^2 \text{ au}. \tag{9}$$

It follows from eqs. (4), (5), (8) and (9) that $\hbar^2/2m = 1$ in atomic units. Another frequently used unit is the electron-Volt, where 1 Ry = 13.6 eV. In this chapter *electronic* energy levels, *E,* will be given in either eV or Ry, whereas *total* energies will be given in either eV/atom or Ry/atom. Conversion to other units may be achieved by using 1 mRy/atom = 0.314 kcal/mole = 1.32 kJ/mole. Length scales will be given either in au or in Å, where 1 au = 0.529 Å.

Solution of the Schrödinger equation (1) for the hydrogen atom leads directly to Bohr's expression *(4)* for the energy levels, E_n, where n is identified as the *principal* quantum number. For the particular case of the hydrogen atom where the potential $v(r)$ varies inversely with distance r from the nucleus, the energy levels do not depend on the angular-momentum quantum numbers l and m. Figure 3 shows the energy levels of atomic *hydrogen* given by eq. (8), where use has been made of the quantum-theory result that for a given n the orbital quantum number I must be such that $0 \leq l \leq (n - 1)$. The total degeneracy of each orbital including spin, namely $2(2l + 1)$, is given at the bottom of the figure and accounts for the structure of the Periodic Table, discussed in the previous chapter. In practice, the energy-level diagram of elements other than hydrogen is different from fig. 3, because the presence of more than one electron outside the nucleus leads to the potential $v(r)$ no longer showing a simple inverse distance behaviour, so that states with the same principal quantum number n but different orbital quantum

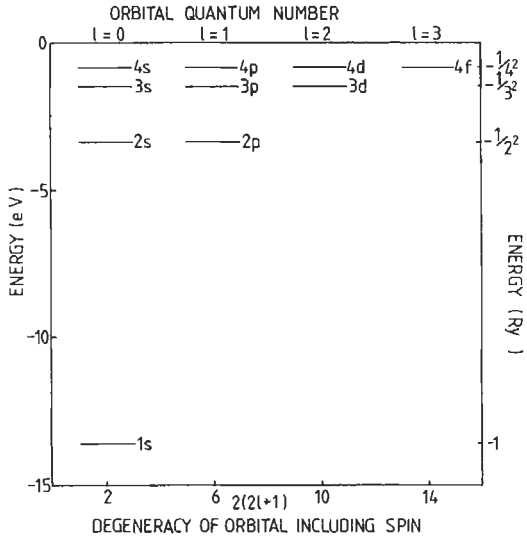

Fig. 3. The energy levels of atomic hydrogen.

numbers l have their degeneracy lifted. This is illustrated in fig. 4, where it is clear, for example, that the 2s level of the second-row elements B to Ne lies well below that of the corresponding 2p level. These atomic energy levels were taken from the tables compiled by HERMAN and SKILLMAN [1963] who solved the Schrödinger equation (1) self-consistently for all the elements in the Periodic Table.

Figure 4 illustrates several important features to which we will be returning throughout this chapter. Firstly, the valence energy levels vary *linearly across* a given period. As

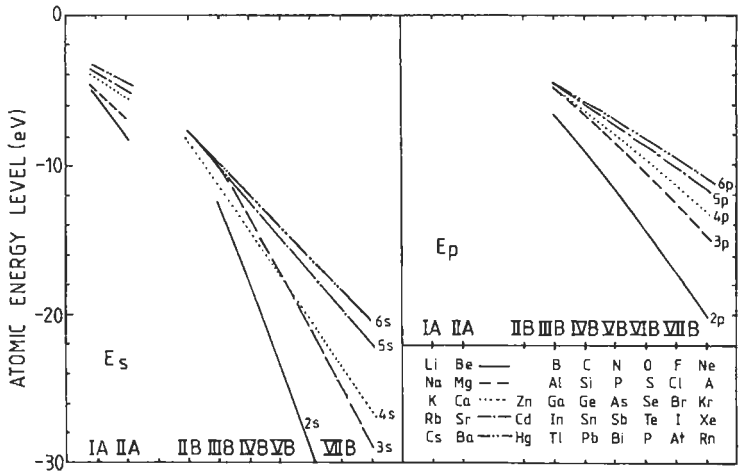

Fig. 4. The valence s and p energy levels (after HERMAN AND SKILLMAN [1963]).

the nuclear charge Ze increases, the electrons are bound more tightly to the nucleus. However, rather than varying as Z^2, which would be the result for the energy levels of a hydrogenic ion of charge Ze, the presence of the other valence electrons induces the linear behaviour observed. Secondly, the valence s and p energy levels become less strongly bound as one moves *down* a given group, which is to be expected from the hydrogenic energy levels displayed in fig. 3. But there is an exception to this rule: the 4s level has come down and crosses below the 3s level to the left of group VB. This is a direct consequence of the presence of the occupied 3d shell (cf. table 2, ch. 2) whose electrons do not completely screen the core from the valence 4s electrons, which therefore feel a more attractive potential than their 3s counterparts in the preceding row. We will see in § 6.2 that this reversal in the expected ordering of the valence s energy levels is reflected in the structural properties of binary AB compounds containing group IIIB elements. Thirdly, it is clear from fig. 4 that the energy *difference* $E_p - E_s$ decreases as one goes from the rare gases to the alkali metals, from right to left across a given period. This will strongly influence the nature of the energy bands and the bonding in the bulk, since if the energy difference is small, s and p electrons will hybridize to form common sp bands.

Figure 5 shows the valence s and d energy levels across the 3d and 4d transition metal series, after HERMAN and SKILLMAN [1963]. The energy levels correspond to the atomic configuration $d^{N-1}s$, where N is the total number of valence electrons, because this is the configuration closest to that of the bulk metal. Again there are several important features. Firstly, we see that the energy variation is *linear across* the transition metal series as the d shell is progressively filled with electrons. However, once the noble metal group IB is reached the d shell contains its full complement of ten electrons, so that any further increase in atomic number Z adds the additional valence electrons to the

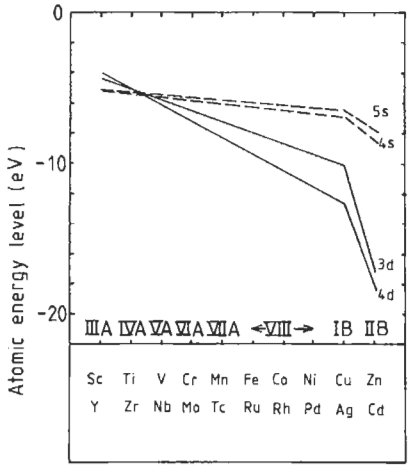

Fig. 5. The valence s and d energy levels across the 3d and 4d transition series (after HERMAN AND SKILLMAN [1963]).

sp outer shell and pulls the d energy rapidly down as is evidenced by the change of slope in fig. 5. Secondly, whereas the *valence* s energy level becomes slightly less strongly bound as one moves *down* a given group, the valence 4d energy level becomes more strongly bound than the valence 3d away from the beginning of the transition-metal series. This behaviour appears to be related to the mutual coulomb repulsion between the negatively charged valence electrons. The 3d orbitals are much more compact than the 4d orbitals, so that the putting of electrons into the 3d shell leads to a more rapid increase in repulsive energy than in the 4d shell. The Sd and 6s energy levels have not been plotted in fig. 5 because *relativistic* effects, which are not included in the Schrödinger equation (1), become important for *heavy* atoms in the Periodic Table. Relativistic corrections are discussed in ch. 2 of HERMAN and SKILLMAN [1963]. Thirdly, since $E_s - E_d$ is about 3 eV in copper but 6 eV in silver, it is not surprising that the noble metals display different physical characteristics.

A concept that is often used in physical metallurgy to discuss and order properties is that of *atomic size.* The microscopic description of the atom, which is provided by quantum mechanics, should be able to give some measure of this quantity. We have seen that quantum mechanics replaces the stationary Bohr *orbits* of radius a_n by orbitals which are not located with a fixed radius but are smeared out in probability-clouds described by $|\psi|^2$. The angular dependence of these probability-clouds has been displayed in fig. 2. We now discuss their radial dependence.

The solution of the Schrödinger equation for a central spherically symmetric potential can be written in separable form, namely:

$$\psi_{nlm}(\boldsymbol{r}) = R_{nl}(r)Y_l^m(\theta, \phi), \tag{10}$$

where r, θ and ϕ are spherical polar coordinates. As expected, the *angular* distribution depends only on the angular-momentum quantum numbers l and m, the functions $Y_l^m(\theta\ \phi)$ being the so-called *spherical harmonics* (see, e.g., SCHIFF [1968]). Y_0^0 is a constant and Y_1^0 is proportional to $\cos\theta$ as we have already mentioned. The *radial* function $R_{nl}(r)$ depends on the principal and orbital quantum numbers, n and l respectively, and therefore changes with energy level E_{nl}. For the hydrogen atom the first few radial functions are (in atomic units)

$$R_{1s}(r) = 2e^{-r}, \tag{11}$$

$$R_{2s}(r) = \frac{1}{\sqrt{2}}\left(1 - \tfrac{1}{2}r\right)e^{-r/2}, \tag{12}$$

$$R_{2p}(r) = \frac{1}{\sqrt{24}}re^{-r/2}. \tag{13}$$

A conceptually useful quantity is the probability of finding the electron at some distance r from the nucleus (in any direction), which is determined by the *radial probability density,* $P_{nl}(r) = r^2R_{nl}^2(r)$.

Figure 6 shows the radial function R_{nl} and the probability density, P_{nl}, as a function

of r for the 1s, 2s and 2p states of hydrogen. We see that there is *maximum* probability of locating the electron at the first Bohr radius a_1 for the 1s state and at the second Bohr radius a_2 for the 2p state. The *average* or expectation value of the radial distance r is given by:

$$\bar{r}_{nl} = n^2\left[1 + \tfrac{1}{2}\left(1 - l(l+1)/n^2\right)\right], \tag{14}$$

so that $\bar{r}_{1s} = 1.5a_1$, $\bar{r}_{2s} = 1.5a_2$ and $\bar{r}_{2p} = 1.25a_2$. Therefore, the 2s orbital is more extended than the corresponding 2p orbital, as is evident from fig. 6. This is due to the fact that all solutions of the Schrödinger equation must be *orthogonal* to one another, i.e., if ψ_{nlm} and $\psi_{n'l'm'}$ are any two solutions and ψ^* is the complex conjugate of ψ, then

$$\int \psi^*_{nlm}\psi_{n'l'm'}\, d\boldsymbol{r} = 0. \tag{15}$$

If the states have *different* angular-momentum character then the angular integration over the spherical harmonics [cf. (eq. 10)] guarantees orthogonality. But if the states have the *same* angular-momentum character then the orthogonality constraint implies that:

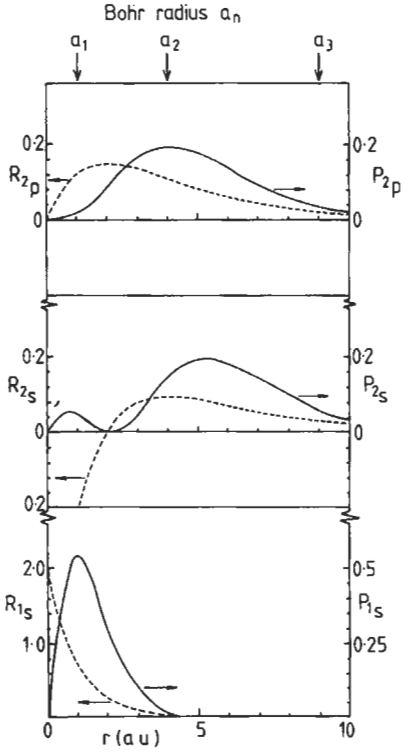

Fig. 6. The radial function R_{nl} (dashed lines) and the probability density, P_{nl} (solid lines) as a function of r for the 1s, 2s and 2p states of hydrogen.

References: p. 129.

$$\int_0^\infty R_{nl}(r)\, R_{n'l}(r) r^2\, dr = 0. \tag{16}$$

For the orbitals drawn in fig. 6, therefore, we must have

$$\int_0^\infty R_{1s}(r)\, R_{2s}(r) r^2\, dr = 0, \tag{17}$$

which can be verified by substituting eqs. (11) and (12) into this equation. This is the origin of the *node* at $r=2$ au in $R_{2s}(r)$, where the radial function changes sign. The 3s radial function must be orthogonal to the 2s and, therefore, has two nodes, the 4s has three nodes, etc. Just as the energetically lowest I s state has *no* nodes, so the 2p, 3d and 4f states are nodeless since they correspond to the states of lowest energy for a given l (see fig. 3).

The position of the outer node of the *valence* electron's radial function may be used as a measure of an l-dependent core size, since we have seen that the node arises from the constraint that the valence state be orthogonal to the more tightly bound core states. This relationship between node and core size has been demonstrated quantitatively for the case of the sp core of the 4d transition metals (PETTIFOR [1977] and § 4.3) and has been discussed for other elements by BLOCH and SCHATTEMAN [1981]. A not unrelated measure of size has been adopted by ZUNGER [1980] who defined l-dependent radii R_l by the condition (cf. ST. JOHN and BLOCH [1974]) that

$$v_l^{\text{eff}}(R_l) = 0, \tag{18}$$

where $v_l^{\text{eff}}(r)$ is some effective angular-momentum dependent atomic potential (which is given by a first-principles screened pseudopotential, cf. § 3.3). Figure 7 shows the resultant values of $-R_s^{-1}$ and $-R_p^{-1}$ for the sp bonded elements. We see a *linear* variation across a given period and a close similarity with the valence energy level behaviour

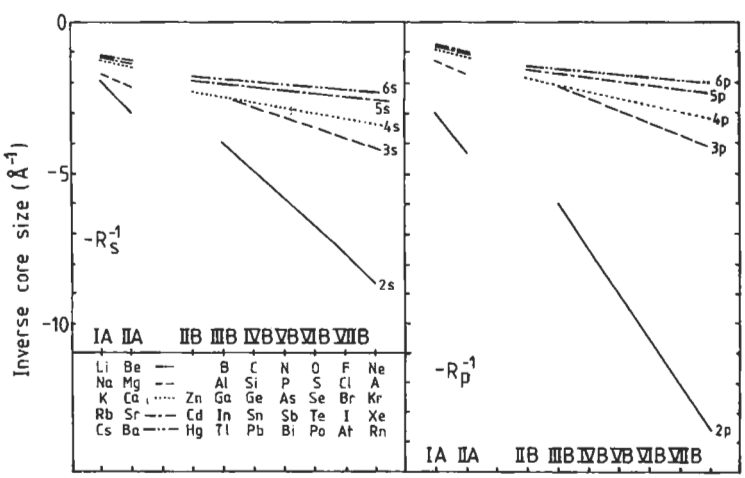

Fig. 7. The negative of the inverse s and p pseudopotential radii (after ZUNGER [1980]).

illustrated in fig. 4. As expected, the s and p radii contract *across* a period as the nuclear charge Ze increases, and they expand *down* a column as additional full orbital shells are pulled into the core region. Figure 7 clearly demonstrates that the sizes of the second-row elements B, C, N and O are a lot smaller than those of the other elements in their respective groups, a fact which manifests itself in their different alloying behaviour (cf. fig. 38, below).

2.2. Bond formation

In this subsection we consider what happens to the atomic energy levels and wave functions as two atoms A and B are brought together from infinity to form the AB diatomic molecule.

Suppose the A and B valence electrons are characterized by the free atomic energy levels E_A and E_B and wave functions ψ_A and ψ_B, respectively. Let us assume, following the experience of theoretical quantum chemists, that the *molecular* wave function ψ_{AB} can be written as a *linear combination of the atomic orbitals*,

$$\psi_{AB} = c_A\psi_A + c_B\psi_B, \tag{19}$$

where c_A and c_B are constant coefficients. Then it follows from the Schrödinger eq. (1) that

$$(\hat{H} - E)(c_A\psi_A + c_B\psi_B) = 0 \tag{20}$$

where $\hat{H}$ is the Hamiltonian operator for the AB dimer, namely $\hat{H} = -\nabla^2 + V_{AB}$ where we have used the fact that $\hbar^2/2m = 1$ in atomic units. Multiplying by ψ_A (or ψ_B) and integrating over all space we find the well-known secular equation (taking $\psi^* = \psi$ as ψ is real)

$$\begin{bmatrix} H_{AA} - E & H_{AB} - ES_{AB} \\ H_{BA} - ES_{BA} & H_{BB} - E \end{bmatrix} \begin{bmatrix} c_A \\ c_B \end{bmatrix} = 0 \tag{21}$$

where the Hamiltonian and overlap matrix elements are given by

$$H_{\alpha\beta} = \int \psi_\alpha \hat{H} \psi_\beta \, \mathrm{d}\boldsymbol{r} \tag{22}$$

and

$$S_{\alpha\beta} = \int \psi_\alpha \psi_\beta \, \mathrm{d}\boldsymbol{r}. \tag{23}$$

The Hamiltonian matrix elements can be simplified by assuming that the molecular potential V_{AB} is given by the sum of the free atom potentials V_A and V_B. The *diagonal* elements H_{AA} and H_{BB} then take the free atom values E_A and E_B respectively, provided the energy shift due to the neighbouring potential fields can be neglected. The *off-diagonal* element H_{AB} can be written

$$H_{AB} = \int \psi_A \overline{V} \psi_B \, \mathrm{d}\boldsymbol{r} + \overline{E}S \tag{24}$$

References: p. 129.

where $\bar{E} = \frac{1}{2}(E_A + E_B)$, $\bar{V} = \frac{1}{2}(V_A + V_B)$, and $S = S_{AB}$. Substituting in equation (21) we obtain the secular equation

$$\begin{bmatrix} -\frac{1}{2}\Delta E - (E - \bar{E}) & h - (E - \bar{E})S \\ h - (E - \bar{E})S & \frac{1}{2}\Delta E - (E - \bar{E}) \end{bmatrix} \begin{bmatrix} c_A \\ c_B \end{bmatrix} = 0 \tag{25}$$

where $\Delta E = (E_B - E_A)$ is the *atomic energy level mismatch* and $h = \int \psi_A \bar{V} \psi_B \, d\boldsymbol{r}$ is the hopping or *bond integral* between atoms A and B. For s orbitals h is negative since the average potential $\bar{V}$ is attractive.

Equation (25) may be solved for the eigenvalues and eigenvectors. To first order in the overlap integral S

$$E_{AB}^{\pm} = \bar{E} - hS \pm (1 + \delta^2)^{1/2} h \tag{26}$$

and

$$\psi_{AB}^{\pm} = c_A^{\pm} \psi_A + c_B^{\pm} \psi_B \tag{27}$$

where

$$c_A^{\pm} = \frac{1}{\sqrt{2}} \left[1 \pm (\delta - S) / (1 + \delta^2)^{1/2} \right]^{1/2} \tag{28}$$

$$c_B^{\pm} = \pm \frac{1}{\sqrt{2}} \left[1 \mp (\delta + S) / (1 + \delta^2)^{1/2} \right]^{1/2} \tag{29}$$

with $\delta = \Delta E / 2|h|$. Therefore, as shown in Fig. 8 s valent diatomic molecules are characterized by bonding and anti-bonding states which are separated in energy by the amount ω_{AB} such that

$$\omega_{AB}^2 = 4h^2 + (\Delta E)^2. \tag{30}$$

The formation of the bond is accompanied by a redistribution of the electronic charge. It follows from equation (27) that the electronic density which corresponds to occupying the bonding state with two valence electrons of opposite spin, namely $\rho_{AB} = 2(\psi_{AB}^{*})^2$ may be written in the form

$$\rho_{AB}(\boldsymbol{r}) = (1 + \alpha_i)\rho_A(\boldsymbol{r}) + (1 - \alpha_i)\rho_B(\boldsymbol{r}) + \alpha_c \rho_{bond}(\boldsymbol{r}) \tag{31}$$

where

$$\rho_{A(B)}(\boldsymbol{r}) = \left[\psi_{A(B)}(\boldsymbol{r}) \right]^2 \tag{31a}$$

and

$$\rho_{bond}(\boldsymbol{r}) = 2\psi_A(\boldsymbol{r})\psi_B(\boldsymbol{r}) - S[\rho_A(\boldsymbol{r}) + \rho_B(\boldsymbol{r})]. \tag{32}$$

α_i and α_c are determined by the normalised energy level mismatch δ through

$$\alpha_i = \delta/\left(1+\delta^2\right)^{1/2} \tag{33}$$

and

$$\alpha_c = 1/\left(1+\delta^2\right)^{1/2}. \tag{34}$$

For the case of *homonuclear* diatomic molecules $\delta = 0$, so that the change in the electronic charge distribution on forming the molecule is given solely by the *bond charge* contribution ρ_{bond} in equation (31). This is illustrated in fig. 9 for the case of the hydrogen molecule where we see that, as expected, the electronic charge has moved from the outer regions of the molecule into the bond region between the atoms. We should note from equations (32) and (23) that the total charge associated with ρ_{bond} over all space is identically zero. Equation (32) shows explicitly that the formation of the bond is a *quantum* interference effect, the charge piling up in the bond region because of the interference contribution $\psi_A\,\psi_B$. In practice, in order to satisfy the virial theorem, the formation of the bond is accompanied by some modification of the free-atom orbitals $\psi_{A,B}$, which has been discussed by RUEDENBERG [1962] and SLATER [1963]. This leads to the energy levels $E_{A,B}$ not being directly identifiable as the *free*-atom energy levels, a point which will be discussed further in § 5.2 on transition-metal bonding.

For the case of a *heteronuclear* diatomic molecule $\delta \neq 0$, so that the electronic charge distribution in equation (31) contains the *ionic* contributions $\alpha_i \rho_A$ and $-\alpha_i \rho_B$ in addition to

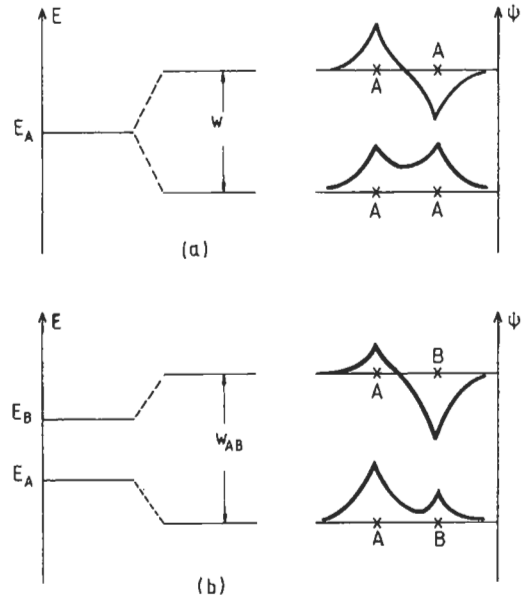

Fig. 8. The bonding (lower lines) and antibonding (upper lines) states for (a) the homonuclear and (b) the heteronuclear diatomic molecule.

the *covalent* bond charge contribution $\alpha_c \rho_{bond}$. α_i and α_c are said to measure the degree of ionicity and covalency of the bond (see, for example, COULSON *et al.* [1962], PHILIPS [1970] and HARRISON [1980]). Note that $\alpha_i^2 + \alpha_c^2 = 1$.

The term covalency will be used in this chapter to describe the bonding which arises from the *quantum* mixing of *valence* states on neighbouring sites into the final state wave function. It is not necessarily associated with *pairs* of electrons of opposite spin, as the lone electron in the hydrogen molecular ion H_2^+, for example, shows all the characteristics of the covalent homonuclear bond discussed above.

A diatomic molecule has cylindrical symmetry about the internuclear axis, so that angular momentum is conserved in this direction. Quantum-mechanically this implies that the state of the molecule is characterized by the quantum number m, where $m\hbar$ gives the component of the angular momentum along the molecular axis. However, unlike the free atom where the $(2l+1)$ different m values are degenerate, the degeneracy is lifted in the molecule. By analogy with the s, p, d, ... states of a free atom representing the orbital quantum numbers $l=0, 1, 2, \ldots$, it is customary to refer to σ, π, δ, ... states of a molecule as those corresponding to $m=0, \pm1, \pm2, \ldots$ respectively.

Figure 10 illustrates the different characteristics of the σ, π and δ bonds. We have seen from our previous discussion on the homonuclear molecule that a given atomic energy level will split into bonding and antibonding states separated by $2|h|$, where h is the matrix element that couples states ψ_A and ψ_B together through the atomic potential

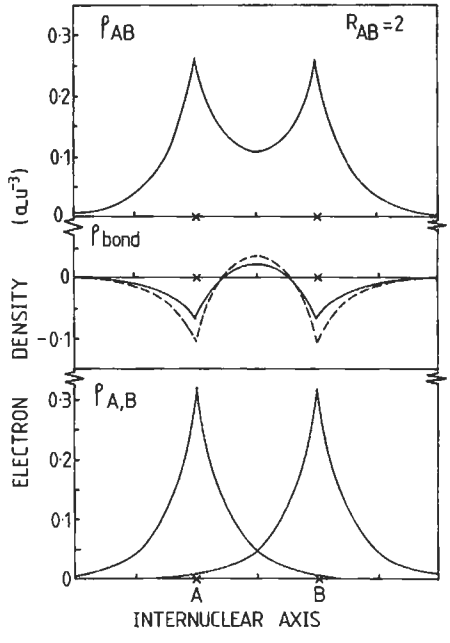

Fig. 9. The electron density of the homonuclear molecule (upper panel) can be regarded as the sum of the *non-interacting* free-atom electron densities (lower panel) and the *quantum-mechanically* induced bond density (middle panel). The dashed curve represents the first-order result, eq. (32), for the bond density.

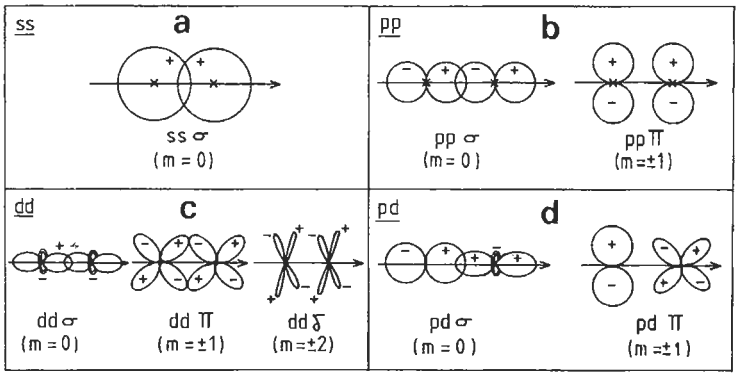

Fig. 10. The formation of σ, π and δ bonds from s, p and d orbitals, see text.

v. If $\psi_{A,B}$ are spherically symmetric s orbitals, then a ssσ bond is formed as shown schematically in fig. 10a. If $\psi_{A,B}$ are p orbitals whose probability clouds are drawn in fig. 2, then the threefold degenerate free atom level (excluding spin degeneracy) splits into the singly degenerate ppσ molecular state (m = 0) and the doubly degenerate ppπ molecular state (m = ±1) shown in fig. 10b. If $\psi_{A,B}$ are d orbitals, whose probability clouds are sketched in fig. 2, then the fivefold degenerate free atom level splits into the singly degenerate ddσ molecular state (m = 0) and the two doubly degenerate molecular states ddπ (m = ±1) and ddδ (m = ±2) as shown in fig. 10c. For the case of a heteronuclear molecule such as NbC where the carbon p orbitals overlap the niobium d orbitals, a pd bond will be formed from the pdσ and pdπ states illustrated in fig. 10d. It is clear from fig. 10 that the σ bond is relatively strong since the angular lobes point along the molecular axis and can give rise to a large overlap in the bonding region. On the other hand, the ppπ and ddδ bonds will be relatively much weaker since their angular lobes extend in the plane perpendicular to the molecular axis. The importance of σ, π and δ bonding in determining the behaviour of the *bulk* band structure will be demonstrated in § 4.1.

The term covalency will be used in this chapter to describe the bonding which arises from the *quantum* mixing of *valence* states on neighbouring sites into the final-state wave function. It is not necessarily associated with *pairs* of electrons of opposite spin, as the lone electron in the hydrogen molecular ion H_2^+, for example, shows all the characteristics of the covalent homonuclear bond discussed above.

2.3. Band formation

Figure 11 illustrates how the free-atom energy levels E_s and E_p broaden into *bands* as the atoms are brought together from infinity to form the bulk. Just as the single atomic energy level splits into two energy levels on bringing two atoms together (cf. fig. 8a), so the single level on a free atom splits into N levels on bringing N atoms together, thereby conserving the total number of electronic states. These levels lie between the bottom of the band, which represents the most bonding state, and the top of the band, which represents the most antibonding state. Since $N \approx 10^{23}$ for 1 cm^3 of bulk material, these N

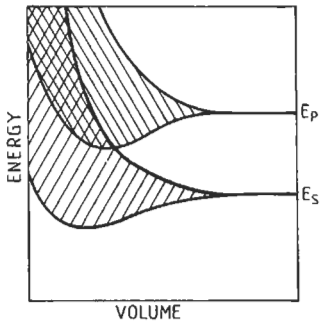

Fig. 11. Energy band formation.

levels form a quasi-continuous band of states and it is customary to work with the *density of states, n(E),* where $dN = n(E)\,dE$ gives the number of states in the energy range from E to $E + dE$. The conservation of states requires that:

$$\int_{-\infty}^{\infty} n_\alpha(E)\,dE = \begin{cases} 2 \\ 6 \\ 10 \end{cases} \quad \text{for } \alpha = \begin{cases} s \\ p, \\ d \end{cases} \tag{35}$$

where $n_\alpha(E)$ is the density of states *per atom* associated with a given atomic s, p or d level.

In metals at their equilibrium volume, the bands corresponding to different valence energy levels overlap and mix as shown on the left-hand side of fig. 11. The mixing or hybridization in *simple* metals is such as to produce *nearly-free-electron*-like behaviour of the energy bands and density of states, which is discussed in the following section. On the other hand, the density of states in *transition* metals is dominated by a well defined d band, which is accurately described within the *tight-binding* approximation by a linear combination of atomic d orbitals and is discussed in § 4.

3. *Simple-metal bands*

3.1. The free-electron approximation

It had been realized before the advent of quantum mechanics that some metallic properties such as electrical or thermal conductivity could be well understood by regarding the valence electrons as a non-interacting gas of particles which were *free* to travel throughout the metal without being affected by the parent ions. However, it remained for quantum mechanics to remove a striking failure of the classical model, namely its inability to explain the *linear* temperature dependence of the electronic heat capacity, since according to classical statistical mechanics a free particle has a *constant* heat capacity of $\frac{3}{2}$, where k_B is the Boltzmann constant.

The Schrödinger equation for a free-electron gas may be written in atomic units as

$$-\left(\frac{\partial^2}{\partial x^2}+\frac{\partial^2}{\partial y^2}+\frac{\partial^2}{\partial z^2}\right)\psi(\boldsymbol{r}) = E\psi(\boldsymbol{r}) \tag{36}$$

If the electrons are contained within a box of side L then a normalized solution of eq. (36) is the *plane wave:*

$$\psi_k(\boldsymbol{r}) = L^{-3/2}\ \mathrm{e}^{\mathrm{i}\boldsymbol{k}\cdot\boldsymbol{r}}, \tag{37}$$

which can be seen by writing $\boldsymbol{k}\bullet\boldsymbol{r}$ as $k_x x+k_y y+k_z z$ and substituting eq. (37) into eq. (36).

This solution corresponds to an electron with kinetic energy E given by:

$$E = k_x^2 + k_y^2 + k_z^2 = k^2. \tag{38}$$

Since the kinetic energy equals $p^2/2m$ where p is the electronic momentum, it follows from eq. (38) that

$$p^2 = 2mE = 2mk^2 = \hbar^2 k^2, \tag{39}$$

using $\hbar^2/2m = 1$. Thus, we have recovered the de Broglie relation

$$p = \hbar k = h/\lambda, \tag{40}$$

because $k = 2\pi/\lambda$ where λ is the wavelength of the plane wave.

The wavelength, λ, of the plane wave is constrained by *boundary conditions* at the surface of the box. For the case of the Bohr orbits in the hydrogen atom, de Broglie had argued that λ must be such that *integer* multiples of the wavelength fit around the circumference of the orbit. Similarly, imposing *periodic* boundary conditions on the box, which in one dimension corresponds to joining both ends in a closed ring, we have that

$$n_x\lambda_x = n_y\lambda_y = n_z\lambda_z = L, \tag{41}$$

where n_x, n_y, n_z are integers. Therefore,

$$\boldsymbol{k} = \frac{2\pi}{L}\left(n_x, n_y, n_z\right) \tag{42}$$

so that the allowed values of the wave vector $\boldsymbol{k}$ are discrete and fall on a fine mesh as illustrated in fig. 12.

By Pauli's exclusion principle each state corresponding to a given $\boldsymbol{k}$ can contain *two* electrons of opposite spin. Therefore, at absolute zero all the states $\boldsymbol{k}$ will be occupied within a sphere of radius k_F, the so-called *Fermi sphere,* because these correspond to the states of lowest energy (cf. fig. 13a). The Fermi wave vector k_F may be related to the total number of valence electrons, N, by

$$\tfrac{4}{3}\pi k_F^3 2V/(2\pi)^3 = N, \tag{43}$$

where $V = L^3$, since it follows from eq. (42) that unit volume of $\boldsymbol{k}$-space contains $V/(2\pi)^3$ states capable of holding two electrons each. Thus,

$$\boldsymbol{k}_F = \left(3\pi^2 N/V\right)^{1/3} \tag{44}$$

References: p. 129.

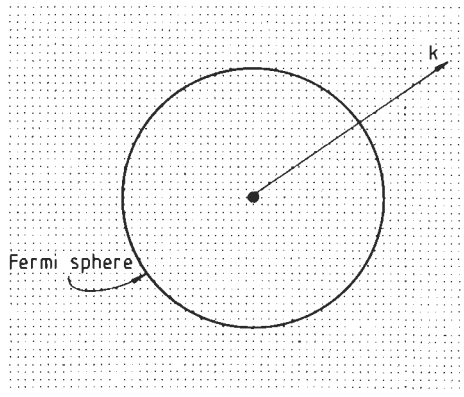

Fig. 12. The fine mesh of allowed $\boldsymbol{k}$ values. At absolute zero only the states $\boldsymbol{k}$ within the Fermi sphere are occupied.

and the corresponding *Fermi energy*, E_F is given by

$$E_F = \left(3\pi^2 N/V\right)^{2/3}. \tag{45}$$

The electron concentration, N/V, for sodium, magnesium and aluminium at their equilibrium atomic volumes is such that the Fermi energy E_F equals 3.2, 7.1 and 11.6 eV respectively.

The free-electron *density of states* $n(E)$ may be obtained from eq. (43) by writing it in the form

$$N(E) = \left(V/3\pi^2\right)E^{3/2}, \tag{46}$$

where $N(E)$ is the total number of states of both spins available with energies less than E. Differentiating eq. (46) with respect to the energy gives the density of states:

$$n(E) = \left(V/2\pi^2\right)E^{1/2}, \tag{47}$$

which is illustrated in fig. 13b. We can now see why the experimental electronic heat capacity did not obey the classical result of $\frac{3}{2}k_B$. By Pauli's exclusion principle the electrons can be excited only into the *unoccupied* states above the Fermi energy E_F.

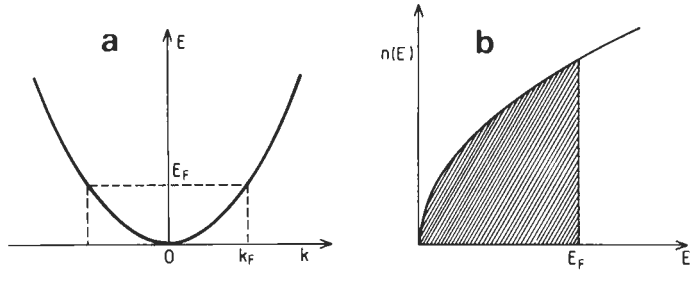

Fig. 13. The free-electron energy dispersion $E(\boldsymbol{k})$ (a) and density of states $n(E)$ (b).

Therefore, only those electrons within about $k_B T$ of E_F will have enough thermal energy to be excited across E_F. Since $k_B T \approx 0.03$ eV at room temperature, these electrons will comprise a very small fraction, $f \approx k_B T/E_F$, of the total number of electrons N. The classical heat capacity is accordingly reduced by this factor f, as is observed experimentally. Using the correct Fermi-Dirac statistics to describe the occupation of the electron states, we find (see, e.g., KITTEL [1971]):

$$C_V = \frac{\pi^2}{2} k_B (k_B T/E_F) \tag{48}$$

in agreement with the previous qualitative argument.

3.2. Nearly-free-electron approximation

The electrons in a real metal are affected by the *crystalline* lattice, since the potential which they feel is not uniform but varies *periodically* as

$$v(\boldsymbol{r} + \boldsymbol{R}) = v(\boldsymbol{r}) \tag{49}$$

where $\boldsymbol{R}$ is any lattice vector. (For simplicity we will be considering only those crystal structures, such as fcc or bcc, in which there is only *one* atom per primitive lattice site, in contrast to hcp or the diamond structure, for example, which have a basis of *two* atoms, cf. KITTEL [1971].) Consider first an infinite *one-dimensional* periodic lattice of atoms with repeat distance a such that

$$v(x + na) = v(x). \tag{50}$$

Because all the atoms are equivalent, the probability of locating the electron about a site must be the same for all sites, so that:

$$|\psi(x + na)|^2 = |\psi(x)|^2. \tag{51}$$

For $n = 1$ this implies that

$$\psi(x + a) = e^{ika}\psi(x), \tag{52}$$

where k is a number (in units of $1/a$) which specifies the *phase factor* e^{ika} linking the wave functions on neighbouring sites. Repeating eq. (52) n times gives:

$$\psi_k(x + na) = e^{ikna}\psi_k(x), \tag{53}$$

which is the usual statement of *Bloch's theorem* in one dimension. Thus the translational symmetry of the lattice leads to the eigenfunctions being characterized by the Bloch vector, k. However, k is only defined modulo $(2\pi/a)$, since $k + m(2\pi/a)$ results in the same phase factor in eq. (53) as k alone. It is, therefore, customary to label the wave function ψ_k by restricting k to lie within the *first Brillouin zone*, defined by

$$-\pi/a \leq k \leq +\pi/a. \tag{54}$$

We note that in one dimension na is a direct lattice vector, whereas $m(2\pi/a)$ is a *reciprocal* lattice vector. Their product is an integer multiple of 2π.

Extending these ideas to three dimensions, Bloch's theorem, eq. (53) may be written as:

$$\psi_k(\boldsymbol{r}+\boldsymbol{R}) = e^{i\boldsymbol{k}\cdot\boldsymbol{R}}\psi_k(\boldsymbol{r}), \tag{55}$$

where $\boldsymbol{R}$ is any *direct lattice* vector which may be expressed in terms of the fundamental translation vectors $\boldsymbol{a}_1$, $\boldsymbol{a}_2$, $\boldsymbol{a}_3$ as:

$$\boldsymbol{R} = n_1\boldsymbol{a}_2 + n_2\boldsymbol{a}_2 + n_3\boldsymbol{a}_3, \tag{56}$$

where n_1, n_2, n_3 are integers. The corresponding *reciprocal lattice* vectors are defined by:

$$\boldsymbol{G} = m_1\boldsymbol{b}_1 + m_2\boldsymbol{b}_2 + m_3\boldsymbol{b}_3, \tag{57}$$

where m_1, m_2, m_3 are integers and the fundamental basis vectors are:*

$$\left.\begin{aligned}\boldsymbol{b}_1 &= (2\pi/\tau)\boldsymbol{a}_2 \times \boldsymbol{a}_3\\ \boldsymbol{b}_2 &= (2\pi/\tau)\boldsymbol{a}_3 \times \boldsymbol{a}_1\\ \boldsymbol{b}_3 &= (2\pi/\tau)\boldsymbol{a}_1 \times \boldsymbol{a}_2\end{aligned}\right\}, \tag{58}$$

with $\tau = |\boldsymbol{a}_1\bullet(\boldsymbol{a}_2 \times \boldsymbol{a}_3)|$ being the volume of the primitive unit cell defined by $\boldsymbol{a}_1$, $\boldsymbol{a}_2$ and $\boldsymbol{a}_3$. It is apparent from their definition (58) that

$$\boldsymbol{a}_i \bullet \mathbf{b}_j = 2\pi\delta_{ij}, \tag{59}$$

where $\delta_{ij}=1$ for $i=j$ but zero otherwise.

The phase factor in eq. (55) only defines the Bloch vector within a reciprocal lattice vector $\boldsymbol{G}$ since it follows from eqs. (56)–(59) that $\boldsymbol{G}\bullet\boldsymbol{R}$ is an integer multiple of 2π. Just as in the one-dimensional case, it is customary to label the wave function ψ_k by restricting $\boldsymbol{k}$ to lie within the *first Brillouin zone* which is the closed volume about the origin in reciprocal space formed by bisecting near-neighbour reciprocal lattice vectors. For example, consider the *simple cubic* lattice with basis vectors $\boldsymbol{a}_1$, $\boldsymbol{a}_2$, $\boldsymbol{a}_3$ along the Cartesian axes x, y, z respectively. Because $a_1=a_2=a_3=a$ it follows from eq. (58) that the reciprocal space basis vectors $\boldsymbol{b}_1$, $\boldsymbol{b}_2$, $\boldsymbol{b}_3$ also lie along x, y and z respectively, but with magnitude $(2\pi/a)$. Thus, the reciprocal lattice is also simple cubic and it is shown in fig. 14 in the x–y plane. It is clear that the bisectors of the first nearest-neighbour (100) reciprocal lattice vectors form a closed volume about the origin which is not cut by the second or any further nearest-neighbour bisectors. Hence, the Brillouin zone is a cube of volume $(2\pi/a)^3$. From eq. (42) it contains as many allowed $\boldsymbol{k}$ points as there are primitive unit cells in the crystal. Figure 15 illustrates the corresponding Brillouin zones for the body-centred cubic and face-centred cubic lattices (see, e.g., KITTEL [1971]).

The solutions E_k of the Schrödinger equation for $\boldsymbol{k}$ lying within the Brillouin zone

* Note the additional factor of 2π compared to the definition of reciprocal lattice vectors in the appendix of ch. 11.

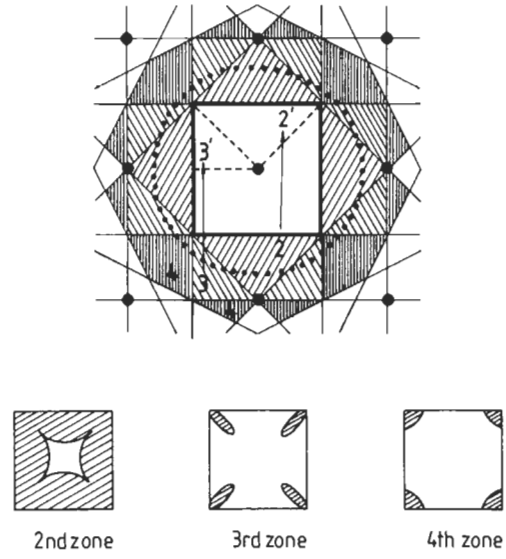

Fig. 14. The first four zones of the simple cubic lattice corresponding to $k_z = 0$. The dotted circle represents the cross-section of a spherical Fermi surface.

determine the *band structure*. Figure 16 shows the band structure of aluminium in the $|100\rangle$ and $|111\rangle$ directions, after MORUZZI *et al.* [1978]. It is very similar to the free-electron band structure

$$E_k = (\boldsymbol{k} + \boldsymbol{G})^2 \tag{60}$$

which results from folding the free-electron eigenvalues shown in fig. 13a into the first Brillouin zone. This "folding-in" is illustrated in fig. 14 for the case of the *simple cubic* lattice. For this two-dimensional cross-section we see that the four contributions to the second zone *2* may be translated through (100) reciprocal lattice vectors into the four

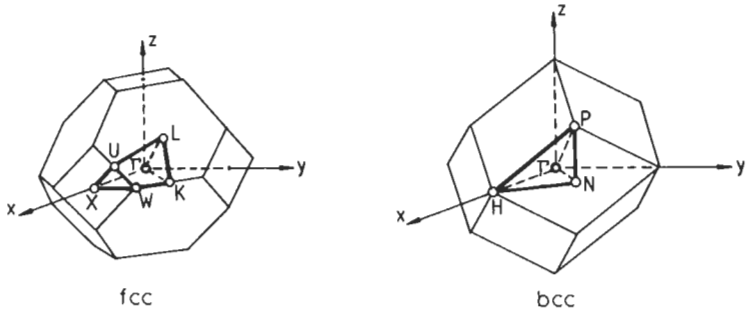

Fig. 15. The fcc and bcc Brillouin zones. Γ labels the centre of the zone. The intersections of the $|100\rangle$ and $|111\rangle$ directions with the Brillouin-zone boundary are labelled X and L in the fcc case and H and P in the bcc case.

zones 2′, which together completely fill the reduced Brillouin zone in the x–y plane. Similarly, the third and fourth zones shown in fig. 14 may each be translated through reciprocal lattice vectors to fill the first Brillouin zone. For the *fcc* lattice the two lowest eigenvalues given by eq. (60) in the $|100\rangle$ direction are:

$$E_k^{(1)} = k^2, \qquad E_k^{(2)} = (\boldsymbol{k}+\boldsymbol{g})^2, \tag{61}$$

where $\boldsymbol{k} = (k_x, 0, 0)$ and $\boldsymbol{g} = (2\pi/a)(\bar{2}, 0, 0)$. These two eigenvalues are degenerate at the zone boundary $\boldsymbol{X}$, where $\boldsymbol{k} = (2\pi/a)(1, 0, 0)$ because from eq. (61) they both take the value $4\pi^2/a^2$. For aluminium $a = 7.60$ au and $4\pi^2/a^2 = 9.3$ eV, so that the two free-electron eigenvalues given by eq. (61) reflect the broad behaviour of the band structure shown along ΓX in fig. 16.

However, in order to recover the *energy gap* at the zone boundary X, it is necessary to lift the free-electron degeneracy by perturbing the free-electron gas with the periodic potential of the crystalline lattice. Within the *nearly-free-electron* (NFE) approximation this is achieved by writing the wave function ψ_k as a linear combination of the plane-wave eigenfunctions corresponding to the two free-electron eigenvalues given by eq. (61); that is:

$$\psi_k = c_1\psi_k^{(1)} + c_2\psi_k^{(2)}, \tag{62}$$

where from eq. (37):

$$\psi_k^{(1)} = V^{-1/2}\exp(i\boldsymbol{k}\cdot\boldsymbol{r}), \tag{63}$$

$$\psi_k^{(2)} = V^{-1/2}\exp[i(\boldsymbol{k}+\boldsymbol{g})\cdot\boldsymbol{r}]. \tag{64}$$

Substituting eq. (62) into the Schrödinger equation (1), pre-multiplying by $\psi_k^{(1)*}$ or $\psi_k^{(2)*}$ and integrating over the volume of the crystal, V, yields the *NFE secular equation*:

$$\begin{pmatrix} k^2 - E & v(200) \\ v(200) & (\boldsymbol{k}+\boldsymbol{g})^2 - E \end{pmatrix}\begin{pmatrix} c_1 \\ c_2 \end{pmatrix} = 0. \tag{65}$$

$v(200)$ is the $(2\pi/a)(2, 0, 0)$ Fourier component of the crystalline potential, where

$$v(\boldsymbol{g}) = \frac{1}{V}\int v(\boldsymbol{r})\, e^{i\boldsymbol{g}\cdot\boldsymbol{r}}\, d\boldsymbol{r}. \tag{66}$$

The energy, E in eq. (65) is measured with respect to the average potential $v(000)$. Non-trivial solutions exist if the secular determinant vanishes, i.e. if

$$\begin{vmatrix} k^2 - E & v(200) \\ v(200) & (\boldsymbol{k}+\boldsymbol{g})^2 - E \end{vmatrix} = 0. \tag{67}$$

This quadratic equation has solutions

$$E_k = \tfrac{1}{2}\left[k^2 + (\boldsymbol{k}+\boldsymbol{g})^2\right] \pm \tfrac{1}{2}\left\{\left[(\boldsymbol{k}+\boldsymbol{g})^2 - k^2\right]^2 + \left[2v(200)\right]^2\right\}^{1/2}. \tag{68}$$

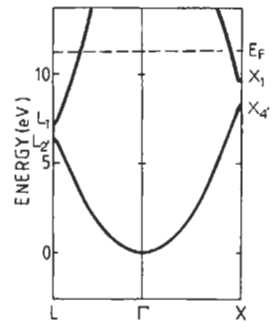

Fig. 16. The band structure of fcc aluminium (after MORUZZI *et al.* [1978]).

Therefore, at the zone boundary X where $k^2=(\boldsymbol{k}+\boldsymbol{g})^2$, the eigenvalues are given by

$$E_X = 4\pi^2/a^2 \pm v(200) \tag{69}$$

and the eigenfunctions are given from eqs. (62) and (65) by:

$$\psi_X = (2/V)^{1/2} \times \begin{cases} \cos(2\pi x/a) \\ \sin(2\pi x/a) \end{cases}. \tag{70}$$

Thus the presence of the periodic potential has opened up a gap in the free electron band structure with energy separation

$$E_{gap}^X = 2|v(200)|. \tag{71}$$

Because the energy gap at X in aluminium is about 1 eV (cf. fig. 16), the magnitude of the Fourier component of the potential within this simple NFE treatment is only 0.5 eV. This is small compared to the free-electron Fermi energy of more than 10 eV in aluminium and, therefore, the band structure E_k and the density of states $n(E)$ are nearly-free-electron-like to a very good approximation.

The NFE behaviour has been observed experimentally in studies of the *Fermi surface,* the surface of constant energy E_F in $\boldsymbol{k}$-space, which separates filled states from empty states at $T=0$. For a free-electron gas the Fermi surface is spherical as illustrated in fig. 12. However, in simple metals we have seen that the free-electron band structure is perturbed by the periodic lattice potential, and energy gaps open up across zone boundaries. As illustrated in fig. 14 for the simple cubic lattice, a spherical free-electron Fermi surface (whose cross-section is represented by the circle of solid dots) will be folded into the first Brillouin zone by the relevant reciprocal lattice vectors. The states in the second zone 2, for example, are folded back into 2′ in the reduced zone, thereby giving rise to the shaded occupied regions of $\boldsymbol{k}$-space and the corresponding Fermi surface indicated in the lower panel of fig. 14. Similarly, the occupied states in the third and fourth zones are folded back into the reduced Brillouin zone as shown. Therefore, even though the crystalline potential may be very weak, it is sufficient to destroy the *spherical* free-

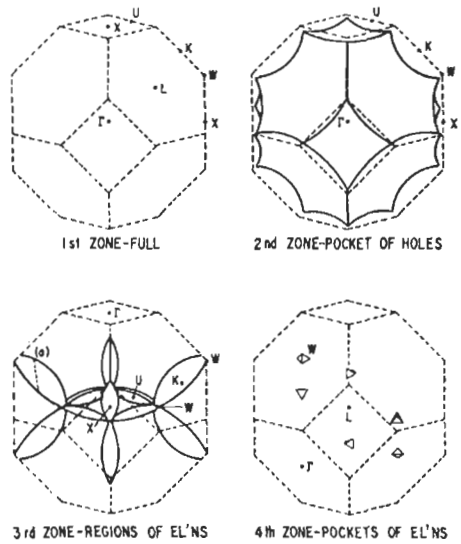

Fig. 17. The free-electron Fermi surface of aluminium (after HARRISON [1959]).

electron Fermi surface and to create a new Fermi surface topology, as is illustrated in fig. 14 by the appearance of the electron *pockets* in the third and fourth zones. A very simple procedure for constructing the Fermi surfaces of free-electron-like materials has been suggested by HARRISON [1959, 1960] and fig. 17 shows the resulting Fermi surface of fcc aluminium. A much more detailed treatment of Fermi surfaces may be found in HARRISON [1966], HEINE and WEAIRE [1970] and KITTEL [1971], where the interested reader is also referred for a discussion of transport properties and concepts such as holes and effective mass.

3.3. Volume dependence

Although the energy bands of simple metals *appear* to be describable by the NFE approximation as discussed in the previous subsection, there is a major difficulty. If the (200) Fourier component of the aluminium lattice potential is estimated from *first principles* using eq. (66), then

$$v(200) \approx -5 \text{ eV}. \tag{72}$$

But the magnitude of this is ten times larger than the value we obtained by *fitting* to the first-principles band structure of MORUZZI *et al.* [1978], namely $|v(200)| = 0.5$ eV. Moreover, by looking at the symmetry of the eigenfunctions at X, we see from fig. 16 that the bottom of the band gap corresponds to X_4, or p-like symmetry whereas the top of the band gap corresponds to X_1 or s-like symmetry (see, e.g., TINKHAM [1964]). It follows from fig. 2 and eq. (70) that the NFE states at the bottom and top of the band gap correspond to $\sin(2\pi x/a)$ and $\cos(2\pi x/a)$, respectively. Therefore, in the state with *lower* energy the electron is never located in the planes containing the ion cores, which

correspond to $x = na/2$ for the fcc lattice, since $\sin(2\pi x/a)$ vanishes. Instead, the electron has maximum probability of being located midway between these atomic planes. This implies that the relevant Fourier component of the atomic potential is *repulsive,* thereby driving the electrons away from the ion cores, i.e.

$$v^{\text{fit}}(200) = +0.5 \text{ eV}. \tag{73}$$

The origin of the discrepancy between eqs. (72) and (73) is easily found once it is remembered that the NFE bands in aluminium are formed from the *valence* 3s and 3p electrons. These states must be orthogonal to the s and p *core* functions as outlined in § 2.1 and they, therefore, contain nodes in the core region as illustrated for the case of the 2s wavefunction in fig. 6. In order to reproduce these very-short-wavelength oscillations, plane waves of *very high* momentum must be included in the plane-wave expansion of ψ_k, so that a linear combination of only the *two* lowest energy plane waves in eq. (62) is an extremely bad approximation. In 1940, HERRING circumvented this problem by starting at the outset with a basis of plane waves that had *already* been orthogonalized to the core states, the so-called orthogonalized plane-wave (OPW) basis. The OPW method led to a secular determinant for the eigenvalues that was identical to the NFE determinant, except that in addition to the Fourier component of the crystal potential $v(\boldsymbol{G})$ there is also a *repulsive* contribution coming from the core-orthogonality constraint. This tended to cancel the *attractive* coulomb potential term in the core region, thereby resulting in much weaker net Fourier components and hence nearly-free-electron-like behaviour of the band structure E_k for the simple metals.

This led to the concept of the *pseudopotential* in which the true potential $v(r)$ in the Schrödinger equation (1) is replaced by a much *weaker* potential $v_{\text{ps}}(\boldsymbol{r})$ which is chosen to preserve the original eigenvalues E_k so that

$$\left(-\nabla^2 + v_{\text{ps}}\right)\phi_k = E_k\phi_k \tag{74}$$

(see, e.g., HARRISON [1966] and HEINE and WEAIRE [1970]). The pseudo-*eigenfunctions*, ϕ_k, however, differ from the true eigenfunctions ψ_k because in general they do *not* contain the nodes in the core region as these have been pseudized-away by the inclusion of the repulsive core component in v_{ps}. A plane-wave expansion of ϕ_k therefore, leads to rapidly convergent eigenvalues E_k in eq. (74). Thus, the NFE approximation will provide a good description of the band structure of simple metals provided the Fourier components of the pseudopotential rather than the true potential are taken in the NFE secular equation (67).

Pseudopotentials are not unique, and certain criteria have been given for their choice (see, e.g., BACHELET *et al.* [1982] and VANDERBILT [1990]). However, in this chapter we shall describe only the Ashcroft *empty-core* pseudopotential because of its simplicity. In 1966, ASHCROFT assumed that the cancellation between the repulsive core-orthogonality contribution and the attractive coulomb contribution is exact within some ion core radius R_c, so that:

$$v_{\text{ps}}^{\text{ion}}(\boldsymbol{r}) = \begin{cases} 0 & r < R_c \\ -2Z/r & \text{for } r > R_c \end{cases} \tag{75}$$

References: p. 129.

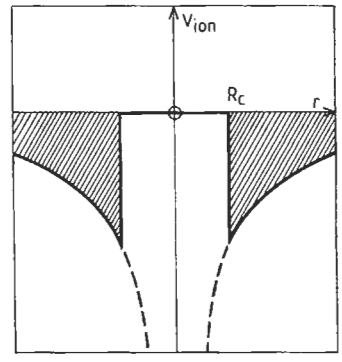

Fig. 18. The Ashcroft empty-core pseudopotential.

where the *ionic* potential falls off coulombically outside the core (cf. $e^2=2$ in atomic units). The Ashcroft empty-core pseudopotential is shown in fig. 18. The resulting ionic lattice has Fourier components given by eq. (66), namely:

$$v_{ps}^{ion}(q) = -\left(8\pi Z/\Omega q^2\right)\cos qR_c, \tag{76}$$

where Ω is the volume per atom. In the absence of the core $R_c=0$ and the Fourier components are *negative* as expected. However, in the presence of the core the Fourier components oscillate in sign and may, therefore, take *positive* values. For the case of aluminium the Ashcroft empty-core radius is about 1.2 au (cf. table 16–1 of HARRISON [1980]) and $v_{ps}^{ion}(200)$ will, therefore, be positive. The corresponding Fourier components $v_{ps}(q)$ are obtained from eq. (76) by allowing the free-electron gas to screen the bare ionic lattice. The resulting Fourier components of the aluminium potential are illustrated in fig. 19 for the more sophisticated HEINE and ABARENKOV [1964] pseudopotential. We see that the values of $v_{ps}(111)$ and $v_{ps}(200)$ are in good agreement with the values, 0.17 and 0.53 eV respectively, which are obtained from fitting the first-principles band structure within the NFE approximation (cf. fig. 16, eq. (71) and p. 52 of MORUZZI *et al.* [1978]).

Figure 20 shows the densities of states, $n(E)$ of the sp-bonded simple metals, which have been computed from first principles by MORUZZI *et al.* [1978]. We see that Na, Mg

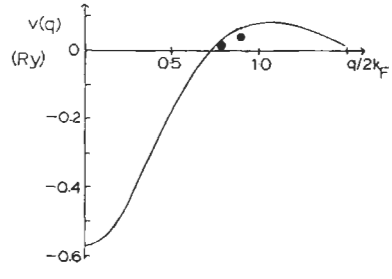

Fig. 19. The HEINE AND ABARENKOV [1964] aluminium pseudopotential $v_{ps}(q)$. The two points give the values of $v_{ps}(111)$ and $v_{ps}(200)$ deduced from fig. 16 using eq. (71).

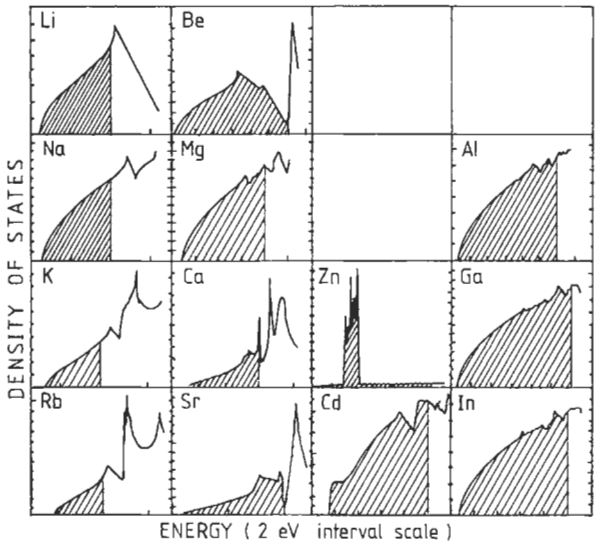

Fig. 20. The density of states, $n(E)$, of sp-bonded metals (after MORUZZI *et al.* [1978]).

and Al across a period and Al, Ga and In down a group are good NFE metals, because their densities of states are only very small perturbations of the free-electron density of states shown in fig. 13b. However, we see that Li and Be display very strong deviations from free electron behaviour. This is a direct consequence of these elements having no p core electrons, so that there is no repulsive core-orthogonality component to cancel the attractive coulomb potential which the valence 2p electrons feel. This leads to sizeable Fourier components of the potential and hence very large band gaps. For example, in fcc Be, $E_{\text{gap}}^{\text{L}} = 5.6$ eV compared to the gap of only 0.34 eV in Al, where L is the point $(2\pi/a)(\frac{1}{2},\frac{1}{2},\frac{1}{2})$ in fig. 15. In fact, the band gaps in different directions at the Brillouin zone boundary (cf. fig. 16) are nearly large enough for a gap to open up in the Be density of states, thereby leading to semiconducting behaviour. We note that the effective potential which the valence electrons feel in Li or Be depends on whether they have s- or p-type character, because there *are* 1s core states but no p core states. Such an l-dependent potential is said to be *non-local* (cf. HARRISON [1966] and HEINE and WEAIRE [1970]), whereas the Ashcroft empty-core pseudopotential of fig. 18 is *local.*

The heavier alkalis K and Rb and alkaline earths Ca and Sr have their occupied energy levels affected by the presence of the respective 3d or 4d band which lies just above the Fermi energy (cf. the relative positions of the s and d free-atom energy levels in fig. 5). This leads to a more than free-electron admixture of $l=2$ component into the occupied energy states, which requires the use of non-local pseudopotential theory for accurate agreement with experimental properties (see e.g., TAYLOR and MACDONALD [1980] and MORIARTY [1982]). It is clear from fig. 20 that Sr is not a simple NFE metal since the perturbation is very strong and the hybridized bottom of the d band has moved

References: p. 129.

below the Fermi energy. Just as in Be, a gap has nearly opened up at E_F, and theoretically it requires only 0.3 Gpa of pressure to turn Sr into a semiconductor, which is in reasonable agreement with high-pressure resistivity data (JAN and SKRIVER [1981]). The group-IIB elements Zn and Cd, on the other hand, have their valence states strongly distorted by the presence of the *filled* d band. In fig. 5 we see that the 5s–4d energy separation in Cd is larger than the 4s 3d separation in Zn, which results in the Cd 4d band lying about 1 eV below the bottom of the valence 5sp band (p. 152 of MORUZZI *et al.* [1978]). Figure 20, therefore, demonstrates that not all simple metals display good NFE behaviour and particular care needs to be taken with Li, Be and the group-II elements on either side of the transition metal series.

The presence of the ion core in simple metals determines the volume dependence of the energy bands. Wigner and Seitz had calculated the behaviour of the bottom of the NFE band in sodium in their classic paper of 1933. They argued that since the bottom of the band corresponded to the most bonding state, it satisfied the *bonding* boundary condition implicit in eq. (27), namely that the gradient of the wave function vanishes across the boundary of the *Wigner–Seitz cell.* This cell is formed in *real* space about a given atom by bisecting the near-neighbour position vectors in the same way that the Brillouin zone is formed in *reciprocal* space. The Wigner-Seitz cell of the bcc lattice is the fcc Brillouin zone and vice versa (cf. KITTEL [1971]). Since there are 12 nearest neighbours in the fcc lattice and 14 first and second nearest neighbours in the bcc lattice, it is a very good approximation to replace the Wigner–Seitz *cell* by a Wigner–Seitz *sphere* of the same volume (cf. fig. 15). Imposing the bonding boundary condition across the Wigner Seitz sphere of radius S, where

$$\Omega = \tfrac{4}{3}\pi S^3, \tag{77}$$

the energy of the bottom of the band Γ_1 is fixed by

$$\left[\mathrm{d}R_s(r,E)/\mathrm{d}r\right]_{r=S,E=\Gamma_1} = 0, \tag{78}$$

where $R_s(r, E)$ is the $l=0$ solution of the radial Schrödinger equation within the Wigner–Seitz sphere. The bonding boundary condition is determined by the $l=0$ radial function because the bottom of the NFE band at Γ_1 is a pure s state (cf. fig. 16).

Figure 21 shows the resulting behaviour of the bottom of the band Γ_1, in sodium as a function of S after WIGNER and SEITZ [1933]. We see that as the free atoms are brought together from infinity, the bonding state becomes more and more bonding until about 3 au when Γ_1, turns upwards and rapidly loses its binding energy. This behaviour is well described *at metallic densities* by the Frohlich–Bardeen expression,

$$\Gamma_1^{\mathrm{ws}} = -(3Z/S)\left[1-(R_c/S)^2\right] \tag{79}$$

since the single valence electron of sodium is assumed to feel only the potential of the *ion* at the Wigner–Seitz sphere centre so that over the boundary

$$v(S) = -2Z/S, \tag{80}$$

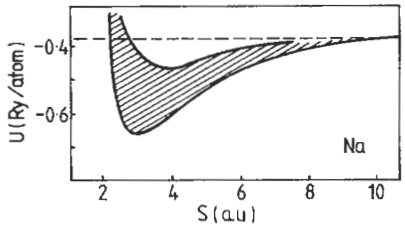

Fig. 21. The total energy, U, as a function of Wigner–Seitz radius, S, for sodium (after WIGNER and SEITZ [1933]). The bottom of the conduction band, Γ_1, is given by the lower curve, to which is added the average kinetic energy per electron (the shaded region).

where $Z=1$ for the monovalent alkali metals (see, e.g., § 3.2 of CALLAWAY [1964]). R_c may be identified as the radius of an Ashcroft empty-core pseudopotential, because the potential energy of one electron distributed uniformly throughout the Wigner–Seitz sphere with an Ashcroft ionic potential at its centre is given by eq. (79). It follows from eq. (79) that the maximum binding energy of this state Γ_1, occurs for

$$S_m = \sqrt{3}R_c. \tag{81}$$

Since for sodium $R_c \approx 1.7$ au (ASHCROFT and LANGRETH [1967] and HARRISON [1980]), eq. (81) predicts that Γ_1, has a minimum at about 2.9 au. This is in good agreement with the curve in fig. 21, which was obtained by solving the radial Schrödinger equation subject to the boundary condition eq. (78).

WIGNER and SEITZ [1933] assumed that the valence electrons of sodium have free-electron-like kinetic energy and density of states, which from fig. 20 is clearly a good approximation. It follows from eqs. (45) and (77) that the Fermi energy E_F may be written as:

$$E_F = \Gamma_1^{WS} + (9\pi/4)^{2/3}/S^2. \tag{82}$$

In § 5 we follow up our understanding of the behaviour of the energy bands by discussing the *total* energy of simple metals and the different factors influencing bulk properties such as equilibrium atomic volume and bulk modulus.

4. *Transition-metal bands*

4.1. Tight-binding approximation

Transition metals are characterized by a partially filled d band, which is well described within the *tight-binding* (TB) approximation by a linear combination of atomic d orbitals. We shall illustrate the TB method (see, e.g., CALLAWAY [1964], PETTIFOR [1992] and SUTTON [1993]) by considering first the simpler case of a lattice of atoms with overlapping *s-state* atomic wave functions ψ_s and corresponding free atomic energy levels E_s. Generalizing eq. (19) for the diatomic molecule to a periodic lattice of N

atoms, we can write the crystal wave function ψ_k as a linear combination of the atomic orbitals:

$$\psi_k(\boldsymbol{r}) = N^{-1/2} \sum_{\boldsymbol{R}} e^{i\boldsymbol{k}\cdot\boldsymbol{R}} \psi_s(\boldsymbol{r} - \boldsymbol{R}), \tag{83}$$

where the phase factor automatically guarantees that $\psi_k(\boldsymbol{r})$ satisfies Bloch's theorem, eq. (55). Assuming that the crystal potential is the sum of the atomic potentials $v(\boldsymbol{r} - \boldsymbol{R})$ and following the method and approximations outlined through eqs. (19)–(30), the eigenvalue E_k may be written as:

$$E_k = E_s + \sum_{R \neq 0} e^{i\boldsymbol{k}\cdot\boldsymbol{R}} \int \psi_s^*(\boldsymbol{r}) v(\boldsymbol{r}) \psi_s(\boldsymbol{r} - \boldsymbol{R})\, d\boldsymbol{r}, \tag{84}$$

where the non-orthogonality and three-centre contributions have been neglected because they do not contribute to first order. Since the atomic s orbitals are spherically symmetric, the ssσ hopping matrix elements in eq. (84) do not depend on the direction of $\boldsymbol{R}$ but only on the magnitude R (see fig. 10), so that

$$E_k = E_s + \sum_{R \neq 0} e^{i\boldsymbol{k}\cdot\boldsymbol{R}} ss\sigma_R. \tag{85}$$

The TB band structure E_k for a *simple cubic* lattice with s orbitals may now be quickly found. Assuming that the hopping matrix elements couple only to the six *first* nearest-neighbour atoms with position vectors $\boldsymbol{R}$ equal to $(\pm a, 0, 0)$ $(0, \pm a, 0)$ and $(0, 0, \pm a)$ eq. (85) gives

$$E_k = E_s + 2ss\sigma_1 \left(\cos k_x a + \cos k_y a + \cos k_z a\right), \tag{86}$$

where $\boldsymbol{k} = (k_x, k_y, k_z)$ Thus the eigenvalues vary *sinusoidally* across the Brillouin zone. The bottom, E^- and top, E^+ of the s band correspond to the Bloch states at the centre of the Brillouin zone (0, 0, 0) and at the zone boundary $(\pi/a)(1, 1, 1)$ respectively. It follows from eq. (86) that

$$E^{\pm} = E_s \pm 6|ss\sigma_1| \tag{87}$$

because $ss\sigma_1$ is negative as can be deduced from fig. 10 and eq. (84). Comparing E^- with eq. (26) and fig. 8a for the diatomic molecule, we see that the most bonding state in the simple cubic lattice corresponds to *maximum* bonding with all six nearest neighbours simultaneously, which from fig. 10 is only possible for the spherically symmetric s orbital case.

The structure of the TB p band may be obtained by writing ψ_k as a linear combination of the *three* p Bloch sums corresponding to the atomic p_x, p_y, and p_z orbitals, where x, y and z may be chosen along the crystal axes for a cubic lattice. That is,

$$\psi_k(\boldsymbol{r}) = N^{-1/2} \sum_{\alpha = x,y,z} c_\alpha \sum_{\boldsymbol{R}} e^{i\boldsymbol{k}\cdot\boldsymbol{R}} \psi_\alpha(\boldsymbol{r} - \boldsymbol{R}), \tag{88}$$

which leads to the 3×3 TB secular determinant for the p band, namely

$$\left|\left(E_p - E_k\right)\delta_{\alpha\alpha'} + T_{\alpha\alpha'}\right| = 0, \tag{89}$$

where

$$T_{\alpha\alpha'} = \sum_{R\neq 0} e^{i\boldsymbol{k}\cdot\boldsymbol{R}} \int \psi_\alpha^*(\boldsymbol{r}) v(\boldsymbol{r}) \psi_{\alpha'}(\boldsymbol{r} - \boldsymbol{R}) d\boldsymbol{r}. \tag{90}$$

It is clear from fig. 10 that the hopping matrix elements in eq. (90) *do* depend on the direction of $\boldsymbol{R}$ because the p_x, p_y, and p_z orbitals are angular dependent. SLATER and KOSTER [1954] showed that they can be written directly in terms of the two fundamental hopping integrals $pp\sigma_R$ and $pp\pi_R$ and the direction cosines (l, m, n) of $\boldsymbol{R}$.

For a *simple cubic* lattice with only first-nearest-neighbour hopping the matrix elements $T_{\alpha\alpha'}$ may be evaluated to give

$$T_{xx} = 2pp\sigma_1 \cos k_x a + 2pp\pi_1\left(\cos k_y a + \cos k_z a\right), \tag{91}$$

with T_{yy} and T_{zz} obtained from T_{xx} by cyclic permutation. The off-diagonal matrix elements vanish for the simple cubic lattice. Therefore, at the centre of the Brillouin zone, Γ, the eigenvalues are *triply* degenerate (if spin is neglected) and given from eqs. (89) and (91) by

$$E_\Gamma^{(3)} = E_p + 2pp\sigma_1 + 4pp\pi_1. \tag{92}$$

This degeneracy is *partially* lifted along the $|100\rangle$ symmetry direction, because from eq. (91) the band structure consists of the *singly* degenerate level

$$E_\Delta^{(1)} = E_p + 4pp\pi_1 + 2pp\sigma_1 \cos k_x a \tag{93}$$

and the *doubly* degenerate level

$$E_\Delta^{(2)} = E_p + 2\left(pp\sigma_1 + pp\pi_1\right) + 2pp\pi_1 \cos k_x a, \tag{94}$$

where the former results from the p_x orbitals and the latter from the p_y and p_z orbitals. The degeneracy is *totally* lifted along a general $\boldsymbol{k}$ direction as from eqs. (89) and (91) there will be three distinct non-degenerate energy levels.

Finally, the structure of the TB d band may be obtained by writing ψ_k as a linear combination of the *five* d Bloch sums corresponding to the five atomic orbitals illustrated in fig. 2. This results in a 5×5 TB secular determinant from which the d band structure may be computed (SLATER and KOSTER [1954]). Starting from first-principles band theory, ANDERSEN [1973] has shown that within the *atomic sphere approximation* (ASA) *canonical* d bands may be derived which depend neither on the lattice constant nor on the particular transition metal, but only on the crystal structure. This approximation leads to hopping integrals of the form

$$\left.\begin{aligned} dd\sigma_R &= -5 \\ dd\pi_R &= 4 \\ dd\delta_R &= -1 \end{aligned}\right\} \times \tfrac{2}{5} W\left(S/R\right)^5, \tag{95}$$

References: p. 129.

where W is the width of the d band, which is obtained by imposing the bonding and antibonding boundary conditions over the Wigner-Seitz *sphere* of radius S. It follows from eq. (95) that the hopping integrals scale uniformly with the band width W and do not depend on the lattice constant as it is the ratio S/R that enters. They fall off quickly with distance as the inverse fifth power.

Figure 22 shows the resulting d band structure for the fcc and bcc lattices along the $|111\rangle$ and $|100\rangle$ directions in the Brillouin zone (ANDERSEN [1973]). We see that at the centre of the Brillouin zone, Γ, there are two energy levels, one of which is *triply* degenerate, the other *doubly* degenerate. The former comprises the xy, yz and xz, T_{2g} orbitals which from fig. 2 are equivalent to one another in a cubic environment. The latter comprises the $x^2 - y^2$, $3z^2 - r^2 E_g$ orbitals which by pointing along the cubic axes are not equivalent to the T_{2g}, orbitals. The degeneracy is partially lifted along the $|111\rangle$ and $|100\rangle$ symmetry directions as indicated in fig. 22, because eigenfunctions which are equivalent at $\boldsymbol{k}=0$ may become non-equivalent for $\boldsymbol{k} \neq 0$ due to the translational phase factor $\exp(i\boldsymbol{k}\cdot\boldsymbol{R})$ (see fig. 8.8 of TINKHAM [1964]).

The band structure of NiO (MATTHEISS [1972]) is shown in fig. 23 because it illustrates s, p and d band behaviour. The three bands arise from the oxygen 2s, 2p and the nickel 3d valence levels, respectively, the ordering being determined by the relative positions of their atomic energy levels in figs. 4 and 5. The Brillouin zone is *face-centred* cubic since the NaCl crystal structure of NiO consists of two interpenetrating fcc lattices, one containing the sodium atoms, the other the chlorine atoms. In the $|100\rangle$ direction along ΓX the s and p band structure is not too dissimilar from that given for the *simple* cubic lattice by eqs. (86), (93) and (94). The d band structure along ΓX in NiO is also similar to that of the fcc canonical d band in fig. 22, except that one level, which joins the upper state at Γ to the *bottom* of the canonical d band at X, has been pushed up and runs across the *top* of the d band in NiO. This is the result of mixing or *hybridization* between the s, p and d blocks in the TB secular determinant (SLATER and KOSTER [1954]), whose strength is determined for example by the non-vanishing $pd\sigma$ and $pd\pi$ hopping matrix elements shown in fig. 10. This mixing can only occur between Bloch states with the same symmetry (TINKHAM [1964]). At the zone boundary X there is only *one* d band state which has the same symmetry X_1 as the s band state. (There are no d band states with the same symmetry as the p band states at X.) The influence of the hybridization on the band structure is enhanced by *orthogonality* constraints which can add a further repulsive contribution to the d states because they must be orthogonal to the valence s and p levels lying beneath them in energy.

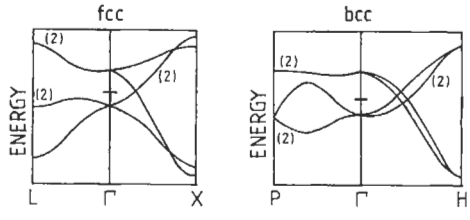

Fig. 22. The fcc and bcc d band structure (after ANDERSEN [1973]).

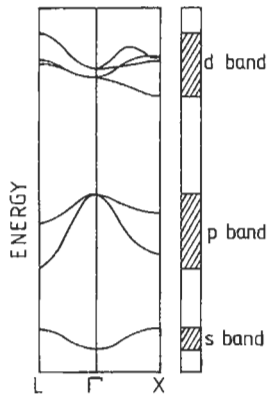

Fig. 23. The band structure of NiO (after MATTHEISS [1972]).

The bands in fig. 23 illustrate an apparent failure of one-electron theory. NiO is an *insulator.* However, adding the ten nickel and six oxygen valence electrons to the bands shown results in the d band containing only eight of its possible ten electrons [cf. eq. (35)]. Thus, the band structure presented in fig. 23 predicts that NiO is a *metal.* The origin of this dramatic failure of band theory was investigated by MOTT [1949], who considered what happens to a lattice of hydrogen atoms as the lattice constant is decreased from some very large value. Initially each atom has a single 1s valence electron associated with it as in the free atom state. The system will, therefore, be *insulating,* because in order for an electron to hop through the lattice it requires an energy given by the difference between the ionization potential of 13.6 eV (corresponding to the atomic 1s level) and the electron affinity of 0.75 eV. This energy difference of about 13 eV is a measure of the coulomb repulsion U between *two* 1s antiparallel spin electrons sitting on the *same* atomic site. However, as the lattice constant decreases the atomic 1s level broadens into a band of states of width W so that the insulating gap will decrease like $U - W$. Therefore, for some sufficiently small lattice spacing W will be large enough for the system to become *metallic* and the hydrogen lattice undergoes a Mott metal-insulator transition.

The very different conducting behaviour of the 3d valence electrons in metallic nickel and insulating nickel oxide can now be qualitatively understood. The width of the d band in NiO is about 2 eV (MATTHEISS [1972]), whereas in pure Ni it is about 5 eV (MORUZZI *et al.* [1978]) since the Ni–Ni internuclear separation is smaller than in the oxide. Because the value of the screened intra-atomic coulomb integral U in 3d transition metals is about 4 eV, U/W is *greater* than unity for NiO but *less* than unity for Ni. Thus, we expect the former to be insulating and the latter metallic as observed experimentally.

The *breakdown* of conventional band theory at *large* lattice spacings can best be illustrated by considering the hydrogen molecule (cf. fig. 8a). In the ground state the two valence electrons 1 and 2 occupy the same bonding molecular orbital ψ_{AB}^{-} with opposite spin, so that the total molecular wave function may be written within the one electron approximation as

$$\psi(1,2) = \psi^{-}_{AB}(1)\psi^{-}_{AB}(2). \tag{96}$$

Substituting from eq. (27), multiplying through and neglecting the normalization factor $[2(1 + S)]^{-1}$ we have

$$\psi(1,2) = \big(\psi_A(1)\psi_B(2) + \psi_B(1)\psi_A(2) + \psi_A(1)\psi_A(2) + \psi_B(1)\psi_B(2)\big). \tag{97}$$

The first two contributions correspond to the two possible *neutral* atom states with a single electron associated with each atom, whereas the latter correspond to the two *ionic* states A^-B^+ and A^+B^- respectively. Since the hydrogen molecule dissociates into two *neutral* atoms, we see that $\psi(1, 2)$ gives the wrong behaviour at large separations (see, e.g., SLATER [1963]).

In practice, the Mott transition to the insulating phase is accompanied by the appearance of local *magnetic* moments (BRANDOW [1977]) so that the band model must be generalized to allow for antiferromagnetic solutions of the Schrödinger equation (SLATER [1951a]; cf. § 8). Within local spin density functional (LSDF) theory (cf. § 1) this leads to a good curve of total energy versus internuclear separation for the hydrogen molecule because the theory now goes over to the neutral free-atom limit (GUNNARSSON and LUNDQUIST [1976]). However, although the antiferromagnetic state leads to a band gap opening up at the Fermi level in NiO (SLATER [1951a]), a proper understanding of CoO and the temperature-dependent properties of these *insulators* can only be obtained by using a more sophisticated *non-local* treatment of exchange and correlation (BRANDOW [1977], JONES and GUNNARSSON [1989]). Fortunately, the bulk properties of simple and transition *metals* considered in this chapter can be well understood within the *local* approximation, even though non-locality can play a role in the finer details of the band structure (see, e.g., Ni; COOKE *et al.* [1980]).

4.2. Hybrid NFE-TB bands

Transition metals are characterized by a fairly tightly-bound d band that overlaps and hybridizes with a broader nearly-free-electron sp band as illustrated in fig. 24. This difference in behaviour between the valence sp and d electrons arises from the d shell lying *inside* the outer valence s shell, thereby leading to small overlap between the d orbitals in the bulk. For example, from eq. (14) the average radial distance of the hydrogenic 3d and 4s wave functions are in the ratio 0.44 :1. Thus, we expect the band structure of transition metals to be represented accurately by a hybrid NFE–TB secular equation of the form (HODGES *et al.* [1966] and MUELLER [1967]):

$$\begin{vmatrix} C - EI & H \\ H^{\dagger} & D - EI \end{vmatrix} = 0 \tag{98}$$

where C and D are sp-NFE and d-TB matrices respectively [cf. eqs. (67) and (89)]. H is the hybridization matrix which couples and mixes together the sp and d Bloch states with the same symmetry, and I is the unit matrix.

A secular equation of this H–NFE–TB form may be derived (HEINE [1967], HUBBARD

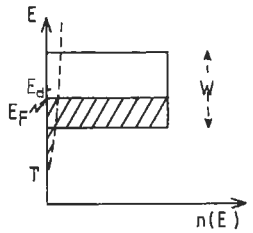

Fig. 24. A schematic representation of transition metal sp (dashed curve) and d (solid curve) densities of states when sp–d hybridization is neglected.

[1967] and JACOBS [1968]) by an exact transformation (PETTIFOR [1972a]) of the first-principle band structure equations of KORRINGA [1946], KOHN and ROSTOKER [1954] (KKR). They have solved the Schrödinger equation (1) by regarding the lattice as a periodic array of scattering sites which individually scatter the electrons with a change in phase η_l. Transition-metal sp valence electrons are found to be scattered very little by the lattice so that they exhibit NFE behaviour with η_0 and η_1 close to zero. Transition-metal d electrons, on the other hand, are strongly scattered, the $l=2$ phase shift showing *resonant* behaviour given by

$$\tan \eta_2(E) = \tfrac{1}{2}\Gamma/(E_d - E), \tag{99}$$

where E_d and Γ determine the position and width of the resonance. This allows the KKR equations to be transformed directly into the H–NFE–TB form, in which the two centre TB hopping integrals and hybridization matrix elements are determined explicitly by the two resonant parameters E_d and Γ. The non-orthogonality contributions to the secular equation (MUELLER [1967]) are obtained by linearizing the implicit energy-dependent matrices C, D and H in a Taylor expansion about E_d.

The nonmagnetic band structure of fcc and bcc iron is shown in fig. 25, being computed from the H–NFE–TB secular equation with resonant parameters $E_d = 0.540$ Ry and $\Gamma = 0.088$ Ry (PETTIFOR [1970a]). The NFE pseudopotential matrix elements were chosen by fitting the first-principle values of WOOD [1962] at the pure p states N_1, $v(_{110} = 0.040$ Ry), L_2' ($v_{111} = 0.039$ Ry) and X_4, ($v_{200} = 0.034$ Ry). Comparing the band structure of iron in the $|100\rangle$ and $|111\rangle$ directions with the canonical d bands in fig. 22, we see there is only the *one* d level with symmetry Δ_1 and Λ_1 respectively which hybridizes with the lowest NFE band, the remaining four d levels being unperturbed. Because of the canonical nature of the pure TB d bands (ANDERSEN [1973]), the band structure of all fcc and bcc transition metals will be very similar to that shown in fig. 25 for iron.

The transition-metal density of states, $n(E)$, is not uniform throughout the band as shown schematically in fig. 24 but displays considerable structure that is characteristic of the given crystal lattice. This is seen in fig. 26 for the bcc, fcc and hcp densities of states, which were calculated by the H–NFE–TB secular equation neglecting non-orthogonality contributions with $E_d = 0.5$ Ry and $\Gamma = 0.06$ Ry (PETTIFOR [1970b]). These early histogram densities of states are displayed rather than more accurate recent

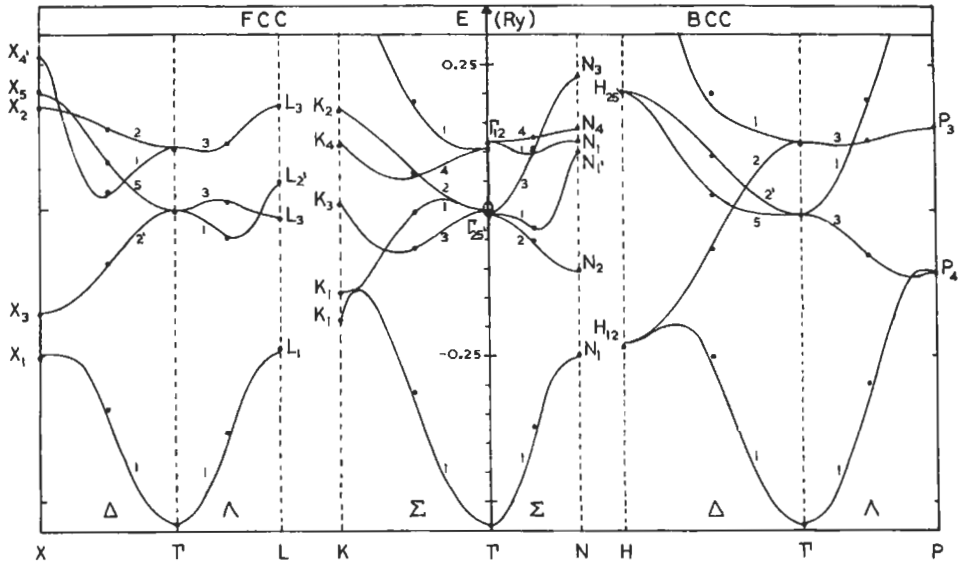

Fig. 25. The H–NFE–TB band structure of fcc and bcc iron in the nonmagnetic state. The solid circles represent the first-principle energy levels of WOOD [1962]. (From PETTIFOR [1970a].)

calculations (see, e.g., RATH and CALLAWAY [1973], JEPSEN *et al.* [1975], MORUZZI *et al.* [1978], PAXTON *et al.* [1990]) because they allow a direct comparison between the bcc, fcc and hcp densities of states for the *same* model element. This will be important when discussing the relative stability of the three different crystal structures in § 6.1 and the stability of the ferromagnetic state in the α, γ and ε phases of iron in § 8.

The structure in the *calculated* densities of states in fig. 26 is reflected in the behaviour of the *experimental* electronic heat constant, γ, across the nonmagnetic 4d and 5d transition metal series. It follows from eqs. (45), (47) and (48) that the electronic heat capacity may be written as

$$C = \gamma T, \tag{100}$$

where

$$\gamma = \tfrac{1}{3}\pi^2 k_B^2 n(E_F). \tag{101}$$

Therefore, ignoring any renormalization effects such as electron–phonon mass enhancement, the linear dependence of the heat capacity gives a direct experimental measure of the density of states at the Fermi level. Figure 27 shows that the H–NFE–TB densities of states in fig. 26 reflect the experimental variation in γ across the series.

4.3. Volume dependence

Figure 28 illustrates the volume dependence of the energy bands of the 4d transition metals Y, Tc and Ag, which were calculated by PETTIFOR [1977] within the atomic–

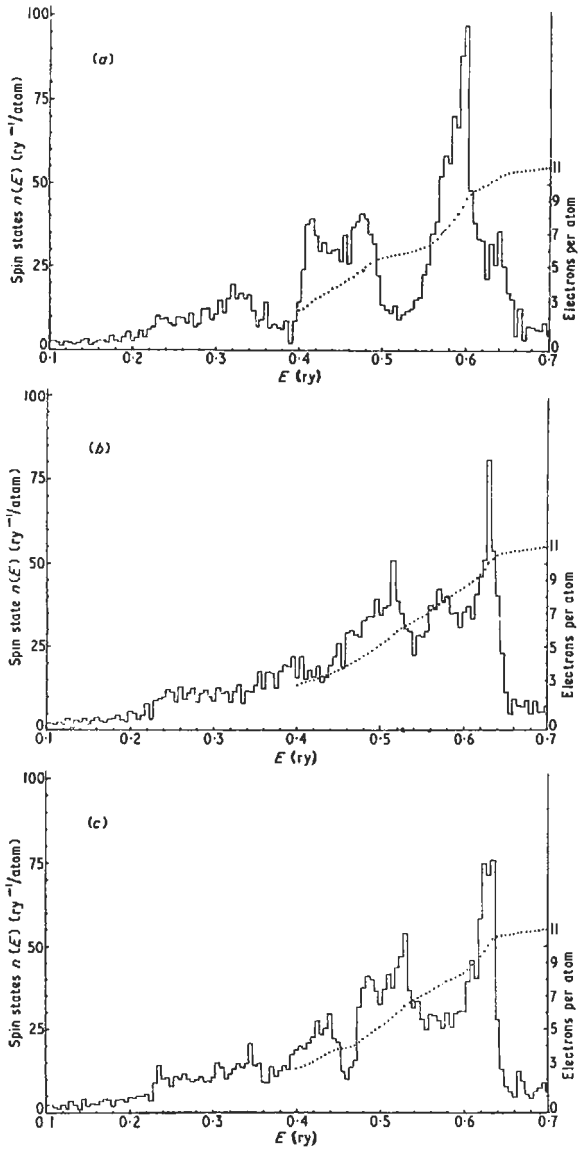

Fig. 26. The density of states for the three structures (a) bcc, (b) fcc, and (c) hcp for a model transition metal. The dotted curves represent the integrated density of states. (From PETTIFOR [1970b].)

sphere approximation of ANDERSEN [1973, 1975]. Similar bands have been obtained by GELATT *et al.* [1977] for the 3d metals Ti and Cu with the renormalized-atom approximation of WATSON *et al.* [1970]. We see from fig. 28 that the bottom of the NFE sp band Γ_1, which was evaluated within LDF theory, is well fitted by the Frohlich–Bardeen expression (79). The values of R_c obtained are found to scale *within 1%* with the position of the outer node of the 5s free-atom radial wave function. This demonstrates quantitat-

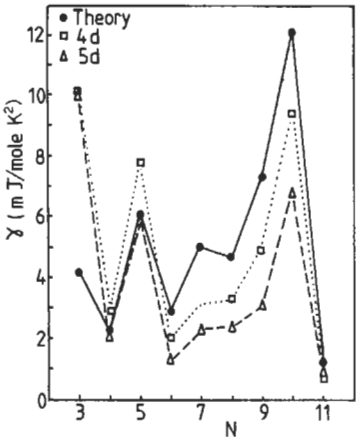

Fig. 27. A comparison of the theoretical and experimental 4d and 5d heat capacities. The theoretical values were obtained directly from eq. (101) and fig. 26, neglecting any changes in the density of states due to band width changes or mass renormalization.

ively that it is the core-orthogonality constraint which is responsible for the rapid turn up in the energy of Γ_1 and that the outer node of the valence s electron is a good measure of the s core size. The free-atom d level broadens into a band of states of width W as the atoms come together from infinity to form the bulk (see figs. 24 and 28). HEINE [1967] has shown that the Wigner–Seitz boundary conditions imply that W should vary approximately as S^{-5}, where S is the Wigner–Seitz radius. Assuming a power-law dependence of W on S, we can write

$$W = W_0(S_0/S)^n, \tag{102}$$

where W_0 and S_0 are the values of the d-band width and Wigner–Seitz radius respectively at the equilibrium lattice spacing of the transition metal. Table 1 gives the values of S_0, W_0 and n for the 4d transition metals (PETTIFOR [1977]). Because of the more extended nature of the d wave functions at the beginning of the transition metal series, n takes a value closer to four than to five which we will see in § 5.2 is reflected in their bulk properties. Values of the band width W for the 3d, 4d and 5d series may be obtained from the table in ANDERSEN and JEPSEN [1977] and are given explicitly in table 20–4 of HARRISON [1980]. The 3d and 5d band widths are approximately 30% smaller and 20% larger respectively than the corresponding 4d widths.

The centre of gravity of the TB-d band, E_d, in fig. 28 rises *exponentially* (PETTIFOR [1977]) as the volume decreases because the potential within the Wigner–Seitz sphere *renormalizes* due to the increase in the electronic charge density (GELATT *et al.* [1977]). This renormalization in position of the free atomic d level plays an important role in transition-metal energetics and will be discussed further in § 5.2.

The different volume dependences of the NFE-sp and TB-d bands displayed in fig. 28 will lead to changes in the relative occupancy of the two bands with volume. This is illustrated in fig. 4 of PETTIFOR [1977] where Y and Zr show a rapid increase in d-band occupancy under compression as the d band widens and the bottom of the sp band moves

Table 1
Equilibrium values of Wigner-Seitz radius S_0 and d band parameters W, n and n/S_0 for 4d series (from PETTIFOR [1977]).

Quantity	Element								
	Y	Zr	Nb	Mo	Tc	Ru	Rh	Pd	Ag
S_0 (au)	3.76	3.35	3.07	2.93	2.84	2.79	2.81	2.87	3.02
W_0 (eV)	6.3	7.8	9.3	9.5	9.1	8.5	7.6	6.0	3.9
n	3.9	4.0	4.1	4.3	4.5	4.6	4.8	5.1	5.6
n/S_0	1.03	1.19	1.33	1.47	1.58	1.65	1.71	1.77	1.84

up (cf. fig. 28a). Eventually Γ_1 moves up through the Fermi level E_F at which point all the NFE-sp states have been emptied into the TB-d states and $N_d = N$. On the other hand, the transition metals with more-than-half-filled d bands display a marked degree of constancy in N_d for volumes about their *equilibrium* values, because the sp core effects are largely counter-balanced by the rapid rise in E_d due to the increasing coulomb repulsion between the d electrons (cf. fig. 28c). However, under very high pressures the bottom of the sp band does eventually move up through the Fermi level, and transition metals with *ten* valence electrons (Ni, Pd and Pt) may become semiconducting (MCMAHAN and ALBERS [1982]). We will return to this dependency of the d-band occupancy on volume and core size when discussing crystal structure stability in § 6.

5. *Bulk properties*

5.1. Simple metals

Within the *free-electron* approximation the total energy per electron may be written (see, e.g., HEINE and WEAIRE [1970]) as:

$$U_{eg} = 2.21/r_s^2 - 0.916/r_s - (0.115 - 0.0313 \ln r_s), \tag{103}$$

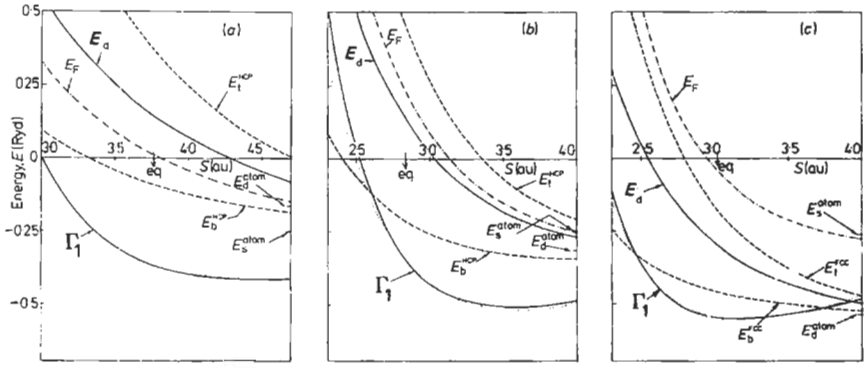

Fig. 28. The energy bands as a function of Wigner–Seitz radius S for (a) Y, (b) Tc, and (c) Ag. The observed equilibrium Wigner–Seitz radii are marked eq. The dotted curve gives the Fröhlich–Bardeen fit (eq. 79) to the bottom of the conduction band Γ_1. E_d, E_t and E_b mark the centre of gravity, and top and bottom of the d band, respectively. (After PETTIFOR [1977].)

where r_s is the radius of the sphere which contains one electron so that

$$r_s = Z^{-1/3} S \tag{104}$$

for a metal with valence Z and Wigner–Seitz radius S. The first term in eq. (103) is the average *kinetic* energy of a free electron gas, namely $\frac{3}{5} E_F$, where E_F is given by eq. (45). The second term is the *exchange* energy which is attractive, because parallel-spin electrons are kept apart by Pauli's exclusion principle, thereby leading to weaker mutual coulomb repulsion. The third term is the *correlation* energy which gives the additional lowering in energy due to the dynamical correlations between the electrons. It follows from eq. (103) that the free electron gas is in equilibrium for $r_s = 4.2$ au with a binding energy per electron of 0.16 Ry or 2.2 eV.

If the electron gas is perturbed to *first order* by the presence of the ionic lattice (HEINE and WEAIRE [1970], GIRIFALCO [1976] and HARRISON [1980]), then the total binding energy *per atom* may be written as:

$$U = Z\left(U_{eg} + U_{ion}\right), \tag{105}$$

where

$$U_{ion} = -\frac{3Z}{S}\left[1 - \left(\frac{R_c}{S}\right)^2\right] + \frac{1.2Z}{S}. \tag{106}$$

The first and second terms in eq. (106) give the electron–ion [cf. eq. (79)] and the electron–electron potential energies, respectively. The potential energy has been evaluated within the WIGNER–SEITZ [1933] approximation of neglecting the coulomb interaction between different Wigner–Seitz cells as they are electrically neutral. Within the free-electron approximation the ion cores had been smeared out into a uniform positive background so that there was zero net potential energy and U_{ion} vanished.

The equilibrium Wigner–Seitz radius, S_0, which is found from eq. (105) by requiring that U is stationary, depends explicitly on the core radius R_c through the equation

$$\left(\frac{R_c}{S_0}\right)^2 = \tfrac{1}{5} + \frac{0.102}{Z^{2/3}} + \frac{0.0035 S_0}{Z} - \frac{0.491}{Z^{1/3} S_0}, \tag{107}$$

where the first four terms are coulomb, exchange, correlation and kinetic contributions respectively. GIRIFALCO [1976] has taken the experimental values of the Wigner–Seitz radius S_0 to determine an effective Ashcroft empty-core radius R_c from eq. (107). The resultant values are given in table 2 where, as expected, the core size increases as one goes down a given group in the Periodic Table. It is clear from table 2 that only sodium has an equilibrium value of r_s that is close to the free-electron-gas value of 4.2 au.

The bulk modulus (or inverse compressibility), which is defined by

$$B = V\left(\mathrm{d}^2 U / \mathrm{d}V^2\right), \tag{108}$$

may be written from eqs. (105) and (107) in the form

$$B/B_{ke} = 0.200 + 0.815 R_c^{\,2}/r_s \tag{109}$$

Table 2
Equilibrium bulk properties of the simple and noble metals.

Metal	Quantity						
	Z	U_{coh}/Z (eV/electron)	S_0 [a] (au)	r_s [a] (au)	R_c (au)	B/B_{ke} (eq. 109)	B/B_{ke} (expt.)
Li	1	1.7	3.27	3.27	1.32	0.63	0.50
Na	1	1.1	3.99	3.99	1.75	0.83	0.80
K	1	0.9	4.86	4.86	2.22	1.03	1.10
Rb	1	0.9	5.31	5.31	2.47	1.14	1.55
Cs	1	0.8	5.70	5.70	2.76	1.29	1.43
Be	2	1.7	2.36	1.87	0.76	0.45	0.27
Mg	2	0.8	3.35	2.66	1.31	0.73	0.54
Ca	2	0.9	4.12	3.27	1.73	0.95	0.66
Sr	2	0.9	4.49	3.57	1.93	1.05	0.78
Ba	2	0.9	4.67	3.71	2.03	1.11	0.84
Zn	2	0.7	2.91	2.31	1.07	0.60	0.45
Cd	2	0.6	3.26	2.59	1.27	0.71	0.63
Hg	2	0.3	3.35	2.66	1.31	0.73	0.59
Al	3	1.1	2.99	2.07	1.11	0.69	0.32
Ga	3	0.9	3.16	2.19	1.20	0.74	0.33
In	3	0.9	3.48	2.41	1.37	0.83	0.39
Tl	3	0.6	3.58	2.49	1.43	0.87	0.39
Cu	1	3.5	2.67	2.67	0.91	0.45	2.16
Ag	1	3.0	3.02	3.02	1.37	0.71	2.94
Au	1	3.8	3.01	3.01	1.35	0.69	4.96

[a] From GIRIFALCO [1976].

at equilibrium, where the correlation contribution has been neglected since it contributes less than a few percent. B_{ke} is the bulk modulus of the non-interacting free electron gas, namely

$$B_{ke} = 0.586/r_s^5. \tag{110}$$

It follows from eq. (109) and table 2 that the presence of the ion core is crucial for obtaining realistic values of the bulk modulus of simple metals, as was first demonstrated by ASHCROFT and LANGRETH [1967]. However, the simple *first*-order expression eq. (109) is leading to large errors for the polyvalent metals with valence greater than two because the *second*-order contribution is not negligible and must be included (ASHCROFT and LANGRETH [1967]). Table 2 also demonstrates that the noble metals are not describable by the NFE approximation, the theoretical bulk moduli being a factor of five too small. We will return to this point in § 5.2.

The *cohesive* energy of the simple metals is observed in table 2 to be about 1 eV *per valence electron*. For example, Na, Mg and Al have cohesive energies of 1.1, 0.8 and 1.1 eV per electron respectively. These are an order of magnitude smaller than the corresponding *binding* energies given by eq. (105), the experimental values being 6.3, 12.1, and 18.8 eV per electron respectively. Although NFE perturbation theory can yield good estimates of *bulk* properties such as the equilibrium atomic volume, structural stability

and heat of formation, it can not provide reliable cohesive energies which require an accurate comparison with the *free* atom whose wave functions are not describable by weakly perturbed plane waves. It is necessary, therefore, to perform *similar* calculations in both the free atom and the bulk as, for example, WIGNER and SEITZ [1933] and MORUZZI *et al.* [1978] have done in their evaluation of the cohesive energies in figs. 21 and 1 respectively. We should point out, however, that eqs. (103)–(106) do yield a *bulk* binding energy for sodium that is very similar to Wigner and Seitz's [cf. eq. (82)], because the additional exchange, correlation and self-energy terms in eqs. (105) and (106) give a net contribution of less than 0.01 eV per sodium atom. CHELIKOWSKY [1981] has linked the cohesive energy of simple metals to a kinetic-energy change which accompanies the transformation of the exponentially damped free-atom wave function to plane-wave bulk states. As expected from table 2 and fig. 20, it is necessary to include an additional *non-local* bulk bonding contribution in order to obtain the stronger cohesion of Li and Be and the weaker cohesion of Zn, Cd and Hg. The anomalously large cohesion of the noble metals Cu, Ag and Au will be discussed in the next subsection.

5.2. Transition metals

The theoretical points in fig. 1 were computed (MORUZZI *et al.* [1978]) by solving the Schrödinger equation (1) with the potential $v(r)$ given by

$$v(r) = v_H(r) + v_{XC}(r), \tag{111}$$

where v_H is the usual Hartree potential and v_{XC} is the exchange-correlation potential evaluated within the local density functional (LDF) approximation of HOHENBERG and KOHN [1964] and KOHN and SHAM [1965], namely

$$v_{XC}(r) = \frac{d}{d\rho}\left(\rho\varepsilon_{XC}(\rho)\right). \tag{112}$$

$\varepsilon_{XC}(\rho)$ is the exchange and correlation energy per electron of a homogeneous electron gas of density ρ. It follows from eqs. (103) and (112) that the *exchange* contribution to the potential may be written as:

$$v_X(r) = \tfrac{3}{4}\,\varepsilon_X(r), \tag{113}$$

where

$$\varepsilon_X(r) = -1.477\left[\rho(r)\right]^{1/3}. \tag{114}$$

Thus the exchange potential varies as the third power of the *local* density, due to the exclusion of parallel spin electrons from the immediate neighbourhood (SLATER [1951b]).

The total energy can *not* be written simply as the sum over the occupied one-electron energies E_i of the Schrödinger equation, because the eigenvalue E_i of the ith electron contains the potential energy of interaction with the jth electron and vice versa. Thus, $E_i + E_j$ *double-counts* the coulomb interaction energy between electrons i and j. The total LDF energy is, therefore, given by

$$U = \sum_i E_i - \tfrac{1}{2}\iint \frac{2\rho(r)\rho(' r')}{|r - r'|}\,dr dr' - \int \rho(r)[v_{XC} - \varepsilon_{XC}]dr, \tag{115}$$

where the second and third contributions correct for the "double-counting" of the coulomb and exchange-correlation energies respectively. The potential energy has been written down in eq. (115) within the Wigner–Seitz sphere approximation, the coulomb interaction between neighbouring Wigner–Seitz cells, or Madelung contribution, being neglected. (Note that $e^2 = 2$ in atomic units, which accounts for the factor of two in the integrand of the coulomb integral.)

The presence of the double-counting contribution in eq. (115) does not allow for a direct interpretation of the *total* energy in terms of the one-electron eigenvalues E_i whose behaviour we have studied in the previous sections. For example, as can be seen from fig. 28b the one-electron sum alone would lead to no binding in Tc because the d-electron eigenvalues at the equilibrium atomic volume are everywhere higher than the free-atom d level. The inclusion of the double-counting term is crucial for bonding since it counters to a large extent the shift in the centre of gravity of the d bands E_d due to the *renormalization* of the potential under volume change. In copper, for example, GELATT *et al.* [1977] found that the band-shift energy of 78.6 eV/atom, which accompanies the formation of the bulk metal, is almost totally cancelled by a change in the double-counting term of 77.7 eV/atom. The remaining net repulsive contribution of about 1 eV/atom is typical for the 3d and 4d transition metal series (see fig. 4 of GELATT *et al.* [1977]).

The problems associated with double-counting can be avoided, however, by working not with the total energy, U, but with *the first-order change* in energy, δU, on change in the Wigner–Seitz sphere volume, $\delta\Omega$, for the bulk metal (PETTIFOR [1976]) or change in the internuclear separation, δR, for the diatomic molecule (PETTIFOR [1978a]). By starting either from the virial theorem in the form derived by LIBERMAN [1971] or from the total-energy expression (115) following NIEMINEN and HODGES [1976], PETTIFOR [1976, 1978a] showed that the first-order change in *total energy*, δU, may be written, neglecting the Madelung contribution, as:

$$\delta U = \sum_i \delta E_i, \tag{116}$$

where δE_i is the first-order change in the *eigenvalue* which accompanies the first-order volume or distance change *while the potential is kept unrenormalized.* The *general* applicability of this first-order result has been proved by ANDERSEN [1980] for force problems involving arbitrary atomic displacements and by NORSKOV [1982] for embedding problems involving a change in the local atomic environment (cf. § 7). SKRIVER [1982], MCMAHAN and MORIARTY [1983] and PAXTON and PETTIFOR [1992] have demonstrated the applicability of eq. (116) to the evaluation of structural energy differences (cf. § 6).

The first-order expression (116) is important because it allows a direct identification of the different roles played by the valence sp and d electrons in bulk transition metal energetics. The eigenstates can be decomposed within the Wigner–Seitz sphere into their different angular momentum components, l, so that eq. (116) may be written as:

$$\delta U = -P\delta\Omega = -\sum_l P_l \delta\Omega, \tag{117}$$

where P is the pressure, given by $P = -\,\mathrm{d}U/\mathrm{d}\Omega$. By working within the atomic-sphere approximation of ANDERSEN [1973] the *partial pressures* P_l may be expressed (PETTIFOR [1976]) directly in terms of parameters describing the energy bands, namely:

$$3P_{sp}\Omega = 3N_{sp}\left(\Gamma_1 - \varepsilon_{xc}\right) + 2U_{sp}^{ke}, \tag{118}$$

$$3P_d\Omega = 2N_d\left(E_d - \varepsilon_{xc}\right)/m_d + 5U_d^{bond}, \tag{119}$$

where

$$U_{sp}^{ke} = \int^{E_F} \left(E - \Gamma_1\right) n_{sp}(E)\mathrm{d}E, \tag{120}$$

$$U_d^{bond} = \int^{E_F} \left(E - E_d\right) n_d(E)\mathrm{d}E, \tag{121}$$

with $\varepsilon_{XC} = \varepsilon_{XC}(S)$. m_d is the d-band effective mass which is related to the width W through $W = 25/(m_d S^2)$. Additional small contributions to eqs. (118) and (119) have been neglected for simplicity in the present discussion (cf. eqs. (13) and (14) of PETTIFOR [1978b]).

The sp partial pressure consists of two terms which give the first-order changes in the *bottom* of the sp band, Γ_1, and in the *kinetic* energy, respectively. In the absence of hybridization with the d band, $n_{sp}(E)$ is free-electron-like and eq. (118) is consistent with the pressure which would be obtained from the simple-metal expression (105) if correlation is neglected. This follows from eqs. (111), (113) and (79) because within LDF theory the bottom of the band is given by

$$\Gamma_1 = \Gamma_1^{WS} + 2.4\,Z/S + \tfrac{4}{3}\varepsilon_X \tag{122}$$

since the electron sees the average Hartree field of the valence electrons and the exchange potential v_X in addition to the ion core pseudopotential.

The d partial pressure also consists of two terms which give the first-order changes in the *centre of gravity* of the d band, E_d, and the d *bond* energy, respectively. In the absence of hybridization we may assume that $n_d(E)$ is rectangular as illustrated in fig. 24, so that from eq. (121) the d bond energy may be written

$$U_d^{bond} = -\tfrac{1}{20} W N_d\left(10 - N_d\right). \tag{123}$$

Assuming that $E_d - E_d^{atom}$ and W vary inversely as the fifth power of S, P_d may be integrated with respect to volume to give the d contribution to the *cohesive* energy, namely:

$$U_d = N_d\left(E_d - E_d^{atom}\right)/4m_d + N_d\left(\tfrac{4}{3}E_d^{atom} - \varepsilon_{xc}\right)/2m_d + U_d^{bond}. \tag{124}$$

It follows from fig. 28a that for Tc at its equilibrium volume $E_d - E_d^{atom} = 6$ eV, $\frac{4}{3}E_d^{atom} - \varepsilon_{XC} = 1$ eV and $m_d = 5$. Therefore, taking, from table 2, $W = 10$ eV and $N_d = 6$, we have

$$U_d = 1.8 + 0.6 - 12 = -10\text{eV/atom}, \tag{125}$$

which is in reasonable agreement with the LDF value of -8 eV/atom for the Tc cohesive energy in fig. 1.

The dominant contribution to the *cohesive energy* of transition metals is, therefore, the d bond term in eq. (125) as emphasized by FRIEDEL [1964, 1969] and illustrated by GELATT *et al.* [1977] in their fig. 4. From eq. (123) it varies parabolically with band filling and accounts for the observed variation of the cohesive energy across the *nonmagnetic* 4d and Sd series shown in fig. 1. It attains a maximum value of $-5\ W/4$ for $N_d = 5$ when all the bonding and none of the antibonding states are occupied. Equation (124) shows that the shift in centre of gravity of the d band contribution $N_d(E_d - E_d^{atom})$ is reduced by at least an order of magnitude through the factor $(4m_d)^{-1}$, thereby accounting *analytically* for the cancellation arising from the double-counting term in eq. (115).

Figure 29 shows the sp and d partial pressures for Tc. As expected from eq. (123) there is a large *attractive* d bond contribution which is pulling the atoms together in order to maximize the strength of the bond. This is opposed for $S < 4.0$ au by a rapidly increasing *repulsive* d centre-of-gravity contribution which reflects the renormalization in E_d. The resulting total d partial pressure is *attractive* at the observed equilibrium volume of Tc (see fig. 29b). As expected from the behaviour of Γ_1 in fig. 28b the bottom of the sp band contribution is attractive for large values of S but becomes repulsive in the vicinity of the equilibrium volume as Γ_1 moves up in energy. Thus, whereas in simple metals this contribution is attractive because the ion cores occupy only about 10% of the atomic volume (see fig. 21 and table 3), in transition metals it is repulsive because

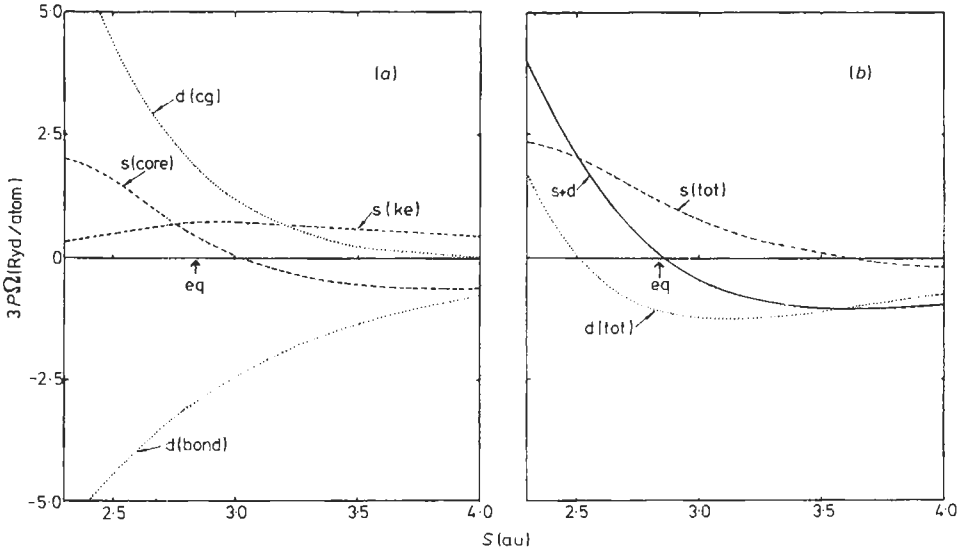

Fig. 29. (a) The *individual* and (b) the *total* sp and d partial pressures as a function of the Wigner-Seitz radius S for T_c. "eq" marks the observed equilibrium Wigner–Seitz radius. (From PETTIFOR [1978b]).

Table 3
The values of λ for the 3d, 4d, and 5d transition metal series.

Period	Element and value of λ (in au^{-1})							
	Sc	Ti	V	Cr	Mn	Fe	Co	Ni
3	1.08	1.23	1.37	1.49	1.61	1.74	1.88	2.07
	Y	Zr	Nb	Mo	Tc	Ru	Rh	Pd
4	1.08	1.23	1.37	1.49	1.60	1.72	1.85	2.02
	Lu	Hf	Ta	W	Re	Os	Ir	Pt
5	1.11	1.25	1.38	1.49	1.60	1.72	1.84	2.01

the ion cores occupy a much larger percentage due to their smaller equilibrium atomic volumes (cf. fig. 1). Together with the sp kinetic energy contribution, the bottom of the sp band contribution provides the necessary repulsion to counter the attractive d partial pressure at equilibrium.

The *size* of a transition-metal atom, which is defined by the equilibrium atomic volume of the pure metal, is not necessarily a helpful quantity for discussing alloy energetics. We have seen that it will be very sensitive to the nature of the local atomic environment, since it is the d bond contribution which is responsible in fig. 1 for the skewed parabolic behaviour of the equilibrium Wigner–Seitz radius across the nonmagnetic 4d series. This may be demonstrated by modifying the simple model of DUCASTELLE [1970] and approximating the total energy of a transition metal by

$$U = U^{\text{rep}} + U_{\text{d}}^{\text{bond}}, \tag{126}$$

where the Born–Mayer contribution, U^{rep}, is:

$$U^{\text{rep}} = aN^2 e^{-2\lambda S} \tag{127}$$

with a being constant across a given series. This form is suggested by the nature of the repulsive d centre-of-gravity contribution in eq. (124) and fig. 29, although we have assumed that U^{rep} is proportional to N^2 rather than N_{d}^2 as a reminder that the sp electrons also contribute to the repulsion. The d bond contribution, eq. (123), is proportional to the band width W which is assumed to vary exponentially as

$$W = b\lambda^2 e^{-\lambda S} \tag{128}$$

with b being constant across a given series.

The cohesive energy, equilibrium Wigner–Seitz radius and bulk modulus are given from eqs. (126)–(128) by:

$$U_{\text{coh}} = \tfrac{1}{2} U_{\text{d}}^{\text{bond}}, \tag{129}$$

$$S_0 \left[\ln\left(-2aN^2 / U_{\text{d}}^{\text{bond}}\right) \right] / 2\lambda, \tag{130}$$

$$B = -\left(\lambda^2 / 12\pi S_0\right) U_{\text{d}}^{\text{bond}}. \tag{131}$$

a and b for a given period are obtained from the known bulk modulus and band width of 3d Cr, 4d Mo and 5d W, the values of *(a, b)* being given in atomic units by (24.3, 11.6), (77.2, 25.8) and (98.9, 31.9) respectively. λ is found by fitting to the *nonmagnetic* Wigner–Seitz radius, assuming that the transition metals have only one sp valence electron. We see from fig. 30 and table 3 that although the equilibrium atomic volume has a minimum in the vicinity of $N=8$, λ varies nearly *linearly* across the series as expected for a parameter characterizing the free atom (cf. figs. 4, 5 and 7). Thus, although Mo and Ag have almost the same size factors with their equilibrium Wigner–Seitz radii of 2.93 and 3.02 au, respectively, they are immiscible because Mo will lose a large part of its attractive d bond contribution in a Ag environment. The logarithmic derivative of the band width, $-\lambda$, predicted by this model is in good agreement at the equilibrium atomic volume with the first-principles value, $-n/S_0$, as can be seen by comparing tables 1 and 3 for the 4d series.

The simple model breaks down at the noble-metal end of the series because the Born–Mayer repulsive term in eq. (126) does not describe correctly the d electron behaviour. This can be seen in fig. 31 where the d partial pressure in Cu *is attractive* at the equilibrium atomic volume, the d electrons contributing about 25% to the cohesive energy (WILLIAMS *et al.* [1980a]). Thus, as first pointed out by KOLLAR and SOLT [1974], the filled d shells in copper interact attractively rather than repulsively as assumed by the Born-Mayer contribution (127). This is due to the second term in eq. (124) which dominates at larger atomic volumes. The sp partial pressure of Cu at its minimum is also more attractive than that of K due to the incomplete screening of the Cu ion core by the 3d valence electrons. The net result is that whereas the simple metal K has a cohesive energy of 0.9 eV/atom and a bulk modulus of 0.3×10^{10} N/m^2, the noble metal Cu has a cohesive energy of 3.5 eV/atom and a bulk modulus of 13.7×10^{10} N/m^2, which is reflected by the behaviour of the curves in fig. 31.

6. *Structural stability*

6.1. Elemental metals

The crystal structure of the *simple* metals can be studied (see, e.g., HARRISON [1966], HEINE and WEAIRE [1970], HAFNER [1974, 1989] and MORIARTY [1982, 1983 and 1988]) by perturbing the free electron gas to *second* order in the pseudopotential, thereby extending the first-order expression (105) considered in § 5.1. The resulting binding energy per atom is given in the real-space representation (FINNIS [1974]) by

$$U = ZU_{e\xi} - \tfrac{1}{2} V\mathrm{ic}_{eg}^{-1} + \tfrac{1}{2}\phi(\boldsymbol{R}=0; r_s) + \tfrac{1}{2}\sum_{\boldsymbol{R}\neq 0}\phi(\boldsymbol{R}; r_s), \tag{132}$$

where κ_{eg} is the compressibility of the free electron gas. $\phi(\boldsymbol{R}=0;\ r_s)$ represents the electrostatic interaction between an ion and its own screening cloud of electrons, whereas $\phi(\boldsymbol{R}\neq 0;\ r_s)$ is a *central* interatomic pair potential which for a local pseudopotential may be written as:

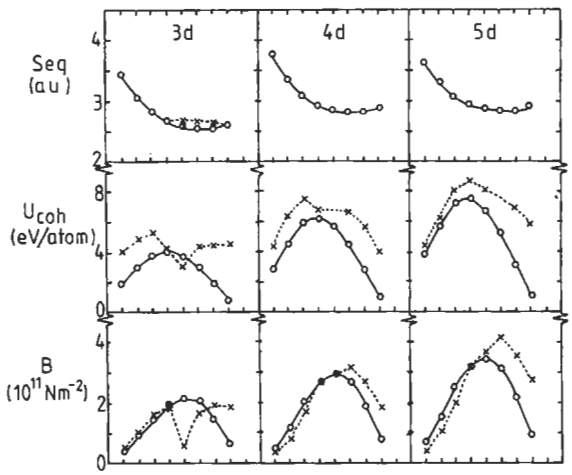

Fig. 30. The theoretical (open circles) and experimental (crosses) values of the equilibrium Wigner-Seitz radius, cohesive energy, and bulk modulus of the 3d, 4d, and 5d transition metals.

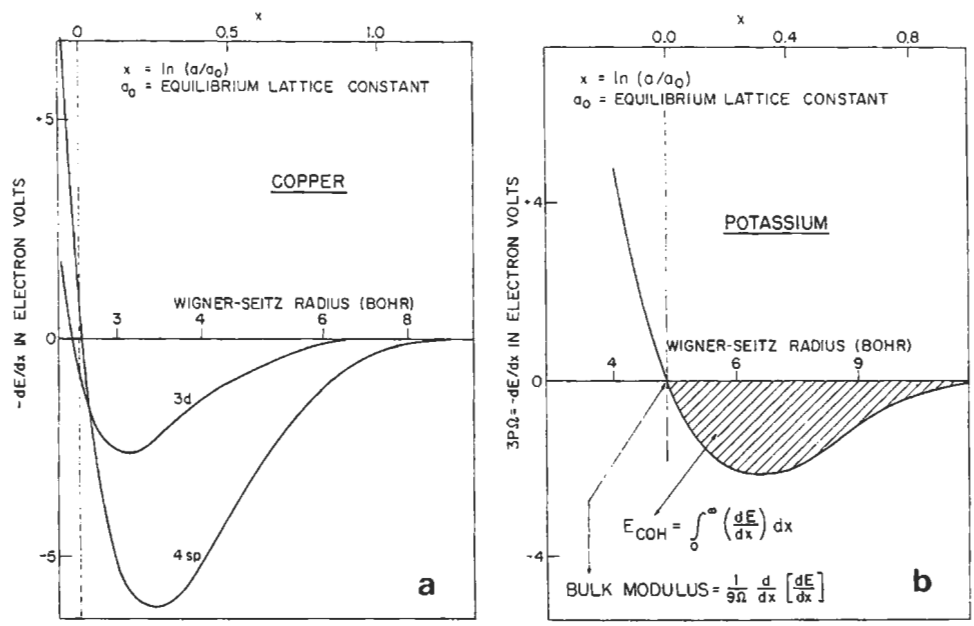

Fig. 31. (a) The sp and d partial pressures for Cu and (b) the sp pressure for K as a function of the Wigner–Seitz radius. The independent variable x is the logarithm of the ratio of the lattice constant a (or Wigner-Seitz radius S) to its equilibrium value a_0 (or S_0), so that equilibrium corresponds to the zero value of x on the upper horizontal axis. The cohesive energy associated with a given pressure curve is the area between the curve and the axis, as illustrated in (b). (From WILLIAMS *et al.* [1980a].)

$$\phi(\boldsymbol{R} \neq 0; r_s) = \frac{2Z^2}{R}\left[1 - \tfrac{2}{\pi}\int_0^\infty \chi(q, r_s)\left[\hat{v}_{ps}^{ion}(q)\right]^2 \frac{\sin qR}{q}\,dq\right]. \tag{133}$$

$\hat{v}_{ps}^{ion}(q)$ is proportional to the Fourier component of the ionic pseudopotential, taking the value $\cos qR_C$ for the Ashcroft potential [cf. eq. (76)]. $\chi(q, r_s)$ is the free-electron-gas response function which screens the ion cores (see, e.g., JACUCCI and TAYLOR [1981]). The first term in eq. (133) gives the direct ion–ion coulomb repulsion, the second the attractive ion–electron contribution.

The interatomic potential (133) may be expressed analytically (PETTIFOR [1982]) at metallic densities as the sum of damped oscillatory terms, namely

$$\phi(\boldsymbol{R} \neq 0; r_s) = (2Z^2/R)\sum_n A_n \cos(2k_n R + \alpha_n)e^{-\kappa_n R}, \tag{134}$$

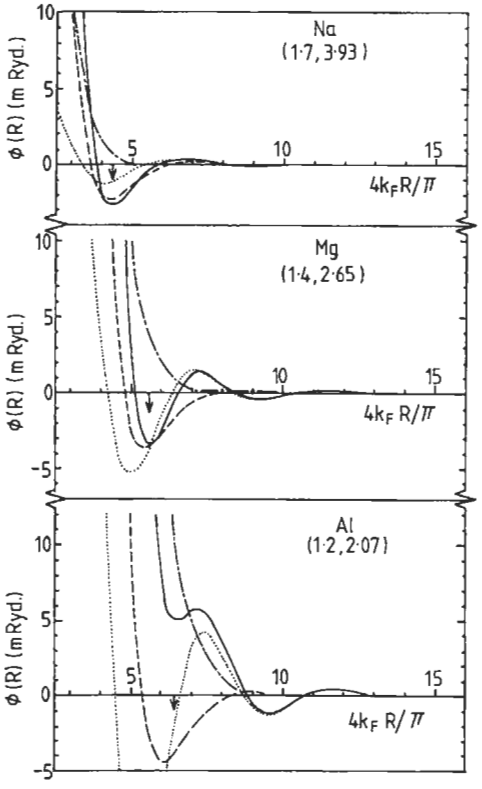

Fig. 32. The analytic pair potential (solid curve) for Na, Mg, and Al, the three individual contributions being given by the dotted–dashed, dashed, and dotted curves respectively. The arrows mark the position of the twelve nearest neighbours in the close-packed fcc and hcp lattices. The values of R_c and r_s are written (R_c, r_s) for each element. (After PETTIFOR and WARD [1984].)

where k_n and κ_n depend only on the density of the free electron gas through r_s, whereas the amplitude A_n and the phase α_n depend also on the ionic pseudopotential (through R_c). The interatomic potentials for Na, Mg and Al are illustrated in fig. 32, where the first three terms in eq. (134) have been retained and an Ashcroft empty-core pseudopotential used (PETTIFOR and WARD [1984]). We see that all three metals are characterized by a repulsive hard-core contribution (dotted–dashed curve), an attractive nearest-neighbour contribution (dashed curve), and an oscillatory long-range contribution (dotted curve). For *very large* interatomic separations the pair potential behaves asymptotically (FRIEDEL [1952]) as

$$\phi(R \neq 0; r_s) \sim A\left[v_{ps}(2k_F)\right]^2 \cos(2k_F R)/R^3, \tag{135}$$

where from eqs. (44) and (104) $k_F = (9\pi/4)^{1/3}/r_s$.

A cautionary note must be sounded concerning the use of interatomic pair potentials for describing the energetics of simple metals. It is clear from fig. 32 that the pair-potential contribution to the binding energy of sodium and magnesium is only about 0.25 eV/atom, which is small compared to their cohesive energies of 1.1 and 1.6 eV/atom, respectively. Moreover, in aluminium the pair contribution acts *against* cohesion. Thus, there is no microscopic justification for describing the bonding in simple metals by pair potentials alone. Their cohesion is determined primarily by the *volume*-dependent terms in eq. (132). However, the pair potential description is valid for tackling problems concerned with *structural* rearrangement in which the volume remains fixed, for example in lattice dynamics or in determining the relative stability of the close- or nearly close-packed fcc, hcp and bcc lattices.

Figure 33 compares the stability of the fcc, hcp and bcc lattices of Na, Mg and Al as their volume is reduced from the equilibrium value by nearly an order of magnitude, which was computed by MORIARTY and MCMAHAN [1982] using a generalized non-local pseudopotential to second order. We see that under pressure Na, Mg and Al are predicted to transform from hcp → bcc → hcp, hcp → bcc → fcc and fcc → hcp → bcc, respectively. The first of these structural transitions occurs at about 1, 57 and 130 GPA for Na, Mg and Al respectively and should, therefore, be verifiable by modern high-pressure technology. The trends displayed in fig. 33 may be understood from the behaviour of the first three contributions to the pair potential in fig. 32 (PETTIFOR and WARD [1984]; see

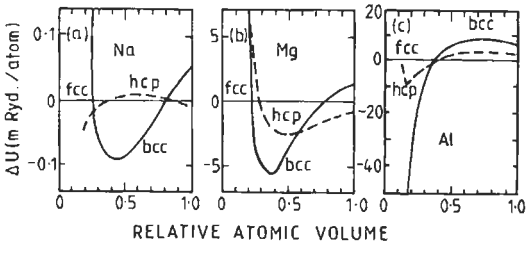

Fig 33. The energy of the bcc and hcp lattices with respect to the fcc lattice for Na, Mg, and Al as a function of their atomic volume relative to the observed equilibrium volumes (after MORIARTY and MCMAHAN [1982]).

also McMAHAN and MORIARTY [1983]). Because the close-packed structures fcc and hcp have identical first and second nearest-neighbour distances their relative stability is determined by the position of their next few neighbours with respect to the long-range oscillatory tail which is drawn dotted in fig. 32. Since the phase α_3 of this contribution depends on r_s, under pressure the minima shift with respect to the neighbour positions and the close-packed phases can reverse their relative stability. On the other hand, the competition between the close-packed phases and bcc is determined primarily by the contribution from the twelve first nearest neighbours and fourteen first and second nearest neighbours respectively. Although at their equilibrium volume the first twelve close-packed neighbours fall at the minimum of the pair potential, thereby favouring the close-packed structures (cf. fig. 32), under pressure this minimum moves and the bcc phase may be stabilized (cf. fig. 33).

The *close-packed* metallic behaviour of Na, Mg and Al gives way to the *open* diamond structure of the semiconductor Si as one proceeds *across* the third row of the Periodic Table. This transition from close-packed to open structure is accompanied by a 30% volume expansion so that the volume-dependent term in the binding energy cannot be neglected when determining structural stability. YIN and COHEN [1980] have solved the Schrödinger equation self-consistently for Si using an ionic pseudopotential, and have evaluated the LDF binding energy [cf. eq. (115)] as a function of volume for seven different crystal structures as illustrated in fig. 34a. They find that the diamond structure has the lowest energy with a predicted equilibrium atomic volume, cohesive energy and bulk modulus within 5% of the experimental values. Moreover, the relative ordering of the metallic bcc and hcp phases and their equilibrium energy of about 0.5 eV/atom with respect to the diamond structure is in good agreement with that deduced from experiment (KAUFMAN and NESOR [1973]). The transition to the open semiconducting phase, therefore, contributes about 10% to the total cohesive energy of 4.6 eV/atom.

In moving *down* group IV we see from figs. 4 and 7 that Ge is very similar to Si with about a 10% larger core, whereas Sn and Pb have approximately 30% and 45% larger cores respectively. Thus the binding–energy–volume curves of Ge are found to be almost identical to those of Si except that the close-packed structures move down relative to the diamond structure by about 20% (compare figs. 34a and b; YIN and COHEN [1980, 1981]). The further increase in core size in going from Ge to Sn is probably responsible for the β-Sn structure being stabilized under only 2 GPA of pressure and the still much larger core of Pb at the bottom of group IV leads to the close-packed fcc structure being most stable. The structural trends across the sp-valent elements within the periodic table has recently been discussed by CRESSONI and PETTIFOR [1991] using the Tight Binding approximation.

The crystal structure of the *transition* metals can be understood by comparing the d bond contribution eq. (121) to the total energy, because we saw in § 5.2 that it dominates the cohesive energy. Figure 35 shows that as the unhybridized tight-binding d band is filled with electrons the structure-trend predicted is hcp → bcc → hcp → fcc → bcc (PETTIFOR [1972b]). Apart from the incorrect stability of the bcc phase at the noble-metal end of the series, this trend agrees with experiment for the *nonmagnetic* 4d and 5d series. The stability of the bcc phase in V and Cr, Nb and Mo, Ta and W, when the d band is

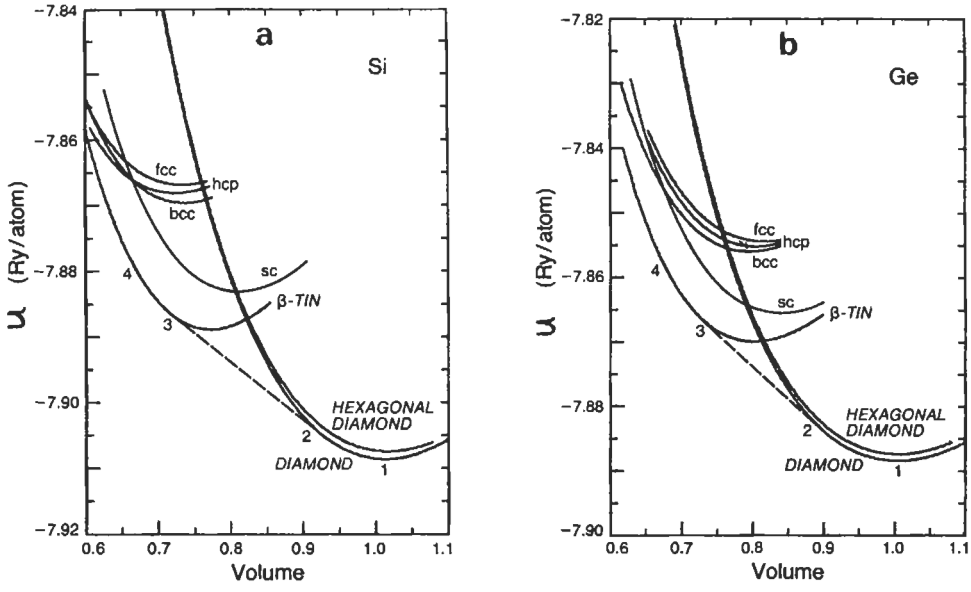

Fig. 34. The binding energy as a function of volume of (a) Si and (b) Ge for seven different crystal structures. The dashed line is the common tangent of the energy curves for the semiconducting diamond phase and the metallic β-tin phase, the system moving from $1 \rightarrow 2 \rightarrow 3 \rightarrow 4$ under pressure. (from YIN and COHEN [1980, 1981] and YIN [1982]).

nearly half-full, is due to the strong bonding-antibonding separation which is manifest in the bcc density of states compared to the close-packed (cf. fig. 26). The appearance of the bcc phase in iron is due to the presence of *ferromagnetism* (see § 8). The stability of different stacking-fault structures shows the same oscillatory behaviour as displayed by the fcc hcp curve in fig. 35 (PAPON *et al.* [1979]).

The number of d electrons, N_d, also influences the structure of the heavier alkalis and alkaline earths (TAKEMURA *et al.* [1982] and SKRIVER [1982]) and the rare earths (DUTHIE and PETTIFOR [1977]). N_d increases on moving down the *alkaline earth* group as the d band starts to fill (cf. fig. 20) so that Ca, Sr and Ba have 0.51, 0.59 and 0.87 $l=2$ electrons within the Wigner–Seitz sphere, respectively (SKRIVER [1982]). Similarly, under pressure N_d increases as the NFE-sp band moves up with respect to the TB-d band (cf. § 4.3). SKRIVER [1982] has computed the structural energy differences, using eq. (116), and has found that the trend hcp $\rightarrow$ fcc $\rightarrow$ bcc $\rightarrow$ hcp correlates with increasing Nd in agreement with the observed behaviour down group IIA (Be,Mg: hcp; Ca,Sr: fcc; Ba,Ra: bcc) and under pressure. The trivalent *rare-earth* crystal structure sequence hcp $\rightarrow$ Sm-type $\rightarrow$ double hcp $\rightarrow$ fcc, which is observed for decreasing atomic number and increasing pressure, can similarly be explained in terms of the change in number of d electrons accompanying valence s to d transfer (DUTHIE and PETTIFOR [1977]). Due to the lanthanide contraction of the ion core La has a 20% larger core radius than Lu, which results in La having 0.6 d electrons more than Lu and taking the double-hcp rather than the hcp crystal structure even though they are both trivalent.

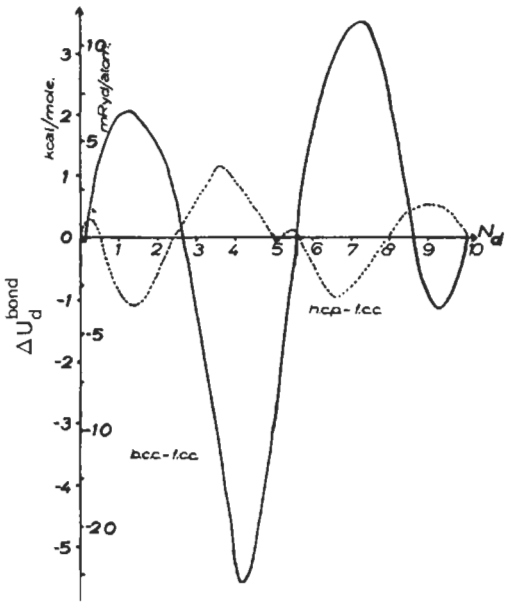

Fig. 35. The d bond energy of the bcc (solid line) and the hcp (dotted line) lattices with respect to the fcc lattice as a function of band filling N_d (from PETTIFOR [1972b]).

Recently *ab initio* Local Density Functional (LDF) calculations have been used to study the transformation path from bcc to hcp in barium under pressure at the absolute zero of temperature (CHEN *et al.* [1988]; HO and HARMAN [1990]). As illustrated in fig. 36, the bcc to hcp transformation involves atomic displacements corresponding to the zone boundary [110] T_1 phonon mode and an additional lattice shear (BURGERS [1934]). The dashed lines in fig. 36b show that a displacement $\delta = \sqrt{2}\,a/12$ in this bcc phonon mode creates a nearly hexagonal geometry, the perfect geometry being achieved in fig. 36c through a subsequent shear which changes the angle θ from 109.47° to 120°. Figure 37 displays the calculated total energy contours as a function of both co-ordinates δ and θ for barium at its equilibrium atomic volume Ω_0, $0.793\Omega_0$ and $0.705\Omega_0$, respectively. The latter volume corresponds to a pressure of 38.4 kbar. We see that at $\Omega = \Omega_0$ the upper contour plot shows that bcc barium is more stable than hcp, in agreement with experiment. However, as pressure is applied, the hcp phase has its energy lowered with respect to bcc. The middle contour plot shows that at $\Omega = 0.793\Omega_0$ their energies are approximately equal, with an energy barrier between them of about 4meV/atom. The lower contour plot shows that at $\Omega = 0.705\Omega_0$ the energy barrier has gone and the bcc phase is no longer metastable. The predicted $T = 0$ transformation pressure is 11 kbar, corresponding to the bcc and hcp lattices having equal enthalpies. However, at low temperatures the system would not be able to overcome the energy barrier so that the bcc phase would probably remain metastable until the T_1 N-point phonon mode became soft at 31 kbar. Experimentally the phase transformation occurs at a pressure of 55 kbar at room temperature so that the LDF predicted pressure appears too low, reflecting the intrinsic errors in the local approximation to density functional theory (see, for example, fig. 1).

References: p. 129.

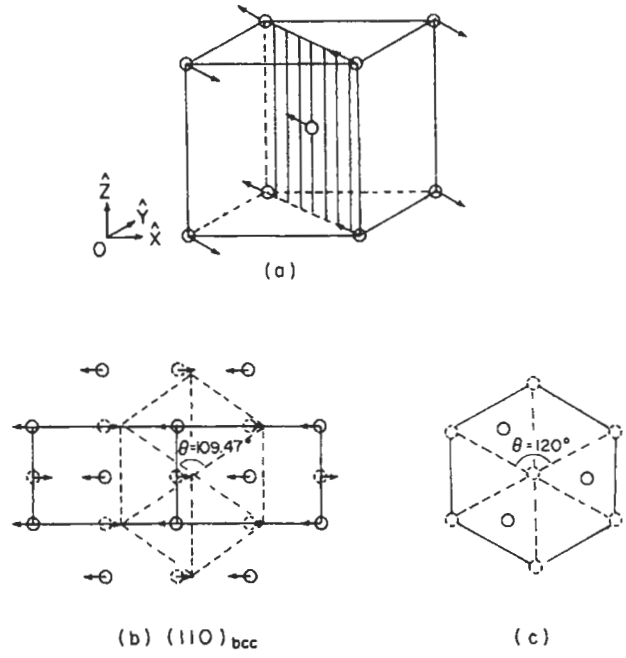

Fig. 36. Illustration of the bcc to hcp phase transformation. The arrows in (a) and (b) indicate the atomic displacements in the bcc lattice corresponding to the polarisation vector of the T_1 N-point phonon mode. A final long-wavelength shear changes the angle from 109.47° to 120° to obtain the hcp lattice in (c) (from Ho and Harmon [1990]; reproduced with permission).

6.2. Binary intermetallic phases

The structural trends within binary intermetallic phases $A_{1-x}B_x$ may be displayed by ordering the structural data base within a single three-dimensional structure map ($\mathfrak{M}_A$, $\mathfrak{M}_B$, x) where $\mathfrak{M}$ is a *phenomenological* co-ordinate which characterises each element in the periodic table (Pettifor [1988a]). The relative ordering *number* $\mathfrak{M}$ is obtained by running a one-dimensional string through the two-dimensional periodic table as shown in fig. 38; pulling the ends of the string apart places all the elements in sequential order, labelled by $\mathfrak{M}$.

The resultant two-dimensional isostoichiometric ground-state structure map ($\mathfrak{M}_A$, $\mathfrak{M}_B$) for the 50:50 AB binary compounds is shown in fig. 39 using the experimental database of Villars and Calvert [1985]. Similar maps for other stoichiometries may be found elsewhere (Pettifor [1988a], [1988b] and [1992])). The bare patches correspond to regions where compounds do not form due to either positive heats of formation or the competing stability of neighbouring phases with different stoichiometry. The boundaries do not have any significance other than they were drawn to separate compounds of

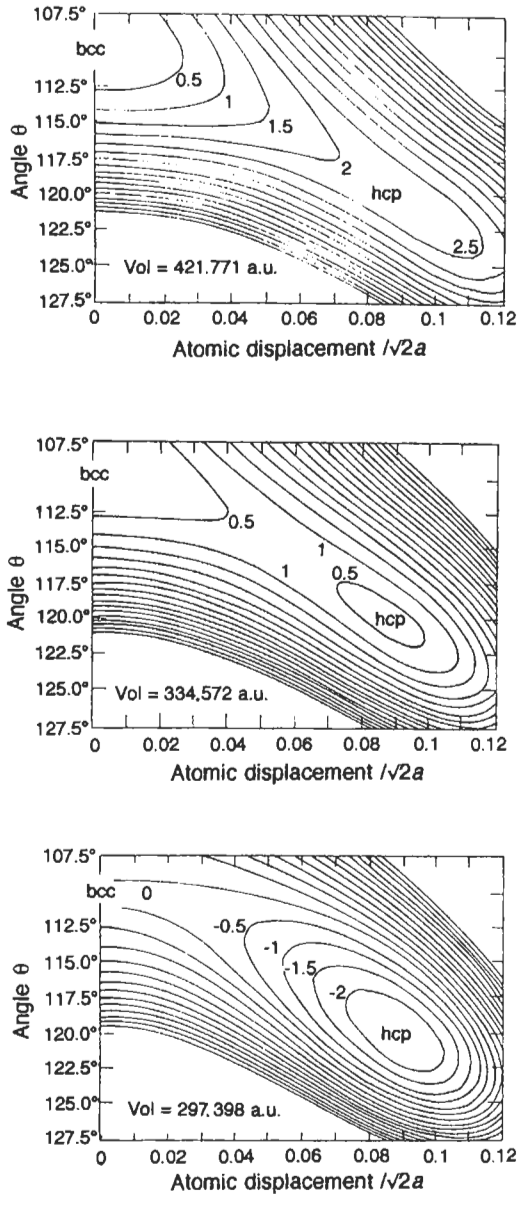

Fig. 37. Contour plots of the LDF energy for barium as a function of the atomic displacement δ corresponding to the T_1 N-point phonon mode and the angle θ of the shear motion. The upper, middle and lower panels correspond to the volumes Ω_0, $0.793\,\Omega_0$ and $0.705\,\Omega_0$, where Ω_0 is the observed equilibrium volume at ambient pressure. The energy contours are in steps of 0.5 mRy/cell (from Ho and HARMON [1990]; reproduced with permission).

References: p. 129.

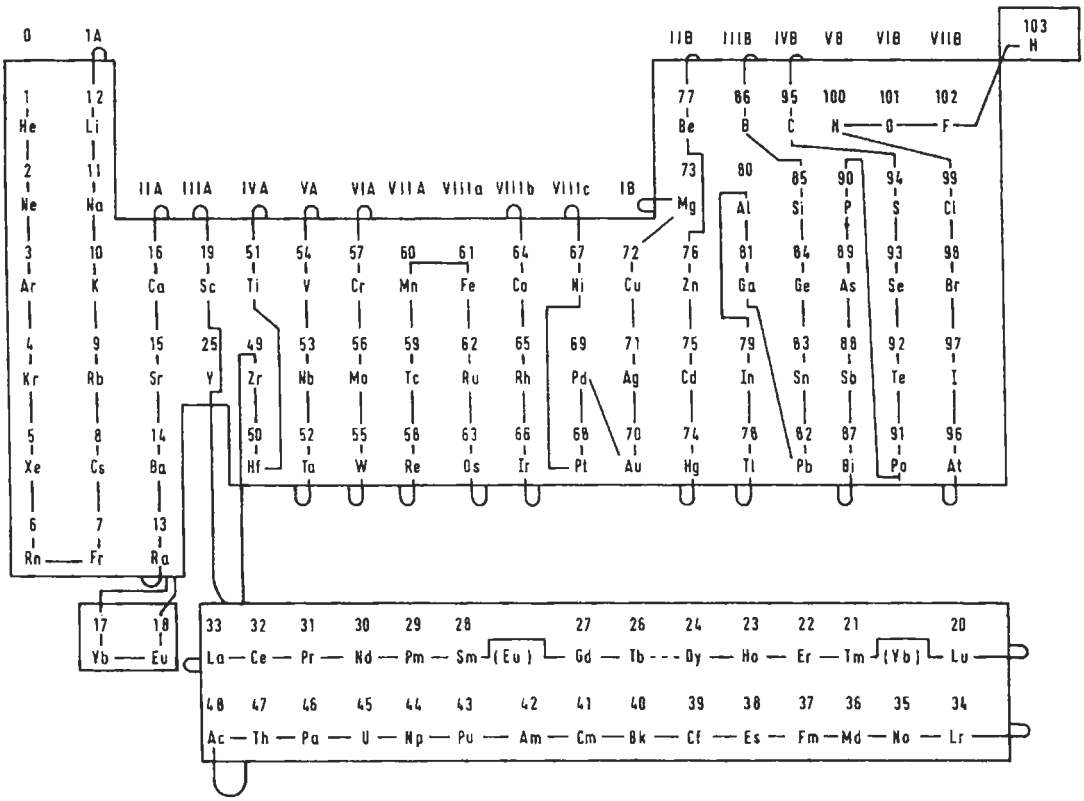

Fig. 38. The string running through this modified periodic table puts all the elements in sequential order according to the relative ordering number. (PETTIFOR [1988a]). Note that group II A elements Be and Mg have been grouped with II B, divalent rare earths have been separated from trivalent, and Y has been slotted between Tb and Dy.

different structure type. In regions where there is a paucity of data the boundary is usually chosen as the line separating adjoining groups in the periodic table. We see that excellent structural separation has been achieved between the 52 different AB structure types that have more than one representative compound each. The two most common structure types, namely B1 (NaCl) and B2 (CsCl), are well separated, the NaCl lattice being found only outside the region defined by $\mathfrak{M}_A$, $\mathfrak{M}_B \leq 81$, which encloses the main CsCl domain. There is only one exception, namely the very small region of Cs-containing salts. The AB structure map successfully demarcates even closely related structure types such as B27 (FeB) and B33 (CrB); $B8_1$ (NiAs) and B31 (MnP); or B3 (cubic ZnS, zincblende) and B4 (hexagonal ZnS, wurtzite). Moreover, coherent phases with respect to the bcc lattice, namely B2 (CsCl), B11 (CuTi), and B32 (NaTl) are also well separated, as too are the close-packed polytypes cubic $L1_0$ (CuAu) and hexagonal B19 (AuCd).

The structural trends within the pd-bonded AB compounds in fig. 39 have been successfully explained by PETTIFOR and PODLOUCKY [1984, 1986] within a simple two-centre, orthogonal Tight Binding (TB) model. The upper panel of fig. 40 shows the

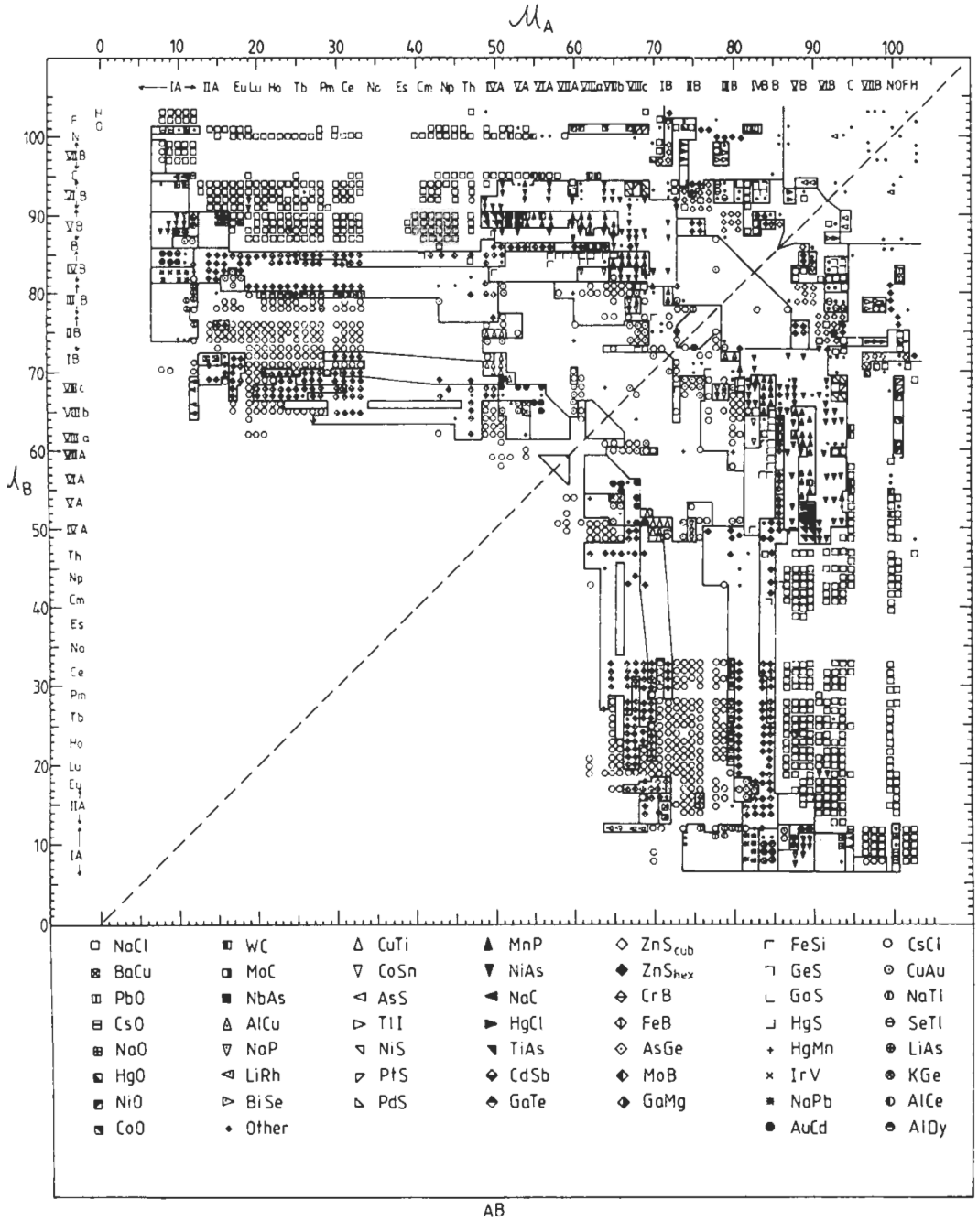

Fig. 39. The AB structure map (PETTIFOR [1988a]).

experimental structural domains for the seven most frequently occurring structure types, namely NaCl, CsCl, NiAs, MnP, FeB, CrB and FeSi respectively (using the socalled chemical scale χ which orders the elements in a similar way to the relative ordering number $\mathfrak{M}$ in fig. 38, PETTIFOR [1984]). The lower panel shows the *predicted* AB structure map (N_p, N_d) where N_p and N_d are the number of p and d valence electrons associated with atoms A and B respectively. We see that the TB model predicts the broad topological features of the experimental map. In particular, NaCl in the top left-hand corner adjoins NiAs running across to the right and boride stability running down to the bottom. MnP stability is found in the middle of the NiAs domain and towards the bottom right-hand corner, where it adjoins CsCl towards the bottom. The main failure of this simple pd TB model is its inability to predict the narrow-tongue of FeSi stability of the transition metal silicides, which is probably due to the total neglect of the valence s electrons within the model.

The theoretical TB calculations allowed the different roles played by relative atomic size, electronegativity difference, and electron per atom ratio in stabilizing a given structure type to be investigated directly (PETTIFOR and PODLOUCKY [1984, 1986]). Fig. 41 shows the fractional change in volume $(\Delta V)/V$ between a given structure type and

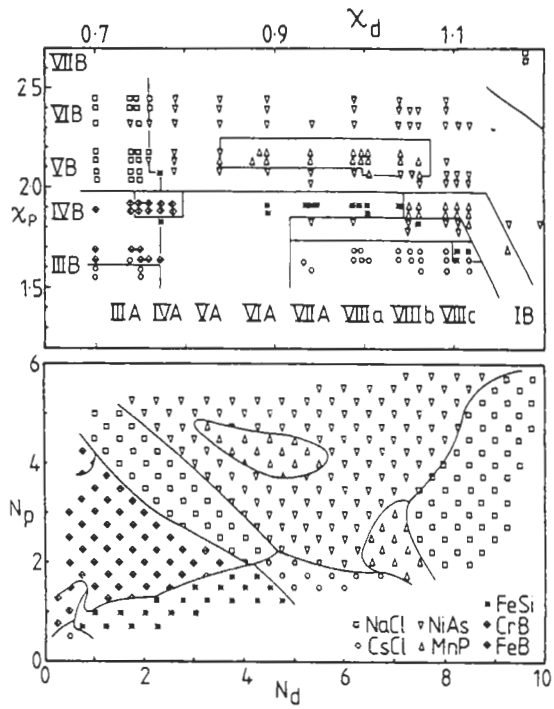

Fig. 40. The *upper* panel shows the structure map (χ_p, χ_d) for 169 pd bonded AB compounds, where χ_p and χ_d are values for the A and B constituents of a certain chemical scale, χ, which orders the elements in a similar way to the relative ordering number $\mathfrak{M}$. The *lower* panel shows the theoretical structure map (N_p, N_d) where N_p and N_d are the number of p and d valence electrons respectively on the CsCl lattice. (From PETTIFOR and PODLOUCKY [1984].)

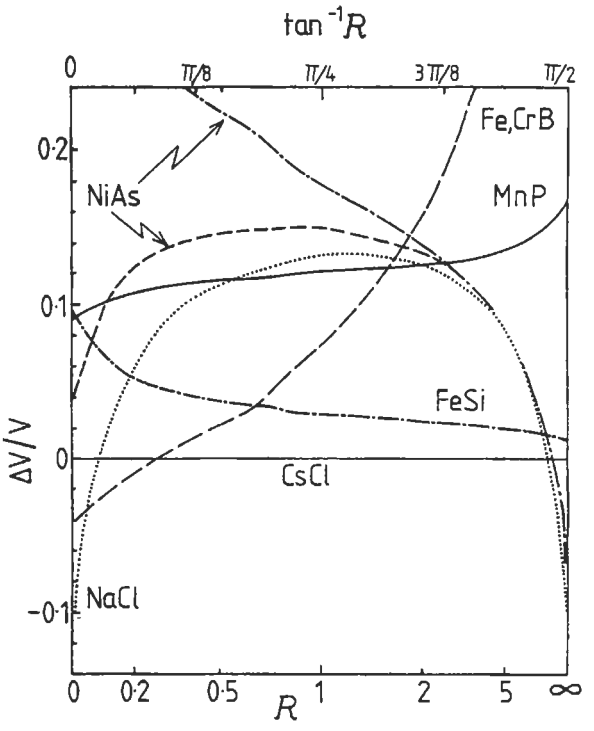

Fig. 41. The fractional change in volume $(\Delta V)/V$ with respect to the CsCl lattice versus the relative size factor $\mathfrak{R}$ (see text). The upper and lower NiAs curves correspond to $c/a = 1.39$ and $(8/3)^{1/2}$ respectively (PETTIFOR and PODLOUCKY [1984]).

the CsCl lattice as a function of the *relative size factor* $\mathfrak{R}$ of the constituent atoms. Within the TB model, $\mathfrak{R}$ had been defined through the relative strength of the pp repulsive pair potential compared to the dd repulsive pair potential. As expected, the NaCl lattice has the smallest volume at either end of the $\mathfrak{R}$ scale, because as the size of either the p-valent atom or the d-valent atom shrinks to zero the repulsion will be dominated by one or other of the close-packed fcc sublattices. On the other hand, in the middle of the scale, where the nearest-neighbour pd repulsion dominates, the volume of the NaCl lattice with six nearest neighbours is about 13% larger than the CsCl with eight nearest neighbours. The packing of hard spheres rather than the softer atoms would have led to the much larger volume difference of 30%.

The structural stability of the pd-bonded AB compounds may then be predicted by comparing the TB band energy of the different structure types at the volumes determined by the relative size factor $\mathfrak{R}$. Fig. 42 shows the resultant structural energies as a function of the *electron per atom ratio* or band filling N for the case where the atomic p level on the A site and the atomic d level on the B site are equal i.e. $E_{pd} = E_p - E_d = 0$. As the electron per atom ratio increases we find the structural sequence CsCl → FeSi → CrB

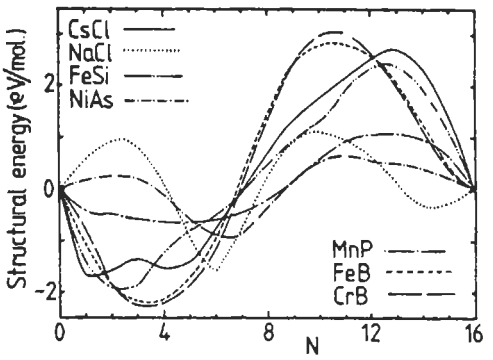

Fig. 42. The structural energy as a function of band filling N for the seven different crystal lattices with E_{pd} = 0 (PETTIFOR and PODLOUCKY [1984]).

→ NaCl → NiAs → (MnP) → NiAs → NaCl, where MnP, a distorted NiAs structure, has been put in parentheses because it does not quite have the lowest energy for $N \approx 9$. The structural energy depends not only on the electron per atom ratio but also on $E_{pd} = E_p - E_d$ which is a measure of a Mulliken-type *electronegativity difference*. Curves similar to fig. 42 have, therefore, been calculated for values of the atomic energy level difference in the range from −10 to +5 eV (in steps of 2.5 eV). Rather than plotting the most stable predicted structure on a structure map of E_{pd} versus N, the lower panel in fig. 40 uses the rotated frame of N_p versus N_d in order to make direct comparison with the experimental results in the upper panel.

The TB model has successfully accounted for the structural trends not only within the pd bonded AB compounds above but also within other families of AB_2 and AB_3 intermetallic phases (see, for example, JOHANNES *et al.* [1976], DUCASTELLE [1991], BIEBER and GAUTIER [1981], LEE [1991a and b], and OHTA and PETTIFOR [1989]). As expected, the structural stability of the binary phases is found to be controlled by four factors, namely the average number of valence electrons per atom (or band filling), a Mulliken-type electronegativity difference (or atomic energy level mismatch), the atomic size mismatch, and the angular character of the valence orbitals (or whether the bonding is pd, dd etc.). Classic ionic Madelung terms appear to play little role in determining the structures of intermetallic phases since the screening in a metal is perfect.

The most famous example of the crystal structure correlating with the average number of valence electrons per atom or band filling N is the Hume-Rothery alloy system of *noble* metals with the sp bonded elements such as Zn, Al, Si, Ge and Sn (see ch. 4). Assuming that Cu and Ag have a valency of 1, then the fcc α-phase is found to extend to a N of about 1.38, the bcc β-phase to be stabilized around 1.48, the γ-phase around 1.62 and the hcp ε-phase around 1.75. MOTT and JONES [1936] pointed out that the fcc and bcc electron-per-atom ratios correlate with the number of electrons required for a free-electron Fermi *sphere* to first make contact with the fcc and bcc Brillouin-zone faces, $N = 1.36$ and 1.48, respectively. This condition corresponds to $2k_F = |G|$ and

implies that the long-range Friedel oscillations (135) are in phase with the lattice, thereby giving an additional stabilizing energy. However, as found by STROUD and ASHCROFT [1971] this only leads to the fcc lattice being stabilized in the *immediate* vicinity of N = 1.36, the hcp lattice being the most stable for N < 1.3. The fcc noble metals with Z = 1 can, therefore, *not* be described by the NFE approximation.

JONES [1937], on the other hand, started with a realisitic value for the Cu energy gap at L, namely 4 eV, which is an order of magnitude larger than that expected for simple NFE metals (cf. fig. 16). This large gap, which arises from hybridization and orthogonality constraints with the underlying d band (MUELLER [1967]), leads to a very *non-spherical* Fermi surface which *already* for Cu with N = 1 just makes contact with the fcc Brillouin-zone face in the <111> direction. Contact is made with the bcc zone for N = 1.23. The resulting fcc and bcc densities of states look very similar to those for Be (fcc) and Li (bcc) in fig. 20, because JONES [1937] neglected the presence of the copper d band (cf. fig. 26). Comparing the fcc and bcc band energies JONES [1937] found that the fcc lattice was indeed the more stable for $1 \leq N < 1.43$. However, no comparison with the hcp lattice was made.

Recently, PAXTON *et al.* [1992] extended Jones' calculations to include not only the hcp lattice but also a proper treatment of the valence d electrons within the Rigid Band Approximation (RBA). Fig. 43 shows the structural predictions where the expected trend from fcc (α phase) to bcc (β phase) to hcp (ε phase) is found as a function of the electron per atom ratio or band filling N. This trend is a direct consequence of rigidly occupying the copper densities of states n(E) in the middle panel and comparing the resultant band energies, i.e.,

$$\Delta U = \Delta\left[\int^{E_F} En(E)dE\right] \tag{136}$$

where

$$N = \int^{E_F} n(E)dE. \tag{137}$$

It follows from equation (136) that

$$\frac{d}{dN}(\Delta U) = \Delta\left[\frac{dE_F}{dN} E_F n(E_F)\right] = \Delta E_F \tag{138}$$

since on differentiating equation (137) with respect to N we have immediately

$$\frac{dE_F}{dN} n(E_F) = 1. \tag{139}$$

Further, it follows from equations (138) and (139) that

$$\frac{d^2}{dN^2}(\Delta U) = \Delta\left[\frac{1}{n(E_F)}\right]. \tag{140}$$

References: p. 129.

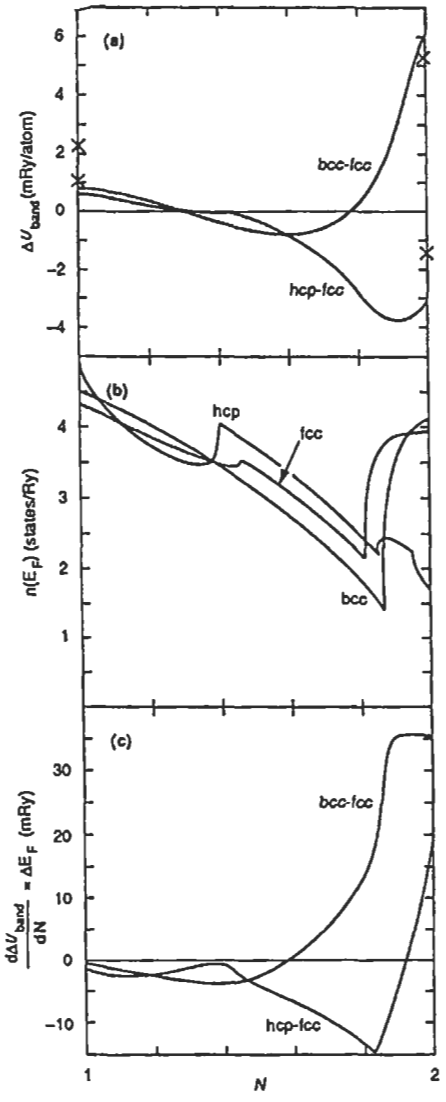

Fig. 43. Analysis of fcc, bcc and hcp relative structural stability within the rigid band approximation for Cu-Zn alloys. (a) The difference in band energy as a function of band filling N with respect to elemental rigid copper bands. (b) The density of states at the Fermi level E_F for fcc, bcc and hcp lattices as a function of band filling N. (c) The difference in the Fermi energies ΔE_F as a function of band filling N (from PAXTON, A. T., M. METHFESSEL and D. G. PETTIFOR [1992] unpublished).

Thus, as first pointed out by JONES [1962], the shape of the band energy difference curves in fig. 43a can be understood in terms of the relative behaviour of the densities of states in the middle panel. In particular, from equation (138) the stationary points in

the upper curve correspond to band occupancies for which ΔE_F vanishes in panel (c). Moreover, whether the stationary point is a maximum or a minimum depends on the relative values of the density of states at the Fermi level through equation (140). In particular, the bcc–fcc energy difference curve has a minimum around N = 1.6, where the bcc density of states is lowest, whereas the hcp–fcc curve has a minimum around N = 1.9, where the hcp density of states is lowest. The fcc structure is most stable around N = 1, where $\Delta E_F \simeq 0$ and the fcc density of states is lowest.

The structural trends in these Hume–Rothery electron phases are thus driven by the van Hove singularities in the densities of states which arise from band gaps at specific Brillouin or Jones zone boundaries as surmised earlier by MOTT and JONES [1936] and JONES [1937]. It is therefore not totally surprising that the NFE second-order perturbation theory results of STROUD and ASHCROFT [1971] and EVANS *et al.* [1979] found energy difference curves that are very similar to those in the top panel of fig. 43 *away* from the copper-rich end. The strong curvature of the bcc–fcc and hcp–fcc curves as a function of band filling can be reproduced only by including explicitly the weak logarithmic singularity in the slope of the Lindhard response function at $q = 2k_F$. It is for this reason that these Hume–Rothery alloys are correctly termed *electron phases* since this singularity is driven solely by the electron-per-atom ratio (through $2k_F$) and does not depend on the particular chemical constituents (through the pseudopotential). The nesting of the Fermi surfaces of noble metal alloys and the implication for long-period superlattices (SATO and TOTH [1961]) have been examined quantitatively by first-principles KRR band calculations (GYORFFY and STOCKS [1983]) assuming total disorder within the coherent-potential approximation (CPA; see, e.g., FAULKNER [1982]).

7. *Heat of formation*

A simple and successful *semi-empirical* scheme for calculating the heats of formation of binary alloys has been developed by MIEDEMA *et al.* [1980], who characterized each element in the Periodic Table by two co-ordinates ϕ^* and $\rho^{1/3}$. The heat of formation of a binary AB alloy is then written (in the simplest case) as:

$$\Delta H = -P(\Delta\phi^*)^2 + Q(\Delta\rho^{1/3})^2, \tag{141}$$

where P and Q are positive constants. The attractive term depends on the difference in the elemental work functions, $\Delta\phi$, (later modified to $\Delta\phi^*$) and is similar in spirit to PAULING'S [1960] electronegativity contribution. The repulsive term depends on the difference in the cube root of the electron densities at the elemental Wigner–Seitz sphere boundaries, $\Delta\rho^{1/3}$, and was argued to arise from the distortion of the charge density across the AB interface. Equation (141) has been useful in providing quantitative values for the heats of formation. In this section the *microscopic* origin of the attractive and repulsive contributions to ΔH will be examined in the light of our understanding of the cohesion of the elemental metals (cf. §§ 5 and 6).

Miedema's expression (141) has been most successful in the treatment of binary

transition-metal alloys, which are well-described by the tight-binding approximation. By analogy with FRIEDEL's [1964] treatment of pure transition metal cohesion, the AB alloy band may be approximated (PETTIFOR [1979, 1987]) by a rectangular density of states of width W_{AB} as shown in fig. 44. It follows from tight-binding theory (CYROT and CYROT-LACKMAN [1976]) that:

$$W_{AB}^2 = W^2 + 3(\Delta E_d)^2, \tag{142}$$

which generalizes the dimer result, eq. (30), to the bulk metal. The first term is the contribution to the square of the alloy band width that arises from nearest-neighbour bonding, whereas the second term reflects the increase in alloy bonding due to the ionicity which is measured by $\Delta E_d = E_d^B - E_d^A$. Thus, the alloy bandwith is given by

$$W_{AB} = \left[1 + 3(\Delta E_d/W)^2\right]^{1/2} W. \tag{143}$$

The heat of formation may now be evaluated explicitly. Filling up the alloy band with the average number of d electrons per atom, $\bar{N}_d$, and comparing the resulting band energy with that obtained from pure metal bands of width W (as illustrated in fig. 44), one finds the contribution to the heat of formation ΔH_0, given by:

$$\Delta H_0/W = -\tfrac{1}{80}(\Delta N_d)^2 - \tfrac{1}{4}\Delta N_d(\Delta E_d/W) - \tfrac{3}{40}\bar{N}_d(10 - \bar{N}_d)(\Delta E_d/W)^2, \tag{144}$$

where eq. (143) has been expanded to second order, and $\Delta N_d = N_d^B - N_d^A$. In addition, there is a further contribution ΔH_1, due to the fact that the elemental equilibrium atomic volumes V_A and V_B are in general different, so that the d bond energy of pure A and B is determined by W_A and W_B, respectively, and not by W as drawn in fig. 44. Assuming that the band width varies inversely with the volume to the five-thirds power (c.f. eq. (102); HEINE [1967]) and that the alloy volume is $V_{AB} = \bar{V} = 1/2(V_A + V_B)$ by Vegard's law, then

$$\Delta W = W_B - W_A = -\tfrac{5}{3} W(\Delta V/\bar{V}). \tag{145}$$

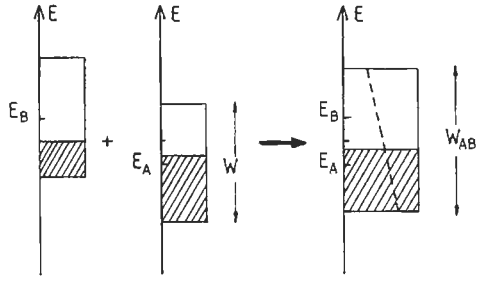

Fig. 44. The rectangular d band model representing AB alloy formation. The dashed line separates the partial density of states associated with atom A from that associated with atom B.

The resulting change in the bond energy due to the change in the band widths of the elemental metals from W to W_A, W_B, respectively is given by

$$\Delta H_1/W = -\tfrac{1}{24}\left(5 - \bar{N}_d\right)\Delta N_d\left(\Delta V/\bar{V}\right). \tag{146}$$

Expressions (144) and (146) may be simplified still further for binary alloys from the *same* transition-metal series. Choosing the 4d series because the 3d row is complicated by the presence of magnetism (cf. § 8), we can write $\Delta E_d = -\Delta N_d$ eV from fig. 5 and $V = V(N_d)$ from fig. 30. Substituting into eqs. (144) and (146) and taking W = 10 eV from table 1, the heat of formation (in eV/atom) is given to second order by

$$\Delta H = \left[f_0\left(\bar{N}_d\right) + f_1\left(\bar{N}_d\right)\right]\left(\Delta N_d\right)^2 \tag{147}$$

where

$$f_0\left(\bar{N}_d\right) = \tfrac{1}{8}\left[1 - \tfrac{3}{50}\,\bar{N}_d\left(10 - \bar{N}_d\right)\right] \tag{148}$$

and

$$f_1\left(\bar{N}_d\right) = -\tfrac{1}{24}\left(5 - \bar{N}_d\right)\left(\frac{\mathrm{d}\,\ln V}{\mathrm{d}N_d}\right)_{\bar{N}_d}. \tag{149}$$

Equation (147) represents the second-order term in a Taylor expansion of $\Delta H(N_d^A, N_d^B)$ in powers of ΔN_d as WILLIAMS *et al.* [1980b] have emphasized.

Figure 45 compares the results of the tight-binding theory with the MIEDEMA *et al.* [1980] semi-empirical values for $\Delta N_d \leq 4$, where we see that reasonable agreement is obtained. The more attractive values of ΔH found by MIEDEMA *et al.* [1980] near $\bar{N}_d = 5$ reflect *structural* bonding effects which are not included in the present model with its uniform alloy density of states (cf. fig. 44). The dependence of the heat of formation on crystal structure has been demonstrated by the first-principles LDF calculations of WILLIAMS *et al.* [1980b] who compared ΔH for the CuAu (fcc) and CsCl (bcc) lattices. It is clear from fig. 45 that the most stable AB alloys will be those for which the average d-band filling is close to 5.5 and ΔN_d is large, for example YPd. On the other hand, for average d-band fillings less than about 4 or greater than 7 the heat of formation will be positive.

The attractive contribution in Miedema's expression (141) may be identified with ΔH_0 provided that ϕ^* is interpreted as the *electronegativity* X rather than the work function ϕ. Within the TB model the charge transfer Q is obtained by assuming partial densities of states $n_A(E)$ and $n_B(E)$ on the A and B sites in the alloy as illustrated in fig. 44. n_A and n_B have been skewed so that their centres of gravity correspond to E_d^A and E_d^A, respectively (PETTIFOR [1980]). The resulting d charge transfer is given by

$$Q_d^B = \tfrac{1}{2}\,\Delta N_d + \tfrac{3}{10}\,\bar{N}_d\left(10 - \bar{N}_d\right)\left(\Delta E_d/W_{AB}\right). \tag{150}$$

The first term reflects the flow of electrons from right to left across the series due to increasing electron density and the second term reflects the flow from left to right due

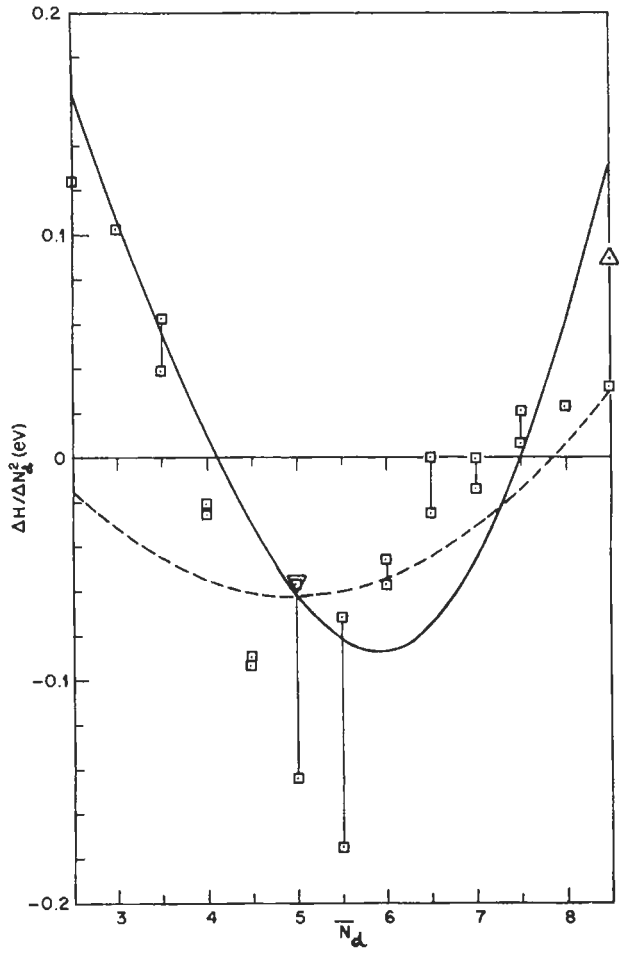

Fig. 45. $\Delta H/(\Delta N_d)^2$ as a function of the average band filling $\bar{N}_d$ for the 4d series. The dashed curve is the ΔH_0 contribution, eq. (148). The squares represent the Miedema values for the 4d alloys with $\Delta N_d \leq 4$, the points with common $\bar{N}_d$ being connected by straight lines. (From PETTIFOR [1979].)

to the increasingly attractive d level as one proceeds across the series (cf. fig. 5). The flow of electrons is, therefore, *not* driven by the difference in the *work functions* $\Delta\phi$ alone, because *all* the electrons throughout the band respond on alloying and not just those in the vicinity of the Fermi level. This can be seen by comparing, in fig. 44, the skewed partial density of states $n_A(E)$ in the AB alloy with the rectangular density of states in the pure metal A.

By implication, the charge transfer is proportional to the difference in the electronegativities, so that we may define a d-electronegativity X_d by

$$\Delta X_d = Q_d. \tag{151}$$

Substituting into eq. (150) and integrating for the 4d series with $\Delta E_d/W = \Delta N_d/10$, the electronegativity is found to be

$$X_d = -\tfrac{1}{2} N_d\left[1 - \tfrac{1}{50} N_d\left(15 - N_d\right)\right] + 1.8, \tag{152}$$

where the constant of integration has been chosen so that Mo with $N_d = 5$ takes the PAULING [1960] value of 1.8. Equation (152) is plotted in fig. 46 and compares surprisingly well with the Pauling electronegativities across the 4d series. It follows from eq. (144) and eqs. (150)–(152) that ΔH_0 can be expressed approximately as:

$$\Delta H_0 = -\tfrac{1}{10} W\left(\Delta X_d\right)^2 \tag{153}$$

for $|\overline{N}_d - 5| \leq 5/\sqrt{3}$. Equation (153) gives the correct value of the dashed curve in fig. 45 at the centre of the band and it vanishes at the correct cross-over points $\overline{N}_d = 5 \pm 5/\sqrt{3}$. Since Miedema's final choice of ordinate ϕ^* is very similar to Pauling's electronegativity X (MIEDEMA *et al.* [1980]), the attractive contribution in eq. (141) may be associated with ΔH_0 through eq. (153). The repulsive contribution in the semi-empirical scheme follows ΔH_1, very closely numerically, but conceptually the latter reflects a mismatch in the d band width rather than the electron density (see also WILLIAMS *et al.* [1982]). The heats of formation of 3d, 4d and 5d transition metal AB alloys have been tabulated by WATSON and BENNETT [1981] who used an optimized version of the d band model.

The heats of formation of *simple*-metal binary alloys may be calculated within second-order perturbation theory provided the valence difference $\Delta Z = Z_B - Z_A$ is not too large (HAFNER [1976] and LEUNG *et al.* [1976]). Neglecting the structurally dependent pair-potential contribution and ignoring the density dependence of $\phi(\boldsymbol{R}=0;\, r_s)$ in eq. (132), the heat of formation ΔH will be determined by the volume-dependent free electron gas terms alone. Assuming Vegard's Law with $V_{AB} = \overline{V} = \frac{1}{2}(V_A + V_B)$, these give (PETTIFOR and GELATT [1983]) the contribution (in eV/atom):

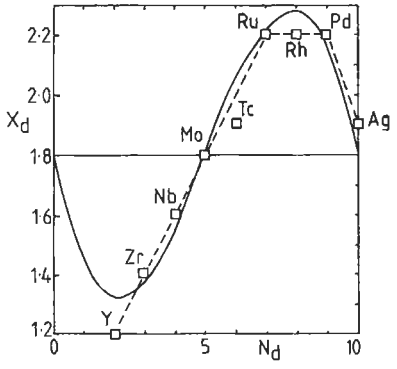

Fig. 46. The d-band electronegativity. X_d, compared to PAULING's [1960] values (squares) for the 4d series.

$$\Delta H_{eg} = \bar{Z} f_{eg}\left(\overline{\rho^{1/3}}\right)\left(\Delta\rho^{1/3}\right)^2, \tag{154}$$

where

$$f_{eg}\left(\rho^{1/3}\right) = -43.39 + 7.81/\rho^{1/3} + 0.17/\left(\rho^{1/3}\right)^2. \tag{155}$$

The three terms in eq. (155) are the kinetic, exchange and correlation contributions respectively, the flow of charge from the more dense to the less dense atom *lowering* the kinetic energy but raising the exchange and correlation energies. Equation (154) is reminiscent of the MIEDEMA *et al.* [1980] repulsive contribution in eq. (141). However, as is clear from fig. 47 the prefactor f_{eg} is not a positive constant Q but is dependent on the average cube root of the density $\rho^{1/3}$. It changes sign from *positive* at low densities (where the exchange and correlation dominate) to *negative* at high densities (where the kinetic energy dominates). The first-principle LDF calculations of ΔH for the Na, Mg, Al, Si, P series with respect to the CsCl (bcc) lattice show the same trend in fig. 47 as eq. (155) although displaced somewhat from the free-electron-gas result because the explicit influence of the core through the last two terms in eq. (132) has been neglected. Figure 6.10 b of HAFNER [1987] shows that equation (154) represents the experimental heat of formation of *liquid* simple metal alloys extremely well.

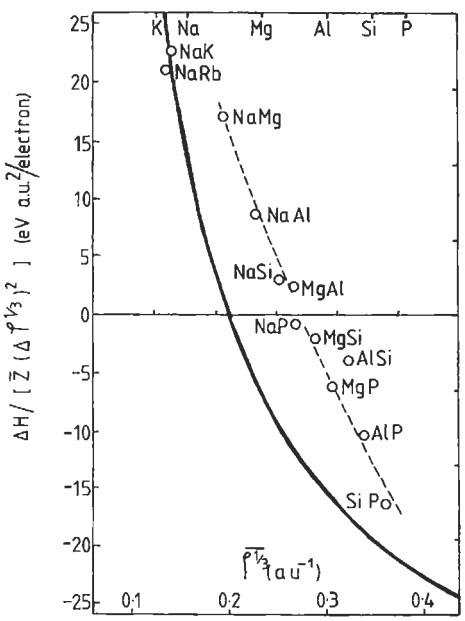

Fig. 47. $\Delta H/[\bar{Z}(\Delta\rho^{1/3})]^2$ as a function of the average cube root of the electron density $\rho^{1/3}$ for the 3s and 3p series. The solid curve is the electron-gas contribution, eq. (155). The open circles are the LDF results for the CsCl lattice. (From PETTIFOR and GELATT [1983]).

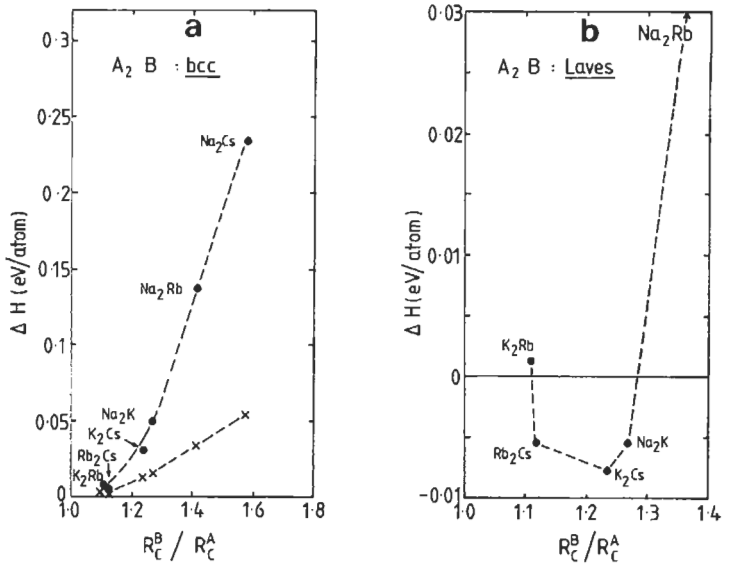

Fig. 48. The *calculated* heats of formation (HAFNER [1977]) of A_2B alkali-metal alloys for (a) the disordered bcc phase and (b) the ordered $MgZn_2$ Laves phase as a function of R_C^B/R_C^A from table 2. The crosses give the electron gas contribution eq. (154) using the *experimental* densities of the elemental metals.

Structural effects can be important in determining the sign of ΔH of simple-metal alloys (cf. § 2.3.2 of MIEDEMA *et al.* [1980]). This has been demonstrated by the second-order pseudopotential calculations of HAFNER [1977] on binary alkali metal alloys, which are illustrated in fig. 48 for the A_2B stoichiometry. (His values of ΔH for the bcc alloys are approximately four times larger than the experimental, LDF or free-electron gas values, because his calculated density differences are larger than experiment.) Whereas the disordered bcc alloys have *positive* heats of formation, the ordered Laves phases Rb_2Cs, K_2Cs and Na_2K have *negative* heats of formation due to the arrangement of the nearest-neighbour atoms with respect to the minimum in the pair potential. Therefore, provided the volume-dependent contribution to ΔH is not too large and positive, the structural contribution due to the pair potential can stabilize the phase. If a semi-conducting gap opens up in the alloy density of states, then this will provide additional stability (MIEDEMA *et al.* [1980]), which requires the theory to be extended beyond second order.

The heats of formation of sp elements with transition metals is illustrated by fig. 49 for the Li-row elements with the 4d transition metals. They were calculated by GELATT *et al.* [1983] using LDF theory for the AB stoichiometry with respect to the NaCl lattice. Their theoretical values agree broadly with the semi-empirical values of MIEDEMA *et al.* [1980] who found it necessary to include for sp-d alloys an additional attractive contribution, $-R$, in their expression (141). R is written as the product of two numbers which are determined by the groups in the Periodic Table from which the sp and d constituents are drawn. GELATT *et al.* [1983] have interpreted their results in terms of an *attractive* sp-d

bonding contribution, which becomes increasingly ionic on proceeding across the sp series from Li to F, and a *repulsive* d-bond contribution. The latter reflects the loss of d-bond energy due to the narrower alloy d band width, which arises from the larger transition-metal-transition-metal nearest neighbour distance in the alloy as compared to the elemental metal. Curves similar to fig. 49 have been obtained by GELATT *et al.* [1978] for the 3d and 4d transition-metal hydrides.

Figure 50 illustrates the reliability of LDF theory for predicting the heats of formation and structural stability of intermetallic phases. Figure 50a gives the LDF heats of formation of different ordered structures with respect to either the fcc or bcc lattices for the aluminium–lithium system (SLUITER *et al.* [1990]). We see that the B32 LiAl structure type is predicted to be much more stable than either the B2 or $L1_0$ equiatomic phases. Moreover, it is this strong stability of the B32 phase that is responsible for the known metastability of the neighbouring $L1_2$ $LiAl_3$ and DO_3 Li_3Al phases. Figure 50b gives the LDF heats of formation of different ordered structures with respect to either the fcc or hcp lattices for the aluminium-titanium system (VAN SCHILFGAARDE *et al.* [1990]). We see that the theory predicts the correct most stable ground state structure for Ti_3Al and $TiAl_3$, namely hexagonal DO_{19} and tetragonal DO_{22} respectively. Furthermore, whereas the metastable cubic $L1_2$ phase is very close to the ground state energy for $TiAl_3$, it is much further removed for Ti_3Al. This accounts for the fact that whereas Ti_3Al has been stabilized as a cubic pseudobinary by suitable alloying additions, it has not been possible to stabilize the cubic phase of Ti_3Al (LIU *et al.* [1989]). This demonstrates the importance of the first principles LDF calculations; they provide information not only about the ground state (which is usually already known experimentally) but also about the metastable phases (which have often not been directly accessed by experiment).

The heat of *solution* of hydrogen and helium in metals may be calculated within the *effective-medium* approximation of STOTT and ZAREMBA [1980], NØRSKOV and LANG

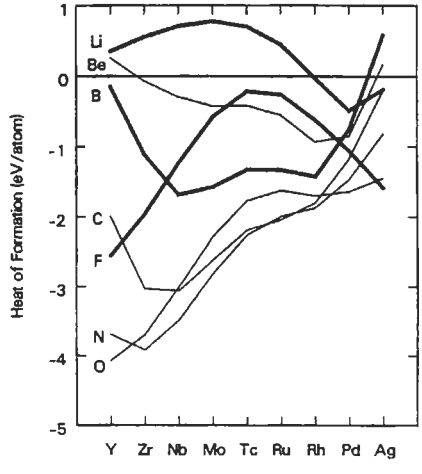

Fig. 49. The heats of formation of 4d transition metals with Li row elements in the NaCl structure (GELATT *et al.* [1983]).

[1980], and JACOBSEN *et al.* [1987]. They assumed that the energy required to embed an atom at some given position $\boldsymbol{R}$ in a host metal which is characterized by an *inhomogeneous* density $\rho(\boldsymbol{r})$, is the same as that required to embed the atom in a *homogeneous* electron gas of density $\rho = \bar{\rho}(\boldsymbol{R})$, where $\bar{\rho}(\boldsymbol{R})$ is the average host electron density seen by the impurity atom at $\boldsymbol{R}$. Then the energy of the impurity atom at position $\boldsymbol{R}$ in the host lattice is given to lowest order by

$$\Delta U(\boldsymbol{R}) = \left[\Delta U_{\text{hom}}(\rho)\right]_{\rho=\bar{\rho}(\boldsymbol{R})}. \tag{156}$$

The homogeneous embedding energy $\Delta U_{\text{hom}}(\rho)$ can be evaluated within LDF theory and the results for H and the rare-gas atoms He and Ne are shown in fig. 51a (PUSKA *et al.* [1981]). We see that the rare-gas atoms display a positive embedding energy at all densities because their full electronic shells *repel* the free electron gas through orthogonality constraints. On the other hand, the open-shell hydrogen atom shows a minimum at $\rho = 0.0026$ au^{-3} (i.e., $\rho^{1/3} = 0.138$ au^{-1}) corresponding to an *attractive* embedding energy of -1.8 eV, although it is repulsive for typical transition-metal densities of 0.02–0.03 au^{-3}.

The heats of solution of H and He across the 3d series are shown in fig. 51b after NØRSKOV [1982] and MANNINEN *et al.* [1982], respectively. The results include an important first-order *electrostatic* correction term to eq. (156), which reduces the slope of the He curve in fig. 51a by half and lowers the *H* curve by -120ρ eV au^3 so that the *H* embedding energy is attractive throughout the entire range of metallic densities (cf. the solid circles in fig. 51b). The behaviour of the helium heat of solution across the 3d series mirrors that of the host metallic density which varies like the bulk modulus shown in fig. 1. The hydrogen heat of solution is measured with respect to the binding energy of the H_2 molecule, namely -2.4 eV/atom. We see in fig. 51b that agreement with experiments is obtained only if a first-order *hybridization* correction is included from eq. (116) which reflects the bonding between the hydrogen impurity and the host nearest neighbour atoms (NØRSKOV [1982]). The effective-medium approximation with first-order electrostatic and hybridization corrections included has been applied successfully to defect problems such as the trapping energies of H and He by interstitials, vacancies and voids (NØRSKOV *et al.* [1982] and MANNINEN *et al.* [1982]). The electron theory of point defects has been reviewed by JENA [1981].

The *ordering* energy of a binary $A_c B_{1-c}$ alloy is defined by

$$\Delta U_{\text{ord}} = U_{\text{ord}} - U_{\text{dis}}, \tag{157}$$

where U_{ord} and U_{dis} are the energies in the completely ordered and disordered states respectively. By using second-order perturbation theory for the NFE *simple* metals (HAYES *et al.* [1968] and INGLESFIELD [1969]) or a generalized perturbation theory for the TB *transition* metals (DUCASTELLE and GAUTIER [1976]) the ordering energy eq. (157) can be expressed directly in terms of effective pair interactions ϕ_1, ϕ_2, ϕ_3,... between the first, second, third,... nearest neighbour atoms. (ϕ_n depends explicitly on $|\Delta v_{\text{ps}}(q)|^2$ for the simple metals and on $|\Delta E_{\text{d}}|^2$ for the transition metals). The ordering energy for $c \leq 0.5$ may be written (see, e.g., DE FONTAINE [1979] and DUCASTELLE [1991]) as:

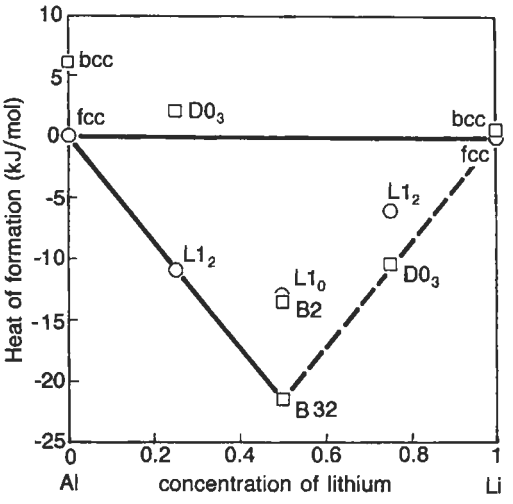

Fig. 50 (a). The predicted heat of formation of fcc- and bcc-based lithium-aluminium ordered compounds (after SLUITER *et al.* [1990]).

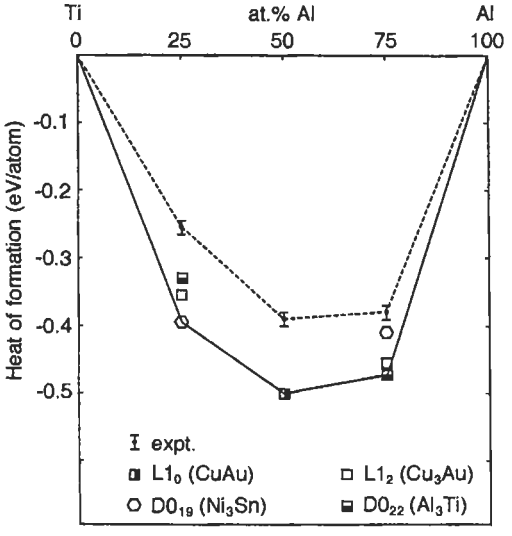

Fig. 50 (b). The predicted heat of formation of fcc- and hcp-based titanium-aluminium ordered compounds (after VAN SCHILFGAARDE *et al.* [1990]).

$$\Delta U_{\text{ord}} = \sum_n \left[p_n - (1-c)^2 z_n \right] \phi_n, \tag{158}$$

where z_n and p_n are the number of nth nearest neighbour atoms and B–B atom pairs respectively.

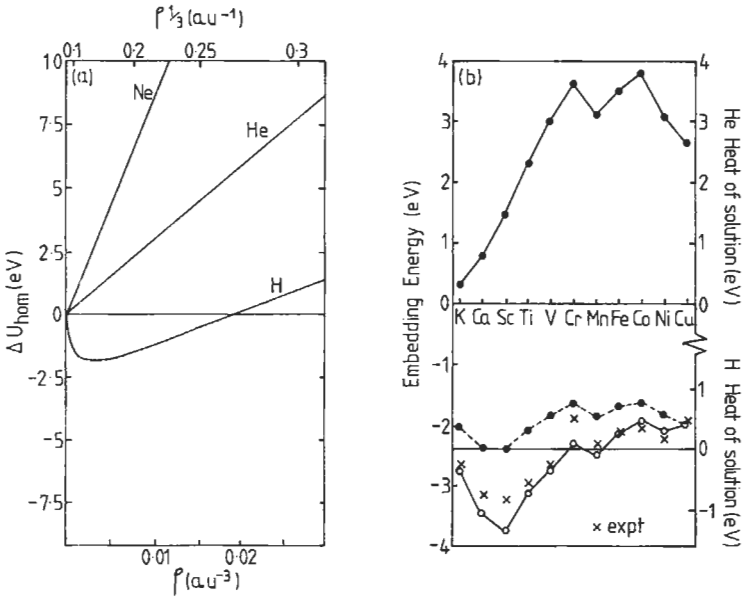

Fig. 51 (a) The homogeneous embedding energy for H and the rare gas atoms He and Ne in a free electron gas of density ρ (after PUSKA *et al.* [1981]). (b) The H and He heats of solution across the 3d series (after NØRSKOV [1982] and MANNINEN *et al.* [1982] respectively). The solid circles include a first-order electrostatic contribution. The open circles include, in addition, a first-order hybridization correction.

The effective pair interaction in transition metals with respect to an fcc lattice is illustrated by fig. 52a where ϕ_1 and ϕ_2 are plotted as a function of average band filling $\overline{N}_d$ for the TB d band alloy with $c = 0.25$ and $\Delta E_d / W = 0.45$ (BIEBER *et al.* [1983]). As expected from the behaviour of the simple-metal pair potentials in § 6.1, the transition-metal pair interactions display oscillations as a function of band filling, $\overline{N}_d$, and nearest neighbour position, n. Figure 52b compares the ordering energy evaluated by the pair interaction of DUCASTELLE and GAUTIER [1976] with the exact TB energy difference from eq. (157). We see that for this particular alloy it is a good approximation in the band-filling region where ordering occurs. Moreover, because the second and further nearest neighbour interactions are at least an order of magnitude smaller than the first nearest neighbour interactions, the ordering energy is dominated by ϕ_1 through eq. (158).

The pair interactions also determine the most stable ordered structure with respect to a given lattice (BIEBER and GAUTIER [1981]). For example, in fig. 53 the Cu_3Au and Al_3Ti structures are shown, which are built on the fcc lattice. They have the same type of first nearest neighbour atoms, so that their relative stability is determined by ϕ_2 and further nearest neighbour interactions. Since ϕ_2 in fig. 52a is negative for $4.4 < \overline{N}_d < 7.3$ when $\Delta E_d / W = 0.45$, the ordered structure with *like* second nearest neighbours will be the more stable, i.e., Cu_3Au. The stability reverses outside this band-filling region, thereby accounting for the nature of the structure map in fig. 53. This displays only a narrow

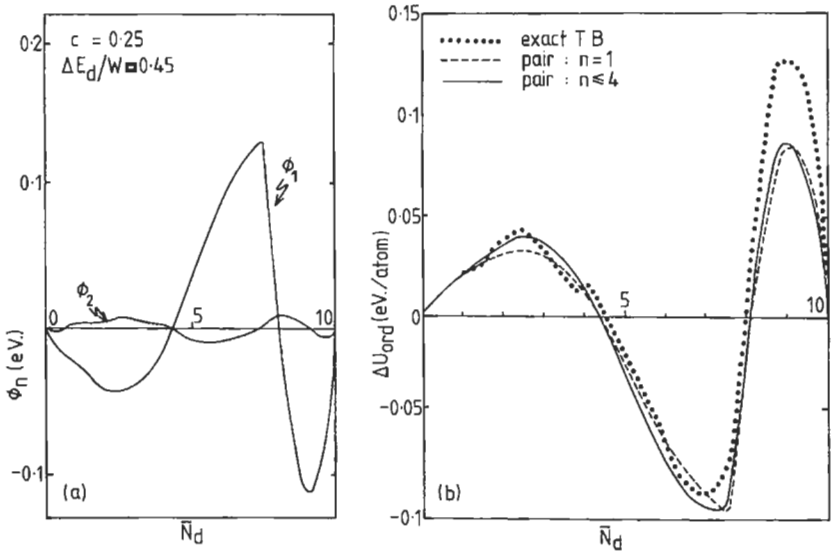

Fig. 52. (a) The first and second nearest neighbour effective pair interactions, ϕ_1 and ϕ_2, as a function of the average band filling, $\bar{N}_d$, for an AB_3 transition-metal alloy with a $\Delta E_d/W = 0.45$ on an fcc lattice. (b) A comparison with the exact result of the ordering energy evaluated using the effective pair interactions. (After BIEBER *et al.* [1983].)

stability range for the Al_3Ti phase, which is in agreement with empirical structure maps (BIEBER and GAUTIER [1981]).

This chapter on Electron Theory has been concerned primarily with the cohesive and structural properties of metals and alloys at the absolute zero of temperature. However, the derivation of effective pair interactions ϕ_n within electron theory allows the first-principles prediction of phase diagram behaviour by using these in an Ising Hamiltonian and performing Monte Carlo or Cluster Variation Method simulations (see, for example, DUCASTELLE [1991] and references therein, and ZUNGER [1994]). Chapter 6 deals explicitly with Phase Diagrams.

8. *Band theory of magnetism*

The magnetic 3d elements have anomalously large equilibrium atomic volumes and small bulk moduli as evidenced by the deviations in fig. 1 between experiment and the non-magnetic LDF theory. In this section we will see that the STONER [1939] theory of band magnetism can explain this anomalous behaviour.

A nonmagnetic system will become magnetic if the lowering in *exchange* energy due to the alignment of the electron spins more than compensates the corresponding increase in kinetic energy. This may be demonstrated by the rectangular d-band model of fig. 54. In the *nonmagnetic* state, the up and down spin electrons are equivalent and, therefore,

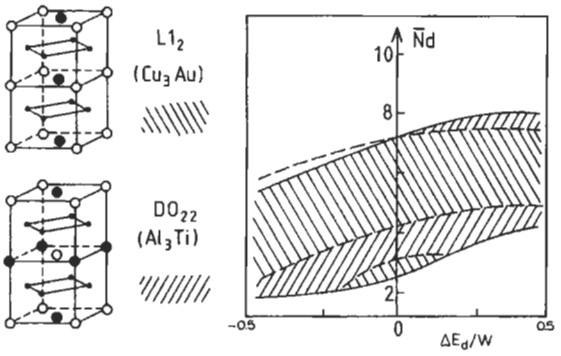

Fig. 53. The relative stability of the Cu_3Au and Al_3Ti structures as a function of the average band filling $\bar{N}_d$, and the renormalized difference in the atomic d levels, $\Delta E_d/W$ (after BIEBER and GAUTIER [1981]).

they have identical density of states $n_\uparrow$ and $n_\downarrow$ as shown in fig. 54a. In the *magnetic* state, the presence of a local magnetic moment, m, produces an exchange field Δ on the atom, of strength

$$\Delta = Im, \tag{159}$$

where I is the Stoner exchange parameter and $m = N_d^{\uparrow} - N_d^{\downarrow}$ in Bohr magnetons (μ_B). In the *ferromagnetic* state, all the atomic moments are aligned in the same direction, so that an up-spin electron sees the atomic level E_d shifted by $-\frac{1}{2}\Delta$ a on every site, the down-spin electron by $+\frac{1}{2}\Delta$. Therefore, the densities of states $n_\uparrow$ and $n_\downarrow$ are shifted *rigidly* apart by Δ as shown in fig. 54b. On the other hand, in the *antiferromagnetic* state, half the atoms have their moments aligned up, the other half have their moment aligned down, so that an electron sees two types of sites, with energies $E_d \pm \frac{1}{2}\Delta$. The problem is, therefore, analogous to that of the AB alloy discussed in the previous section (cf. fig. 44) and the densities of states $n_\uparrow$ and $n_\downarrow$ (corresponding to an atom with net moment up) are obtained by *skewing* the rectangular nonmagnetic densities of states as shown in fig. 54c.

The magnetic energy which accompanies the formation of a local moment m at each site, may be written as:

$$U_{\text{mag}} = \delta T - \tfrac{1}{4} Im^2, \tag{160}$$

where the first term is the change in the kinetic energy and the second is the lowering in energy due to exchange. The *ferromagnetic* (fm) state is created by flipping $\frac{1}{2}m$ down-spin electrons from just below the nonmagnetic Fermi level into the unoccupied up-spin states just above the nonmagnetic Fermi level. This is accompanied by an increase in kinetic energy of $(\frac{1}{2}m)/n(E_F)$ per electron, so that, to second order,

$$U_{\text{fm}} = \tfrac{1}{4} m^2/n(E_F) - \tfrac{1}{4} Im^2 \tag{161}$$

where in this section $n(E_F)$ refers to the nonmagnetic density of states *per spin*. Therefore, the nonmagnetic state will be unstable to ferromagnetism if $U_{\text{fm}} < 0$, i.e. if:

References: p. 129.

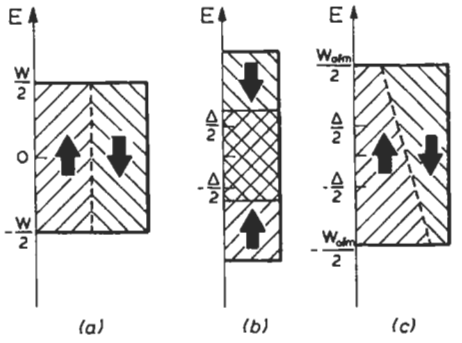

Fig. 54. The rectangular d band model of the (a) nonmagnetic, (b) ferromagnetic, and (c) antiferromagnetic states (after PETTIFOR [1980]).

$$In(E_F) > 1 \tag{162}$$

which is the famous *Stoner criterion.* The *equilibrium* value of m in the ferromagnetic state is determined by the condition

$$\overline{In(N_d, m)} = 1, \tag{163}$$

where $\overline{n(N_d, m)}$ is the average of the nonmagnetic density of states per spin between the two energies corresponding to a band-filling of $N_d^{\downarrow}$ and $N_d^{\uparrow}$ respectively (see, e.g., GUNNARSSON [1976]).

The magnetic energy of the *antiferromagnetic* (afm) state can be obtained (PETTIFOR [1980]) by adding up the band energies in fig. 54c and subtracting off the exchange energy which has been double-counted, i.e.:

$$U_{afm} = -\tfrac{1}{20}(W_{afm} - W)N_d(10 - N_d) + \tfrac{1}{4} Im^2, \tag{164}$$

where from eq. (142)

$$W_{afm} = \left\{1 + 3(\Delta/W)^2\right\}^{1/2} W. \tag{165}$$

Expanding eq. (165) to second order and using eq. (159), the nonmagnetic state is found to be unstable to antiferromagnetism if

$$I/W > \left[\tfrac{3}{10} N_d(10 - N_d)\right]^{-1}. \tag{166}$$

This is the rectangular d-band model criterion equivalent to the exact second-order result, namely

$$I\chi_q(E_F) > 1 \tag{167}$$

where $\chi_q(E_F)$ is the response function corresponding to the afm ordering wave vector $\boldsymbol{q}$ (see, e.g., FEDDERS and MARTIN [1966]). The usefulness of the present model is that eqs.

(164) and (165) include terms beyond second order so that the *equilibrium* value of the magnetic moment and energy may be obtained explicitly. Equation (164) is stationary for

$$m = \left(1/\sqrt{3}\right)\left\{\left[\tfrac{3}{10} N_d\left(10 - N_d\right)\right]^2 - \left(W/I\right)^2\right\}^{1/2} \tag{168}$$

when

$$U_{afm} = \left[\tfrac{1}{20} W N_d\left(10 - N_d\right) - \tfrac{1}{6} W^2/I\right] - \tfrac{1}{4} Im^2. \tag{169}$$

The first term in eq. (169) represents the change in kinetic energy, δT. The value of the moment given by eq. (168) is identical to that obtained by filling the up and down spin bands in fig. 54c and solving eq. (159) self-consistently.

Figure 55 shows the regions of stability of the ferromagnetic and antiferromagnetic phases as a function of the renormalized exchange integral, I/W, and band filling, N_d, for the rectangular d-band model (see also PENN [1966]). The fm and afm phases are stable for values of I/W above the critical curves ABC (fm) and DBE (afm), which are defined by eq. (162) with $n(E_F) = 5/W$ and eq. (166), respectively. In the region where both phases are stable, the fm and afm state have the lower energy in region FBE and ABF respectively.

The magnetic behaviour across the 3d series can be accounted for qualitatively (see also MORIYA [1965]) by assigning the 3d transition-metals values of N_d in fig. 55 which fix Ni with 0.6 holes. Values of I/W are chosen as marked by the crosses in fig. 55, the numbers lying in the range expected from first-principles LSDF calculations where $I \approx$ 1 eV and $W \approx 5$ eV for the 3d series (see, e.g., KÜBLER [1981]). I is approximately constant across the series but W increases from Ni to Cr just as observed in table 1 for the corresponding 4d series from Pd to Mo. Therefore, we expect I/W to decrease in moving from Ni to Cr, as shown in fig. 55. The positions of the crosses in fig. 55 imply that Ni and Co are strong ferromagnets with moments of 0.6 and 1.6 μ_B respectively,

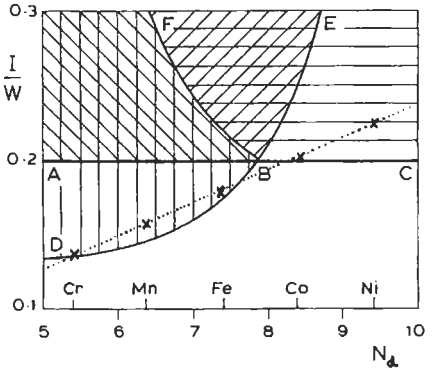

Fig. 55. The regions of stability of the ferromagnetic and antiferromagnetic states as a function of the renormalized exchange integral, I/W, and d band filling, N_d. The crosses mark plausible values of I/W across the 3d series. (After PETTIFOR [1980].)

whereas Fe ($I/W=0.180$), Mn($I/W=0.158$), and Cr ($I/W=0.136$) are anti-ferromagnets with local moments from eq. (168) of 0.9, 1.6 and 0.7 μ_B, respectively.

In practice, the rectangular d band model is not too bad a description of the *close-packed* fcc and hcp metals whose densities of states are fairly constant away from the top of the d band (c.f. fig. 26). This is demonstrated in fig. 56 by the band structure calculations of ASANO and YAMASHITA [1973] who evaluated the fm and afm local moments across the 3d series. Their fcc results are similar to those obtained from fig. 55. In particular, fcc iron is unable to maintain a fm moment, being instead a weak antiferromagnet. However, if I/W were to increase (by volume expansion), then fig. 55 implies that fcc iron eventually stabilizes in the fm state as has been observed experimentally by GRADMANN and ISBERT [1980] and theoretically by the LSDF calculations of KÜBLER [1981].

On the other hand, bcc transition metals have a very non-uniform density of states and are characterized by a very marked antibonding peak for $N \approx 8$ electrons (cf. fig. 26a). $n(E_F)$ is sufficient for the 3d transition metal iron to satisfy the Stoner criterion (162) and the resulting magnetic energy of – 0.3 eV/atom (JANAK and WILLIAMS [1976]) stabilizes the bcc lattice with respect to the nonmagnetic or weakly afm close-packed lattices. Under pressure, however, the d band broadens and the density of states decreases, thereby leading to an increased kinetic-energy contribution in eq. (161). At just over 10 GPA the nonmagnetic structural energy contribution in fig. 35 wins out and ferromagnetic bcc α-iron transforms to the nonmagnetic hcp ε-phase (MADSEN *et al.* [1976]). This is the most stable structure of the isovalent 4d and 5d elements Ru and Os at their equilibrium volume because their wider d bands prevent them from satisfying the Stoner criterion. At atmospheric pressure bcc α-iron transforms to the fcc γ-phase at 1184 K and changes back to the bcc δ-phase at 1665 K just before melting at 1809 K. The occurrence of the α, γ, δ and ε-phases in the temperature–pressure phase diagram of iron can be understood qualitatively (HASEGAWA and PETTIFOR [1983]) within a band theory of magnetism which extends Stoner theory to finite temperatures (CYROT [1970], HASEGAWA [1980] and HUBBARD [1981]).

The simple rectangular d band model of antiferromagnetism presented in fig. 54c does not include any Fermi-surface *nesting* effects which LOMER [1962] argued were

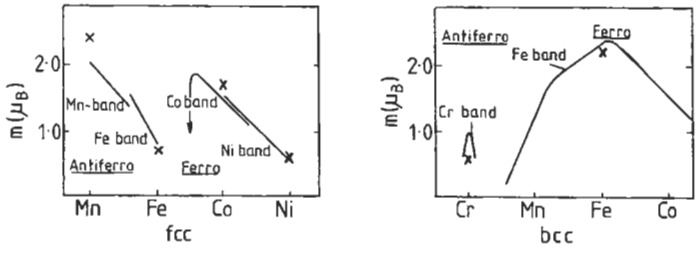

Fig. 56. The magnetic moments of the 3d metals in the ferromagnetic and antiferromagnetic states calculated as a function of band filling by ASANO and YAMASHITA [1973] for the fcc and bcc lattices. The crosses mark the experimental values.

responsible for the observed periodicity of the bcc Cr spin density wave. In practice, even though nesting provides only a small contribution to $\chi_q(E_F)$ in eq. (167), it is sufficient to take *bcc* Cr across the afm stability curve DBE in fig. 55 (WINDSOR [1972] and SKRIVER [1981a]).

The anomalous behaviour of the equilibrium atomic volumes and bulk moduli of the 3d series observed in fig. 1 is due to the *magnetic pressure*, $P_{mag} = -\,dU_{mag}/dV$, which accompanies moment formation (SHIGA and NAKAMURA [1969] and JANAK and WILLIAMS [1976]). Assuming that I is volume-independent (MADSEN *et al.* [1976]) and W varies inversely with volume to the five-thirds power (HEINE [1967]), it follows from eqs. (161), (164) and (169) that

$$3P_{mag}V = 5\delta T, \tag{170}$$

because $\delta U_{mag}/\delta m = 0$ at equilibrium.

In particular, for the *ferromagnetic* state the kinetic-energy change, δT, may be approximated by the first term in eq. (161), so that

$$3P_{fm}V = \tfrac{5}{4}\, m^2/n(E_F). \tag{171}$$

JANAK and WILLIAMS [1976] have shown that this simple expression accounts for the increase in equilibrium volume on going to the ferromagnetic state which the LSDF results display in fig. 57. For example, iron and nickel have moments of 2.2 and 0.6 μ_B, respectively, and LDF nonmagnetic density of states per spin of 1.5 and 2.2 states per eV atom respectively. Substituting into eq. (171) gives a magnetic pressure for iron and nickel of 21.2 and I GPA, respectively, which leads to an increase in the equilibrium volume of 7% and $\frac{1}{2}$%, respectively. The increase in atomic volume reduces the bulk modulus because the valence s electrons are now no longer compressed to the same extent into the core region where they are repelled by orthogonality effects (cf. § 5.2).

Figure 57 shows that the experimental *trend* in the equilibrium atomic volume and bulk modulus across the ferromagnetic metals Fe, Co and Ni is well accounted for by the LSDF results (JANAK and WILLIAMS [1976]). Similarly, SKRIVER *et al.* [1978] have obtained good agreement with experiment across the 5f actinide series, where the LSDF calculations reproduce the sudden 30% volume expansion that is observed in going from Pu to Am, due to the formation of a 5f moment. The 4f rare earths Ce and Pr have also been studied within LSDF theory, by GLOTZEL [1978] and SKRIVER [1981b] respectively, as too has the permanent magnet $Nd_2Fe_{14}B$ (COEHOORN [1992]) and various magnetic mutilayers (EDWARDS [1992]). However, errors remain in figs. 1 and 50 (for the 3d metals in particular) which must be attributed to the *local* approximation to the exchange and correlation energy functional. For example, LDF theory does not position the valence s and d bands in exactly the correct relative position (HARRIS and JONES [1978]) or provide the correct exchange splitting in nickel (WOHLFARTH [1980] and COOKE *et al.* [1981]). Although the correlations can be treated perturbatively within a TB framework (FRIEDEL and SAYERS [1977]), a simple *non-local* extension of the LDF approximation will be required for the next generation of higher-accuracy first-principles calculations (see, e.g., JONES and GUNNARSSON [1989]).

References: p. 129.

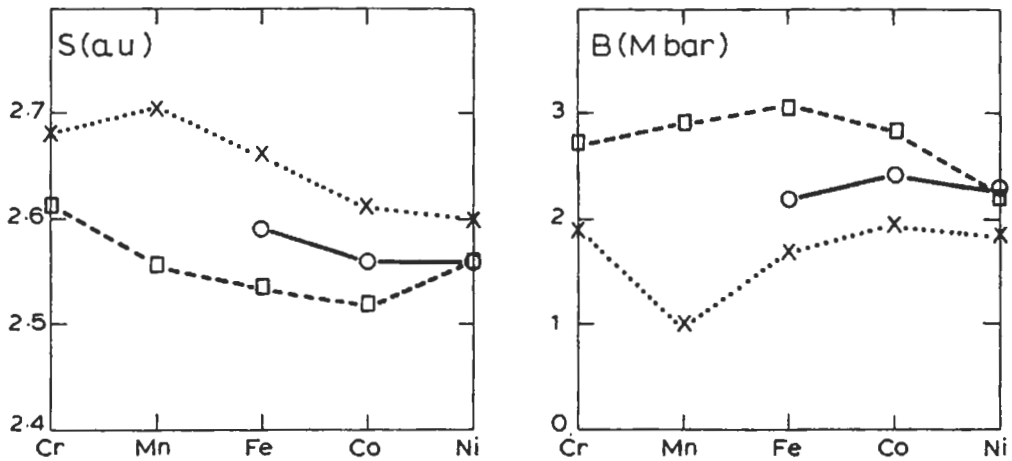

Fig. 57. The equilibrium Wigner-Seitz radius, S, and bulk modulus, B, across the magnetic 3d transition metals. The crosses, circles. and squares are the experimental, spin-polarized LSDF and nonmagnetic LDF results, respectively. (After JANAK and WILLIAMS [1976].)

References

ANDERSEN, O.K., 1973, Solid State Commun. **13**, 133.
ANDERSEN, O.K., 1975, Phys. Rev. **B12**, 3060.
ANDERSEN, O.K., 1980, §5.3 of A.R. MACKINTOSH and O.K. ANDERSEN, in: Electrons at the Fermi Surface, ed. M. Springford (Cambridge Univ. Press).
ANDERSEN, O.K., and O. JEPSEN, 1977, Physica **B91**, 317.
ASANO, S., and J. YAMASHITA, 1973, Prog. Theor. Phys. **49**, 373.
ASHCROFT, N.W., 1966, Phys. Lett. **23**, 48.
ASHCROFT, N.W., and D.C. LANGRETH, 1967, Phys. Rev. **155**, 682.
BACHELET, G.B., D.R. HAMANN and M. SCHLUTER, 1982, Phys. Rev. **B26**, 4199.
BIEBER, A., and F. GAUTIER, 1981, Solid State Commun. **38**, 1219.
BIEBER, A., F. DUCASTELLE, F. GAUTIER, G. TREGLIA and P. TURCHI, 1983, Solid State Commun. **45**, 585.
BLOCH, A.N., and G.C. SCHATTEMAN, 1981, in: Structure and Bonding in Crystals, vol. I, eds. O'Keefe and Navrotsky (Academic, New York).
BRANDOW, B.H., 1977, Adv. Phys. **26**, 651.
BURGERS, W.G., 1934, Physica **1**, 561.
*CALLAWAY, J., 1964, Energy Band Theory (Academic, London).
CHELIKOWSKY, J.R., 1981, Phys. Rev. Lett. **47**, 387.
CHEN, Y., K.M. HO, and B.N. HARMON, 1988, Phys. Rev. **B37**, 283.
*COEHOORN, R., 1992, in: Electron Theory in Alloy Design, eds. D.G. Pettifor and A.H. Cottrell (Institute of Materials, London) ch. 8.
COOKE, J.F., J.W. LYNN and H.L. DAVIS, 1980, Phys. Rev. **B21**, 4118.
COULSON, C.A., L.R. REDEI and D. STOCKER, 1962, Proc. Roy. Soc. **A270**, 357.
CRESSONI, J.C., and D.G. PETTIFOR, 1991, J. Phys.: Condens. Matter **3**, 495.
CYROT, M., 1970, Phys. Rev. Lett. **25**, 871.
CYROT, M., and F. CYROT-LACKMANN, 1976, J. Phys. **F6**, 2257.
DE FONTAINE, 1979, Solid State Physics, vol. 34 (Academic, New York).
DUCASTELLE, F., 1970, J. Physique **31**, 1055.
*DUCASTELLE, F., 1991, Order and Phase Stability in Alloys (North-Holland, Amsterdam).
DUCASTELLE, F., and F. GAUTIER, 1976, J. Phys. **F6**, 2039.
DUTHIE, J.C., and D.G. PETTIFOR, 1977, Phys. Rev. Lett. **38**, 564.
EDWARDS, D.M., 1992, in: Electron Theory in Alloy Design, eds. D.G. Pettifor and A.H. Cottrell (Institute of Materials, London) ch. 9.
FAULKNER, J.S., 1982, Prog. Mater. Sci. **27**, 1.
FEDDERS, P.A., and P.C. MARTIN, 1966, Phys. Rev. **143**, 245.
FINNIS, M.W., 1974, J. Phys. **F4**, 1645.
*FINNIS, M.W., 1992, in: Electron Theory in Alloy Design, eds. D.G. Pettifor and A.H. Cottrell (Institute of Materials, London) ch. 2.
FRIEDEL, J., 1952, Phil. Mag. **43**, 153.
FRIEDEL, J., 1964, TMS AIME **230**, 616.
FRIEDEL, J., 1969, in: The Physics of Metals, ed. J.M. Ziman (Cambridge Univ. Press, New York) p. 494.
FRIEDEL, J., and C.M. SAYERS, 1977, J. Physique **38**, 697.
GELATT, C.D., H. EHRENREICH and R.E. WATSON, 1977, Phys. Rev. **B15**, 1613.
GELATT, C.D., H. EHRENREICH and J.A. WEISS, 1978, Phys. Rev. **B17**, 1940.
GELATT, C.D., A.R. WILLIAMS and V.L. MORUZZI, 1983, Phys. Rev. **B27**, 2005.
GIRIFALCO, L.A., 1976, Acta Metall. **24**, 759.
GLÖTZEL, D., 1978, J. Phys. **F8**, L163.
GRADMANN, U., and H. ISBERT, 1980, J. Magn. Magn. Mater. **15-18**, 1109.
GUNNARSSON, O., 1976, J. Phys. **F6**, 587.
GUNNARSSON, O., and B.I. LUNDQUIST, 1976, Phys. Rev. **B13**, 4274.

GYORFFY, B. L., and G. M. STOCKS, 1983, Phys. Rev. Lett. **50**, 374.
HAFNER, J., 1974, Phys. Rev. **B10**, 4151.
HAFNER, J., 1976, J. Phys. **F6**, 1243.
HAFNER, J., 1977, Phys. Rev. **B15**, 617.
*HAFNER, J., 1987, From Hamiltonians to Phase Diagrams: The Electronic and Statistical Mechanical Theory of sp-bonded Metals and Alloys, Solid State Sciences **70** (Springer, Berlin).
HAFNER, J., 1989, in: The Structures of Binary Compounds, eds. F. R. de Boer and D. G. Pettifor (North-Holland, Amsterdam) p. 147.
HARRIS, J., and R. O. JONES, 1978, J. Chem. Phys. **68**, 3316.
HARRISON, W. A., 1959, Phys. Rev. **116**, 555.
HARRISON, W. A., 1960, Phys. Rev. **118**, 1190.
*HARRISON, W. A., 1966, Pseudopotentials in the Theory of Metals (Benjamin, New York).
*HARRISON, W. A., 1980, Electronic Structure and the Properties of Solids (Freeman, San Francisco).
HASEGAWA, H., 1980, J. Phys. Soc. Japan **49**, 963.
HASEGAWA, H., and D. G. PETTIFOR, 1983, Phys. Rev. Lett. **50**, 130.
HAYES, T. M., H. BROOKS and A. R. BIENENSTOCK, 1968, Phys. Rev. **175**, 699.
HEINE, V., 1967, Phys. Rev. **153**, 673.
HEINE, V., and I. ABARENKOV, 1964, Phil. Mag. **9**, 451.
*HEINE, V., and D. WEAIRE, 1970, Solid State Physics, vol. 24 (Academic, New York).
HERMAN, F., and S. SKILLMAN, 1963, Atomic Structure Calculations (Prentice Hall, Englewood Cliffs, NJ).
HERRING, C., 1940, Phys. Rev. **57**, 1169.
HO, K., and B. N. HARMON, 1990, Mater. Sci. Eng. **A127**, 155.
HODGES, L., H. EHRENREICH and N. D. LANG, 1966, Phys. Rev. **152**, 505.
HOHENBERG, P., and W. KOHN, 1964, Phys. Rev. **136**, B864.
HUBBARD, J., 1967, Proc. Phys. Soc. **92**, 921.
HUBBARD, J., 1981, Phys. Rev. **B23**, 5974.
INGLESFIELD, J. E., 1969, J. Phys. **C2**, 1285.
JACOBS, R. L., 1968, J. Phys. **C1**, 492.
JACOBSEN, K. W., J. K. NØRSKOV, and M. J. PUSKA, 1987, Phys. Rev. **B35**, 7423.
JACUCCI, G., and R. TAYLOR, 1981, J. Phys. **F11**, 787.
JAN, J-P., and A. R. WILLIAMS, 1976, Phys. Rev. **B14**, 4199.
JENA, P., 1981, Treatise Mater. Sci. Tech. **21**, 351.
JEPSEN, O., O. K. ANDERSEN and A. R. MACKINTOSH, 1975, Phys. Rev. **B12**, 3084.
JOHANNES, R. L., R. HAYDOCK and V. HEINE, 1976, Phys. Rev. Lett. **36**, 372.
JONES, H., 1973, Proc. Phys. Soc. (London) **49**, 250.
JONES, R. O., and O. GUNNARSSON, 1989, Rev. Mod. Phys. **61**, 689.
KAUFMAN, L., and H. NESOR, 1973, in: Titanium Science and Technology, vol. 2, eds R. I. Jaffe and H. Burte (Plenum, New York) p. 773.
*KITTEL, C., 1971, Introduction to Solid State Physics (Wiley, New York).
KOHN, W., and N. ROSTOKER, 1954, Phys. Rev. **94**, 1111.
KOHN, W., and L. J. SHAM, 1965, Phys. Rev. **140**, A1133.
KOLLAR, J., and G. SOLT, 1974, J. Phys. Chem. Solids **35**, 1121.
KORRINGA, J., 1946, Physica **13**, 392.
KÜBLER, J., 1981, Phys. Lett. **81A**, 81.
LEE, S., 1991a, J. Am. Chem. Soc. **113**, 101.
LEE, S., 1991b, Acc. Chem. Res. **24**, 249.
LEUNG, C. H., M. J. STOTT and W. H. YOUNG, 1976, J. Phys. **F6**, 1039.
LIBERMAN, D. A., 1971, Phys. Rev. **B3**, 2081.
LIU, C. T., J. A. HORTON, and D. G. PETTIFOR, 1989, Mat. Res. Soc. Symp. Proc. **133**, 37.
LOMER, W. M., 1962, Proc. Phys. Soc. **A80**, 489.

MADSEN, J., O. K. ANDERSEN, U. K. POULSEN and O. JEPSEN, 1976, in: Magnetism and Magnetic Materials, 1975, Philadelphia, eds. J. J. Becker and G. H. Lander (AIP Conf. Proc. 29, New York) p. 327.
MANNINEN, M., J. K. NØRSKOV and C. UMRIGAR, 1982, J. Phys. **F12**, L1.
MATTHEISS, L. F., 1972, Phys. Rev. **B5**, 290.
MCMAHAN, A. K., and R. C. ALBERS, 1982, Phys. Rev. Lett. **49**, 1198.
MCMAHAN, A. K., and J. A. MORIARTY, 1983, Phys. Rev. **B27**, 3235.
MIEDEMA, A. R., P. F. DE CHATEL and F. R. DE BOER, 1980, Physica **B100**, 1.
MORIARTY, J. A., 1982, Phys. Rev. **B26**, 1754.
MORIARTY, J. A., 1983, Int. J. Quantum Chem. **17**, 541.
MORIARTY, J. A., 1988, Phys. Lett. **131**, 41.
MORIARTY, J. A., and A. K. MCMAHAN, 1982, Phys. Rev. Lett. **48**, 809.
MORIYA, T., 1965, Prog. Theor. Phys. **33**, 157.
MORUZZI, V. L., J. F. JANAK and A. R. WILLIAMS, 1978, Calculated Electronic Properties of Metals (Pergamon, New York).
MOTT, N. F., 1949, Proc. Phys. Soc. **A62**, 416.
MOTT, N. F., and H. JONES, 1936, Properties of Metals and Alloys (Dover, New York) ch. 7.
MUELLER, F. M., 1967, Phys. Rev. **153**, 659.
NIEMINEN, R. M., and C. H. HODGES, 1976, J. Phys. **F6**, 573.
NØRSKOV, J. K., 1982, Phys. Rev. **B26**, 2875.
NØRSKOV, J. K., and N. D. LANG, 1980, Phys. Rev. **B21**, 2131.
NØRSKOV, J. K., F. BESENBACHER, J. BOTTIGER, B. B. NIELSEN and A. A. PISAREV, 1982, Phys. Rev. Lett. **49**, 1420.
OHTA, Y., and D. G. PETTIFOR, 1989, J. Phys.: Condens. Matter **2**, 8189.
PAPON, A. M., J. P. SIMON, P. GUYOT and M. C DESJONQUERES 1979, Phil. Mag. **39**, 301.
PAULING, L., 1960, The Nature of the Chemical Bond (Cornell Univ. Press, New York).
PAXTON, A. T., M. METHFESSEL and H. M. POLATOGLOU, 1990, Phys. Rev. **B41**, 8127.
PAXTON, A. T., and D. G. PETTIFOR, 1992, Scripta Metall. **26**, 529.
PENN, D. R., 1966, Phys. Rev. **142**, 350.
PETTIFOR, D. G., 1970a, Phys. Rev. **B2**, 3031.
PETTIFOR, D. G., 1970b, J. Phys. **C3**, 367.
PETTIFOR, D. G., 1972a, J. Phys. **C5**, 97.
PETTIFOR, D. G., 1972b, in: Metallurgical Chemistry, ed. O. Kubaschewski (Her Majesty's Stationery Office, London) p. 191.
PETTIFOR, D. G., 1976, Commun. Phys. **1**, 141.
PETTIFOR, D. G., 1977, J. Phys. **F7**, 613.
PETTIFOR, D. G., 1978a, J. Chem. Phys. **69**, 2930.
PETTIFOR, D. G., 1978b, J. Phys. **F8**, 219.
PETTIFOR, D. G., 1979, Phys. Rev. Lett. **42**, 846.
PETTIFOR, D. G., 1980, J. Magn. Magn. Mater. **15-18**, 847.
PETTIFOR, D. G., 1982, Phys. Scripta **T1**, 26.
PETTIFOR, D. G., 1984, Solid State Commun. **51**, 31.
*PETTIFOR, D. G., 1987, Solid State Physics **40**, 43.
PETTIFOR, D. G., 1988a, Mater. Sci. Technol. **4**, 2480.
PETTIFOR, D. G., 1988b, Physica B **149**, 3.
*PETTIFOR, D. G., 1992, in: Electron Theory in Alloy Design, eds. D. G. Pettifor and A. H. Cottrell (Institute of Materials, London) ch. 4.
PETTIFOR, D. G., and C. D. GELATT, 1983, fig. 8 of Cohesion and Decohesion in the Metallic Bond, in: Atomistics of Fracture, Proc. Nato Adv. Res. Inst., Corsica, 1981, ed. R. Latanision (Plenum, New York).
PETTIFOR, D. G., and R. PODLOUCKY, 1984, Phys. Rev. Lett. **53**, 1080.
PETTIFOR, D. G., and R. PODLOUCKY, 1986, J. Phys. **C19**, 315.
PETTIFOR, D. G., and M. A. WARD, 1984, Solid State Commun. **49**, 291.

PHILLIPS, J. C., 1970, Rev. Mod. Phys. **42**, 317.
PUSKA, M. J., R. M. NIEMINEN and M. MANNINEN, 1981, Phys. Rev. **B24**, 3037.
RATH, J., and J. CALLAWAY, 1973, Phys. Rev. **B8**, 5398.
RUEDENBERG, K., 1962, Rev. Mod. Phys. **34**, 326.
ST. JOHN, J., and A. N. BLOCH, 1974, Phys. Rev. Lett. **33**, 1095.
SATO, H., and R. S. TOTH, 1961, Phys. Rev. **124**, 1833.
SCHIFF, L. I., 1968, Quantum Mechanics, 3rd Ed. (McGraw-Hill, New York).
SHIGA, M., and Y. NAKAMURA, 1969, J. Phys. Soc. Japan **26**, 24.
SKRIVER, H. L., 1981a, J. Phys. **F11**, 97.
SKRIVER, H. L., 1981b, in: Physics of Solids under High Pressure, eds. J. S. Schilling and R. N. Shelton (North-Holland, Amsterdam) p. 279.
SKRIVER, H. L., 1982, Phys. Rev. Lett. **49**, 1768.
SKRIVER, H. L., O. K. ANDERSEN and B. JOHANNSSON, 1978, Phys. Rev. Lett. **41**, 42.
SLATER, J. C., 1951a, Phys. Rev. **82**, 538.
SLATER, J. C., 1951b, Phys. Rev. **81**, 385.
SLATER, J. C., 1963, Quantum Theory of Molecules and Solids, vol. I (McGraw-Hill, Maidenhead).
SLATER, J. C., and G. F. KOSTER, 1954, Phys. Rev. **94**, 1498.
SLUITER, M., D. DE FONTAINE, X. Q. GUO, R. PODLOUCKY and A. J. FREEMAN, 1990, Phys. Rev. **B42**, 10460.
STONER, E. C., 1939, Proc. Roy. Soc. **A169**, 339.
STOTT, M. J., and E. ZAREMBA, 1980, Phys. Rev. **B22**, 1564.
STROUD, D., and N. W. ASHCROFT, 1971, J. Phys. **F1**, 113.
*SUTTON, A. P., 1993, Electronic Structure of Materials (Clarendon Press, Oxford).
TAKEMURA, K., S. MINOMURA and O. SHIMOMURA, 1982, Phys. Rev. Lett. **49**, 1772.
TAYLOR, R., and A. H. MACDONALD, 1980, J. Phys. **F10**, 2387.
TINKHAM, M., 1964, Group Theory and Quantum Mechanics (McGraw-Hill, New York).
VAN SCHILFGAARDE, M., A. T. PAXTON, A. PASTUREL and M. METHFESSEL, 1990, Mat. Res. Soc. Symp. Proc. **186**, 107.
VANDERBILT, D., 1990, Phys. Rev. **B41**, 7892.
VILLARS, P., and L. D. CALVERT, 1985, Pearson's Handbook of Crystallographic Data for Intermetallic Phases, vols. 1, 2, 3 (American Society for Metals, Metals Park, Ohio).
WATSON,. R. E., and L. H. BENNETT, 1981, Calphad **5**, 25.
WATSON, R. E., H. EHRENREICH and L. HODGES, 1970, Phys. Rev. Lett. **24**, 829.
WIGNER, E. P., and F. SEITZ, 1933, Phys. Rev. **43**, 804.
WILLIAMS, A. R., C. D. GELATT and V. L. MORUZZI, 1980a, in: Proc. Metallurg. Soc. AIME, New Orleans 1979, ed. L. H. Bennett (Met. Soc. AIME, Warrendale, PA).
WILLIAMS, A. R., C. D. GELATT and V. L. MORUZZI, 1980b, Phys. Rev. Lett. **44**, 429.
WILLIAMS, A. R., C. D. GELATT and V. L. MORUZZI, 1982, Phys. Rev. **B25**, 6509.
WINDSOR, C. G., 1972, J. Phys. **F2**, 742.
WOHLFARTH, E. P., 1980, in: Ferromagnetic Materials, vol. 1, ed. E. P. Wohlfarth (North-Holland, Amsterdam) ch. 1.
WOOD, J. H., 1962, Phys. Rev. **126**, 517.
YIN, M. T., 1982, Ph. D. thesis, Univ. of California, Berkeley, figs. 5 and 6.
YIN, M. T., and M. L. COHEN, 1980, Phys. Rev. Lett. **45**, 1004.
YIN, M. T., and M. L. COHEN, 1981, Solid State Commun. **38**, 625.
ZUNGER, A., 1980, Phys. Rev. **B22**, 5839.
ZUNGER, A., 1994, in: Statics and Dynamics of Alloy Phase Transformations, eds. P. E. A. Turchi and A. Oonis (Plenum, New York), 361.

Further reading

References marked with an asterisk in the list above can also be used for general reading.

CHAPTER 3

STRUCTURE AND STABILITY OF ALLOYS*

T.B. MASSALSKI

Department of Materials Science
and Engineering
Carnegie–Mellon University
Pittsburgh, PA, USA

* This chapter is dedicated to the memory of my good friend Professor Peter Haasen. Much of the revision which I undertook was done in Göttingen, in the summer of 1993, and many suggestions for changes and improvements came from Peter during our walks in Göttingen woods. I am very grateful to the Alexander von Humboldt Foundation for the award of the Humboldt Prize which made my stay in Göttingen during that summer possible.

R. W. Cahn and P. Haasen†, eds.
Physical Metallurgy; fourth, revised and enhanced edition

1. Solid solubility

A *solid solution* is obtained when atoms of different elements are able to share together, and with changing proportions, various sites of a common crystalline lattice. It is now generally recognized that all metals and compounds show some solubility in the solid state; a question of great interest is, however, the extent of solid solubility in a given case. For example, only 0.2 wt% of phosphorus can be dissolved in γ-iron, but nearly 39 wt% of zinc can be dissolved in copper without changing its structure. On alloying copper with nickel, on the other hand, the same fcc structure is maintained throughout the entire alloy system (fig. 1a), providing an example of *complete solid solubility*. The Au–Cu alloys have complete solid solubility at high temperatures, but show different behavior at low temperatures (see fig. 1b and § 11). In the great multitude of phase diagrams now known, the above cases, and even the case of only a partial but extensive solid solubility (of several atomic percent), are relatively rare. Complete solid solubility can occur only if the structures of the elements involved are basically the same, but it need not always occur when this condition is fulfilled (i.e., the system Cu–Ag which is a simple eutectic). In the case of close-packed hexagonal solid solutions

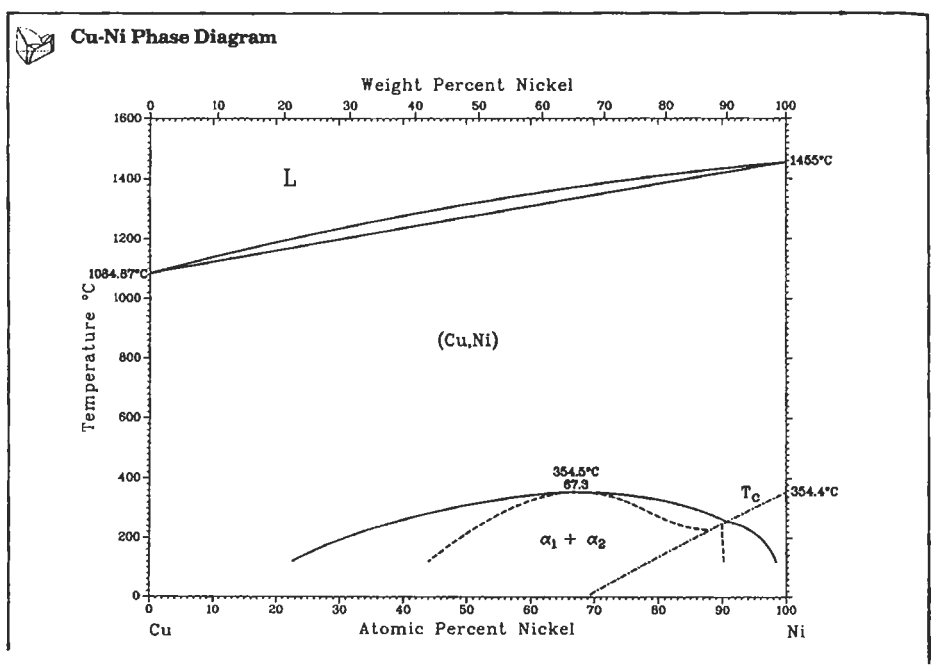

Fig. 1a. Complete solid solubility in the system Cu–Ni which maintains fcc structure throughout the whole composition range (from MASSALSKI [1990].)

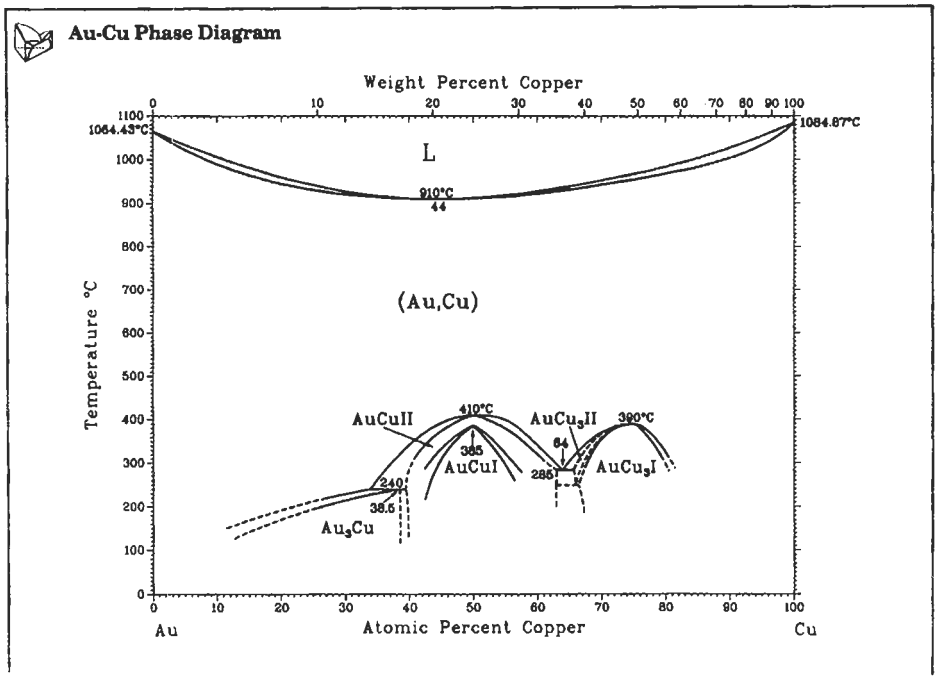

Fig. 1b. The Au–Cu system has complete solid solubility and fcc structure at high temperatures. At low temperatures superlattices form (see § 11). (From MASSALSKI [1990].)

considerable difference between the values of the axial ratio can usually be accommodated on changing from one element to another; for example, the axial ratio, c/a, changes from 1.5873 for Ti to 1.5931 for Zr in the Ti–Zr system, and from 1.6235 for Mg to 1.8856 for Cd in the Mg–Cd system. The phase diagrams of these systems are shown in figs. 1c and 1d. In the case of Ti–Zr the pure elements exist in two allotropic forms (cubic at high temperatures and hexagonal at low temperatures), and complete solid solubility occurs between both modifications on alloying. In the Mg–Cd system, on the other hand, complete solubility occurs only at high temperatures and is interrupted at lower temperatures by the formation of superlattices (see § 11).

From the point of view of solid solubility, chemical compounds can be compared with pure metals and may be said to show alloying behavior if they exhibit wide solid solubility in a phase diagram. Since compounds are usually formed at fixed ratios of the numbers of atoms, the occurrence of solid solubility represents a departure from stoichiometry. If a compound is truly ionic in nature, the extent of such departure may be extremely small, amounting perhaps to a fraction of an at%; and for all practical purposes this is usually ignored and the compound is then drawn as a vertical line in the phase diagram. However, in typical metallic systems a large number of phases have been

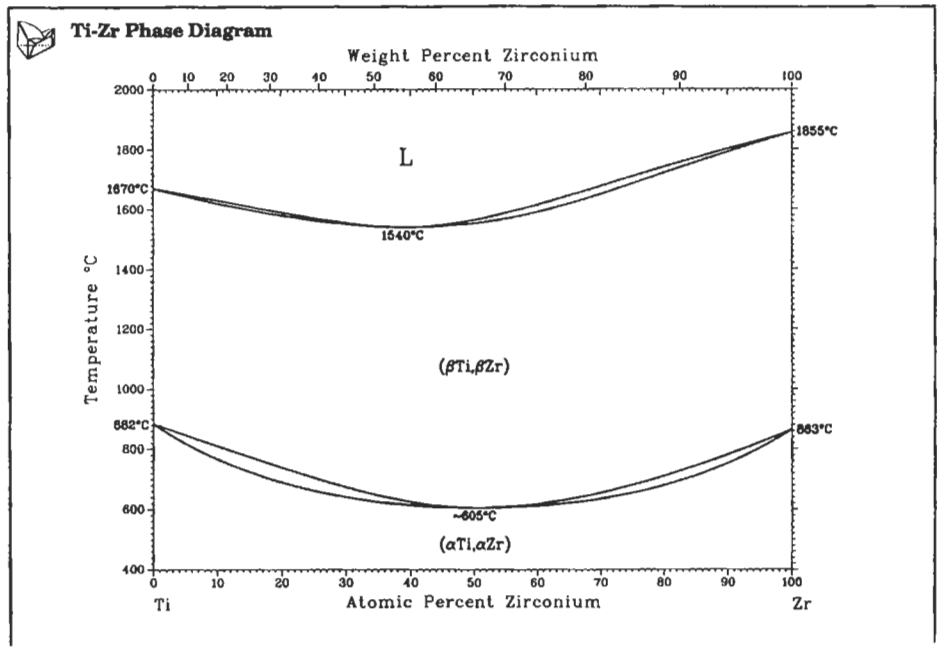

Fig. 1c. The Ti–Zr system has complete solid solubility, with cubic structure at high temperatures and hexagonal structure at low temperatures (from MASSALSKI [1990].)

observed at atomic compositions which bear no apparent relation to the rules of stoichiometry. Such phases frequently possess wide ranges of solid solubility and resemble the solid solutions obtained on initial alloying of pure metals. To an engineer concerned with materials the occurrence of wide solid solubility, both between pure metals and in compounds, is of great practical interest because it is often associated with relatively simple metallic structures which possess desirable mechanical and physical properties.

In this chapter we shall examine some of the factors which determine the limits of solid solubility in metallic systems and then consider some properties of the structure of extended solid solutions, such as lattice spacings, defects, departure from randomness, size effects, etc.

2. *Terminology (types of solid solutions)*

Solid solutions are phases of variable composition, and in principle any number of components can be alloyed together to form a series of solid solutions. However, for simplicity we shall consider mainly the binary alloys. The replacement of copper atoms by nickel on the lattice of pure copper is an example of a *substitutional* solid solution.

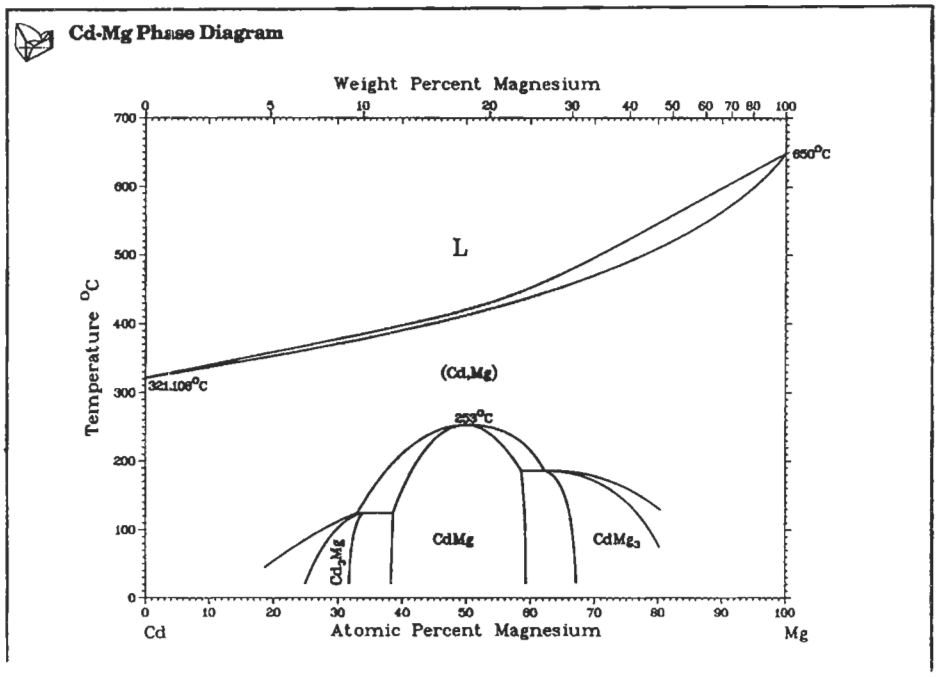

Fig. 1d. In the Mg–Cd system complete solid solubility occurs at high temperatures. Superlattices form at low temperatures (see § 11). (From MASSALSKI [1990].)

Since the two elements can be substituted at all proportions throughout the whole system, they form a *continuous series of solid solutions.* If the solid solubility is limited to only those portions of the phase diagram which are linked to pure elements, the resulting phases are known as *primary (or terminal) solid solutions.* Such solutions have, of course, the same structure as the elements on which they are based. All other phases are usually known as *intermediate phases;* they may be called *intermetallic compounds* or *valence compounds* if their solid solubility is unusually restricted around a stoichiometric composition. Intermediate phases typically possess structures which are different from the structure of either of the component elements.

If the size-difference between the component atoms which participate in forming a solid solution is sufficiently large, it may become possible on alloying for the one kind of atoms to be merely deposited in the holes (or interstices) between the other atoms on their space lattice. An *interstitial* solid solution is then formed. Such solutions can occur for example when nonmetallic elements such as boron, oxygen, nitrogen or carbon are dissolved in a metal lattice.

Both interstitial and substitutional solid solutions can be *random,* with statistical distribution of atoms, or they may be partially or completely *ordered,* in which case the unlike atoms show preference for one another. A fully ordered solid solution is some-

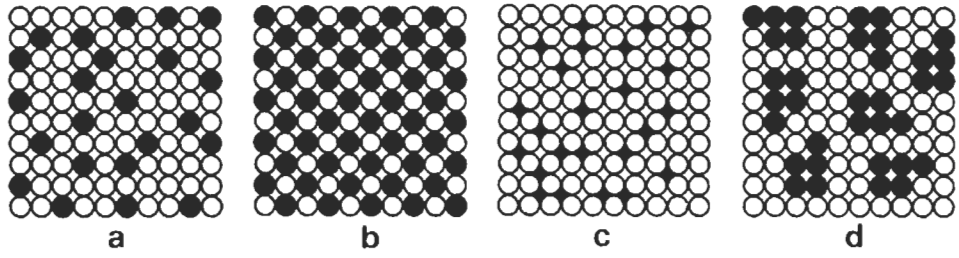

Fig. 2. Schematic models of solid solutions: (a) substitutional random; (b) substitutional ordered; (c) interstitial random; (d) solute clusters in solid solution.

times known as a *superlattice*. Alternatively, the like-atoms may tend to associate together to form clusters within the solid solution. Again, the clusters may be dispersed randomly or they may be ordered or oriented in various ways, producing a variety of complex substructures within the solid solution. A diagrammatical illustration of the various types of solid solution is given in fig. 2.

While it is possible to consider the case of a random solid solution as an idealized example, the mounting experimental evidence, based mainly on diffuse X-ray scattering, suggests that complete randomness (like perfect crystallinity) is probably never found in nature. Hence, solid solutions which are in a thermodynamical equilibrium (ch. 5) may be considered to be truly *homogeneous* on a macroscopic scale, but they need not be homogeneous down to the scale where atoms are considered individually.

3. *Energy of solid solutions and phase stability considerations*

The extent of solid solubility of phases, the stability of phases, the temperature dependence of stability, and the choice of structures that are actually observed in phase diagrams are the result of competition among numerous possible structures that could be stable in a given system. This competition is based on the respective values of the *Gibbs Free Energy* of each competing phase and the variation of this energy with temperature, pressure, composition and possibly other extensive parameters. The details are presented in chapter 5. Here, we shall merely state that the most general form of the Gibbs energy (G) can be expressed as a function of the intensive parameters, enthalpy (H) and entropy (S), and the absolute temperature (T):

$$G = H - TS. \tag{1}$$

As is well known, numerous factors contribute to the H and S parameters. The major contribution to the entropy is from statistical mixing of atoms (ΔS_{mix}), but there can be additional contributions from vibrational effects (ΔS_{vib}), distribution of magnetic moments, clustering of atoms and various long range configurational effects. The main interest in this chapter is in the contributions to the enthalpy resulting from atomic mixing (ΔH_{mix}), which are in turn related to the interaction energies between neighbouring and further distant atoms in a given structure based upon electronic, elastic, magnetic and vibrational effects. Much progress has been made in measuring, calculating and

predicting many such effects, and hence progress continues to be made in the evaluation of the related thermodynamic quantities and ultimately the phase diagrams.
Some recent reviews of these topics are listed in the bibliography for further reading (and in chapter 6).

Typical values of the enthalpy of formation (ΔH) and its relation to the type of bonding are given as an illustration in table 1. As discussed in chapter 6, a change by 10–20 kJ/mole in the interaction parameter that determines the enthalpy of formation can profoundly affect the form of the resulting phase diagram. The estimation of the ΔH values, particularly for systems where the experimental data are meager or lacking, has been therefore of great practical interest to the workers in the area of phase stability. Semi-empirical values of the heats of formation have been predicted for many systems by Miedema and co-workers (MIEDEMA and NIESSEN [1988]) and have found many uses.

Along with the progress achieved in the measurements that established the details of phase diagrams and the associated phases, it is natural that the observed phase stabilities should be tested against basic theory. In this connection, two aspects stand out sharply ([MASSALSKI 1989]):

(1) The need to calculate phase stability from "first principles" in order to understand the basic parameters that control the energy of a phase.

Table 1
Heats of formation at 298K of some typical intermediate phases and compounds.*

Compound or phase	Structure**	Predominant bonding	Heat of formation $-\Delta H$ (kJ/g atom)
MgSe	NaCl (B2)	Ionic	135.9 ± 8.3
MgTe	ZnS (B4)	Ionic	104.3 ± 10.4
ZnTe	ZnS (B3)	Ionic	60.0 ± 2.1
Mg_2Ge	CaF_2 (C1)	Partially ionic	38.4 ± 0.08
Mg_3Bi_2	Ca_2O_3 (D5c)	Partially ionic	30.9 ± 0.8
Mg_2Si	CaF_2 (C1)	Partially ionic	26.3 ± 1.3
InAs	ZnS (B3)	Covalent	30.9 ± 2.5
GaSb	ZnS (B3)	Covalent	20.9 ± 0.8
InSb	ZnS (B3)	Covalent	14.6 ± 0.4
NiTe	NiAs (B8)	Partially metallic	18.8 ± 6.3
CoSn	NiAs (B8)	Partially metallic	15.0 ± 1.3
Co_3Sn_2	NiAs (B8)	Partially metallic	11.3 ± 0.8
$CaMg_2$	$MgZn_2$ (C14)	Metallic	13.3 ± 0.4
Ag_5Zn_8 (0.61 Zn)	γ-brass (D8c)	Metallic	4.6 ± 0.21
AgZn (0.50 Zn)	β-brass (B2)	Metallic	3.1 ± 0.21

*Data taken from ROBINSON and BEVER [1967].

**For meaning of the symbols, see ch. 4.

References: p. 199.

(2) The need to utilize the successful theories of phase stability for predicting phase diagrams in systems where measurements have not yet been done, or are particularly difficult. Here, progress will ultimately permit technologically relevant complex or multicomponent phase diagrams to be predicted.

It was Hume–Rothery and his associates who more than a half century ago laid the foundations for a systematic study of phase diagrams and their interpretation. A suitable testing ground at that time was the stability of alloy phases based on the so-called noble metals, Cu, Ag, and Au (HUME–ROTHERY [1955]; HUME–ROTHERY *et al.* [1969]). From this work has emerged the emphasis on three general metallurgical parameters. Stated very broadly they are:

(1) the difference in atomic sizes of the components,
(2) the electrochemical differences among the components, and
(3) the "electron concentration" change on alloying.

Their importance is often expressed in terms of the so called "Hume–Rothery Rules" (see section 4).

Regarding the basic theory, the understanding and prediction of phase stability of alloys and compounds in terms of the electronic structure calculations is a subject of paramount importance in materials science. There has been much progress in the "first principles" (or the so called "*ab initio*" approach to the band theory of both ordered compounds and, more recently, also of random metallic alloys (STOCKS and WINTER [1984]). At the same time, because of the pressing need of technology, many semi-empirical or partially qualitative schemes of phase stability have been pursued, often very successfully. The results of such attempts are usually the estimated heats of formation (ΔH) (see also ch. 2, § 6.2.).

Basic theoretical guidelines are needed to classify phase diagrams, in order to be able to extrapolate from known binaries to higher order systems. A theoretical derivation of energies of specific structures and phase equilibria between them, eventually will yield reasonably accurate free energy and entropy changes, and a description of states of partial order, relative stability of metastable phases, etc. Clearly, the first step towards true theoretical determination of phase diagrams is to calculate the energies of phases involved in simple binaries and compare them with experimentally determined values, where possible. A number of theoreticians in excellent reviews (LOMER [1967], FAULKNER [1982]; HAFNER [1983]) have outlined the different operations that must be performed to calculate a composition-temperature phase diagram of a binary alloy, starting first with the stability of individual phases. Essentially, these steps are as those enumerated in table 2.

From the point of view of phase stability, the result of such a detailed calculation would be a sufficiently precise set of values of the enthalpies of the various competing alloy phases and their variations with composition. The calculation of the phase diagrams, including temperature and entropy, would be the next step. Clearly, from the point of view of phase stability, even these initial calculations represent a monumental task. Yet, a glance at table 3 quickly shows that theoretical assessments are our only reasonable hope of dealing with higher-order systems in the near future. In table 4, a brief

Table 2
Phase stability calculations.*

(First principles) *General procedure*	
(1)	Calculate self-consistent atomic potentials of components.
(2)	Fix alloy composition.
(3)	Assume a possible crystal structure.
(4)	Choose lattice parameters.
(5)	Introduce the atomic potentials on the lattice, calculate self-consistent band structure and ground state energy, and add interionic energy.
Result: total energy	
(6)	Repeat (4) and (5) for different values of lattice constants.
(7)	Repeat (3) through (6) for other possible crystal structures.
(8)	Repeat (2) through (7) for other compositions.
Result: enthalpy of the possible alloy phases as a function of composition.	

*LOMER [1967], FAULKNER [1982], HAFNER [1983]

summary is given of some of the more recent theoretical calculations that have been developed. This summary is not intended to be comprehensive or complete. (See also ch. 5, § 6.).

Table 3
Possible number of systems.

	$\frac{n!}{(m!(n-m)!}$
binary	$\frac{90!}{2!88!} = 4{,}005$
ternary	$\frac{90!}{3!87!} = 117{,}480$
quaternary	$\frac{90!}{4!86!} = 2{,}555{,}190$

n = number of elements (say 90)
m = number of elements in a system

As emphasized by many authors (MASSALSKI [1989]), the majority of existing models, from the semi-empirical to those providing detailed density maps and electronic parameters of alloys, have the same major drawback as far as phase diagrams are concerned: it is difficult to treat theoretically the temperature dependence of the energy. For example, the calculations that predict enthalpies at 0 K (for first principles calculations), or at some undefined temperature (for the semiempirical models), rarely provide sufficient information about the thermal behavior of such enthalpies or the thermal

entropy contributions. Yet, for the purpose of phase diagrams determination the Gibbs free energies must be calculated by adding to each enthalpy derived from the static models the vibrational energy and the thermal entropy contributions. The latter in turn consist of vibrational and configurational parts. It is clear that the prediction of entropies, particularly for possible metastable phases in phase diagrams, will become the necessary step before the full potential of the theoretically calculated stabilities can be utilized. Only a few interesting examples of phase stability, compound stability and alloying effects are reviewed below.

4. *Factors governing solid solubility (Hume–Rothery rules for primary solid solutions)*

Since all interactions between atoms are a function of electronic forces, they should ultimately be subject to the laws of quantum mechanics. At the present time, however, the available theories of the solid state of the type summarized in table 4 are unable to incorporate or to account for the many factors which have been known to materials scientists as important in determining the structure and various properties of solid solutions. Such factors, for example, as chemical affinity or the size-difference between atoms can be considered only semi-empirically, and even the electronic structure, for which more elaborate theories exist, has been discussed satisfactorily only in a few rather simple cases. Nevertheless, mainly as a result of studies by Hume–Rothery and his associates (HUME–ROTHERY [1961a] and HUME–ROTHERY *et al.* [1969]), extending over more than thirty years, certain general rules have been formulated concerning the limits of primary solid solubility and, to some measure, also the width and stability of certain intermediate phases. As already mentioned above, these rules refer to the difference between the relative atomic radii of the participating elements, their electrochemical differences and their relative valencies. *Hume–Rothery rules* may be summarized as follows:

(i) If the difference between the atomic sizes of the component elements forming an alloy exceeds about 14–15%, solid solubility should become restricted. This is known as the 15% *rule*. The general concept may be illustrated by reference to fig. 3 (HUME–ROTHERY [1961a]) in which the ranges of favorable atomic sizes with respect to copper, silver and γ-iron are shown diagrammatically. If the atomic diameter of a particular solute element lies outside the favorable size zone for the solvent, the *size factor* is said to be unfavourable and the primary solid solubility will be restricted usually in some proportion to the increasing difference between the two atomic diameters. Within the favorable zone the size factor is only of secondary importance and other factors will determine the total extent of solid solubility. In a sense, therefore, the 15% rule is a negative rule stressing the role of size differences only when they *restrict* alloy formation. In this connection, WABER *et al.* [1963] have shown that when the size rule alone was applied to 1423 terminal solid solutions, in 90.3% of the systems where little solid solubility was predicted, little solid solubility was in fact observed, but the prediction of extensive solid solubility on the basis of small size difference was only 50% successful. Theoretical justification for the 15% rule has been obtained from considerations of elastic strain energy in a solid solution (see below).

Table 4
Recent theoretical calculations of phase stability or phase diagrams.

Type of calculation	Quantities calculated	Typical references
semi-empirical (charge density, size and electronegativity effects)	enthalpy of mixing, ΔH_f	MIEDEMA *et al.* [1980] MIEDEMA and NIESSEN [1988]
Pair potentials	alloy stabilities ΔH_{transf} (at 0 K)	MACHLIN [1981]
Mainly *d*-band effects	maps of related structures and their stability, ΔH_f	PETTIFOR [1986, 1979] WATSON and BENNETT [1979, 1983] YUKAWA *et al.* [1985]
Mainly valence band effects	relative alloy stabilities density of states	MOTT and JONES [1936] BREWER [1968] MASSALSKI and MIZUTANI [1978]
Cluster variation models	ordering energies, order–disorder	DE FONTAINE [1983] R. KIKUCHI [1981]
	ΔH_f (at 0 K) of simple systems	WILLIAMS *et al.* [1982]
First principles calculation using various atomic potentials: DFT, LSDA, KKR-CPA, LMTO	ΔH_{transf} (at 0 K) lattice dynamics, ordered compound stabilities	YIN and COHEN [1982] XU *et al.* [1987] PEI *et al.* [1989]
	simple phase diagrams	STOCKES and WINTER [1984] HAFFNER [1983] TERAKURA *et al.* [1987, 1988]

(ii) Formation of stable intermediate compounds will restrict primary solid solubility. The likelihood of the formation of such compounds in an alloy system is related to the chemical affinity of the participating elements and will be increased the more electronegative one of the elements and the more electropositive the other. The general principle leading to the restriction of solid solubility is illustrated in fig. 4 using hypothetical free-energy curves for a primary solid solution and for an intermediate phase. The width of the shaded area represents the extent of primary solid solubility; it becomes more restricted the greater the stability of the intermediate phase. The above

References: p. 199.

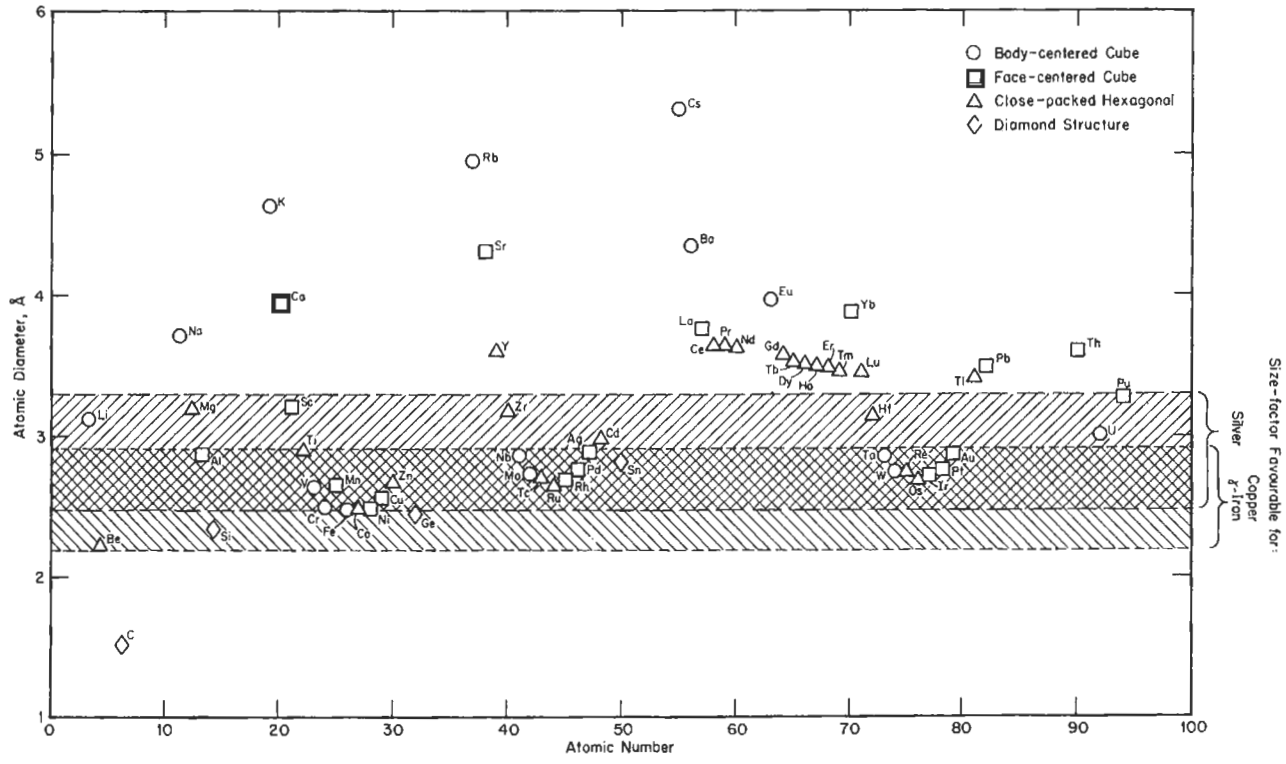

Fig. 3. Illustration of the application of the size-factor principle to solid solutions in copper, silver and γ-iron. The ordinates show the atomic diameters as defined by the closest distance of approach of the atoms in the crystals of elements. The shaded areas show the ranges of favorable size-factor, bounded by the limits ± 15% of the atomic diameters of silver, copper, and γ-iron, respectively. The types of structures involved are indicated by different symbols. (After HUME-ROTHERY [1961a].)

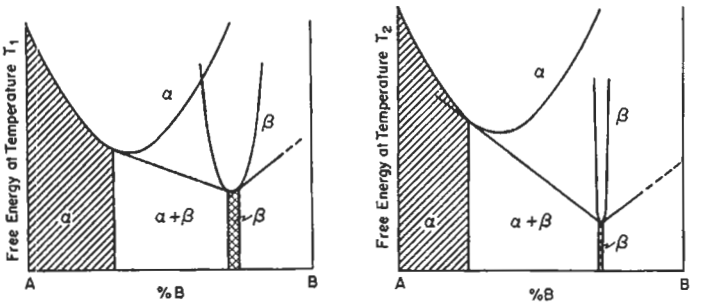

Fig. 4. Restriction of primary solid solubility due to stability of an intermediate phase.

principle has become known as the *electrochemical effect*, which is related to the difference in the electronegativities of the two components.

(iii) Empirical studies have shown that in many alloy systems one of the most important factors determining the extent of solid solubility and the stability of certain intermediate phases is *the electron concentration*. This parameter is usually taken to denote the number of all valence electrons per unit cell provided that all atomic sites within the structure are occupied. Alternatively, electron concentration may be taken as the ratio of all valence electrons to the number of atoms. It is then denoted as e/a.

Following the early investigations by Hume–Rothery and his associates it was also suggested that the mutual solid solubility of two given elements was related to their respective valencies, namely, that the amount of the solid solution in the element of lower valency was always greater than vice versa. This general principle is sometimes known as the *relative valency effect*. It appears to be valid when copper, silver or gold, which are monovalent, are alloyed with the B-subgroup elements of the Periodic Table which possess valencies greater than one. It may be associated in part with the fact that the Brillouin zones of the noble metals are only partially filled with electrons; and, although they are touched by the Fermi surface, they are not overlapped as are the Brillouin zones of the B-subgroup elements. A more likely cause, however, has its origin in the long-range charge oscillations around the impurity atoms as discussed by FRIEDEL [1964] and BLANDIN [1965].

Subsequent appraisals by HUME–ROTHERY [1961a] and GSCHNEIDNER [1980] suggest that the relative valency effect is not really a general principle, and that when two elements which are both of high valency are alloyed together it is often not possible to predict which of the two will form the more extensive solid solution with respect to the other.

5. *The meaning of "electron concentration"*

In the study of alloys it is often convenient to use the electron concentration, rather than atomic or weight composition, as a parameter against which various properties can be plotted. In the case of the alloys of the noble metals, the use of electron concentration has been particularly successful since it almost never fails to bring about interesting

correlations when applied to experimental data. Nevertheless, the physical meaning of electron concentration is by no means as simple as that of chemical composition, and as time progresses it has become increasingly more difficult to "visualize" the process by means of which valence electrons which belong to the solvent and the solute atoms become a common property of the conduction band of an alloy. Usually only the s and p electrons are considered as taking part in such a process, but occasionally the total number of electrons outside the inert-gas core (i.e., s + p + d electrons) has been used to denote the electron concentration (see below). In the B-subgroup elements which follow the noble metals in the respective horizontal rows of the Periodic Table the d bands in the free atoms are fully occupied by electrons. It has been considered for a long time, therefore, that on alloying only the s and p electrons are involved, but the possibility of transfer of electrons from the d band to the conduction band, and the s–d hybridization, makes the situation more complex. There is no doubt that the presence of d-band electrons sufficiently near the Fermi level in alloys of the noble metals and the changes in the energy of the d-band electrons on alloying constitute an important contribution to the electronic structure. This contribution is at present not fully understood but progress continues to clarify the picture. Calculations of the cohesive energy of the noble metals, using the assumption that only the s electrons are important, yield values which are far too low when compared with experimental data. In fact, as pointed recently by COTTRELL [1988], the cohesion of a metal like copper is mainly the result of attraction brought about by the sd hybridized electrons and the positive ions, while that part of the electronic system which corresponds to the classical free-electron gas is actually pushing the atoms apart (see below).

On the other hand, on alloying, even if it is assumed that the d band may be ignored and that certain elements possess a well-defined valence (for example, copper = 1, zinc = 2, gallium = 3, etc.), it is not certain whether all of the (s + p) electrons of a solute element go into the conduction band of the alloy. FRIEDEL [1954a] has suggested that in an alloy some of the s + p electrons may lie in *bound states* near the solute nuclei. According to MOTT [1952] such elements as zinc, gallium, germanium, etc., when dissolved in copper certainly contribute at least one electron to the conduction band. The next electron may or may not be in a bound state, while the additional electrons in gallium and germanium almost certainly are in bound states. Nevertheless, it has been suggested by FRIEDEL [1954a] and others that the valence-electron concentration rules may remain valid if one assumes that the potential acting on conduction electrons in an alloy "subtracts" from the bottom of the conduction band as many bound states as there are electrons in the bound atomic orbitals. Hence, the relationship between the effective conduction electrons and the band structure may be such that the Brillouin-zone effects, associated with the stability of phases and certain other alloy properties, may remain relatively unaltered. For further discussion of this and related subjects see FRIEDEL [1954a], HUME–ROTHERY and COLES [1954], COTTRELL [1988], and the proceedings of recent symposia (RUDMAN *et al.* [1967], BENNETT [1980], GONIS and STOCKS [1989]).

In alloy systems which involve transition elements, rare earths, actinides, lanthanides and transuranic elements, the assessment of valence and the corresponding changes in electron concentration are open to quite wide speculation. Often they depend on the

nature of the particular problem to be considered. Thus, many striking regularities are frequently revealed in a group of related elements, or alloy systems, provided that some valence scheme is adopted against which various properties within the group can be compared. For example, a rather abrupt change occurs in the electronic specific heat, magnetic susceptibility, Hall coefficient, hydrogen absorption, etc., in the transition metals and alloys of the first long period at an electron concentration of about 5.7 (MOTT [1962]) provided that the numbers of electrons outside the inert-gas core are considered to represent their valence, i.e., 4, 5, 6, 7, 8 and 9 for Ti, V, Cr, Mn, Fe and Co respectively. At the same time the valencies of these same elements when in dilute solution in the noble metals or aluminium are usually assessed according to a diffferent scheme in which only the predominantly s electrons are included. Considerations of phase stability (HUME–ROTHERY [1966] and RAYNOR [1956]) and changes of axial ratio (MASSALSKI [1958], MASSALSKI and KING [1960], COCKAYNE and RAYNOR [1961] and HENDERSON and RAYNOR [1962]) suggest that the above transition elements possess much lower, and possibly variable, valencies in the range between 0 and 2.

In a similar way, valence schemes have been suggested for other alloy groups, but will not be discussed here.

5.1. Progress in the electronic theories of metals and alloys

The distinction between metals, semi-metals and insulators, in terms of Brillouin zones, energy bands and the related overlapping or separation of bands, which has been for many years the basis in physics for defining what is a metal, has become somewhat blurred in recent years. COTTRELL [1988] points out that there are many substances that show metallic conductivity (or even superconductivity) even though clearly they are not metals in other aspects. (For example TCNQ, or certain ceramic oxides). When sufficient pressure is applied, electronic clouds of individual atoms are forced to overlap more and more, with the result that additional outer electrons in atoms will cease to belong to any particular atomic orbital and will behave as nearly free, contributing to metallic conductivity and bonding. Thus, the traditional view that the outer electrons (i.e., the valence electrons) become the "bonding glue" when atoms are assembled into crystals has become quite blurred.

In the earlier theories of Brillouin zones and Fermi surfaces the Bloch wavefunctions were used as a basis for calculation. Metals and solid solutions were considered as regular arrays of ions immersed in a "sea" of conduction electrons. The potential in a crystal was considered to be a periodically varying quantity corresponding to the periodicity of the ionic lattice and being more or less atomic (i.e. rapidly falling) in character near each ion. Bloch was able to show that wave functions of the conduction electrons for which the potential energy was modulated by the periodicity of the lattice were valid solutions of the Schrödinger equation. The resulting Bloch model has served as a very successful basis for discussion of the motion of electrons in metals and alloys. Only the conduction electrons, moving without electrostatic interactions with one another, were considered, and their motion was described by one-particle functions. Hence only the kinetic energy of the electrons was involved.

References: p. 199.

Subsequent developments in the electron theory have introduced a number of important modifications to the above model. It was found that the description of electronic properties was more consistent with experimental data if only weak *electron-ion* interactions were assumed, i.e., if the periodical potential was not considered to be atomic in character near each ion but only weakly changing from ion to ion. At the same time the additional problem of having to allow for possible strong *electron-electron* interactions was removed by considering that the Bloch model describes the motion, not of one-electron particles but of more complex entities, called *quasi particles*, introduced by Landau. Quasi particles have an electron at the center, surrounded by a region of electron deficiency (correlation hole) and a further region containing electrons that have been pushed out by the Coulombic repulsion away from the central electron and "flow around it much as water flows around a moving particle" (COHEN [1965]).

The problem of looking realistically at electron-atom interactions in order to reconcile the difference between the atomic and the effective potential in a metallic lattice has been tackled by introducing the notion of a *pseudopotential*. In this treatment the electron wave functions near the ions are ignored to some extent and substituted by pseudo wave functions which have the effect of statistically excluding the valence electrons from regions of space occupied by core electrons. (See ch. 2, § 3.3.) The application of the theory of pseudo-potentials has been very useful to the understanding of some problems in the theory of alloys (HEINE [1967] and STROUD [1980]). Other developments, as already mentioned in section 3, involve calculations of electronic energies "ab initio", and various elaborate treatments of the atomic potentials in solid solutions (see for example, FAULKNER [1982] and COTTRELL [1988]).

6. *Termination of primary solid solubility*

6.1. Electronic theories of primary solid solutions based on noble metals

A survey of binary systems of copper, silver and gold with a large number of elements, and in particular with the B-subgroup elements, has shown that the observed ranges of primary solid solubility may be correlated with electron concentration (HUME–ROTHERY and RAYNOR [1940]). In fig. 5 the maximum ranges* of primary solid solutions based on the three noble metals are indicated as linear plots in terms of e/a for the cases where these solutions are followed by an intermediate phase with a close-packed hexagonal structure (fig. 5a) and, separately, when they are followed by an intermediate phase with the body-centred cubic structure (fig. 5b). Apart from the systems Cu–In and Cu–Sn, the primary solutions followed by the cubic phase reach somewhat higher values of e/a than when followed by the close-packed hexagonal phase.

* It must be remembered that these maximum ranges occur at different temperatures in each system. Strictly speaking the correlation with *e/a* should apply only at the absolute zero of temperature. The fact that a significant correlation is observed at relatively high temperatures suggests that the electronic factors play a predominant role even at those high temperatures, although entropy considerations undoubtedly also play a role.

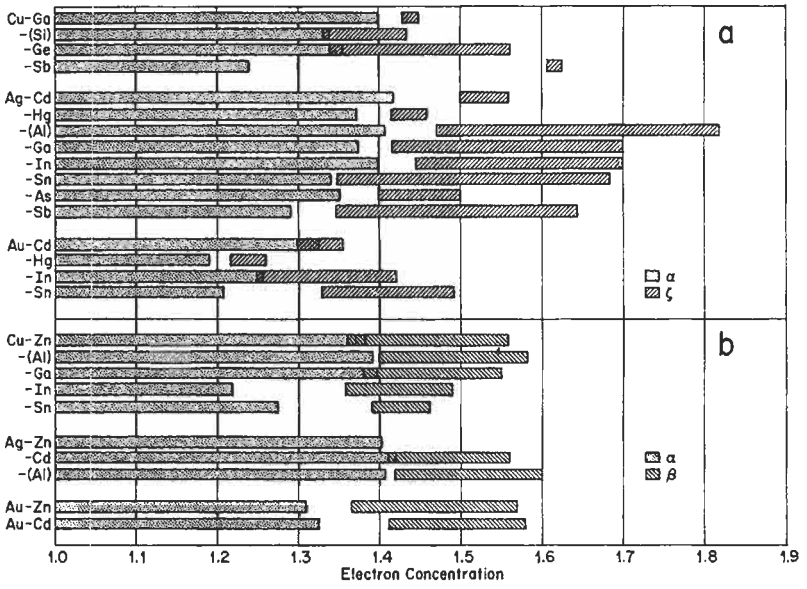

Fig. 5. Extent of the maximum primary solid solubility and of the following intermediate phase in alloys based on the noble metals (see text).

Examination of fig. 5 reveals that in silver-based alloys the primary solid solutions terminate within a fairly close range of values near $e/a = 1.4$, whereas in copper-based alloys the e/a values show a wider scatter, but the range of maximum values is again only a little less than 1.4. In the case of gold-based alloys the primary solid solubility is further restricted ranging between 1.2 and 1.3.

The above correlation between the primary solubility and e/a does not lead to any unique value, but it is quite striking when compared with similar plots drawn as a function of composition. Hence, it has been suspected for a long time that there must be an important link between the primary solid solubility and the electronic structure. During the 1930s an attempt was made by JONES [1937] to calculate the primary solid solubility of alloys based on copper using the theory of Brillouin zones and Bloch functions. This approach, and subsequent developments, are extensively quoted in metallurgical literature and will be discussed briefly below.

The main assumptions of the Jones model were: (i) that the *nearly-free-electron approximation* could be extended from pure metals to random solid solutions, and (ii) that the *rigid-band condition* was applicable on alloying (i.e., that the shape of the density of states curve $N(E)$ for a pure solvent remains unchanged on alloying and that the band gaps in the Brillouin zone do not change in magnitude, the only change being in the number of loosely-bound electrons). The general idea regarding stability of alloy phases was that at certain values of the electron concentration the Brillouin zone of one structure may be associated with a high density of quantum states, $N(E)$, at relatively low values of energy and thus "accommodate" the available electrons within lower total energy than

would be possible in the zone of some other structure. This condition is particularly likely to occur in the range of energies associated with contact between the Fermi surface and Brillouin-zone faces since it results in a peak in the density of states. The connection between phase stability and a peak in the density-of-states curve had been established earlier (JONES [1934a]) for the case of the γ-brass structure.

In 1937 JONES considered in detail the theory of the α–β phase boundary in the Cu–Zn system where the face-centred cubic primary solid solution (α) is succeeded by the body-centred cubic intermediate phase (β). Using the same values of the atomic volume for both α and β phases and making them equal to that of copper, and using the same values of energy gaps as those obtained for copper from optical properties ($\Delta E = 4.1$ eV), Jones calculated the density-of-states curves for both phases in terms of energy expressed in electron volts. The result of the calculation is shown schematically* in fig. 6a. The first peak in the density-of-states curve for the α-phase occurs at about 6.6 eV. When compared with the free electron energy at the center of the {111} faces in the Brillouin zone, 6.5 eV, this suggested that the contact between the Fermi surface and these faces should occur in the α-phase already at an early stage of alloying. Many years later PIPPARD [1958] showed that this contact in fact already exists in pure copper. Interpreted in terms of e/a, the two peaks shown in fig. 6a correspond to $e/a \approx 1.0$ for the α phase and $e/a \approx 1.23$ for the β phase, respectively, and are therefore unlikely to be associated in a simple way with the termination of the primary solid solubility ($e/a \approx 1.4$), or the optimum range of stability for the β phase ($e/a \approx 1.5$). The diagram in fig. 6a is, nevertheless, of interest because of its general emphasis on the relationship between phase stability and the density of states. Actual electronic energy relationships are more likely to be like those shown in fig. 6b, according to which the largest differences between the Fermi energy of free-electron gas and the Fermi energies of electrons in the Brillouin zone of the α and β phases occur at some points to the right of the peaks $\{111\}\alpha$ and $\{110\}\beta$ in the density of states (JONES [1962]). The actual α–β phase boundary will then be determined by the common tangent principle (BLANDIN [1965]). Thus, it appears that while the e/a parameter is indeed important in the α phases, as was thought by Hume–Rothery, their stability ranges also are very strongly influenced by additional factors. For example, each particular range strongly depends on the type of crystal structure that follows a given α phase in a given phase diagram (this is illustrated in fig. 5), as would be expected from phase competition. In addition, it has also been shown by AHLERS [1981] that the part of the configurational cohesive energy in the α phases, which is related to the third nearest neighbor interactions constitutes a large additional part of their total energy. Configurational energy is the difference between the ground state energy (at 0 K) and the heat of formation. While this complicates the simple original picture of α-phase stability in terms of e/a (and the related notions connected with the density of states [$N(E)$] and Fermi surfaces), there is outstanding agreement between the experimentally determined behavior of the electronic specific heats (from

* For actual curves, reference should be made to the original paper (JONES [19371]). Additional discussion may be found in a later review article (MASSALSKI and MIZUTANI [1978]).

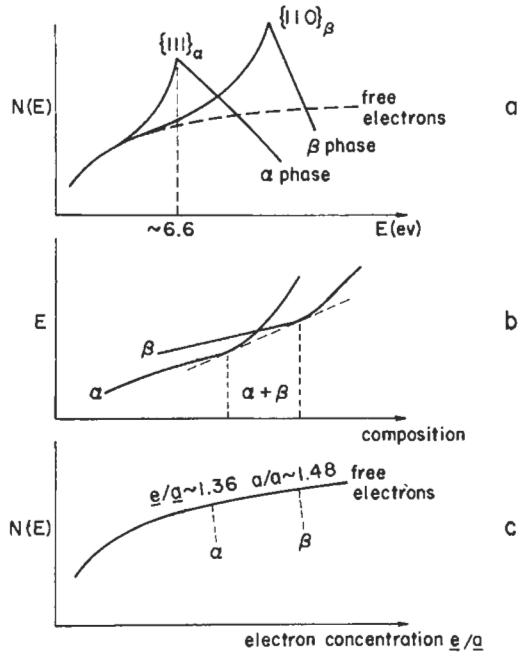

Fig. 6. Schematic models proposed to account for the primary solid solubility of alloys based on copper: (a) Jones model: band gap across the {111} faces of the zone for the fcc structure = gap across the {110} faces of the zone for the bcc structure ≈ 4.1 eV; (b) total electronic energy $E=\int_0^{E_F} N(E)\mathrm{d}E$, corresponding to the density of states as modified by the interactions with the respective Brillouin zones; (c) density of states for free electrons.

which the density of states at the Fermi level can be derived) and the predicted density of states obtained from a parameter-free calculation based on the KKR-CPA approximation (FAULKNER and STOCKS [1981]). This means that the electronic structure of the α phases is now well understood and the path is clear for a detailed stability calculation of these phases in the near future.

Incorporation of the original Jones model into metallurgical literature has led to a good deal of confusion about the relationship between phase stability and the contact between the Fermi surface and the Brillouin-zone faces. One must appreciate the difference between the attempt by Jones to calculate the relative stability of two adjoining phases in terms of the contact between Fermi surfaces and certain Brillouin-zone faces with assumed large energy gaps and in terms of additional thermodynamic quantities, and similar attempts in terms of *spherical* Fermi surfaces. The use of spherical surfaces amounts to merely calculating the electron concentration at which an inscribed *Fermi sphere* would contact the zone faces. In the latter case, the zone faces by implication should possess zero energy gaps. As pointed out by HUME–ROTHERY [1964], this important conclusion has been often overlooked in metallurgical literature. Free-electron calculation shows that contact of a Fermi *sphere* with the Brillouin zone would be obtained in the α phase at 1.36 electrons per atom and in the β phase at 1.48 electrons

per atom (see fig. 6c), and these values are strikingly close to the experimental observation. This, however, must now be regarded as rather fortuitous, at least for the α phases, because it has been proved beyond dispute that the Fermi surface is considerably distorted from a sphere in the [111] direction and touches the set of {111} Brillouin-zone faces in all three noble metals, Cu, Ag and Au (HARRISON and WEBB [1960]). Further comments of developments in this field may be found in a review article by MASSALSKI and MIZUTANI [1978].

6.2. Primary solid solubility in transition metal alloys

Hume–Rothery's further work has shown that electron-concentration principles similar to those established for the noble metals and their alloys apply also to the solid solutions of a number of transition metals, particularly those with the fcc structure (HUME–ROTHERY [1966]). Figure 7 shows the limits of solid solutions in Rh, Pd, Ir and Pt in terms of the *average group number* (AGN) which denotes all electrons outside the rare-gas shell. The general tendency appears to be for the fcc solid solutions to extend back to an AGN value of about 8.4. A similar effect is found for solid solutions of V and Cr in fcc γ-Fe, and in Ni. The behavior in bcc metals has not been generally examined. However, similar correlations may exist. For example, the solid solubilities of Rh and Ru in bcc Mo terminate at a similar value of AGN of about 6.6 (HUME–ROTHERY [1967]).

7. *The atomic size in solid solutions*

On forming a solid solution of element A with element B, two different kinds of atoms come in contact on a common lattice. This inclusion of new centers of disturbance will affect the existing electronic force fields between atoms, both short range and long range; the resulting effects will be of several kinds. On the atomic scale some atoms of the solvent and the solute will be shifted from the mean atomic positions on the lattice and thus suffer a permanent static displacement. The resulting average distance between any two neighboring atoms in a solid solution will depend on whether they are of the like kind, either both solvent or both solute, or of the opposite kind. We may thus talk of the average AA, BB or AB bond distances which may, even for an identical pair of atoms, depend also on the direction in the lattice.

In addition to local displacements, the average distances between lattice planes may also change and we may talk of the change in the *lattice spacings* and, related to them, the volume of the unit cell. Both the lattice spacings and the volume of the unit cell are not related to the actual size of any particular atom.

The relationship between lattice spacings, space lattice and the individual position of atoms may be summarized as follows: the space lattice represents a repetition in space of an elementary unit known as the *unit cell* (fig. 8). The lattice spacings describe the linear dimensions of the unit cell. To a certain extent a unit cell may be chosen quite arbitrarily so that, for example, in the face-centred cubic structure shown in fig. 8b three different unit cells are possible — rhombohedral, face-centred cubic and body-centred tetragonal. The cell which reveals the essential symmetry is cubic; if the X-ray reflections

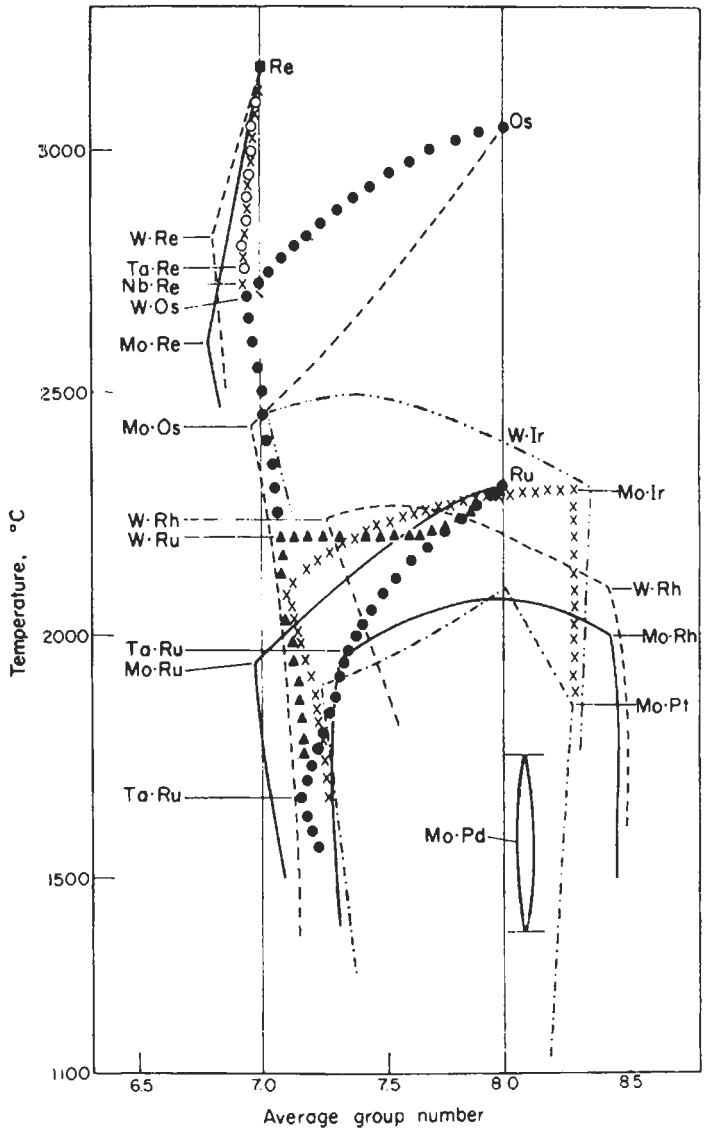

Fig. 7. The composition limits, in terms of AGN, of terminal solid solutions of Nb, Ta, Mo and W in Re, of Mo and W in Os, of Ta, Mo and W in Ru, and of the intermediate σ-phases in the systems Mo–Rh, Mo–Ir, Mo–Pd, Mo–Pt, W–Rh and W–Ir (from HUME–ROTHERY [1966].)

are indexed according to this cell, then the lattice spacing a is associated with the average spacing of atoms located at the corners of the cube and is larger than the spacings between the neighboring atoms within the cube or in other possible unit cells. The a spacing therefore exceeds the closest distance of approach of atoms. For example,

References: p. 199.

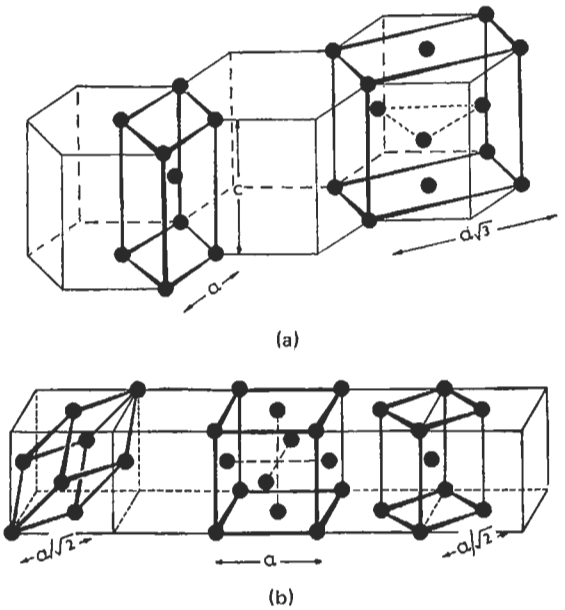

Fig. 8. (a) The close-packed hexagonal structure, showing the tetragonal and orthorhombic unit cells, and (b) the face-centred cubic structure, showing the rhombohedral, the face-centred cubic and the body-centred cubic unit cells.

the *closest distance of approach* of atoms in fig. 8b is $a/\sqrt{2}$. In a simple structure, one can easily calculate this distance from the known dimensions of the unit cell; but this may be very difficult if the structure is complex as, for example, that of γ brass (fig. 16, below).

In some structures there are considerable variations in the distance between pairs of atoms at their closest distance of approach, according to position and direction in the lattice; and in order to study these a more complex analysis, involving all average interatomic spacings, may become necessary. The *cementite* structure (fig. 9) provides a good example. In this structure the iron-carbon distances vary in the unit cell and the determination of spacings between specified pairs of atoms of iron and carbon requires the knowledge of X-ray line intensities in addition to the Debye–Scherrer analysis. (The nature of the bonding in cementile has recently been reexamined by COTTRELL [1993]).

Throughout a range of solid solutions the average "sizes" of individual atoms may be expected to change depending on the degree and nature of local displacements. A change in the average lattice spacings may mean a contraction of solute atoms and expansion of solvent atoms or vice versa, and such local changes may bear little relation to the total macroscopic distortion of the unit cell. Therefore it is very desirable to be able to assess the changes in individual atomic sizes in a solid solution, whenever possible. For this purpose methods involving measurement of diffuse X-ray scattering or changes in the intensity of principal (Bragg) reflections have been developed.

From a materials science point of view, the important questions regarding the atomic size are as follows:

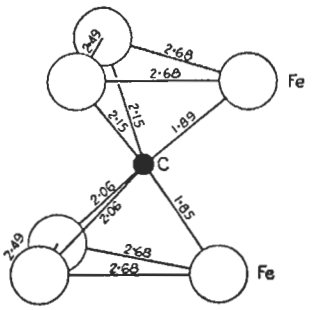

Fig. 9. The variable iron-carbon distances in the structure of cementite, Fe_3C (from GOLDSCHMIDT [1948].)

1) What is the actual size of an atom in a pure element and what are the best ways of estimating and defining that size?

2) Having decided upon atomic sizes of pure elements, which is the best method of estimating the influence of atomic sizes in a solid solution?

3) Can one assess this influence of the disparity between initial atomic sizes without additional measurements in a solid solution?

One would like to know, for example, how successful can be the prediction of the influence of the size difference merely from the knowledge of the atomic sizes of the pure elements and perhaps one other physical property, or whether it is always necessary to perform some kind of a measurement in a solid solution before the importance of the atomic size can be assessed more accurately. Yet another question concerns the relationship between the strain in the crystal lattice and the atomic size. The contribution of the strain energy to the total free energy affects the thermodynamical properties, and recently several attempts have been made to estimate the strain energy using methods of continuum elasticity.

The empirical success of the 15% rule (§ 4) already suggests that initial sizes of atoms can, in some cases, give a guide to the extent of solid solubility on alloying. However, when formulated in this way the atomic-size difference merely provides a guide to the hindrance which it may cause to the formation of extensive primary solid solubility. In some systems, for example in systems Ag-Sn or Ag–Sb, the limits of primary solid solubility are less than average (for silver-based alloys), yet the widths of the close-packed hexagonal intermediate phases are surprisingly large. In both systems the disparity beween atom radii is within the 0–15% range (i.e., the 15% rule is satisfied), and is appears that the actual value of the size difference may be of importance.

7.1. The size factor

The original formulation of the size-factor concept for binary alloy systems involved the assumption that the atomic diameter of an element may be given by the closest

distance of approach of atoms in its structure * (see ch. 1). This approach to estimating atomic size often meets with difficulties when the structures are anisotropic, or complex, or when the coordination numbers are low. For example, when there are several close distances of approach in the structure (as in gallium with $d_1 = 2.437$, $d_2 = 2.706$, $d_3 = 2.736$ and $d_4 = 2.795$ Å), the closest distance of approach, d_1, does not adequately express the size of the gallium atom when in a solid solution. A similar consideration may apply even in the case of an element which crystallizes in a typically metallic structure. For example, in zinc, with the close-packed hexagonal structure but a high value of the axial ratio, four possible values can be considered to represent the size of a zinc atom: spacings between atoms in the basal planes which also correspond to closest packing ($d_1 = 2.6649$ Å); spacings between the nearest neighbors of the adjoining basal planes which strongly depend on the axial ratio ($d_2 = 2.9129$ Å); an atomic diameter derived from the average volume per atom of the unit cell of zinc ($d_3 = 3.0762$ Å); and finally an atomic diameter calculated for a hypothetical structure with coordination number 12 ($d_4 = 2.7535$ Å). For the purpose of the 15% rule, d_1, has been chosen to represent the size of the zinc atom. However, when the behavior of lattice spacings of solid solutions

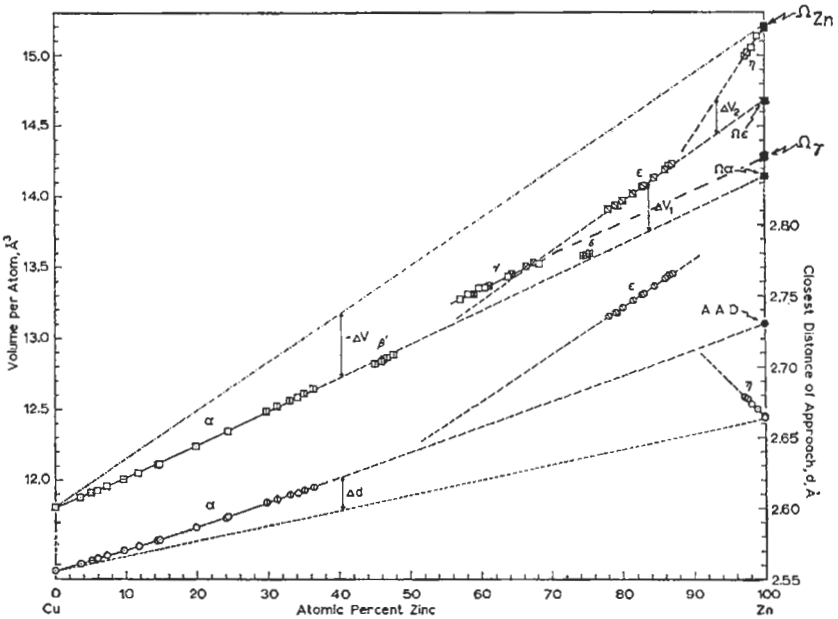

Fig. 10. Trends in lattice spacings and volume per atom in the Cu–Zn system; circles indicate closest distance of approach, d, squares indicate volume per atom. (From MASSALSKI and KING [1961].)

* The size factor is given by $[(d_B - d_A)/d_A] \times 100$ where d_A and d_B are values of the closest distance of approach of atoms in the solvent and solute respectively. For a detailed account of the possible role of the size factor as defined above reference may be made to a review article by RAYNOR [1956].

containing zinc is studied in detail, it appears that frequently the lattice spacings expand, or contract, when an opposite behavior might be expected from the value of the closest distance of approach. In fig. 10 the changes with composition in the closest distance of approach, d, and volume per atom in Cu–Zn alloys are shown. Within the primary solid solution based on copper the lattice spacings follow a curve which indicates that zinc behaves as if it possessed a larger size than that derived from its a spacing, since the lattice spacings of the alloys show a positive deviation from a line joining the closest distances of approach of copper and zinc. On the other hand, within the primary solid solution of copper in zinc, addition of copper to zinc again expands the a spacing of the latter despite the fact that the value of d for copper is indicated to be smaller than that for zinc. Thus, on a finer scale there are often discrepancies between the behavior of lattice spacings in the alloys and the estimated atomic sizes. For such reasons other attempts have been made to derive the average atomic size. For example, in fig. 10 the trend in the α lattice spacing within the α phase may be extrapolated towards pure zinc to give a hypothetical size of a zinc atom for the case where the face-centred cubic structure is maintained throughout the Cu–Zn system and on the assumption that the behavior of lattice spacings is linear. The obtained value is marked AAD in the figure, and it is close to the d_4 value mentioned above. This method of estimating *apparent atomic diameters* (AAD), is due to AXON and HUME–ROTHERY [1948]. Another approach makes use of the trend in the volume per atom (MASSALSKI and KING [1961]). Comparison between the atomic sizes estimated from the volume per atom in the pure elements and the behavior of the volume per atom trends in the Cu–Zn system is shown in the upper portion of fig. 10.

7.2. The measurement of atomic size in terms of volume

By analogy to the use of the apparent atomic diameter, a measure of the size of a solute atom in any particular primary solid solution or an intermediate phase may be obtained by extrapolating to the solute axis the plot of the mean volume per atom within that phase. In fig. 10 such a procedure is illustrated for the α, γ and ε phases of the Cu–Zn system, providing values of the *effective atomic volumes* (MASSALSKI and KING [1961]) or *partial molar atomic volumes*. The different effective atomic volumes estimated in this way for the solute in each phase are independent of the coordination number or the structural anisotropy effects mentioned above. Thus, when the coordination number changes, the atomic volume rather than the interatomic distance tends to remain constant (MOTT [1962]). An extensive study of solid solutions of various B-sub-group metals (Zn, Cd, In, Tl etc.) in late transition elements such as Ni, Pd or Pt has shown that often the initial effective atomic volume of a solute, extrapolated to the pure-solute side, is practically the same in a number of different solvents (ELLNER [1978,1980]). A good example is provided by the behavior of Ga, fig. 11. At the same time, it may be seen from fig. 10 that the effective atomic volumes of zinc in the different phases are smaller than the atomic volume of pure zinc. Since these effective volumes are different in each phase, it appears that the *contribution of the atomic size is variable according to composition* and hence it may be desirable to designate several size

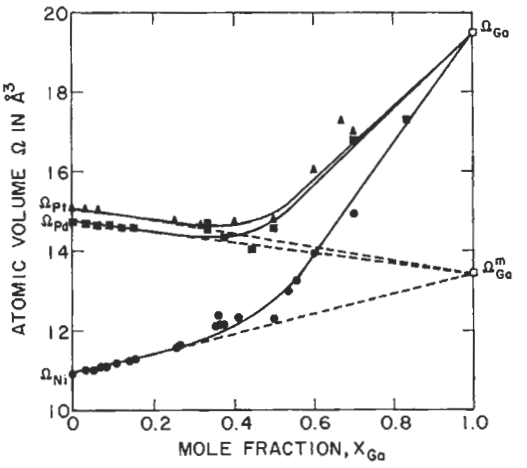

Fig. 11. Changes of atomic volume with composition in the binary Pt–Ga, Pd–Ga and Ni–Ga (from ELLNER [1978].)

Table 5
Effective atomic volume of solutes in electron phases of the noble metals
(from MASSALSKI and KING [1961].)

Sub-group	Solute	Ω_s (Å³)	Effective atomic volume of solute (Å³)					
			Cu ($\Omega_0 = 11.8$)		Ag ($\Omega_0 = 17.05$)		Au ($\Omega_0 = 16.95$)	
			$\Omega_{(\alpha,\beta',\mu)}$	$\Omega_{(\zeta,\varepsilon)}$	$\Omega_{\alpha,\beta',\mu}$	$\Omega_{(\zeta,\varepsilon)}$	$\Omega_{\alpha,\beta',\mu}$	$\Omega_{(\zeta,\varepsilon)}$
II B	Zn	15.2	14.15	14.7	14.7	14.8	14.5	14.8
	Cd	21.6	18.8	–	19.95	20.7	19.25	n.m.
	Hg	23.7	n.m.	–	20.75	22.4	20.2	n.m.
III B	(Al)	16.6	14.2	–	15.5	16.1	15.2	–
	Ga	19.6	14.7	n.m.	16.2	16.7	16.2	–
	In	26.15	20.8[a] 21.3	–	21.4	22.9	21.4[a] 20.5	n.m.
	Tl	28.6	n.m.	–	23.85	–	n.m.	–
IV B	(Si)	20.0	12.5	n.m.	n.m.	–	n.m.	–
	Ge	22.6	15.1	15.8	17.5	–	17.4	–
	Sn	27.05	21.9	–	22.7	23.3	22.2	22.5
	Pb	30.3	n.m.	–	26.7	–	n.m.	–
V B	As	21.5	16.5	n.m.	18.85	n.m.	n.m.	–
	Sb	30.2	22.3	n.m.	24.8	25.5	23.5	–
	Bi	35.4	n.m.	–	29.3	–	n.m.	–

[a] Alternative data

factors in each binary system. The values of the effective atomic volumes, Ω_α, Ω_β, Ω_ζ for solutes in several noble metal electron phases are listed in table 5 together with the atomic volumes of pure solvents, Ω_0, and of pure solutes, Ω_s. An examination of the table shows that without exception all solutes show a decrease of the volume per atom on alloying and that this decrease appears to be greatest with solutes of highest valency. Hence, the atomic sizes of such elements as aluminium, indium, thallium or lead, which are considered to be an exception when measured in terms of the closest distance of approach, are found to be typical of a general trend for the B-subgroup elements with the noble metals when considered in terms of atomic volume (MASSALSKI and KING [1961]). This generalization does not apply to transition elements and other solvents. MOTT [1962] has pointed out that if the volume of a solute atom in the solid solution is nearly the same as in its own pure metal one can expect the heat of solution to be small. Why a solute atom when placed in a hole similar to its own volume in the solvent tends to retain its original energy, even when the valencies of solvent and solute are different, is not altogether clear.

7.3. Combined effects of size and electronegativity

In the early 1950s, DARKEN and GURRY [1953] suggested that the extent of solid solubility in a given solvent metal may be assessed by testing simultaneously both the size and electronegativity differences between solvent and solute elements. They showed that in a combined plot of electronegativity (ordinate) and size (abscissa), which they called a map (see fig. 12) each element can be represented by a point (see also ch. 5, § 1.5). The closer any two points are on the map, the more likely is a high mutual solid solubility between the elements involved. In a typical Darken–Gurry (D–G) plot, as in fig. 12, substantial solubility is usually indicated by an ellipse drawn around a given solvent point. WABER *et al.* [1963] have shown subsequently, following a statistical survey of 1455 systems for which experimental data exists, that over 75% of the systems obeyed the prediction of solid solubility assessed on the basis of a D-G plot. The usefulness of the D–G method is particularly well demonstrated for the actinide metals and rare-earths (GSCHNEIDNER [1980]).

7.4. Strain in solid solutions

A simple model which takes into account the difference between atomic sizes, and which can yield estimates of lattice strain, may be constructed using basic ideas of continuum elasticity. Several such models have been considered (DARKEN and GURRY [1953], ESHELBY [1956] and FRIEDEL [1955]). The general approach is illustrated schematically in fig. 13.

Consider a rubberlike elastic matrix of a large volume V_2 in which a very small cavity has been drilled away of volume V_1. Then, through an infinitesimally small opening (shown as a capillary opening in the figure) an amount of incompressible fluid of volume $(V_1 + \Delta V_1)$ is introduced which, therefore, expands the cavity by the amount ΔV_1. Both the fluid and the matrix are now under stress and the matrix suffers an

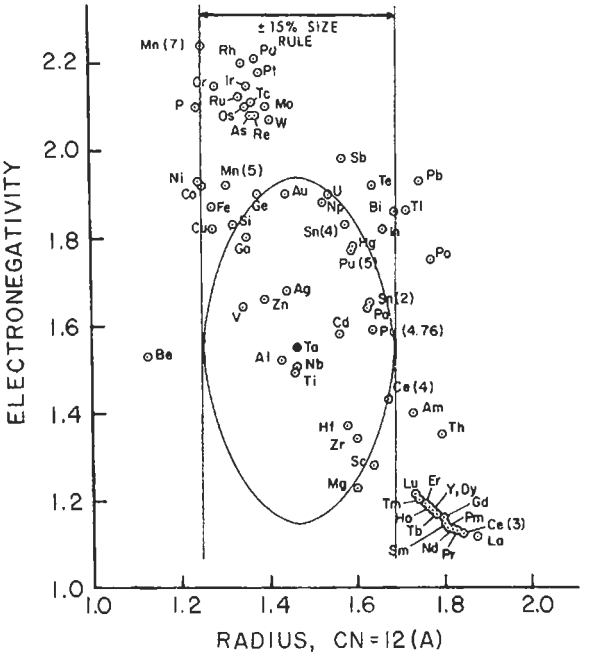

Fig. 12. The Darken–Gurry map with an ellipse drawn about the solvent tantalum. The two vertical lines are the tangents to the ellipse at the termini of the minor axis (±15% of tantalum's radius). (From GSCHNEIDNER [1980].)

expansion ΔV_2, shown in the figure by the shaded portion, which is related to the increase in the volume of the cavity by the relationship

$$\Delta V_2 / \Delta V_1 = 3(1 - \nu)/(1 + \nu), \tag{2}$$

where ν is Poisson's ratio. As pointed out by DARKEN and GURRY [1953], for most metals Poisson's ratio is about 0.3 and hence $\Delta V_2/\Delta V_1$, equals about 1.6, i.e., the volume-increase of a metal bulk will be larger than the increase in the volume of the cavity. The above model can be related to a solid solution in which the expanded cavity is replaced by several solute atoms and the bulk by a metal solvent matrix. In analogy to the expanded volume of the elastic matrix we may expect that in a substitutional solid solution on replacing an atom of the solvent (a cavity) by a somewhat larger-sized atom of the solute (the incompressible fluid) we should obtain a net expansion of the entire unit cell. The estimates of the strain energy associated with such an expansion have enabled a number of authors (DARKEN and GURRY [1953], ESHELBY [1956]) to show a direct link between the limitation of primary solid solubility and Hume–Rothery's 15% rule. Lattice spacing measurements in solid solutions are also in qualitative agreement with the above model, but sometimes a lattice expansion is observed even if the solute atoms are considered to be smaller than those of the solvent. This discrepancy is usually due to the difficulty of being able to assess correctly the sizes of atoms and to the fact

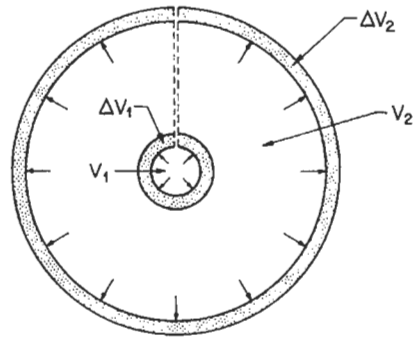

Fig. 13. Model of an incompressible particle in an elastic matrix.

that, on alloying, other factors not included in a crude assessment of size come into play, to mention only that the size of the solute atom in the pure element may differ considerably from its size in solid solution because of such factors as electron concentration, electrochemical effects and static displacements, etc.

Calculations based on simple elastic models permit one to relate the strain energy to composition and atomic volume. A general equation expressing strain energy in a solid solution may be written as (MASSALSKI and KING [1961]):

$$E_S(c) = A\mu\Omega\left(\frac{1}{\Omega}\frac{\partial\Omega}{\partial c}\right)^2 f(c), \tag{3}$$

where A is a numerical constant, μ is the shear modulus, Ω is the mean atomic volume and c the composition. In many alloy phases the variation of atomic volume with composition is nearly linear and hence for dilute solutions (for which $\Omega_0 \approx \Omega$) one may write:

$$\left(\frac{1}{\Omega}\frac{\partial\Omega}{\partial c}\right) \approx \left(\Omega_\alpha - \Omega_0\right)/\Omega_0, \tag{4}$$

where Ω_0 is the atomic volume of the pure solvent and Ω_α the effective atomic volume of the solute in the α phase. The relationship $(\Omega_\alpha - \Omega_0)/\Omega_0$ represents a measure of a volume-size-factor (MASSALSKI and KING [1961]) within a given alloy phase and a comparison of eqs. (3) and (4) shows that the strain energy for dilute alloys is related to the square of the volume-size-factor. Volume-size-factors have been calculated for numerous solid solutions and are available in tabulated form (KING [1966]). It should be pointed out that the use of a volume-size-factor rather than one based on the closest distance of approach necessitates the knowledge of the extrapolated effective atomic volumes of the solute within different phases and hence necessitates additional measurements within solid solutions.

Ellner's studies, for example the plot shown in fig. 11, confirm that in many solid solutions the initial behavior of the atomic volume with composition is practically linear (usually in the composition range up to about 30–40 at% of solute). The corresponding

effective atomic volume obtained from extrapolation to the pure solute side provides a measure of the departure of the atomic volume trend from a possible linear behavior between the atomic volumes of the pure components. If the difference ($\Omega_{solvent} - \overline{\Omega}_{solute}$) is plotted against the difference between the partial molar heats of mixing ($\Delta H_{solvent} - \overline{\Delta H}_{solute}$) obtained from measurements (or calculations), a nearly linear relationship is obtained (ELLNER [1978, 1980]). Thus, size effects find their expression in the corresponding chemical manifestations.

7.5. Deviation from Vegard's law

A study of available systems based on copper, silver and gold with the B-subgroup elements indicates that, when volume-per-atom trends are considered, alloying between any two elements causes a decrease in the volume per atom from a straight line joining the two values for the pure elements. A similar behavior is observed also when various interatomic spacings are measured and plotted within a solid solution, although in such cases the deviation can have positive or negative sign. The trends usually observed are illustrated in fig. 14.

The expected linear dependence on composition of lattice spacing trends, to follow a line joining the values for the pure elements, has come to be known as *Vegard's Law*, although this law has only been found valid for a number of ionic salts (VEGARD [1921, 1928]) and is never quite true in metallic systems. Nevertheless, it is tempting to be able to calculate deviations from assumed linear behavior, without actually performing any measurement in a solid solution, and using solely the knowledge of various parameters in the pure components. Such an attempt has been made by FRIEDEL [1955] for the cases of dilute and concentrated primary solid solutions. Friedel used the atomic volumes,

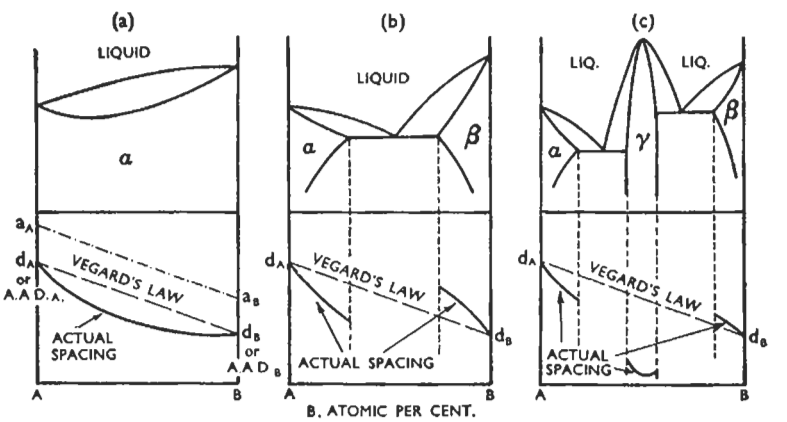

Fig. 14. The commonly observed trends in lattice-spacing-composition curves in three typical binary alloy systems: (a) complete solid solubility; (b) partial solid solubility, A has higher valency than B; (c) presence of an intermediate phase, large electrochemical interaction between A and B. (After MASSALSKI [1958].)

Poisson's ratio, bulk moduli, and compressibilities. The elastic model illustrated in fig. 13 is extended to the case in which both the matrix and the introduced fluid are compressible with compressibility coefficients χ_1 and χ_2. The atoms of solvent and solute are represented by radii r_1, and r_2 which are derived from the atomic volumes of the elements using the relationship $\Omega = \frac{4}{3}\pi r^3$. The holes in the matrix are represented by the atoms of the solvent with radius r_1 and the introduced distortions by atoms of the solute with radius r_2. On replacing an atom of the solvent by an atom of solute both suffer an elastic adjustment which may be represented by an average radius a common to both. Freidel has shown that at *infinite dilution*

$$(a - r_1)/(r_2 - a) = \alpha = (1 + \nu)\chi_1 / 2(1 - 2\nu)\chi_2, \tag{5}$$

where ν is again Poisson's ratio and χ_1, and χ_2 are the compressibilities of the solvent and solute respectively. At a finite concentration c the total volume of the solvent will suffer an increase and the average radius of an atom in the solid solution may now be represented by r (derived from average atomic volume) which will be different from the initial radii r_1 and r_2 of both the solvent and solute. Following Friedel, the initial deviation of the average atomic radius r in a solid solution from a line joining the atomic radii of the solvent and solute, may be expressed-as follows:

$$\frac{r - r_1}{cr_1} = \frac{r_2 - r_1}{r_1} \frac{\alpha + (\chi_1/\chi_2)}{\alpha + 1} \tag{6}$$

Comparison between calculated deviations using the above elastic model and the observed deviations (FRIEDEL [1955]) from the assumed Vegard's Law shows a good general agreement for the cases where the solute atoms are considered to be bigger than the solvent atoms, but usually not vice versa.

7.6. Measurement of actual atomic sizes in solid solutions

The static distortions in a solid solution which can be related to the individual atomic sizes may be estimated from a *modulation in diffuse X-ray scattering* (WARREN *et al.* [1951], ROBERTS [1954] and AVERBACH [1956]) and from a *quasi-temperature reduction in the Bragg reflections* (HUANG [1947], HERBSTEIN *et al.* [1956] and BORIE [1957, 1959]). In the former case the modulations of the diffuse X-ray intensity diffracted by a solid solution are described by coefficients, α_i, related to the nature of local atomic order of atoms, and by size effect coefficients, β_i, related to the differences in the sizes of the component atoms. According to theory,

$$\alpha_i = 1 - P_A^i / X_A \tag{7}$$

and

$$\beta_i = \left(\frac{1}{\eta - 1}\right)\left[-\left(\frac{X_A}{X_B} + \alpha_i\right)\varepsilon_{AA}^i + \left(\frac{X_B}{X_A} + \alpha_i\right)\eta\varepsilon_{BB}^i\right], \tag{8}$$

where

References: p. 199.

$$\eta = f_B / f_A, \quad \varepsilon^i_{AA} = \left(r^i_{AA} - r_i\right)r_i, \quad \varepsilon^i_{BB} = \left(r^i_{BB} - r_i\right)r_i,$$

and P^i_A = probability of finding an A atom in the i^{th} shell about a B atom; X_A = mol fraction of A atoms; f_A, f_B = scattering factors of A and B atoms; r_i = average interatomic distance to the i^{th} neighbor, calculated from lattice spacings; r^i_{AA} = distance between two A atoms in the i^{th} shell; r^i_{BB} = distance between two B atoms in the i^{th} shell.

8. *Intermediate phases with wide solid solubility*

8.1. The electron phases

Of all intermediate phases which possess wide solid solubility the most typically metallic are the *electron phases.* Their discovery and studies have a historical aspect, and it is of interest to outline this briefly.

In the first quarter of this century, even before X-ray analysis had been applied to the study of such phases as the Cu–Al and Cu–Sn β-brasses, HUME-ROTHERY indicated the possibility that they possessed the same crystallographic structure as that of Cu–Zn β-brass. Systematic and detailed work of Westgren and his collaborators (WESTGREN and PHRAGMEN [1926], WESTGREN [1930]), has subsequently established the validity of this and similar suppositions. The circumstance that the formulas CuZn, Cu_3Al and Cu_5Sn could be ascribed to the three phases with identical β-brass structure caused Hume–Rothery to postulate the principle that the stability of these phases was in some way related to the ratio 3/2 between the number of valence electrons and the number of atoms. Following this empirical formulation many similarities between crystal structures of other intermediate phases have been noted and studied systematically particularly in systems based on copper, silver and gold; and they led to the recognition of the now well-established term *electron compound.* At present it is known that such phases are not compounds in the chemical sense and that they may exist over wide ranges of composition. For this reason they should perhaps be called *electron phases.*

In the Cu–Zn system, which is somewhat typical of systems based on the noble metals, there are three characteristic electron phases commonly known as β-brass, γ-brass and ε-brass. Although these phases possess quite wide ranges of homogeneity, it had been thought originally that their ranges of stability were in each case based upon a characteristic stoichiometric ratio of atoms, and the formulae suggested for the β-, γ- and ε-brasses were CuZn, Cu_5Zn_8 and $CuZn_3$ respectively. From these formulae one obtains the electron/atom values of 3/2, 21/13 and 7/4 (1.50, 1.62 and 1.75) which have become widely accepted as characteristic of greatest stability of electron phases despite the fact that in some cases these values fall outside the range of stability of known electron phases.

Following mainly the work of JONES [1934a,b, 1937, 1952], the stability of electron phases has been linked via a simple electronic theory of metals with possible interactions between the Fermi surface and the Brillouin zones, with the emphasis on the influence of such interactions on the density of states $N(E)$ at the Fermi surface. The β-, γ- and ε-brasses possess the body-centred cubic, complex cubic and hexagonal close-packed

structures respectively; and it can be shown that at the onset of contact between the Fermi surface of free electrons and the principal faces of the respective Brillouin zones the zones are relatively full. The values of e/a associated with the free-electron concept of the Fermi surface are: $e/a = 1.48$ for contact between the Fermi surface and the zone for β-brass, $e/a = 1.54$ for contact between the Fermi surface and the {300} and {411} faces of the large zone for γ-brass, and $e/a = 1.75$ associated with the filling of the inner zone of ε-brass. These electron/atom values based on the Brillouin zone models bear similarity to the original e/a ratios based on chemical formulae (compare 1.5, 1.62 and 1.75 with 1.48, 1.54 and 1.75), but it must be remembered that in both cases the actual values are derived from particular models put forward to interpret the stability of electron phases. The chemical formulae are now known not to be applicable, and the simple Brillouin-zone models suffer from the limitation already mentioned before that for the e/a values quoted above the band gaps across the Brillouin zone must be assumed to be zero or near zero. Thus, as in the case of the theory of primary solid solutions, we are left with two possibilities: (i) The band gaps in the Brillouin zones are relatively large, and the Fermi surfaces are not spherical, but the stability may be described qualitatively by

Table 6
Typical electron phases based on noble metals, zinc and cadmium, and some transition elements.

Phases with cubic symmetry						Phases with hexagonal symmetry (hcp)	
disordered bcc structure e/a range 1.36–1.59			γ-brass structure e/a range 1.54–1.70		β-Mn structure e/a range 1.40–1.54	$c/a = 1.633$ e/a range 1.22–1.83	$c/a = 1.57$ e/a range 1.65–1.89
β			γ		μ	ζ	ε
Cu–Be	Ag–Zn	Au–Al	Cu–Zn	Mn–Zn	Cu–Si	Cu–Ga	Cu–Zn
Cu–Zn	Ag–Cd		Cu–Cd	Mn–In	Ag–Al	Cu–Si	Ag–Zn
Cu–Al	Ag–Al		Cu–Hg	Fe–Zn	Au–Al	Cu–Ge	Ag–Cd
Cu–Ga	Ag–In		Cu–Al	Co–Zn	Co–Zn	Cu–As	Au–Zn
Cu–In			Cu–Ga	Ni–Zn		Cu–Sb	Au–Cd
Cu–Si			Ci–In	Ni–Cd		Ag–Cd	Li–Zn
Cu–Sn			Cu–Si	Ni–Ga		Ag–Hg	Li–Cd
Mn–Zn			Cu–Sn	Ni–In		Ag–Al	
			Ag–Li	Pd–Zn		Ag–Ga	
			Ag–Zn	Pt–Zn		Ag–In	
			Ag–Cd	Pt–Cd		Ag–Sn	
			Ag–Hg			Ag–As	
			Ag–In			Ag–Sb	
			Au–Zn			Au–Cd	
			Zu–Cd			Au–Hg	
			Au–Ga			Au–In	
			Au–In			Au–Sn	
						Mn–Zn	

References: p. 199.

a model as that shown in fig. 6b which points to the existence of a relationship between the density of states and phase stability. (ii) The band gaps in the Brillouin zone are variable with composition and are small in the range of electron phases so that the nearly spherical model of the Fermi surface describes the situation adequately. Experimental estimates of the Fermi surfaces in alloys are still limited, but some measurements have been made in both dilute and concentrated solid solutions, and they indicate that the Fermi surface is distorted from the spherical shape, but not substantially (see for example PEARSON [1967], Massalski and MIZUTANI [1978] and KOLKE *et al.* [1982]). Although the details are still not clear, one is left with indisputable experimental correlations that show e/a to be an important factor in the stability of electron phases. Modelling of such stability in terms of electronic energy alone suggests that very small differences of the order of a few hundred cal/mole are involved between respective competing electron phases (MASSALSKI and MIZUTANI [1978]).

A list of typical electron phases is shown in table 6 in which are also shown the experimentally established ranges of stability of these phases.

8.2. Electron phases with cubic symmetry

The range of stability of the β-phases is shown in fig. 5b, above. The disordered β-phases are stable only at high temperatures and upon cooling or quenching they usually decompose, unless they become ordered as in the Cu–Zn system. In all cases the range of homogeneity of the disordered β-phases decreases with the fall of temperature, causing the phase fields to have the characteristic V-shape as illustrated in fig. 15. The electronic structure of the β-phases appears to be closely linked with the Brillouin zone for the bcc structure formed by 12 {110} faces, which constitute a rhombic dodecahedron. As mentioned in the preceding section, in the free electron approximation a spherical Fermi surface would just touch these faces at $e/a = 1.48$ (see fig.6c). If the

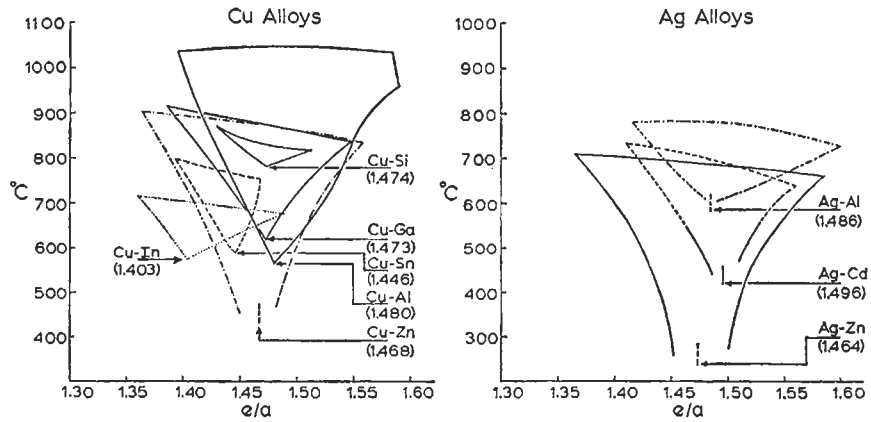

Fig. 15. The typical V-shaped phase fields of the disordered β-phases (from MASSALSKI and KING [1961].)

Brillouin-zone faces have a finite discontinuity, the density-of-states curve should show a peak near the value of e/a associated with the contact between the Fermi surface and the Brillouin zone. This possibility has been made the basis of a theory of the occurrence and stability of the β-phases (JONES [1937, 1952]). However, as pointed out above, if the gap across the faces of the Brillouin zone is assumed to be about 4.2 eV, the position in terms of e/a of the calculated peak in the density-of-states curve appears to occur at relatively low values of e/a and bears no relation to the actual ranges of stability. Nevertheless, it is remarkable that the most stable compositions of the β-phases, represented by eutectoid points at the tips of the V-shaped portions of the phase fields (see fig. 15), very nearly correspond to electron-concentration values associated with the free-electron model. More recent developments have centered on the measurement of properties, such as electronic specific heats, or the de Haas van Alphen effect (dHvA), that can be more directly related to the electronic structure. They show that the band gaps in the Brillouin zone are relatively small (~ 3.5 eV), and that the Fermi surface contours approximate a free-electron sphere. However, the stability of the β-phases is undoubtedly related to the total electronic energy integrated from the density-of-states trends from the bottom of the energy band to the Fermi level, and not just to some specific condition such as an initial contact between the Fermi surface and the Brillouin zone (MASSALSKI and MIZUTANI [1978]).

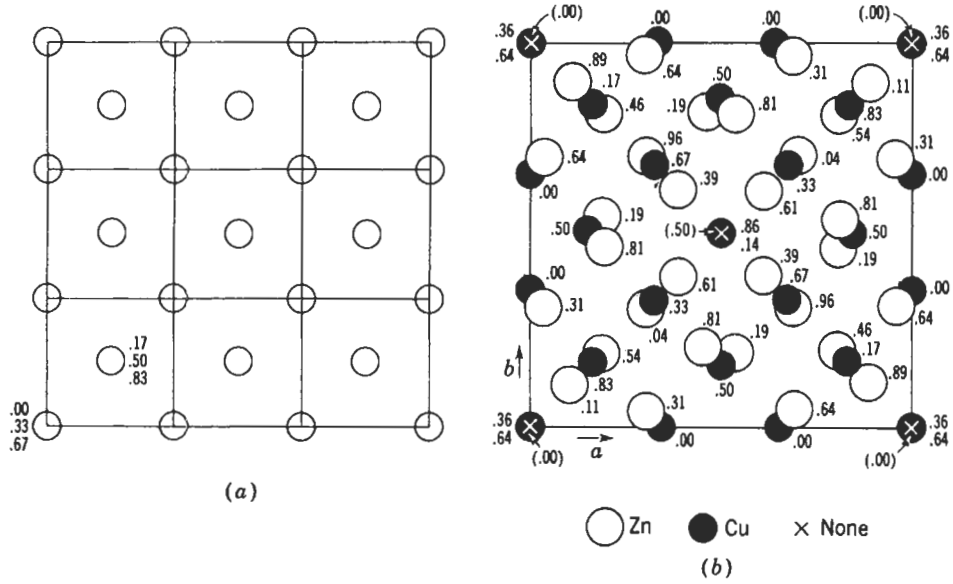

Fig. 16. The structure of γ-brass. (a) Planar view. The structure is built up from 27 bcc cells stacked in three dimensions. Distances above the projection plane are indicated in terms of the large cell edge. (b) The gamma-brass structure derived from (a) by removing the corner and central atoms and displacing others. (From BARRETT and MASSALSKI [1966].)

The range of stability of the γ-phases appears to be associated with no particular single value of electron concentration (see table 6) although there does seem to be a strong connection between the stability of γ-phases and the *large (Brillouin) zone* (see JONES [1934a, b, 1960]). The γ-phases have a complex bcc structure with approximately 52 atoms per cell (see fig. 16). They are usually ordered, certain related atomic sites being occupied by solute atoms and others by solvent atoms. The electronic structure of the γ-phases and certain of their physical properties have been reviewed by MASSALSKI and KING [1961] and MASSALSKI and MIZUTANI [1978]. On the whole, the γ-phases are brittle and they are therefore of no primary metallurgical interest. However, from the point of view of electronic theories the γ-phases are of historical interest because they were the first to be identified with a possible peak in the density-of-states curve associated with the contact of the Fermi surface with the Brillouin zone. Detailed calculations show that actually two closely positioned peaks are involved, corresponding to small band gaps, of the order of 1–2 eV. It is not surprising, therefore, that the Fermi surface associated with the γ-phases appears to be nearly spherical. The interaction of such a spherical Fermi surface with a Brillouin zone which itself resembles a sphere (the zone is bounded by 48 faces), should produce a rapid decrease in the density of states once contact has occurred between the Fermi surface and the zone. This is indeed confirmed by experimental measurements of electronic specific heats which show a rapid decrease of the electronic specific heat coefficient γ with composition. A similar effect is also observed in the cubic μ-phases which possess the β-Mn structure (MASSALSKI and MIZUTANI [1978]).

8.3. Electron phases with hexagonal symmetry

Apart from the more complex σ-, μ- and certain other phases which possess cubic symmetry (see, e.g., MASSALSKI and KING [1961]), the remaining group of electron phases possess the close-packed hexagonal structure. These phases are most numerous of all intermediate phases based on the noble metals, and they may occur anywhere within the electron-concentration range between 1.32 and 2.00 except for the narrow region 1.89–1.93. Together with the close-packed hexagonal primary solid solutions of zinc and cadmium with the noble metals (the η-phases) the close-packed hexagonal phases fall into three natural groups and are usually denoted by the Greek symbols ζ, ε and η on the basis of electron concentration, axial ratio and solute content. The known ε-phases always contain zinc or cadmium as their principal constituents (MASSALSKI and KING [1961]) and their range of stability varies between $e/a = 1.65$ and $e/a = 1.89$ (see table 6). The stability of close-packed hexagonal electron phases again appears to be intimately linked with both contact and overlap of electrons across the Brillouin zone.

The Brillouin zone for the close-packed hexagonal structure is shown in fig. 17 for an ideally close-packed structure. This zone is bounded by twenty faces, six of the {10.0} type, two of the {00.2} type, and twelve of the {10.1} type. The energy discontinuity vanishes across certain lines in the {00.1} faces (JONES [1960]) unless the structure is ordered, and hence these planes do not form a part of the energy zone. However, the {00.1} faces together with the {10.1} faces may be used to obtain a

slightly smaller zone for the structure as described by JONES [1960]. Many of the measured electronic properties in hcp structures may be related to the Brillouin zone. The dHvA (de Haas van Alphen) data for pure hcp metals, for instance, are often interpreted in terms of the reduced zone scheme, while the low-temperature specific heat data can be more conveniently discussed in terms of the extended zone. If the extended "roofs" formed beyond the {10.0} planes by the intersection of the {10.1} planes are removed, the resulting zone is still surrounded by energy discontinuities in all directions except along the lines of intersection between the {10.1} and {10.0} zone planes (line HL in fig. 17a). This smaller zone is sometimes known as the *Jones zone* and its electron content per atom is:

$$e/a = 2 - \frac{3}{4}\left(\frac{a}{c}\right)^2\left[1 - \frac{1}{4}\left(\frac{a}{c}\right)^2\right], \tag{9}$$

where c/a is the axial ratio.

The importance of the electron concentration, e/a, as the major parameter controlling the properties and behavior of the hcp phases became clearly evident only after the relationship between c/a and e/a was established in detail. When e/a is constant, for example in a ternary system, c/a also remains constant. However, when e/a is allowed to change c/a changes accordingly. In binary systems, the axial-ratio trends of all known ζ and ε phases conform to a general pattern as shown in fig. 18. Consideration of this

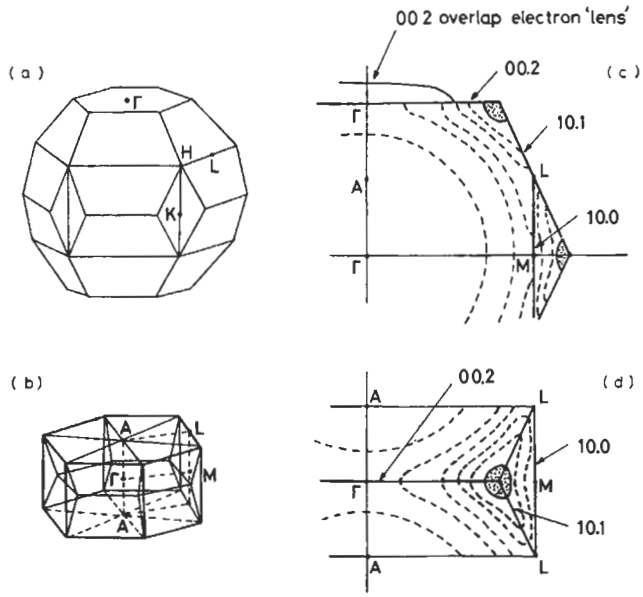

Fig. 17. The Brillouin zone of the hcp structure in the extended scheme (a) and in the reduced scheme (b). The possible contours of the Fermi surface in the vertical section of the corresponding Brillouin zone are shown in (c) and (d). The shaded areas correspond to the holes in pure Zn. The hole in (d) is known as a portion of the "monster". (After MASSALSKI *et al.* [1975].)

References: p. 199.

behavior suggests a direct dependence of the structural parameters a and c on the interaction between Fermi surface and Brillouin zone (FsBz interaction): as the electron concentration increases, the resulting contacts and overlaps of the Fermi surface with respect to different sets of zone planes cause a distortion of the Brillouin zone. This in turn affects the lattice parameters in real space. The earlier models of the electronic structure of the hcp phases have been derived mainly from the interpretation of the trends in lattice parameters, but more recently the electronic structure has also been explored by additional techniques using, e.g., electronic specific heat, superconductivity, magnetic

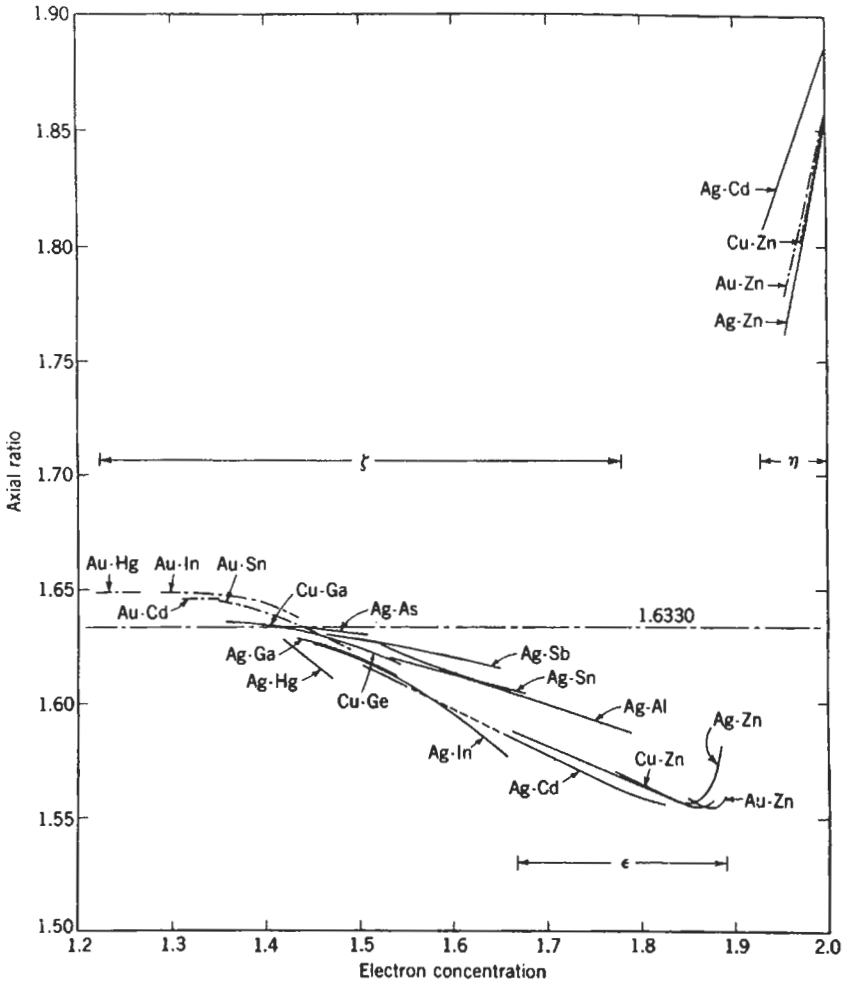

Fig. 18. The trend of the axial ratio as a function of the electron concentration in various hcp alloy systems (from MASSALSKI and MIZUTANI [1978].)

susceptibility, thermodynamic activity and positron annihilation.

The distance from the origin to the respective zone plane in k-space is given by:

$$k_{10.0} = \frac{2\pi}{\sqrt{3}a}, \quad k_{00.2} = \frac{2\pi}{c} \quad \textit{and} \quad k_{10.1} = \frac{2\pi}{\sqrt{3}a}\left(1 + \frac{3}{4}\left(\frac{a}{c}\right)^2\right)^{1/2}, \tag{10}$$

and hence depends on the axial ratio. In the range of c/a higher than $\sqrt{3}$, the {00.2} zone planes are closest to the origin, leading to the sequence $k_{00.2} < k_{10.0} < k_{10.1}$ which holds in the η-phases, where c/a exceeds 1.75. The sequence $k_{10.0} < k_{00.2} < k_{10.1}$ holds for all ζ- and ε-phase structures. The corresponding Jones zone holds, at most, only 1.75 electrons per atom. Therefore, overlaps of electrons from the Jones zone into higher zones are expected at relatively low values of e/a. The interpretation of the lattice-spacing trends in the ζ-phase Ag-based alloys, whose axial ratios vary between 1.63 and 1.58, strongly suggests that overlaps of electrons across the {10.0} zone planes already occur at about 1.4 electrons per atom. The occurrence of possible overlaps across the {00.2} zone plane within the range of the ε-phases has been inferred from measurements of the lattice spacings, electronic specific heat coefficient, the Debye temperature, the superconductivity transition temperature, the magnetic susceptibility and the thermodynamic activity (MASSALSKI and MIZUTANI [1978]). This is shown in fig. 19. In each case the onset of electron overlaps across the {00.2} zone planes has been proposed for the range of e/a exceeding approximately 1.85 electrons per atom. All such measurements imply the occurrence of FsBz interactions that should be reflected also in the corresponding density-of-states changes on alloying.

The available calculated density-of-states curves for the hcp structure are at the moment limited to several pure metals, such as Mg, Zn or Be. All these metals have two valence electrons per atom and may be represented by relatively similar features in the corresponding density-of-state curves. The positions of peaks and subsequent declining slopes occur more or less at the same electron concentration for all three cases, in spite of a large difference in the axial ratios, atomic volumes and electronic interactions. This strongly indicates that the main features of the respective density-of-states curves originate from the FsBz interactions in which e/a plays an essential role. From this, one can conclude that a density-of-states curve for a disordered hcp alloy may also have essentially the same characteristic features. This is confirmed by experiments involving the measurement of electronic specific heats, which are directly proportional to the density of states at the Fermi level (fig. 20).

The experimental coefficients γ plotted in fig. 20 as a function of e/a show that, irrespective of the solute or solvent species, all available γ_{exp} values follow a very similar general trend over a wide range of electron concentrations. An increasing trend is evident in the lower e/a range, culminating in a broad maximum at about 1.5 electrons per atom, and followed by a decreasing trend at higher e/a values. The theoretical density-of-states curve for the hcp Zn, shown in units of mJ/mole K^2 in the same figure allows a direct comparison between a relevant calculation and the experimental data. This shows that the large peak in the theoretical curves more or less coincides with the experimental peak on the abscissa.

References: p. 199.

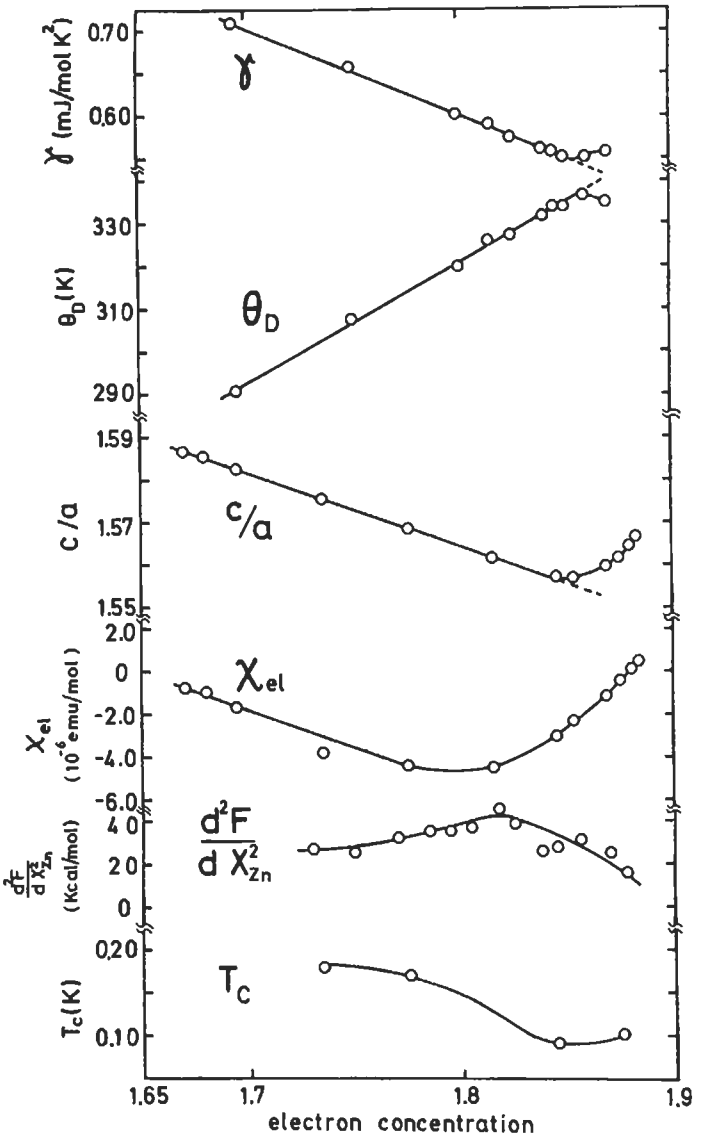

Fig. 19. Behavior of various physical properties in the ε-phase Ag–Zn alloy system: electronic specific heat coefficient γ; Debye temperature θ_D; axial ratio c/a; magnetic susceptibility due to conduction electrons χ_{el}; second derivative of the free energy with respect to concentration (d^2F/dX_{Zn}^2) (in units of 4.2 kJ/mol); superconducting transition temperature T_c. (From MASSALSKI and MIZUTANI [1978].)

The combination of contacts and overlaps with respect to a large number of zone planes is clearly responsible for the large peak in the $N(E)$ curve in hcp metals. The distance of the {10.1} planes from the origin of the zone is relatively insensitive to the

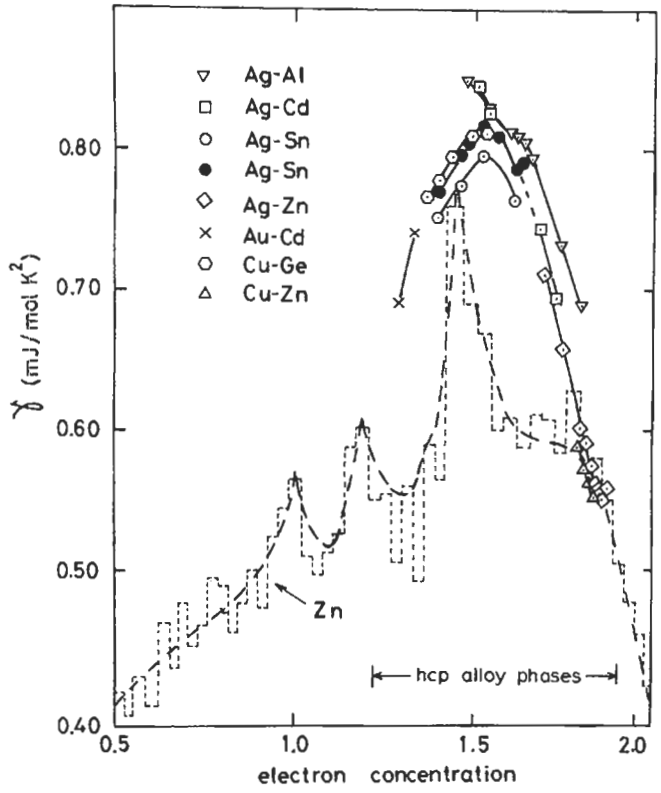

Fig. 20. Trends of electronic specific heat coefficients as a function of electron concentration for hcp Hume–Rothery alloys, shown against the band calculation for pure Zn (from MASSALSKI and MIZUTANI [1978].)

axial ratio (eq. 9). Hence, the large peak may be expected to occur at similar e/a values in most hcp structures. Once contact with the {10.1} planes occurs, additional electrons will be allocated in the remaining hole regions of the Brillouin zone until overlaps across the {10.1} or {00.2} zone planes become possible. Thus, until a sufficiently high e/a is reached, a progressive decrease in the $N(E)$ curve is expected as is actually seen in fig. 20. Based on the above interpretation the likely Fermi surface topography for a typical hcp Hume–Rothery phase may be expected to be like that shown in fig. 21. The recent positron-annihilation studies of the Fermi surface in the ζ-phase Cu–Ge alloys, by SUZUKI *et al.* [1976] and KOIKE *et al.* [1982] are entirely consistent with the conclusions drawn from the electronic specific heat data and earlier work on lattice spacings and axial ratios. Indeed, because of zone contacts and overlaps that are likely to occur in all hcp alloy phases, this particular group of alloys offers a most challenging research area for the positron-annihilation method. For the first time it has become possible to provide

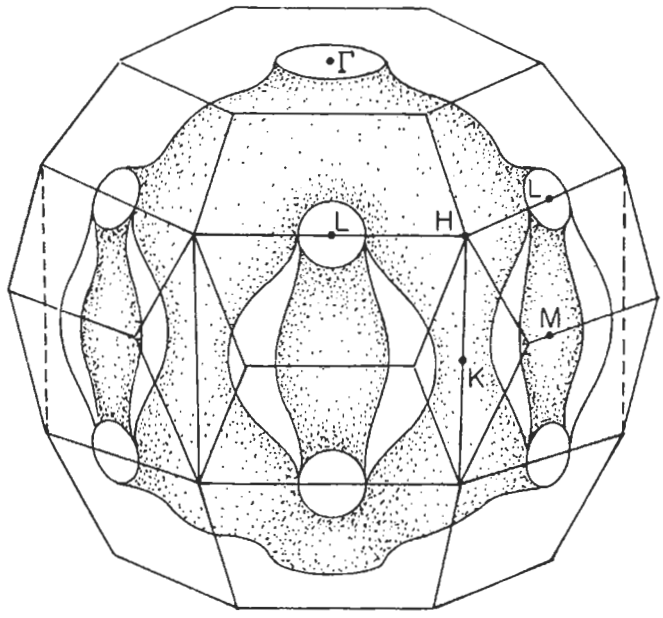

Fig. 21. A very likely Fermi surface topography in an hcp Hume–Rothery electron phase alloy. The 101 contact and 100 overlap are assumed to be present. (From MASSALSKI and MIZUTANI [1978].)

a direct evidence for the existence of the Fermi-surface concept in disordered electron phases, precisely along the lines predicted by numerous earlier interpretations based on indirect data.

8.4. Laves phases

An important group of related intermediate phases is obtained by alloying of elements whose atomic diameters, d_{AA} and d_{BB}, are approximately in the ratio 1.2 to 1. The exact lattice geometry requires that d_{AA}/d_{BB} should be 1.225, but in known examples of this type of intermediate phases the ratio varies from about 1.1 to about 1.6. Much of the original work concerning the above phases is due to Laves and his co-workers. For this reason they are often called *Laves phases* (see ch. 4).

Laves phases are close packed, of approximate formula AB_2, crystallizing in one of the three structural types:

1) C_{14} structure, typified by the phase $MgZn_2$, hexagonal, with packing of planes of atoms represented by the general sequence ABABAB etc;

2) the C_{15} structure, typified by the phase $MgCu_2$, cubic, with packing ABCABCABC;

3) the C_{36} structure, typified by the phase $MgNi_2$, hexagonal, with packing ABACABAC.

The main reason for the existence of Laves phases appears to be one of geometrical origin — that of filling space in a convenient way. However, within the given range of atomic diameters which satisfy the space-filling condition, it appears that often the choice as to which particular modification will be stable is determined by electronic considerations. The evidence

for this is particularly striking in the magnesium alloys studied by LAVES and WITTE [1935, 1936]. The experimental results concerning the three modifications occurring in several ternary systems based on magnesium are shown in fig. 22 and are plotted in terms of electron concentration. Witte and his co-workers have carried out experiments suggesting that the phase boundaries on the electron-rich side of typical Laves structures occur at very nearly the same e/a, suggesting that the homogeneity of a particular structure may be restricted by an appropriate Brillouin zone. Measurements of the changes in magnetic susceptibility and hydrogen solubility of several alloys within the pseudobinary sections $MgCu_2$–$MgZn_2$, $MgNi_2$–$MgZn_2$, $MgCu_2$–$MgAl_2$ and $MgZn_2$–$MgAl_2$, appear to support this hypothesis. The changes of the magnetic susceptibility in the pseudo-binary $MgCu_2$–$MgZn_2$ system are shown in fig. 23. KLEE and WITTE [I954] proposed that they may be interpreted in terms of interactions between the Fermi surface and the Brillouin zone, the dip in the susceptibility prior to the termination of solid solubility indicating a dip in the density of states.

Measurements of the electronic specific heats, that can be related to the density of states at the Fermi surface, have provided a further evidence of the importance of electronic factors in Laves phases. Examination of the trends of the electronic specific heat coefficient γ, as it varies in pseudobinary systems of $MgCu_2$ with polyvalent metals such as Zn, Al and Si, has shown that a sharp decrease of the density of states occurs near the phase boundary before the $MgCu_2$ structure is replaced by a two-phase field. A possible interpretation of this is that an appropriate Brillouin zone becomes filled with electrons. In this respect the electronic specific heat data and the magnetic susceptibility data shown in fig. 23 are very similar (SLICK *et al.* [1965]).

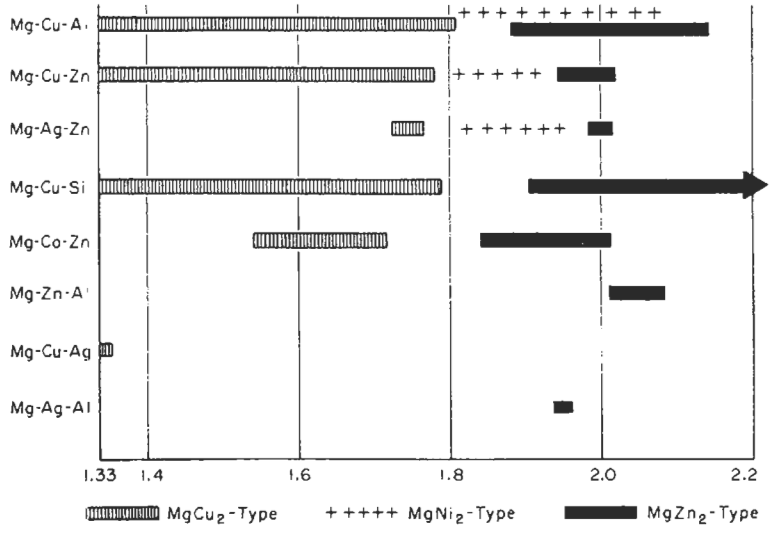

Fig. 22. The ranges of homogeneity in terms of electron concentration of several ternary magnesium alloys which possess the three typical Laves structures (from MASSALSKI [1956] after LAVES and WITTE [1936].)

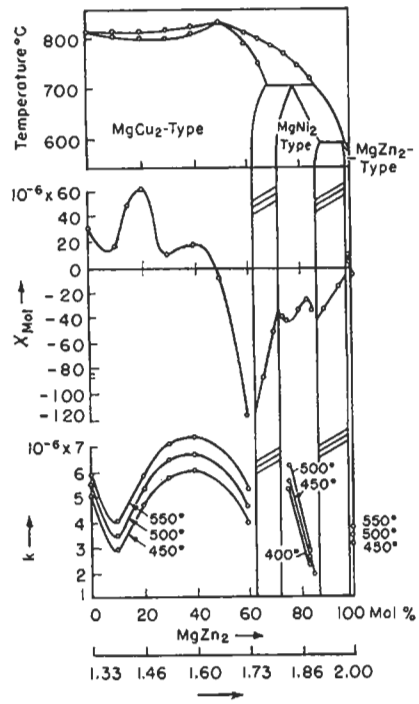

Fig. 23. Variation of hydrogen solubility and magnetic susceptibility with electron concentration in quasi-binary systems $MgCu_2$–$MgZn_2$ (from MASSALSKI [1956] after KLEE and WITTE [1954].)

8.5. Phases with wide solubility formed by the transition elements

A number of intermediate phases formed by the transition elements possess wide ranges of solid solubility. They are often designated by various Greek or Latin symbols such as σ, μ, δ, χ, P or R. For details reference may be made to TAYLOR [1961], NEVITT [1963] and ch. 5 which deals specifically with alloy compounds.

The σ-phase, the unit cell of which is tetragonal with $c/a \approx 0.52$ and 30 atoms per cell, has received much detailed attention, chiefly because of the detrimental effect which the formation of this phase has on mechanical properties of certain steels. In the system Fe–Cr, for example, the σ-phase separates out of the ferritic matrix and causes brittleness, but in more complex steels such as Fe–Cr–Mn σ-phases can also precipitate from the austenite phase.

X-ray and neutron diffraction studies have shown that many of the phases listed above are structurally related to one another because they can be built up from layers that show close similarities. Thus, undoubtedly, atomic packing plays an important role in determining their stability. At the same time studies of stability ranges, particularly in ternary systems, have shown that the contours of the phase fields of the above phases often bear relation to the value of the average group number (AGN). Hence, much

speculation has been advanced about the electronic nature of their stability that might be similar to the electron phases of the noble metals. In fig. 24 the ternary phase relationships of some 19 ternary systems are shown at various temperatures as collected by NIEMIEC [1967]. The relationship between AGN and the contours of the σ-phase fields is particularly noticeable. It must be kept in mind however, that since the d-electrons

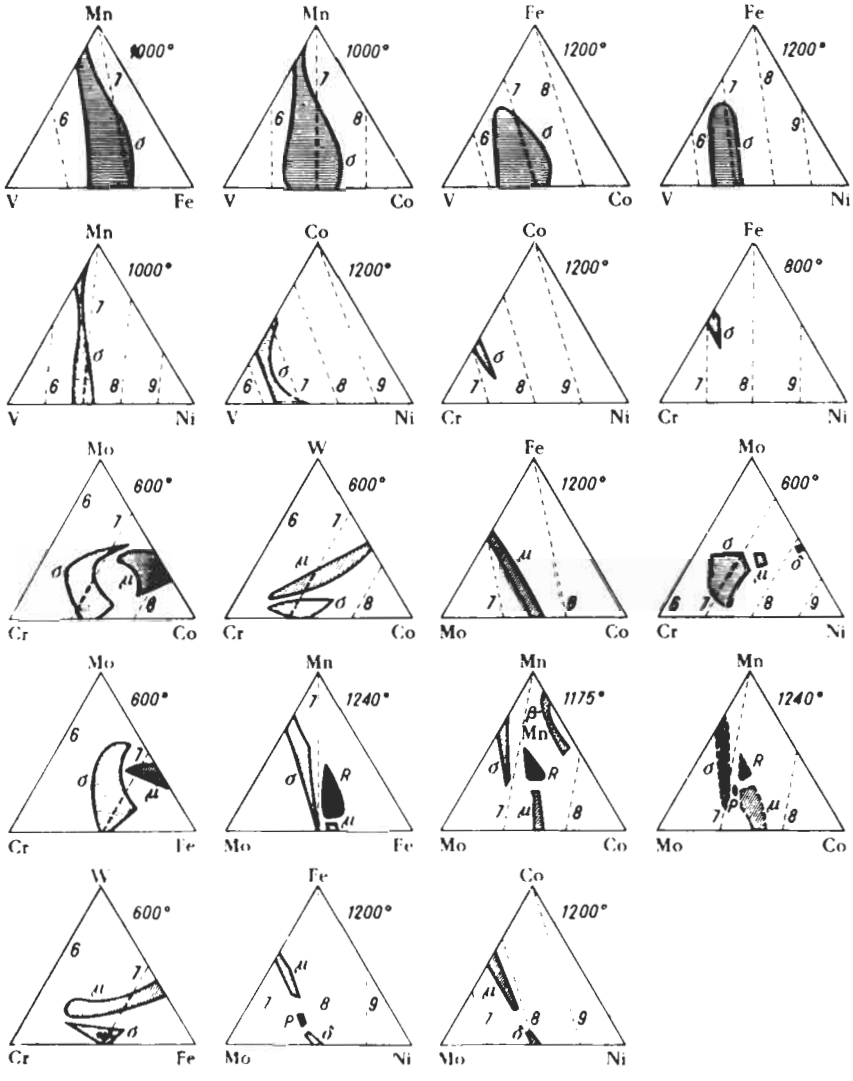

Fig. 24. Isothermal sections through a number of ternary phase diagrams between transition elements showing phase fields of phases with wide solid solubility. Values of average group number are indicated by dashed lines. (From NIEMIEC [1966].)

unquestionably contribute to e/a in these phases, and since the d-bands are incompletely filled, the details of possible electronic interactions are bound to be complex and not necessarily related solely to some simple Brillouin-zone-Fermi-surface effects. For example, some of the bonding forces may be highly directional, or the number of "d-band vacancies" rather than electrons, may play a role.

9. *Lattice spacings in solid solutions*

The measurement of precise values of lattice spacings in solid solutions has contributed to the understanding of a number of factors which influence their stability and properties. Since the introduction of the Debye–Scherrer powder method some sixty years ago, the interest in the knowledge of lattice spacings in alloys has developed in three distinct directions:

1) in connection with precision measurements of lattice parameters for studies of systematic structural similarities between related alloy phases;

2) in connection with studies of relationships between lattice spacings, composition, electronic structure, size effects, local order, magnetic effects and numerous other properties of solid solutions;

3) in connection with the use of the lattice-spacing method as a tool for determining phase boundaries in alloy systems.

Detailed measurements of lattice spacing trends within individual alloy phases date back to the early 1930s. They were done mostly in terminal solid solutions of the noble metals and a few intermediate phases *. Today the available data fill large volumes (PEARSON [1958, 1967]), and further additions are rapidly growing. The importance of the behavior of lattice spacings in hcp electron phases, in connection with their electronic structure, has already been discussed in § 8.3. Some additional aspects are discussed below.

9.1. Lattice spacings in primary solid solutions

The problem of lattice distortion in primary solid solutions of the *monoralent noble metals* has been considered by Hume–Rothery and by Owen and their associates (HUME–ROTHERY [1964] and OWEN [1947]). The relationships obtained by OWEN [1947] between the percentage lattice distortion and the solute valency in binary systems based on a common solvent are shown in figs. 25 and 26. The importance of valence difference is clearly demonstrated in the figures, but there appear to be departures from the general trends which have not been explained. In order to gain further insight into the particular role of the difference beween valencies of the component elements, RAYNOR [1949a] attempted to eliminate size contributions by assuming that the electronic and size effects in certain solid solutions are additive and can be analyzed separately. Raynor's analysis was based on the assumption that a linear Vegard's Law may be applied to the sizes of

* For a review of some of these measurements see MASSALSKI [1958].

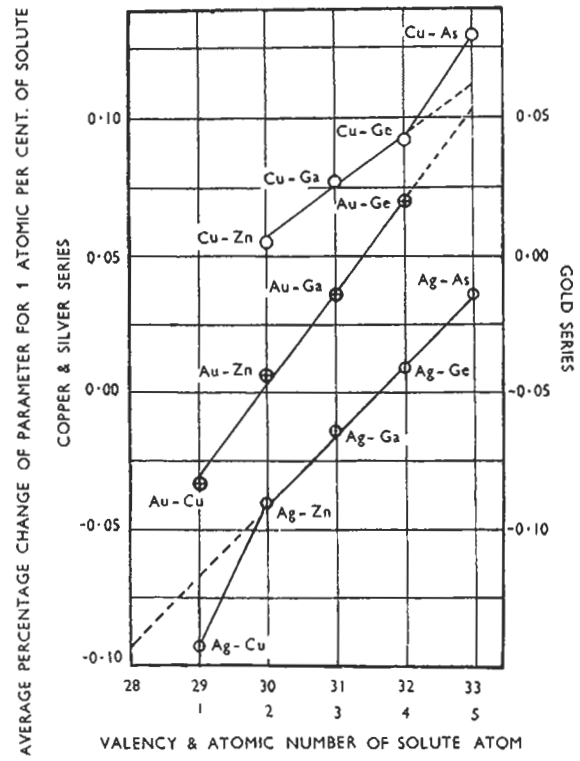

Fig. 25. Percentage lattice distortion as a function of solute valency in solid solutions. Cu, Ag and Au with Zn, Ga, Ge and As. (From PEARSON [1958] after OWEN [1947].)

atoms as given by the closest distance of approach and is therefore open to some doubt (MASSALSKI and KING [1961]).

Nevertheless, a detailed analysis of numerous solid solutions has shown that, after the assumed size contribution has been subtracted, the remaining lattice-spacing variation appears to be proportional to $(V_{so} - V_{bv})^2$ for solutes (so) and solvents (sv) of the same period, and to $(V_{so} - V_{sv})^2 + (V_{so} - V_{sv})$ for solutes and solvents from different periods. Subsequently, PEARSON [1982] has shown that a more general correlation is obtained, valid for a larger number of systems, if a size-effect correction, $\overline{D}$, is calculated from a relationship of the form $a = f\overline{D} + k$, where a is the lattice parameter, $\overline{D}$ is the average atomic diameter calculated from a linear relationship involving initial atomic diameters based on coordination 12, and f and k are constants. If an additional assumption is made that Ga, Ge, Sn, As, Sb and Bi contribute only two electrons to the conduction-electron concentration when alloyed with the noble metals, fifteen more systems appear to obey a uniform correlation.

Studies of binary systems have been extended to *ternary systems* where it is found that lattice spacings of ternary alloys may often be calculated from binary data using empirical additive relationships. An example of a linear relationship between lattice

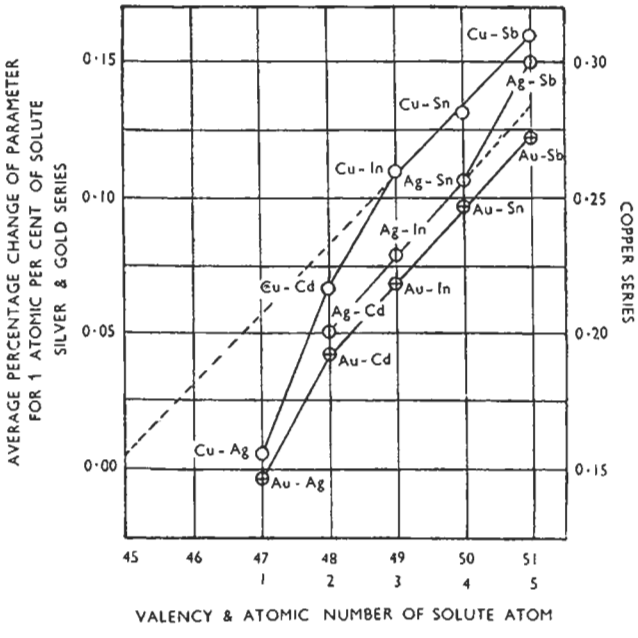

Fig. 26. Percentage lattice distortion as a function of solute valency in solid solutions. Cu, Ag and Au with Ag, Cd, In, Sn and Sb. (From PEARSON [1958] after OWEN [1947].)

spacings and composition in the system Cu–Al–In (STIRLING and RAYNOR [1956]) is shown in fig. 27. ARGENT and WAKEMAN [1957] have shown that the expansion of the copper lattice by additions of zinc and gallium or zinc and germanium is additive in the respective ternary systems. Similar results hold also for additions of gallium and germanium to copper. Additive linear behavior suggests that in simple ternary solid solutions there is no appreciable solute–solute interaction, at least in dilute solutions where atoms of copper can effectively prevent contact beween solutes. Even in the system Ag–Mg–Sb (HILL and AXON [1956–7]) the strictly additive behavior of lattice spacings is still observed despite the fact that strong electrochemical differences between magnesium and antimony, and the tendency towards compound formation (Mg_3Sb_2), might be expected to favor clustering of magnesium and antimony atoms which should lead to the contraction of the lattice. However, when magnesium and silicon are dissolved in an aluminium lattice, contractions are observed which point to electrochemical interactions (HILL and AXON [1954–5]).

The lattice spacings of solid solutions of lithium, magnesium, silicon, copper, zinc, germanium and silver *in aluminium* have been studied and discussed by AXON and HUME-ROTHERY [1948] whose data are plotted in fig. 28. It may be seen from the figure that apart from silver, which produces virtually no change of lattice spacings, the aluminium lattice is expanded by magnesium and germanium and contracted by lithium, silicon, copper and zinc. Aluminium is an example of a trivalent solvent with a face-centered cubic structure. The first Brillouin zone can hold only two electrons per atom and must therefore be overlapped; but it has been shown (HARRISON [1959] and HARRISON

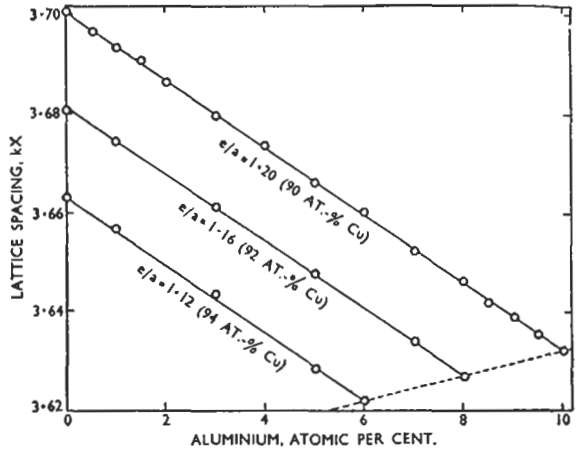

Fig. 27. Lattice spacings of α solid-solution alloys in the Cu–Al–In system along lines of constant copper content (from MASSALSKI [1958] after STIRLING and RAYNOR [1956]).

and WEBB [1960]) that the various portions of the overlapped and unoverlapped Fermi surface, when assembled together, resemble a free electron sphere. Hence, although overlaps exist in the aluminium structure and its alloys, their influence upon lattice spacings may be small.

AXON and HUME-ROTHERY [1948] have shown that the extrapolated AAD (§ 6.1) values for various elements dissolved in aluminium are influenced by the interplay of a number of factors such as relative volume per valence electron in the crystals of the solvent and the solute, the relative radii of the ions, and the relative difference in the electrochemical affinities.

The changes in the lattice spacings in the system *magnesium–cadmium* at temperatures at which complete solid solubility occurs in this system (see fig. 1) have been studied by HUME-ROTHERY and RAYNOR [1940]. When magnesium is alloyed with cadmium, no change occurs in the nominal electron concentration, both elements being two-valent. The initial additions of cadmium to magnesium cause a contraction of the a lattice spacing but only a very slight increase in the axial ratio because the c lattice spacing decreases at about the same rate as does the a lattice spacing. When magnesium is added to cadmium at the opposite end of the phase diagram, both a and c also decrease, but c more rapidly, causing a rapid decrease of c/a. The presence of at least two electrons per atom in this system means that there must exist overlaps from the first Brillouin zone (see fig. 17) since the alloys are conductors of electricity. It is now known from direct measurements of the Fermi surface that in both pure cadmium and pure magnesium overlaps exist across the horizontal and vertical sets of planes in the Brillouin zone, and although the amounts of these overlaps are different in both cases the nature of the overlaps is similar. Hence the relationship between overlaps and trends in the lattice spacings and the axial ratio in the Mg–Cd system is open to speculation.

In a similar way, because of the complexity of factors involved, the interpretation of

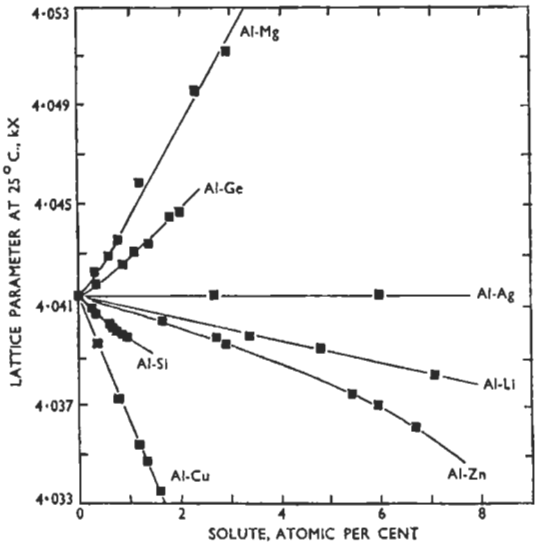

Fig. 28. The lattice-spacing-composition curves of alloys based on aluminium as solvent (from MASSALSKI [1958] after AXON and HUME-ROTHERY [1948].)

the lattice spacings of alloys of transition elements may be expected to meet formidable difficulties. The inner-core d-band shells are incomplete, and it is known that electrons from these shells can contribute both to bonding and to conductivity.

The trends in the lattice spacings of the *transition elements* of the Second Long Period (zirconium, niobium, molybdenum, rhodium and palladium), when dissolved in the hexagonal close-packed ruthenium, have been studied by HELLAWELL and HUME-ROTHERY [1954]. In all cases the parameters c and c/a are increased by the formation of a solid solution and, at equal percentages of each solute, the increases are in the order zirconium → niobium → molybdenum → palladium → rhodium. The a parameters are diminished by zirconium and rhodium and increased by palladium, niobium and molybdenum. The axial ratio of ruthenium (1.5824) is considerably less than the ideal value (1.633), and the interatomic distance in the basal plane is greater than the distance between an atom and its nearest neighbor in the plane above or below. Hellawell and Hume-Rothery interprete the observed lattice spacings on the basis of "size differences" between component atoms as expressed by the minimum distance of approach between atoms in the pure elements and by a possible directional sharing of the electron cloud of zirconium which may take place on alloying.

9.2. The relationship between lattice spacings and magnetic properties

A survey of the lattice spacings of transition metal alloys as a function of composition shows (PEARSON [1958]) that there are many inflections in the lattice spacing curves reflecting changes in the magnetic properties. The magnetic properties of metals and

alloys depend on the arrangement and separation of atoms in a structure, and therefore such changes as the ferromagnetic-paramagnetic transition might be expected to be related to some changes in the lattice spacings and the volume of the unit cell.

The ferromagnetic–paramagnetic changes (F–P) and the antiferromagnetic–paramagnetic changes (A–P) are *second-order transitions* in which the ordering of the spin orientation develops gradually on cooling below the transition temperature, T_c. Such changes are usually accompanied by a sharp change in the slope of the lattice-spacing curve as a function of temperature, such that the derivative da/dT is discontinuous at T_c (WILLIS and ROOKSBY [1954]). Ferromagnetic-antiferromagnetic changes (F-A), on the other hand, are a first-order transition involving a discontinuous change of electron spin orientation and are accompanied by a discontinuous change in lattice spacing (WILLIS and ROOKSBY [1954]). The second order F–P and A–P changes are truly reversible while the first order changes are accompanied by the usual thermal hysteresis in the transition region.

An example of the lattice-spacing changes accompanying an F–P transition is shown in fig. 29a for the system Mn-Sb (WILLIS and ROOKSBY [1954]). In cases of a first-order transition at the Curie point, the discontinuous change in the lattice spacings may also be associated with some displacements of the different types of atoms in a structure, so that in such a case the change in the lattice spacing represents two processes occurring at the same time. According to ROBERTS [1956], the first-order transition at the Curie point is associated with a movement of about 10% of the manganese atoms into interstitial positions. The actual trend in the lattice spacings with temperature in the Mn-Bi system as determined by WILLIS and ROOKSBY [1954] is shown in fig. 29b.

A definite anomaly is found in the temperature variation of the lattice spacings accompanying the F–P transition of pure nickel, but no pronounced anomalies are observed in the slope of the lattice spacings as a function of composition in nickel alloys at compositions at which the F–P change should occur (PEARSON [1958]). COLES [1956]

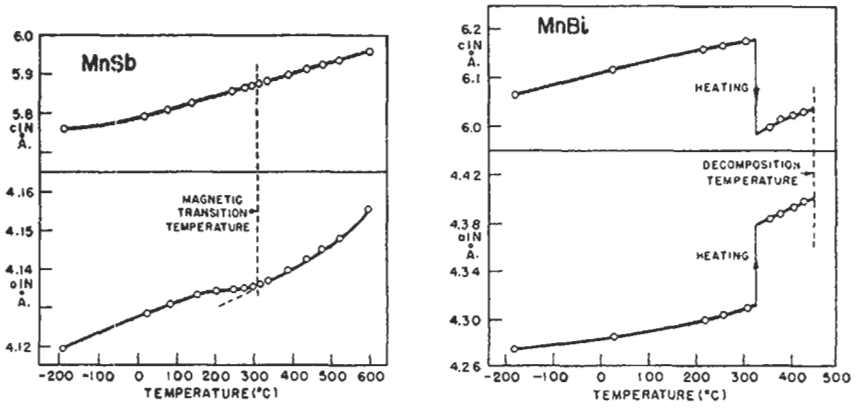

Fig. 29. (a) Lattice spacing of MnSb, which has a $B8_1$ type of structure as a function of temperature. (b) Lattice spacing of MnBi, which has a $B8_1$ type of structure as a function of temperature. (From PEARSON [1958] after WILLIS and ROOKSBY [1954].)

References: p. 199.

has reported a slight change of slope accompanying the F–P change in an alloy of nickel–35at. copper. This composition corresponds to alloys in which the Curie point occurs at room temperature.

10. Defect structures

In addition to the occurrence of clustering or ordering of atoms, which constitutes a departure from randomness, solid solutions can contain various imperfections which can be of three general types: point-, line- and surface imperfections, according to whether they are vacant sites or interstitial atoms, various types of dislocations, stacking faults, or small-angle boundaries. The nature of dislocations, their interactions and their properties are discussed in ch. 20. Below we shall briefly consider some aspects of vacancies in solid solutions and the presence of various stacking disorders.

From the point of view of energy relationships, the presence of vacant sites in solid solutions may enhance stability, owing to their association with the entropy, the strain energy, or the electronic energy. Vacancies may be introduced by quenching from higher temperatures where their equilibrium number, due to entropy considerations, is higher than at lower temperatures, or they may be introduced by various irradiation processes, plastic deformation or, finally, by alloying. The calculation of the energy associated with the formation of vacancies or interstitials in a solid solution at finite concentrations presents several difficulties (see, for example, FUMI [1955], FRIEDEL [1954b], BROOKS [1955] and MANN and SEEGER [1960]). The subject is presented in great detail in ch. 18.

10.1. Vacancies and vacant sites in structures of alloys

From the point of view of the theory of alloys, vacancies are believed to be produced on alloying under certain conditions when the number of electrons per atom is kept constant or reduced. Evidence of this is provided by terminal solutions or electron phases with lattice defects. With the increase or decrease in the number of solute atoms a change can occur in the number of atoms per unit cell in a way which produces vacant lattice sites. It is believed that this takes place in order to maintain optimum electronic energy. Such vacancy populations, determined by composition and not by temperature, are distinguished as *constitutional vacancies.* (CAHN [1979], AMELINCKX [1988]).

The work of BRADLEY and TAYLOR [1937] and TAYLOR and DOYLE [1972] on Ni–Al, and of LIPSON and TAYLOR [1939] on some ternary alloys based on this phase, are first-known examples of this phenomenon. The Ni–Al alloy may be regarded as an electron phase analogous to β-brass if nickel, a transition element, is assumed to have zero to near zero valency. At 50 at% this phase possesses a Cs–Cl ordered structure in which one kind of atoms, say nickel, occupy cube centers and the other kind of atoms, cube corners. The diameter of a nickel atom is smaller than that of an aluminium atom and hence, if nickel content is increased above 50 at%, the lattice parameter of the structure decreases in the expected manner while the density is increased. However, when the aluminium content is increased above 50 at%, an anomalous behavior is observed since

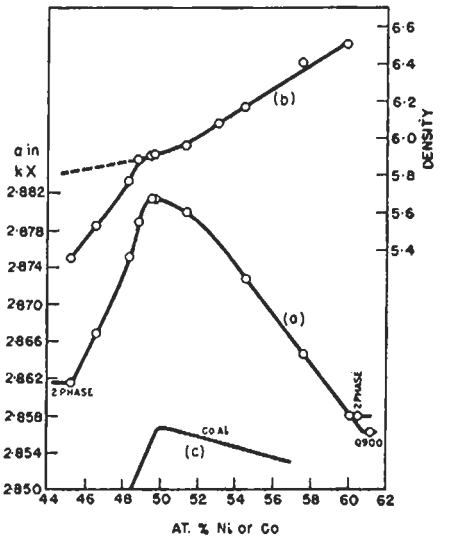

Fig. 30. (a, b) Lattice spacing and density of β-AlNi as a function of composition. (c) Lattice spacing of β-AlCo as a function of composition. (From PEARSON [1958] after original work of BRADLEY and TAYLOR [1937] and BRADLEY and SEAGER [1939].)

the lattice spacing of the Ni–Al phase does not increase but actually decreases, and the fall in the density is much more rapid than would be expected from the replacement of nickel atoms by aluminium. This behavior is shown in fig. 30 in which the lattice spacing data for Co-Al (BRADLEY and SEAGER as quoted by PEARSON [1958]) are also included. BRADLEY and TAYLOR [1937] concluded that the observed anomalies could be explained if one supposed that in the aluminium-rich alloys there are less than two atoms per unit cell and that omission of atoms occurs from some lattice points with the creation of vacancies. On the nickel-rich side, the extra nickel atoms substitute in the usual way for aluminium atoms on the aluminium sublattice. The aluminium-rich side, however, is quite different: hardly any aluminium substitutes on the nickel sublattice; instead nickel atoms disappear from the nickel sublattice, leaving nickel vacancies. For instance, according to the most recent measurements (KOGACHI *et al.* [1992, 1995]) at 46 at% Ni, 10% of the nickel sites are vacant, most of the aluminium sites are filled. In this way the number of electrons per unit cell is kept constant and equal to approximately 3, corresponding to an e/a ratio of 3/2 characteristic of the β-brass structures. Several other studies showed that a stoichiometric β-NiAl quenched from a high temperature (as opposed to that slowly cooled) contained a high concentration of *thermal* vacancies; the most recently cited figure is 1.08% of vacancies at 1600°C. This is a very much larger thermal vacancy concentration than is found in other metals or alloys, even just below the melting temperature; so large that on cooling the vacancies will separate out into a population of voids visible in the electron microscope (EPPERSON *et al.* [1978]). 50/50 NiAl containing such vacancies, all on the nickel sublattice, must also contain substitutional defects – that is some nickel atoms in the aluminium sublattice, also called

References: p. 199.

nickel antistructure atoms — to preserve the overall chemical composition: specifically, two vacancies must be accompanied by one substitutional defect. Such a trio of linked defects is now termed a triple defect. Parallels for the behavior of the NiAl alloys at high temperatures are found in other systems isomorphous with NiAl (see CAHN [1979]).

The conclusion related to the dependence of constitutional vacancies on electron concentration has been criticized on the basis that the omission of atoms could also be interpreted in terms of size-effects. Since there is only one atom of aluminium in the unit cell of the Ni–Al alloy, it appears possible that the omission of atoms with addition of aluminium in excess of 50% occurs as a result of an inability to squeeze an additional large aluminium atom in the place of a small nickel atom. A possible differentiation between an interpretation in terms of electronic considerations and one in terms of size considerations could be made by introduction of a further element into the Ni–Al alloy. The size-effect spatial theory requires that the loss of atoms should take place when the concentration of aluminium exceeds more than one per unit cell whereas the electronic theory requires that it should occur when a definite electron concentration, approximately 1.5, is exceeded. LIPSON and TAYLOR [1939] have shown that in two ternary systems, Fe–Ni–Al and Cu–Ni–Al, the general shape of the phase field of the ternary alloys based on Ni–Al falls into the composition regions which indicate that electron concentration, rather than size, is the main factor determining the phase stability. A detailed analysis of constitutional vacancies in Ni–Al based on band energies has just been published by COTTRELL [1995].

The interpretation of the lattice spacings and density behavior in alloys based on Ni–Al is limited by the fact that nickel, a transition element, must be assumed to possess zero valency in order to make it possible to assume that the above phase is an electron phase of the 3/2 type. However, further evidence of omission of atoms from sites in a unit cell has also been obtained in the study of some γ-brasses (HUME-ROTHERY *et al.* [1952]) and Al—Zn primary solid solutions (ELLWOOD [1948, 1951–2]), in which no transition elements are involved so that the valence of the participating atoms is more definite. In the case of γ-brass two particular binary systems were studied, Cu–Al and Cu–Ga (HUME-ROTHERY *et al.* [1952]). In the former system, lattice spacing work and density data show that the number of atoms in the unit cell of the γ-phase remains constant at about 52 as aluminium is increased to approximately 35.3 at%, after which the number steadily decreases. A similar effect has been observed in the Cu–Ga γ-brass to occur at about 34.5 at% gallium. The data for Cu–Al and Cu–Ga alloys are shown in fig. 31. HUME-ROTHERY *et al.* [1952] have interpreted the creation of vacant sites in γ-brass structures in terms of the Brillouin zone of the γ-brasses, suggesting that both the normal and the defect y-structures can hold no more than about 87–88 electrons per cell in order not to exceed an electron concentration of about 1.68–1.70. It appears that the high-temperature δ-phase in the Cu–Zn system resembles a defect γ-brass structure in that it possesses numerous lattice defects and vacant atomic sites. Other constitutional vacancies in brass-type alloys have been discussed by NOVER and SCHUBERT [1980].

Creation of lattice defects in which vacancies or excess atoms are involved occurs in intermediate phases probably more frequently than it was thought likely in the past. For example, in intermediate phases which crystallize in structures closely related to the NiAs structure, the basic structure, corresponding to the formula AB, can gradually

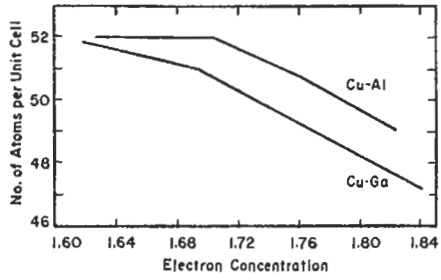

Fig. 31. The number of atoms per unit cell in the γ-phases of the system Cu–Ga and Cu–Al as a function of electron concentration (after HUME-ROTHERY *et al.* [1952].)

change in the direction of compositions A_2B by a gradual filling of certain vacant spaces* in the structure by the excess atoms of one of the components. In the series of phases such as NiS → NiSe → NiAs → Ni_3Sb_2 → Ni_3Sn_2 → Ni_2Ge → Ni_2In. The number of nickel atoms becomes greater than 50 at% and X-ray work has shown that this is accomplished by nickel atoms gradually filling certain interstitial positions in the ideal NiAs structure. The typical NiAs structure may be regarded as based on a close-packed hexagonal lattice of metalloid atoms in which the metal atoms occupy the octahedral spaces between the close-packed hexagonal layers (see ch. 5). As the structure becomes filled with the excess of the more metallic atoms, it gradually acquires a pseudo-cubic symmetry and the metallic character increases considerably so that, for example, in the series quoted above the Ni_2In phase is almost indistinguishable from the Cu–Al or Cu–Ca γ-brasses.

Constitutional vacancies in large concentrations have also been found in a number of oxides, especially those of the transition metals, and in some hydrides (e.g., TiH_x) and carbides. In some instances there is also evidence of vacancy ordering.

10.2. Stacking faults

The possibility of the formation of stacking faults in typically metallic solid solutions has recently come to play an ever-increasing role in the understanding of many properties of solid solutions, particularly those with the face-centred cubic and the close-packed hexagonal structures. Such phenomena, for example, as the changes in electrical resistivity, work-hardening, recrystallization, creep, deformation texture, crystallography of phase transformations, corrosion, phase morphology and a number of others have been shown to be related to the presence of stacking faults and therefore to the *stacking-fault energy.*

The face-centred cubic and close-packed hexagonal structures are closely related and, being both close packed, differ essentially only in the way in which the closest-packed planes are stacked together. It has been shown originally by BARRETT [1950] that stacking disorders exist in a cold-worked metal. Subsequently, several authors (PATERSON

* These are analogous to the octahedral, tetrahedral and other vacant spaces which exist in the simple metallic structures as discussed in ch. 2.

[1952], WARREN and WAREKOIS [1955], WAGNER [1957], WILKENS [1957] and JOHNSON [1963]) developed theories which relate the effect of the presence of various types of stacking faults to the changes in the X-ray diffraction pattern of the face-centred cubic structure. The normal sequence of {111} planes in a face-centred cubic structure can be described as ABCABCABC using the usual A, B, C notation. The three typical stacking errors are illustrated by the characteristic stacking patterns shown in fig. 32. They are: (1) the *intrinsic fault*, corresponding to the removal of a close-packed layer of atoms, (2) the *extrinsic fault*, corresponding to the insertion of an extra close-packed layer of atoms, and (3) the *twin (growth) fault*, produced at the interface between two perfect crystallites which are in twin relation (see READ [1953]). The intrinsic faults have received the most attention, and calculations based upon idealized models suggest that such faults should produce broadening and shifts in X-ray peak positions. This prediction has been verified experimentally in a number of pure metals (Cu, Au, Ag, Pb, Ni, etc.) and alloy systems (mostly based on the noble metals Cu, Ag and Au). Theoretical considerations of the influence of twin faults and extrinsic faults indicate that the corresponding X-ray line-broadening should be asymmetric in both cases and that the peak shifts resulting from the presence of extrinsic faults should occur in a direction opposite to the shift produced by intrinsic faulting (JOHNSON [1963]). Published work to date indicates that in metals intrinsic faults predominate. However in other materials, for example in silicon (AERTS *et al.* [1962a, b]), the stacking-fault energy of intrinsic and extrinsic faults may be of about equal magnitude. If, in addition, one considers the less idealized cases in which the distribution of stacking-fault density is variable in a specimen, the prediction of the over-all X-ray pattern becomes very complex (see for example, BARRETT and MASSALSKI [1966] p. 464). Nevertheless, the X-ray work has served as a useful means for comparison between various metals and alloys and for the studies of trends in faulting probability with composition and temperature.

In addition to the above mentioned X-ray analysis a direct estimate of stacking-fault energy γ can also be made by studies of certain annealing or deformation features in metals and alloys and their changes with temperature, by studies of twinning frequency in metallographic samples (FULLMAN [1951] and BOLLING and WINEGARD [1958a, b]), by interpretation of dissociated dislocations (nodes) in transmission electron photomicrographs (HOWIE and SWANN [1961] and CHRISTIAN and SWANN [1965]) and other features such as cross-slip, creep, texture etc. [GALLAGHER [1970]).

The possibility of the existence of stacking faults in hcp and bcc structures has been

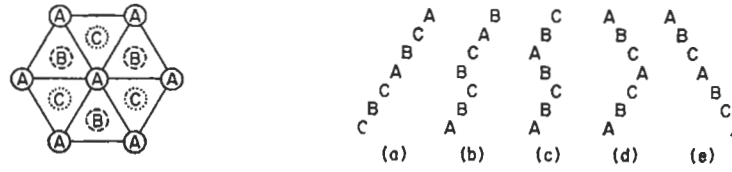

Fig. 32. Planar view of atomic positions and stacking sequences for: (a) perfect fcc crystal; (b) intrinsic fault; (c) extrinsic fault; (d) twin fault; (e) twin crystal. (After JOHNSON [1963].)

considered in a number of publications both from the experimental and the theoretical point of view. In bcc and hcp metals stacking faults do not produce line shifts (see WARREN [1959a]). In hexagonal metals they produce broadening of certain reflections, which has been observed experimentally, particularly in the case of cobalt (EDWARDS and LIPSON [1942]).

A number of attempts have been made to elucidate the factors which influence the changes of stacking-fault energy upon alloying. Although all such factors must be electronic in nature, it appears at the moment that a detailed interpretation is not possible. In a number of publications the changes of stacking-fault energy have been related to the electron concentration, certain size effects, the changes in the density of stat.es, and the changes in the topology of the Fermi surface (See GALLAGHER [1970].)

In the case of fcc *metals*, recent measurements of the rate of loop annealing, the stability of tetrahedra introduced by deformation, of faulted dipoles, and of texture developed by rolling have led to the availability of quite precise information on the magnitude of γ for materials in which extended nodes or extrinsic-intrinsic fault pairs cannot be observed. Thus, it is no longer essential to estimate the fault energy of such metals as Cu, Au, Al, and Ni by extrapolating node data or normalized X-ray faulting probability results, although the extrapolation procedures, too, have been improved and now lead to more reliable results. Reasonable estimates of γ, probably accurate to ±20%, are: $\gamma_{Ag} = 21.6$ mJ/m^2, $\gamma_{Ph} = 30$ mJ/m^2, $\gamma_{Au} = 50$ mJ/m^2, $\gamma_{Cu} = 55$ mJ/m^2, $\gamma_{Al} = 200$ mJ/m^2 and $\gamma_{Ni} = 250$ mJ/m^2. Estimates of γ in other elements from scaled rolling-texture data are subject to rather larger errors, but are the best values available at the present time: $\gamma_{Ce} <$ 5 mJ/m^2, $\gamma_{Yb} < 10$ mJ/m^2, $\gamma_{Th} = 70$ mJ/m^2, $\gamma_{Pt} = 75$ mJ/m^2, $\gamma_{Pd} = 130$ mJ/m^2 and $\gamma_{Rh} = 330$ mJ/m^2 (GALLAGHER [1970]). Advances have been made in theoretical estimates of γ for pure materials (BLANDIN *et al.* [1966]), but difficulties are still experienced in applying the treatments to noble metals on account of their complex electronic structure.

In fcc *solid solutions*, a satisfactory amount of numerically accurate information is now available for the variation of γ (effective) with alloying, particularly in systems with copper, silver, and nickel as solvents. The form of the variation with B-group solutes in all cases follows the pattern established in the earliest studies in that γ decreases with increasing solute concentration, and a considerable normalization of the data is achieved in plots with the electron/atom ratio as abscissa.

Several authors have noted that straight-line relationships for the change of γ with alloying can be obtained if γ is plotted on a log scale and the abscissa is expressed in terms of a composition-dependent function $[c/(1+c)]^2$, where $c =$ (alloying concentration)/(solubility limit) at high temperatures. Expressing the abscissa in this form appears to provide a normalizing effect similar to that which arises by using the e/a ratio, but with the advantage that the solubility limit is in some systems more accurately known than is the effective valence of the solute. The relationship obtained for the fcc Cu–Si alloys is shown in fig. 33. Recent studies also suggest that in alloys of two fcc elements having complete mutual solubility, all compositions have γ intermediate in value between the fault energies of the component metals. Such noble-metal–transition-metal alloys as have been studied have γ of the same order as in the pure noble metal. Contrary to early studies, considerable extrinsic–intrinsic faulting has recently been observed in copper-,

References: p. 199.

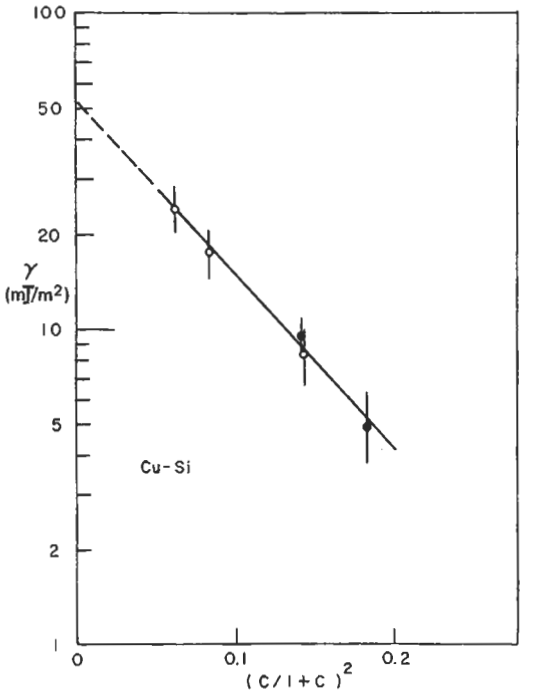

Fig. 33. Semi-log plot of γ versus $[c/(1+c)]^2$ in the Cu–Si series (from GALLAGHER [1970]).

silver-, and gold-base alloys, and measurements on fault pairs have revealed that the extrinsic and intrinsic fault energies are approximately equal (GALLAGHER [1970]).

10.3. Metastable structures*

Many solid solutions whose properties have been outlined in the preceding sections can exist in a metastable condition at temperatures which fall outside the equilibrium range of stability but at which the rate of approach to equilibrium is so slow as to be negligible. One of the most frequently used methods for producing metastability is rapid quenching from a high temperature. During quenching a single-phase solid solution may be retained untransformed, or it may transform by changing its crystal structure, either by a martensitic or a "massive" process (see BARRETT and MASSALSKI [1966]). Metastable solid solutions have also been obtained by a rapid cooling from the liquid state, using the "splat" or "crusher" cooling techniques (DUWEZ [1965, 1967]), by a rapid cooling from the vapor state, using vacuum deposition techniques (MADER *et al.* [1963]) or sputtering (MASSALSKI and RIZZO [1988]), by various methods involving the quenching of liquid metals on a rapidly revolving copper wheel, and by surface melting methods

* See also chapter 19.

using laser beams, electron beams, etc. (See DUWEZ [1978] and also ch. 7, § 9.1.).

Following these procedures, enhanced solubilities, non-equilibrium phases and unusual crystalline and amorphous structures have been obtained. For example, a continuous series of *metastable solid solutions* can be obtained in the Cu–Ag system in place of the well-known eutectic phase diagram corresponding to equilibrium conditions. In other instances solid solutions have been obtained that are *amorphous,* resembling a frozen liquid. A large number of metastable phases obtained by the various rapid-cooling techniques have most unusual crystalline (or non-crystalline) electrical, semiconducting, superconducting, magnetic and thermal properties. The research area of metallic glasses, in particular, has seen very rapid growth during the past two decades and numerous symposia and reviews on this subject have been published (see, e.g., MASUMOTO and SUZUKI [1982], PEREPEZKO and BOETTINGER [1983]; TURNBULL [1981]; JOHNSON [1986]). In order to produce a metallic glass, crystallization has to be prevented during rapid cooling of the liquid. Cooling rates exceeding 10^6 K/s are usually needed to achieve this, and the most likely regions in phase diagrams where metallic glasses can be produced are the deep eutectic regions. The reason for this has been discussed in numerous publications. One of the possibilities is that, in deep eutectics, the crystallization competing with metallic-glass formation must be of a multi-phase form, which is kinetically difficult. Here, the T_0 concept provides a very useful guide to the search for glass formation regions in metallic systems (MASSALSKI [1982]). Hence, the chilled liquid becomes more and more viscous without crystallization until a glass transition temperature is reached when the liquid becomes a solid. The subject is discussed more fully in ch. 7, § 9.1.

11. Order in solid solutions

The phenomena related to order–disorder (O–D) changes in solid solutions comprise a very extensive literature and a detailed review of these is beyond the scope of this chapter. Nevertheless, the tendency for unlike atoms to occupy adjoining sites of a crystalline lattice, leading towards formation of superlattices, is a very prominent feature of many solid solutions; and we shall briefly consider this subject from the structural point of view.

On the basis of thermodynamics (see ch. 5) it can be shown that an ordered arrangement of atoms in an alloy may produce a lower internal energy compared to a disordered arrangement, particularly if the segregation of atoms to designated atomic sites occurs at relatively low temperatures where entropy, associated with randomness, plays a lesser role. The condition of perfect order, such that the like atoms are never nearest neighbors, could be achieved only in a perfect single crystal with a simple metallic lattice and at compositions corresponding to stoichiometric ratios of atoms like AB, AB_2, AB_3, etc. Actually, the presence of various imperfections and grain boundaries precludes this possibility in most cases. In addition, it is known that an ordered solid solution consists of *ordered domains* which may be perfectly ordered within themselves but which are *out of step* with one another. This results in more contact between like atoms at the boundaries of adjacent domains. Ordered domains are sometimes called *antiphase domains* and

usually their number is quite large within each grain of the material. With the development of electron microscopy techniques, the presence of antiphase domains has been confirmed by direct observation in thin films (GLOSSOP and PASHLEY [1959], SATO and TOTH [1961]).

A further departure from maximum order occurs in solid solutions whose compositions deviate from the optimum stoichiometric ratios of atoms. This is often associated with the fall of the ordering temperature on both sides of the ideal composition and by the change of other properties such as hardness, electrical resistivity, etc.

When the interaction between unlike atoms is very strong, the critical temperature T_c, at which disordering occurs, may lie above the melting point of the material. Alloys with this characteristic closely resemble chemical compounds. When the interaction forces are less intense, an ordered solid solution may become disordered at a critical temperature even though the composition corresponds to a stoichiometric compound-like formula. Many typical alloy phases show this behavior with temperature. Finally, if the ordering forces are weak, as for example at low atomic concentrations in terminal solid solutions, the critical temperature may lie below the temperature at which attainment of equilibrium is possible within a reasonable time. One may then speak of the disordered state being frozen in. It has been found that the activation energy necessary to switch atoms into disordered positions in a fully ordered alloy is of the same order of magnitude as the heat of activation for diffusion or for recovery from cold work, usually about 1.5–2 eV. References to recent work on long range order in alloys are given by LAUGHLIN [1988].

11.1. Types of superlattices

Simple superlattices in binary alloys with cubic structure occur near compositions corresponding to formulas A_3B, AB and AB_3. The Cu–Au system (see fig. 1b, above) provides a well-known prototype of ordered solid solutions based on the fcc structure. The superlattices Cu_3Au, CuAu and $CuAu_3$ have been investigated in great detail. In the case of Cu_3Au the low-temperature structure, (fig. 34a) is cubic, but in the case of CuAu (fig. 34c) alternate (002) planes contain either all copper or all gold atoms and a contraction occurs in the c direction, presumably as a result of attraction between atoms in these planes. This results in a tetragonal fcc structure with c/a ratio of 0.92.

Order in bcc alloys again depends on composition. At 50 at% of solute the AB type of order results in the well-known CsCl structure (fig. 34b) which occurs, for example, in ordered β-brass. When the composition is between approximately 25 and 50 at% of solute, a sequence of ordered structures based on the simple body-centred cube sometimes becomes possible and such structures have been studied in detail (e.g., RAPACIOLI and AHLERS [1977], for β-Cu, Zn, Al). The superlattices that occur in the Fe–Al system (fig. 34d) and the *Heusler alloys* (Cu_2MnAl), which are ordered when in the ferromagnetic condition, have received particular attention (see, for example, TAYLOR [1961]). With solute contents exceeding 50 at% the γ-brass type of order and other more complex superlattices are possible.

By analogy with the cubic structures, ordered superlattices occur frequently in close-packed hexagonal solid solutions. For example, in the Mg–Cd system the continuous

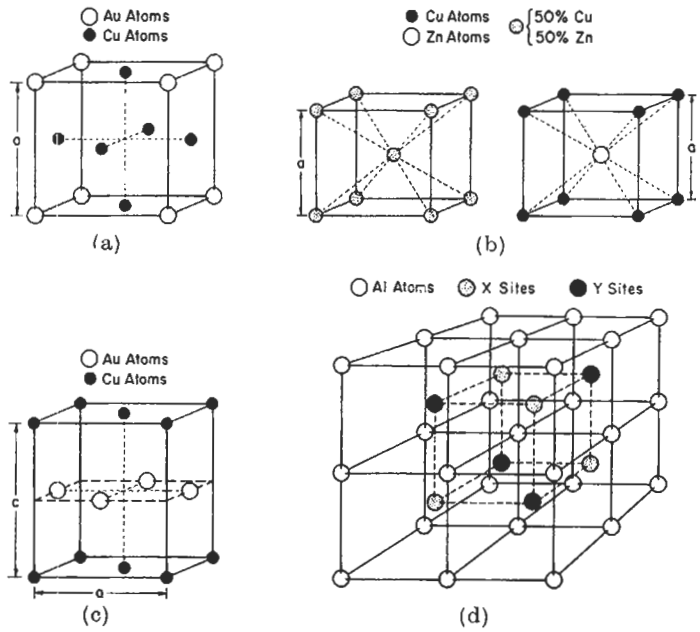

Fig. 34. Various types of ordered superlattices: (a) ordered cubic superlattice Cu_3Au; (b) disordered and ordered structures of β-brass; (c) the tetragonal superlattice of AuCu; (d) the structure of Fe_3Al and FeAl: Al atoms fill the X sites in Fe_3Al and the X and Y sites in FeAl.

series of solid solution at high temperatures is broken at lower temperatures by the formation of ordered superlattices at compositions $MgCd_3$, MgCd and Mg_3Cd (see fig. 1d, above). $MgCd_3$ orders to form the DO_{19} type of structure which is distorted from close-packed hexagonal, while the Mg_3Cd is closepacked hexagonal but with the a axis doubled and the basal layers so arranged that each cadmium atom is in contact with three magnesium atoms in the adjacent layers. Cooling of alloys in the MgCd composition region produces an ordered orthorhombic structure.

11.2. Long-period superlattices

As mentioned in the previous section, the low-temperature annealing of CuAu alloys (below 380°C) produces a face-centred tetragonal structure whose unit cell is shown in fig. 34b. This structure is usually referred to as CuAu I. In the temperature interval between 380–410°C another ordered structure has been detected (by JOHANSSON and LINDE [1936]) which is often described as CuAu II. The superlattice CuAu II is a modification of CuAu I and the unit cell of this structure is orthorhombic as shown in fig. 35a. The long cell is obtained by stacking five CuAu I unit cells in a row in the direction of one of the long-cell edges ($\boldsymbol{b}$) and then repeating this unit at five cell intervals with a simultaneous *out-of-step* shift at the boundary through a distance equal to the vectorial distance $\frac{1}{2}(\boldsymbol{a}+\boldsymbol{c})$. The distance between each antiphase boundary may thus

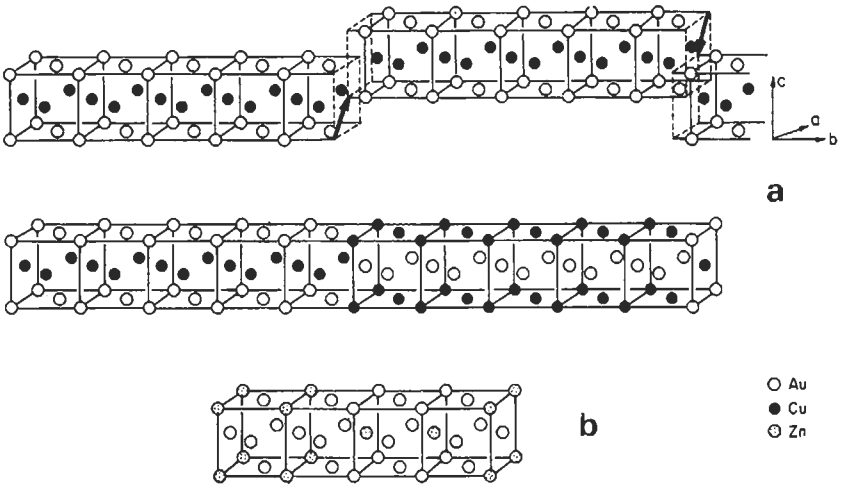

Fig. 35. Long-period superlattices: (a) the structure of CuAu II; (b) the structure of Au–Zn. (After SCHUBERT *et al.* [1955].)

be specified by $M \times b$ where M denotes the domain size *or the period.* For CuAu II, $M = 5$. This superlattice is therefore called a *one-dimensional long-period superlattice* with a period equal to five. OGAWA and WATANABE [1954] have shown that a repulsive force arises at the junction of the long antiphase domains, which leads to a small local lattice-parameter increase in the direction of the long axis. This has the effect of a small periodic error in the diffracting lattice in this direction, and in electron-diffraction patterns it produces "satellite" reflections around the normal reflections.

Many other long-period superlattices have been discovered in cubic alloys, particulary at the A3B compositions. Long-period superlattices have also been reported in hexagonal alloys (SCHUBERT *et al.* [1955]). The structure shown in fig. 35b corresponds to the orthorhombic structure Au_3Zn. This long-period superlattice is based on Cu_3Au and consists of four face-centred cells stacked together with a half-diagonal shift as shown in the figure. Most of the long-period superlattices at compositions A_3B retain the cubic symmetry of atomic distribution and they can be either one-dimensional long-period superlattices or two-dimensional superlattices. Much of the recent work in this field is due to SCHUBERT *et al.* [1955] and to SATO and TOTH [1961, 1962, 1965].

The discovery of the long-period superlattices has presented a challenge to the theory of alloys because the usual atom-pair interaction models adopted for explanation of the order-disorder phenomena cannot be used unless one assumes extremely long-distance interactions. The most successful interpretation at the moment appears to be that such superlattices are a result of a complex interaction between the Fermi surface and the Brillouin zone (SATO and TOTH [1961, 1962, 1965]) and is therefore connected with the collective behavior of the free electrons. The Brillouin zone for the CuAu alloys is shown in fig. 36. The thin lines represent the zone for the disordered fcc structure. This zone is bounded by the octahedral {111} and cubic {200} faces and can hold two

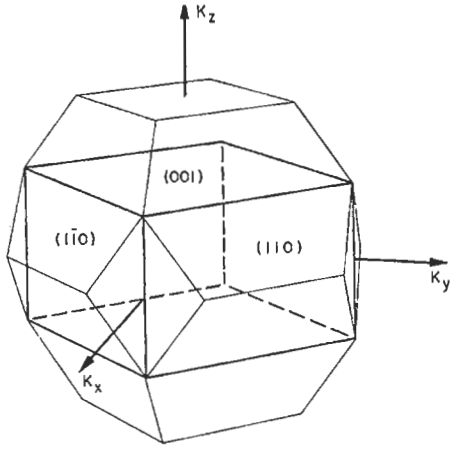

Fig. 36. The Brillouin zone of the disordered (thin lines) and ordered (thick lines) fcc structures (from SATO and TOTH [1962].)

electrons per atom. The thick lines represent the zone for the ordered CuAu I superlattice. This zone, as a result of order in the lattice, is now bounded by the {001} and {110} faces and is therefore no longer symmetrical, the {100} faces being much closer to the origin than the {110} faces. The free-electron energies at the centers of the {100} and {110} faces are 2.4 eV and 4.8 eV respectively, while the energy at the Fermi surface corresponding to one electron per atom (Cu–Au system) is 6.5 eV. Therefore electrons should overlap into the larger zone. The existence of "satellite" reflections around the normal reflections in the *b* direction, corresponding to the long-range periodicity in the CuAu II superlattice, suggests that the Brillouin zone would show a slight splitting of certain faces. This is illustrated in fig. 37b and c which represents a horizontal section in the reciprocal lattice throught the zone shown in fig. 36. SATO and

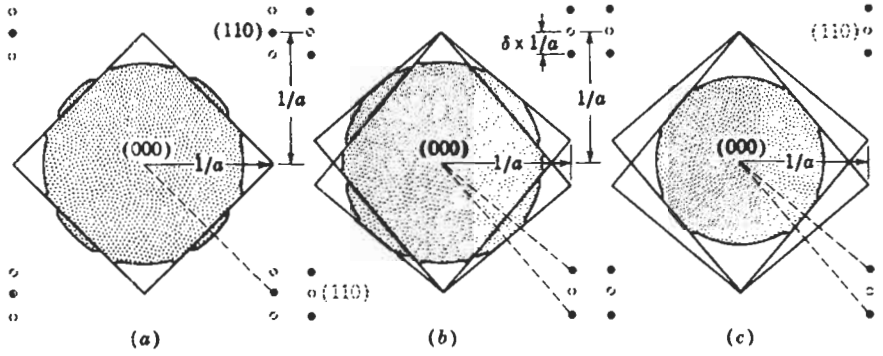

Fig. 37. Horizontal section in reciprocal space through the Brillouin zone of fig. 36, showing possible Fermi surface contours for the Cu–Au superlattice: (a) CuAu I; (b,c) CuAu II. (From BARRETT and MASSALSKI [1966].)

References: p. 199.

TOTH [1962] have proposed that at one electron per atom, the Fermi surface comes rather close to the {110} faces and, when the CuAu II superlattice is formed, the interaction between the Fermi surface and these split faces produces extra stabilization of the long-period structure. Since the period M governs the extent to which the satellite spots are separated in the reciprocal lattice, there should be a relationship between M and the electron concentration which governs the volume of the Fermi "sphere". It can be shown that as e/a increases, the Fermi "sphere" would fit better with respect to the {110} faces if their splitting were increased. This requires that the period M should decrease. SATO and TOTH [1961] have shown that additions of alloying elements to the CuAu II superlattice, resulting in changes of e/a, also poduce changes of the long-range period in the direction suggested by the above model. Furthermore, the model makes also possible the explanation of other characteristics of the long-period superlattices such as the nature of the distortion of the lattice, the concentration and temperature dependence of the distortion and of the periods, and the question whether or not the superlattice will be one-dimensional or two-dimensional. (Ordering in CuAu is treated by RAPSON [1995].)

11.3. Long-range order and short-range order

Attempts to formulate a theory of ordering date back to the 1930s and are associated with the names of Borelius, Johansson and Linde, Dehlinger, Bragg and Williams, Bethe, Peierls, Takagi and others. Several comprehensive reviews exist on both the mechanisms of ordering and on various treatments of the subject, and they may be consulted for details; for example, those of NIX and SHOCKLEY [1938], LIPSON [1950] and GUTTMAN [1956].

The essential condition for a solid solution of suitable composition to become ordered is that dissimilar atoms must attract each other more than similar atoms in order to lower the free energy upon ordering. In terms of interaction energies between pairs of atoms of two atomic species A and B this condition is usually expressed as follows:

$$E_{AB} < \tfrac{1}{2}\left(E_{AA} + E_{BB}\right), \tag{11}$$

where E_{AA} and E_{BB} represent energies of like pairs of atoms and E_{AB} represents the energy of the unlike pair. If this condition is satisfied for a given alloy of a stoichiometric composition, then at some suitably low temperature the structure will become perfectly ordered, the A and B atoms occupying designated sites in the lattice, which may be called the α and β sites. On warming up the energy will be supplied in the form of heat and will cause some A atoms to migrate into "wrong" β sites and vice versa, causing the atomic distribution to become more *random*. With perfect order at a low temperature the mathematical probability of finding an A atom on an a site and a B atom on a β site is unity. At higher temperatures, however, the probability that an a site is occupied by an A atom will be reduced to a fraction of unity, say p. BRAGG and WILLIAMS [1934] have used this description to define the *long-range order parameter*, S,

$$S = (p - r)/(1 - r), \tag{12}$$

where r is the fraction of A atoms in the alloy. According to eq. (11), S varies from one to zero as order decreases.

The order-disorder change, like the magnetic change, is a *cooperative phenomenon*. As more atoms find themselves in "wrong" atomic sites due to thermal agitation the energy difference indicated by eq. (10) decreases and it becomes easier to produce further disorder. Eventually a critical temperature is reached, Tc, at which all distinction between different sites is lost.

The simple approach as outlined above does not allow for the possibility of the existence of magnetic domains and other types of interruptions in the ordered array of atoms that may cause a departure from perfect order (as mentioned in a previous section) which makes it possible for a high degree of local order to exist even though its perfection is not absolute on a large volume scale. In order to describe such situations an alternative method of defining the state of order is possible which, instead of considering the probability of finding A or B atoms on designated α or β lattice sites, takes into acount the number of unlike nearest neighbors around a given atom. For example, the BETHE [1935] *short-range order parameter*, σ, is defined by:

$$\sigma = (q - q_r)/(q_m - q_r), \tag{13}$$

where q denotes the fraction of unlike nearest neighbors at a given temperature and q_r and q_m correspond to the fractions of unlike nearest neighbors at conditions of maximum randomness and maximum order. As may be seen, σ is defined in such a way that it would become unity for perfect order and zero for randomness.

Actually, instead of reaching zero on disordering, σ usually remains a definite value above T_c. In terms of the relationship between atoms, σ measures the state of order in the immediate vicinity of a given atom unlike the long-range order parameter, S, of Bragg and Williams which deals with the whole lattice. The description of the immediate surroundings of a given atom can be extended further to include several successive concentric shells corresponding to the first, second, third, etc., nearest neighbors (COWLEY [1950]).

References

AAERTS, E., P. DELAVIGNETTE, R. SIEMS and S. AMELINCKX, 1962a, Electron Microscopy (Academic, New York).

AAERTS, E., P. DELAVIGNETTE, R. SIEMS and S. AMELINCKX, 1962b, J. Appl. Phys. **33**, 3078.

AHLERS, M., 1981, *J. Phys. F* **11**, 1775.

AMELINCKX, S., 1988, in: Encyclopedia of Materials Science and Engineering, Supp. Vol. 1, ed. R.W. CAHN, Pergamon Press, Oxford, p. 77.

ARGENT, B.B., and D.W. WAKEMAN, 1956–7, J. Inst. Metals **85**, 413.

AVERBACH, B.L., 1956, in: Theory of Alloy Phases (ASM, Metals Park, OH).

AXON, H.J., and W. HUME-ROTHERY, 1948, Proc. Roy. Soc. **A193**, 1.

BARRETT, C.S., 1950, Trans. AIME **188**, 123.

BARRETT, C.S., and T.B. MASSALSKI, 1966, Structure of Metals, 3rd Ed. (McGraw-Hill, New York).

BENNETT, L.H., ed., 1980, Proc. Conf. on theory of Alloy Phase Formation (AIME, Warrendale, PA).

BETHE, H.A., 1935, Proc. Roy. Soc. (London) **A150**, 552.

BLANDIN, A., 1965, in: Alloying Behavior and Effects in Concentrated Solid Solutions, ed. T. B. MASSALSKI (Gordon and Breach, New York).
BLANDIN, A., and J. FRIEDEL and G. SAADA, 1966, J. Phys. Suppl. C3, **27**, 128.
BOLLING, G. F., and W. C. WINEGARD, 1958a, J. Inst. Metals **86**, 492.
BOLLING, G. F., and W. C. WINEGARD, 1958b, Acta Metall. **6**, 288.
BOLLING, G. F., T. B. MASSALSKI and C. J. MCHARGUE, 1965, Phil. Mag. **6**, 491.
BORIE, B. S., 1957, Acta Cryst. **10**, 89.
BORIE, B. S., 1959, Acta Cryst. **12**, 280.
BRADLEY, A. J., and A. TAYLOR, 1937, Proc. Roy. Soc. (London) **A159**, 56.
BRAGG, W. L., and E. J. WILLIAMS, 1934, Proc. Roy. Soc. (London) **A145**, 669.
BREWER, L., 1968, Science, **161**, 115.
BROOKS, H., 1955, in: Impurities and Imperfections, ASM Seminar (ASM, Metals Park, OH).
CAHN, R. W., 1979, Nature **279**, 579.
CHRISTIAN, J. W., and P. R. SWANN, 1965, in: Alloying Behavior and Effects in Concentrated Solid Solutions, ed. T. B. MASSALSKI (Gordon and Breach, New York) p. 105.
COCKAYNE, B., and G. V. RAYNOR, 1961, Proc. Roy. Soc. **A261**, 175.
COHEN, M. H., 1965, in: Alloying Behavior and Effects in Concentrated Solid Solutions, ed. T. B. MASSALSKI (Gordon and Breach, New York).
COLES, B. R., 1956, J. Inst. Metals **84**, 346.
COTTRELL, A. H., 1988, Introduction to the Modern Theory of Metals, Institute of Metals, London.
COTTRELL, A. H., 1993, Mat. Sci and Tech. **9**, 277.
COTTRELL, A. H., 1995, Intermetallics **3**, 341.
COWLEY, J., 1950, Phys. Rev. **77**, 669.
DARKEN, L. S., and R. W. GURRY, 1953, Physical Chemistry of Metals (McGraw-Hill, New York).
DE FONTAINE, D., 1983, M. R. S. Symp., vol. 19, p. 149.
DUWEZ, P., 1965, in: Alloying Behavior and Effects in Concentrated Solid Solutions, ed. T. B. MASSALSKI (Gordon and Breach, New York).
DUWEZ, P., 1967, Trans. ASM **60**, 607.
DUWEZ, P., ed., 1978, Metallic Glasses, ASM seminar (ASM, Metals Park, OH).
EDWARDS, Os., and H. LIPSON, 1942, Proc. Roy. Soc. **A180**, 208.
ELLNER, M., 1978, J. Less-Common Met. **60**, 15.
ELLNER, M., 1980, J. Less-Common Met. **75**, 5.
ELLWOOD, E. C., 1948, Nature, **163**, 772.
ELLWOOD, E. C., 1951–2, J. Inst. Metals **80**, 217.
EPPERSON, J. E., K. W. GERSTENBERG, D. BRENER, G. KOSTORZ and C. ORTIZ, 1978, Phil. Mag. **A38**, 529.
ESHELBY, J. D., 1956, Solid State Phys. **3**, 79.
FAULKNER, J. S. and G. M. STOCKS, 1981, *Phys. Rev. B*, **23**, 5628.
FAULKNER, J. S. , 1982, Prog. Mater. Sci. **27**, 1.
FRIEDEL, J., 1954a, Adv. Phys. **3**, 446.
FRIEDEL, J., 1954b, Les Electrons dans les Métaux, 10th Solvay Conference (ed. R. STOOPS, Bruxelles, 1955).
FRIEDEL, J., 1955, Phil. Mag. **46**, 514.
FRIEDEL, J., 1964, Trans. AIME **230**, 616.
FULLMAN, R. L., 1951, J. Appl. Phys. **22**, 488.
FUMI, F., 1955, Phil./ Mag. **45**, 1007.
GALLAGHER, P. C. J., 1970, Metallurg. Trans. **1**, 2450.
GLOSSOP, A. B., And D. W. PASHLEY, 1959, Proc. Roy. Soc. **A250**, 132.
GOLDSCHMIDT, H. J., 1948, J. Iron Steel Inst. **160**, 345.
GSCHNEIDNER, K. A., 1980, in: Theory of Alloy Phase Formation, ed. L. H. BENNETT (AIME, Warrendale, PA).
GUTTMAN, L., 1956, Solid State Phys. **3**, 145.
HAFNER, J., 1983, in: Mat. Res. Soc. Symp. Proc., Vol. 19, eds. H. BENNETT, T. B. MASSALSKI and B. C. GIESSEN, Elsevier Science Publ. Co., p. 1.
HARRISON, W. A., 1959, Phys. Rev. **116**, 555; 1960, **118**, 1190.
HARRISON, W. A., and M. B. WEBB, eds., 1960, The Fermi Surface (Wiley, New York).

HEINE, V., 1967, in: Phase Stability in Metals and Alloys, eds. P. S. RUDMAN, J. STRINGER and R. I. JAFFEE (McGraw-Hill, New York).
HELLAWELL, A., and W. HUME–ROTHERY, 1954, Phil. Mag. **45**, 797.
HENDERSON, B., and G. RAYNOR, 1962, Proc. Roy. Soc. **A267**, 313.
HERBSTEIN, F. H., B. S. BORIE and B. L. AVERBACH, 1956, Acta Cryst. **9**, 466.
HILL, R. B., and H. J. AXON, 1954–5, J. Inst. Metals **83**, 354.
HILL, R. B., and H. J. Axon, 1956–7, J. Inst. Metals **85**, 102.
HOWIE, A., and P. R. SWANN, 1961, Phil. Mag. **6**, 1215.
HUANG, K., 1947, Proc. Roy. Soc. **A190**, 102.
HUME–ROTHERY, W., 1955, Atomic theory for the Students of Metallurgy (The Institute of Metals, London); enlarged edition, 1960.
HUME–ROTHERY, W., 1961a, Elements of Structural Metallurgy (The Institute of Metals, London) Monograph and Report Series, no. 26).
HUME–ROTHERY, W., 1961b, J. Inst. Metals **9**, 42.
HUME–ROTHERY, W., 1964, The Metallurgist, p. 11.
HUME–ROTHERY, W., 1966, The Structure of Alloys of Iron (Pergamon Press, Oxford).
HUME–ROTHERY, W., 1967, in: Phase Stability in Metals and Alloys, eds. P. S. RUDMAN, J. STRINGER and R. I. JAFFEE (McGraw-Hill, New York).
HUME–ROTHERY, W., and B. R. COLES, 1954, Adv. Phys. **3**, 149.
HUME–ROTHERY, W., and G. V. RAYNOR, 1949), Proc. Roy. Soc. **A174**, 471.
HUME–ROTHERY, W., J. O. BETTERTON and J. REYNOLDS, 1952, J. Inst. Metals **80**, 609.
HUME–ROTHERY, W., R. E. SMALLMAN and C. W. HAWORTH, 1969, The Structure of Metals and Alloys , 5th edn. (The Institute of Metals, London), p. 349.
JOHANNSON, C. H., and J. O. LINDE, 1936, Ann. Phys. **25**, 1.
JOHNSON, C. A., 1963, Acta Cryst. **16**, 490.
JOHNSON, W. L., 1986, Prog. Mat. Sci. **30**, 81.
JONES, H., 1934a, Proc. Roy. Soc. **A144**, 225.
JONES, H., 1934b, Proc. Roy. Soc. **A147**, 396.
JONES, H., 1937, Proc. Roy. Soc. **A49**, 250
JONES, H., 1952, Phil. Mag. **43**, 105.
JONES, H., 1960, The Theory of Brillouin Zones and Electronic States in Crystals (North-Holland, Amsterdam).
JONES, H., 1962, J. Phys. Radium **23**, 637.
KIKUCHI, R., Physica, 1981, **103B**, 41.
KING, H. W., 1966, J. Mater. Sci. **1**, 79.
KING, H. W., and T. B. MASSALSKI, 1961, Phil. Mag. **6**, 669.
KLEE, H., and H. WITTE, 1954, Z. Phys. Chem. **202**, 352.
KOGACHI, M., S. MINAMIGAWA and K. NAKAHIGASHI, 1992, Acta Metall. et Mater. **40**, 1113.
KOGACHI, M., Y. TAKEDA and T. TANAHASHI, 1995, *Intermetallics*, in press.
KOIKE, S., M. HIRABAYASHI and To. SUZUKI, 1982, Phil. Mag. **45**, 261.
LAVES, F., and H. WITTE, 1935, Metallwirtschaft **14**, 645.
LAVES, F., and H. WITTE, 1936, Metallwirtschaft **15**, 840.
LAUGHLIN, D. E. , 1988, "Long-Range Order in Alloys", Encyclopedia of Materials Science and Engineering, Supp. Vol. 1, (Pergamon Press, Oxford) pp. 263–268.
LIESER, K. H., and H. WITTE, 1954, Z. Phys. Chem. **202**, 321.
LIPSON, H., 1950, Prog. Metals Phys. **2**, 1.
LIPSON, H., and A. TAYLOR, 1939, Proc. Roy. Soc. (London) **A173**, 232.
LOMER, 1967, in: *Phase Stability in Metals and Alloys*, eds. P. S. RUDMAN, J. STRINGER and R. I. JAFFEE, McGraw Hill, New York.
MACHLIN, E. S., 1981, CALPHAD vol. 5, p. 1.
MANN, E., and A. SEEGER, 1970, J. Phys. Chem. Solids **12**, 314.
MASSALSKI, T.B., 1958, Met. Rev. **3**, 45.
MASSALSKI, T.B., and H. W. KING, 1961, Prog. Mater. Sci. **10**, 1.
MASSALSKI, T.B., and U. MIZUTANI , 1978, Prog. Mater. Sci. **22**, 151.

MASSALSKI, T.B., U. MIZUTANI and S. NOGUCHI, 1975, Proc. Roy. Soc. **A343**, 363.
MASSALSKI, T.B., 1982, in: Proceedings of RQ4 Conference, T. MASUMOTO and U. SUZUKI, eds. Jap. Inst. of Metals, p. 203.
MASSALSKI, T. B., and H. F. RIZZO, 1988, Proc. of JIMIS-5 on Non-Equilibrium Solid Phases of Metals and Alloys, Suppl. to Trans. JIM, vol. 29, p. 217.
MASSALSKI, T. B., 1989 , The Campbell Lecture, Metallurgical Transactions, **20A**, 1295; and **20B**, 445.
MASSALSKI, T. B., 1990, Binary Alloy Phase Diagrams, second edition, T. B. MASSALSKI editor-in-chief, H. OKAMOTO and L. KACPRZAK, editors, American Society for Metals.
MIEDEMA, A. R., P. F. DE CHATEL and F. R. DE BOER, 1980, *Physica*, **100B**, 1.
MIEDEMA, A. R., and A. K. NIESSEN, 1988, *Proc. JIMIS-5*, "Non-Equilibrium Solid Phases of Metals and Alloys", JIM Suppl. vol. 29, p. 209.
MOHRI, T., K. TERAKURA, T. OGUCHI and K. WATANABE, 1988, Acta Metall., **36**, 547.
MORINAGA, M., N. YUKAWA and H. ADACHI, 1985,J. Phys. F, **15**, 1071.
MOTT, N. F., and H. Jones, 1936. The Theory of the Properties of Metals and Alloys (Oxford University Press).
MOTT, N. F., 1952, Prog. Met. Phys. **3**, 76.
MOTT, N. F., 1962, Rept. Prog. Phys. **25**, 218.
NEVITT, M., 1963, in: Electronic Structure and Alloy Chemistry of Transition Elements, ed. P. A. BECK (Wiley, New York).
NIEMIEC, J., 1966, in: Fizykochemia Ciala Stalego, ed. B. STALINSKI (Panstwowe Wydawnictwo Naukowe, Warsaw).
NIX., F. C., and W. SHOCKLEY, 1938, Rev. Mod. Phys. **10**, 1.
NOVER, R. G., and K. SCHUBERT, 1980, Z. Metallk. **71**, 329.
OGAWA, S., and D. WATANABE, 1954, Acta Cryst. **7**, 377.
OWEN, E. A., 1947, J. Inst. Metals, **73**, 471.
PATERSON, M. S., 1952, J. Appl. Phys. **23**, 805.
PEARSON, W. B., 1958 and 1967, A Handbook of Lattice Spacings and Structures of Metals and Alloys (Pergamon Press, London and New York) vol. 1, 1958; vol. 2, 1967.
PEARSON, W. B., 1967, in: Phase Stability in Metals and Alloys, P. S. RUDMAN, J. STRINGER and R. I. JAFFEE, eds., McGraw Hill, New York.
PEREPEZKO, J. H. and W. J. BOETTINGER, 1983, in Alloy Phase Diagrams, L. H. BENNETT, T. B. MASSALSKI and B. C. GIESSEN, eds. MRS Symposium, Vol. 19, p. 223. Elsevier Publ., Inc.
PEI, S., T. B. MASSALSKI, W. M. TEMMERMAN, P. A. STERNE and G. M. STOCKS, 1989, Physical Review B, **39**, 5767.
PETTIFOR, D. G., 1979, Phys. Rev. Letters **42**, 846.
PETTIFOR, D. G., 1986, J. Phys. C, **19**, 285.
PIPPARD, A. B., 1957, Phil. Trans. Roy. Soc. **A250**, 325.
RAPACIOLI, R., and M. AHLERS, 1977, Scripta Metall. **11**, 1147.
RAPSON, W. S., 1995, in: Intermetallic Compounds — Principles and Practice, eds. J. H. Westbrook and R. L. Fleischer (Wiley, Chichester), Vol. 2, p. 559.
RAYNOR, G. V., 1949a, Trans. Farad. Soc. **45**, 698.
RAYNOR, G. V., 1949b, Prog. Met. Phys. **1**, 1.
RAYNOR, G. V., 1956, The Theory of Alloy Phases, (ASM, Metals Park, OH), p. 321.
READ, W. T., Jr., 1953, Dislocations in Crystals (McGraw-Hill, New York).
ROBERTS, R. W., 1954, Acta Metall. **2**, 597.
ROBERTS, B. W., 1956, J. Metals **8**, 1407, Phys. Rev. 104, 607.
ROBINSON W. M., and M. B. BEVER, 1967, Metallurgical Transactions, **239**, p. 1015.
RUDMAN, P. S., J. STRINGER and R. I. JAFFEE, eds. 1968, Phase Stability in Metals and Alloys, (McGraw Hill, New York).
SATO, H., and R. S. TOTH, 1961, Phys. Rev. **124**, 1833.
SATO, H., and R. S. TOTH, 1962, Phys. Rev. Lett. **8**, 239.
SATO, H., and R. S. TOTH, 1965, in: Alloying Behavior and Effects in Concentrated Solid Solutions, ed. T. B. MASSALSKI (Gordon and Breach, New York).
SCHUBERT, K., B. KIEFER, M. WILKENS and R. HAUFLER, 1955, Z. Metallk. **46**, 692.

STIRLING, P. H., and G. V. RAYNOR, 1956, J. Inst. Metals, **84**, 57.
SLICK, P. I., C. W. MASSENA and R. S. CRAIG, 1965, J. Chem. Phys. **43**, 2792.
STOCKS, G. M., and H. WINTER, 1984, The Electronic Structure of Complex Systems, eds. P. PHARISEAU and W. M. TAMMERMAN, Plenum Press, New York.
STOCKS, G. M. and A. GONIS, Eds., 1989, NATO Symposium on "Alloy Phase Stability", Kluwer Academic Publishers, vol. 163, series E.
STROUD, D., 1980, in: Proc. Conf. on Theory of Alloy Phase Formation, ed. L. H. BENNETT, (AIME, Warrendale, PA), p. 84.
SUZUKI, To., M. HASEGAWA and M. HIRABAYASHI, 1976, J. Phys. **F6**, 779.
TAYLOR, A., 1961, X-Ray Metallography (Wiley, New York).
TAYLOR, A., and N. J. DOYLE, 1972, J. Appl. Cryst. **5**, 201.
TERAKURA, K., T. OGUCHI, T. MOHRI and K. WATANABE, 1987, Phys. Rev. B, **35**, 2169.
TURNBULL, D., 1980, Met. Transactions **12A**, p. 695.
VEGARD, L., 1928, Z. Cryst. **67**, 239.
WABER, J. T., K. A. GSCHNEIDNER, A. C. LARSON and M. Y. PRINCE, 1963, Trans. AIME **227**, 717.
WAGNER, C. N. J., 1957, Acta Metall. **5**, 427 and 477.
WARREN, B. E., B. E. AVERBACH and B. W. ROBERTS, 1951, J. Appl. Phys. **22**, 1943.
WARREN, B. E., and E. P. WAREKOIS, 1955, Acta Metall. **3**, 473.
WARREN, B. E., 1959a, Acta Cryst. **12**, 837.
WARREN, B. E., 1959b, Prog. Met. Phys. **8**, 147.
WATSON, R. E., and L. H. BENNETT, 1979, Phys. Rev. Letters, **43**, 1130.
WATSON, R. E., and L. H. BENNETT, 1983, in: Alloy Phase Diagrams, MRS Symposium, L. H. BENNETT, T. B. MASSALSKI and B. C. GIESSEN, eds. Vol. 19, p. 99.
WESTGREN, A., and G. PHRAGMEN, 1926, On the Chemistry of Metallic Compounds, Z. Metallk. **18**, 279.
WESTGREN, A., 1930, Z. Metallk. **22**, 368.
WILKENS, M., 1962, Phys. Stat. Sol. **2**, 692.
WILLIAMS, A. R., C. D. GELATT and V. L. MORUZZI, 1980, Phys. Rev. Lett. **44**, 429.
WILLIS, M., and H. F. ROOKSBY, 1954, Proc. Phys. Soc. **B67**, 290.
XU, J. H., T. OGUCHI and A. J. FREEMAN, 1987, Phys. Rev. **B35**, 6940.
YIN, M. T., and M. L. COHEN, 1982, Phys. Rev. **26B**, 3259.

Further reading

(a) In the present chapter the main emphasis has been placed on solid solutions and structures with wide solid solubility. However, this subject is closely bound with the much wider area of the stability of all alloy phases and crystal structures. Further reading on early ideas on the theories of alloy phases may be found in: ASM Symposium on the Theory of Alloy Phases (ASM, Metals Park, OH, 1956) and the Symposium on Metallic Solid Solutions, Orsay, France, eds. J. FRIEDEL and A. GUINIER (Benjamin, New York, 1963). More recent symposia or reviews include:
AIME Symposium on The Alloying Behavior and Effects in Concentrated Solid Solutions, ed. T. B. MASSALSKI, Gordon and Breach, New York (1965).
Battelle Inst. Symposium on Phase Stability in Metals and Alloys, eds. P. S. RUDMAN, J. STRINGER and R. I. JAFFEE, eds., McGraw Hill, (1967).
Structure of Metals, 3rd edition, C. S. BARRETT and T. B. MASSALSKI, McGraw-Hill, New York (1966).
A discussion of the theories of alloys based on the noble metals, Cu, Ag and Au, is given by:
W. HUME-ROTHERY, J. Inst. Metals **9** (1961–2) 42. T. B. MASSALSKI and H. W. KING, Prog. Mater. Sci. **10** (1961) 1. T. B. MASSALSKI and U. MIZUTANI, Prog. Mater. Sci. **22** (1978) 151.

(b) Problems concerning the transition elements and their alloys are discussed in:
AIME Symposium on Electronic Structure and Alloy Chemistry of Transition Elements, ed. P. A. BECK, Wiley, New York (1963).
Electrons in Transition Elements, by N. F. MOTT, Adv. Phys. **13** (1964) 325.

Battelle Inst. Symposium on Phase Stability in Metals and Alloys, eds. P. S. RUDMAN, J. STRINGER and R. I. JAFFEE, McGraw Hill (1967.

(c) Relations between phase stability and phase diagrams are discussed in:
T. B. MASSALSKI, the Campbell Lecture, Metallurgical Transactions, **20A**, 1295; and **20B**, 445 (1989).

(d) Size effects in alloy phases are discussed by:
H. W. KING, in: AIME Symposium (1965) listed above.
F. LAVES, in: Advances in X-ray Analysis, eds. W. M. MUELLER and M. F. FAY, **6** (1962) 43. For electron theory connections to size effects see F. J. PINSKI, B. GINATEMPO, D. D. JOHNSON, J. B. STAUNTON, G. M. STOCKS and B. L. GYOFFRY, 1991, Phys. Rev. Lett., **66**, 766.

(e) Long-period superlattices and stacking faults are discussed by H. SATO and R. S. TOTH, and J. W. CHRISTIAN and P. SWANN, respectively, in the AIME Symposium (1965) listed above under (a), and more recently in the NATO Symposium on Alloy Phase Stability listed under (g).

(f) Stability and electronic structure of metallic glasses are discussed by:
U. MIZUTANI, Prog. Mater. Sci. **28** (1983).

(g) Recent concepts related to the electronic interactions in metals and alloys are discussed in a NATO Symposium on "Alloy Phase Stability" G. M. STOCKS and A. GONIS, eds., Kluwer Academic Publishers, vol. 163, series E, (1989); and in a book by Alan H. COTTRELL, "Introduction to the Modern Theory o Metals", Institute of Metals, London (1988). Interested readers should perhaps consult first the chapter on electronic theories in this book.

CHAPTER 4

STRUCTURE OF INTERMETALLIC COMPOUNDS AND PHASES

RICCARDO FERRO AND ADRIANA SACCONE

Istituto di Chimica Generale
Università di Genova
Genova, Italy

R. W. Cahn and P. Haasen†, eds.
Physical Metallurgy; fourth, revised and enhanced edition

1. Introduction

1.1. Preliminary remarks and definition of an intermetallic phase

In the field of solid state chemistry an important group of substances is represented by the intermetallic compounds and phases. A few general and introductory remarks about these substances may be presented by means of figs. 1 and 2. In binary and multicomponent metal systems, in fact, several crystalline phases (terminal and intermediate, stable and metastable) may occur.

Simple schematic phase diagrams of binary alloy systems are shown in fig. 1. In all of them the formation of solid phases may be noticed. In fig. 1a we observe the formation of the AB_x phase (which generally crystallizes with a structure other than those of the constituent elements) and which has a negligible homogeneity range. Thermodynamically, the composition of any such phase is variable. In a number of cases, however, the possible variation in composition is very small (invariant composition phases or stoichiometric phases, or "compounds" proper, also called "point compounds" in binary alloys).

In fig. 1b and 1c, on the contrary, we observe that solid phases with a variable composition are formed (non-stoichiometric phases). In the reported diagrams we see examples both of terminal (1b, 1c) and intermediate phases (1c). These phases are characterized by homogeneity ranges (solid solubility ranges) which, in the case of the terminal phases, include the pure components and which, generally, have a variable temperature-dependent extension. (In the older literature, stoichiometric and non-stoichiometric phases were often called "daltonides" and "berthollides", respectively. These names, however, are no longer recommended by the Commission on the Nomenclature of Inorganic Chemistry (IUPAC), LEIGH [1990].

More complex situations are shown in fig. 2, where some typical examples of isobarothermal sections of ternary alloy phase diagrams are presented. In the case of a ternary system, such as that reported in fig. 2a, we notice the formation of several, binary and ternary, stoichiometric phases. In the case shown in fig. 2b, different types of variable composition phases can be observed. We may differentiate between these phases by using terms such as: "*point compounds*" (or *point phases*), that is, phases represented in the composition triangle, or, more generally, in the composition simplex by points, "*line phases*", "*field phases*", etc.

As a summary of the aforementioned considerations, we may notice that several types of substances may be included in a preliminary broad *definition of an intermetallic phase*. Both *stoichiometric (compounds) phases* and *variable-composition (solid solutions) phases* may be considered and, as for their structures, both fully ordered or (more or less completely) disordered phases.

For all the intermetallic phases the identification (and classification) requires information about their chemical composition and structure. To be consistent with the other field of descriptive chemistry, this information should be included in specific chemical (and structural) formulae built up according to well-defined rules. This task, however, in the specific area of the intermetallic phases (or more generally in the area of solid state chemistry) is much more complicated than for other chemical compounds.

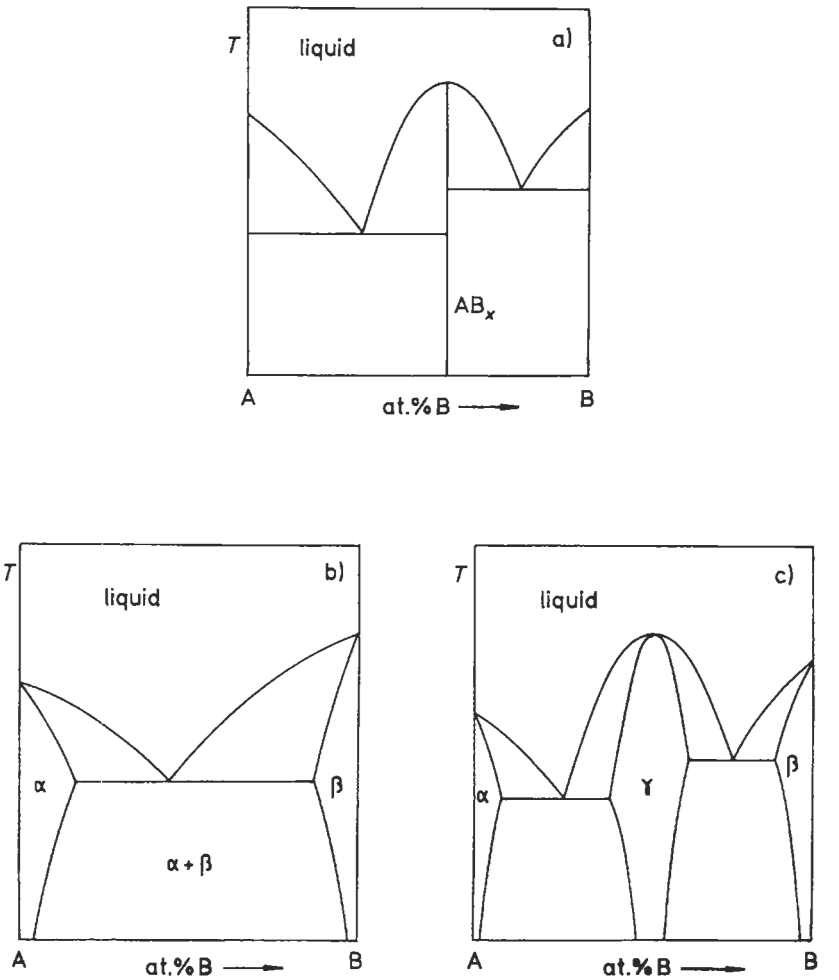

Fig. 1. Examples of simple binary diagrams.

a) A stoichiometric, congruently melting, compound is formed at the composition corresponding to the AB_x formula.

b) No intermediate phase is formed. The components show a certain limited mutual solid solubility.

c) The two components show limited mutual solid solubility (formation of the α- and β-phases). Moreover, an intermediate phase (γ) is formed: it is homogeneous in a certain composition range.

This complexity is related both to the chemical characteristics (formation of variable composition phases) and to the structural properties (the intermetallic compounds are generally non-molecular in nature, while the conventional chemical symbolism has been mainly developed for the representation of molecular units). As a consequence there is not a complete, or generally accepted, method of representing the formulae of intermetallic compounds.

References: p. 363.

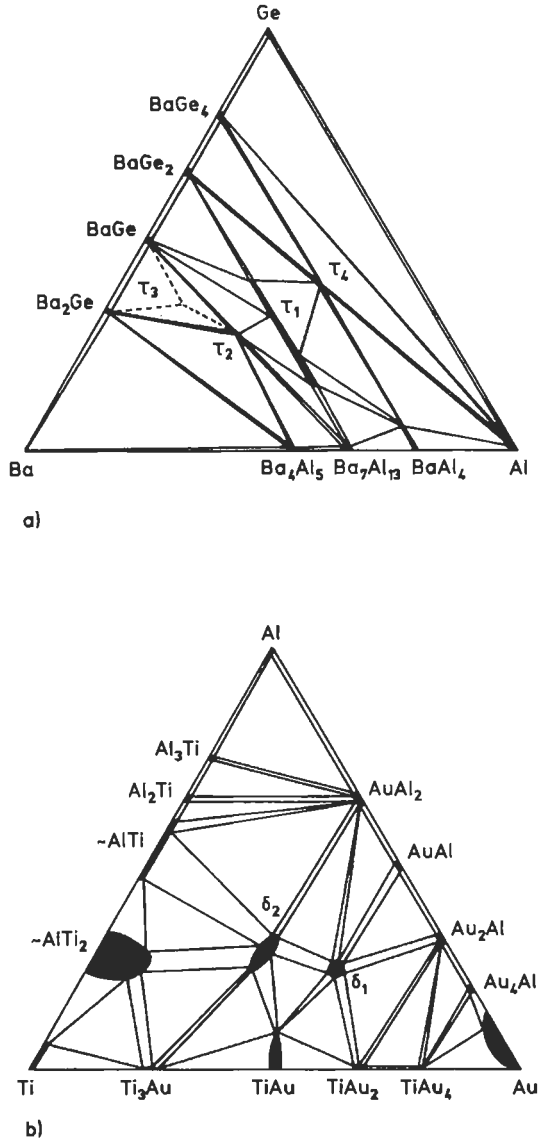

Fig. 2. Isobarothermal sections of actual ternary systems (from "Ternary Alloys", PETZOW and EFFENBERG, [1988 *et seg.*]).

a) Ba–Al–Ge system. A number of binary compounds are formed in the side binary systems. Moreover, a few ternary phases have been observed.
τ_1: ≈$Ba(Al_xGe_{1-x})_2$, line phase, stable for $0.41 < x < 0.77$;
τ_2: $Ba_3Al_2Ge_2$, τ_3: $Ba_{10}Al_3Ge_7$, τ_4: $BaAl_2Ge_2$, point phases.

b) Ti–Au–Al system. The binary systems show the formation of several intermediate phases, generally characterized by certain composition ranges (ideal simple formulae are here reported). Two ternary field phases are also formed. Their homogeneity ranges are close to $TiAu_2Al$ (δ_1) and TiAuAl (δ_2), respectively.

Some details on these points will be given in the next sections. These will then be used for a description of selected common phases and a presentation of a few characteristic general features of intermetallic crystallochemistry. For an exhaustive description of all the intermetallic phases and a comprehensive presentation and discussion of their crystallochemistry, general reference books and catalogues, such as those reported in the list of references, should be consulted. More references to specific topics will be reported in the following sections.

Those who are interested in the historical development of the intermetallic compound concept and science may refer to the review written by WESTBROOK [1977] on the past and future potential of intermetallic compounds. In this review Westbrook selected the following topics for the examination of their historic roots:

a) the development of the modern concept of the intermetallic compound;
b) the development of the phase diagram;
c) the role of electron concentration in determining intermetallic phase stability;
d) the role of geometrical factors in determining intermetallic phase stability;
e) the point defect concept and its relation to non-stoichiometric compounds;
f) the unusual role of grain boundaries in intermetallic compounds.

He reported information on the chronological growth in the number of binary metallic phase diagrams studied (starting from the year about 1830 with the systems Pb–Sn, Sn–Bi, etc.,) and of the intermetallic compounds.

The first problems encountered while studying these substances are pointed out: typically that simple valence concepts were not applicable for rationalizing compound formulation and that several compounds seemed to exist over a range of composition and not at some specific ratio as with ordinary salts. The development of the systematics of the intermetallic phases and of their applications is then discussed and compared with the history of the rise of thermodynamics and crystallochemistry.

The complexity and variability of solid state phenomena add to more practical reasons of interest in defining the peculiar approach to a systematic investigation of solid intermetallic phases.*

1.2. Identification of the intermetallic phases

The identification and crystallochemical characterization of an intermetallic solid phase requires the definition and analysis of the following points:

a) Chemical composition (and the homogeneity composition range and its temperature and pressure dependence).

* This chapter, as previously stated, will highlight the particular subject of the intermetallic solids. It may be worth reminding, however, that intermetallic substances can be found also in different aggregation states. (For the liquid state see, for instance, fig. 1). Important contributions to understanding systems in the liquid state (experimental measurements, thermodynamic properties forecasting, liquid state structure, theories and models) were brought about, for instance, by HOCH, ARPSHOFEN and PREDEL [1984], SOMMER [1982] and SINGH and SOMMER [1992]). A systematic description of the structure of amorphous and molten alloys (basic equation for the description of the structure of non-crystalline systems, experimental techniques and elements of systematics) has been presented by LAMPARTER and STEEB [1993].

References: p. 363.

b) Structure type (or crystal system, space group, number of atoms per unit cell and list of occupied atomic positions).

c) Values of a number of parameters characteristic of the specific phase within the group of isostructural phases (unit cell edges, occupation characteristics and, if not fixed, coordinate triplets of every occupied point set).

d) Volumetric characteristics (molar volume of the phase, formation volume contraction, or expansion, space filling characteristics, etc.).

e) Interatomic connection characteristics (local atomic coordination, long distance order, interatomic distances, their ratios to atomic diameters, etc.).

Clearly, not all the data relevant to the aforementioned points are independent of each other. The strictly interrelated characteristics listed under d) and e), for instance, may be calculated from the data indicated in b) and c), from which the actual chemical composition of the phase may also be obtained.

For each of the aforementioned points (and for their symbolic representation) a few remarks may be noteworthy: these will be presented in the following. *Crystallographic conventions, nomenclature and symbols* will be used. For a summary of these and of the corresponding definitions the most important reference book is "International Tables for Crystallography", HAHN [1989]. Several books, mentioned here in the reference list, contain, more or less detailed, introductions to the crystallographic notations. A few remarks on these points will be presented in this chapter (see especially table 3 and Sec. 3.1 and 3.5.5); some examples moreover have been given in chapter 1.

2. *Chemical composition of the intermetallic phase and its compositional formula*

Simple compositional formulae are often used for intermetallic phases; these (for instance, Mg_2Ge, $ThCr_2Si_2$,...) are useful as quick references, especially for simple, stoichiometric, compounds. The following remarks may be noteworthy:

Order of citation of element symbols in the formula

The symbol sequence in a formula ($LaPb_3$ or Pb_3La) is, of course, arbitrary and, in some particular cases, may be a matter of convenience. Alphabetical order has often been suggested (for example by IUPAC, LEIGH [1990]). A symbol sequence based on some chemical properties, however, may be more useful when, for instance, compounds with analogous structures have to be compared (Mg_2Ge and Mg_2Pb). Recently, in 1990, an international group of materials scientists coordinated by the Max Planck Institute for Metals Research of Stuttgart (Germany) (the so-called MSIT: Materials Science International Team) performing the critical assessment of a new series on ternary alloys edited by PETZOW and EFFENBERG [1988 *et seq.*] decided to adopt a symbol quotation order based on a parameter introduced by PETTIFOR [1984, 1986a] In fact, in order to stress the chemical character of the elements and to simplify their description, PETTIFOR [1984, 1985, 1986a, 1986b] (see also chapter 2) created a new *chemical scale* (χ) which orders the elements along a simple axis. The progressive order number of the elements in this scale (the so-called Mendeleev number) may also be considered. The Mendeleev

numbers M (which, of course, are different from the atomic numbers) start, according to Pettifor, with the least electronegative elements He 1, Ne 2,... and end with the most electronegative ones ...N 100, O 101, F 102 up to H 103. The Mendeleev Number (M) and the correlated "chemical scale χ" are shown in table 1. The chemical meaning of these parameters may be deduced not only by their relation to the Periodic Table. By using them, in fact, excellent separation of similar structures is achieved for numerous A_mB_n phases with a given stoichiometry within single two-dimensional M_A/M_B maps, (see Sec. 8.7.). Notice, however, that in subsequent papers, on the basis of a progressive improvement of the structure maps, slightly different versions of the chemical scale had been reported.

On the basis of the Pettifor's scale, the suggestion has been made that the element E with a lower value M_E (or χ_E) is quoted first in the formulae of its compounds. This will be generally adopted here.

Indication of constituent proportions

No special comments are needed for stoichiometric compounds ($LaPb_3$, $ThCr_2Si_2$,...).

More complex notation is needed for non-stoichiometric phases. Selected simple examples will be given below and more detailed information will subsequently be reported, when discussing crystal coordination formulae.

a) *Ideal formulae*

While considering a variable composition phase, it is often possible to define an "ideal composition" (and formula) relative to which the composition variations occur (or are considered to occur). This composition may be that for which the ratio of the numbers of different atoms corresponds to the ratio of the numbers of the different crystal sites in the ideal (ordered) crystal structure (as suggested by IUPAC, LEIGH [1990]). These formulae may be used even when the "ideal composition" is not included in the homogeneity range of the phase (Nb_3Al for instance, shows a homogeneity range from 18.6 at% Al which hardly reaches 25 at% Al. At the formation peritectic temperature of 2060°C the composition of the phase is about 22.5 at% Al).

b) *Approximate formulae*

A general notation which has been suggested by IUPAC when only little information has

Table 1

Chemical order of the elements, according to PETTIFOR [1986a]

1a. For the elements, arranged here in alphabetical order, the values of the so-called Mendeleev number are reported.

Ac	48	Be	77	Cm	41	Fe	61	Ho	23	Md	36	No	35	Pr	31	Sb	88	Te	92	Yb	17
Ag	71	Bi	87	Co	64	Fm	37	I	97	Mg	73	Np	44	Pt	68	Sc	19	Th	47	Zn	76
Al	80	Bk	40	Cr	57	Fr	7	In	79	Mn	60	O	101	Pu	43	Se	93	Ti	51	Zr	49
Am	42	Br	98	Cs	8	Ga	81	Ir	66	Mo	56	Os	63	Ra	13	Si	85	Tl	78		
Ar	3	C	95	Cu	72	Gd	27	K	10	N	100	P	90	Rb	9	Sm	28	Tm	21		
As	89	Ca	16	Dy	24	Ge	84	Kr	4	Na	11	Pa	46	Re	58	Sn	83	U	45		
At	96	Cd	75	Er	22	H	103	La	33	Nb	53	Pb	82	Rh	65	Sr	15	V	54		
Au	70	Ce	32	Es	38	He	1	Li	12	Nd	30	Pd	69	Rn	6	Ta	52	W	55		
B	86	Cf	39	Eu	18	Hf	50	Lr	34	Ne	2	Pm	29	Ru	62	Tb	26	Xe	5		
Ba	14	Cl	99	F	102	Hg	74	Lu	20	Ni	67	Po	91	S	94	Tc	59	Y	25		

References: p. 363.

Table 1—*Continued*

1b. The elements are arranged in the order of the Mendeleev Number M (and of the related chemical scale χ).

M	Element	χ	M	Element	χ	M	Element	χ
1	He	0.00	36	Md	0.7125	70	Au	1.16
2	Ne	0.04	37	Fm	0.715	71	Ag	1.18
3	Ar	0.08	38	Es	0.7175	72	Cu	1.20
4	Kr	0.12	39	Cf	0.72	73	Mg	1.28
5	Xe	0.16	40	Bk	0.7225	74	Hg	1.32
6	Rn	0.20	41	Cm	0.725	75	Cd	1.36
7	Fr	0.23	42	Am	0.7275	76	Zn	1.44
8	Cs	0.25	43	Pu	0.73	77	Be	1.50
9	Rb	0.30	44	Np	0.7325	78	Tl	1.56
10	K	0.35	45	U	0.735	79	In	1.60
11	Na	0.40	46	Pa	0.7375	80	Al	1.66
12	Li	0.45	47	Th	0.74	81	Ga	1.68
13	Ra	0.48	48	Ac	0.7425	82	Pb	1.80
14	Ba	0.50	49	Zr	0.76	83	Sn	1.84
15	Sr	0.55	50	Hf	0.775	84	Ge	1.90
16	Ca	0.60	51	Ti	0.79	85	Si	1.94
17	Yb	0.645	52	Ta	0.82	86	B	2.00
18	Eu	0.655	53	Nb	0.83	87	Bi	2.04
19	Sc	0.66	54	V	0.84	88	Sb	2.08
20	Lu	0.67	55	W	0.88	89	As	2.16
21	Tm	0.675	56	Mo	0.885	90	P	2.18
22	Er	0.6775	57	Cr	0.89	91	Po	2.28
23	Ho	0.68	58	Re	0.935	92	Te	2.32
24	Dy	0.6825	59	Tc	0.94	93	Se	2.40
25	Y	0.685	60	Mn	0.945	94	S	2.44
26	Tb	0.6875	61	Fe	0.99	95	C	2.50
27	Gd	0.69	62	Ru	0.995	96	At	2.52
28	Sm	0.6925	63	Os	1.00	97	I	2.56
29	Pm	0.695	64	Co	1.04	98	Br	2.64
30	Nd	0.6975	65	Rh	1.05	99	Cl	2.70
31	Pr	0.70	66	Ir	1.06	100	N	3.00
32	Ce	0.7025	67	Ni	1.09	101	O	3.50
33	La	0.705	68	Pt	1.105	102	F	4.00
34	Lr	0.7075	69	Pd	1.12	103	H	5.00
35	No	0.71						

to be conveyed and which can be used even when the mechanism of the variation in composition is unknown, is to put the sign ≈ (read as circa or approximately) before the formula; for instance ≈CuZn.

c) *Variable composition formulae*

(Ni,Cu) or Ni_xCu_{1-x} $(0 \leq x \leq 1)$ are the equivalent representations of the continuous solid solution between Ni and Cu, homogeneous in the complete range of compositions; other examples are: $Ce_{1-x}La_xNi_5$ $(0 \leq x \leq 1)$; $(Ti_{1-x}Cr_x)_5Si_3$ $(0 \leq x \leq 0.69)$; etc....

Similar formulae may also be used in more complicated cases to convey more information: $A_{m+x}B_{n-x}C_p$ $(... < x < ...)$ (phase involving substitution of atoms A for B).

$A_{1-x}B$ may indicate that there are A-type vacant sites in the structure.

$LaNi_5H_x$ ($0 < x < 6.7$) indicates the solid solution of H in $LaNi_5$.

d) *Site occupation formulae*

According to the Recommendations by the Commission on the Nomenclature of Inorganic Chemistry, (LEIGH [1990]), additional information may be conveyed by using a more complicated symbolism; suggestions have also been made about the indication of site occupation and of their characterization. These points will be discussed in more detail in the following sections; in the meantime we may mention that, for the indication of site occupation, the following criteria have been suggested by the Commission:

The site and its occupancy is represented by two right lower indexes separated by a comma. The first index indicates the type of site, the second one indicates the number of atoms in this site. (A_A, for instance, means an atom A on a site occupied by A in the ideal structure, whereas A_B represents an atom A in a site normally (ideally) occupied by B).

A formula such as:

$M_{M,1-x}N_{M,x}M_{N,x}N_{N,1-x}$ or $(M_{1-x}N_x)_M(M_xN_{1-x})_N$ represents a disordered alloy (whereas the ideal composition is MN with an ideal M_MN_N structure). In this notation vacant sites may be represented by □ or by v_.

The following examples of alloy formulae have been reported:

$Mg_{Mg,2-x}Sn_{Mg,x}Mg_{Sn,x}Sn_{Sn,1-x}$ shows a partially disordered alloy with some of the Mg atoms on Sn sites, and vice versa;

$(Bi_{2-x}Te_x)_{Bi}(Bi_xTe_{3-x})_{Te}$ shows the composition changes from the ideal Bi_2Te_3 formula;

$Al_{Al,1}Pd_{Al,x}Pd_{Pd,1-x}\,□_{Pd,2x}$ which shows that in the phase (corresponding to the ideal composition PdAl), every Al is on an Al site, but x Pd atoms are on Al sites (1–x Pd atoms in Pd sites) and 2x Pd sites are vacant.

This type of formula may be especially useful when discussing thermodynamic properties of the phase and dealing with solid solution models and quasi-chemical equilibria between point defects.

e) *Polymorphism descriptors*

Several substances may change their crystal structure because of external conditions such as temperature and pressure. These different structures (polymorphic forms) may be distinguished by using special designators of the stability conditions. (If the various crystal structures are known, explicit structural descriptors may obviously be added). A very simple, but systematic notation has been introduced by the MSIT (see before) which in the meanwhile has been adopted worldwide (see Introduction of all volumes on "Ternary Alloys" edited by PETZOW and EFFENBERG, [1988 *et seq.*]). The different temperature modifications are indicated by lower case letters in parenthesis behind the phase designation, with (h) = high temperature modification, (r) = room temperature modification and (l) = low temperature modification; (h_1, h_2, etc. represent different high temperature modifications). In the description of a number of modifications which are stable at different temperatures, the letters are used in the sequence h_2, h_1, r, l_1, l_2,..., in correspondence to the decreasing stability temperature.

Table 2, taken from Volume 3 of the series edited by PETZOW and EFFENBERG [1988], shows a few examples of this notation. (In this case, of course, the temperature and composition ranges of stability explicitly indicated for all the phases give additional, more detailed information).

References: p. 363.

Table 2
An example of crystallochemical description of alloy system.
Binary solid phases in the Ag–Al system
(from PETZOW and EFFENBERG [1988 *et seg.*] and MASSALSKI [1990]).

Phase Trivial Name, Ideal Formula, Temperature Range (°C)	Pearson Symbol/ Prototype	Lattice Parameters (pm)	Maximum Composition Range (at% Al)
(Ag) < 961.93	cF4 Cu	a = 408.53 (23°C)	0 to 20.4 (at ≈ 450°C)
β-Ag_3Al (h) 778–605	cI2 W	a = 330.2 (700°C)	20.5 to 29.8 (at 726°C)
μ-Ag_3Al (r) < 448	cP20 β-Mn	a = 693	≈ 21 to 24
δ-Ag_2Al < 726	hP2 Mg	a = 287.1 (27at%Al) c = 466.2 a ≈ 288.5 (Al-rich c ≈ 458.2 limit)	22.9 to 41.9
(Al) < 660.45	cF4 Cu	a = 404.88 (24°C)	76.5 to 100 (at 567°C, Al-rich eutectic temperature)

In connection with this group of descriptors we may perhaps remember indicators such as (am), (vt), etc. for amorphous, vitreous substances. For instance:
SiO_2(am) amorphous silica; Si(am)H_x amorphous silicon doped with hydrogen.

3. *Crystal structure of the intermetallic phase and its representation*

3.1. Unit cell description (general remarks, lattice complexes)

The characterization of a phase requires a complete and detailed description of its structure. As examples of such a description, we may consider the data (as obtained, for instance, from X-ray diffraction experiments) reported in table 3 for stoichiometric and variable composition phases. (For an explanation of the various symbols used in the table see the International Tables of Crystallography (HAHN [1989]. See also the examples reported in chapter 1).

Following information is included in the table:
— *Crystallographic system*, that is the coordinate system (and metrical relationships between the lattice parameters of the adopted unit cell: for instance, cubic: $a = b = c$, $\alpha = \beta = \gamma = 90°$; tetragonal: $a = b \neq c$, $\alpha = \beta = \gamma = 90°$, etc.); and the specific values (in picometers) of the *unit cell dimensions*.

Table 3
Examples of crystallographic description of phase structures
(from VILLARS and CALVERT [1991]).

CsCl (stoichiometric compound);
Primitive cubic; a = 411.3 pm; space group $Pm\bar{3}m$, No. 221,
1 Cs in a): 0,0,0;
1 Cl in b): $\frac{1}{2},\frac{1}{2},\frac{1}{2}$;
(The two special a) and b) Wyckoff positions have no free coordinate parameter.) The two occupancy parameters are 100%.

Mg_2Ge (stoichiometric compound):
Face-centered cubic; a = 638.7 pm; space group $Fm\bar{3}m$, N. 225,
Equivalent positions (0,0,0; $0,\frac{1}{2},\frac{1}{2}$; $\frac{1}{2},0,\frac{1}{2}$; $\frac{1}{2},\frac{1}{2},0$) +
4 Ge in a): 0,0,0
8 Mg in c): $\frac{1}{4},\frac{1}{4},\frac{1}{4}$; $\frac{1}{4},\frac{1}{4},\frac{3}{4}$
(No free parameters in the atomic positions of Mg and Ge. In this case the two occupancy parameters have been found to be 100%.)

$MoSi_2$ (nearly stoichiometric compound):
body-centered tetragonal; a = 319.6 to 320.8 pm and c = 787.1 to 790.0 pm, according to the composition; space group I4/mmm, No. 139,
Equivalent positions (0,0,0; $\frac{1}{2},\frac{1}{2},\frac{1}{2}$) +
2 Mo in a): 0,0,0
4 Si in e): 0,0,z; 0,0,−z ; z = 0.333
(The Si position has the free parameter z, for which, in this particular case, the value 0.333 has been determined; the two occupancy parameters are 100%.)

≈ Ce_2NiSi_3 (disordered structure):
hexagonal; a = 406.1 to 407.1 pm; c = 414.9 to 420.2 pm; space group P6/mmm, N. 191
1 Ce in a): 0,0,0,
2 (Ni + Si) (in a ratio 1:3) in d): $\frac{1}{3},\frac{2}{3},\frac{1}{2}$; $\frac{2}{3},\frac{1}{3},\frac{1}{2}$;
(In this case the atomic sites corresponding to the d) Wyckoff position are randomly occupied by Ni and Si atoms in the given ratio and the overall composition correspond to 1Ce + 2 × (0.25 Ni + 0.75Si)).

$Cr_{12}P_7$ (simple structure showing partially occupied sites):
hexagonal; a = 898.1 pm; c = 331.3 pm; space group $P6_3/m$, No. 176.
2 P in a): $0,0,\frac{1}{4}$; $0,0,\frac{3}{4}$; (occupancy 50%)
6 P in h): $x,y,\frac{1}{4}$; $-y,x-y,\frac{1}{4}$; $-x+y,-x,\frac{1}{4}$; $-x,-y,\frac{3}{4}$; $y,-x+y,\frac{3}{4}$; $x-y,x,\frac{3}{4}$ (x= 0.2851, y = 0.4462); (occupancy 100%)
6 Cr in h): $x,y,\frac{1}{4}$; $-y,x-y,\frac{1}{4}$; $-x+y,-x,\frac{1}{4}$; $-x,-y,\frac{3}{4}$; $y,-x+y,\frac{3}{4}$; $x-y,x,\frac{3}{4}$ (x= 0.5109, y = 0.3740); (occupancy 100%)
6 Cr in h): $x,y,\frac{1}{4}$; $-y,x-y,\frac{1}{4}$; $-x+y,-x,\frac{1}{4}$; $-x,-y,\frac{3}{4}$; $y,-x+y,\frac{3}{4}$; $x-y,x,\frac{3}{4}$ (x= 0.2108, y = 0.0144); (occupancy 50%)
6 Cr in h): $x,y,\frac{1}{4}$; $-y,x-y,\frac{1}{4}$; $-x+y,-x,\frac{1}{4}$; $-x,-y,\frac{3}{4}$; $y,-x+y,\frac{3}{4}$; $x-y,x,\frac{3}{4}$ (x= 0.2638, y = 0.0137); (occupancy 50%)

In this case several groups of atoms have the same type of Wyckoff positions: the h) position which has free parameters. These, of course, have different values for the different groups of atoms. The parameter values experimentally determined in this case for each atom group are reported.

The partial occupancies found for the different positions are also reported. In this case in the a) Wyckoff position, for instance, only half of the sites are randomly occupied by P atoms; the others are vacant. The total number of atoms in the unit cell is: P: 0.5×2 + 6 = 7; Cr: 6 + 0.5×6 + 0.5×6 = 12.

— Bravais point lattice and *space group* (this describes the spatial symmetry of the structure on a microscopic (atomic) level, and is represented by means of the Hermann–Mauguin symbol, composed by a letter representing the lattice type (P = primitive, I = body centered, etc., see table 4) followed by the symbols of the symmetry elements

Table 4
Pearson Symbols

System symbol	Lattice symbol
a triclinic (anorthic)	**P** primitive
m monoclinic	**I** body centred
o orthorhombic	**F** all-face centred
t tetragonal	**C** side face centred *
h hexagonal (and trigonal and rhombohedral)	**R** rhombohedral
c cubic	

* Instead of **C**, in the future, the symbol **S** will probably be adopted according to the recommendation of the International Union of Crystallography.

ordered according to their positions relative to the axes (for instance $Pm\bar{3}m$ is the symbol of the space group of the CsCl structure).

As usual, the space group is also identified by the *serial number* (221 for $Pm\bar{3}m$) reported in several compilations such as the "International Tables" which is the fundamental reference book for crystallography (HAHN [1989]).

A *list* of the *atoms* contained in the unit cell and their *coordinates* (fractional coordinates related to the adopted system and unit cell edges) are then reported. These are usually presented in a format as *M El in n: x,y,z*. In the $MoSi_2$ structure, also reported in table 3, we have, for instance, four silicon atoms (that is: M El = 4 Si) in the position set coded as *e* and corresponding to the 4 coordinate triplets 0,0,0; 0,0,z; $\frac{1}{2},\frac{1}{2},\frac{1}{2}+z$; $\frac{1}{2},\frac{1}{2},\frac{1}{2}-z$. Such entries correspond to the so-called *Wyckoff positions* characterized by a well-defined site symmetry and by a *multiplicity M*. For each Wyckoff position M, is the number of equivalent points (positions) in the unit cell with the same site symmetry. The highest multiplicity M_{max} of the given space group corresponds to the lowest site symmetry (each point is mapped onto itself only by the "identity operation"). This is the "*general position*": the coordinate triplets of the M_{max} sites include the reference triplet indicated as x,y,z (having *three variable parameters*). In a given space group, moreover, it is possible to have several *special positions*. In this case points are considered which are located on symmetry elements (without translations) or at the intersection of several such symmetry elements. Each point will be mapped onto itself by at least one of these symmetry operations: we will have as a consequence a reduction in the number of different equivalent points in the unit cell generated by all the characteristic symmetry operations. The multiplicity of these positions will be lower than M_{max} (M in a special position is a divisor of that of the general position). We may also say that specific costraints are imposed on the coordinates of each point of a special position leading to triplets such as x,y,0 (that is z = 0) or x,x,z (that is x = y), with two variable parameters, or $x,\frac{1}{2},\frac{1}{2}$ or x,x,0 (with one variable parameter) or 0,0,0 or $\frac{1}{2},\frac{1}{2},0$ (with no variable parameter). In the International Tables of Crystallography, for each of the 230 space groups, the list of all the positions is reported. For each of the positions (the general and the special ones) the coordinate triplets of the equivalent points are also given. The different positions are coded by means of the Wyckoff letter, ***a***, ***b***, ***c***, etc., starting with ***a*** for the position with the lowest multiplicity and continuing in alphabetical order up to the general position.

In the examples reported in table 3 it is also shown that for the positions with *free parameters* the specific values of the parameters themselves have to be experimentally determined in order to present a complete description of the structure.

Notice that, for instance, in the case of the $MoSi_2$ structure the different atomic positions in the unit cell are the following: 2 Mo in 0,0,0, and in $\frac{1}{2},\frac{1}{2},\frac{1}{2}$ and 4 Si in 0,0,z; in 0,0,−z; in $\frac{1}{2},\frac{1}{2}$, $\frac{1}{2}+z$ and in $\frac{1}{2},\frac{1}{2},\frac{1}{2}-z$ (corresponding, on the basis of the experimental value z=0.333, to 0,0,0.333; 0,0,0.667; $\frac{1}{2},\frac{1}{2}$,0.833; $\frac{1}{2},\frac{1}{2}$,0.167). These positions have been described, according to the International Tables of Crystallography conventions, explicitly indicating the centring translations $(0,0,0;\ \frac{1}{2},\frac{1}{2},\frac{1}{2})+$ before the coordinate triplets. The symbol + means that, in order to obtain the complete Wyckoff position the components of these centring translations have to be added to each of the listed triplets.

A similar presentation has been used for the Mg_2Ge structure description. Notice that the coordinates are formulated modulo 1: thus, for instance, −x,−y,−z is written rather than 1−x,1−y,1−z.

Finally, in the table, some more examples are reported as an introduction to more complex, partially disordered structures (random distribution of different atom types in the same positions, partially occupancy of certain positions).

Considering now the simple structure of CsCl as an example we see that the "crystallographic description" reported in table 3 corresponds to the atom arrangement presented (with alternative representations) in fig. 3 and, in more details, in sec. 6.1.2).

More generally, we may say that, from descriptions, such as those reported in table 3, the interatomic distances may be computed and, consequently, the coordinations and grouping of the various atoms may be derived: an example of this computation will be presented in sec. 3.5.5. (A systematic listing of the crystal data relevant to all the known phases has been reported in a number of fundamental reference books such as (PEARSON [1967], LANDOLT–BÖRNSTEIN [1971], VILLARS–CALVERT [1985], VILLARS–CALVERT [1991], etc).

For the criteria to be followed, especially when complex structures are involved, in the preparation and presentation of coordinate lists see PARTHE and GELATO [1984]. Their paper describes a proposal for a standardized presentation of inorganic crystal structure data with the aim of recognizing identical (or nearly identical) structures from the similarity of the numerical values of the atom coordinates. Different, equivalent (but not easily recognizable) descriptions could, in fact, be obtained by shift of origin of the coordinate system, rotation of the coordinate system, inversion of the basis vector triplet. (See also PARTHE *et al.* [1993]).

A description which in some simple cases could in a way be considered alternative to those exemplified in table 3 is based on the *lattice complex concept.* (Listing the symbols of the lattice complexes occupied by the different atoms in a structure, for instance, symbol P for the point 0,0,0, and its equivalent points, provides in fact a means of describing and classifying structures. This may be especially convenient for relatively simple structures particularly in the cubic system).

A *lattice complex* may be defined as an arrangement of equivalent points that are related by space group symmetry operations including lattice translations (PEARSON [1972]). The same lattice complex may occur in different space group types and may have more than one location in regard to a chosen origin for the unit cell. The number

References: p. 363.

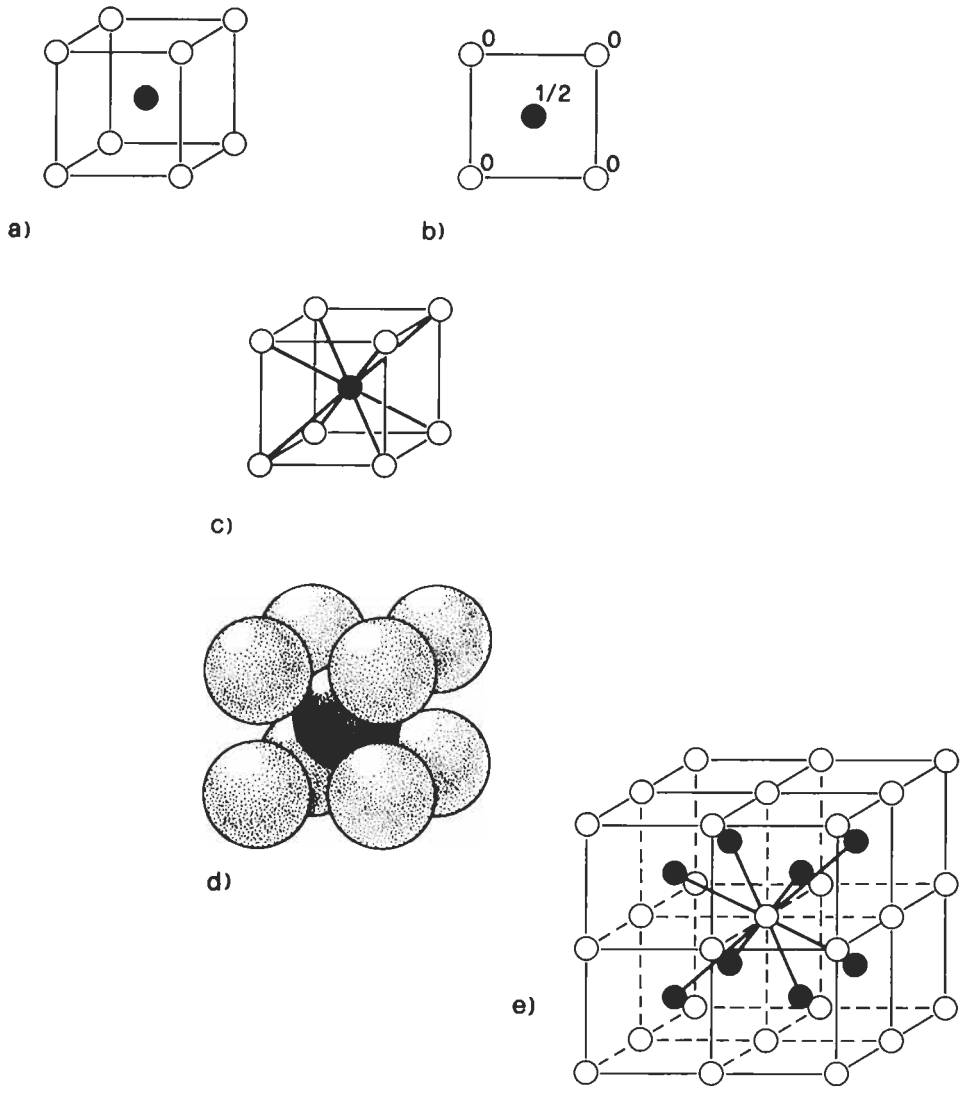

Fig. 3. Alternative representations of the unit cell of the CsCl compound. The two types of atoms are represented by means of the differently coloured spheres.

a) the positions of the centers of the atoms in the unit cell are indicated.
b) projection of the unit cell on the base plane. The values of the 3rd (vertical) coordinate are given.
c) the shortest interatomic distances are presented.
d) packed spheres model.
e) a group of 8 cells is represented in order to show that the actual structure of CsCl corresponds to a three-dimensional infinite repetition of unit cells. Notice the coordination around the white atom; it is similar to that around the black atom shown in c).

of *degrees of freedom* of a lattice complex, normally, is the same as that of any of its Wyckoff positions and is the number of coordinate (free) parameters x,y,z, that can vary independently. According to its number of degrees of freedom a lattice complex is called invariant, uni-, bi-, or trivariant.

The *invariant lattice complexes* in their characteristic Wyckoff positions are represented mainly by capital letters. Those with equipoints at the nodes of the Bravais lattice are designated by their appropriate lattice symbols. (Lattice complexes, from different crystal families that have the same coordinate description for their characteristic Wyckoff positions, receive the same symbol: for instance, lattice complex P corresponding to coordinate 0,0,0. In such a case, unless it is obvious from the context which lattice is meant, the crystal family may be stated by a small letter, preceding the lattice-complex symbol as follows: c = cubic, t = tetragonal, h = hexagonal, o = orthorhombic, m = monoclinic, a = anorthic = triclinic). Other invariant complexes are designated by letters that recall some structural features of a given complex, for instance D from the diamond structure, E from the hexagonal close-packing. Examples of two-dimensional invariant complexes are G (from graphite layer) and N (from kagomé net). (See table 4 and sec. 3.5.2.)

A short list of invariant lattice complex symbols is reported in the following. (For a complete list, for a more systematic description and formal definition, see chapter 14, Vol. A, of the International Tables of Crystallography, HAHN [1989]).

— *Lattice complex P*: (multiplicity, that is the number of equivalent points in the unit cell, 1);
coordinates 0,0,0;
(crystal families: c, t, h, o, m, a).
— *Lattice complex I*: (multiplicity 2);
coordinates 0,0,0; $\frac{1}{2},\frac{1}{2},\frac{1}{2}$;
(crystal families: c, t, o).
— *Lattice complex J*: (multiplicity 3);
coordinates $0,\frac{1}{2},\frac{1}{2}$; $\frac{1}{2},0,\frac{1}{2}$; $\frac{1}{2},\frac{1}{2},0$;
(crystal families: c).
— *Lattice complex F*: (multiplicity 4);
coordinates 0,0,0; $0,\frac{1}{2},\frac{1}{2}$; $\frac{1}{2},0,\frac{1}{2}$; $\frac{1}{2},\frac{1}{2},0$;
(crystal families: c, o).
— *Lattice complex D*: (multiplicity 8);
(D from "Diamond", see sec. 6.3.1)
coordinates 0,0,0; $\frac{1}{2},\frac{1}{2},0$; $\frac{1}{2},0,\frac{1}{2}$; $0,\frac{1}{2},\frac{1}{2}$; $\frac{1}{4},\frac{1}{4},\frac{1}{4}$; $\frac{3}{4},\frac{3}{4},\frac{1}{4}$; $\frac{3}{4},\frac{1}{4},\frac{3}{4}$; $\frac{1}{4},\frac{3}{4},\frac{3}{4}$;
(crystal families: c, o).
— *Lattice complex E*: (multiplicity 2);
coordinates $\frac{1}{3},\frac{2}{3},\frac{1}{4}$; $\frac{2}{3},\frac{1}{3},\frac{3}{4}$;
(crystal families: h).

— *Lattice complex G*: (multiplicity 2);
(G fom "Graphite" layer, see sec. 6.3.4).
coordinates $\frac{1}{3},\frac{2}{3},0$; $\frac{2}{3},\frac{1}{3},0$;
(crystal families: h).
— *Lattice complex R*: (multiplicity 3);
coordinates 0,0,0; $\frac{1}{3},\frac{2}{3},\frac{2}{3}$; $\frac{2}{3},\frac{1}{3},\frac{1}{3}$;
(crystal families: h).

The coordinates indicated in the reported (partial) list of invariant lattice complexes correspond to the so called "standard setting". Some of the non-standard settings of an invariant lattice complex may be described by a shifting vector (defined in terms of fractional coordinates) in front of the symbol. The most common shifting vectors have also abbreviated symbols: P′ represents $\frac{1}{2}\ \frac{1}{2}\ \frac{1}{2}$ P (coordinates $\frac{1}{2},\frac{1}{2},\frac{1}{2}$), J′ represents $\frac{1}{2}\ \frac{1}{2}\ \frac{1}{2}$ J (coordinates $\frac{1}{2},0,0,$; $0,\frac{1}{2},0$; $0,0,\frac{1}{2}$); F″ represents $\frac{1}{4}\ \frac{1}{4}\ \frac{1}{4}$ F (coordinates $\frac{1}{4},\frac{1}{4},\frac{1}{4}$; $\frac{1}{4},\frac{3}{4},\frac{3}{4}$; $\frac{3}{4},\frac{1}{4},\frac{3}{4}$; $\frac{3}{4},\frac{3}{4},\frac{1}{4}$) and F‴ represents $\frac{3}{4}\ \frac{3}{4}\ \frac{3}{4}$ F. (The following notation is also used J∗ = J + J′ (complex of multiplicity 6). It can be seen, moreover, that the complex D corresponds to the coordinates F + F″.

Simple examples of structure descriptions in terms of combination of invariant lattice complexes, may be: **Cs**Cl type **P** + P′ (Cs in 0,0,0; Cl in $\frac{1}{2},\frac{1}{2},\frac{1}{2}$), see table 3 and sec. 6.1.2.; **Na**Cl type structure: **F** + F′, see sec. 6.4.1; **Zn**S type structure: **F** + F″, see sec. 6.3.2.; **Na**Tl type structure: **D** + D′, see sec. 6.1.4.

Such combination of, original or transformed, invariant lattice complexes, are also indicated as *connection patterns* or *construction patterns* or *frameworks* (or *Bauverbände* in the German literature, according to LAVES [1930]). These patterns are *homogeneous* if they may be described by the parameters of one point position, *heterogeneous* if, for their description, the parameters of two or more independent point positions are necessary. This terminology may give a short informative description of the crystal structure and is specially useful for cubic substances. (For its use in a systematic description and classification of cubic structures see HELLNER [1979]). For non-invariant complexes and/or in crystal systems with symmetry lower than cubic, the geometrical configuration of the complex (and the coordination) may change significantly with free parameter value and with axial ratios and angles between the crystal axes.

3.2. Structural types

Several intermetallic phases are known which have the same (or a similar) stoichiometry and crystallize in the same crystal system and space group with the same occupied point positions.

Such compounds are considered as belonging to the same structure type. The reference to the structure type may be a simpler and more convenient way of describing the structure of the specific phase. The *structure type is generally named after the formula of the first representative* identified: the "*prototype*". Trivial names and symbols are also used in some cases (see sec. 3.4.).

The various representatives of a specific structure type generally have different unit cell edges, different values of the occupancy parameters and of the free coordinates of

the atomic positions and, in the same atomic positions, different atoms (see, for instance, sec. 3.5.5.).

If these differences are small, we may consider the general pattern of the structure unaltered.

On the other hand, of course, if these differences become larger, it might be more convenient to describe the situation in terms of a "family", instead of a single structural type, of different (more or less strictly interrelated) structural (sub) types. According to PARTHE and GELATO [1984], some structures may not really be *isotypic* but only *isopointal*, which means that they have the same space group and the same occupation of Wyckoff positions with the same adjustable parameters but *different unit-cell ratios* and *different atom coordinations* (and/or different values of Wyckoff free parameters).

An interesting example may be given by the structures of $MoSi_2$, reported in table 3, and CaC_2. In this compound, Ca and C are respectively in the same positions as Mo and Si in the same space group I4/mmm:
2 Ca in a): 0,0,0; $\frac{1}{2},\frac{1}{2},\frac{1}{2}$;
4 C in e): 0,0,z; 0,0,$-$z; $\frac{1}{2},\frac{1}{2},\frac{1}{2}+z$; $\frac{1}{2},\frac{1}{2},\frac{1}{2}-z$.
The unit cell dimensions, however, correspond to a = 388 pm, c = 638 pm (c/a = 1.644 instead of 2.463 as in $MoSi_2$) and the free parameter z has the value 0.4068 (instead of 0.333). These differences result in two different space arrangements (see fig. 4). Diatomic groups, such as C_2, clearly evident in CaC_2 (and in a number of isostructural dicarbides and peroxides) are not formed in $MoSi_2$.

Very interesting general comments and definitions on this question have been proposed, for instance, by PEARSON [1972], and more recently by LIMA DE FARIA *et al.* [1990] According to these authors, two structures are *isoconfigurational* (configurationally isotypic) if they are isopointal and are similar with respect to the corresponding Wyckoff positions and their geometrical interrelationships (same or similar positional coordinates, same or similar values of the unit cell axial ratios, c/a, a/b, b/c and cell angles α, β, γ).

Isotypism is found particularly with inorganic compounds. This behaviour has been discussed by PARTHE *et al.* [1993]. It has been underlined that to explain why two compounds adopt the same atom arrangement is not always simple. Following examples have been presented:
— The isotypism of $Gd_4Ni_6Al_{23}$ and $Y_4Ni_6Al_{23}$ may be easily explained because Gd and Y (elements of the same group of the Periodic Table) have comparable electron configuration and nearly the same atomic dimensions.
— Li_2SiO_3 and $LiSi_2N_3$ are isotypic (even if not in a rigorous sense owing to slightly different distorsions of the coordination polyhedra). They adopt an adamantine structure type (see sec. 6.3. and 7.2.1.) for which particular values of the electron concentration may be relevant even if obtained with elements from different parts of the Periodic Table.
— GdNi and NiB represent another couple of isotypic compounds. The role (the position in the crystal structure), however, of the same atom, Ni, in the two compounds is exchanged. In NiB, the Ni atoms are those centring the trigonal prism (formed by Gd atoms). A reason for the existence of this structure type could possibly be related to the

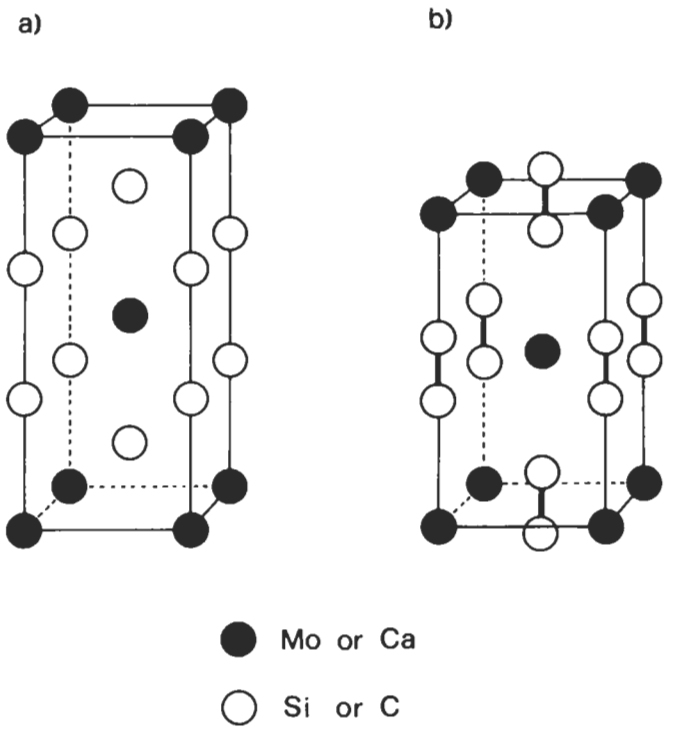

Fig. 4. $MoSi_2$ (a) and CaC_2 (b) type structures: an example of isopointal structures. Notice that, due to the different values of the c/a ratios and of the z parameters, there are different coordinations and atomic groupings (formation in CaC_2 of C–C, dumb-bell, discrete groups).

atomic size difference of the elements involved (or, perhaps, to their relative position in Pettifor's chemical scale).

— The last (and most intriguing) example reported by PARTHE *et al.* [1993] is the couple of compounds $Pu_{31}Rh_{20}$ and $Ca_{31}Sn_{20}$. For the present, the isotypism of these compounds of unusual stoichiometry cannot be expected and explained.

As a conclusion to these comments, we may mention that two structures are defined *crystal-chemically isotypic* if they are isoconfigurational and the corresponding atoms (and bonds) have similar chemical/physical characteristics.

Those interested in these concepts and in their historical development may refer also to a contribution by LAVES [1944], translated and reported by HELLNER [1979]. Conditions to be defined for calling crystal structures "equal" (isotypism), "similar" (homeotypism) or "different" (heterotypism) were suggested, discussed and exemplified.

We have finally to observe that, when considering phases having certain polar characteristics (salt-like "bonding"), the concept *type* and *antitype* may be useful. Antitypic phases have the same site occupations as the typic ones, but with the cation-anion positions exchanged (or more generally some important physical/chemical

characteristics of the corresponding atoms interchanged). As examples the structure types CaF_2 and CdI_2 and their antitypes reported in sec. 6.4.2. and 6.5.2. may be considered. Notice, however, that for a structure such as the CsCl type, it does not matter whether we describe it as 1 Cs in 0,0,0 and 1 Cl in $\frac{1}{2},\frac{1}{2},\frac{1}{2}$, or as 1 Cs in $\frac{1}{2},\frac{1}{2},\frac{1}{2}$, and 1 Cl in 0,0,0. In this case the two descriptions are undistinguishable (see fig. 3): they correspond to a mere shift of the origin of the reference axes. The CsCl type is its *own antitype*. Similar considerations are valid also for other structures such as the NaCl, ZnS types, etc.

3.3. Unit cell Pearson symbol

The use of the so-called Pearson notation (PEARSON, [1972]) is highly recommended (IUPAC, LEIGH [1990], "Ternary Alloys", PETZOW and EFFENBERG [1988 *et seg.*]) for the construction of a compact symbolic representation of the structure of the phase. As far as possible, it should be completed by a more detailed structural description by using the prototype formula which defines (as previously mentioned) a certain structure type.

The Pearson symbol is composed of a sequence of two letters and a number. The first (small) letter corresponds to the crystal system of the structure type involved; the second (capital) letter represents the lattice type (see table 4). The symbol is completed by the number of the atoms in the unit cell. A symbol as tP10, for example, represents a structure type (or a group of structure types) corresponding to 10 atoms in a primitive tetragonal cell.

In this chapter, the Pearson symbol will be used throughout; the convention has been adopted indicating in every case the number of atoms contained in the chosen unit cell. *In the case*, therefore, *of rhombohedral substances* for which the data of the (triple primitive) hexagonal cell are generally reported, the number of atoms is given which is in the hexagonal cell and *not* the number of atoms in the equivalent rhombohedral cell (FERRO and GIRGIS [1990]). So, for instance, at variance with VILLARS and CALVERT [1985, 1991], hR9 (and not rP3 or hR3) for the Sm-type structure.

If the structure is not known exactly, the prototype indication cannot be added to the Pearson symbol. In some cases, moreover, only incomplete Pearson symbols (such as o?60, cF?, etc.) can be used.

A criterion similar to Pearson's for the unit cell designation was used by SCHUBERT [1964] in his detailed and systematic description of the structural types of the intermetallic phases and of their classification.

A slightly more detailed notation, moreover, for the unit cell of a given structure has been suggested by FREVEL [1985]. Four items of information are coded in Frevel's notation:
— the number of different elements contained in the compound,
— the total number of atoms given by the chemical formula,
— the appropriate space group expressed in the HERMANN–MAUGUIN notation and
— the number of formulae for unit cell.
The notation for the CaF_2 structure, for instance, is:
2,3 $Fm\bar{3}m$ (4).

Possible augmentation of the notation has been discussed by Frevel and its use for classification and cataloguing the different crystal structures suggested.

References: p. 363.

According to PARTHE *et al.* [1993], a standardization procedure is at first necessary in the presentation of the relevant data characteristic of a crystal structure (see also PARTHE and GELATO [1984]). A convenient description of the structure types is then possible using the "*Wyckoff sequence*" (the letters of the occupied Wyckoff sites). This allows a finer classification of structure types and offers suggestions not only for recognizing isotypic structures but also possible structural relationships (substitution, formation of vacancy or filled-in structure variants).

3.4. Structure trivial names and symbols

A number of trivial names and symbols have been used (and are still in use) both as indicators, of a single phase in specific systems or as descriptors of certain structural types (or of families of different interrelated structural types).

Among the trivial symbols, we may mention the use of Greek (and Roman) letters to denote phases. These have often been used to indicate actual phases in specific systems, for instance in a given binary system, phase α, β, γ, etc., in alphabetical order according to the increasing composition from one component to the other, while in a unary system the α, β, etc., symbols have often been used to denote different allotropic forms.

Obviously this notation (or other similar ones such as τ_1, τ_2, τ_3, denoting "1st", "2nd", etc., phase) may be useful as a quick reference code while discussing and comparing phase properties of alloys in a single specific system, but in general cannot be used as a rational criterion for denoting structural types. In a few cases, however, certain Greek (and Roman) letters have assumed a more general meaning (as symbols of groups of similar phases): for instance, the name "γ-phases" which is an abbreviation of a sentence such as phases having the γ-brass (the γ-Cu–Zn) type structure. A short list, taken from LANDOLT–BÖRNSTEIN [1971], of (Greek and Roman) letters which have also been used as descriptors of structural types, may be the following:

γ : γ-brass type or similar structures
ε : Mg type
ζ : Mg type
η : W_3Fe_3C or Ti_2Ni type
μ : W_6Fe_7 type
σ : σ phase or σ-CrFe type
χ : α-Mn or Ti_5Re_{24} type
ω : ω_2 -(Cr,Ti) type (similar to the AlB_2 type)
E : $PbCl_2$ or Co_2Si type
G : G phase, Th_6Mn_{23} or $Cu_{16}Mg_6Si_7$
P : P phase or P-(Cr, Mo, Ni)
R : R phase or R-(Co, Cr, Mo)
T_1 : W_5Si_3 type
T_2 : Cr_5B_3 type

In a number of cases, names of scientists are used as descriptors. We may mention the following groups of structures (some of which will be described in more detail later).

Chevrel phases. A group of compounds having a general formula such as $M_xMo_3S_4$

(M = Ag, As, Ca, Cd, Zn, Cu, Mn, Cr, etc.). Many representatives of these structure types are superconducting with critical T_c as high as 10–15 K.

Frank–Kasper phases. (For all of which the structure can be described as composed of a collection of distorted tetrahedra which fill the space: see sec. 6.6). This family of phases includes those of the structural types: *Laves phases* (a family of polytypic structures including the hP12–$MgZn_2$, cF24–Cu_2Mg and hP24–Ni_2Mg types), *tP30 σ–phases*, *oP56–P phases* and *hR39–W_6Fe_7 type phases*.

Hägg phases. According to HÄGG [1931], a number of compounds of the transition metals with small non-metal atoms (H, B, C, N) have structures which can be described as "*interstitial*". These correspond, generally, to a simple structures in which the small non metal atoms occupy interstices in a face centered cubic or body centered cubic framework of metal atoms or, the interstices in other close packed structures. In the Hägg interstitial phases the relative atomic size of the two elements is of particular importance to the stability of the structure.
See sec. 6.2.2. for a classification of the interstices ("holes") in close packed structures, sec. 6.4.1. for NaCl-type related phases and sec. 6.5.5. for WC-type phases.

Heusler phases. Magnetic compounds of the cF16–$MnCu_2Al$-type. (See sec. 6.1.3. on this structure which can be considered "derivative" of the CsCl type).

Hume–Rothery phases. These designations can be connected to the research carried out as far back as 1926 by HUME–ROTHERY, WESTGREN and PHRAGMEN, etc. They observed that several compounds (electron compounds) crystallize in the same structural type if they have the average number of valence electrons per atom (the so-called VEC: valence electron concentration) included within certain well-defined ranges. Some groups of these phases (brasses, etc.) will be presented in sec. 6.1.5. and 7.2.2. (See also ch. 3, § 8.1.)

Nowotny phases. Chimney-ladder phases (see sec. 4.4.).

Samson phases. Complex intermetallic structures with giant unit cells, based on framework of fused truncated tetrahedra (see sec. 6.6.5.)

Zintl phases. This term was first applied to the binary compounds formed between the alkali or alkaline-earth elements and the main group elements from group 14 on, that is to the right of the "Zintl boundary" of the Periodic Table. These combinations not only yield some Zintl anions (homopolyatomic anions) in solution but also produce many rather polar or salt-like phases. A simple example may be a classical valence compound in which the more "noble" member achieves a filled "octet" and an 8–N oxidation state in salt-like structure (for example Na_3As, Mg_2Sn) (CORBETT [1985]). An important intermetallic structure discovered by Zintl (ZINTL and WOLTERSDORF [1935]) was that of the cF16–NaTl-type (superstructure of the bcc lattice, see sec. 6.1.4.). The Na and Tl atoms are arranged according to two (interpenetrating) diamond type sublattices; each atom is tetrahedrally coordinated by four like neighbours on the same sublattice and has four unlike neighbours on the other sublattice. This could be interpreted as a Tl^- array, isoelectronic with carbon in the limit of complete charge transfer. For a critical discussion on the NaTl-type structure, its stability, the role of the size factor, the comparative trend of the stabilities of CsCl and NaTl type structures, the application of modern

band-structure techniques, see HAFNER [1989]. Subsequent applications of the term "Zintl Phases" have been based on the structural characteristic of such polar phases. A review on this subject has been published by CORBETT [1985]. In this paper several phases are mentioned: starting from compounds such as hR18–$CaSi_2$ (containing rumple double layers of Si atoms resembling those of the As structure), mP32–NaGe and mC32–NaSi (respectively containing Ge, or Si atom, tetrahedra with the Na atoms arranged in the intervening spaces), up to complex alkali metal-gallium compounds exhibiting complex structures containing large interconnected usually empty gallium polyhedra, reminiscent of boron chemistry. It may be added that the concept of Zintl ions has been used also in the description of selected liquid alloys. It was proposed (VAN DER LUGT and GEERTSMA [1984], REIJERS *et al.* [1990]) that in the equiatomic liquid alkali alloys with Sn and Pb the liquid consists of poly-anion clusters, such as Pb_4^{4-} tetrahedra, formed by covalent bonding which are separated by alkali ions.

Within the group of trivial names we may also include a few "*personal*" *names* such as *austenite* (solid solution of C in γ-Fe), *ferrite* (solid solution of C in α-Fe), *martensite* (see sec. 6.1.5.), etc., and a few *mineralogical names* such as pyrite, blende, cinnabar, etc. According to the IUPAC recommendations (LEIGH [1990]), mineralogical names should be used to designate actual minerals and not to define chemical composition. They may, however, be used to indicate a structure type. They should be accompanied by a representative chemical formula:
cF8–ZnS sphalerite, hP4–ZnS wurtzite, cF8–NaCl rock salt, cP12–FeS_2 pyrite, etc.

In closing this section we have to mention the *Strukturbericht designation* adopted from pre-war time by the editors of the Strukturbericht publications (and later Structure Reports) in abstracting crystal-structure determination. This designation is no longer recommended by the International Union of Pure and Applied Chemistry, but it is still used.

According to this designation, each structure type is represented by a symbol generally composed of a letter (**A**, **B**, **C**,etc.) and a number (possibly in some cases followed by a third character). The letter was related to the stoichiometry according to the following form: **A**: unary phases (or believed to be unary), **B**: binary compounds having 1:1 stoichiometry, **C**: binary 1:2 compounds, **D**: binary m:n compounds, **E**...**K** types: more complex compounds; **L**: alloys, **O**: organic compounds and **S**: silicates.

In every class of stoichiometries, the different types of structures were distinguished by a number and/or a letter. (For instance, in the element class the frequently encountered fcc structure, cF4–Cu-type, was called A1, in the 1:1 group the common cF8–NaCl type was represented by B1, etc.). Equivalence tables between the Strukturbericht designation and the Pearson symbol-prototype may be found in PEARSON [1972], MASSALSKI [1990].

The following is a partial list of these old *Strukturbericht symbols* for some types frequently occurring in metallic systems:

A1: cF4–Cu; **A2**: cI2–W; **A3**: hP2–Mg; **A3'**: hP4–αLa; **A4**: cF8–C (diamond); **A5**: tI4–βSn; **A6**: tI2–In; **A7**: hR6–αAs;...; **A9**: hP4–C (graphite);...; **A12**: cI58–αMn; ... ; **A15**: cP8–Cr_3Si; ....The A15 structure was previously considered to be that of a W

modification (and therefore a unary structure): later on the substance concerned was recognized to be a W oxide: W_3O (isostructural with Cr_3Si); ...; $\mathbf{A_b}$: tP30–βU;...; $\mathbf{A_h}$: cP1–αPo;...; $\mathbf{A_i}$: hR3–βPo; ...

B1: cF8–NaCl; **B2**: cP2–CsCl; **B3**: cF8–ZnS (sphalerite or zinc blende); **B4**: hP4–ZnS (wurtzite);...; $\mathbf{B8_1}$: hP4–NiAs; $\mathbf{B8_2}$: hP6–Ni_2In; ... ; **B11**: tP4–γCuTi;...; **B19**: oP4–AuCd; **B20**: cP8–FeSi; ... ; **B27**: oP8–FeB;...; **B31**: oP8–MnP; **B32**: cF16–NaTl; ...; **B35**: hP6–CoSn;...; $\mathbf{B_a}$: cI16–UCo;...; $\mathbf{B_f}$: oC8–CrB;...; $\mathbf{B_h}$: hP2–WC;...; $\mathbf{B_i}$: hP8–TiAs;...

C1: cF12–CaF_2; $\mathbf{C1_b}$: cF12–AgMgAs; **C2**: cP12–FeS_2 (pyrite); ... ; $\mathbf{C11_a}$: tI6–CaC_2; $\mathbf{C11_b}$: tI6–$MoSi_2$, (the two $\mathbf{C11_a}$ and $\mathbf{C11_b}$ structures are closely interrelated, see fig. 4); ...; **C14**: hP12–$MgZn_2$; **C15**: cF24–Cu_2Mg; $\mathbf{C15_h}$: cF24–$AuBe_5$ (this structure is a derivative structure of the cF24–Cu_2Mg, C15 type, see figs. 42 and 44); **C16**: tI12–$CuAl_2$; ...; **C22**: hP9–Fe_2P;...; **C32**: hP3–AlB_2; ...; **C36**: hP24–Ni_2Mg; ...; **C38**: tP6–Cu_2Sb;...; $\mathbf{C_a}$: hP18–$NiMg_2$; $\mathbf{C_b}$: oF48–$CuMg_2$; $\mathbf{C_c}$: tI12–$ThSi_2$;...

$\mathbf{D0_2}$: cI32–$CoAs_3$; ... ; $\mathbf{D0_{18}}$: hP8–Na_3As; ... ; $\mathbf{D1_a}$: tI10–$MoNi_4$; $\mathbf{D1_b}$: oI20–UAl_4;...; $\mathbf{D1_3}$: tI10–$BaAl_4$;...; $\mathbf{D2_b}$: tI26–$ThMn_{12}$;...; $\mathbf{D8_1}$: cI52–Fe_3Zn_{10}; $\mathbf{D8_2}$: cI52–Cu_5Zn_8; $\mathbf{D8_3}$: cP52–Cu_9Al_4; $\mathbf{D8_4}$: cF116–$Cr_{23}C_6$; ...

$\mathbf{E1_a}$: oC16–$MgCuAl_2$;...;$\mathbf{E9_a}$: tP40–$FeCu_2Al_7$;..

$\mathbf{H2_4}$: cP8–Cu_3VS_4;..

$\mathbf{L1_0}$: tP2–AuCu (I); $\mathbf{L1_2}$: cP4–$AuCu_3$; $\mathbf{L2_1}$: cF16–$MnCu_2Al$; $\mathbf{L1_a}$: cF32–$CuPt_3$;...; $\mathbf{L2_a}$: tP2–δCuTi;...; $\mathbf{L6_0}$: tP4–$CuTi_3$.

3.5. Rational crystal structure formulae

We know that all of the requisite structural information for a solid phase is contained (either explicitly or implicitly) in its unit cell and this can be obtained from the Pearson symbol-prototype notation (complemented, if necessary, by data on the values of lattice parameters, atomic positions, etc.). A number of features, however, which are especially relevant for chemical-physical considerations, such as local coordination geometries, the existence of clusters, chains or layers, etc., are not self-evident in the aforementioned structural descriptions and can be deduced only by means of a more or less complicated series of calculations. It should, moreover, be pointed out that the same structure can be differently viewed and described (FRANZEN [1986], PARTHE and GELATO [1984]). The simple rock-salt structure, for instance, (see sec. 6.4.1.) can be viewed as cubic close packed anions with cations in octahedral holes, as XY_6 octahedra sharing edges, as a stacking sequence of superimposed alternate triangular nets respectively of X and Y atoms or as a cubic-close packed structure of a metal with non-metals in octahedral interstices. As a further example we may consider the Cu structure which, for instance, could be conveniently compared with those of Mg, La and Sm, or from another point of view, with the AuCu and $AuCu_3$ structures. In the two cases, as we will see in sec. 6.2, one would choose a different description and representation of the aforementioned Cu structure.

In the different cases, some criteria may therefore be useful in order to give (in a systematic and simple way) explicit information on the characteristic structural features.

References: p. 363.

In the following sections some details will be given on a few complementary, alternative notations.

3.5.1. Coordination and dimensionality symbols in the crystal coordination formula

Several attempts have been carried out in order to design special formulae (crystal coordination formulae) which (in a convenient linear format) may convey explicit information on the local coordination geometry. A detailed discussion of these attempts and of their development (through the work, inter alios, of NIGGLI [1945, 1948], MACHATSCHKI [1938, 1953], LIMA DE FARIA and FIGUEIREDO [1976, 1978], PARTHE [1980a] and JENSEN [1984]) may be found in a review by JENSEN [1989], who presented and systematically discussed a flexible notation for the interpretation of solid-state structures. A short description of Jensen's notation will be given below. The different symbols used will be briefly presented. For the notation concerning the common coordination geometries a summary is reported in table 5. A report by the International Union of Crystallography Commission on Crystallographic Nomenclature (LIMA DE FARIA *et al.* [1990]) presents a concise description of similar alternative notations, a summary of which is also presented in table 5.

The symbols suggested by Jensen, based on Niggli's proposals, indicate the local coordination environments by means of *coordination number ratios*. For instance, a *formula* $AE_{m/n}$ will indicate a binary compound where m is the coordination number (the nearest neighbour number) of atoms E around A and n will be considered the coordination number of E by A. The ratio m/n will be equal to the stoichiometric compositional ratio. For instance, we will write $NaCl_{6/6}$ to represent the hexa-coordination

Table 5
Suggested notations for common coordination geometries.

a)	from JENSEN [1989]		
1	Terminal	7″	Monocapped trigonal prism
2	Bent CN 2	8	Cube
2′	Linear CN 2	8′	Square antiprism
3	Pyramidal or in general non-planar CN 3	8″	Dodecahedron
3′	Trigonal planar	8‴	Bicapped trigonal prism
3″	T-planar	$\hat{8}$	Hexagonal bipyramid
4	Tetrahedral	9	Tricapped trigonal prism
4′	Square planar	10	Bicapped square antiprism
4″	Base of a square pyramid with the central atom as the apex	11	Monocapped pentagonal antiprism
		12	Cubic closest-packed or cuboctahedron
5	Trigonal bipyramid	12′	Hexagonal close-packed or twinned cuboctahedron
5′	Square based pyramid with the central atom inside	12″	Isocosahedron
		$\hat{12}$	Hexagonal prism
6	Octahedron or trigonal antiprism	$\tilde{n}$	Complex, distorted n-hedron
6′	Trigonal prism	$\bar{n}$	Disordered structure in which it is possible to define only an average coordination number n
6″	Hexagonal planar		
7	Pentagonal bipyramid		
7′	Monocapped octahedron		

Table 5—*Continued*

b) from LIMA DE FARIA *et al.*[1990]

Coordination polyhedron around atom A	Complete Symbol		Alternative simplified symbols	
Single neighbour	[1l]		[1]	
Two atoms collinear with atom A	[2l]		[2]	
Two atoms non-collinear with atom A	[2n]		[2]	
Triangle coplanar with atom A	[3l]		[3]	
Triangle non-coplanar with atom A	[3n]		[3]	
Triangular pyramid with atom A in the centre of the base	[4y]		[4]	
Tetrahedron	[4t]	[t]	[4]	t
Square coplanar with atom A	[4l] or [4s]	[s]	[4]	s
Square non-coplanar with atom A	[4n]		[4]	
Pentagon coplanar with atom A	[5l]		[5]	
Tetragonal pyramid with atom A in the centre of the base	[5y]		[5]	
Trigonal bipyramid	[5by]		[5]	
Octahedron	[6o]	[o]	[6]	o
Trigonal prism	[6p]	[p]	[6]	p
Trigonal antiprism	[6ap]	[ap]	[6]	ap
Pentagonal bipyramid	[7by]		[7]	
Monocapped trigonal prism	[6p1c]		[7]	
Bicapped trigonal prism	[6p2c]		[8]	
Tetragonal prism	[8p]		[8]	
Tetragonal antiprism	[8ap]		[8]	
Cube	[8cb]	[cb]	[8]	cb
Anticube	[8acb]	[acb]	[8]	acb
Dodecahedron with triangular faces	[8do]	[do]	[8]	do
Hexagonal bipyramid	[8by]		[8]	
Tricapped trigonal prism	[6p3c]		[9]	
Cuboctahedron	[12co]	[co]	[12]	co
Anticuboctahedron (twinned cubooctahedron)	[12aco]	[aco]	[12]	aco
Icosahedron	[12i]	[i]	[12]	i
Truncated tetrahedron	[12tt]		[12]	
Hexagonal prism	[12p]		[12]	
Frank-Kasper polyhedra with				
14 vertices	[14FK]		[14]	
15 vertices	[15FK]		[15]	
16 vertices	[16FK]		[16]	

(in this case octahedral coordination) of Cl around Na (and vice versa) in sodium chloride. Similarly we will have: $ZnS_{4/4}$; $PH_{3/1}$; $CsCl_{8/8}$; $CaF_{8/4}$; $UCl_{9/3}$; etc. According to one of Jensen's suggestions it is possible to add *modifiers* to the coordination numbers in order to specify not only *topological* but also *geometrical* characteristics of the primary coordination sphere. (For examples, 6: octahedral; 6′: trigonal prismatic; 6″: hexagonal planar; etc., see table 5a.

Similar symbols were proposed by DONNAY *et al.* [1964] who suggested adding to the coordination number, one or two letters to indicate the geometry: y, pyramidal; l, planar; c, cubic; etc. Detailed descriptions of the coordination polyhedra are obtained by means of the LIMA DE FARIA *et al.* [1990] symbols presented in table 5b. An advantage of the

References: p. 363.

Lima de Faria symbolism may be the existence of two alternative sets of symbols: complete and simplified. The simplified symbols give only a numerical indication, without any distinction between different geometries; the complete symbols (clearly distinguishible from the previous ones) contain beside the numeric indication a description of the coordination polyhedron. A selection of the Lima de Faria symbols, together with the Jensen's suggestions, will be used here.

According to Jensen, the *dimensionality* of a structure (or of a substructure of the same) is indicated by enclosing its compositional formula in *square brackets* and prefixing an appropriate *symbol* $\underset{\sim}{d}$. The dimensionality index, d, may be d = 0 for a discrete molecular (cluster, ring) structure, d = 1 for a one-dimensional, infinite chain structure, d = 2 for a two-dimensional, infinite layer structure and d = 3 for an infinite three dimensional, framework structure. These are the Machatschki symbols (MACHATSCHKI [1947]).

More complex symbols such as $d\text{-}d$ or $d'\underset{\sim}{d}''d$ will represent intermediate dimensionality (between d and d') or, second, the dimensionality indexes of different substructures (d' and d'') followed by that of the overall structure (d). A few examples:

Molecular structures	$\underset{\sim}{0}$[HI], $\underset{\sim}{0}$[CO_2],
Linear structures	$\underset{\sim}{1}$[$BeCl_2$]
Layer structures	$\underset{\sim}{2}$[C] graphite, $\underset{\sim}{2}$[As]
Framework structures	$\underset{\sim}{3}$[C] diamond,
Substructures	$\underset{\sim}{0}$Ca[CO_3] (finite ions);
	$\underset{\sim}{1}$K[PO_3] (infinite anionic PO_3^- chain)

etc.....

If, in a A–B structure, one wishes to show not only the A/B coordination but also the B/B, or A/A, self-coordinations this is done, according to the suggestion by Jensen via the use of a composite dimensionality index and the relative positions of the various ratios and brackets in the formula, with the last unbracketed ratio always referring to the B/A coordination. So, for instance, $\underset{\sim}{03}$[$(H_2O)_{4/4}$] is a compact form for $\underset{\sim}{03}$[$(H_2O)(H_2O)_{4/4}$] to indicate the molecular packing in the ice structure. The formula $\underset{\sim}{23}$Al[$B_{3/3}$]$_{12/6}$ or $3\underset{\sim}{23}$[$Al_{8by/8by}$][$B_{3l/3l}$]$_{12p/6p}$ correspond to a more or less detailed description of the AlB_2 type structure where the coordination of B around Al is 12 (12p: hexagonal prismatic) and that of Al around B is 6 (6p: trigonal prismatic). The self-coordinations are bipyramidal for Al/Al (8by: hexagonal bipyramidal) and trigonal-planar (3l) for B/B (the B atoms form a two-dimensional net).

Considering as a further example the compounds AB having the CsCl type structure, we may mention that according to Jensen, the two descriptions $3\underset{\sim}{33}$[$A_{6/6}$][$B_{6/6}$]$_{8/8}$ and $\underset{\sim}{3}$[$AB_{8/8}$] (with and without the indication of the self-coordination) may also be used to suggest the bonding type (metallic if the A–A and B–B interactions contribute to the overall bonding, ionic, or covalent, if only A–B interactions have to be considered).

More complex examples of the use of this notation may be given by the structures of typical fluorides for which ionic type, coordination formulae are here reported:

oP16 YF_3 : $\underset{\sim}{3}$[$YF_{8/3}F_{1/3}$];
hP8 LaF_3 : $\underset{\sim}{3}$[$LaF_{8/4}F_{3/3}$];
cF16 BiF_3: $\underset{\sim}{3}$[$BiF_{8/4}F_{6/6}$].

In all these cases the sum of the numerators of the coordination ratios gives the total coordination (of two groups of F atoms) around the metal atom. (The sums of the ratios give, of course, the stoichiometric coefficients).

Another example may be represented by the hP6–Ni_2In structure ($^{3}_{\infty}[InNi_{6/6}Ni_{5/5}]$) described in sec. 6.5.3.

A detailed example ($AuCu_3$) of the application of the aforementioned notation to the description of a simple intermetallic structure will be presented in sec. 3.5.5. (with the pertinent figs. 12 to 15).

A few more examples will be reported in the following descriptions of a number of typical structures.

In conclusion to this description of "crystal coordination formulae" we have, however, to notice that the term "*coordination number*" (CN) may be used in two ways in crystallography (FRANK and KASPER [1958]). According to the first the coordination number, as previously mentioned, is the number of nearest neighbours to an atom. According to the other way, the definition of the coordination should be based on an "*interpretation*" *of the structure* which depends not only on an evaluation of the interatomic distances to assign bonding versus non-bonding contacts but on considerations on the bonding mechanism (JENSEN [1989]). These considerations are particularly important when thinking of metallic phases where it may be difficult to make distinctions between X–X, X–Y or Y–Y contacts. So, for instance, when considering the bc cubic structure of the W type, some authors define the coordination number as 8 (in agreement with the nearest-neighbours definition) but others prefer to regard it as 14 (including a group of 6 atoms at a slightly higher distance). Further considerations on this subject is delayed to a discussion, in sec. 7.2.6., on alternative definitions of coordination numbers (weighted coordination number, effective coordination number). In sec. 7.2.7., on the other hand, the *atomic-environment types* will be introduced, their codes presented and the results of their use in the classification of the selected groups of intermetallic structure types summarized.

3.5.2. Layer stacking sequence representation

A large group of structures of intermetallic phases can be considered to be formed by the successive stacking of certain polygonal nets of atoms (or, in more complex cases, by the successive stacking of characteristic "slabs"). These structural characteristics can easily be described by using specific codes and symbols, which can be very useful for a compact presentation and comparison of the structural features of several structures. Many different notations have been devised to describe the stacking pattern (for a summary see PARTHE [1964], PEARSON [1972]). A few of them will be presented here. *As an introduction to this point* we may consider figs. 5–7 where typical simple close-packed structures are shown and presented as built from the superimposition of close-packed atomic layers. If spheres of equal sizes are packed together as closely as possible on a plane surface they arrange themselves as shown in fig. 5. (Their centres are in the points of a triangular net.) Each sphere is in contact with six others. Such layers may be stacked to give three-dimensional close packed arrays. If we label the positions of the (centres of the) spheres in one layer as A, then an identical layer may be superimposed

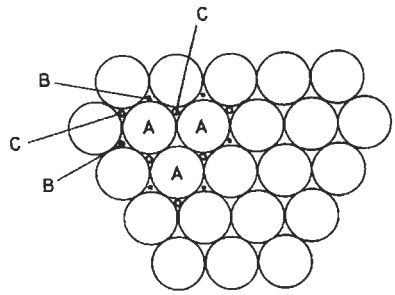

Fig. 5. Close-packed bidimensional arrangement of equal spheres. The A, B, C coding used to indicate different relative positions is shown. (See also fig. 8.)

on the first so that the centres of the spheres of the second layer are vertically above the positions B (for two layers, it is insignificant whether we choose the positions B or the equivalent position C). When we superimpose a third layer above the second (B) we have two alternatives: the centres of the spheres may be above either the A or the C positions. The two simplest sequences of layers correspond to the superimpositions ABABAB... and ABCABCABC... (more complex sequences may of course be considered). The sequence ABAB..., corresponding to the so-called hexagonal close-packed structure (Mg-type structure) is shown in fig. 6. The sequence ABCABC... having a cubic symmetry, is shown in fig. 7. It is the cubic (face-centered cubic) close-packed structure (also described as cF4–Cu type structure).

A more complete representation of different layer sequences (which can be used not only for the description of close packed structures) may be obtained by using *stacking symbols* such as those shown in fig. 8, together with layer stacking indications. Fig. 8a

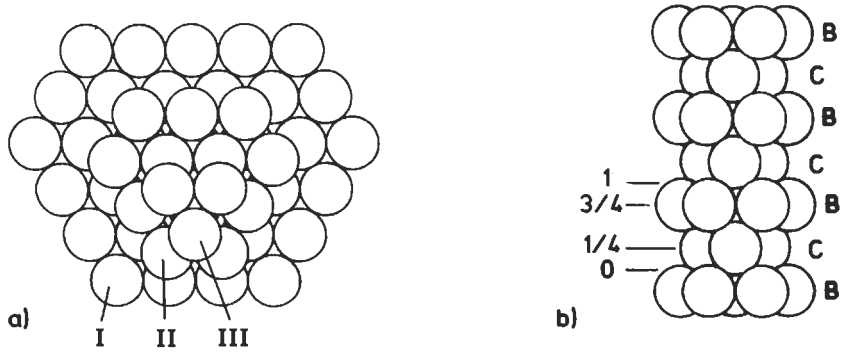

Fig. 6. Hexagonal close-packing.

a) A few spheres of three superimposed layers are shown. In this structure, the spheres of the layer III are just above those of the first one.

b) Lateral view of the same arrangement. The stacking symbols corresponding to the Mg unit cell description reported in sec. 6.2.6. (Mg in $\frac{1}{3},\frac{2}{3},\frac{1}{4}$ and $\frac{2}{3},\frac{1}{3},\frac{3}{4}$) are shown. (The ...BCBCBC... sequence description is identical to a ...ABABAB... or ...CACACA... symbol). The heights of the layers are reported as fractions of the repeat unit along the z axis of the hexagonal cell (that is of the distance between levels 0 and 1).

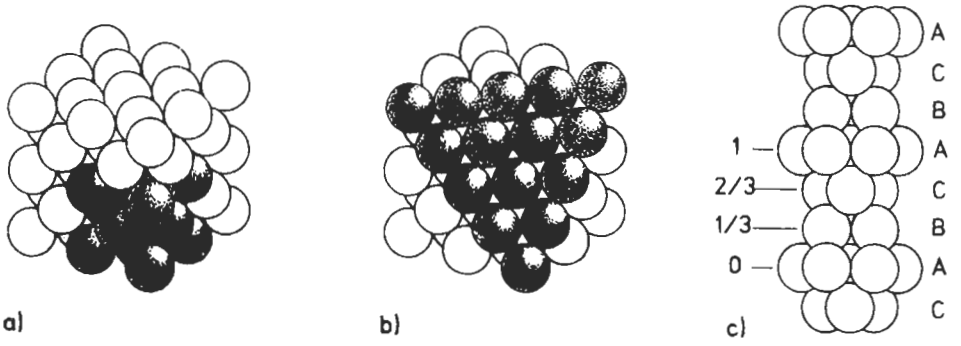

Fig. 7. Face-centered cubic close-packed structure of equal spheres.

a) Sphere-packing: a group of eight cubic unit cells is shown. (One of the unit cell is indicated by the black atoms).

b) A section of the same structure shown in a) is presented; it corresponds to a plane perpendicular to the cube diagonal. The typical arrangement of layers similar to that shown in fig. 5 is evidenced.

c) A lateral view of the stacking of the layers in the fcc structure is presented. The layer positions along the superimposition direction (which corresponds to the cubic cell diagonal) are shown as fractions of the repeat unit (cell diagonal)).

shows a network of atoms which can be considered as a triangular net, T net, that is the 3^6 net. We may incidentally notice that this notation, the Schläfli notation P^N, describes the characteristics of each node in the network, that is the number N of P-gon polygons surrounding the node. In the reported 3^6 net all the nodes are equivalent: their polygonal surrounding corresponds to 6 triangles. (More complex symbols are used for nets containing non equivalent nodes: for instance, the symbol $3^2434 + 3^24^2$ (2:1) means that, in the given net, two type of nodes, 3^2434 and 3^24^2, occur with a relative 2:1 frequency. A symbol such as 3^24^2 means that the given node is surrounded, in this order, by 2 triangles and 2 squares).

In the case of the simple, *3^6, triangular net* the aforementioned *stacking symbols A, B, C,* as can be seen in fig. 8c relate the positions of the nodes to the origin of the cell (which is defined as in fig. 8b). In the *layer stacking sequence full symbol*, the component atoms occupying the layers are written on the base line, with the stacking symbols as exponents and the layer spacings in the form of suffixes, denoting the fractional height of the repetition constant along the direction perpendicular to the layers. In the case of Mg, for instance, with reference to the standard choice of the unit cell origin (two equivalent atomic positions for the two Mg atoms in $\frac{1}{3},\frac{2}{3},\frac{1}{4}$ and $\frac{2}{3},\frac{1}{3},\frac{1}{4}$), the symbol will be $Mg^B_{1/4}Mg^C_{3/4}$ (which, with a zero point shift, is equivalent to $Mg^A_0Mg^B_{1/2}$). The symbol $Cu^A_0Cu^B_{1/3}Cu^C_{2/3}$, on the other hand, represents the cubic Cu structure as a stacking sequence of triangular layers viewed along the direction of the unit cell diagonal (which is perpendicular to the layers themselves).

A few other nets, based on the hexagonal cell, are of frequent structural occurrence. Following Pearson's suggestions, the corresponding sequences of stacking symbols which have a wide application are here presented. Fig. 9 shows the *hexagonal* (honeycomb) *net*

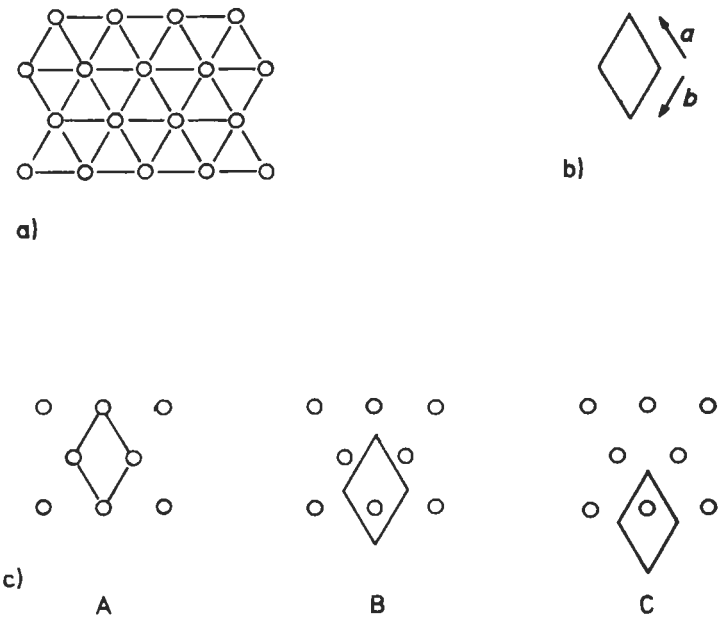

Fig. 8. Triangular net of points.

a) and b) The 3^6 net and the corresponding (bidimensional) cell are shown. Notice that, in this case, the selected coordinate system corresponds to an interaxial angle of 120°.

c) Different point positions (relative to the cell origin) and corresponding coding:
A) the representative point, in the x,y plane (a, b plane with a = b), has the coordinate 0,0;
B) with reference to the a, b constants the coordinate "doublet" of the representative point is $\frac{1}{3}, \frac{2}{3}$;
C) the representative point is in $\frac{2}{3}, \frac{1}{3}$.

(H net) and the stacking symbols (a, b, c) used for relating the different positions of the nodes to the cell origin. (Notice that two nodes are contained in the unit cell.)

A simple structure which can be described in terms of superposition of (even if far away, not close-packed) hexagonal layers is that of graphite: $C^{b}_{1/4}C^{c}_{3/4}$. The hexagonal net is also called "graphitic" net. (see sec. 6.3.4. and fig. 33).

Fig. 10 shows the three-ways bamboo weave net, known as *kagomé*, a net of triangles and hexagons (*K net*, the *3636 net* of points). The different positions of the nodes (three nodes in the unit cell) are represented by the symbols (α, β, γ) shown in fig. 10b.

Several (especially hexagonal, rhombohedral and cubic) structures may be conveniently described in terms of stacking triangular, hexagonal and/or kagomé layers of atoms. Examples will be given in the following sections. The specification of the spacing between the layers is useful in order to compare different structures, to recognize the close-packed ones (A, B, C symbols with appropriate layer distances) and to deduce atomic coordinations.

We have to notice, however, that the A, B, C notation previously described is not the

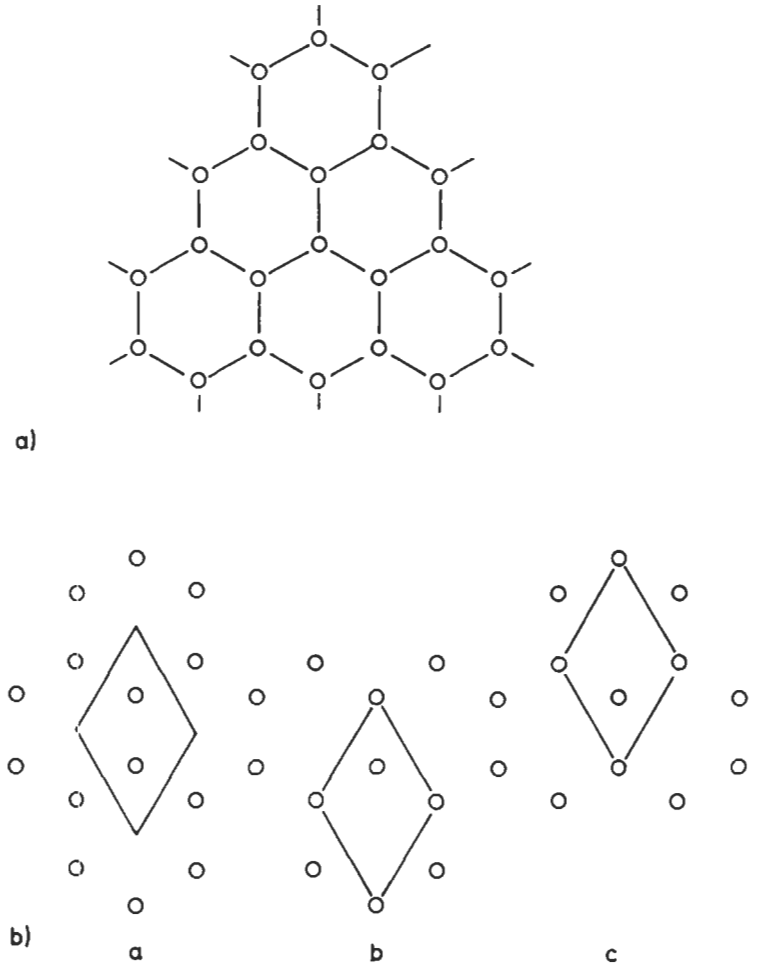

Fig. 9. Hexagonal (6^3) net of points.
The net is shown in a). In b) the different positions of the points in the unit cell are indicated with the stacking symbols a, b, c. Notice that the unit cell contains two points. (Every point in the corner is in common with (belongs to) four adjacent hexagonal cells).

only one devised. Several different symbols have been suggested to describe stacking patterns. (For a description of the more frequently used notations see PARTHE [1964], PEARSON [1972]).

A very common *notation* is that by JAGODZINSKI [1954]. This notation involving *h and c symbols* is applicable only to those structure type groups which allow not more than three possible positions of the unit layer (or more generally of the "unit slabs". See sec. 4.3. on polytypic structures). The h, c notation cannot therefore be applied, for instance, to disilicide types. The letters h and c have the following meaning:

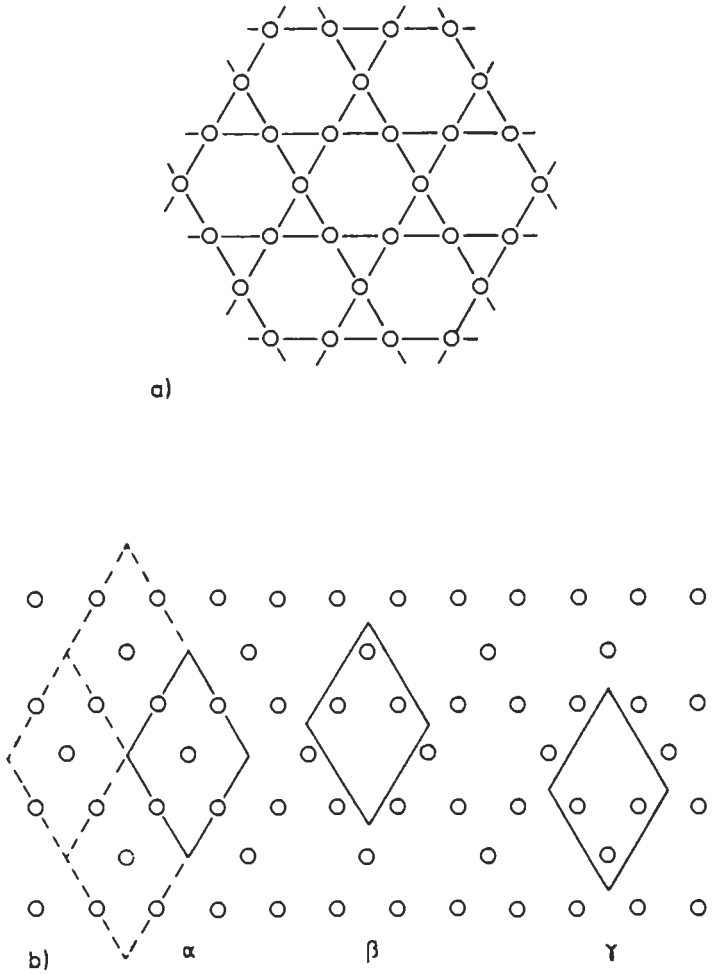

Fig. 10. The 3636 (kagomé) net of points.
The net is shown in a). In b) the different positions (relative to the hexagonal cell origin) are indicated by the symbols α, β, γ. Three points of the net are contained in the unit cell: notice that every point in an edge belongs to two adjacent cells.

— the *letter h* is assigned to a unit slab, whose neighbouring (above and below) unit slabs are displaced sideways, in the same direction for the same amount:
for instance ABABA or CBCBCB
hhh hhhh
(h comes from *hexagonal*: this is the stacking sequence of simple hexagonal structures such as hP2–Mg, hP4–ZnS wurtzite and hP12–$MgZn_2$ types).
— the *letter c*, on the other hand, is assigned to unit slabs whose neighbouring slabs

have different sideways displacements:
for instance ABCABC or CABCAB
cccc cccc
(c comes from *cubic*: this is the stacking sequence found in cubic structures such as cF4–Cu, cF8–ZnS sphalerite and cF24–Cu_2Mg types).

To denote the stacking sequence of the different structures it is sufficient to give only one identity period of the *h, c symbol series*. For instance:
cF4–Cu, c (instead of ABC); cF8–ZnS sphalerite, c; hP4–ZnS wurtzite, h; hP4–La, hc; hR9–Sm, hhc.

As can be seen from the previously reported examples, the identity period of the h, c symbols is generally shorter than the A, B, C... letter sequence. The h, c...symbols may be condensed, e.g., hcchcchchc to $(hcc)_2(hc)_2$. (If the number of c letters in a Jagodzinski symbol is divided by the total number of letters one obtains the percentage of "cubic stacking" in the total structure).

Another, common, *notation* for describing stacking of close-packed 3^6 nets (T nets) is that devised by ZHDANOV [1945] (a number notation equivalent to Jagodzinski's notation). A short description of the Zhdanov symbol is the following: a "+" is assigned if the order between a layer and its previous partner follows the sequence corresponding to any two subsequent layers in the face-centered cubic type structure, that is

A → B, B → C, C → A. Otherwise a "–" is assigned. For instance, the sequence "+++– – –" (shortened $3\underline{3}$) corresponds to ABCACB.

Finally, as another simple example of description (and symbolic representation) of structures in terms of layer stacking sequence we may now examine structures which can be considered as generated by *layer networks containing squares*. A typical case will be that of structures containing 4^4 *nets* of atoms (*Square net: S net*). The description of the structures will be made in term of the separation of the different nets (along the direction perpendicular to their plane) and of the origin and orientation of the unit cell).

Fig. 11 shows the different symbols (in this case numbers) suggested by PEARSON [1972] which will be used to indicate origin and orientation of the nets. These numbers will be reported as exponents of the symbols of the atoms forming the different nets. In this case too the relative height of the layers will be indicated by a fractional index. A few symbols of square net stacking sequences are the following:

Po_0^1: the simple cubic cell of Po (containing 1 atom in the origin) corresponds to a stacking sequence of type 1 square nets.

$W_0^1W_{1/2}^4$: the body-centered cubic structure of W (1 atom in 0,0,0 and 1 atom in $\frac{1}{2},\frac{1}{2},\frac{1}{2}$) corresponds to a sequence of type 1 and type 4 square nets at the heights 0 and $\frac{1}{2}$, respectively.

For more *complex polygonal nets*, their symbolic representation and use in the description, for instance, of the Frank-Kasper phases, see FRANK and KASPER [1958] and PEARSON [1972]. (Brief comments on this point will be reported in sec. 6.6.)

3.5.3. Assembly of polyhedra

A complementary approach to the presentation and analysis of the intermetallic phase

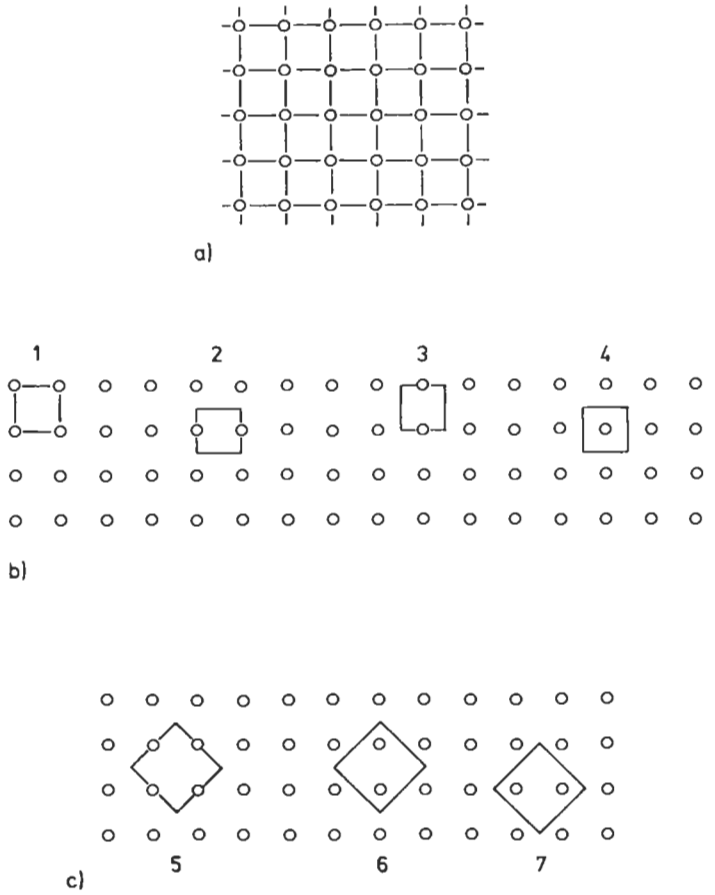

Fig. 11. A bidimensional square (4^4) net is shown in a).
b) Different positions of the representative point in the unit square are presented and coded (net of points aligned parallel to the cell edge).
c) Codes used for different positions of a square net of points referred to a larger square cell with axes at 45° to the net alignment (and edges equal to $\sqrt{2}$ times the repeat unit of the net).
In b) one point of the net is contained in the unit square, in c) there are two.

structures consists of their description with *coordination polyhedra* as *building blocks*.

A classification of types of intermetallic structures based on the coordination number, configurations of coordination polyhedra and their method of combination has been presented by KRIPYAKEVICH [1963].

According to Kripyakevich, a coordination polyhedron of an atom is the polyhedron, the vertices of which are defined by the atoms surrounding this atom: a coordination polyhedron should have a form as close as possible to a sphere, that is, it should be convex everywhere and have the maximum number of triangular faces. At the vertices of a coordination polyhedron of a given atom (in addition to atoms of different elements)

there can also be atoms of the same kind. A considerable variety of coordination polyhedra exists. In some cases, plane coordination polygons have to be considered. The number of vertices may vary from, say, 3 to 24. Generally, the structure consists of atoms with different coordination numbers; according to Kripyakevich, structures are most conveniently classified considering the type of coordination polyhedron of the atoms with the lowest coordination number. (For a general approach to the classification of atomic environment types and their description and coding in terms of coordination polyhedra see also sec. 7.2.7.).

An important contribution to the structure analysis of intermetallic phases in terms of the coordination polyhedra has been carried out by FRANK and KASPER [1958]. They described several structure types as the result of the *interpenetration* of a group of *polyhedra*, which give rise to a distorted tetrahedral close-packing of the atoms. (The Frank–Kasper structures will be presented in sec. 6.6).

In particular, SAMSON [1967, 1969] developed the analysis of the structural principles of intermetallic phases having giant unit cells. These structures have been described as arrangements of fused polyhedra rather than the full interpenetrating polyhedra (see a short description in sec. 6.6.5.).

The principles of describing structures in terms of *polyhedron-packing* has been considered by GIRGIS and VILLARS [1985]. To this end they consider, in a given structure, the coordination polyhedra of all the atomic positions; structures are then described by *packing* the *least* number of polyhedra types. All the atoms in the unit cell are included in the structure-building polyhedra. The *polyhedra considered should not penetrate each other.*

According to GIRGIS and VILLARS [1985] structures are then classified mainly on the basis of the following criteria:

— *Number of polyhedra types* employed in the description of the structure,
— *Characteristics of the polyhedra* (number of vertices, symmetry),
— *Types of polyhedra packing* (either *three-dimensional distribution of discrete polyhedra sharing corners, edges or faces,* or *layer-like distribution of polyhedra).*

As examples of structures described by *packing of one polyhedron type* we may mention:
cP4–$AuCu_3$ type, three-dimensional arrangement of cubooctahedra (coordination number, CN, 12);
tP30–σ(Cr,Fe) type, layer-like arrangement of icosahedra (CN 12).

For a general approach to the problem of *structure descriptions in term of polyhedron packing* a paper by HAWTHORNE [1983] should also be consulted. The following hypothesis is proposed: crystal structures may be ordered or classified according to the polymerization of those coordination polyhedra (not necessarily of the same type) with the higher bond valences. *The linkage of polyhedra to form "clusters"* is then considered from a graph-theoretic point of view. Different kinds of isomers are described and their enumeration considered. According to Hawthorne, moreover, it has to be pointed out that many classifications of complex structures recognize families of structures based on different arrangements of a fundamental building block or module (see the sec. 3.5.4. and

References: p. 363.

4.5. on recombination structures). *If this* building *module is a tightly bound unit* within the structure it could be considered, for instance, as the analogue of a molecule in an organic structure. Such *modules* can be considered the *basis of structural hierarchies* that include, for instance, simple and complex oxides and complex alloy structures. These modules may be considered as formed by polymerization of those coordination polyhedra that are most strongly bonded and may be useful for a classification and systematic description of crystal structures.

As a conclusion to this section we may mention also the "environment polyhedra", defined and coded by DAAMS *et al.* [1992]. A short decsription of this topic will be presented in sec. 7.2.7.

3.5.4. Modular aspect of crystal structure

A very general, mainly geometric, approach to the description and classification of the different inorganic structures may be based on a systematic "*construction of complex structural types*" *by means of a few operations applied to some building units*. As has been suggested by ANDERSSON and HYDE [1982, 1989] a formal description and classification of the various crystal structures could be obtained in terms of a classification of the *building units* and of the *construction mechanism*. Building units may correspond to *packets of points* (atoms) (blocks, clusters, bounded in three dimensions) or to *groups of lines* (rods, columns bounded in two dimensions, infinite in the third) or to *groups of planes* (slabs, sheets, layers, lamellae bounded in only one dimension, infinite in the other two). Structures may then be constructed from such portions by (discontinuous) symmetry operations (translation, reflection, or their combinations) repeated in a *parallel way* or by similar symmetry operations repeated in a cyclic way (involving rotation) (see, for instance, fig. 36).

Emphasis to similar approach has been given by ZVYAGIN [1993]. He pointed out that many crystal structures can be represented as a composite of certain standard "*construction modules*" and various combinations, distributions and arrangements of them. The simplest example of a modular structures is the densest packing of identical atoms (the atomic planes represent the construction modules forming various structures owing to a variation of the two possible placements of the successive plane relative to the preceding one).

A classification of the different structures may be based on:

— *module types* (sheets, rods, blocks),
— *dimension* of the modules,
— *variety* of module type (single or mixed-module structures),
— *relative number* of module types,
— *arrangement* of adjacent modules (*variations* in these arrangements, *periodicity/aperiodicity* of successive variations, etc.).

Strictly related to this kind of description may be the concepts of "*Recombination Structures*" and of "*Intergrowth Structure Series*" which will be presented in sec. 4.5.

3.5.5. An exercise on the use of alternative structural notations ($AuCu_3$ type as an example)

In the following, data concerning a few selected structures, will be presented. In this section, by using a simple structural type (cP4–$AuCu_3$, $3^3_\infty 3[Au_{6/6}][Cu_{8/8}]_{12/4}$, or, in more detail, $3^3_\infty 3[Au_{6o/6o}][Cu_{8p/8p}]_{12co/4l}$) a presentation will be given on the different ways of describing the structure.

$AuCu_3$ is primitive, cubic. The space group is $Pm\bar{3}m$ (N. 221 in the International Tables for Crystallography, HAHN [1989]). In the unit cell there are 4 atoms in the following positions:

1 Au in a) 0,0,0;
3 Cu in c) $0,\frac{1}{2},\frac{1}{2}$; $\frac{1}{2},0,\frac{1}{2}$; $\frac{1}{2},\frac{1}{2},0$;

Several phases are known which have this structure; in the VILLARS and CALVERT compilation [1991] there are around 450 listed: 1.7 % of all the reported phases. This structural type is the 8th in the frequency rank order (see sec. 7.1.). A short selection is presented in the following list:

≈$HfPt_3$ a = 398.1 pm	Pt_3Al a = 387.6 pm.
$LaIn_3$ a = 473.21 pm	Ti_3Hg a = 416.54 pm
La_3In a = 509.0 pm	$TiZn_3$ a = 393.22 pm
Mn_3Pt a = 383.3 pm	UPb_3 a = 479.3 pm
$MnZn_3$ a = 386 pm	YAl_3 a = 432.3 pm
Ni_3Al a = 357.0 pm	Y_3Al a = 481.8 pm

(Note that, in this structure type, in some cases, according to the phase stoichiometry, the same element may occupy either the a) or the c) Wyckoff position).

In the reported list the unit cell edges have been given. In the following, while discussing the characteristics of this structural type, we will consider the data referring to the prototype itself (a = 374.84 pm).

The structure is shown in fig. 12, where the tridimensional sequence of the atoms is suggested by presenting a small group (eight) of contiguous cells. The unit cell itself is shown in figs. 13a and 13b, by using two different drawing styles.

The subsequent figures 14a, 14b, 14c, 14d correspond to an analysis of the structure carried out in order to show the different local atomic arrangements (coordinations around the atoms in the two crystal sites).

In the analysis of a structure, however, it is also necessary to take into consideration the values of the *interatomic distances*. It may be useful to consider both absolute and so called "reduced" values of the interatomic distances. In the case of the $AuCu_3$ phase, the minimum interatomic distance corresponds to the Au-Cu distance (Au in 0, 0, 0 and Cu in $0,\frac{1}{2},\frac{1}{2}$) which is the same as the Cu–Cu distance between Cu in $0,\frac{1}{2},\frac{1}{2}$ and Cu in $\frac{1}{2},0,\frac{1}{2}$. This distance is given by $a\sqrt{2}/2$.

For the $AuCu_3$ phase a = 374.8 pm and, therefore, $d_{min} = 265.0$ pm. This value could be compared, for instance, to the value 272 pm, sum of the radii of Cu and Au (as defined for a coordination number of 12) or to the value 256 pm of the Cu–Cu distance in the metal (Cu atom "diameter"). *Reduced interatomic distances* ($d_r = d/d_{min}$) may be defined as the ratios of the actual distance values to the minimum value.

References: p. 363.

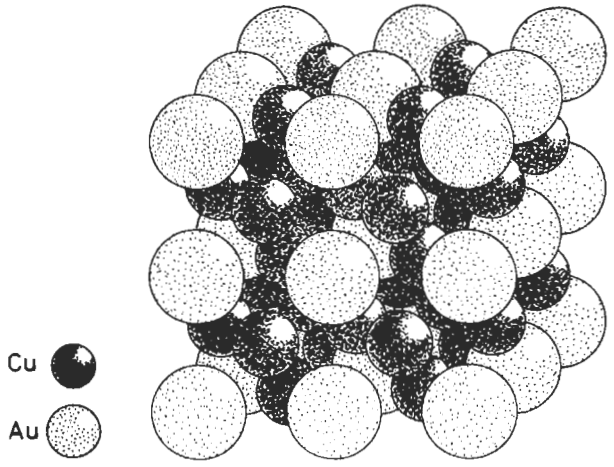

Fig. 12. cP4–$AuCu_3$ type structure. A group of eight cells is shown. The light spheres represent Au atoms. In order to get a better view of the structure inside, the atomic diameters are not to scale.

A first set of interatomic distances (and coordination) which can be considered in the $AuCu_3$ phase is that corresponding to the Au coordination around Au atoms (see fig. 14a):

Considering as the *reference atom*, the atom Au in 0,0,0, the next neighbours Au atoms are the six Au shown in fig. 14a, corresponding to the same Wyckoff position and having, in comparison with the reference atom, the coordinates 0,0,1; 0,0,$\bar{1}$; 0,1,0; 0,$\bar{1}$,0; 1,0,0; $\bar{1}$,0,0; all at a distance $d = a = 374.8$ pm, corresponding to a reduced distance $d_r = d/d_{min} = 1.414$.

In the same group of Au–Au interatomic distances a subsequent set is represented by distances such as those between $Au_{0,0,0}$ and $Au_{0,\bar{1},1}$ (or $Au_{0,\bar{1},\bar{1}}$, $Au_{0,1,\bar{1}}$, $Au_{1,0,1}$, etc.). This set corresponds to a group of 12 atoms (all at an absolute distance of $a\sqrt{2} = 530.1$ pm, that is, at a reduced distance $d_r = d/d_{min} = 2.000$).

A compact representation of these data is given by means of the bar-graph in fig. 15a).

A second set of interatomic distances (and coordination) corresponds to the Cu coordination around Au atoms:

Considering as the *reference atom*, the atom Au in 0,0,0, the next neighbours Cu atoms are the 12 Cu reported in fig. 4–14b, in the coordinates: $0,\frac{1}{2},\frac{1}{2}$; $0,\frac{1}{2},\frac{\bar{1}}{2}$; $0,\frac{\bar{1}}{2},\frac{1}{2}$; $0,\frac{\bar{1}}{2},\frac{\bar{1}}{2}$; $\frac{1}{2},0,\frac{1}{2}$; $\frac{1}{2},0,\frac{\bar{1}}{2}$; $\frac{\bar{1}}{2},0,\frac{1}{2}$; $\frac{\bar{1}}{2},0,\frac{\bar{1}}{2}$; $\frac{1}{2},\frac{1}{2},0$; $\frac{1}{2},\frac{\bar{1}}{2},0$; $\frac{\bar{1}}{2},\frac{1}{2},0$; $\frac{\bar{1}}{2},\frac{\bar{1}}{2},0$; all at a distance $d = a\sqrt{2}/2 = 265.1$ pm, corresponding to a reduced distance $d/d_{min} = 1.000$.

Considering also the subsequent sets of Au–Cu distances, 24 atoms at $d = 459.1$ pm ($d_r = d/d_{min} = \sqrt{3} = 1.732$), 24 Cu at $d = 592.7$ pm ($d_r = 2.236$), etc. we obtain the histogram reported in fig. 15b.

A third group of interatomic distances (and coordination) which has to be considered is that corresponding to the Cu coordination around Cu atoms (see fig. 14c):

Considering as the *reference atom*, the atom Cu in $\frac{1}{2},\frac{1}{2},0$, the next neighbours Cu

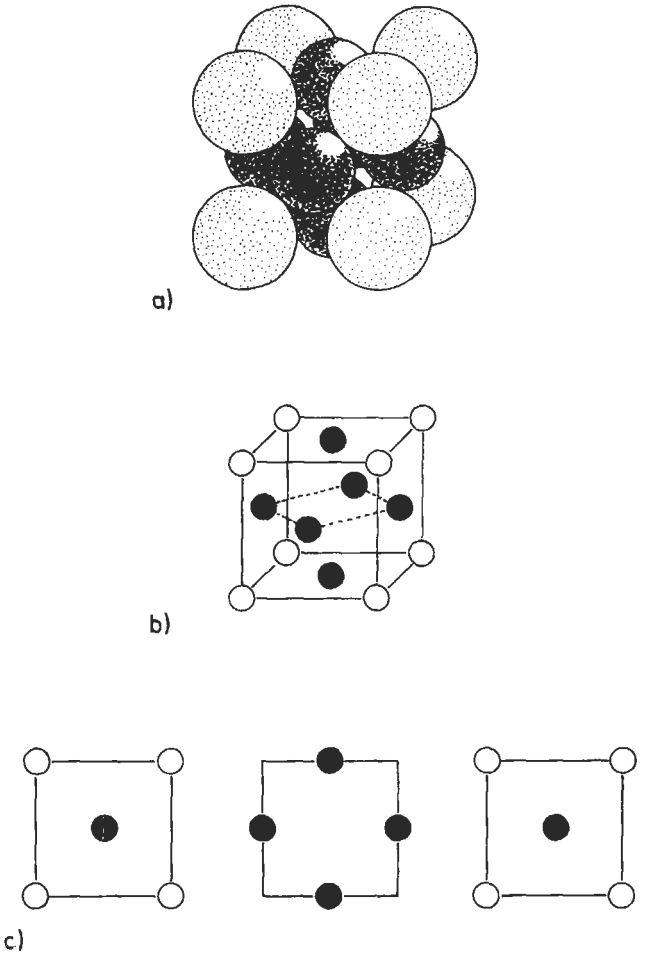

Fig. 13. The cP4–$AuCu_3$ unit cell is presented in different drawing styles. In a) an (approximate) indication of the packing and space filling is given. In b) the positions of the different atoms are reported in a perspective view of the unit cell and in c), in some typical sections of the same at different heights: notice the square net arrangement. The first (and the third) section corresponds to the height 0 or 1 * c. The second to the height $\frac{1}{2}$ * c. For the first section the position codes of the two atoms, in the square net, are 1 and 4; for the second the code is 5. (Compare with fig. 11.)

atoms are the 8 Cu atoms in $\frac{1}{2},0,\frac{1}{2}$; $0,\frac{1}{2},\frac{1}{2}$; $1,\frac{1}{2},\frac{1}{2}$; $\frac{1}{2},1,\frac{1}{2}$; $\frac{1}{2},0,\bar{\frac{1}{2}}$; $0,\frac{1}{2},\bar{\frac{1}{2}}$; $1,\frac{1}{2},\bar{\frac{1}{2}}$; $\frac{1}{2},1,\bar{\frac{1}{2}}$; all at a distance $d = a\sqrt{2}/2 = 265.1$ pm, corresponding to a reduced distance $d/d_{min} = 1.000$.

The subsequent sets of Cu–Cu distances correspond to 6 Cu atoms (in coordinates such as $\frac{1}{2},\frac{1}{2},1$; $\frac{1}{2},\frac{1}{2},\bar{1}$; $\frac{3}{2},\frac{1}{2},0$; etc.) at a distance $d = 374.8$ pm ($d_r = 1.414$), 16 Cu atoms at $d = 459.1$ pm ($d_r = 1.732$), 12 Cu atoms at $d = 530.1$ pm ($d_r = 2.000$), 16 Cu atoms at 592.7 pm ($d_r = 2.236$), etc. The corresponding histogram is presented in fig. 15c).

References: p. 363.

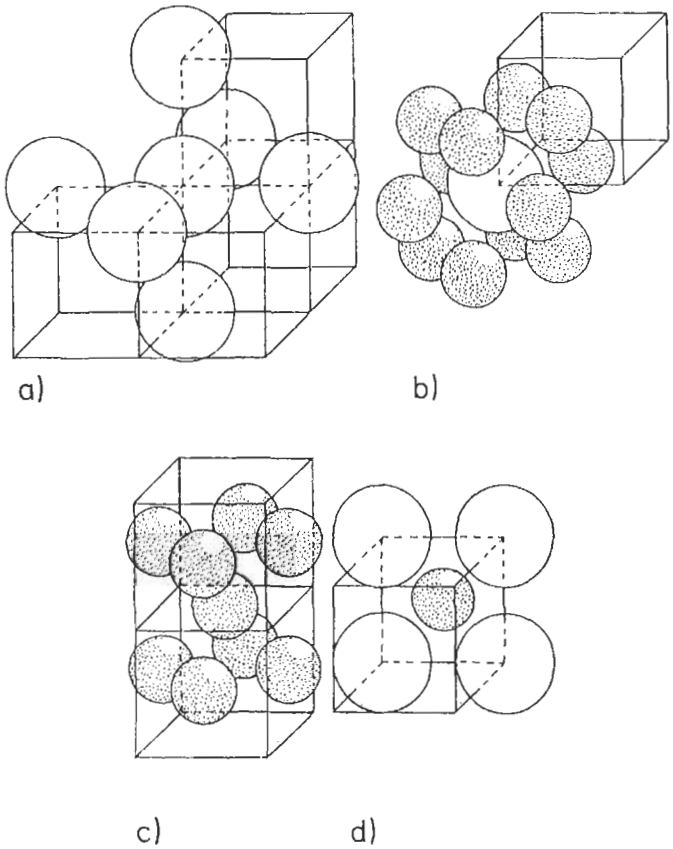

Fig. 14. cP4–$AuCu_3$ type structure. Different fragments of the structure (of a few unit cells) are presented in order to show the various typical coordinations. (Cu atoms are represented by small dotted spheres)
a) Au – 6 Au (octahedral); b) Au – 12 Cu (cuboctahedral);
c) Cu – 8 Cu (tetragonal prismatic); d) Cu – 4 Au (square).
The 8 Cu+4 Au at the same distance from Cu form a heterogeneous cuboctahedron. (Compare also with fig. 25.)

The fourth (and last) type of interatomic distances (and coordination) characteristic of the $AuCu_3$ structure is given by Au coordination around Cu atoms (see fig. 14d).

Considering as the *reference atom* one of the three equivalent atoms Cu in c), for instance, the atom in $0,\frac{1}{2},\frac{1}{2}$, the next neighbours Au atoms are 4 Au in 0,0,0; 0,0,1; 0,1,0; 0,1,1, respectively; all at a distance $d = a\sqrt{2}/2 = 265.1$ pm, corresponding to a reduced distance $d/d_{min} = 1.000$.

Subsequent sets of Cu–Au distances correspond to a group of 8 Au atoms (in coordinates such as 1,0,0; 1,0,1; 1,1,0; etc.) at a distance $d = 459.1$ pm (reduced distance $d/d_{min} = 1.732$), to a group of 8 Au (in coordinates such as $0,0,\bar{1}$; $0,1,\bar{1}$; 0,0,2; etc.), at a

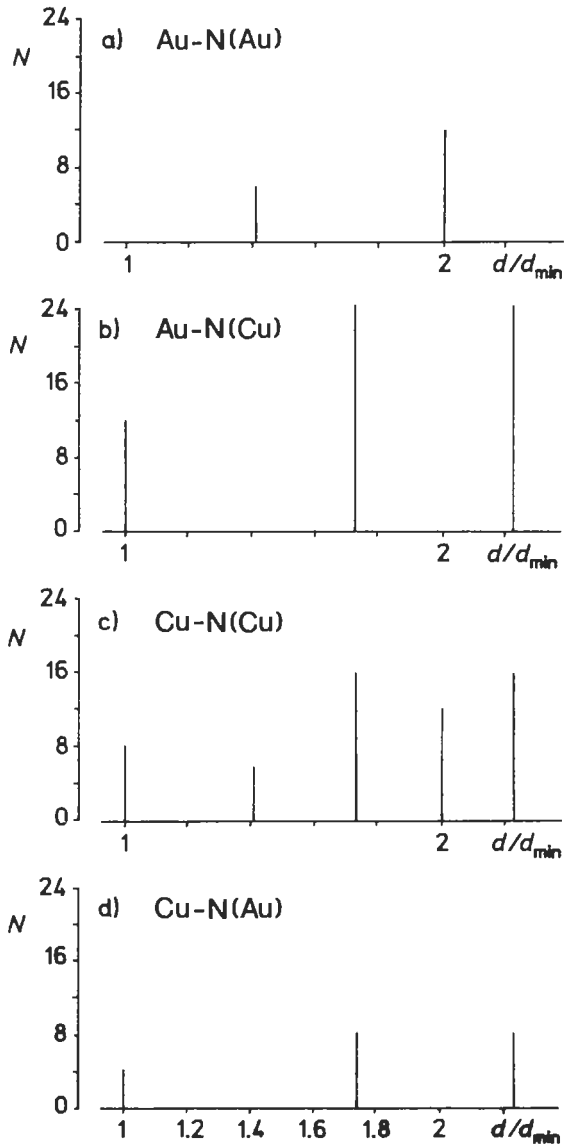

Fig. 15. cP4–$AuCu_3$ type structure. Coordinations and distances. For each type of coordination the numbers (N) of near-neighbours atoms are plotted as a function of their distances from the central atom. (Relative values of the distances, d/d_{min}, have been used. In these histograms and in the subsequent ones d_{min} is the shortest interatomic distance observed in the structure. For details see the comments reported in sec. 3.5.5.)

distance d = 592.7 pm, $d/d_{min} = 2.236$, etc. The corresponding coordination histogram is presented in fig. 15d.

Lists of coordinating atoms (with distances from the references atom), coordination polyhedra, and next-neighbor histograms are presented systematically by DAAMS *et al.* [1991]. They, however, use a more compact representation giving for each atom in a given site the histogram corresponding to the total coordination. In our case, for Au the sum of the two histograms reported in figs. 15a and b and for Cu the sum of the histograms of figs. 15c and d. (Compare with fig. 25). For the different structures, moreover, the distances are related by Daams et al. to the d_{min} observed in each coordination group instead of to the d_{min} of the overall structure as adopted here.

As a conclusion to the *description* of the different *coordinations* we may observe that those corresponding to the first distance sets are summarized in the symbol $3^{3}_{\infty}3\,[A_{6/6}][B_{8/8}]_{12/4}$. ($3^{3}_{\infty}3\,[Au_{6/6}][Cu_{8/8}]_{12/4}$ for the prototype). In terms of *polyhedra packing*, therefore, this structure may be described as a tridimensional arrangement of cubooctahedra (see sec. 3.5.3.).

Fig. 16, on the other hand, shows how for the same structure, alternative descriptions (*layer stacking sequence descriptions*) may be obtained and, according to Pearson, symbolized. In this figure the structure (viewed along the cube diagonal) is presented as a *stacking sequence* of *triangular* and *kagomé nets*. It corresponds to the symbol $Au^{A}_{0}\,Cu^{\alpha}_{0}\,Au^{C}_{1/3}\,Cu^{\gamma}_{1/3}\,Au^{B}_{2/3}\,Cu^{\beta}_{2/3}$ (In the symbol we have the same number of triangular (A,B,C) Au atom nets and of kagomé (α,β,γ) Cu atom nets. These two net types are characterized by the presence of 1 and 3 points in the unit cell (see figs. 8 and 10). This, of course, corresponds to the total 1:3 stoichiometric ratio). The same structure, viewed along the unit cell edge direction, corresponds to a *square net stacking sequence* (see fig. 13). The stacking symbol is $Au^{1}_{0}Cu^{4}_{0}Cu^{5}_{1/2}$ (These different symbols may be useful when comparing this structure with other structural types: for instance, the cF4–Cu type, sec. 6.2.1., tP2–AuCu(I) type, sec. 6.2.4., etc.).

With reference to a description in terms of *lattice complex combination*, we may

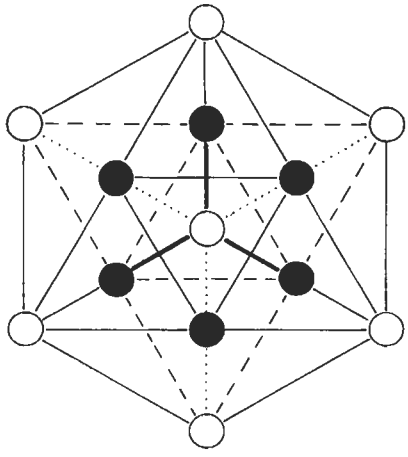

Fig. 16. cP4–$AuCu_3$ type structure. The unit cell is viewed along its diagonal. (Au atoms white, Cu black). The triangular arrangements of the atoms around the cube diagonal are evident.

finally note that the $AuCu_3$ type structure corresponds to a combination of P and J complexes (**Au**Cu_3: **P** + J; see sec. 3.1.). According to HELLNER [1979] this structure may be considered as pertaining to a F-family as a consequence of a particular splitting of the points of the F complex.

A few other comments on the $AuCu_3$ type structure and some remarks on the relationship with other structural types will be reported in the following sec. 6.2.3.).

4. Relationships between structures and structure "families"

As clearly pointed out, for instance, by BÄRNIGHAUSEN [1980] (see sec. 4.6.), one of the main objectives of crystal chemistry is to order the profusion of structure types and to show the general principles involved. To this end relations between cognate structures evidently play an important role.

The structures corresponding to different types may often be interrelated on the basis of some transformation schemes. These schemes can be used as criteria for classifying structure types and showing structural relationships.

A few selected groups of interrelated structural types will be presented in the following sections.

4.1. Degenerate and derivative structures, superstructures (defect, filled-up, derivative structures)

An important and general scheme of structure transformation and interrelation is that described, for instance, by PEARSON [1972], by means of the concept of *derivative structures* and *degenerate structures.*

A *derivative structure* can be considered being obtained from a reference structure by ordered atomic substitution, subtraction or addition processes or by unit cell distortions (or both). The opposite kinds of transformation correspond to the so-called *degeneration processes.* A derivative structure has fewer symmetry operations than the reference structure (a degenerate one has more). A derivative structure has either a larger cell or a lower symmetry (or both) than the reference structure.

It is possible, for instance, that a set of equipoints of a certain structure (considered as the reference structure) has to be subdivided into two (or more) subgroups in order to obtain the description of another ("derivative") structure. The structure of the Cu type (cF4-type), for instance, corresponds to 4 Cu atoms in the unit cell, placed in 0,0,0; $\frac{1}{2},\frac{1}{2},0$; $\frac{1}{2},0,\frac{1}{2}$; $0,\frac{1}{2},\frac{1}{2}$, whereas in the cP4–$AuCu_3$ type structure the same atomic sites are subdivided into two groups with an ordered distribution of the two atomic species (1 Au atom in 0,0,0, and 3 Cu atoms in $\frac{1}{2},\frac{1}{2},0$; $\frac{1}{2},0,\frac{1}{2}$; $0,\frac{1}{2},\frac{1}{2}$). The $AuCu_3$ type structure can, therefore, be considered as a derivative structure of the Cu type. On the other hand, if we consider the $AuCu_3$ type as the reference structure, we may describe the Cu type as a degenerate structure.

The aforementioned subdivision of a set of equipoints in more groups can be described in this case in terms of similar cubic cells (both of the original and of the derivative structures). Notice, however, that in the case of Cu the conventional cubic cell

is face-centered. It is not primitive: it corresponds to 4 (rhombohedral) primitive cells, whereas, in the case of $AuCu_3$ the primitive unit cell is larger and it is identical to the cube. Because of the observation that these ordering processes may lead to a cell *multiple* of the original one, they are also referred to as forming *superstructures* (also called *superlattices*) (BARRETT and MASSALSKI [1966]) of the original structure. An example where, due to ordering, we observe, perhaps in a more evident immediate way, the increase of the unit cell size (formation of a multiple cell) may be the structure of $MnCu_2Al$ type (see fig. 24 and sec. 6.1.3) which can be considered a derivative structure (*superstructure*) of the cP2–CsCl type structure (which in turn is a superstructure of the W-type structure, corresponding to a, non-primitive cubic, cI2 cell).

Notice that the ordering may not lead to a multiple cell, if the symmetry of the ordered structure is reduced, relative to the original one. Nevertheless the name *superstructure* is generally used especially when we have the formation of a disordered solid solution regardless of whether there is multiplication of the edges of the cell.

A contribution to the study of *order-disorder interrelations between structures* and to their *classification into two groups on the basis of the presence/absence of a difference in the translational symmetry* (unit cell edge variations) has been given by WONDRATSCHEK and JEITSCHKO [1976] and by ALBERING *et al.* [1994]. (The detectability of the two types of ordering by means of X-ray diffraction studies has been also discussed).

ALBERING *et al.* [1994] especially studied the hP3–AlB_2 type structure and its derivatives. A few of these are presented in fig. 17. A detailed description is given in sec. 6.5.6. Main features of several deformation and substitution derivatives of the AlB_2-type were discussed by GLADYSHEVSKII *et al.* [1992].

A more complex case of structure interrelation which can be presented in terms of (even if "formal") substitution is that which can be exemplified by considering structures such as those of NaCl (see fig. 18 and a detailed description in sec. 6.4.1.) and FeS_2 or CaC_2. These structures may be compared: the cP12–FeS_2 type may be described as having Fe atoms in the sodium ion positions and the centers of the discrete S_2 dumb-bell groups at the chlorine ion positions. The passage from a structure containing spherical atoms to another one in which atomic groups substituted single atoms will generally result in a symmetry reduction. A clear example may be given by the tI6–CaC_2 type which can also be compared with the NaCl type: Ca is in the sodium positions and the C_2 group in the chlorine positions. In this case, however, the long axes of the C–C groups are all aligned in one direction so that the unit cell is tetragonal instead of cubic. (See fig. 4 and a description of this structure and a comparison with the $MoSi_2$-type in sec. 3.2.). In a similar way, we may, for instance, consider the K_2PtCl_6 structure essentially the same as the CaF_2–antitype: the K ions are in the F ion positions and the centers of the $PtCl_6$ octahedral groups in the Ca ion positions.

Derived structures may also be formed with the *ordered introduction of vacant sites*. As an example we may consider the hP3–CdI_2 type structure (see sec. 6.5.2) which can be related to the hP4–NiAs type structure in which the set of equivalent points 0,0,0 and $0,0,\frac{1}{2}$ is considered as being subdivided into two groups (each of 1 site) 0,0,0, (occupied by 1 atomic species) and $0,0,\frac{1}{2}$ (vacant). We can, therefore, regard the hP3–CdI_2 type structure as a *defect derivative* form of the hP4–NiAs type.

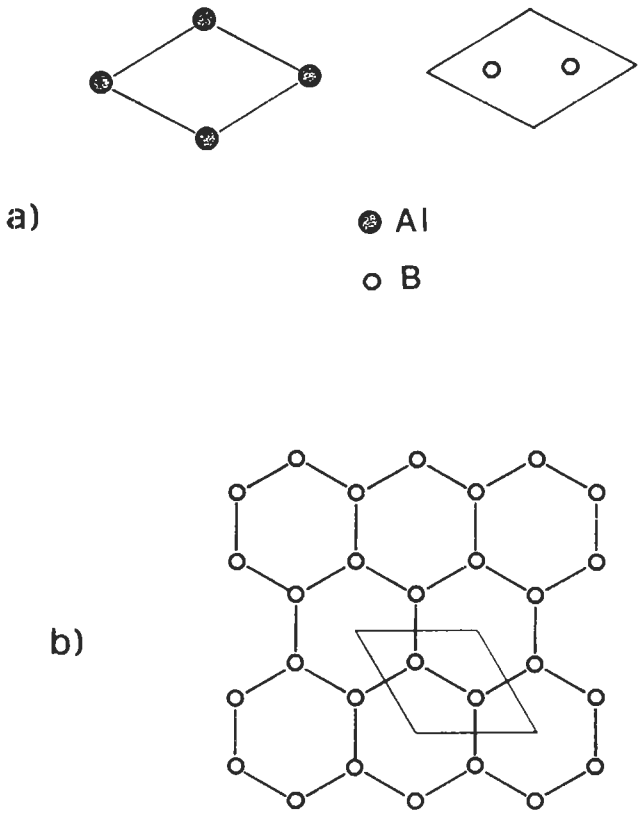

Fig. 17a,b. AlB_2–type and derivative structures.

a) Two sections of the hP3–AlB_2 unit cell are presented at the height $z=0$ (Al atoms) and $z=\frac{1}{2}$ (B atoms), respectively.

b) The corresponding hexagonal net of B atoms in AlB_2 is shown (a projection of the unit cell is superimposed. (Compare with fig. 9). The Al atoms (at the cell origin) are surrounded by 12 B, arranged in a hexagonal prism, and the B atoms are in sixfold coordination with Al, in the center of an Al trigonal prism.

Similar considerations may be extended to include (besides substitution and subtraction) *ordered addition of atoms*. In this case *stuffed* or *filled-up derivative structures* are considered in which extra atoms have been added in an ordered way, on sites unoccupied in the reference structure. An example is the hP6–Ni_2In structure, which is a stuffed derivative structure of the previously mentioned NiAs structure.

Another interesting example may be the fcc-derivative *interstitial cP5 Fe_4N phase*. It may be described as corresponding to the following atomic positions in the $Pm\bar{3}m$ (or $P\bar{4}3m$) space group:

1 Fe in a): 0,0,0; 1 N in b): $\frac{1}{2},\frac{1}{2},\frac{1}{2}$ and 3 Fe in c): $0,\frac{1}{2},\frac{1}{2}$; $\frac{1}{2},0,\frac{1}{2}$; $\frac{1}{2},\frac{1}{2},0$.

References: p. 363.

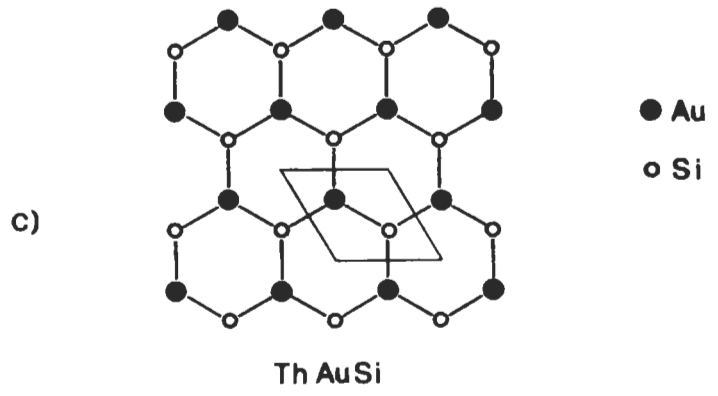

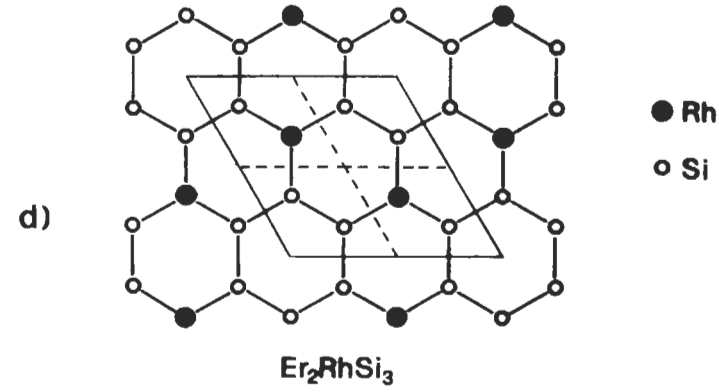

Fig. 17c, d. AlB_2–type and derivative structures.
c) and d) Hexagonal nets observed in AlB_2 derivative structures. In c) the AuSi net of the ThAuSi type structure and in d) the $RhSi_3$ net of the Er_2RhSi_3 structure are shown. In c) and d) the Th and Er positions, corresponding to those of Al in AlB_2, are not shown. The projections of the unit cells are presented: notice the larger cell of the Er_2RhSi_3 structure.

This filled-up superstructure may therefore be described in terms of the occupation by N of an interstice (centered in $\frac{1}{2},\frac{1}{2},\frac{1}{2}$) of a Cu-type (or $AuCu_3$-type) structure. The N atom results octahedrally surrounded by 6 Fe atoms. This structure could also be described as a deficient NaCl-type derivative structure (see sec. 6.4.1.): the Fe atoms are in the same positions as the Na atoms in NaCl and one out of the four Cl positions is occupied by the N atoms.

(For a description and a classification of the "holes", octahedral and tetrahedral, in

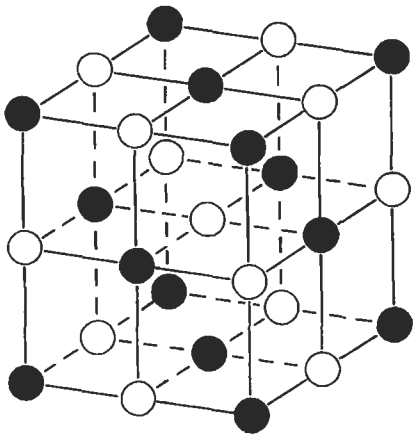

Fig. 18. NaCl-type structure (see sec. 6.4.1.). The positions in the unit cell of the two types of atoms are indicated.

closed packed structures see sec. 6.2.2, see also Hägg phases in sec. 3.4.).

As a footnote to these observations, we have also to mention that frequently structural distortions (axial ratio and/or interaxial angle variations) accompany the formation of derivative structures (especially because of the ordered distribution of atoms of different sizes or of vacant sites).

4.1.1. Ordering-disordering transformation

In a number of metal systems for a given range of compositions depending, for instance, on the temperature, it is possible to observe alloys having both a certain degenerate structure and a corresponding (more or less) ordered derivative structure. The transformation from one structure to the other corresponds to a real process (*ordering–disordering transformation*). A large number of solid solutions become ordered at low temperature.

In the specific case, for instance, of the Au–Cu system an alloy with the $AuCu_3$ composition at high temperature, has the (disordered) cF4–Cu type structure. The two atomic species are equally distributed in the four atomic sites (which are therefore equivalent: each one is occupied by Au with a 25% probability and by Cu with a 75% probability). This random distribution may be also related to the possibility of gradually changing the overall composition of the alloy maintaining the same structure and giving the formation of *solid solutions*. For the Cu–Au alloys we have, at high temperature, a continuous solid solution ranging from Cu to Au (both having the same cF4–Cu type structure): in all the intermediate alloys we have the equivalence of all the atomic sites whose occupation gradually changes from pure Cu to pure Au. By lowering the temperature we have ordering processes corresponding to a change from a nearly random distribution of atoms among the structure sites into more ordered arrangements where certain sites are predominantly occupied by one kind of atom. In the specific case of the

$AuCu_3$ composition we have the transformation from the cF4–Cu type into the described, derivative type (cP4–$AuCu_3$ type) structure.

Typical examples of ordering processes are also the transformation from the β to β' phases in the Cu–Zn system (from cI2–W type to cP2–CsCl type) and the ordering of the FeAl phase in the CsCl type structure (see sec. 6.1.2.). Notice that, ordering in these metallic phases, may be an extremely complex sluggish process requiring slow cooling and/or long annealing of the alloys. Alloy samples with different degrees of ordering can be obtained by quenching at various cooling times. As a consequence the effects of ordering on a number of properties have been studied. Alloys such as Cu_3Au and Fe_3Al have been the subject of many of these studies.

The Au–Cu system, in particular, is one of the earliest systems for which order-disorder type transformations were established. As a result, a very large volume of work has been carried out on the ordered AuCu and $AuCu_3$ phases. The description of the gold–copper system, reported by OKAMOTO and MASSALSKI [1987], may be considered as a reference to the review and to the assessment, not only for the specific system, but also for the investigation methods and discussion criteria of general interest. The following topics have been considered:

Au–Cu phase diagram, Au_3Cu, AuCu, $AuCu_3$ ordered phases (phase boundaries determination by X-ray studies, electrical resistometry, electron microscopy), crystal structure determination (by X-ray and electron diffraction methods), nature of ordering transformation in AuCu, short range order, anomalous behaviour in $AuCu_3$ at high temperatures (specific heat, thermal expansion measurements, etc.). Kinetic studies carried out by measuring gradual shift and intensity variation of the X-ray lines from a disordered to an ordered (superlattice) structure on samples after different quenching and annealing are reported.

For a review on site preference of substitutional additions to CsCl type intermetallic compounds see KAO *et al.*[1994]. In this work dilute additions to NiAl, FeAl and CeAl are especially discussed. As another example we may mention that the addition of a third element to ordered Ni_3Al (cP4–$AuCu_3$ type) occurs in different ways (OCHIAI *et al.* [1984]). For instance Sb, Si, Ge and Ga atoms replace preferably Al, while Cu and Co replace Ni.

As a conclusion to this section, we may mention that a systematic description of ordering processes in alloys and of the superstructures which can be generated has been presented, for instance, by KHACHATURYAN [1983] in the framework of a theoretical treatment of structural transformation in solids. *Two groups of superstructures* have been specially considered: *substitutional and interstitial.*

a) Examples of substitutional superstructures.

tI10–$MoNi_4$: a = 572.0, c = 356.4 pm. Space group I4/m, N.87.

2 Mo in a): 0,0,0; $\frac{1}{2},\frac{1}{2},\frac{1}{2}$.

8 Ni in h): x,y,0; −x,−y,0; −y,x,0; y,−x,0; $\frac{1}{2}+x,\frac{1}{2}+y,\frac{1}{2}$;

$\frac{1}{2}-x,\frac{1}{2}-y,\frac{1}{2}$; $\frac{1}{2}-y,\frac{1}{2}+x,\frac{1}{2}$; $\frac{1}{2}+y,\frac{1}{2}-x,\frac{1}{2}$, with $x \approx 0.2$, $y = 0.4$.

This superstructure is based on a fc cubic pseudocell. The atoms form close packed layers stacked in a 15 layer close packed repeat sequence.

oI6–$MoPt_2$: a = 276.5, b = 829.6, c = 393.8 pm. Space group Immm, N.71.
2 Mo in a): 0,0,0; $\frac{1}{2},\frac{1}{2},\frac{1}{2}$.
4 Pt in g): 0,y,0; 0,−y,0; $\frac{1}{2},\frac{1}{2}+y,\frac{1}{2}$; $\frac{1}{2},\frac{1}{2}-y,\frac{1}{2}$, with y = 0.353.
It is a close packed superstructure based on a fc cubic pseudocell. Distorted close packed triangular layers are stacked in close packed ABC sequence.

tI8–$TiAl_3$: a = 383.6, c = 857.9 pm, c/a = 2.236. Space group I4/mmm, N.139.
2 Ti in a): 0,0,0; $\frac{1}{2},\frac{1}{2},\frac{1}{2}$.
2 Al in b) 0,0,$\frac{1}{2}$; $\frac{1}{2},\frac{1}{2}$,0.
4 Al in d): 0,$\frac{1}{2},\frac{1}{4}$; $\frac{1}{2}$,0,$\frac{1}{4}$; $\frac{1}{2}$,0,$\frac{3}{4}$; 0,$\frac{1}{2},\frac{3}{4}$.
The superstructure may be described in terms of two, distorted, $AuCu_3$ type subcells stacked one above the other.

tI16–$ZrAl_3$: a = 400.5, c = 1728.5 pm, c/a = 4.316. Space group I4/mmm, N.139.
4 Al in c): 0,$\frac{1}{2}$,0; $\frac{1}{2}$,0,0; $\frac{1}{2}$,0,$\frac{1}{2}$; 0,$\frac{1}{2},\frac{1}{2}$.
4 Al in d): 0,$\frac{1}{2},\frac{1}{4}$; $\frac{1}{2}$,0,$\frac{1}{4}$; $\frac{1}{2}$,0,$\frac{3}{4}$; 0,$\frac{1}{2},\frac{3}{4}$.
4 Al in e): 0,0,z; 0,0,−z; $\frac{1}{2},\frac{1}{2},\frac{1}{2}+z$; $\frac{1}{2},\frac{1}{2},\frac{1}{2}-z$; with z = 0.361.
4 Zr in e): 0,0,z; 0,0,−z; $\frac{1}{2},\frac{1}{2},\frac{1}{2}+z$; $\frac{1}{2},\frac{1}{2},\frac{1}{2}-z$; with z = 0.122.
This structure may be considered another, more complex, superstructure based on close packing. The height of the superstructure cell in the c direction corresponds to four cubic pseudocells. Fig. 19 gives a comprehensive presentation of some structural features of the $MoNi_4$, $MoPt_2$, $TiAl_3$ and $ZrAl_3$ structural types.

Fe_3Al, cF16–Li_3Bi type structure: This structure may conveniently be described as derived from bcc solid solution (see in sec. 6.1. the interrelated types *cI2–W*, the previously mentioned types *cP2–CsCl*, *cF16–$MnCu_2Al$ and cF16–Li_3Bi*; see also fig. 24). The Li_3Bi-type structure, however, may be also considered as composed of four interpenetrating fc cubic arrays of atoms with Bi (or Al) at the cell corners and face centers and Li (or Fe) in the centers of the interstices.
tP2–AuCu(I), cP4–$AuCu_3$ and tP4–Ti_3Cu: These structures described in the following sections, 6.2. and in fig. 20, can be considered fcc based substitutional ordered superstructures.
hR96–CuPt(I): The equilibrium phase diagram of the Cu–Pt system shows the fcc continuous solid solution stable at high temperature and a number of ordered superstructure phases (with composition ranges) stable at lower temperatures. CuPt(I) is a complex, slightly distorted superstructure built up by 8 face centered cubic pseudocells. In the same Cu–Pt system other superstructures have been described for compositions around Cu_3Pt_5 (rhombohedral CuPt(II) type), $CuPt_3$ and $CuPt_7$.
hP8–Ni_3Sn: This structure may be considered an example of a superstructure based on the hexagonal close packed structure. In the same way as by ordering the Cu-type structure the $AuCu_3$ type may be obtained, the Ni_3Sn-type may be derived from the Mg type. Details of the structure are given in sec. 6.2.7.

b) Examples of interstitial superstructures
tP3–FeNiN: a = 283.0, c = 371.3 pm, c/a = 1.312. Space group P4/mmm, N.123.
1 Fe in a): 0,0,0; 1 N in c): $\frac{1}{2},\frac{1}{2}$,0 and 1 Ni in d): $\frac{1}{2},\frac{1}{2},\frac{1}{2}$.

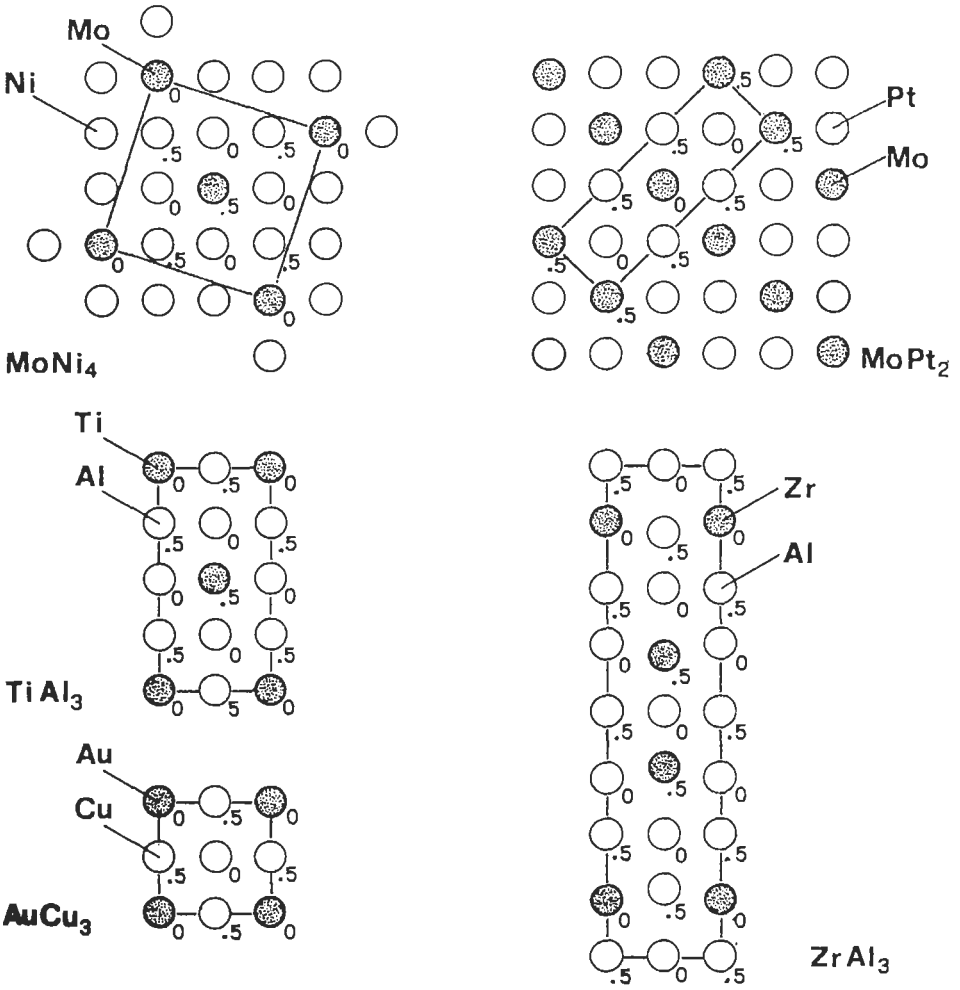

Fig. 19. Examples of face centered based, substitutional superstructures. The unit cells of a few selected superstructures are shown by means of their projection on a convenient plane and compared with a similar projection of the cP4–$AuCu_3$ type cell (on the face a,a): tI10–$MoNi_4$ (on the face a,a), oI16–$MoPt_2$ (a,b), tI8–$TiAl_3$ (a,c) tI16–$ZrAl_3$ (a,c). (The values of the coordinate along the third axis are indicated).

This structure can be considered a superstructure of the AuCu(I) type, with 1 N atom inserted in an octahedral interstitice. This structure, as the previously described *cP5–Fe_4N type*, can be considered an interstitial ordered phase. The *oP5–Ta_4O* phase and the *tI8–Fe_8N* phase are examples of bcc-based interstitial ordered phases.

oP5–Ta_4O: a = 719.4, b = 326.6, c = 320.4 pm. Space group Pmmm, N.47.

1 Ta in a): 0,0,0; 1 Ta in b): $\frac{1}{2}$,0,0; 1 O in h): $\frac{1}{2},\frac{1}{2},\frac{1}{2}$; 2 Ta in l): $x,\frac{1}{2},\frac{1}{2}$; $-x,\frac{1}{2},\frac{1}{2}$ (with x = 0.225).

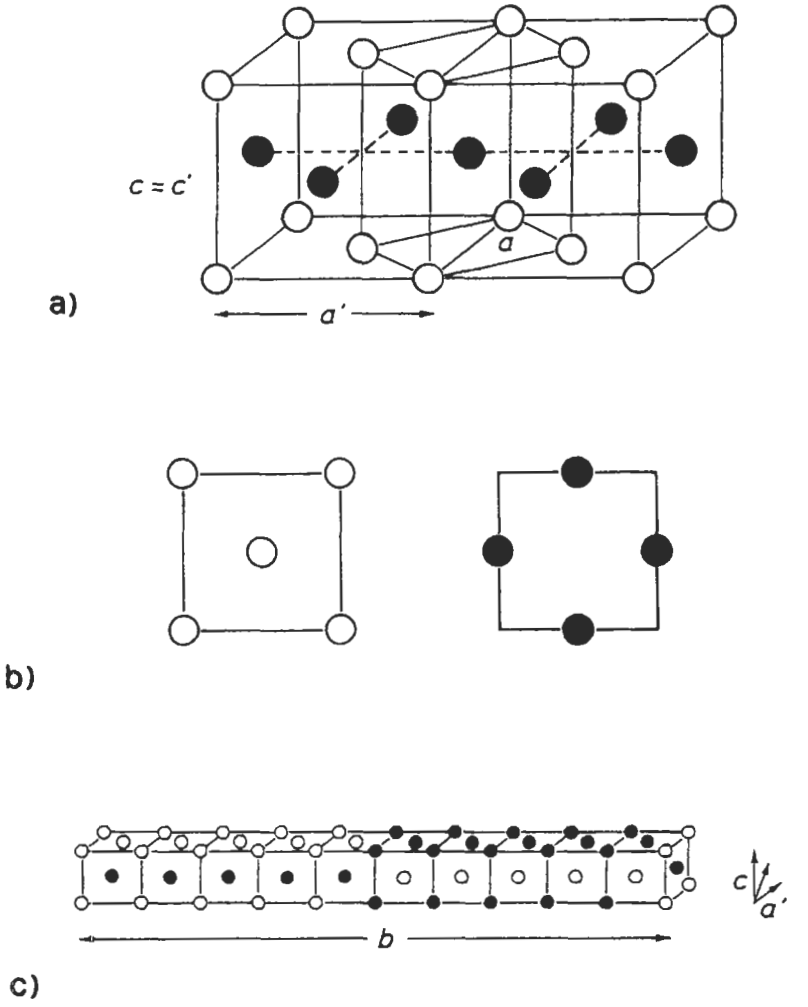

Fig. 20. AuCu type structures. The two types of atoms are shown.

a) AuCu(I) type structure. Both the tP2 cell (a and c edges) and a tP4 pseudocell (a′ and c edges) are shown. (The tetragonal pseudocell is shown in order also to make easier the comparison with the cubic, Cu-type, structure).

b) Sections of the large tP4–pseudo-cell. (Compare with fig. 13.)

c) oI40–AuCu(II) type structure.

The cell can be described as formed by two superimposed slightly distorted bcc subcells of the metal atoms. The O atom is surrounded by a (slightly compressed) Ta atom octahedron.

4.2. Antiphase domain structures

A special case of superstructures may now be considered. A typical example can be observed in the oI40–AuCu(II) type structure (fig. 20 and sec. 6.2.4.). We first have to mention that ordering of the Au–Cu face-centered cubic (cF4–Cu type) solid solution, having a 50–50 atomic composition, distributes Cu and Au atoms alternatively on two layers, resulting in a tetragonal structure, tP2–AuCu(I)) with the c axis perpendicular to the layers (see fig. 20a). The more complex structure, oP40–AuCu(II) type, is obtained by a *long-period ordering* which results in an orthorhombic cell containing 10 (slightly distorted) AuCu(I) pseudocells (fig. 20b). This ordering corresponds to a periodic shift (every 5 cells along the orthorhombic *b* axis) of the structure by $\frac{1}{2}$ (a′ + c) in the a′,c plane. This out-of step shift corresponds to a "so-called" *antiphase boundary*. An *antiphase domain* may correspondingly be defined; in this case it contains 5 AuCu(I) type pseudocells. Several examples of one-dimensional long period structures found in 1:1 and 1:3 alloys and of two-dimensional long period structures (characterized by two different domain periods and two steps-shifts) found in 1:3 alloys have been presented by PEARSON [1972]; the role of the valence-electron concentration in defining the superstructure period has also been discussed. A general presentation of several antiphase boundaries (not only planar, but also cylindrical) and related structure groups may be found in the book of HYDE and ANDERSSON [1989].

It may be useful to mention here that antiphase domain boundaries play an important role in phase changes and microstructural stability of ordered alloys and intermetallics as well as affecting mechanical behaviour. The origin of antiphase domain boundaries has been examined and discussed by MORRIS [1992], emphasis has been given to the differences between a sharp boundary, as produced by crystal shear, and a relaxed fault structure. The kinetics of relaxation of shear produced fault have examined and it was shown by MORRIS [1992] that fast relaxation may affect the movement of dislocation by creating locking stresses as well as affecting cross slip behaviour significantly affecting mechanical properties. An important point in this study, as far as the origin of the antiphase domain boundaries are concerned, is the principle that a disordered crystal exists initially which subsequently becomes ordered. According to CAHN [1987], the observation of grown-in domain network is proof that the material existed, even if momentarily, in a disordered crystalline state before becoming ordered. In agreement with this, domain networks are commonly observed in weakly ordered alloys, for example $AuCu_3$, $FeNi_3$ and sometimes FeAl, but not in strongly ordered intermetallics such as Ni_3Al and TiAl. A review on the interactions of ordering and recrystallization has been published by CAHN [1990]. Aspects of recovery and recrystallization in the $L1_2$ $(Co_{0.78}V_{0.22})_3V$ ordered alloy have been reported by GIALANELLA and CAHN [1993].

4.3. Homeotect structure types (polytypic structures)

According to PARTHE [1964], two different structure types of the same formula X_mY_n are called *homeotect structure types*, if every X atom has the same number of nearest X neighbours and the same number of nearest Y neighbours, and, conversely, if every Y

atom has the same number of nearest X and Y neighbour atoms. It is possible for several structure types to show this feature.

All the different structure types of equal composition, which have (for corresponding atoms) the same kind of surroundings, form a *set of homeotect structure types* (the term *polytypic structures* is also used to denote the relationships observed with homeotect structures).

According to PARTHE [1964] all structure types which belong to a homeotect set can be described as different stacking variants of *identical structural unit slabs* ("*minimal sandwiches*"). All structure types of a set are constructed by stacking identical unit slabs one on top of another. The various types differ only in the relative horizontal displacement of these units. (The vertical unit cell edges of the different types are integer multiples of a common unit which is the height of the unit slab characteristic for the homeotect structure type set). All structure types which belong to a homeotect set have the same space-filling curve. (See sec. 7.2.4.)

A few important examples of groups of homeotect structure types will be described in the following sections. A short index of the same is the following list (in which the Jagodzinski–Wyckoff notation of the stacking pattern has been inserted, according to the indications given in sec. 3.5.2.).

— *Close-packed element structure types* (see sec. 6.2.): Mg-type (h), Cu-type (c), La-type (hc), Sm-type (hhc).
— *Equiatomic tetrahedral structure types (Carborundum Structure types)* (see sec. 6.3.): Wurtzite-type (h), Sphalerite-type (c), SiC polytypes (hc, hcc, hccc, hcchc, ..$(hcc)_5(hccc)(hcc)_5$hc ... $(hchcc)_{17}(hcc)_2$, .. $(hcc)_{43}$hc...).
— *Laves phases* (see sec. 6.6.4.): hP12 $MgZn_2$-type (h), cF24 Cu_2Mg-type (c), hP24 Ni_2Mg-type (hc), Laves polytypes (hhc, hhccc, etc.).

Other important sets of homeotect structure types are those related to disilicide structure types ($MoSi_2$, $CrSi_2$, etc.), cadmium halide structure types, etc. (See PARTHE [1964], HYDE and ANDERSSON [1989]), or presented by certain groups of compounds such as rare earth trialuminides (VAN VUCHT and BUSCHOW [1965]).

From a general point of view, *polytypism* may be considered a special case of polymorphism: the two-dimensional translations within the layers are (essentially) preserved whereas the lattice spacings normal to the layers vary between polytypes and are indicative of the stacking period (GUINIER *et al.* [1984]). As evidenced by ZVYAGIN [1987], we may distinguish various forms of polytypic structures, including (besides close-packing of like and unlike atoms) polytypes of tetrahedral, octahedral and prismatic layers packed according to the laws of closest packings. Complex silicate structures, for instance, may be considered which are characterized by much variety in the orientations and displacements of the layers and also structures in which two-dimensional layers are conjoined with one-dimensional band and island groups.

The aforementioned papers (GUINIER *et al.* [1984], ZVYAGIN [1987]) contain also suggestions and recommendations on the nomenclature and symbolism for use in the general case of either simple or complex polytypic structures.

Another method for discussing polytypic structures has been suggested by BOKII and

References: p. 363.

LAPTEV [1994]. The polytypic structures, described by means of special unit cell diagrams and crystal-chemical formulae, are distinguished by the number and type of Wyckoff positions.

4.4. Chimney-ladder structures (structure commensurability, structure modulation)

In the cases of ordered alloys, described in the foregoing sections, long period structures were considered in which the near-neighbour coordination of the atoms remains essentially unchanged between one structural modification and another.

More complex cases can, however, be considered. As an introduction to this point, we may remember that it is often convenient to describe structures as consisting, for instance, of two interpenetrating substructures (two different atom sets).

As an example, an interesting group of phases T_nX_m may be considered which are tetragonal and are formed between transition metals T and p-block elements X (of the Ga and Si groups). In these phases, along the *c* axis, the unit cell (superstructure cell, supercell) contains *n* pseudocells of T atoms and *m* interpenetrating pseudocells of X atoms. These phases (*Nowotny phases or "chimney-ladder" structures*) contain rows of atoms X (the "ladder"), with variable interatomic spacing from one compound to another, which are inserted into channels ("chimneys") in the T array. The T metals in all of the superstructures form a βSn–like array with the number of T metal atoms in the formula of the compound corresponding to the number of βSn–like pseudocells stacked in the *c* direction of the supercell (see sec. 6.3.1.). The arrangement of the atoms in these phases can be compared to that found in the structure of $TiSi_2$.

The following is a list of some chimney-ladder phases (phases containing as many as 600 atoms in the unit cell have been described):

tP20 Ru_2Sn_3 ($a = 617.2$ pm, $c = 991.5$ pm, $c/(2a\sqrt{2}) = 0.568$)
The Ru atoms form a βSn–like array with two pseudocells along the *c* direction of the supercell).
tP32 Ir_3Ga_5 ($a = 582.3$ pm, $c = 1420$ pm, $c/(3a\sqrt{2}) = 0.575$)
tP36 Ir_4Ge_5 ($a = 561.5$ pm, $c = 1831$ pm, $c/(4a\sqrt{2}) = 0.576$)
...
tP192–$V_{17}Ge_{31}$ ($a = 591$ pm, $c = 8365$ pm, $c/(17a\sqrt{2}) = 0.589$)
(In $V_{17}Ge_{31}$, for instance, there are 17 βSn like pseudocells of V atoms and 31 Ge pseudocells stacked along the *c* axis).

The atomic arrangements in a few chimney-ladder phases are shown in fig. 21 and compared with that found in $TiSi_2$. (This structure corresponds to the orthorhombic cell oF24–$TiSi_2$-type with $a_0 = 826.7$ pm, $b_0 = 480.0$ pm, $c_0 = 855.1$ pm. It can be approximately described in terms of a smaller body-centered tetragonal pseudocell, shown in fig. 21a, having $a' \approx a_0/\sqrt{2} \approx c_0/\sqrt{2}$; $c' = b_0$ and $c'/a_0 \approx 0.58$ (close to the "ideal" value $1/\sqrt{3} = 0.577...$).

The electron concentration appears to play some role in control of this family of structures as noted by Nowotny (SCHWOMMA *et al.* [1964a, 1964b], FLIEHER *et al.* [1968a, 1968b]), JEITSCHKO and PARTHE [1967] and PARTHE [1969] and reported by PEARSON [1972].

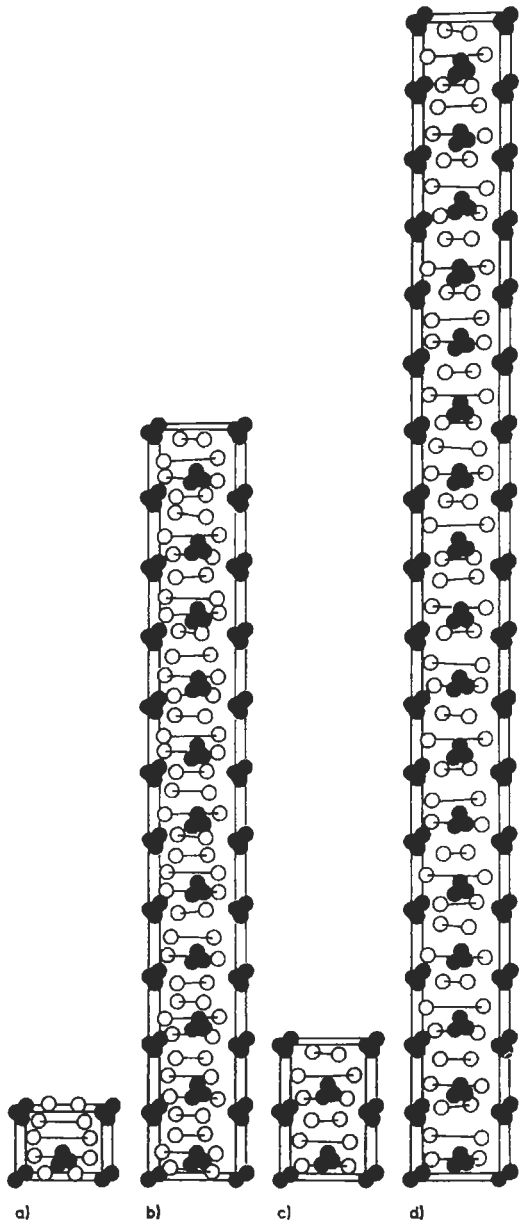

Fig. 21. Nowotny phases, chimney-ladder structures (JEITSCHKO and PARTHE [1967]).

a) The reference oF24–$TiSi_2$ type structure presented in terms of a tetragonal pseudo-cell (12 atoms in the pseudo-cell).

b) tP120–$Mn_{11}Si_{19}$; c) tP20–Ru_2Sn_3 and d) tI156–$Rh_{17}Ge_{22}$ phases.
(Notice that the metal atoms, black circles, form sequences of β-Sn like cells; compare with fig. 32 below).

References: p. 363.

In the book of HYDE and ANDERSSON [1989], the Nowotny phases are presented as a special case of a group of "*one-dimensional, columnar misfit structures*" which also include compounds such as $Ba_m(Fe_2S_4)_n$ and other complex sulphides. *Layer misfit structures*, such as those of some oxide-fluorides, arseno-sulphides, etc., are also presented and classified with reference to a concept of *structure commensurability* based on the recognition that (along one or more axes) the ratios between the different repeat units of various interpenetrating substructures can (or cannot) be represented as ratios between integer numbers.

The *coexistence of different kinds of periodicity* has also to be considered in the description of a quite different type of structure which is becoming increasingly common. In this, some atomic parameters (and/or the partial occupancy of some sites) vary in a periodic way through the structure. The periodicity may or may not be commensurate with the unit cell of the basic structure. (The ratio between the repetition length of this parameter and the lattice constant may or may not correspond to the ratio between two integer numbers). Structures having these characteristics are often termed *modulated structures* (HYDE and ANDERSSON [1989]). Several non-stoichiometric compounds present such modulations (FeS_x, Yb_3S_4, etc.). Various modulated structures have also been considered, for instance, for the NiAs-type structure (see sec. 6.5.1.).

An interesting case of *magnetic modulated structure* is that reported for $EuCo_2P_2$ (REEHUIS *et al.* [1992]). The *positional structure* of the atoms (of the atomic nuclei, nuclear structure) corresponds to the tI10–$ThCr_2Si_2$ type (see sec. 6.5.9). A magnetic structure has been also determined, which is related to the ordering of the magnetic moments of the Eu atoms. These moments are oriented perpendicular to the *c* axis and form an incommensurate spiral with the turning axis parallel to the *c* axis. The magnetic moments lie in the basal planes and they order parallel within these planes. Along the *c* axis, from one basal plane to the next one, there is a periodic rotation of the moments. The ratio, along the *c* axis, of the characteristic lengths of the magnetic and nuclear structures, is slightly dependent on temperature. At 64 K it is close to 5/6 (that is: there are 5 translation lenghts of the magnetic cell for 6 translation lengths of the nuclear structures). At 15 K the ratio was found to be close 6/7. If this magnetic structure is maintained at still lower temperatures, it may correspond to the exact 6/7 value. The ground state may then be called a commensurate structure with this ratio.

4.5. Recombination structures, intergrowth structure series

Some of the previously reported relationships between structures may be included in the general term "*recombination*" *structures*. Such structures (see LIMA DE FARIA *et al.* [1990]) are formed when topologically simple parent structures are periodically divided into blocks, rods or slabs (that is structure portions which are finite or infinite in one or two dimensions, respectively) which are recombined into derivative structures by means of one or more structure building operations. The most important operations are: *unit cell twinning*, *crystallographic shear planes*, *intergrowth* of blocks, rods or slabs of different structural types (for instance, intergrowth of cF24–$MgCu_2$ type and hP6–$CaCu_5$ type slabs to obtain the hP36–Ce_2Ni_7 type structure), *periodic out-of-plane*, antiphase boundaries

(AuCu(II), as an example), *rotation* of rods or blocks. The frequency of structure building operators (and, therefore, the size of undisturbed structure portions) can vary by well defined increments, so that many phases may occur as members of homologous series.

A few considerations about possible schemes of relationships between inorganic crystal structures based on a systematic "construction" of complex structural types by means of a few operations (symmetry operations, topological transformations) applied to some building units (point systems, clusters, rods, sheets), have been previously reported in sec. 3.5.4, following criteria suggested, for instance, by HYDE and ANDERSSON [1989] and by ZVYAGIN [1993].

We may add here that, within the "recombination" scheme, a very interesting method of describing, interpreting and interrelating complex structures is that based on the aforementioned "*intergrowth*" *concept* (KRIPYAKEVICH *et al.* [1972, 1976, 1979], GRIN′ *et al.* [1982, 1990], PARTHE *et al.* [1985], LIMA DE FARIA [1990], PANI and FORNASINI [1990]). According to this concept, selected structure types may be considered as belonging to certain intergrowth structure series. *The different structure types of an intergrowth series are described as being constructed from structure segments of more simple structures (the so-called "parent structures").*

In an other way, we may say that, according to this approach, the *construction modules* instead of being defined on a mere geometrical basis, are *selected* with reference to specific *crystallochemical criteria*. To this end, groups (series) of similar complex structures are analysed in order to recognize "fragments" which could be identified as structure segments of more simple structural types.

The structure series are then classified according to the *kind of fragments* and the *method of construction*. On the basis of the kind of fragments the structure series is described as homogeneous or inhomogeneous: *the homogeneous intergrowth structures* consist of identical fragments, the *inhomogeneous intergrowth structures* consist of segments (differing in composition and/or coordination) belonging to different parent structures. According to the method of construction, the intergrowth structure series can be classified into *one-dimensional* (linear), *two-* or *three-dimensional series*. In a *linear series* we have the one-dimensional stacking (along one direction) of two-dimensional, infinite segments (slabs) of the parent structures. The different structures of a *two-dimensional intergrowth series*, on the other hand, are built up by aggregations of several one-dimensional fragments (infinite rods, columns). Finally, the structures of a *three-dimensional intergrowth series* are constructed from (zero-dimensional, finite) parent structure blocks stacked in three dimensions.

It has been pointed out (GRIN′ [1992]) that slicing the parent structure into segments can be done in different ways. For a segment to be used in a particular structure series, for the members of which we are interested in predicting composition and symmetry, a number of requirements should be fulfilled. The segments should contain certain symmetry elements (in a linear series, for instance, all the segments used for the description usually contain some symmetry elements, mostly parallel to the stacking direction, which are retained in any stacking sequence, and represent the "minimal symmetry" of the series). The segments interfaces necessarily pass through atom centers.

References: p. 363.

(The composition of the segment is proportional to the stoichiometry of the parent structure: by addition it is possible to obtain the compositions of all possible structures of the series). The segments, moreover, selected from different parent structures, must have, at least, one topologically equal interface in order to make the intergrowth possible. Additional requirements are necessary when the atomic arrangement on the interface permits more than one possibility of intergrowing and when more complex (two-, three-dimensional) series are studied.

Considering, for instance, the particular case of the "linear intergrowth structure series", we may mention that many, binary and ternary, intermetallic phases can be considered members of those series (both homogeneous and inhomogeneous).

A representative of a structure belonging to a linear inhomogeneous series is presented in fig. 22. In this case, the parent structures are the oC8–CrB and oC12–UPt_2 types. The intergrowth structure presented is the oC28–W_3CoB_3 (or Y_3Co_3Ga) type. Its unit cell contains a segment arrangement corresponding to two repetition of a sequence containing a UPt_2 fragment followed by two CrB-type fragments. A simple code of this structure may be $(2_{CrB}1_{UPt2})_2$. Other members of the series have been described, for instance:

$1_{CrB}1_{UPt2}$ (corresponding to the oI10–W_2CoB_2 type);
$3_{CrB}1_{UPt2}$ (corresponding to the mC18–Y_4Co_4Ga type);
$(4_{CrB}1_{UPt2})_2$ (corresponding to the oC44–Y_5Co_5Ga type).

It is interesting to observe that many real representatives of this series may be found in the Y–Co–Ga system. This may be considered an example of the fact that, often, *several members* of a *certain intergrowth series* have representatives in the *same* (binary and ternary) *alloy system*. In the same system (or in chemically analogous systems) representatives of the parent structures may also be found (in the example reported, for instance, YCo has the CrB type structure). The interest of a crystallochemical description based on the intergrowth concept is thus evident.

As a further simple example, we may mention the structure of the oC16–$NdNiGa_2$ type belonging to the series $BaAl_4$–AlB_2. Its unit cell contains indeed two $BaAl_4$-type segments and two AlB_2-type segments. The simple code, previously considered, will be $(1_{BaAl4}1_{AlB2})_2$. (Notice, however, that in a more complex and detailed notation, superscripted indexes may be added to the formulae of the segments in order to specify, for instance, their symmetry (GRIN′ *et al.* [1982], PARTHE *et al.* [1985]).

General compositional formulae are often used for representing a series (GRIN′ [1992]). $Me_{m+n}X_{5m+3n}Y_{2n}$, for instance, may be the overall formula of a series consisting of intergrown $CaCu_5$-type and $CeCo_3B_2$-type slabs. (For the hP6–$CaCu_5$ type and its ordered variant hP6–$CeCo_3B_2$ type structures, see sec. 6.2.8.). Members of this series are the following structure types: hP12–$CeCo_4B$ (corresponding, in the aforementioned formula, to m = 1, n = 1), hP18–$Ce_3Co_{11}B_4$ (m = 1, n = 2), hP24–$Ce_2Co_7B_3$ (m = 1, n = 3), hP18–$Nd_3Ni_{13}B_2$ (m = 2, n = 1) and hP30–$Lu_5Ni_{19}B_6$ (m = 2, n = 3). We may notice in this case too, the close chemical analogy among the alloy systems (rare earth, nickel or cobalt, borides) forming structures corresponding to the different members of a given series.

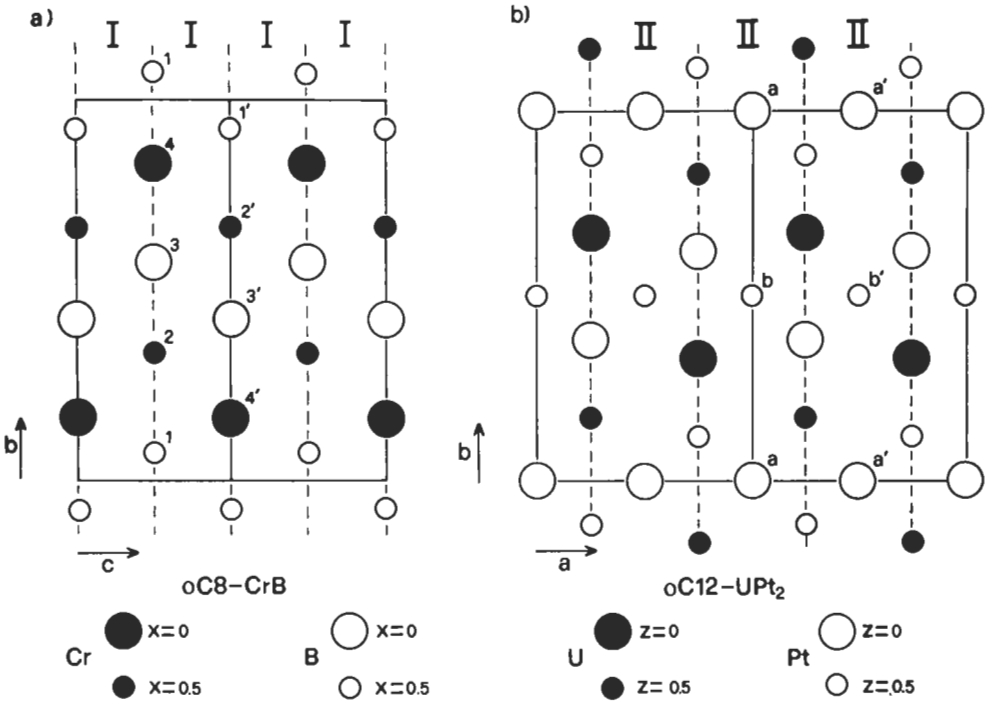

Fig. 22a, b

4.6. Group-subgroup relations for the representation of crystal-chemical relationships

According to the presentation given by BÄRNIGHAUSEN [1980], if two structures are topologically equivalent their interrelation may be conveniently expressed by *group–subgroup* relations between their space groups. Graphic representation of these relations leads to hierarchic ordering resembling a "*family tree*". At the top of the tree there is the so-called "*aristotype*" (a highly symmetrical structure). From the aristotype the other structures of the tree may be derived along specific routes of symmetry reduction. In order to obtain a well-defined description, the symmetry reduction is presented in terms of *minimal steps* (that is a given structure is followed by another whose space group is a so-called maximal subgroup (M) (see HAHN [1989]) of the space group (G) of the former structure). The minimal steps of symmetry reduction are characterized by the terms *lattice-equivalent* (M contains all the translations of G, the crystal class of M is of lower symmetry than that of G), or *class-equivalent* (M and G have the same crystal class but belong to different space-group types: M has lost translational symmetry, that is the primitive cell corresponding to M is larger than that of G) or *crystallographically-equivalent* (G and M belong to the same space group type, that is, as in the previous case, M has lost translational symmetry).

References: p. 363.

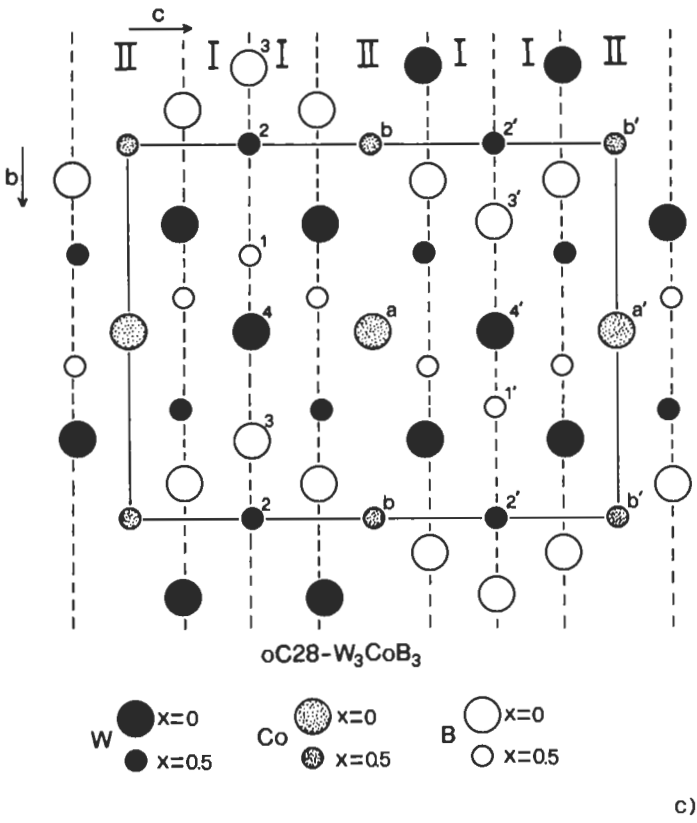

Fig. 22. An example of the application of the intergrowth concept. In a) and in b) two "parent" structures (CrB and UPt_2) are presented. The projections of a few unit cells (defined by the continuous lines) on the b,c and a,b planes respectively are shown. The structure segments which have been correspondingly identified are shown by dotted lines. In c) a member (W_3CoB_3 type structure) of the linear inhomogeneous series CrB-UPt_2 is presented (the sequence of parallel building segments is indicated). The segments characteristic of the CrB and UPt_2 structures have been indicated by I and II. In order to make easier the comparison, a few atoms with similar environments have been marked by the same numbers (or letters) in the parent and in the derived structures.

5. *Elements of systematic description of structure types. General remarks and references*

By means of the considerations previously presented some typical structures will be described in the following sections. On the basis of somewhat arbitrary criteria (such as high frequency of the structural type, existence of phases of considerable practical importance, possibility of presenting some features of general interest, etc.) the types to be described have been selected and presented in a few sections. This description, therefore, should be considered as only an initial introduction to a vast subject. As

already mentioned, complete and updated descriptions may be found in some reference books such as: LANDOLT–BÖRNSTEIN (HELLWEGE [1971], PREDEL [1991]), VILLARS and CALVERT [1985, 1991], MASSALSKI [1990] and DAAMS *et al.* [1991] that report (in alphabetical order) all the known binary systems. They can be considered complete riformulation of "classic" books such as: HANSEN [1936], HANSEN and ANDERKO [1958], ELLIOTT [1965], SHUNK [1969], MOFFATT [1986]. Phase diagrams are presented and discussed; crystal structure data of the intermediate phases, moreover, are systematically given. A similar lay-out has been adopted in the Monograph Series on Alloy Phase Diagrams published by ASM International. The book of VILLARS and CALVERT [1991] consists of an "*Handbook of Crystallographic Data*" (in 4 volumes); DAAMS *et al.* [1991] published an "*Atlas of Crystal Structure Types*" (in 4 volumes). The "Handbook" reports all the data available for binary (and complex) intermetallic phases. The "Atlas" describes the different structural types presenting (both by using tables and drawings) atomic coordinates, interatomic distances and coordination polyhedra.

For a general presentation of the Inorganic Crystallochemistry, see, for instance, WELLS [1970].

For a *systematic classification* of the *intermetallic structure types*, the *following monographs* may be consulted.

SCHUBERT [1964] in his book "*Kristallstrukturen Zweikomponentiger Phasen*" (Crystal Structures of Binary Phases) described a few hundred structural types. In this book, Schubert paid great attention to chemical criteria for the description, classification and discussion of the properties of the different phases. The position of the elements involved in the Periodic Table was considered particularly relevant. For this purpose, the elements were considered by Schubert to be subdivided into the following families: A-metals (elements of the s-block of the periodic table), T-metals (transition metals), B-elements (elements of the p-block of the Periodic Table). The different structural types were then described according to the following chapter subdivision:

Brass-type alloys and *close-packed* sphere stacking and superstructure variants: $AuCu_3$, AuCu, $SrPb_3$, $ZrAl_3$, $ZrGa_2$, Nb_5Ga_{13}, etc.; Mg-type structure and superstructures Ni_3Sn, etc.; body-centered sphere packing W structure and derivatives Fe_3Si, CsCl, NaTl, Cu_5Zn_8, Ni_2In, etc.

T–T phases (among which the T element structures of the so-called Cr_3Si family such as the βU, cI58–αMn, hR39–W_6Fe_7, Th_6Mn_{23}, etc., and then the Laves phase structures).

B–B phases (structures considered as deformation variants of close-packed structures, such as Zn, In, etc., structures of B, graphite, structures of the diamond-family, of the P and As families, etc.).

A–B phases (several types partly classified according to the stoichiometry: Li_3Bi, Mg_2Sn, Mg_3Sb_2, NaCl, etc.).

T–B phases (T-rich borides, carbides, nitrides, oxides and hydrides, $CuAl_2$, $MoSi_2$, NiAs, FeS_2 structures and their variants).

PEARSON [1972], in his book "*The Crystal Chemistry and Physics of Metals and Alloys*", discussed the characteristics and specific features (coordination, stability, relationships

References: p. 363.

with other structures, etc.) of about a thousand structure types. He was able to classify all these structures in 12 different families. The most important 10 are summarized here below.

1) *Valence compounds of non-metals* (semiconducting compounds with anions forming close packed arrays, polyanionic compounds, polycationic compounds, group IV, V and VI elements and IV-VI and V-VI compounds, etc.).
2) *Metastable phases, interstitial phases, martensite* (in this group of phases the Hägg interstitial phases formed by transition metal and small non-metal atoms such as H, B, C, N have been especially considered: in these phases the non-metals occupy the interstices, generally the octahedral ones of the close-packed structures of the transition metals).
3) *Structures based on the close packing of the 3^6 close-packed nets* (Cu and Mg structures and their derivative structures $AuCu_3$, AuCu, Ti_3Cu, $TiAl_3$, $ZrGa_2$, $MoNi_4$, etc.).
4) *Structures derived by filling tetrahedral, octahedral (and other) holes in close-packed arrays of atoms* (sphalerite structure and derivative structures oP12–CuAsS, tI16–$FeCuS_2$, tI16–Cu_3AsS_4, etc., wurtzite structure and derivative structures, oP16–$CuSbS_2$, oP16–Cu_3AsS_4, hP30–In_2Se_3, etc.; CaF_2 structure and distorted, defective, superstructures of CaF_2; NaCl structure and derivative structures of the NaCl type; NiAs structure, etc.).
5) *Structure types dominated by triangular prismatic arrangements* (hP2–WC, hR9–MoS_2, tI8–NbAs, tP6–Cu_2Sb, oP36–Ta_2P, hP3–AlB_2, hP6–$CaIn_2$, hP6–Ni_2In and their variants, are examples of structure types included in this group).
6) *Structures based on simple cubic and body centered cubic packing* (in this group the structure types cI2–W, tI2–Pa, martensite, cP6–Cu_2O, cP2–CsCl, tP4–TiCu, cF16–Li_3Bi, cF16–NaTl, cF16–$MnCu_2Al$, tP3–$FeSi_2$, cI52–Cu_5Zn_8 and several variants are considered. In this structure family the Nowotny chimney-ladder phases are also included).
7) *Structures generated by square-triangle nets of atoms: cubes and cubic antiprisms* (for instance tI12–$CuAl_2$, oP24–$AuSn_2$, mC12–PdP_2, oC20–$PtSn_4$, tP10–U_3Si_2, tP40–$FeCu_2Al_7$, oP16–ThNi, oI20–UAl_4, etc.)
8) *Structures generated by alternate stacking of triangular and kagomé nets.* (The structures of hP6–$CaCu_5$, tI26–$ThMn_{12}$, hP38–Th_2Ni_{17} and their variants are included in this family. The Laves phases cF24–Cu_2Mg, hP12–$MgZn_2$ and hP24–Ni_2Mg types and several variants are considered in this family. However, they are also described, as Frank–Kasper structures, in the subsequent group).
9) *Structures in which icosahedra and CN 14, 15 and 16 polyhedra play a dominant role.* (Laves phases, μ phases: hR39–W_6Fe_7; P phases: oP56–Mo-Cr-Ni phase, (which, at a composition corresponding to 42 at% Mo and 18 at% Cr, has a unit cell containing 56 atoms in partial substitutional disorder); R phases: hR159–Mo-Co-Cr, etc. are included in this family, as well as a number of intermetallic phases with giant cells such as the cF1124–Cu_4Cd_3, cF1192–$NaCd_2$, cF1832–Mg_2Al_3 types studied by SAMSON [1969].

10) *Structures with large coordination polyhedra.* (Structures are presented in which large coordination polyhedra are contained: for instance cP36–$BaHg_{11}$ in which Ba is surrounded by 20 Hg, tI92–Ce_5Mg_{41}, tI48–$BaCd_{11}$, cF112–$NaZn_{13}$ in which coordination polyhedra corresponding to coordination numbers (CN) 20, 22 and 24 are present respectively).

As a comment to the Pearson's classification and description of structure types we may mention a paper by PEARSON [1985b] himself on the classification of the crystal structures of intermetallic phases according to building principles and properties. Five groups of phases have been evidenced:

1) Phases based on geometrical packings;
2) Phases in which the band-structure energy is an unusually large fraction of the total energy;
3) Valency compounds;
4) Framework structures;
5) Hybrid framework structures with geometrical packings.

A substantially geometrical approach has been adopted in their book "*Inorganic Crystal structures*", by HYDE and ANDERSSON [1989] who presented and discussed the structure of more than a thousand inorganic compounds, explicitly ignoring "the artificial barrier between inorganic and mineral structures on the one hand and metallurgical structures (intermetallic compounds, borides, carbides, etc.) on the other." In their treatment and classification of the structural types, they generate complex structures starting with relatively few basic structures and applying to segments of such structures, one or more of a few geometrical operations that are essentially symmetry operators. The "segments" or building units considered may be blocks (or clusters, bounded in 3 dimensions), rods, (or columns, bounded in 2 dimensions, infinite in the third), slabs (or lamellae, sheets, layers, the latter bounded in 1 dimension and infinite in the other two).

6. *Description of a few selected structural types*

The selected structural types which will be presented in the following sections arranged in a few groups according to their crystallochemical interrelations are also alphabetically summarized, for reader convenience, in Appendix 1: "Gazetteer of Intermetallic Phases".

For the different phases described, the values of the lattice parameters have been generally reported: this may indeed be useful in comparing different structures and in order to get a better idea of the real atomic packing. Notice, however, that, generally, for the various phases, several slightly different values have been reported in the literature (owing to different preparation and measurement techniques and/or to the existence of certain, often not well-defined, homogeneity ranges). The reader interested in accurate values of the lattice parameters should therefore consult the original literature.

References: p. 363.

6.1. bcc W-type structure and derivative structures

In this section a few structural types are presented which can be described as related to the simple body-centered cubic structure, cI2–W type. For some of them, fig. 23 shows the normalized interatomic distances and the corresponding numbers of equidistant atoms.

6.1.1. Structural type: cI2–W

Body-centered cubic, space group $Im\bar{3}m$, No. 229.
Atomic positions:
2 W in a) 0,0,0; $\frac{1}{2},\frac{1}{2},\frac{1}{2}$
Coordination symbol: $\overset{3}{\underset{\infty}{}}[W_{8/8}]$
Layer stacking symbols:
Triangular (T) nets: $W_0^A W_{1/6}^B W_{1/3}^C W_{1/2}^A W_{2/3}^B W_{5/6}^C$
Square (S) nets: $W_0^1 W_{1/2}^4$
For the prototype itself, W, a = 316.5 pm.

This structure can be compared with the CsCl type structure (which can be obtained from the W type by an ordered substitution of the atoms) and the $MnCu_2Al$ type structure ("ordered" superstructure of the CsCl type): see fig. 24a and 24b and notice the typical 8 (cubic) coordination.

The W-type structure is shown by a number of unary systems: Li, Na, K, Rb, Ba, Cr, Eu, Cr, Mo, V, Ta, W, etc., (as the only form or the room temperature stable form), Be, Ca, Sr, several rare earth elements, Th, etc., (as a high temperature form) and α and δ Fe forms.

The same structure is formed in a number of binary (or ternary) phases, for which a random distribution of the two (or three) atomic species in the two equivalent sites is possible. Typical examples are the β-Cu–Zn phase (in which the equivalent 0,0,0; $\frac{1}{2},\frac{1}{2},\frac{1}{2}$ positions are occupied by Cu and Zn with a 50% probability) and the β-Cu–Al phase having a composition around Cu_3Al (in which the two crystal sites are similarly occupied, on average by Cu, with a 75% occupation probability, and by Al, with a 25% occupation probability). A number of these phases can be included within the group of the "Hume–Rothery" phases (see sec. 3.4.). In the Villars–Calvert compilation 380 phases (about 1.5% of the total number of phases considered) are listed under this structural type (which is the 11th in the frequency order).

6.1.2. Structural type: cP2–CsCl

Cubic, space group $Pm\bar{3}m$, No.221.
Atomic positions:
1 Cs in a) 0,0,0
1 Cl in b) $\frac{1}{2},\frac{1}{2},\frac{1}{2}$
Coordination formulae:
$\overset{3}{\underset{\infty}{}}[CsCl]_{8/8}$ or $\overset{3}{\underset{\infty}{}}[CsCl]_{8cb/8cb}$ (ionic description)
$\overset{333}{\underset{\infty}{}}[X_{6/6}][Y_{6/6}]_{8/8}$ or $\overset{333}{\underset{\infty}{}}[X_{6o/6o}][Y_{6o/6o}]_{8cb/8cb}$ (metallic description)

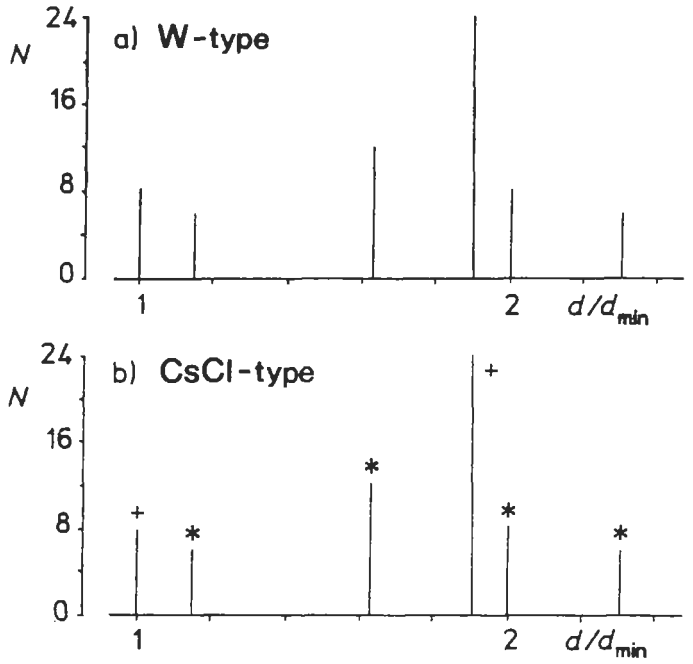

Fig. 23a,b. Trends of interatomic distances and coordinations in a group of closely interrelated structures.
a) cI2–W type structure: coordination around W.
b) XY compounds of cP2–CsCl type structure:
(+) X–Y (or Y–X) coordination.
(*) X–X (or Y–Y) coordination.

Layer stacking symbols:
Triangular (T) nets: $Cs_0^A Cl_{1/6}^B Cs_{1/3}^C Cl_{1/2}^A Cs_{2/3}^B Cl_{5/6}^C$
Square (S) nets: $Cs_0^1 Cl_{1/2}^4$
For the prototype itself, CsCl, a = 411.3 pm.

See also fig. 3. The 8 coordination (cubic) of the two atomic species is apparent.

The normalized interatomic distances and numbers of equidistant neighbours are shown in fig. 23. In the same figure data are also reported for the W type structure, which can be considered a degenerate structure of the CsCl type structure (in the W type structure the two atomic sites are equivalent) and of the derivative (superstructure) $MnCu_2Al$ type.

The CsCl type structure is adopted by many of the 1:1 intermetallics and by a few halide and chalcogenide 1:1 (ionic) compounds (for which, however, it is in competition with the NaCl type structure (see sec. 6.4.1)). Of the monohalides only CsCl, CsBr, CsI, TlCl, TlBr and TlI (and of the monochalcogenides only, ThTe) have the CsCl type structure, while the rest with a lower atomic (ionic) ratio have the NaCl type structure (corresponding to a lower coordination, 6 instead of 8).

References: p. 363.

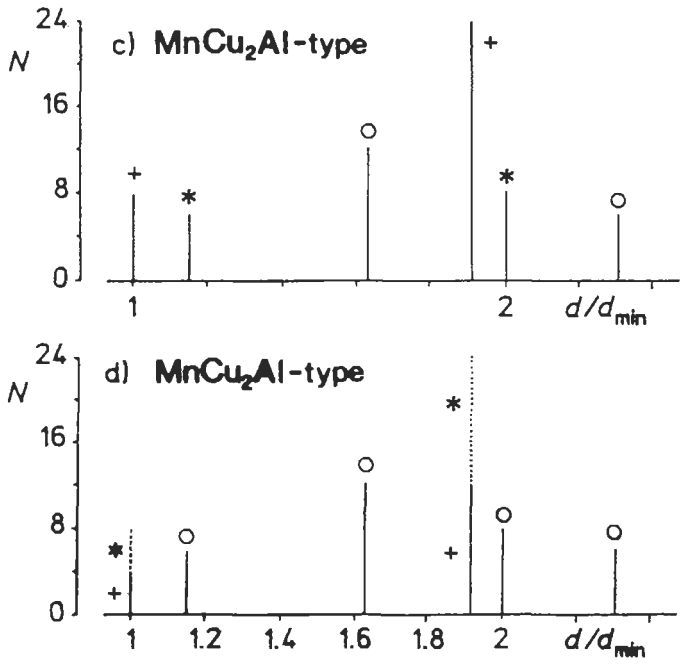

Fig. 23c,d. Trends of interatomic distances and coordinations in a group of closely interrelated structures.
c) cF16–$MnCu_2Al$ type structure: coordination around Al (or Mn)
(+) Al–Cu (or Mn–Cu); (*) Al–Mn (or Mn–Al);
(o) Al–Al (or Mn–Mn).
d) cF16–$MnCu_2Al$ type structure: coordination around Cu
(+) Cu-Mn; (*) Cu–Al; (o) Cu–Cu.

As for the intermetallics, in the Villars-Calvert compilation, about 460 compounds (≈ 1.8% of the total number of phases considered) are listed under this structural type (7th in the frequency rank order); about 300 phases are binary, the others are (more or less disordered) ternary phases. Among the binary phases we may mention 1:1 compounds such as those of alkaline earth and rare earth elements with Mg, Zn, Cd, Hg (and often with In, Tl, Ag, Au), those of Al and Ga with Fe and Pt group metals. The β' Cu–Zn phase (stable at room temperature) belongs to this structural type; at higher temperature it undergoes the order–disorder transformation into the disordered cI2–W-type, β phase. FeAl also is an example of a phase having this (more or less) ordered structure. It corresponds to a solid solution range from ≈ 23 to ≈ 55 at% Al. It forms through ordering of the α Fe, cI2–W type, phase which has a solubility range from 0 to ≈ 45 at% Al.

Other interesting phases belonging to this structural type are:

Ni_xAl_{1-x} (homogeneous between 42 and 69 at% Ni) with good mechanical and oxidation resistance properties. (By quenching from high temperatures the formation of an ordered martensite is obtained which can be considered for shape memory behaviour).

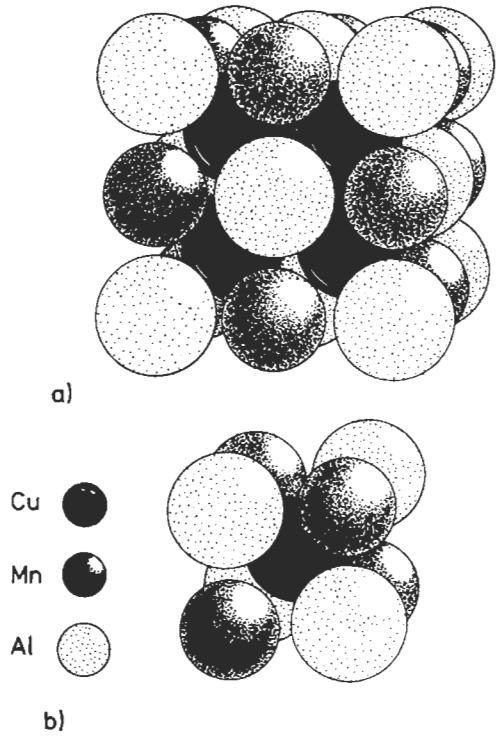

Fig. 24. cF16–$MnCu_2Al$ type structure. The unit cell is shown in a). This structure degenerates in the Li_3Bi type if the Cu and Mn positions become equivalent. The small cube presented in b) corresponds to $\frac{1}{8}$ of the $MnCu_2Al$ unit cell and degenerates into a CsCl type cell if the atoms at the vertices (Mn + Al positions) are equal. Moreover a further degeneration in the W type will be obtained if all the atoms are equal.

Co_xAl_{1-x} (≈ 48 to 79 at% Co), Co_xBe_{1-x} (26 to 53 at% Co), Ni_xBe_{1-x} (≈ 25 to 52 at% Ni), PdBe (≈ 50 at% Pd), Cu_xBe_{1-x} (≈ 51 to 53 at% Cu), etc.

For a discussion on substitutional additions to CsCl type alloys (site preference for dilute additions to NiAl, FeAl, CoAl, etc.) see KAO *et al.* [1994].

Finally, we may mention Ti_xPd_{1-x} (47 to 53 at%Pd) and Ti_xPt_{1-x} (46 to 54 at% Pt) which have the CsCl type structure at high temperature and the oP4–AuCd structure at low temperature.

6.1.3. Structural type: cF16–$MnCu_2Al$

Face-centered cubic, space group $Fm\bar{3}m$, No. 225.

Atomic positions:

4 Al in a) 0,0,0; $\frac{1}{2},\frac{1}{2},0$; $\frac{1}{2},0,\frac{1}{2}$; $0,\frac{1}{2},\frac{1}{2}$

4 Mn in b) $\frac{1}{2},\frac{1}{2},\frac{1}{2}$; $0,0,\frac{1}{2}$; $0,\frac{1}{2},0$; $\frac{1}{2},0,0$

8 Cu in c) $\frac{1}{4},\frac{1}{4},\frac{1}{4}$; $\frac{3}{4},\frac{3}{4},\frac{1}{4}$; $\frac{3}{4},\frac{1}{4},\frac{3}{4}$; $\frac{1}{4},\frac{3}{4},\frac{3}{4}$; $\frac{3}{4},\frac{3}{4},\frac{3}{4}$; $\frac{1}{4},\frac{1}{4},\frac{3}{4}$; $\frac{3}{4},\frac{1}{4},\frac{1}{4}$; $\frac{1}{4},\frac{3}{4},\frac{1}{4}$

Coordination formula:
$^{3}_{\infty}[AlCu_{8/4}Mn_{6/6}]$

For the layer stacking symbols, the data are reported in the next section in comparison with the Li_3Bi and NaTl type structures.

For the prototype itself, $MnCu_2Al$, a = 596.8 pm.

The structure is shown in fig. 24. In this figure a comparison is also made with the CsCl type structure. It is apparent that if the two a) and b) sites are occupied by the same atomic species, the cell degenerates into a block of 8 equal cells (of the CsCl-type). We may also observe that, on the contrary, if a single atomic species were assigned to the b) and c) sites, another ordered structure would be obtained, corresponding to the 1:3 stoichiometric ratio (Li_3Bi-type or BiF_3-type).

In the Villars–Calvert compilation the phases belonging to the $MnCu_2Al$ and Li_3Bi types are listed together. (See also sec. 6.1.3. and 6.1.4.). They are about 380 (≈ 1.5% of the total number of phases considered and 12th in the frequency rank order).

Among the ternary alloys, we may mention several $Me'Me''Me'''_2$ phases (with Me′ = Al, Ga, Ge, Sn; Me″ = Ti, Zr, Hf, V, Nb, Mn, etc. and Me‴ = Co, Ni, Cu, Au, etc.). The compounds which crystallize with the $MnCu_2Al$ type structure (and particularly the magnetic compounds having this structure) are called *Heusler Phases*. In the specific case of the Al–Cu–Mn system this phase is ferromagnetic and stable above 400°C, but it can be frozen by quenching to room temperature. It is assumed that its whole moment is due to the spin moment of Mn which has an unfilled d shell (5 electrons). Magnetic properties of Heusler phases are strongly dependent on the ordering of the atoms.

6.1.4. Structural types: cF16–Li_3Bi and cF16–NaTl

cF16–Li_3Bi type is face-centered cubic, space group $Fm\bar{3}m$, No. 225.
Atomic positions:
4 Bi in a) 0,0,0; $\frac{1}{2},\frac{1}{2},0$; $\frac{1}{2},0,\frac{1}{2}$; $0,\frac{1}{2},\frac{1}{2}$
4 Li in b) $\frac{1}{2},\frac{1}{2},\frac{1}{2}$; $0,0,\frac{1}{2}$; $0,\frac{1}{2},0$; $\frac{1}{2},0,0$
8 Li in c) $\frac{1}{4},\frac{1}{4},\frac{1}{4}$; $\frac{3}{4},\frac{3}{4},\frac{1}{4}$; $\frac{3}{4},\frac{1}{4},\frac{3}{4}$; $\frac{1}{4},\frac{3}{4},\frac{3}{4}$; $\frac{3}{4},\frac{3}{4},\frac{3}{4}$; $\frac{1}{4},\frac{1}{4},\frac{3}{4}$; $\frac{3}{4},\frac{1}{4},\frac{1}{4}$; $\frac{1}{4},\frac{3}{4},\frac{1}{4}$
Coordination formula:
$^{3}_{\infty}[BiLi_{8/4}Li_{6/6}]$ (ionic description)
For the layer stacking symbols, see under the following description of the NaTl type.
For the prototype itself, Li_3Bi, a = 672.2 pm.

This structure (or BiF_3 structure) could also be described as derived from a cubic close-packed array of atoms (Bi atoms) by filling all the tetrahedral and octahedral holes with Li (or F) atoms.

The *cF16–NaTl type* structure is face-centered, cubic, space group $Fd\bar{3}m$, No. 227.
Atomic positions:
8 Tl in a) 0,0,0; $0,\frac{1}{2},\frac{1}{2}$; $\frac{1}{2},0,\frac{1}{2}$; $\frac{1}{2},\frac{1}{2},0$; $\frac{3}{4},\frac{1}{4},\frac{3}{4}$; $\frac{3}{4},\frac{3}{4},\frac{1}{4}$; $\frac{1}{4},\frac{1}{4},\frac{1}{4}$; $\frac{1}{4},\frac{3}{4},\frac{3}{4}$.
8 Na in b) $\frac{1}{2},\frac{1}{2},\frac{1}{2}$; $\frac{1}{2},0,0$,; $0,\frac{1}{2},0$; $\frac{1}{2},\frac{1}{2},0$; $\frac{1}{4},\frac{3}{4},\frac{1}{4}$; $\frac{1}{4},\frac{1}{4},\frac{3}{4}$; $\frac{3}{4},\frac{3}{4},\frac{3}{4}$; $\frac{3}{4},\frac{1}{4},\frac{1}{4}$.
For the prototype, NaTl, a = 747.3 pm.

LiZn, LiCd, LiAl, NaIn have this structure.

This structure may be regarded as a completely filled-up fcc arrangement in which each component occupies a diamond like array of sites (see sec. 6.3.1. and, in sec. 3.4., "Zintl Phases".)

The structure may thus be presented as **NaTl**: **D** + D′ (see the descriptions in terms of combination of invariant lattice complexes reported in sec. 3.1.).

The coordination formula is $^{33}_{88}Na[Tl_{4/4}]_{4/4}$.

All the three cF16–NaTl, Li_3Bi and $MnCu_2Al$ types, which may also be considered as composed of four interpenetrating face centered cubic arrays (F + F′ + F″ + F‴), correspond to the same space filling as in 8 b.c. cubic (or in 8 CsCl type) cells (see fig. 24).

The layer stacking symbols of the NaTl structure are here reported in comparison with those of the cF16–Li_3Bi and cF16–$MnCu_2Al$ types.

Triangular (T) nets:

NaTl type:

$Na_0^A\ Tl_{1/12}^B\ Tl_{1/6}^C\ Na_{1/4}^A\ Na_{1/3}^B\ Tl_{5/12}^C\ Tl_{1/2}^A\ Na_{7/12}^B\ Na_{2/3}^C\ Tl_{3/4}^A\ Tl_{5/6}^B\ Na_{11/12}^C$

Li_3Bi type

$Bi_0^A\ Li_{1/12}^B\ Li_{1/6}^C\ Li_{1/4}^A\ Bi_{1/3}^B\ Li_{5/12}^C\ Li_{1/2}^A\ Li_{7/12}^B\ Bi_{2/3}^C\ Li_{3/4}^A\ Li_{5/6}^B\ Li_{11/12}^C$

$MnCu_2Al$ type

$Al_0^A\ Cu_{1/12}^B\ Mn_{1/6}^C\ Cu_{1/4}^A\ Al_{1/3}^B\ Cu_{5/12}^C\ Mn_{1/2}^A\ Cu_{7/12}^B\ Al_{2/3}^C\ Cu_{3/4}^A\ Mn_{5/6}^B\ Cu_{11/12}^C$

Square (S) nets:

NaTl type:

$Na_0^1\ Na_0^4\ Tl_0^5\ Na_{1/4}^6\ Tl_{1/4}^7\ Tl_{1/2}^1\ Tl_{1/2}^4\ Na_{1/2}^5\ Tl_{3/4}^6\ Na_{3/4}^7$

Li_3Bi type

$Bi_0^1\ Bi_0^4\ Li_0^5\ Li_{1/4}^6\ Li_{1/4}^7\ Li_{1/2}^1\ Li_{1/2}^4\ Bi_{1/2}^5\ Li_{3/4}^6\ Li_{3/4}^7$

$MnCu_2Al$ type:

$Al_0^1\ Al_0^4\ Mn_0^5\ Cu_{1/4}^6\ Cu_{1/4}^7\ Mn_{1/2}^1\ Mn_{1/2}^4\ Al_{1/2}^5\ Cu_{3/4}^6\ Cu_{3/4}^7$

6.1.5. Comments on the bcc derivative structures

In the family of bcc derivative structures we may include several other structural types.

As an important *defect superstructure* based on the bcc structure we may mention the **cP52–Cu_9Al_4** type structure (Ag_9In_4, Au_9In_4, Pd_8Cd_{43}, Co_5Zn_{21}, Cu_9Ga_4, $Li_{10}Pb_3$ can be considered reference formulae of selected solid solution phases having this structure). The large cell (a = 870.4 pm in the case of Cu_9Al_4) can be considered to be obtained by assembling 27 CsCl type pseudocells with two vacant sites. One vacant site occurs on each sublattice $Al_{16}Cu_{10}\square$ and $Cu_{26}\square$.

The **γ-brass, cI52–Cu_5Zn_8**-type structure can be similarly described as a distorted defect superstructure of the W type structure, in which 27 pseudocells are assembled together with two vacant sites (corner and body center of the supercell). In this case, however, the atoms, are considerably displaced from their ideal sites. The structure could also be described as built up of interpenetrating, distorted, icosahedra (each atom being sur-

rounded by 12 neighbours). This description applies also to the cP52–Cu_9Al_4 type structure. (Ag_5Cd_8, Li_7Ag_3, Ag_5Zn_8, V_5Al_8, Au_5Cd_8, Au_5Hg_8, Fe_3Zn_{10}, $NiGa_4$, V_6Ga_7, Ni_2Zn_{11}, etc. crystallize in the cI52–Cu_5Zn_8 structural type).

Martensite. The iron-carbon martensite structure can be considered a tetragonal distortion of the body-centered cubic cell of Fe (a = 285 pm, c = 298 pm at ≈ 1 mass% C (≈ 4.5 at%), in comparison to a = 286.65 pm for α-Fe, cI2–W type). Carbon is randomly distributed in the octahedral holes having coordinates $0,0,\frac{1}{2}$ and $\frac{1}{2},\frac{1}{2},0$. Typically an occupancy of these sites of only a few % has to be considered. For a 100% occupancy the structure of the tI4–CoO type (low-temperature form) is obtained with 2 Co in a) $0,0,0$; $\frac{1}{2},\frac{1}{2},\frac{1}{2}$; and 2 O in b) $0,0,\frac{1}{2}$; $\frac{1}{2},\frac{1}{2},0$ in the space group I4/mmm, No. 139. In the martensitic cell the position parameters of the Fe atoms have a range along the fourfold axis, so there is a displacement from the cell corners and body center and an enlargement of the octahedral holes containing carbon. (Notice, however, that "*martensite*" is also a general name used by metallurgists to denote all phases formed by diffusionless shear).

Al–Cu–Ni continuous sequence of ordered structures. An interesting series of superstructures have been described by LU and CHANG [1957a, 1957b]. For an assessed description of the system and of the intermediate phases see PRINCE [1991]. They all have hexagonal unit cells (some corresponding to rhombohedral structures) based on ordered sequences of pseudo cubic subcells slightly distorted in rhombohedra having the constant a_{rhom} included between 289 and 291 pm and the interaxial angle α_{rhom} included between 90.34 and 90.10°. (These data may be compared with the values a = ≈ 288 pm and, of course, $\alpha = 90°$, for the cubic CsCl type unit cell of NiAl at the 50 at% Al composition). The hexagonal cells of the superstructures have a certain number of subcells stacked along c. Al atoms occupy the corners of the subcells and Ni,Cu (Me) atoms or vacancies (Vac) occupy the centers in ordered array, vacancies occurring along the three triad axes ($0,0,0$; $\frac{1}{2},\frac{2}{3},z$; $\frac{2}{3},\frac{1}{3},z$). All together these phases corresponds to the τ-region lying in the ternary system in a domain included between ≈ 7 and 12 at% Ni and between ≈ 27 and 38 at% Cu. The different τ_i ordered structures correspond to the stacking of i subcells centred according to a definite sequence of Vac or Me atoms.

Following stacking variants have been described:

$\tau_5 \approx (Ni,Cu)_3Al_5$, hR24, a = 411.9 pm, c = 2512.5 pm (= 5 * 502.5)
stacking sequence VacMeMeMeVac = $VacMe_3Vac$

$\tau_6 \approx (Ni,Cu)_4Al_6$, hP30, a = 411.3 pm, c = 3013.5 pm (= 6 * 502.3)
stacking sequence $VacMe_4Vac$

$\tau_7 \approx (Ni,Cu)_5Al_7$, hP36, a = 410.6 pm, c = 3493.8 pm (= 7 * 499.1)
stacking sequence $VacMe_5Vac$

$\tau_8 \approx (Ni,Cu)_6Al_8$, hR42, a = 410.5 pm, c = 3990 pm (= 8 * 498.8)
stacking sequence $VacMe_6Vac$

$\tau_{11} \approx (Ni,Cu)_6Al_{11}$, hP51, a = 411.5 pm, c = 5528.9 pm (= 11 * 502.6)
stacking sequence $VacMe_3Vac_3Me_3Vac$

$\tau_{13} \approx (Ni,Cu)_8Al_{13}$, hR63, a = 411.3 pm, c = 6517.3 pm (= 13 * 501.3)
stacking sequence $VacMe_4Vac_3Me_4Vac$

$\tau_{15} \approx (Ni,Cu)_{10}Al_{15}$, hP75, a = 409.6 pm, c = 7464.5 pm (= 15 * 497.6)
stacking sequence $VacMe_5Vac_3Me_5Vac$
$\tau_{17} \approx (Ni,Cu)_{12}Al_{17}$, hP87, a = 410.1 pm, c = 8449.9 pm (= 17 * 497.1)
stacking sequence $VacMe_6Vac_3Me_6Vac$

These structures appeared to be determined by the free electron concentration. They represent a so-called "*continuous sequence of ordered structures*" or, infinitely adaptive structures (HYDE and ANDERSSON [1989]). These structures occupy a single-phase field in the system: it has been observed that, in such cases, may be ambiguous to define a phase in terms of a unit cell of structure.

6.2. Close-packed structures and derivative structures

In this section, a few important elemental structures are described. Particularly the cubic (cF4–Cu type) and hexagonal close-packed (hP2–Mg) structures are presented. A few other stacking variants of identical monoatomic triangular nets are also reported. A group of structures which can be considered as derivative structures of Cu are also described.

Normalized interatomic distances and numbers of equidistant neighbours are shown in figs. 25 and 26.

6.2.1. Structural type: cF4–Cu

Face-centered cubic, space group $Fm\bar{3}m$, No. 225.
Atomic positions:
4 Cu in a) 0,0,0; $0,\frac{1}{2},\frac{1}{2}$; $\frac{1}{2},0,\frac{1}{2}$; $\frac{1}{2},\frac{1}{2},0$;
Coordination formula: $\frac{3}{\infty}[Cu_{12/12}]$
Layer stacking symbols:
Triangular (T) nets: $Cu_0^A\, Cu_{1/3}^B\, Cu_{2/3}^C$
Square (S) nets: $Cu_0^1\, Cu_0^4\, Cu_{1/2}^5$
For the prototype itself, Cu, a = 361.46 pm.

The atoms are arranged in close packed layers stacked in the ABC sequence (see sec. 3.5.2.).

Several metals, such as Al, Ag, Au, α Ca, α Ce, γ Ce, α Co, Cu, γ Fe, Ir, β La, Pb, Pd, Pt, Rh, α Sr, α Th and the noble gases Ne, Ar, Kr, Xe crystallize in this structural type. Several binary (and complex) phases having this structure have also been reported (solid solutions with random distribution of several atomic species in the four equivalent positions).

6.2.2. Cu-derivative, substitutional and interstitial superstructures (tetrahedral and octahedral holes)

Derivative structures may be obtained from the Cu type structure by ordered substitution or by ordered addition of atoms. As examples of *derivative structures* obtained *by ordered substitution* (and/or distortion) in the Cu type we may mention the $AuCu_3$, AuCu, Ti_3Cu types, which are described here below. (In the specific case of the $AuCu_3$ type structure and the Cu–$AuCu_3$ types interrelation, see also sec. 3.5.5.). For a

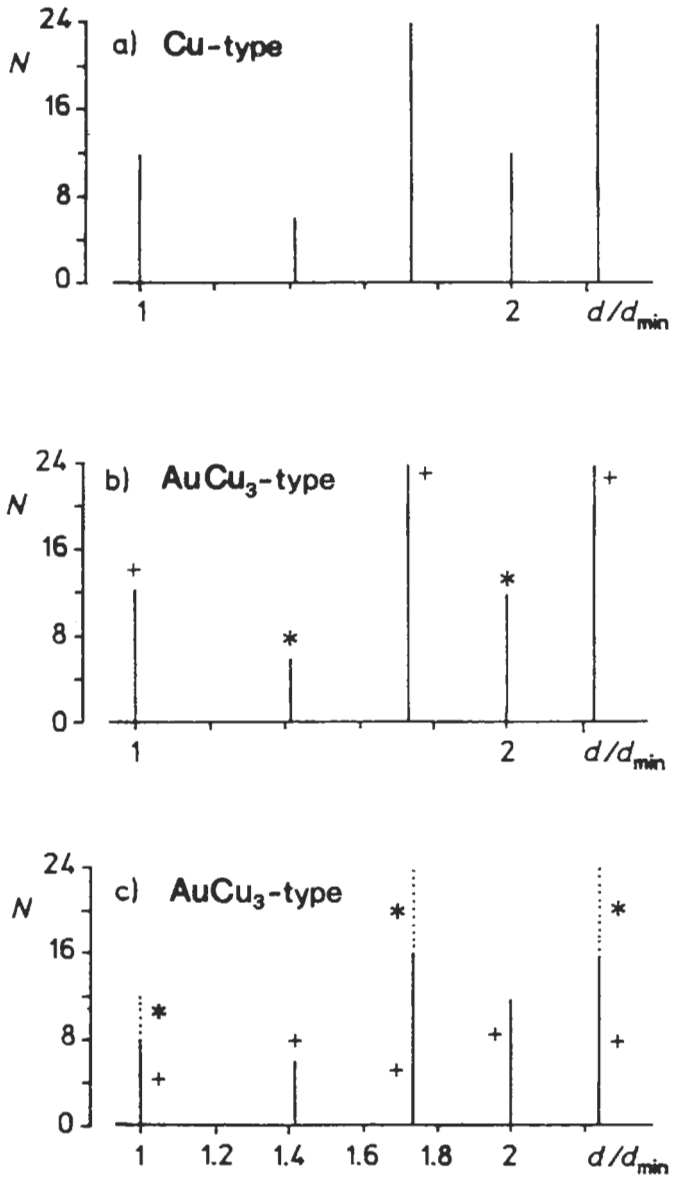

Fig. 25. Distances and coordinations in the cF4–Cu and cP4–$AuCu_3$ types structures. (Compare also with figs. 14 and 15.)

a) cF4–Cu type structure

b) cP4–$AuCu_3$ type structure: coordination around Au
(+) Au-Cu; (*) Au-Au.

c) $AuCu_3$ type structure: coordination around Cu
(+) Cu-Cu; (*) Cu-Au.

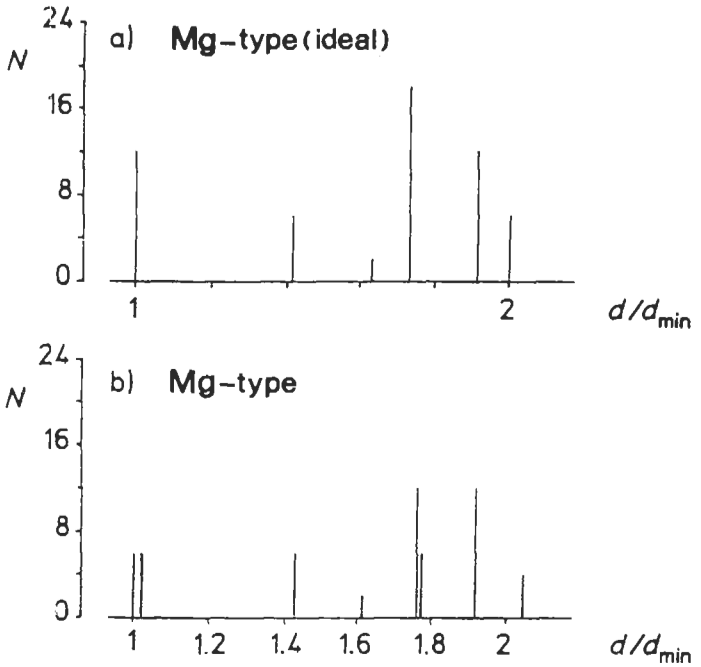

Fig. 26. Distances and coordinations in the hexagonal close-packed (Mg-type) structure.
a) Ideal structure, c/a = 1.633 (first coordination shell corresponding to 12 atoms at the same distance).
b) Mg-type structures with c/a = 1.579.
The group of the first 12 neighbours is subdivided into 6 + 6 atoms at slightly different distances.

systematic description of the *derivative structures* which may be obtained from the Cu type *by ordered filling-up* it may be useful to consider that in a closest packing of equal spheres there are, among the spheres themselves, essentially two kinds of interstices (holes). These are shown in fig. 27. The smallest holes surrounded by a polyhedral group of spheres are those marked by T. An atom inserted in this hole will have four neighbours whose centres lie at the vertices of a regular tetrahedron (*tetrahedral holes*). The larger holes (*octahedral holes*) are surrounded by octahedral groups of six spheres. In an infinite assembly of close-packed spheres the ratios of the numbers of the tetrahedral and octahedral holes to the number of spheres are, respectively, 2 and 1.

Considering the Cu type structure (in which the 4 close-packed spheres are in 0,0,0; $0,\frac{1}{2},\frac{1}{2}$; $\frac{1}{2},0,\frac{1}{2}$; $\frac{1}{2},\frac{1}{2},0$) the centers of the tetrahedral and octahedral holes have the coordinates:

4 octahedral holes in:
$\frac{1}{2},\frac{1}{2},\frac{1}{2}$; $\frac{1}{2},0,0$; $0,\frac{1}{2},0$; $0,0,\frac{1}{2}$;
2 sets of 4 tetrahedral holes in:
$\frac{1}{4},\frac{1}{4},\frac{1}{4}$; $\frac{1}{4},\frac{3}{4},\frac{3}{4}$; $\frac{3}{4},\frac{1}{4},\frac{3}{4}$; $\frac{3}{4},\frac{3}{4},\frac{1}{4}$;
and in:
$\frac{3}{4},\frac{3}{4},\frac{3}{4}$; $\frac{3}{4},\frac{1}{4},\frac{1}{4}$; $\frac{1}{4},\frac{3}{4},\frac{1}{4}$; $\frac{1}{4},\frac{1}{4},\frac{3}{4}$.

References: p. 363.

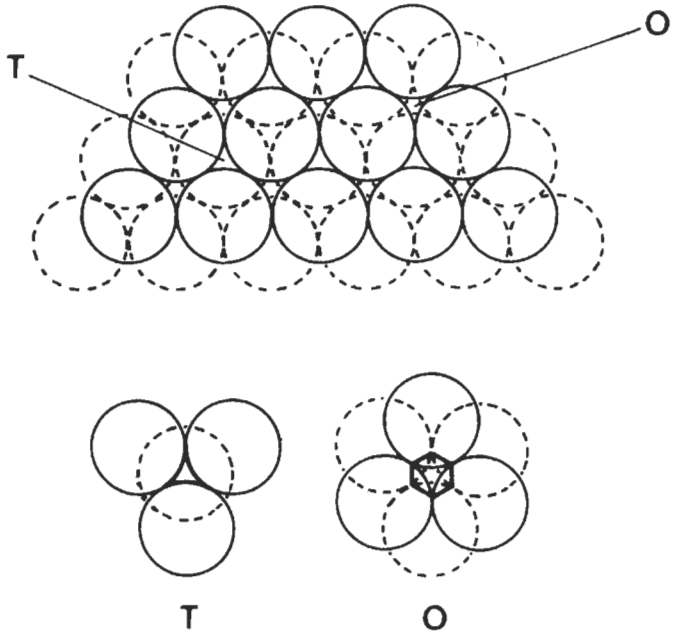

Fig. 27. Voids in the closest packing of equal spheres; tetrahedral (T) and octahedral holes (O) are evidenced within two superimposed triangular nets.

Several cubic structures, therefore, in which (besides 0,0,0; $0,\frac{1}{2},\frac{1}{2}$; $\frac{1}{2},0,\frac{1}{2}$; $\frac{1}{2},\frac{1}{2},0$) one (or more) of the reported coordinate groups are occupied could be considered as filled-up derivatives of the cubic close-packed structures. The NaCl, CaF_2, ZnS (sphalerite), AgMgAs and Li_3Bi type structures could, therefore, be included in this family of derivative structures. For this purpose, however, it may be useful to note that the radii of small spheres which fit exactly into tetrahedral and octahedral holes are 0.225... and 0.414..., respectively, if the radius of the close-packed spheres is 1.0. For a given phase pertaining to one of the aforementioned types (NaCl, ZnS, etc.) if the stated dimensional conditions are not fulfilled, alternative descriptions of the structure may be more convenient than the reported derivation schemes.

Notice, moreover, that a fc cubic cell of atoms X in which all the interstices are occupied (the octahedral by X and the tetrahedral by Z atoms) is equivalent to a block of 8 XZ, CsCl type, cells (see figs. 3 and 24). This relationships (and other ones with other structures such Li_3Bi and $MnCu_2Al$) should be kept in mind when considering, for instance, phase transformations occurring in ordering processes.

Similar considerations may be made with reference to the other simple close-packed structure, that is to the hexagonal Mg type structure. In this case two basic derived structures can be considered: the NiAs type with occupied octahedral holes and the wurtzite (ZnS) type with one set of occupied tetrahedral holes.

6.2.3. Structural type: cP4–$AuCu_3$

Cubic, space group $Pm\bar{3}m$, No. 221;

Atomic positions:
1 Au in a) 0,0,0
3 Cu in c) $0,\frac{1}{2},\frac{1}{2}$; $\frac{1}{2},0,\frac{1}{2}$; $\frac{1}{2},\frac{1}{2},0$
Coordination formula: $3^3_3 3\,[Au_{6/6}][Cu_{8/8}]_{12/4}$
Layer stacking symbols:
Triangular, kagomé (T,K) nets:
$Au^{A}_{0}\,C^{\alpha}_{0}\,Au^{C}_{1/3}\,Cu^{\gamma}_{1/3}\,Au^{B}_{2/3}\,Cu^{\beta}_{2/3}$
Square (S) nets: $Au^{1}_{0}\,Cu^{4}_{0}\,Cu^{5}_{1/2}$
For the prototype itself, $AuCu_3$, a = 374.8 pm.
(See also sec. 3.5.5. for a detailed description of this structure.)

This structure can be considered a derivative structure (ordered substitution) of the cF4–Cu type.

A discussion of the characteristics of a number of ordered layer (super)structures involving a XY_3 stoichiometry has been reported by MASSALSKI [1989]. Sequences of layer structures (among which those corresponding to the cP4–$AuCu_3$, hP16–$TiNi_3$, hP24–VCo_3, hR36–$BaPb_3$ types) as observed in V (or Ti) alloys with Fe, Co, Ni, Cu are described. The relative stabilities of the different stacking sequences have been analyzed in terms of a few parameters which characterize the interactions between various layers.

6.2.4. Structural types: tP2–AuCu (I) and oI40–AuCu(II)

tP2–AuCu(I) is tetragonal, space group P4/mmm, No. 123;

Atomic positions:
1 Au in a) 0,0,0;
1 Cu in d) $\frac{1}{2},\frac{1}{2},\frac{1}{2}$;
For the prototype itself, AuCu(I), a = 280.4 pm, c = 367.3 pm, c/a = 1.310.

The unit cell could be considered either as a distorted CsCl type cell greatly elongated in the c direction or, better, as a deformed (and orderly substituted) Cu type cell. This is apparent from fig. 20 where the tP2 unit cell and two tP4 supercells having $a' = a\sqrt{2} = 396.6$ pm, $c' = c = 367.3$ pm are also shown. The larger cell is similar to a Cu type cell, slightly compressed ($c'/a' = 0.926$) and in which the atoms placed in the center of the sidefaces have been orderly substituted. The coordinates in the tP4 super(pseudo)cell are:

Au in 0,0,0, and $\frac{1}{2},\frac{1}{2},0$;
Cu in $\frac{1}{2},0,\frac{1}{2}$ and $0,\frac{1}{2},\frac{1}{2}$;
and the corresponding square nets stacking sequence is $Au^{1}_{0}\,Au^{4}_{0}\,Cu^{5}_{1/2}$.
The *long period superstructure of AuCu(I)*, discussed in sec. 4.2., resulting in the antiphase-domain structure of AuCu(II) is shown in fig. 20c.

6.2.5. Structural type: tP4–Ti_3Cu

Tetragonal, space group P4/mmm, No. 123;

Atomic positions:
1 Cu in a) 0,0,0
1 Ti in c) $\frac{1}{2},\frac{1}{2},0$;
2 Ti in e) $0,\frac{1}{2},\frac{1}{2}$; $\frac{1}{2},0,\frac{1}{2}$;
Coordination formula: $^{3}_{\infty}3[Cu_{6/6}][Ti_{8/8}]_{12/4}$
Layer stacking symbols:
Square (S) nets: $Cu^{1}_{0}\,Ti^{4}_{0}\,Ti^{5}_{1/2}$.
For the prototype itself, Ti_3Cu, a = 415.8 pm, c = 359.4 pm, c/a = 0.864. This structure can be described as a tetragonal distortion of the $AuCu_3$ type structure. It may also be considered a variant of the previously described AuCu(I) type (compare with its tP4 pseudocell).

6.2.6. Structural types: hP2–Mg, hP4–La and hR9–Sm

hP2–Mg type. Hexagonal, Space group $P6_3/mmc$, No. 194.

Atomic positions:
2 Mg in c) $\frac{1}{3},\frac{2}{3},\frac{1}{4}$; $\frac{2}{3},\frac{1}{3},\frac{3}{4}$;
Coordination formula: $^{3}_{\infty}[Mg_{(6+6)/(6+6)}]$ and ideally: $^{3}_{\infty}[Mg_{12/12}]$.
For the prototype itself, Mg, a = 320.89 pm, c = 521.01 pm, c/a = 1.624.
Normalized interatomic distances and numbers of equidistant neighbours are presented in fig. 26a for an "ideal" hexagonal close-packed structure ($c/a = \sqrt{8/3} = \approx 1.633$), which corresponds to 12 nearest neighbours at the same distance, and, in fig. 26b, for a slightly distorted cells.

The atoms are arranged in close-packed layers stacked in the sequence ABAB... (or BCBC... see sec. 3.5.2.). The corresponding layer symbol (triangular nets) is $Mg^{B}_{0.25}\,Mg^{C}_{0.75}$.

Several metals have been reported with this type of structure, such as: αBe, Cd, εCo, αDy, Er, Ho, Lu, Mg, Os, Re, Ru, Tc, αY, Zn, etc. Several binary (and complex) phases have also been described with this type of structure. These are generally solid solution phases with a random distribution of the different atomic species in the two equivalent positions.

Other *stacking variants* of close-packed structures are the *La type* and *Sm type structures*. Characteristic features of these types are presented here below.

hP4–La type. Hexagonal, Space group $P6_3/mmc$, No. 194.
Atomic positions:
2 La in a) 0,0,0; $0,0,\frac{1}{2}$;
2 La in c) $\frac{1}{3},\frac{2}{3},\frac{1}{4}$; $\frac{2}{3},\frac{1}{3},\frac{3}{4}$;
For the prototype itself, αLa, a = 377.0 pm, c = 1215.9 pm, c/a = 3.225.
Layer stacking symbols:
Triangular (T) nets: $La^{A}_{0}\,La^{B}_{0.25}\,La^{A}_{0.5}\,La^{C}_{0.75}$.

hR9–Sm type. Rhombohedral, space group $R\bar{3}m$, No. 166.
Atomic positions:
3 Sm in a) 0,0,0; $\frac{2}{3},\frac{1}{3},\frac{1}{3}$; $\frac{1}{3},\frac{2}{3},\frac{2}{3}$;

6 Sm in c) 0,0,z; 0,0,−z; $\frac{2}{3},\frac{1}{3},\frac{1}{3}+z$; $\frac{2}{3},\frac{1}{3},\frac{1}{3}-z$; $\frac{1}{3},\frac{2}{3},\frac{2}{3}+z$; $\frac{1}{3},\frac{2}{3},\frac{2}{3}-z$;
For the prototype itself, αSm, a = 362.90 pm, c = 2620.7 pm, c/a = 7.222 and z = 0.222.
Layer stacking symbols:
Triangular (T) nets:
$Sm_0^A\, Sm_{0.11}^C\, Sm_{0.22}^A\, Sm_{0.33}^C\, Sm_{0.45}^B\, Sm_{0.55}^C\, Sm_{0.67}^B\, Sm_{0.78}^A\, Sm_{0.89}^B$.

The La and Sm type structures belong to the same *homeotect type* set as Mg and Cu (see sec. 4.3.). All these close-packed element structures are stacking variants of identical slab types (monoatomic triangular nets).

6.2.7. Structural type: hP8–Ni_3Sn

Hexagonal, Space group $P6_3/mmc$, No. 194.
Atomic positions:
2 Sn in c): $\frac{1}{3},\frac{2}{3},\frac{1}{4}$; $\frac{2}{3},\frac{1}{3},\frac{3}{4}$;
6 Ni in h): x,2x,$\frac{1}{4}$; −2x,−x,$\frac{1}{4}$; x,−x,$\frac{1}{4}$; −x,−2x,$\frac{3}{4}$; 2x,x,$\frac{3}{4}$; −x,x,$\frac{3}{4}$.
For the prototype itself a = 527.5 pm, c = 423.4 pm, c/a = 0.802 and x = 0.833.
(A projection of the cell is shown in fig. 28 and compared with that of the hP2–Mg type).
The layer stacking symbol (triangular and kagomé nets) is:
$Sn_{0.25}^B\, Ni_{0.25}^{\beta}\, Sn_{0.75}^C\, Ni_{0.75}^{\gamma}$.
(which may be compared with the symbol $Mg_{0.25}^B\, Mg_{0.75}^C$ of the Mg type).

This type is a superstructure of the closed packed (hP2–Mg) hexagonal structure in the same way as the $AuCu_3$ type is of the close-packed cubic (cF4–Cu) structure. It can, therefore, be considered a stacked polytype of the $AuCu_3$ type.

Several phases belong to this type, for instance, Ti_3Al, Fe_3Ga, Fe_3Ge, Fe_3Sn, $ZrNi_3$, $ThAl_3$, YAl_3, etc.

In the specific case of the rare earth trialuminides $REAl_3$, the Ni_3Sn type structure has been observed for $LaAl_3$ to $GdAl_3$ (and YAl_3). For $ErAl_3$ to $YbAl_3$ and $ScAl_3$ the $AuCu_3$ type structure is formed. For the intermediate $REAl_3$, intermediate stacking variants of similar layers have been described and their relative stabilities discussed (VAN VUCHT and BUSCHOW [1965]). In fig. 28b, the oP8–β $TiCu_3$ type structure is also shown. The close relationship between the two structures may be noticed.

6.2.8. Structural type: hP6–$CaCu_5$

As another example of structures in which more complex stacking sequences can be observed we may mention here the hP6–$CaCu_5$ type structure, which is the reference type for a family of structures in which 3^6 nets (and 6^3) are alternatively stacked with 3636 (kagomé) nets of atoms.

The hP6–$CaCu_5$ structure is hexagonal, space group P6/mmm, No. 191, with:
1 Ca in a) 0,0,0,
2 Cu in c) $\frac{1}{3},\frac{2}{3},0$; $\frac{2}{3},\frac{1}{3},0$;
3 Cu in g) $\frac{1}{2},0,\frac{1}{2}$; $0,\frac{1}{2},\frac{1}{2}$; $\frac{1}{2},\frac{1}{2},\frac{1}{2}$;
For the prototype, a = 509.2 pm, c = 408.6 pm, c/a = 0.802.
The layer stacking symbol, triangular (T: A,B,C), hexagonal (H: a,b,c) and kagomé (K: α,β,γ) nets is: $Ca_0^A\, Cu_0^a\, Cu_{0.5}^{\alpha}$ (see fig. 29).

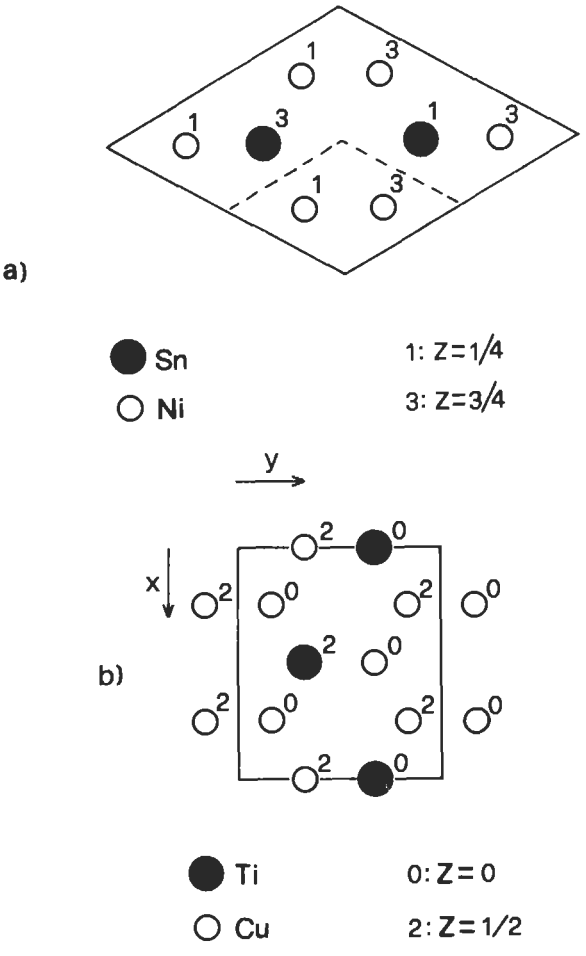

Fig. 28. hP8–Ni_3Sn type unit cell.

a) Projection of the hP8–Ni_3Sn type unit cell on the x,y plane (the values of the coordinate z are indicated). A Mg-type subcell is represented by the dotted lines.

b) Projection of the oP8–β-$TiCu_3$ type cell. Compare the similar arrangements of the atoms in the two structures.

A large coordination is obtained in this structure: Ca is surrounded by 6 Cu + 12 Cu + 2 Ca at progressively higher distances and the Cu atoms have 12 neighbours (in a non-icosahedral coordination).

Several phases belonging to this structure are known (alkali metal compounds such as KAu_5, $RbAu_5$, alkaline earth compounds such as $BaAu_5$, $BaPd_5$, $BaPt_5$, $CaPt_5$, $CaZn_5$, etc., rare earth alloys such as $LaCo_5$, $LaCu_5$, $LaPd_5$, $LaPt_5$, $LaZn_5$, etc., The compounds as $ThFe_5$, $ThCo_5$, $ThNi_5$, etc.). Ternary phases have been also described, both correspon-

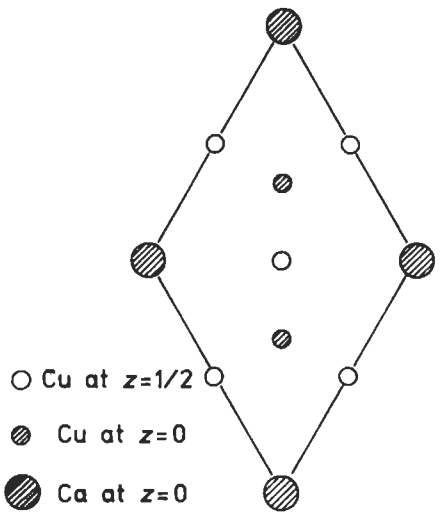

Fig. 29. Projection of the hP6–$CaCu_5$ type unit cell on the x,y plane.

ding to the *ordered derivative hP6–$CeCo_3B_2$ type* (1 Ce in a), 2 B in c) and 3 Co in g)) and to disordered solid solutions of a third component in a binary $CaCu_5$ type phase.

According to PEARSON [1972] several structures may be described as derived from the $CaCu_5$ type (for instance, the tI26–$ThMn_{12}$ type; hR57–Th_2Zn_{17} type; hP38–Th_2Ni_{17} type; etc.).

As for the building principles of the $CaCu_5$ type some analogies with the Laves phases (see sec. 6.6.4) may be noticed.

Cobalt-based rare earth alloys such as $SmCo_5$ (hP6–$CaCu_5$ type) are important materials for permanent magnets. A short review on the properties of alloys for permanent magnetic materials has been reported by RAGHAVAN and ANTIA [1994]. Complex (especially iron) alloys have been mentioned starting from the Alnico (Fe–Al–Ni–Co) alloys introduced in the thirties followed by ferrites and Co-based rare earth alloys (such as $SmCo_5$) and then by $Sm_2(Co,Fe,Cu)_{17}$ and $Nd_2Fe_{14}B$ (tP68) with a progressive decreasing of volume and weight of magnets per unit energy product.

6.3. Tetrahedral structures

This section is mainly dedicated to the presentation of a few typical so-called tetrahedral structures. For the simplest ones, normalized interatomic distances and numbers of equidistant neighbours are shown in fig. 30. The graphite structure will also be described.

6.3.1. cF8–C (diamond) and tI4–βSn structural types

cF8–C (diamond) type.

Face-centered cubic, space group $Fd\bar{3}m$, No. 227.

Atomic positions:

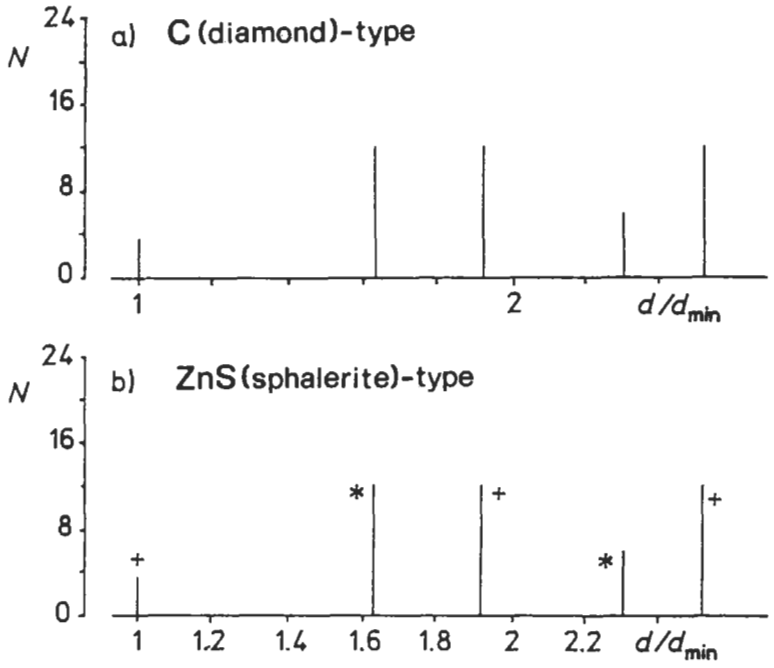

Fig. 30. Distances and coordinations in the cF8–C diamond and cF8–ZnS sphalerite type structures.
a) cF8–C (diamond) type structure.
b) XY compounds of cF8–ZnS type structure:
(+) X–Y (or Y–X) coordination.
(*) X–X (or Y–Y) coordination.

8 C in a) 0,0,0; $0,\frac{1}{2},\frac{1}{2}$; $\frac{1}{2},0,\frac{1}{2}$; $\frac{1}{2},\frac{1}{2},0$; $\frac{1}{4},\frac{1}{4},\frac{1}{4}$; $\frac{1}{4},\frac{3}{4},\frac{3}{4}$; $\frac{3}{4},\frac{1}{4},\frac{3}{4}$; $\frac{3}{4},\frac{3}{4},\frac{1}{4}$;
(This group of atomic positions corresponds to the so-called invariant lattice complex D; see sec. 3.1.).
The coordination formula is $^{3}_{\infty}[C_{4/4}]$
The layer stacking symbols are:
Triangular (T) nets: $C_0^A\, C_{1/4}^A\, C_{1/3}^B\, C_{7/12}^B\, C_{2/3}^C\, C_{11/12}^C$
Square (S) nets: $C_0^1\, C_0^4\, C_{1/4}^6\, C_{1/2}^5\, C_{3/4}^7$
For the prototype itself, C diamond, a = 356.69 pm.

The diamond structure is a 3–dimensional adamantine network in which every atom is surrounded tetrahedrally by four neighbours. The 8 atoms in the unit cell may be considered as forming two interpenetrating face centered cubic networks. If the two networks are occupied by different atoms we obtain the derivative cF8–ZnS (sphalerite) type structure. As a further derivative structure, we may mention the tI16–$FeCuS_2$ type structure (See fig. 31). These are all examples of a family of "tetrahedral" structures which have been described by Parthé and will be briefly presented in sec. 7.2.1.

Si, Ge and αSn have the diamond-type structure. The *tI4–β Sn structure* (a = 583.2

pm, c = 318.2 pm) (4 Sn in a) 0,0,0; $0,\frac{1}{2},\frac{1}{4}$;; $\frac{1}{2},\frac{1}{2},\frac{1}{2}$; $\frac{1}{2},0,\frac{3}{4}$; space group $I4_1/amd$, No. 141) can be considered a very much distorted diamond type structure. Each Sn has 4 close neighbours, 2 more at a slightly larger (and 4 other at a considerably larger) distance. The βSn unit cell is reported in fig. 32.

6.3.2. Structural types: cF8–ZnS sphalerite and hP4–ZnO (ZnS wurtzite)

cF8–ZnS sphalerite

Face-centered cubic, space group $F\bar{4}3m$, No. 216.
Atomic positions:

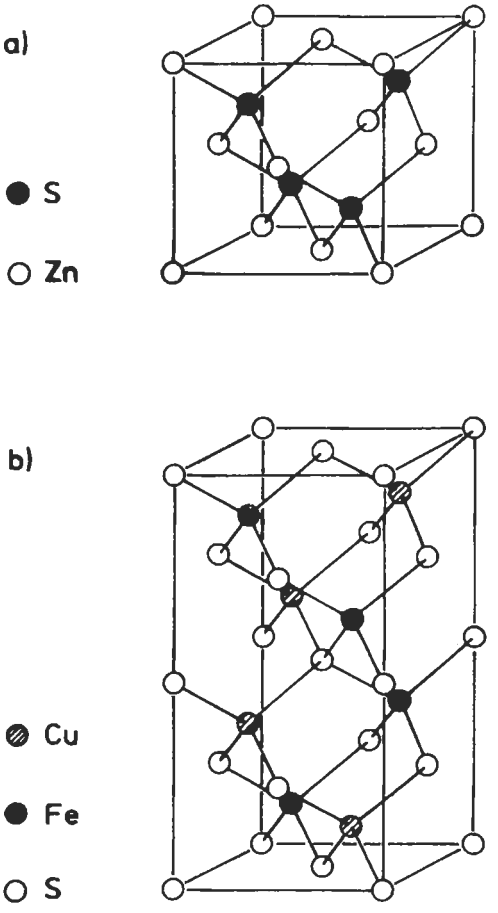

Fig. 31. a) cF8–ZnS sphalerite and b) tI16–$FeCuS_2$ (chalcopyrite) type structures.

References: p. 363.

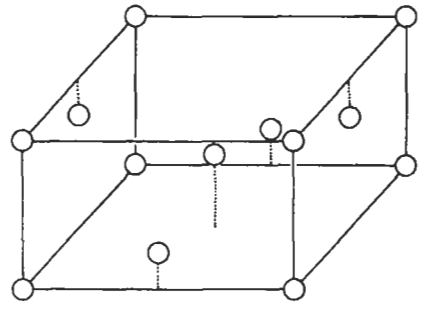

Fig. 32. tI4–βSn type structure.

4 Zn in a) 0,0,0; $0,\frac{1}{2},\frac{1}{2}$; $\frac{1}{2},0,\frac{1}{2}$; $\frac{1}{2},\frac{1}{2},0$;
4 S in c) $\frac{1}{4},\frac{1}{4},\frac{1}{4}$; $\frac{1}{4},\frac{3}{4},\frac{3}{4}$; $\frac{3}{4},\frac{1}{4},\frac{3}{4}$; $\frac{3}{4},\frac{3}{4},\frac{1}{4}$;
In terms of a combination of invariant lattice complexes (see sec. 3.1) we may therefore describe the sphalerite structure as **ZnS**: $\mathbf{F}+\mathrm{F}''$.
Coordination formulae:
$^{3}_{\infty}[ZnS_{4/4}]$ (ionic or covalent description)
$^{333}_{\infty}[Zn_{12/12}][S_{12/12}]_{4/4}$ (metallic description)
For the prototype itself, ZnS sphalerite, a = 541.1 pm.

Structural type ***hP4–ZnO or ZnS wurtzite***
hexagonal, $P6_3mc$, No. 186.
Atomic positions:
2 Zn in b (1) $\frac{1}{3},\frac{2}{3},z$; $\frac{2}{3},\frac{1}{3},\frac{1}{2}+z$; $(z=z_1)$
2 O or 2 S in b (2) $\frac{1}{3},\frac{2}{3},z$; $\frac{2}{3},\frac{1}{3},\frac{1}{2}+z$; $(z=z_2)$
Coordination formula: $^{3}_{\infty}[ZnO_{4/4}]$
For the prototypes themselves, ZnO: a = 325.0 pm, c = 520.7 pm, c/a = 1.602; ZnS (wurtzite): a = 382.3 pm, c = 626.1 pm, c/a = 1.638. The atomic positions correspond, for both types of atoms, to similar coordinate groups (to the same Wyckoff positions) with different values of the z parameter. For ZnO $z_{Zn}=0$, $z_O=0.382_5$ and for ZnS $z_{Zn}=0$, $z_S=0.371$.

6.3.3. General remarks on "tetrahedral structures" and polytypes. tI16–FeCuS2, hP4–C lonsdaleite, oP16–BeSiN2 types and polytypes

Compounds, isostructural with the cubic cF8–ZnS sphalerite include AgSe, AlP, AlAs, AlSb, AsB, AsGa, AsIn, BeS, BeSe, BeTe, BePo, CdSe, CdTe, CdPo, HgS, HgSe, HgTe, etc. (possibly in one of their modifications).

The sphalerite structure can be described as a derivative structure of the diamond type structure. Alternatively we may describe the same structure as a derivative of the cubic close-packed structure (cF4–Cu type) in which a set of tetrahedral holes has been filled-in. (This alternative description would be especially convenient, when the atomic diameter ratio of the two species is close to 0.225: see the comments reported in sec. 6.2.2.).

In a similar way the closely related hP4–ZnO structure can be considered as a derivative of the hexagonal close-packed structure (hP2–Mg type) in which, too, a set of tetrahedral holes has been filled-in.

Compounds, isostructural with ZnO include some forms of AgI, BeO, CdS, CdSe, CuX (X = H, Cl, Br, I), MnX (X = S, Se, Te), MeN (Me = Al, Ga, In, Nb), ZnX (X = O, S, Se, Te).

In order to have around each atom in this hexagonal structure, four exactly equidistant neighbouring atoms, the axial ratio should have the ideal value $\sqrt{8/3}$, that is ≈ 1.633. The experimental values range from 1.59 to 1.66. The ideal value of one of the parameters (being fixed at zero the other one by conventionally shifting the origin of the cell) is $z = 3/8 = 0.3750$.

The C diamond, sphalerite and wurtzite type structures are well-known examples of the "*normal tetrahedral structures*" (see sec. 7.2.1.).

Several *superstructures* and *defect superstructures* based on sphalerite and on wurtzite have been described. The *tI16–$FeCuS_2$ (chalcopyrite) type structure* (tetragonal, a = 525 pm, c = 1032 pm, c/a = 1.966) (see fig. 31b), for instance, is a superstructure of sphalerite in which the two metals adopt ordered positions. The superstructure cell corresponds to two sphalerite cells stacked in the c-direction. The c/2a ratio is nearly 1. As another example we may mention the *oP16–$BeSiN_2$ type structure* which similarly corresponds to the wurtzite type structure.

The degenerate structures of sphalerite and wurtzite (when, for instance, both Zn and S are replaced by C) corresponds to the previously described cF8–diamond type structure and, respectively, to the *hP4–hexagonal diamond or lonsdaleite* which is very rare compared with the cubic, more common, gem diamond. The unit cell dimensions of lonsdaleite (prepared at 13 GPa and 1000°C) are a = 252 pm, c = 412 pm, c/a = 1.635. (Compare with ZnS wurtzite).

While discussing the sphalerite and wurtzite type structures we have also to remember that they belong to a homeotect structure type set. (See sec. 4.3.)

The layer stacking sequence symbols (triangular nets) of the two structures are:
Sphalerite: $Zn_0^A\, S_{1/4}^A\, Zn_{1/3}^B\, S_{7/12}^B\, Zn_{2/3}^C\, S_{11/12}^C$
Wurtzite: $Zn_0^B\, S_{0.37}^B\, Zn_{1/2}^C\, S_{0.87}^C$.

In the first case we have (along the direction of the diagonal of the cubic cell) a sequence ABC of identical "unit slabs" ("minimal sandwiches") each composed of two superimposed triangular nets of Zn and S atoms. The "thickness" of the slabs, between the Zn and S atom nets is 0.25 of the lattice period along the superimposition direction (cubic cell diagonal: $a\sqrt{3}$). It is $(0.25\sqrt{3} * 541)$ pm = 234 pm. In the wurtzite structure we have a sequence BC of slabs formed by sandwiches of the same triangular nets of Zn and S atoms (their thickness is $\approx 0.37 * c = (0.37 * 626.1)$ pm = 232 pm).

With reference to the aforementioned structural unit slab the Jagodzinski-Wyckoff symbol of the two structures will be:
ZnS sphalerite: c; ZnS wurtzite: h.

In the same (equiatomic tetrahedral structure type) homeotect set many more structures occur often with very long stacking periods. Several other polytypes of ZnS itself have

been identified and characterized. The largest number of polytypic forms and the largest number of layers in regular sequence have, however, been found for silicon monocarbide. A cubic form of SiC is known and many tenths of rhombohedral and hexagonal polytypes. (In commercial SiC a six-layer structure, hcc, is the most abundant). All have the same $a_{hex} \approx 308$ pm, the c_{hex} of their hexagonal (or equivalent hexagonal) cells are all multiples of ≈ 252 pm and range from 505 pm to more than 150000 pm (up to more than 600 Si-C slabs in a regular sequence).

6.3.4. An important non-tetrahedral C structure. The hP4–C graphite

In comparison with the previously described tetrahedral structures of C we may mention here the very different structure that carbon adopts in graphite (see fig. 33).
hP4–C graphite. Hexagonal, space group $P6_3/mmc$, No. 194.
Atomic positions:
2 C in b) $0,0,\frac{1}{4}$; $0,0,\frac{3}{4}$;
2 C in c) $\frac{1}{3},\frac{2}{3},\frac{1}{4}$; $\frac{2}{3},\frac{1}{3},\frac{3}{4}$;
Coordination formula: $^{2}_{\infty}[C_{3/3}]$
The lattice parameters are $a = 246.4$ pm and $c = 671.1$ pm; $c/a = 2.724$.
Different varieties, however, of graphite may be considered: the actual structure, in fact, and unit cell dimensions and layer stacking can vary depending on the preparation conditions, degree of crystallinity, disorientation of layers, etc.

In crystalline hP4–graphite, sheets of six-membered rings are situated so that the atoms in alternate layers lie over one other, and the second layer is displaced according to the stacking symbol $C^{b}_{1/4}\,C^{c}_{3/4}$ (compare with fig. 9). Whereas in diamond the bond length is 154 pm, in graphite the C–C minimum bond lenght is 142 pm in the sheets and 335 pm between sheets. This may be related to the highly anisotropic properties of this substance. (It may be said, for instance, that properties of graphite in the sheets are similar to those of a metal while perpendicularly are more like those of a semiconductor).

In conclusion, notice also that in terms of combinations of invariant lattice complexes the positions of the atoms in the level $\frac{1}{4}$ may be represented by $\frac{2}{3},\frac{1}{3},\frac{1}{4}$ G and those in the level $\frac{3}{4}$ by $\frac{1}{3},\frac{2}{3},\frac{3}{4}$ G (where G is the symbol of the "graphitic" net complex, here presented in non-standard settings by means of shifting vectors; see sections 3.1. and 3.5.2.).

6.4. cF8–NaCl, cF12–CaF_2, and cF12–AgMgAs types

In this section the NaCl type, CaF_2 type (and the related AgMgAs type) structures are described.

In fig. 34 the normalized interatomic distances and the equidistant neighbours are shown for the NaCl and CaF_2 structures.

6.4.1. cF8–NaCl type structure and compounds

Face-centered cubic, space group $Fm\bar{3}m$, No. 225.
Atomic positions:
4 Na in a) $0,0,0$; $0,\frac{1}{2},\frac{1}{2}$; $\frac{1}{2},0,\frac{1}{2}$; $\frac{1}{2},\frac{1}{2},0$;
4 Cl in b) $\frac{1}{2},\frac{1}{2},\frac{1}{2}$; $\frac{1}{2},0,0$; $0,\frac{1}{2},0$; $0,0,\frac{1}{2}$;

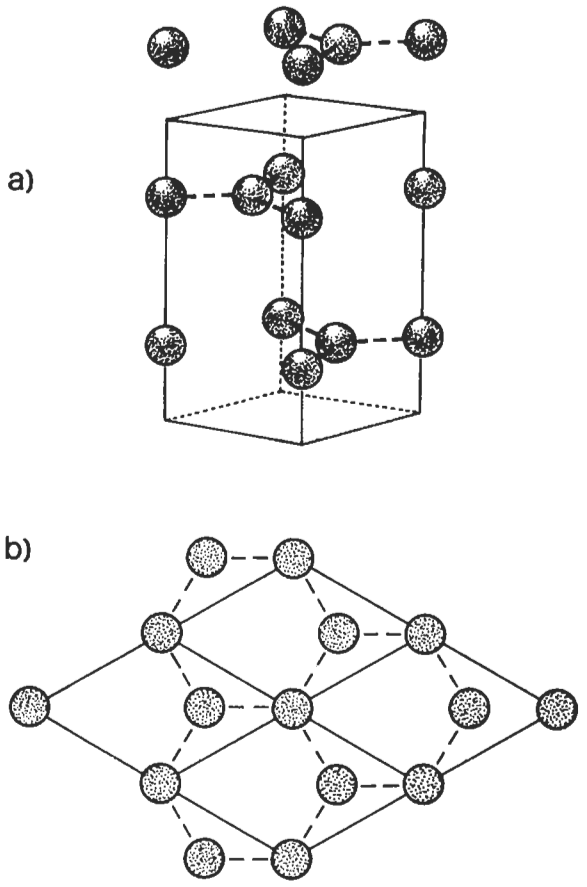

Fig. 33. Graphite structure.

a) unit cell with the indication of the atoms at the levels $z=\frac{1}{4}$ and $\frac{3}{4}$ (part of a second, superimposed cell is also shown).

b) the hexagonal net formed at level $z=\frac{1}{4}$ is shown (four adjacent cells are indicated).

Coordination formula: $3\frac{3}{\infty}3\,[Na_{12/12}][Cl_{12/12}]_{6/6}$

Layer stacking symbols:

Triangular (T) nets: $Na_0^A\,Cl_{1/6}^C\,Na_{1/3}^B\,Cl_{1/2}^A\,Na_{2/3}^C\,Cl_{5/6}^B$

Square (S) nets: $Na_0^1\,Na_0^4\,Cl_0^5\,Cl_{1/2}^1\,Cl_{1/2}^4\,Na_{1/2}^5$

For the prototype itself, NaCl, a = 564.0 pm.

(A sketch of the NaCl unit cell is shown in fig. 18.)

A large number of compounds belong to this structure type, besides several alkali metal halides, for instance, nearly all the (partially ionic covalent) 1:1 compounds formed by the rare earths and the actinides with N, P, As, Sb, Bi, S, Se, Te, Po, by the alkaline earths with O, S, Se, Te, Po, etc.

Notice that we may also describe this structure as a derivative of the cubic close-

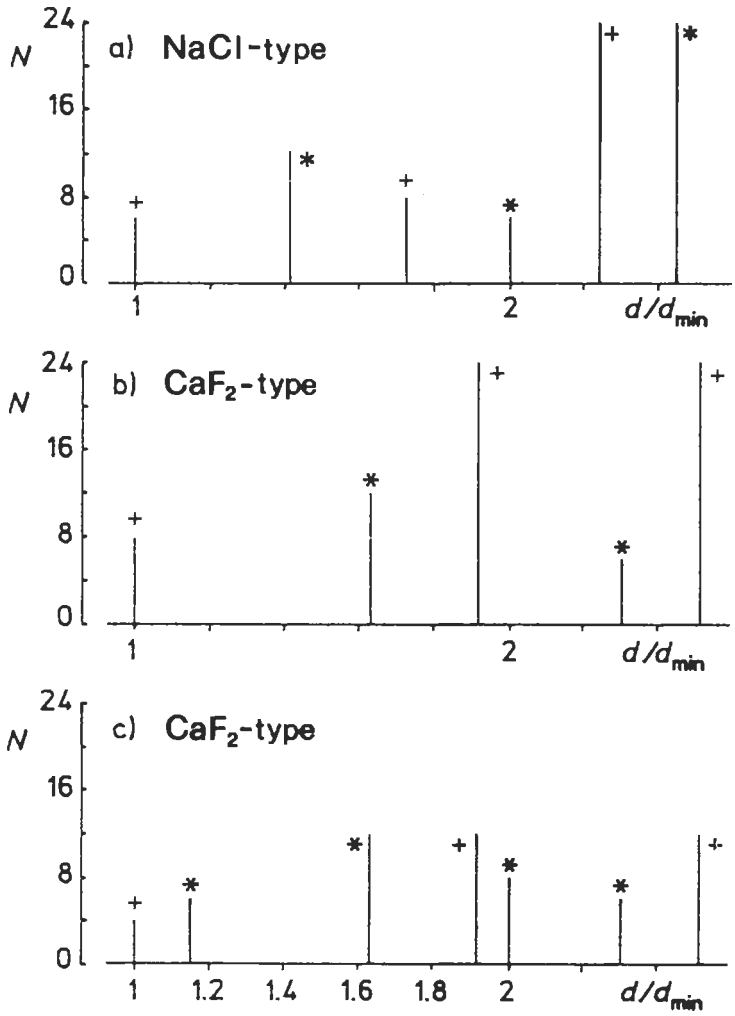

Fig. 34. Distances and coordinations in the cF8–NaCl and cF12–CaF_2 types structures.
a) XY compounds of cF8–NaCl type structure:
(*) X–X (or Y–Y) coordination.
(+) X–Y (or Y–X) coordination.
b) cF12–CaF_2 type structure. Coordination around Ca:
(*) Ca–Ca; (+) Ca–F;
c) CaF_2 type structure. Coordination around F
(*) F–F; (+): F–Ca.

packed structure (cF4–Cu type), in which the octahedral holes have been filled in. This description, however, may be specially convenient when the atomic diameter ratio between the two elements is close to the theoretical value 0.414. In this case the small

spheres will fit exactly into the octahedral holes of the close-packed arrangement of the metal atoms. (See sec. 6.2.2.). This could be the case of a number of "*interstitial compounds*". Compounds of the transition metals having relatively large atomic radii with non metals having small radii (H, B, C, N, possibly O) may be simple examples of this type. (General properties of these compounds were discussed by HÄGG [1931]).

Examples of typical phases belonging to this group may be a number of "mono" carbides, nitrides, etc.

The NaCl type structure is shown by several monocarbides MeC (or more generally MeC_{1-x}) such as TiC_{1-x} (homogeneous in the composition range ≈ 32–49 at% C), ZrC_{1-x} (≈ 33–50 at% C), HfC_{1-x} (≈ 33–50 at% C) and ThC_x (with a very large homogeneity range at high temperature). All the aforementioned monocarbides are stable from room temperature up to the melting points (which are among the highest known: ≈ 3500°C for ZrC and ≈ 4000°C for HfC). The carbides VC_{1-x} (37–48 at% C), NbC_{1-x} (40–50 at% C) are stable only at high temperature: at lower temperature, transformations associated with C-atom ordering have been reported, resulting in the formation of V_8C_7, V_6C_5, Nb_6C_5 structures. WC_{1-x} is a NaCl type high temperature phase homogeneous between 37–39 at% C. At 50 at% C another structure is formed: the hP2–WC type.

Among the NaCl type mononitrides we may mention VN_{1-x}. At high temperature (up to the melting point ≈ 2340°C) we have a large homogeneity field (≈ 33–50 at% N). The composition changes result from variation in the number of vacancies on sites in the N sublattice, with x being the fraction of sites randomly vacant. At lower temperature, in the composition range 43–46 at% N, an ordering of the N atoms has been observed, resulting in a tetragonal superstructure containing 32 V atoms and 26 N atoms in the unit cell. In the W–N system, a WN_{1-x}, NaCl type phase, has been observed in the composition range ≈ 33–50(?) at% N; hP2–WC type structure, however, has been described at 50 at% N.

As a final example, we may mention the NaCl type phases formed in the V–O and Ti–O systems. The ($VO_{1\pm x}$) phase is homogeneous in the composition range 42 to 57 at% O. Lattice parameter determination in combination with density measurements evidenced that, in the structure, vacancies occur in both V and O sub-lattices through the entire range of composition. At the stoichiometric composition VO there are ≈ 15% of sites vacant in each sublattice.

In the Ti–O system, γTiO (high temperature form, homogeneous in the composition range 35 to 55 at% O) has the NaCl type structure. (Other forms of the monooxide βTiO, αTiO, $\beta Ti_{1-x}O$, $\alpha Ti_{1-x}O$ have ordered structures based on γTiO.) In the structure there are atoms missing from some of the sites. According to what is summarized by HYDE and ANDERSSON [1989], in $TiO_{0.64}$ ≈ 36% of the oxigens are missing, in $TiO_{1.26}$ (which, of course, can be represented also with the stoichiometry $Ti_{0.79}O$) ≈ 20% of the Ti atoms are missing and in ≈ TiO both kinds of atoms are missing (≈ 15% of each): see fig. 35.

6.4.2. cF12-CaF_2 type and antitype structures and compounds

Face-centered cubic, space group $Fm\bar{3}m$, No. 225.
Atomic positions:

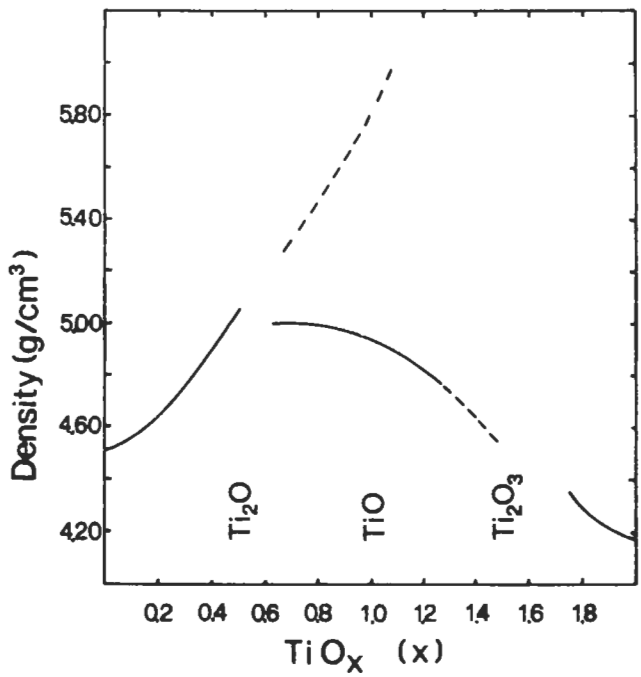

Fig. 35. Experimental densities of titanium oxides (continuous lines). The upper dotted line gives the values computed for a 100% occupancy of the cation sites in the NaCl structure type (from HYDE and ANDERSSON [1989]).

4 Ca in a) 0,0,0; $0,\frac{1}{2},\frac{1}{2}$; $\frac{1}{2},0,\frac{1}{2}$; $\frac{1}{2},\frac{1}{2},0$;
8 F in c) $\frac{1}{4},\frac{1}{4},\frac{1}{4}$; $\frac{1}{4},\frac{1}{4},\frac{3}{4}$; $\frac{1}{4},\frac{3}{4},\frac{3}{4}$; $\frac{1}{4},\frac{3}{4},\frac{1}{4}$; $\frac{3}{4},\frac{1}{4},\frac{3}{4}$; $\frac{3}{4},\frac{1}{4},\frac{1}{4}$; $\frac{3}{4},\frac{3}{4},\frac{1}{4}$; $\frac{3}{4},\frac{3}{4},\frac{3}{4}$;
Coordination formula: $3\underset{\sim}{3}3\,[Ca_{12/12}][F_{6/6}]_{8/4}$
Layer stacking symbols:
Triangular (T) nets:
$Ca_0^A\,F_{1/12}^B\,F_{1/4}^A\,Ca_{1/3}^B\,F_{5/12}^C\,F_{7/12}^B\,Ca_{2/3}^C\,F_{3/4}^A\,F_{11/12}^C$
Square (S) nets: $Ca_0^1\,Ca_0^4\,F_{1/4}^6\,F_{1/4}^7\,Ca_{1/2}^5\,F_{3/4}^6\,F_{3/4}^7$
For the prototype itself, CaF_2, a = 546.3 pm.

As pointed out in the description of the cubic close-packed structure (cF4–Cu type) this structure may be described (especially for certain values of the atomic diameter ratio) as a derivative of the Cu type structure in which two sets of tetrahedral holes have been filled in.

A ternary ordered derivative variant of this structure is the cF12–AgMgAs type.

Several (more or less ionic) compounds such as CeO_2, UO_2, ThO_2, etc. belong to this structural type.

Several Me_2X compounds, with Me = Li, Na, K, X = O, S, Se, Te), also belong to this type. In this case, however, the cation and anion positions are exchanged, Me in c) and X in a) and these compounds are sometimes referred to a *CaF_2–antitype*. Typical (more

metallic) phases having this structure are also, for instance, $AuAl_2$, $PtAl_2$, Mg_2Pb, Mg_2Sn, Mg_2Ge, Mg_2Si.

6.4.3. Structural type: cF12–AgMgAs

Face-centered cubic, space group $F\bar{4}3m$, No. 216.
Atomic positions:
4 As in a) 0,0,0; $0,\frac{1}{2},\frac{1}{2}$; $\frac{1}{2},0,\frac{1}{2}$; $\frac{1}{2},\frac{1}{2},0$;
4 Ag in c) $\frac{1}{4},\frac{1}{4},\frac{1}{4}$; $\frac{1}{4},\frac{3}{4},\frac{3}{4}$; $\frac{3}{4},\frac{1}{4},\frac{3}{4}$; $\frac{3}{4},\frac{3}{4},\frac{1}{4}$;
4 Mg in d) $\frac{3}{4},\frac{3}{4},\frac{3}{4}$; $\frac{3}{4},\frac{1}{4},\frac{1}{4}$; $\frac{1}{4},\frac{3}{4},\frac{1}{4}$; $\frac{1}{4},\frac{1}{4},\frac{3}{4}$;
Layer stacking symbols:
Triangular (T) nets:
$As_0^A\, Mg_{1/12}^B\, Ag_{1/4}^A\, As_{1/3}^B\, Mg_{5/12}^C\, Ag_{7/12}^B\, As_{2/3}^C\, Mg_{3/4}^A\, Ag_{11/12}^C$
Square (S) nets: $As_0^1\, As_0^4\, Ag_{1/4}^6\, Mg_{1/4}^7\, As_{1/2}^5\, Mg_{3/4}^6\, Ag_{3/4}^7$
For the prototype itself, AgMgAs, a = 624 pm.

In systematic investigations of MeTX ternary alloys (Me = Th, U, rare earth metals, etc., T = transition metal, X element from the V, IV main groups) several tens of phases pertaining to this structure type have been identified. For the same group of alloys, however, other structural types are also frequently found. The hP6–$CaIn_2$ type and its derivative types often represent a stable alternative. The relative stabilities of the two structures (especially as a function of the atomic dimensions of the metals involved) have been discussed, for instance, by DWIGHT [1974], MARAZZA *et al.* [1980, 1988], WENSKI and MEWIS [1986].

6.5. hP4–NiAs, cP3–CdI_2, hP6–Ni_2In, oP12–Co_2Si, oP12–TiNiSi types; hP2–WC, hP3–AlB_2, hP6–$CaIn_2$, hP9–Fe_2P types, tI8–NbAs, tI8–$AgTlTe_2$ and tI10–$BaAl_4$ ($ThCr_2Si_2$) types, tI12–$ThSi_2$ and tI12–LaPtSi types

In this section a number of important interrelated structures are presented. A first group is represented by the cP3–CdI_2, hP4–NiAs and hP6–Ni_2In types. Some comments on the interrelations between these structures have been reported in sec. 4.1. A further comparison may also be made by considering their characteristic triangular net stacking sequences:

hP3–CdI_2 $\quad Cd_0^A\, I_{1/4}^B\, I_{3/4}^C$
hP4–NiAs $\quad Ni_0^A\, As_{1/4}^B\, Ni_{1/2}^A\, As_{3/4}^C$
hP6–Ni_2In $\quad Ni_0^A\, Ni_{1/4}^C\, In_{1/4}^B\, Ni_{1/2}^A\, Ni_{3/4}^B\, In_{3/4}^C$

We see, on passing from CdI_2 to the NiAs type the insertion of a new layer at level $\frac{1}{2}$ and, from NiAs to $NiIn_2$, the ordered addition of atoms at levels $\frac{1}{4}$ and $\frac{3}{4}$.

In this section, moreover, the typical non-metal atom frameworks characteristic of the AlB_2, and derivative structures ("graphitic" layers) and of $\alpha ThSi_2$, and derivative structures ("hinged", tridimensional framework) will also be presented, compared and discussed.

The groups of more or less strictly interrelated structures which will be considered in this section are those corresponding to the hP2–WC, hP3–AlB_2, hP6–$CaIn_2$ and hP9–Fe_2P

References: p. 363.

types, and, respectively, to the tI8–NbAs, tI8–$AgTlTe_2$, tI10–$BaAl_4$ (and tI10–$ThCr_2Si_2$) types and to the tI12–α-$ThSi_2$ and tI12–LaPtSi types.

6.5.1. Structural type: hP4–NiAs

Hexagonal, space group $P6_3/mmc$, N.194,
Atomic positions:
2 Ni in a) 0,0,0; $0,0,\frac{1}{2}$;
2 As in c) $\frac{1}{3},\frac{2}{3},\frac{1}{4}$; $\frac{2}{3},\frac{1}{3},\frac{3}{4}$;
Coordination formula: $^{13}_{\infty}[Ni_{2/2}]As_{6/6}$
For the prototype itself, a = 361.9 pm, c = 504 pm, c/a = 1.393.

According to HYDE and ANDERSSON [1989], the data reported have to be considered as corresponding to an average slightly idealized structure, corresponding for several compounds to the form which is stable at high temperature. At room temperature, in the real structure, there are very small displacements of both Ni and As from their ideal average positions. The structure should, therefore, be better described by:

2 Ni in a) 0,0,z; $0,0,\frac{1}{2}+z$; $(z=0)$
2 As in b) $\frac{1}{3},\frac{2}{3},z$; $\frac{2}{3},\frac{1}{3},\frac{1}{2}+z$; $(z\approx\frac{1}{4})$
in the space group $P6_3mc$, No. 186.

The small (probably correlated) displacements of the atoms produce several sorts of modulated structures (see sec. 4.4.).

6.5.2. Structural type: hP3–CdI_2

Hexagonal, space group $P\bar{3}m1$, No. 164.
Atomic positions:
1 Cd in a) 0,0,0
2 I in d) $\frac{1}{3},\frac{2}{3},z$; $\frac{2}{3},\frac{1}{3},-z$;
Coordination formula: $^{2}_{\infty}[CdI_{6/3}]$
For the prototype itself, CdI_2, a = 424.4 pm, c = 685.9 pm, c/a = 1.616 and z = 0.249.

Typical phases pertaining to this structural type are $CoTe_2$, HfS_2, PtS_2, etc. and also Ti_2O (which, owing to the exchange in the unit cell of the metal/non-metal positions may be considered to be a representative of the *CdI_2-antitype*).

6.5.3. Structural type: hP6–Ni_2In

Hexagonal, space group $P6_3/mmc$, No. 194.
Atomic positions:
2 Ni in a) 0,0,0; $0,0,\frac{1}{2}$;
2 In in c) $\frac{1}{3},\frac{2}{3},\frac{1}{4}$; $\frac{2}{3},\frac{1}{3},\frac{3}{4}$;
2 Ni in d) $\frac{1}{3},\frac{2}{3},\frac{3}{4}$; $\frac{2}{3},\frac{1}{3},\frac{1}{4}$;
Coordination formula: $^{3}_{\infty}[InNi_{6/6}Ni_{5/5}]$
For the prototype itself, a = 419 pm, c = 512 pm, c/a = 1.222.

Typical phases assigned to this structural type are, for instance: Zr_2Al, Co_2Ge, La_2In, Mn_2Sn, Ti_2Sn and several ternary phases such as: BaAgAs, CaCuAs, CoFeSn, LaCuSi,

VFeSb, KZnSb, etc.

A distorted variant of the $InNi_2$ type structure is the oP12–orthorhombic structure of the Co_2Si, (or $PbCl_2$) type: $\frac{3}{\infty}[SiCo_{6/5}Co_{4/5}]$, that is total coordination 10 of Co around Si with $\frac{6}{5}+\frac{4}{5}=\frac{10}{5}=2$ Co atoms for each Si atom). A ternary derivative of this type is the oP12–TiNiSi type (prototype of the so-called E phases).

6.5.4. Structural types: oP12–Co_2Si ($PbCl_2$) and oP12–TiNiSi

Orthorhombic, space group Pnma, N.62.

In these structural types the atoms are distributed in three groups of positions corresponding (obviously with different values of the x and z free parameters) to the same type of Wyckoff positions (Wyckoff position c).

Atomic positions:	in Co_2Si	in TiNiSi
c (1)) $x,\frac{1}{4},z$; $\frac{1}{2}-x,\frac{3}{4},\frac{1}{2}+z$; $-x,\frac{3}{4},-z$; $\frac{1}{2}+x,\frac{1}{4},\frac{1}{2}-z$;	4 Co	4 Ti
c (2)) $x,\frac{1}{4},z$; $\frac{1}{2}-x,\frac{3}{4},\frac{1}{2}+z$; $-x,\frac{3}{4},-z$; $\frac{1}{2}+x,\frac{1}{4},\frac{1}{2}-z$;	4 Co	4 Ni
c (3)) $x,\frac{1}{4},z$; $\frac{1}{2}-x,\frac{3}{4},\frac{1}{2}+z$; $-x,\frac{3}{4},-z$; $\frac{1}{2}+x,\frac{1}{4},\frac{1}{2}-z$;	4 Si	4 Si

For the prototypes:

Co_2Si: a = 491.8 pm, b = 373.8 pm, c = 710.9 pm, a/c = 0.692; $x_{c(1)}=0.038$, $z_{c(1)}=0.782$; $x_{c(2)}=0.174$, $z_{c(2)}=0.438$; $x_{c(3)}=0.702$, $z_{c(3)}=0.389$.

TiNiSi: a = 614.84 pm, b = 366.98 pm, c = 701.73 pm, a/c = 0.876; $x_{c(1)}=0.0212$, $z_{c(1)}=0.8197$; $x_{c(2)}=0.1420$, $z_{c(2)}=0.4391$; $x_{c(3)}=0.7651$, $z_{c(3)}=0.3771$.

Co_2Si is the prototype of a group of phases (also called $PbCl_2$ type) which can be subdivided into two sets according to the value of the axial ratio a/c which is in the range from 0.67 to 0.73 for one set (for instance, Co_2Si, Pd_2Al, Rh_2Ge, Pd_2Sn, Rh_2Sn, etc.) and in the range from 0.83 to 0.88 for the other set (for instance $PbCl_2$, BaH_2(h), Ca_2Si, Ca_2Pb, $GdSe_2$, ThS_2, TiNiSi, etc.) (PEARSON [1972]).

The ternary variant TiNiSi type is also called E-phase structure. Many ternary compounds belonging to a MeTX formula (Me = rare earth metal, Ti, Hf, V, etc., T = transition metal of the Mn, Fe, Pt groups, X = Si, Ge, Sn, P, etc.) have this structure.

6.5.5. Structural type: hP2–WC

Hexagonal, space group $P\bar{6}m2$, No. 187.

Atomic positions:

1 W in a) 0,0,0,;

1 C in d) $\frac{1}{3},\frac{2}{3},\frac{1}{2}$;

For the prototype itself, a = 290.6 pm, c = 283.7 pm, c/a = 0.976.

This structure type with the axial ratio c/a close to 1 is an example of the Hägg interstitial phases formed when the ratio between non-metal and metal radii is less than about 0.59. The structure can be described as a tridimensional array of trigonal prism of W-atoms (contiguous on all the faces). Alternate trigonal prisms are centered by C-atoms.

References: p. 363.

Compounds belonging to this structure type, for instance, are: IrB, OsB, RuB, MoC, WC (compare, however, with the NaCl type phase), NbN, WN, MoP, etc.

6.5.6. Structural types: hP3–AlB_2 and hP3–BaPtSb; hP3-ω, Cr-Ti phase

Structural type: hP3–AlB_2
Hexagonal, space group P6/mmm, No. 191.
Atomic positions:
1 Al in a) 0,0,0;
2 B in d) $\frac{1}{3},\frac{2}{3},\frac{1}{2}$; $\frac{2}{3},\frac{1}{3},\frac{1}{2}$;
Coordination formula: $\underset{\omega\omega}{323}[Al_{8/8}][B_{3/3}]_{12/6}$
For the prototype itself, a = 300.5 pm, c = 325.7 pm, c/a = 1.084.

The structure can be considered a filled-up WC structure type. The B-atoms form a hexagonal net and center all the Al trigonal prisms. The arrangement of the boron atoms in their layers is the same as that in graphite (see fig. 9 and sec. 6.3.4). (See sec. 6.5.10. for a comparison between the planar graphitic net and similar threedimensional networks).

Several B, Si, Ge, Ga, etc., binary and ternary compounds have been described as pertaining to this structure or, possibly, to its variants (many of them deficient in the second component and corresponding to different stoichiometries in the 1:2 to 1:1.5 range). The axial ratio of phases with this structure varies between very wide limits. The relationships between axial ratio, atomic radii ratio of the elements involved and the role of the different bonds have been discussed by PEARSON [1972]. In the specific case of AlB_2 ($c/a \approx 1.08$) the important role of the graphite-like net of B-atoms in determining the phase stability has been evidenced.

A disordered, AlB_2 type, ternary phase ($\approx Ce_2NiSi_3$) has been presented in table 3.

A variant (ordered derivative structure) of the hP3–AlB_2 type, previously discussed in sec. 4.1 and presented in fig. 17, is the hP3–BaPtSb type, hexagonal, space group $P\bar{6}m2$, No. 187. Another compound with this structure is, for instance, ThAuSi. The atomic positions are the following:

1 Ba (or Th) in a): 0,0,0;
1 Pt (or Au) in d) $\frac{1}{3},\frac{2}{3},\frac{1}{2}$;
1 Sb (or Si) in f): $\frac{2}{3},\frac{1}{3},\frac{1}{2}$.

The layer-stacking sequence symbols of the three previously mentioned structures are:

WC type, triangular (T) nets;
$W_O^A C_{0.5}^B$;
AlB_2 type, triangular, hexagonal (T, H) nets:
$Al_0^A B_{0.5}^a$;
ThAuSi type, triangular, hexagonal (T,H) nets:
$Th_0^A Au_{0.5}^B Si_{0.5}^C$.

Another ordered derivative structure of the AlB_2 type is the Er_2RhSi_3 type, hexagonal, space group $P\bar{6}2c$, No. 190 with the following atomic positions:

2 Er in b): $0,0,\frac{1}{4}$; $0,0,\frac{3}{4}$;
4 Rh in f): $\frac{1}{3},\frac{2}{3},z$; $\frac{1}{3},\frac{2}{3},\frac{1}{2}-z$; $\frac{2}{3},\frac{1}{3},-z$; $\frac{2}{3},\frac{1}{3},\frac{1}{2}+z$;
6 Er in h): $x,y,\frac{1}{4}$; $-y,x-y,\frac{1}{4}$; $y-x,-x,\frac{1}{4}$; $y,x,\frac{3}{4}$; $x-y,-y,\frac{3}{4}$; $-x,y-x,\frac{3}{4}$
12 Si in i): x,y,z; $-y,x-y,z$; $y-x,-x,z$; $x,y,\frac{1}{2}-z$; $-y,x-y,\frac{1}{2}-z$; $y-x,-x,\frac{1}{2}-z$;
$y,x,-z$; $x-y,-y,-z$; $-x,y-x,-z$; $y,x,\frac{1}{2}+z$; $x-y,-y,\frac{1}{2}+z$; $-x,y-x,\frac{1}{2}+z$.
(with $z_{Rh}=0$; $x_{Er}=0.481$; $y_{Er}=0.019$; $x_{Si}=0.167$; $y_{Si}=0.333$; $z_{Si}=0$).

The different ordering relationships between these structures have been discussed in sec. 4.1. (see also fig. 17).

Finally, while considering the structural characteristics of the AlB_2 type phases, we may mention that boron-centered triangular metal prisms are the dominating structural building elements in the crystal structures of simple and complex metal borides. Building blocks of centered triangular prisms as base units for classification of these substances have been considered by ROGL [1985, 1991] in a systematic presentation of the crystal chemistry of borides.

We may mention here, also as an example of "modular" description, that several structures may be described in terms of cyclic translations about a 6_3 axis of blocks of AlB_2 type columns: see fig. 36.

Structural type: hP3–ω,Cr-Ti

The ω-phase, a ubiquitous metastable phase in Ti (or Zr or Hf)-transition metal systems, is approximately isotypic with AlB_2. (The axial ratio of the unit cell, however, instead of being close to unity, is very much smaller and has a value of about 0.62.) The components are randomly arranged. One third of the atoms are distributed in a triangular net at $z=0$ forming trigonal prisms. Two thirds of the atoms are placed near the centers of the prisms (slightly displaced alternately up and down) forming a rumpled 6^3 net at $z\approx\frac{1}{2}$. (The space group is $P\bar{3}m1$.)

6.5.7. Structural type: hP6–$CaIn_2$

Hexagonal, space group $P6_3/mmc$, No. 194.
Atomic positions:
2 Ca in b) $0,0,\frac{1}{4}$; $0,0,\frac{3}{4}$;
4 In in f) $\frac{1}{3},\frac{2}{3},z$; $\frac{2}{3},\frac{1}{3},\frac{1}{2}+z$; $\frac{2}{3},\frac{1}{3},-z$; $\frac{1}{3},\frac{2}{3},\frac{1}{2}-z$;
Layer stacking symbol:
Triangular (T) nets:
$In^{B}_{1/20}\,Ca^{A}_{1/4}\,In^{B}_{9/20}\,In^{C}_{11/20}\,Ca^{A}_{3/4}\,In^{C}_{19/20}$
For the prototype itself, $a=489.5$ pm, $c=775.0$ pm, $c/a=1.583$ and $z=0.455$.

This structure can be described as a distortion (a derivative form) of the AlB_2 type structure. Ca-atoms form trigonal prisms alternatively slightly off-centered up and down by In-atoms.

In fig. 37 the normalized interatomic distances and the equidistant neighbours are shown for the NiAs and $CaIn_2$ structures.

References: p. 363.

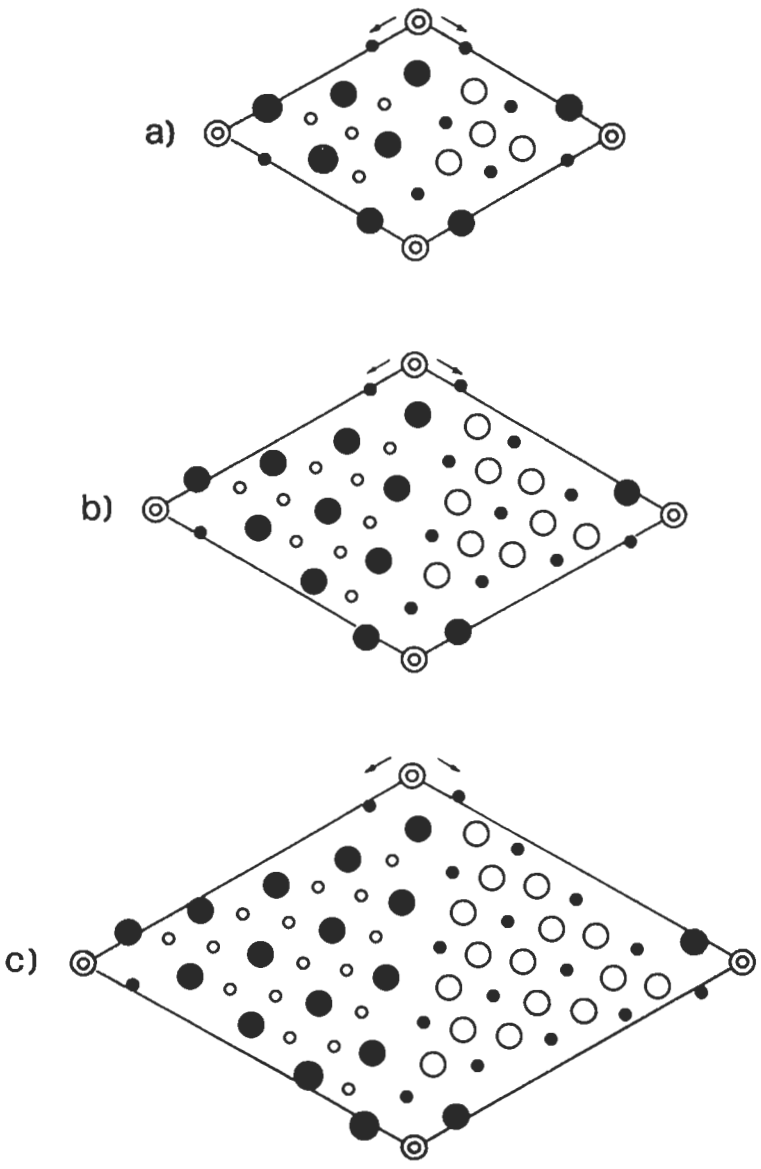

Fig. 36a,b,c. AlB_2–type derivative structures generated by cyclic translation of blocks of AlB_2–type columns. The projections of the unit cells (all having the same c value) on the x,y plane are shown.

a) hP22–$Ce_6Ni_2Si_3$ structure (a = 1211.2 pm, c = 432.3 pm).

b) hP40–≈$Ce_5Ni_2Si_3$ structure (a = 1612.0 pm, c = 430.9 pm).

c) hP64–≈$Pr_{15}Ni_7Si_{10}$ structure (a = 1988.1 pm, c = 425.5 pm)

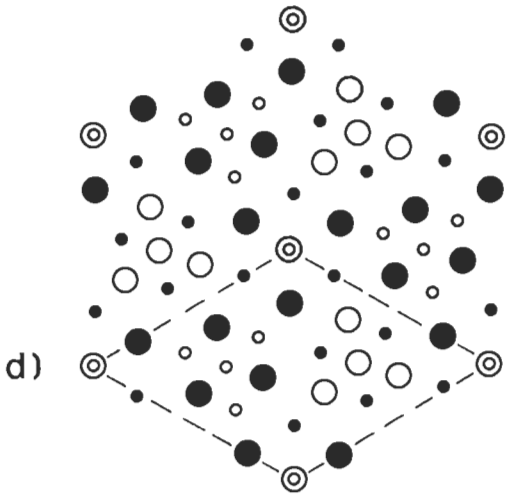

Fig. 36d. AlB_2–type derivative structures generated by cyclic translation of blocks of AlB_2–type columns. The projections of the unit cells (all having the same c value) on the x,y plane are shown.

d) hP22–$Ce_6Ni_2Si_3$ structure (compare with a)): the arrangement of the building blocks around the z-axis (6_3 symmetry axis) is shown.

Black circles represent the rare earth atoms (Ce or Pr), open circles Si (and Si + Ni); small circles are atoms at level $\frac{1}{4}$, large circles at level $\frac{3}{4}$. Double circles (at cell origin) represent Ni atoms at level 0 and at level $\frac{1}{2}$.

6.5.8. Structural type: hP9–Fe_2P

Hexagonal, space group $P\bar{6}2m$, No. 189.

Atomic positions:

1 P in b) $0,0,\frac{1}{2}$

2 P in c) $\frac{1}{3},\frac{2}{3},0$; $\frac{2}{3},\frac{1}{3},0$;

3 Fe in f) x,0,0; 0,x,0; $-x,-x,0$;

3 Fe in g) $x,0,\frac{1}{2}$; $0,x,\frac{1}{2}$; $-x,-x,\frac{1}{2}$;

For the prototype itself, a = 586.5 pm, c = 345.6 pm, c/a = 0.589 and x (f) = 0.256 and x (g) = 0.594.

In the Fe_2P type structure there are 4 different groups of equipoints. The distribution of P and Fe atoms in different groups of positions is reported. A number of isostructural binary compounds are known. To the same structure, however, ternary (or even more complex) phases may be related if different atomic species are distributed in the different sites.

This structure can be considered as an example of more complex structures built up by linked triangular prisms of Fe-atoms.

Several ordered ternary phases have structures related to the Fe_2P type.

6.5.9. Structural types: tI8–NbAs, tI8–$AgTlTe_2$ and tI10–$BaAl_4$ ($ThCr_2Si_2$)

The three structural types tI8–NbAs, tI8–$AgTlTe_2$ and tI10–$BaAl_4$ (with its ordered ternary variants such as the tI10–$ThCr_2Si_2$) belong to a group of interrelated structures.

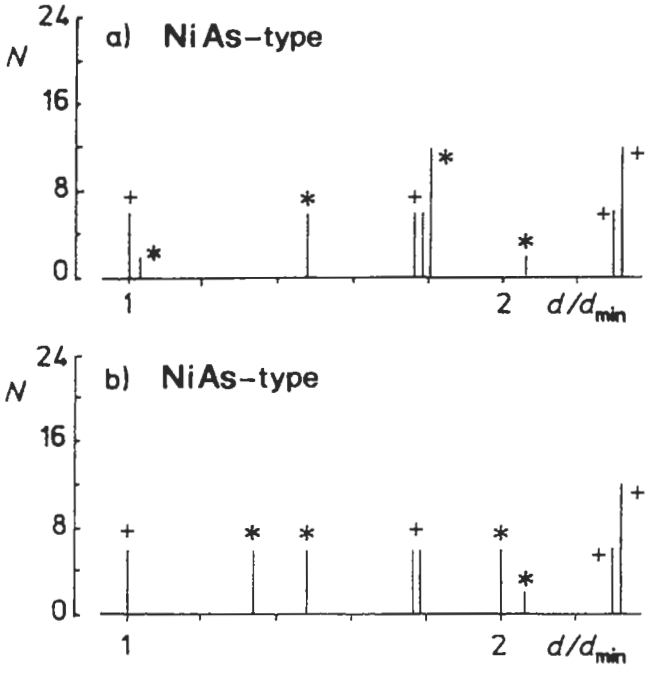

Fig. 37a,b. Distances and coordinations in the hP4–NiAs and hP6–$CaIn_2$ types structures.
a) hP4–NiAs type structure. Coordination around Ni:
(+) Ni–As; (*) Ni–Ni.
b) hP4–NiAs type structure. Coordination around As:
(+) As–Ni; (*) As–As.

All these structures contain among their building parts layers of (metal atoms) triangular prisms with specific distributions of the (non-metal) atoms centering the prisms (PEARSON [1972]). The prisms are parallel to the basal planes of the tetragonal unit cells.

Features of the hP2–WC type structure (characterized by an array of trigonal prisms alternatively centered by C-atoms) are, therefore, present in the aforementioned structures. (In the hP2–WC structure, of course, the prism axes are lying in the *c*-direction of the hexagonal cell.)

Another convenient description of these group of structures may be in term of 4^4 net layer stacking. The corresponding square net symbols for the 8–layers stacks are the following ones:

tI8–NbAs:
$Nb_0^1\, As_{0.17}^2\, Nb_{0.25}^3\, As_{0.42}^1\, Nb_{0.5}^4\, As_{0.67}^3\, Nb_{0.75}^2\, As_{0.92}^3$
tI8–$AgTlTe_2$:
$Tl_0^1\, Te_{0.13}^4\, Ag_{0.25}^3\, Te_{0.37}^1\, Tl_{0.5}^4\, Te_{0.63}^1\, Ag_{0.75}^2\, Te_{0.87}^4$
tI10–$ThCr_2Si_2$:
$Th_0^1\, Si_{0.13}^4\, Cr_{0.25}^5\, Si_{0.38}^1\, Th_{0.5}^4\, Si_{0.63}^1\, Cr_{0.75}^5\, Si_{0.88}^4$

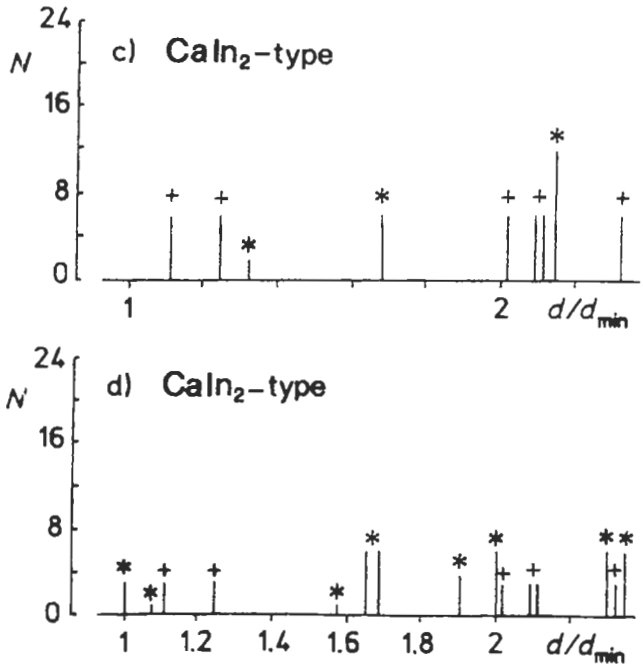

Fig. 37c,d. Distances and coordinations in the hP4–NiAs and hP6–$CaIn_2$ types structures.
c) hP6–$CaIn_2$ type structure. Coordination around Ca:
(+) Ca–In; (*) Ca–Ca;
d) hP6–$CaIn_2$ type structure. Coordination around In:
(+) In–Ca; (*): In–In.

Structure type: tI8–NbAs
Body-centered tetragonal, space group $I4_1md$, No. 109.
4 Nb in a(1): $0,0,z;\ 0,\frac{1}{2},\frac{1}{4}+z;\ \frac{1}{2},\frac{1}{2},\frac{1}{2}+z;\ \frac{1}{2},0,\frac{3}{4}+z;$
4 As in a(2): $0,0,z;\ 0,\frac{1}{2},\frac{1}{4}+z;\ \frac{1}{2},\frac{1}{2},\frac{1}{2}+z;\ \frac{1}{2},0,\frac{3}{4}+z;$
For the prototype itself a = 345.2 pm, c = 1168 pm, c/a = 3.384, z(Nb) = 0, z(As) = 0.416.

Structural type: tI8–$AgTlTe_2$
Body-centered tetragonal, space group $I\bar{4}m2$, No. 119.
2 Tl in a): $0,0,0,;\ \frac{1}{2},\frac{1}{2},\frac{1}{2};$
2 Ag in c): $0,\frac{1}{2},\frac{1}{4};\ \frac{1}{2},0,\frac{3}{4};$
4 Te in e): $0,0,z;\ 0,0,-z;\ \frac{1}{2},\frac{1}{2},\frac{1}{2}+z;\ \frac{1}{2},\frac{1}{2},\frac{1}{2}-z;$
For the prototype itself, a = 392 pm, c = 1522 pm, c/a = 3.883 and z(Te) = 0.369.

Structural type: tI10–$BaAl_4$ and tI10–$ThCr_2Si_2$
The $ThCr_2Si_2$ is one of the ordered ternary variant of the $BaAl_4$ type, frequently found in several ternary compounds.

The two structures may be described by the following occupation of the same atomic positions in the space group I4/mmm (No. 139).

References: p. 363.

	in $BaAl_4$	in $ThCr_2Si_2$
a) 0,0,0; $\frac{1}{2},\frac{1}{2},\frac{1}{2}$	2 Ba	2 Th
d) $0,\frac{1}{2},\frac{1}{4}$; $\frac{1}{2},0,\frac{1}{4}$; $\frac{1}{2},0,\frac{3}{4}$; $0,\frac{1}{2},\frac{3}{4}$;	4 Al	4 Cr
e) 0,0,z; 0,0,−z; $\frac{1}{2},\frac{1}{2},\frac{1}{2}+z$; $\frac{1}{2},\frac{1}{2},\frac{1}{2}-z$;	4 Al	4 Si

For the prototypes themselves:
$BaAl_4$, a = 453.9 pm, c = 1116 pm, c/a = 2.459 , z = 0.38
$ThCr_2Si_2$: a = 404.3 pm, c = 1057.7 pm, c/a = 2.616, z = 0.37$_5$
The unit cell is presented in fig. 38.

Normalized interatomic distances and numbers of equidistant neighbours are reported in fig. 39 for the ternary $ThCr_2Si_2$ type.

Many ternary alloys MeT_2X_2 (Me = Th, U, alkaline-earth, rare earth metal, etc., T = Mn, Cr, Pt family metal, X = element of the fifth, fourth and occasionally third main group) have been systematically prepared and investigated (PARTHE and CHABOT [1984], ROSSI *et al.* [1979]). A few hundreds of them resulted in the $ThCr_2Si_2$ (or other Al_4Ba derivatives) structure. The peculiar superconductivity and magnetic properties of these materials have been reported. The $ThCr_2Si_2$ type structure, can be described as formed by T_2X_2 layers interspersed with Me layers. The bonding between Me and T_2X_2 layers has been considered as largely ionic. In the T_2X_2 layers T–X (covalent) and some T–T bonding have to be considered. A detailed discussion of this structure and of the bonding involved has been reported by HOFFMANN [1987].

In the specific case of the RET_2X_2 phases (RE = rare earth metal) the data concerning

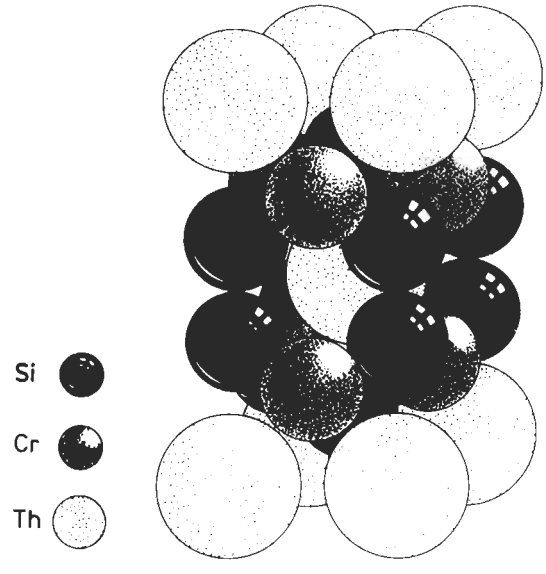

Fig. 38. Unit cell of the tI10–$ThCr_2Si_2$ type structure (a derivative structure of the tI10–$BaAl_4$ type).

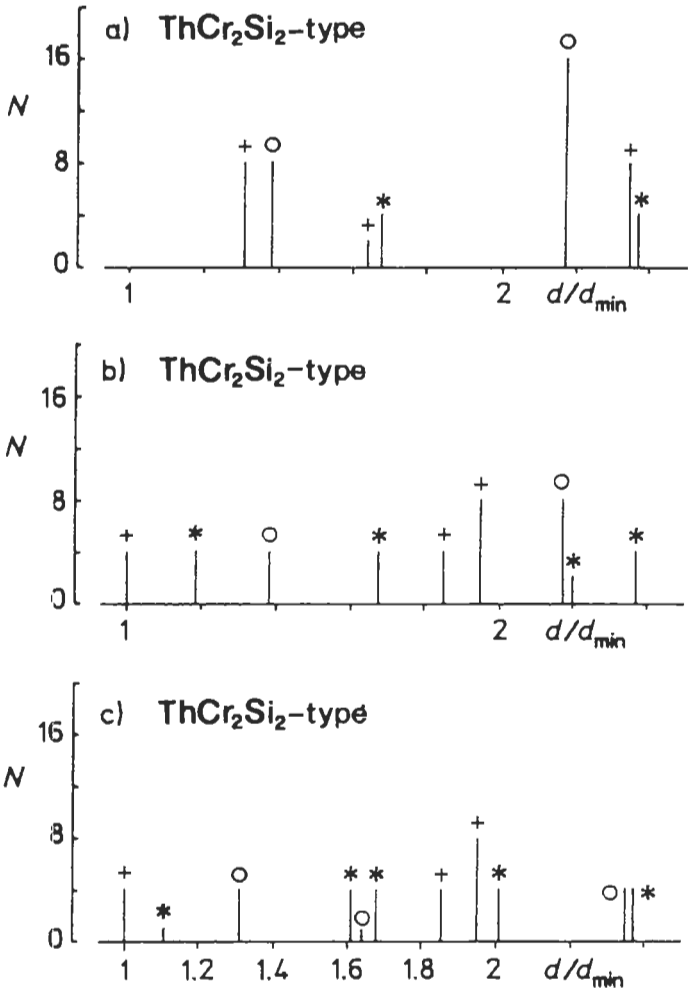

Fig. 39. Distances and coordinations in the tI10–$ThCr_2Si_2$ type structure.
a) Coordination around Th:
(+) Th-Si; (*) Th–Th; (o) Th–Cr;
b) Coordination around Cr:
(+) Cr–Si; (*) Cr–Cr; (o) Cr–Th.
c) Coordination around Si:
(+) Si–Cr; (*) Si–Si; (o) Si–Th.

ten series (T = Mn, Fe, Co, Ni, Cu; X = Si, Ge) have been analysed by PEARSON [1985a]. It has been observed that the cell dimensions are generally controlled by RE–X contacts. In the case of Mn, however, the RE-Mn contact has to be assumed to control the cell dimensions (see sec. 7.2.5.).

Magnetic phase transition in RET_2X_2 phases have been described by SZYTULA [1992].

References: p. 363.

Structural distortions in some groups of RET_2X_2 phases ($REPt_2Sn_2$), leading to less symmetric cells, have been reported by LATROCHE *et al.* [1992].

An interesting compound belonging to the RET_2X_2 family is $EuCo_2P_2$. In a neutron diffraction investigation of this phase carried out by REEHUIS *et al.* [1992] the positional (nuclear) and the magnetic structures were determined. The ordering of the magnetic moments of the Eu-atoms and the relation (commensurability) between this ordering and that of the atomic positions were studied (see sec. 4.4.).

6.5.10. Structural types: tI12–$\alpha ThSi_2$ and tI12–LaPtSi

The $\alpha ThSi_2$ type structure, and its lattice-equivalent ternary LaPtSi type derivative can be considered, filled up tI8–NbAs type derivative. These structures can be described in terms of layers of (metal atoms) triangular prisms parallel to the basal planes of the tetragonal cells, the prism axes in one layer being rotated 90° relative to those of the layers above and below.

In the NbAs type structure the As atoms only center alternate Nb prisms. In the $\alpha ThSi_2$ type structure all the Th-prisms are centered by Si instead of only half of them (PEARSON [1972]).

We may also compare the three structures in terms of 4^4 net layer stacking (along the c-direction of the tetragonal cells): See also fig. 40.

tI8–NbAs:
$Nb_0^1\ As_{0.17}^2\ Nb_{0.25}^3\ As_{0.42}^1\ Nb_{0.5}^4\ As_{0.67}^3\ Nb_{0.75}^2\ As_{0.92}^4$
tI12–$\alpha ThSi_2$:
$Th_0^1\ Si_{0.08}^4\ Si_{0.17}^2\ Th_{0.25}^3\ Si_{0.33}^2\ Si_{0.42}^1\ Th_{0.5}^4\ Si_{0.58}^1\ Si_{0.67}^3\ Th_{0.75}^2\ Si_{0.83}^3\ Si_{0.92}^4$
tI12–LaPtSi:
$La_0^1\ Pt_{0.08}^4\ Si_{0.17}^2\ La_{0.25}^3\ Pt_{0.33}^2\ Si_{0.42}^1\ La_{0.5}^4\ Pt_{0.58}^1\ Si_{0.67}^3\ La_{0.75}^2\ Pt_{0.83}^3\ Si_{0.92}^4$

Structural type: tI12–$\alpha ThSi_2$
body-centered, tetragonal, space group $I4_1/amd$, No. 141.
4 Th in a): 0,0,0; $0,\frac{1}{2},\frac{1}{4}$; $\frac{1}{2},\frac{1}{2},\frac{1}{2}$; $\frac{1}{2},0,\frac{3}{4}$;
8 Si in e): 0,0,z; $0,\frac{1}{2},\frac{1}{4}+z$; $\frac{1}{2},0,\frac{3}{4}-z$; $\frac{1}{2},\frac{1}{2},\frac{1}{2}-z$; $\frac{1}{2},\frac{1}{2},\frac{1}{2}+z$; $\frac{1}{2},0,\frac{3}{4}+z$; $0,\frac{1}{2},\frac{1}{4}-z$; 0,0,−z.
For the prototype itself a = 412.6 pm, c = 1434.6 pm, c/a = 3.477 and $z(Si) = 0.416_5$.

Structural type: tI12–LaPtSi
body-centered, tetragonal, space group $I4_1md$, N.109.
4 La in a(1): 0,0,z; $0,\frac{1}{2},\frac{1}{4}+z$; $\frac{1}{2},\frac{1}{2},\frac{1}{2}+z$; $\frac{1}{2},0,\frac{3}{4}+z$;
4 Pt in a(2): 0,0,z; $0,\frac{1}{2},\frac{1}{4}+z$; $\frac{1}{2},\frac{1}{2},\frac{1}{2}+z$; $\frac{1}{2},0,\frac{3}{4}+z$;
4 Si in a(3): 0,0,z; $0,\frac{1}{2},\frac{1}{4}+z$; $\frac{1}{2},\frac{1}{2},\frac{1}{2}+z$; $\frac{1}{2},0,\frac{3}{4}+z$.
For the prototype itself a = 424.90 pm, c = 1453.9 pm, c/a = 3.422 and z(La) = 0 (fixed conventionally), z(Pt) = 0.585 and z(Si) = 0.419.
The unit cells of the two structures are presented in fig. 40.

The $ThSi_2$ type structure according to PEARSON [1972] is primarily controlled by the Th-Si contacts, with the Si-Si contacts exerting a certain influence. Each Si atom has three close Si neighbours resulting in the three dimensionally connected framework schematically shown in fig. 40d. This framework (and the Si–Si coordination) can be compared

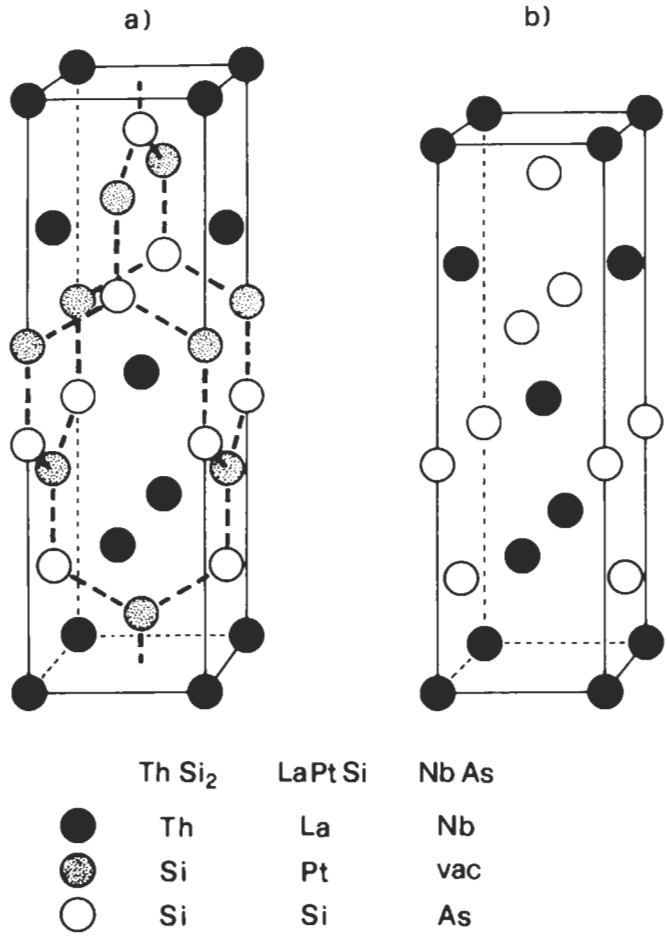

Fig. 40a,b. Crystal structures of $ThSi_2$ and LaPtSi (a) and NbAs (b) with the indication of the atoms which, in the three structures, occupy the different sites. (Notice the defective character of the NbAs type structure in comparison with the $ThSi_2$ type.) In c) different sections of the LaPtSi structure unit cell are presented with the indication of the heights along the z-direction and of the codes used for the different atomic position in a square net (compare with fig. 11). In the NbAs structure, the sections at $z = 0.08$, 0.33, 0.58 and 0.83 are not occupied by any atoms. The dotted lines in a) show a part of the three-connected framework of Si (or Pt,Si) atoms. A larger portion of the framework is presented in d).

with the planar graphite hexagonal nets and therefore with, for instance, the hP3–AlB_2 type structure (and its ordered variants). In the case of $ThSi_2$, however, one vertex of each hexagon is always missing and we have parallel sets of planar chains interconnected to similar perpendicular sets.

It may be interesting to mention that the characteristic structure of this network described as "*hinged*" *network* should have the peculiar feature that the entire framework could undergo reorganisation by a nearly barrierless twisting type motion. According to

References: p. 363.

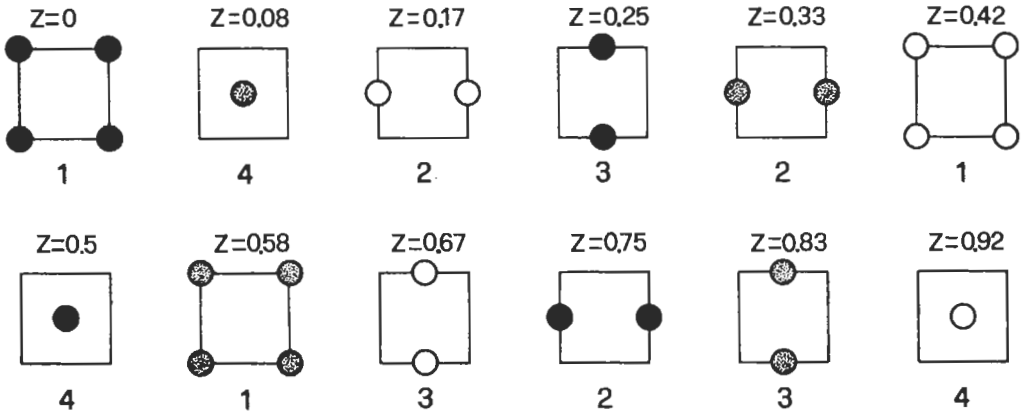

c)

d)

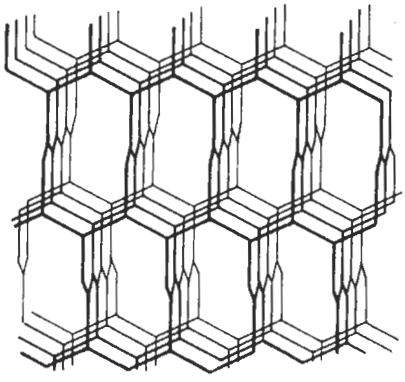

Fig. 40c,d.

BAUGHMAN and GALVAO [1993] and MOORE [1993], unusual mechanical and thermal properties may be predicted for substances having all their atoms arranged in such a framework. These special properties, therefore, may be envisaged for hypothetical compounds such as polyacetylene, polydiacetylene, polyphenylene, $(BN)_x$ phases, etc. and perhaps for substances containing the hinged network as a part of their structure (*"crowded" hinged network* crystals) such as $ThSi_2$ compounds.

Finally considering the AlB_2 and the $\alpha ThSi_2$ type structures we may notice that the similarity of their bonding arrangements may be further confirmed by the existence of the AlB_2 structure also for a different form of $ThSi_2$ (β form, high temperature form) and (as a defective structure) for $\approx Th_3Si_5$. Following the description presented by BAUGHMAN and GALVAO [1993]) the AlB_2 type structure could be called a "crowded" graphitic network structure.

6.6. Tetrahedrally close-packed, Frank–Kasper structures, Laves phases, Samson phases

6.6.1. General remarks

A number of structures of several important intermetallic phases can be classified as tetrahedrally close-packed structures. As an introduction to this subject we may remember, according to SHOEMAKER and SHOEMAKER [1969] that in packing spheres of equal sizes the best space filling is obtained in the cubic or hexagonal close-packed structures (or in their variants). In those arrangements there are tetrahedral and octahedral holes (see the comments on this point reported in the description of the cF4–Cu type structure in sec. 6.2.2). The local mean atomic density (the average space filling) is somewhat higher at the tetrahedral holes than in the larger octahedral ones. A more compact arrangement might, therefore, be obtained if it were be possible to have only tetrahedral interstices. It is, however, *impossible to fill space* with *regular tetrahedra* throughout. By introducing some variability in the sphere dimensions it is possible to obtain packing containing only tetrahedral holes. The tetrahedra are now no longer regular: the ratio of the longest tetrahedron edge to the shortest, however, needs not exceed about $\frac{4}{3}$ in a given structure. The corresponding crystal structure can be considered to be obtained from the space filling of these tetrahedra (which share faces, edges and vertices). In structures containing atoms of approximately the same size and within the aforementioned limits of edge-length ratio, the sharing of a given tetrahedron edge (i.e. an interatomic link ligand) either among 5 or 6 tetrahedra has to be considered the most favored situation (according to the systematic analysis of these structures carried out by FRANK and KASPER [1958, 1959]). On the assumption that only 5 or 6 tetrahedra may share a given edge the number of tetrahedra that share a given vertex is limited to the values 12, 14, 15 and 16. The 12 (or 14, 15, 16) tetrahedra sharing a given vertex form, *around this point*, a coordination polyhedron with triangular faces. The radii of this polyhedron are the edges shared among 5 or 6 component tetrahedra and connect the central atom with the polyhedron vertices, five-fold or six-fold vertices, that is vertices in which 5 or 6 faces meet.

The four possible coordination polyhedra are shown in fig. 41 and correspond to the following properties:

coordination 12 (regular, or approximately regular, icosahedron): 12 vertices (12 five-fold vertices) and 20 faces.
coordination 14: 14 vertices (12 five-fold and 2 six-fold) and 24 faces.
coordination 15: 15 vertices (12 five-fold and 3 six-fold) and 26 faces.
coordination 16: 16 vertices (12 five-fold and 4 six-fold) and 28 faces.
(For symbols used in the coding of the vertex-characteristics see sec. 7.2.7).

Several structures (*Frank–Kasper structures*) can be considered in which all atoms have either 12 (icosahedral), 14, 15 or 16 coordinations. These can be described as resulting from the polyhedra presented in fig. 41. These polyhedra interpenetrate each other so that every vertex atom is again the center of another polyhedron. All structures in this family contain icosahedra and at least one other coordination type.

Frank and Kasper demonstrated that structures formed by the interpenetration of the four polyhedra contain planar or approximately planar layers of atoms. (*Primary layers* made up by tessellation of triangles with hexagons and/or pentagons were considered,

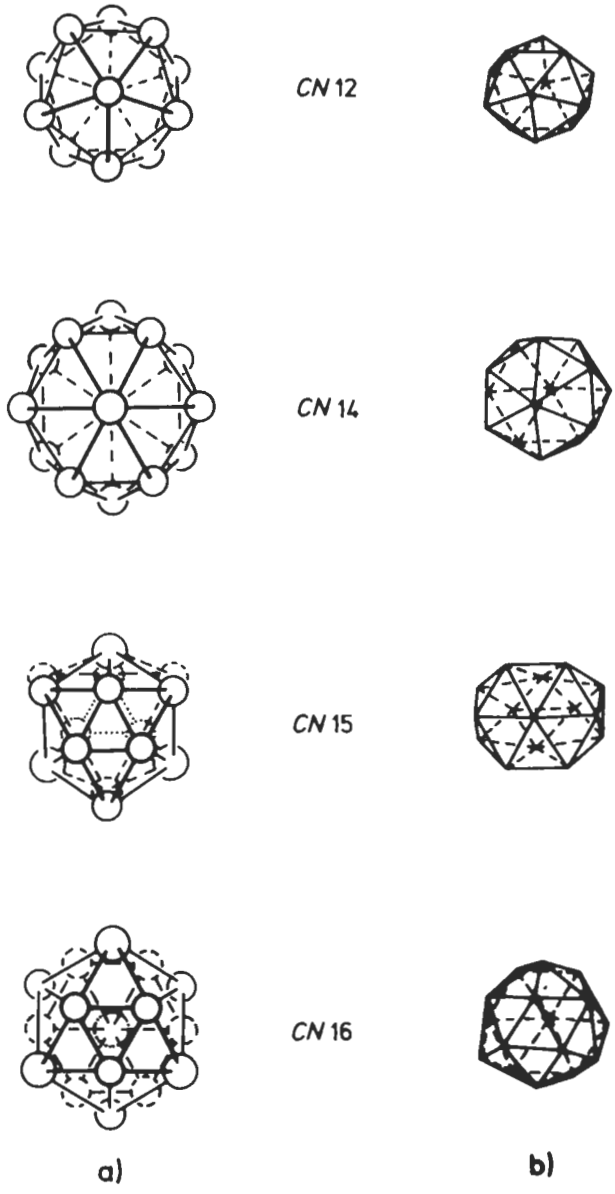

Fig. 41. The coordination polyhedra of the Frank–Kasper structures, are shown in two different styles.

a) the relative positions of the coordinating atoms are shown (the central atoms are not reported). (For the coordination numbers (CN) 12 and 14, one atom of the coordination shell is not visible).

b) the corresponding triangulated polyhedra are shown. Vertices in which 5 or 6 triangles meet are easily recognizable.

and intervening *secondary layers* of triangles and/or squares). For a classification and coding of the nets and of their stacking see PEARSON [1972] and also SHOEMAKER and SHOEMAKER [1969] or FRANK and KASPER [1958, 1959].

A short summary of structural types pertaining to this family is reported in table 6; for a few of them, some details or comments are reported in the following.

6.6.2. cP8–Cr_3Si type structure

This structure is also called W_3O or β-W type (it was previously believed to be a W modification instead of an oxide) or A15 type (see section 3.4).
Cubic, space group $Pm\bar{3}n$, No. 223.
Atomic positions:
2 Si in a) 0,0,0; $\frac{1}{2},\frac{1}{2},\frac{1}{2}$;
6 Cr in c) $\frac{1}{4},0,\frac{1}{2}$; $\frac{3}{4},0,\frac{1}{2}$; $\frac{1}{2},\frac{1}{4},0$; $\frac{1}{2},\frac{3}{4},0$; $0,\frac{1}{2},\frac{1}{4}$; $0,\frac{1}{2},\frac{3}{4}$.

This structure type is observed for many phases formed in the composition ratio 3:1 by several transition metals with elements from the III, IV, V main groups (or with Pt metals or Au). Phases having this structural type are, for instance, Mo_3Al, Nb_3Al, V_3Al, Ta_3Au, Ti_3Au, Cr_3Pt, Cr_3Os, Cr_6AlSi, V_6AlSn, Nb_6GaGe, etc. A number of compounds with this structure have been found to have significantly high superconducting transition temperature, T_c (among the highest known, before the discovery of the families of superconducting complex oxides, such as $Ba_2YCu_3O_{7-x}$ or $\approx Bi_2(Ca,Sr)_3Cu_2O_{9-x}$, etc.). Examples of superconducting, Cr_3Si type, phases are:

Nb_3Ge ($T_c = 23.2$ K, sputtered films), Nb_3Ga ($T_c = 20.7$ K, bulk), Nb_3Sn ($T_c = 18.1$ K), V_3Si ($T_c = 16.8$ K), V_3Ga ($T_c = 14.1$ K), Nb_3Au ($T_c = 11.5$ K), Nb_3Pt ($T_c = 9.2$ K), Mo_3Ir ($T_c = 8.8$ K), etc.

The Cr_3Si type structure does not always remain stable in these materials down to 0 K, yet the change in crystal structure, when it occurs (for instance, with a tetragonal structure formed at low temperature as a result of a martensitic transformation) seems not correlated with T_c. Solid solutions in general have lower T_c values than the stoichiometric compounds. (Other superconducting intermetallic phases belonging to different structural types are, for instance, $LuRh_4B_4$ ($T_c = 11.7$ K, $YPd_5B_3C_x$ ($T_c = 23$ K), quaternary lanthanum nickel boro-nitrides, etc. See CAVA *et al.* [1994a, 1994b]).

6.6.3. σ phase type structure, (tP30–σCr-Fe type)

In the space group $P4_2/mnm$, No. 136, the two atomic species, Cr and Fe, are distributed in several sites with a nearly random occupation. Different atom distributions have been proposed in the literature (also owing to different preparation methods and heat treatments). The following distribution is one of those reported in DAAMS *et al.* [1991]: two atoms in sites a) (with a 12% probability for Cr and 88% for Fe), 4 atoms (75% Cr, 25% Fe) in sites f), 8 atoms (62% Cr, 38% Fe) in a set i) of sites, 8 atoms (16% Cr, 84% Fe) in another set i) and 8 atoms (66% Cr, 34% Fe) in j). The structure can be considered as made up of primary hexagon–triangle layers containing $3636 + 3^26^2$ and 6^3 nodes (in a 3:2:1 ratio) at height ≈ 0 and $\frac{1}{2}$ separated (at height $\approx \frac{1}{4}$ and $\frac{3}{4}$) by secondary 3^2434 layers (that is layers, in which every node is surrounded, in order, by 2

Table 6
Examples of tetrahedral close-packed structures.

Structural types	Unit cell dimensions (rounded values) for the reported prototype [pm]	% of atoms in the center of a polyhedron with CN 12	14	15	16
cP8–Cr_3Si (also called W_3O or ß-W type or A15 type phase).	a = 456	25	75		
tP30–σ-$Cr_{46}Fe_{54}$* σ phases	a = 880 c = 456	33	53	13	
hR39– W_6Fe_7 μ phases	a = 476 c = 2562	55	15	15	15
hP7–Zr_4Al_3	a = 543 c = 539	43	28	28	
oP52 ≈ $Nb_{48}Ni_{39}Al_{13}$* M phases	a = 930 b = 493 c = 1627	55	15	15	15
oP56 ≈ $Mo_{21}Cr_9Ni_{20}$* P phases	a = 1698 b = 475 c = 907	43	36	14	7
hR159 ≈ $Mo_{31}Cr_{18}Co_{51}$* R phases	a = 1090 c = 1934	51	23	11	15
cI162–$Mg11Zn_{11}Al_6$*	a = 1416	61	7	7	25
Laves Phases:					
cF24–Cu_2Mg	a = 704	67	33		
hP12–$MgZn_2$	a = 522 c = 856	67	33		
hP24–Ni_2Mg	a = 482 c = 1583	67	33		

* For these phases the reported formulae generally correspond to an average composition within a solid solution field. This also in relation with a (partially) disordered occupation of the different sites.

triangles, 1 square, 1 triangle and 1 square).

As pointed out by Pearson (by studying the near-neighbours diagram: see sec. 7.2.5.a) the σ-phase structure is a good example of a structure which is controlled by the coordination factor: all the known phases are closely grouped around the intersection of lines corresponding to high coordination numbers. (The most favorable radius ratio for the component atoms is included between 1.0 and 1.1.) It is also possible that the electron concentration plays some role in controlling the phase stability. The different phases are grouped in the range 6.2 to 7.5 electrons (s, p and d) per atoms.

6.6.4. Laves phases: cF24–Cu_2Mg (and cF24–Cu_4MgSn and cF24–$AuBe_5$), hP12–$MgZn_2$ (and hP12–U_2OsAl_3) and hP24–Ni_2Mg types

General remarks

The Laves phases form a *homeotect structure type set* (a family of polytypic structures). In all of them (described in terms of a hexagonal cell) three closely spaced 3^6 nets of atoms are followed (in the z direction of the same cell) by a 3636 net (see figs. 8 and 10). The 3^6 nets are stacked on the same site as the kagomé 3636 nets which they surround (for instance: β-BAC–γ-CAB in the "two slabs" $MgZn_2$ type (h) structure, β-BAC–γ-CBA–α-ACB in the "three slabs" $MgCu_2$ type (c) structure, α-ABC–γ-CBA–α-ACB–β-BCA in the "four slabs (hc)" Ni_2Mg type structure, etc.: see sec. 4.3. on homeotect structure type). The Laves phases, as Frank–Kasper structures, (see table 6), can also be described by alternative stacking of pentagon–triangle main layers of atoms and secondary triangular layers (parallel to (110) planes of the hexagonal cell). The importance of the geometrical factor in determining the stability of these phases has been pointed out (PEARSON [1972]). The role of the electron concentration in controlling the differential stability of the different Laves phase types has been also observed. By studying, for instance, solid solutions of Cu_2Mg and $MgZn_2$ with Ag, Al, Si (LAVES and WITTE [1936], KLEE and WITTE [1954]) it was observed that for an average VEC (valence electron concentration) between 1.3 and 1.8 e/a (electrons per atom) the Cu_2Mg structure is generally formed, for VEC values in the range from ≈ 1.8 to 2.2 e/a generally the $MgZn_2$ type structure is obtained. The Ni_2Mg type can be observed for intermediate values of VEC between 1.8 and 2.0.

It may be useful, however, to mention that depending, for instance, on the temperature different Laves type structures may be observed in the same chemical system. An example may be the Ti–Cr system for which 3 different structures have been described: α-$TiCr_2$ ($MgCu_2$ type, homogeneous in the composition range $\approx$ 63–65 at% Cr), stable from room temperature up to $\approx$ 1220°C; β-$TiCr_2$ ($MgZn_2$ type, homogeneous from 64 to 66 at% Cr), high temperature phase stable from 800°C up to $\approx$ 1270°C; and γ-$TiCr_2$ (Ni_2Mg type, $\approx$ 65–66 at% Cr), high temperature phase stable from 1270°C up to the melting point (1370°C). Notice that the α and β forms, which can coexist in the temperature range from 800°C up to 1220°C have slightly different compositions.

Many (binary and complex solid solutions) Laves phases are known. Typically Laves compounds XM_2 are formed in several systems of X metals such as alkaline-earths, rare earths, actinides, Ti, Zr, Hf, etc, with M = Al, Mg, VIII group metals, etc.

Before passing to a detailed description of the principal Laves types, a few more remarks can be made concerning the *Laves polytypes*. An interesting example may be given by the Li–Mg–Zn alloys (MELNIK [1974], MALLIK [1987]). This system is one of the richest in the Laves phases among the known ternary systems. It contains, besides $MgZn_2$, eight ternary compounds L_n (the index n denotes the number of slabs) in the following sequence:

L_2: $MgZn_2$ (hP), a = 521.4 pm; c = 856.3 pm ($\equiv 2*428.1$)
L_8: $Mg(Li_{0.07}Zn_{1.93})$ (hP), a = 521.3 pm; c = 3422 pm ($\equiv 8*427.8$)
L_{14}: $Mg(Li_{0.11}Zn_{1.89})$ (hP), a = 521.5 pm; c = 5989 pm ($\equiv 14*427.8$)
L_9: $Mg(Li_{0.20}Zn_{1.80})$ (hR), a = 522 pm; c = 3841 pm ($\equiv 9*426.8$)

L_{10}: $Mg(Li_{0.23}Zn_{1.77})$ (hP), a = 522.3 pm; c = 4278 pm (≡ 10 * 427.8)
L_4: $Mg(Li_{0.25}Zn_{1.75})$ (hP), a = 522.7 pm; c = 1709 pm (≡ 4 * 427.3)
L'_4: $Mg(Li_{0.50}Zn_{1.50})$ (hP), a = 1046 pm; c = 1705 pm (≡ 4 * 426.3)
L'_3: $Mg(Li_{0.56}Zn_{1.44})$ (hR), a = 1051 pm; c = 1285 pm (≡ 3 * 428.3)
L_3: $Mg(Li_{0.77}Zn_{1.23})$ (cF), a = 522.6 pm; c = 1290 pm (≡ 3 * 430)

Notice that the structures with n = 3 and 4 exist not only in an ordinary form L_4, Ni_2Mg, and L_3, $MgCu_2$ type cubic, (a = 744.8 pm, here described in terms of an equivalent set of hexagonal axes) but also with doubled unit cell edge *a* (Ni_2Mg type and $MgCu_2$ type superstructures L'_4 and L'_3).

Structural type: cF24–Cu_2Mg and derivative structures
Face-centered cubic cF24–Cu_2Mg, space group $Fd\bar{3}m$, No. 227.
Atomic positions:
8 Mg in a) 0,0,0; $0,\frac{1}{2},\frac{1}{2}$; $\frac{1}{2},0,\frac{1}{2}$; $\frac{1}{2},\frac{1}{2},0$; $\frac{3}{4},\frac{1}{4},\frac{3}{4}$; $\frac{3}{4},\frac{3}{4},\frac{1}{4}$; $\frac{1}{4},\frac{1}{4},\frac{1}{4}$; $\frac{1}{4},\frac{3}{4},\frac{3}{4}$;
16 Cu in d) $\frac{5}{8},\frac{5}{8},\frac{5}{8}$; $\frac{5}{8},\frac{1}{8},\frac{1}{8}$; $\frac{1}{8},\frac{5}{8},\frac{1}{8}$; $\frac{1}{8},\frac{1}{8},\frac{5}{8}$; $\frac{3}{8},\frac{7}{8},\frac{1}{8}$; $\frac{3}{8},\frac{3}{8},\frac{5}{8}$; $\frac{7}{8},\frac{7}{8},\frac{5}{8}$; $\frac{7}{8},\frac{3}{8},\frac{1}{8}$; $\frac{7}{8},\frac{1}{8},\frac{3}{8}$; $\frac{7}{8},\frac{5}{8},\frac{7}{8}$; $\frac{3}{8},\frac{1}{8},\frac{7}{8}$; $\frac{3}{8},\frac{5}{8},\frac{3}{8}$; $\frac{1}{8},\frac{3}{8},\frac{7}{8}$; $\frac{1}{8},\frac{7}{8},\frac{3}{8}$; $\frac{5}{8},\frac{3}{8},\frac{3}{8}$; $\frac{5}{8},\frac{7}{8},\frac{7}{8}$;
Coordination formula: $3^3_\infty[Mg_{4/4}][Cu_{6/6}]_{12/6}$
For the prototype itself, Cu_2Mg, a = 704 pm.
Fig. 42 shows the $MgCu_2$ packing spheres structure.
Normalized interatomic distances and numbers of equidistant neighbours are shown in fig. 43.

Ordered variants of this type of structure are the *Cu_4MgSn* type structure and the *$AuBe_5$* type structure. The packing spheres structure of $AuBe_5$ is shown in fig. 44. The atomic positions of the two structures correspond to the following occupation of the same equipoints in the space group $F\bar{4}3m$ (No. 216).

	in Cu_4MgSn	in $AuBe_5$
a) 0,0,0; $0,\frac{1}{2},\frac{1}{2}$; $\frac{1}{2},0,\frac{1}{2}$; $\frac{1}{2},\frac{1}{2},0$	4 Sn	4 Au
c) $\frac{1}{4},\frac{1}{4},\frac{1}{4}$; $\frac{1}{4},\frac{3}{4},\frac{3}{4}$; $\frac{3}{4},\frac{1}{4},\frac{3}{4}$; $\frac{3}{4},\frac{3}{4},\frac{1}{4}$;	4 Mg	4 Be
e) x,x,x; −x,−x,x; −x,x,−x; x,−x,−x $x,\frac{1}{2}+x,\frac{1}{2}+x$; $-x,\frac{1}{2}-x,\frac{1}{2}+x$; $-x,\frac{1}{2}+x,\frac{1}{2}-x$; $x,\frac{1}{2}-x,\frac{1}{2}-x$; $\frac{1}{2}+x,x,\frac{1}{2}+x$; $\frac{1}{2}-x,-x,\frac{1}{2}+x$; $\frac{1}{2}-x,x,\frac{1}{2}-x$; $\frac{1}{2}+x,-x,\frac{1}{2}-x$; $\frac{1}{2}+x,\frac{1}{2}+x,x$; $\frac{1}{2}-x,\frac{1}{2}-x,x$; $\frac{1}{2}-x,\frac{1}{2}+x,-x$; $\frac{1}{2}+x,\frac{1}{2}-x,-x$. ($x \cong 0.625 = \frac{5}{8}$)	16 Cu	16 Be

We can see that the 8-atom equipoint of the Cu_2Mg type structure has been subdivided into two different, ordered, 4-point subsets in the two derivative structures.

Layers stacking symbols, triangular, kagomé (T,K) nets:

Cu_2Mg:
$Mg_0^A\ Cu_{0.13}^{\alpha}\ Mg_{0.25}^A\ Cu_{0.29}^C\ Mg_{0.33}^B\ Cu_{0.46}^{\beta}\ Mg_{0.58}^B\ Cu_{0.63}^A\ Mg_{0.67}^C\ Cu_{0.79}^{\gamma}\ Mg_{0.92}^C\ Cu_{0.96}^B$
Cu_4MgSn:
$Mg_0^A\ Cu_{0.13}^{\alpha}\ Sn_{0.25}^A\ Cu_{0.29}^C\ Mg_{0.33}^B\ Cu_{0.46}^{\beta}\ Sn_{0.58}^B\ Cu_{0.63}^A\ Mg_{0.67}^C\ Cu_{0.79}^{\gamma}\ Sn_{0.92}^C\ Cu_{0.96}^B$
$AuBe_5$:
$Au_0^A\ Be_{0.13}^{\alpha}\ Be_{0.25}^A\ Be_{0.29}^C\ Au_{0.33}^B\ Be_{0.46}^{\beta}\ Be_{0.58}^B\ Be_{0.63}^A\ Au_{0.67}^C\ Be_{0.79}^{\gamma}\ Be_{0.92}^C\ Be_{0.96}^B$

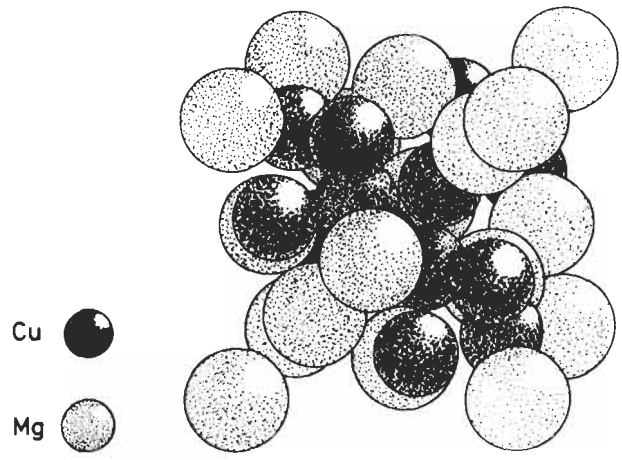

Fig. 42. cF24–$MgCu_2$ type structure (1 unit cell is shown).

Structural type: hP12–$MgZn_2$
Hexagonal, space group $P6_3/mmc$, N. 194,
Atomic positions:
2 Zn in a) 0,0,0; $0,0,\frac{1}{2}$;
4 Mg in f) $\frac{1}{3},\frac{2}{3},z$; $\frac{2}{3},\frac{1}{3},\frac{1}{2}+z$; $\frac{2}{3},\frac{1}{3},-z$; $\frac{1}{3},\frac{2}{3},\frac{1}{2}-z$;
6 Zn in h) $x,2x,\frac{1}{4}$; $-2x,-x,\frac{1}{4}$; $x,-x,\frac{1}{4}$; $-x,-2x,\frac{3}{4}$; $2x,x,\frac{3}{4}$; $-x,x,\frac{3}{4}$;
For the prototype itself, $MgZn_2$, a = 522 pm, c = 856 pm, c/a = 1.640, $z_{Mg} = 0.062$ and $x_{Zn} = 0.830$.
Coordination formula: $3^3_\infty 3\,[Mg_{4/4}][Zn_{6/6}]_{12/6}$
Layer stacking symbols, triangular, kagomé (T,K) nets:
$Zn_0^A\ Mg_{0.06}^B\ Zn_{0.25}^\beta\ Mg_{0.44}^B\ Zn_{0.50}^A\ Mg_{0.56}^C\ Zn_{0.75}^\gamma\ Mg_{0.94}^C$
Fig. 45 shows the packing spheres structure for the $MgZn_2$ compound.

A ternary ordered variant of this structure corresponds to three different atomic species in the three equipoint set. An example may be U_2OsAl_3 (2 Os in a), 4 U in f) and 6 Al in h)).

Structural type: hP24–Ni_2Mg
Hexagonal, space group $P6_3/mmc$, No. 194.
Atomic positions:
4 Mg in e) $0,0,z$; $0,0,\frac{1}{2}+z$; $0,0,-z$; $0,0,\frac{1}{2}-z$;
4 Mg in f) $\frac{1}{3},\frac{2}{3},z$; $\frac{2}{3},\frac{1}{3},\frac{1}{2}+z$; $\frac{2}{3},\frac{1}{3},-z$; $\frac{1}{3},\frac{2}{3},\frac{1}{2}-z$;
4 Ni in f) $\frac{1}{3},\frac{2}{3},z$; $\frac{2}{3},\frac{1}{3},\frac{1}{2}+z$; $\frac{2}{3},\frac{1}{3},-z$; $\frac{1}{3},\frac{2}{3},\frac{1}{2}-z$;
6 Ni in g) $\frac{1}{2},0,0$; $0,\frac{1}{2},0$; $\frac{1}{2},\frac{1}{2},0$; $\frac{1}{2},0,\frac{1}{2}$; $0,\frac{1}{2},\frac{1}{2}$; $\frac{1}{2},\frac{1}{2},\frac{1}{2}$;
6 Ni in h) $x,2x,\frac{1}{4}$; $-2x,-x,\frac{1}{4}$; $x,-x,\frac{1}{4}$; $-x,-2x,\frac{3}{4}$; $2x,x,\frac{3}{4}$; $-x,x,\frac{3}{4}$;
For the prototype itself, Ni_2Mg, a = 482 pm, c = 1583 pm, c/a = 3.284 and z (e_{Mg}) = 0.094, z (f_{Mg}) = 0.8442, z (f_{Ni}) = 0.1251, and x (h_{Ni}) = 0.1643.

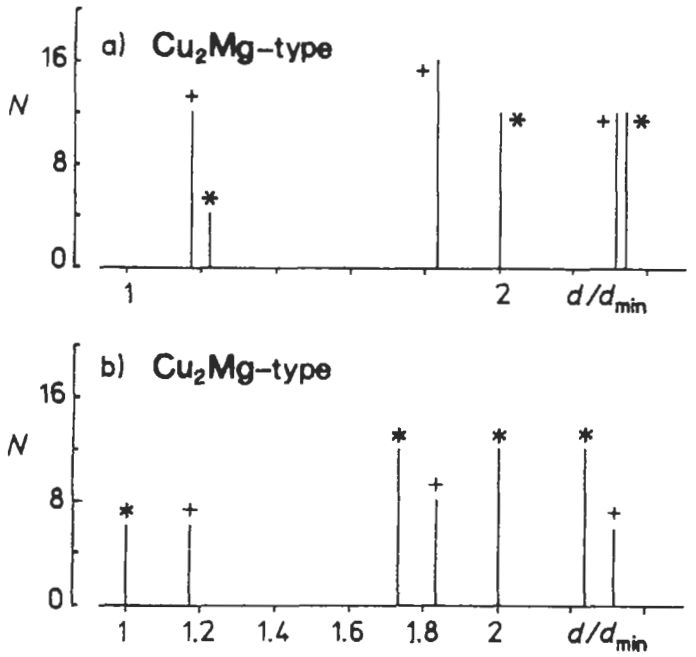

Fig. 43. Distances and coordinations in the cF24–$MgCu_2$ type structure.
a) Coordination around Mg:
(+) Mg–Cu; (*) Mg–Mg.
b) Coordination around Cu:
(*) Cu–Cu; (+) Cu–Mg.

The structure can be described by the following layer stacking sequence triangular, kagomé (T,K) nets:
$Ni_0^{\alpha}\, Mg_{0.09}^{A}\, Ni_{0.13}^{B}\, Mg_{0.16}^{C}\, Ni_{0.25}^{\gamma}\, Mg_{0.34}^{C}\, Ni_{0.37}^{B}\, Mg_{0.41}^{A}\, Ni_{0.50}^{\alpha}$
$Mg_{0.59}^{A}\, Ni_{0.63}^{C}\, Mg_{0.66}^{B}\, Ni_{0.75}^{\beta}\, Mg_{0.84}^{B}\, Ni_{0.87}^{C}\, Mg_{0.91}^{A}$
Coordination formula:
$3^3_{\infty}3\,[Mg_{4/4}][Ni_{6/6}]_{12/6}$

6.6.5. Structures based on frameworks of fused polyhedra, Samson phases

In addition to the Frank–Kasper phases, other structures may be considered in which the same four coordination polyhedra prevail although some regularity is lost. Many of these structures and, in particular the giant cell structures studied by SAMSON [1969] can be described as based on frameworks of fused polyhedra rather than the full interpenetrating polyhedra. Among the most important polyhedra we may mention the truncated tetrahedron: it is shown in fig. 46. It can be related to the CN 16 polyhedron (Friauf polyhedron) of fig. 41. The two polyhedra can be transformed into each other by removing (adding) the 4 six-fold vertices of the CN 16 polyhedron (corresponding to positions out from the center of each of the 4 hexagons of the truncated tetrahedron).

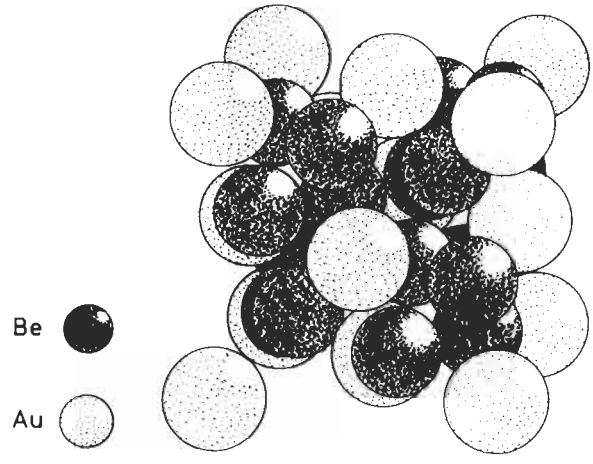

Fig. 44. Unit cell of the cF24–$AuBe_5$ type structure. (Compare with the cF24–$MgCu_2$ type structure, fig. 42.)

Several other coordination polyhedra occur in giant cell structures in addition to the Frank–Kasper polyhedra and to the truncated tetrahedron. (The most important are polyhedra corresponding to CN between 11 and 16).

The following phases represent a few examples of structures to which the aforementioned considerations specially apply:

cI58–α-Mn (a = 891.4 pm) type structure (and its binary variants, cI58–Ti_5Re_{24} or χ-phase and cI58–γ-$Mg_{17}Al_{12}$), cF1124–Cu_4Cd_3 type (a = 2587.1 pm); cF1192–$NaCd_2$ type (a = 3056 pm); cF1832–Mg_2Al_3 (a = 2823.9 pm), etc. (In the giant cell structures partial disorder and/or partial occupancy in some atomic positions have been generally reported, for cF1124–Cu_4Cd_3, for instance, the structure was described as corresponding to the occupation, in several Wyckoff positions, of 388 atomic sites by Cd-atoms, 528 by Cu-atoms and of 208 by Cu- and Cd-atoms in substitutional disorder.)

7. *On some regularities in the intermetallic compound formation and structures*

7.1. Preliminary remarks

As already mentioned in the previous sections, several thousands of binary, ternary and quaternary intermetallic phases have been identified and their structures determined. In a comprehensive compilation such as that by VILLARS and CALVERT about 2200 (in the first edition, [1985]) or about 2700 (second edition, [1991]) different structural types have been described. The specific data concerning about 17500 different intermetallic phases (pertaining to the aforementioned structural types) have been reported in the 1st edition and 26000 in the 2nd one.

As an introductory remark, a little *statistical information* about the *phase* and *structure type distributions* may be interesting.

References: p. 363.

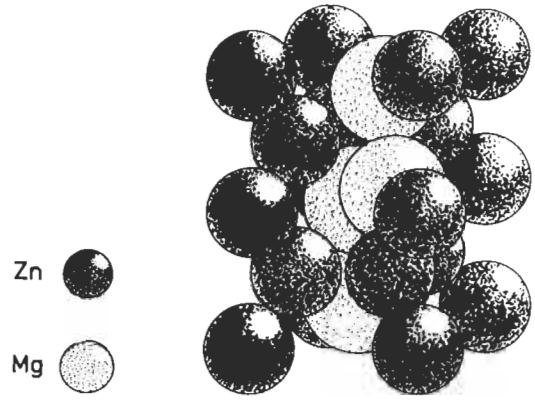

Fig. 45. Unit cell of the hP12–$MgZn_2$ type structure.

For this purpose, we may consider the group of phases described in the compilation by VILLARS and CALVERT [1991]. This, in fact may be considered a fairly representative sample even if the number of new intermetallic phases (and structural types) is constantly increasing.

As a first observation we may notice that the number of phases pertaining to each structural type is not at all constant. Table 7 shows that a very high number of phases crystallize in a few more common structure types. About 25% of the known intermetallic phases belong to the first 12 more common structure types and about 50% of the phases belong to 44 types (that is less than 2% of the known structural types).

This kind of distribution seems to be significant even if table 7 contains only an approximate list. (Some changes may actually be obtained by a more accurate attribution of different phases to a certain structural type or to its degenerate or derivative variants).

The distribution of the phases among the different types is summarized in fig. 47, where (in a double logaritmic scale) the number of phases belonging to each structural type is plotted against the rank order of the type itself. According to a suggestion of the authors of this chapter, in the same figure a curve is presented which has been computed by fitting the reported data by means of eq. (1):

$$N_f = A(r + r_O)^{-B} \tag{1}$$

where N_f is the number of phases corresponding to the structure type having rank r (A, B and r_0 are empirical constants whose values have been determined by the fitting (see also FERRO *et al.* [1995]).

It may be interesting to point out that the aforementioned equation is that suggested by MANDELBROT [1951] as a generalization of ZIPF's law [1949] (which corresponds to the special case of $r_0 \approx 0$ and B = 1). This law, in linguistics, relates for a given text the recurrence frequency (N_f) of a word to its rank (recurrence order). The formula had been deduced to define a cost function for the transmission of linguistic information and minimizing the average cost. (The word "cost" was considered to be related to the complexity of the word

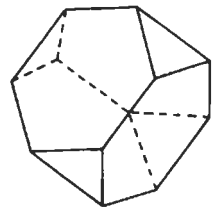

Fig. 46. Truncated polyhedron (12 vertices) related, by the addition of 4 more coordinate atoms out from the centers of the hexagonal faces to the Friauf polyhedron (CN 16), reported in fig. 41.

itself). (Eq. (1) may be considered a special case of a general "Rank Size Rule".)

We note, moreover, the larger numbers of phases having highly symmetric structures (cubic, hexagonal or tetragonal structures). The most frequent orthorhombic and monoclinic structures are the 6th and the 58th respectively in a general list such as reported in table 7. This may be partially related to a certain greater ease in solving highly symmetric structures but probably also contains an indication of a stability criterion. The Laves' stability principles (presented in sec. 7.2.3.) and, specially, the "symmetry principle" may be mentioned.

Considering then the phase composition as a significant parameter, we obtain the histogram shown in fig. 48 for the distribution of the structural types and of the intermetallic phases (as obtained from the 2nd edition of Villars–Calvert) according to the *stoichiometry* of *binary prototypes* (that is, for instance, the binary and ternary Laves phases, the AlB_2, $CaIn_2$, etc., type phases are all included in the number reported for the 66 to 67.99 stoichiometry range, even if the real stoichiometry of the specific phase is different). We may note the overall prevalence of phases and (to a certain extent) of structural types, which, at least ideally, may be related to simple (1:2, 1:1, 1:3, 2:3, etc.) stoichiometric ratios.

The restriction of the phases concentration to a limited number of stoichiometric ratios is also valid (and, perhaps, more evident) for the ternary phases. We may notice in fig. 49 (adapted from a paper by RODGERS and VILLARS [1993]) that seven stoichiometric ratios (1:1:1, 2:1:1, 3:1:1, 4:1:1, 2:2:1, 3:2:1, 4:2:1) are the most prevalent. According to Rodgers and Villars they represent over 80% of all ternary known compounds.

We have, however, to remark that, considering only selected groups of (binary or ternary) alloys, quite different stoichiometric ratios may be predominant. As an example we may mention the binary alloys formed by an element such as Ca, Sr, Ba, rare earth metals, actinides, etc., with Be, Zn, Cd, Hg and, to a certain extent, Mg. Many compounds are generally formed in these alloys. Among them, phases having very high stoichiometric ratios are frequently observed, such as, for instance: $CaBe_{13}$, $LaBe_{13}$, $BaZn_{13}$, $BaCd_{11}$, $BaHg_6$, $BaHg_{11}$, $BaHg_{13}$, La_2Zn_{17}, $LaZn_{13}$, La_2Cd_{17}, $LaCd_{11}$, Th_2Zn_{17}, Pu_3Zn_{22}, Ce_5Mg_{41}, La_2Mg_{17}, $LaMg_{12}$, etc.

7.2. On some factors which control the structure of intermetallic phases

A systematic description of bond characterization from thermodynamic properties in intermetallic compounds (and considerations concerning the stability of intermetallic

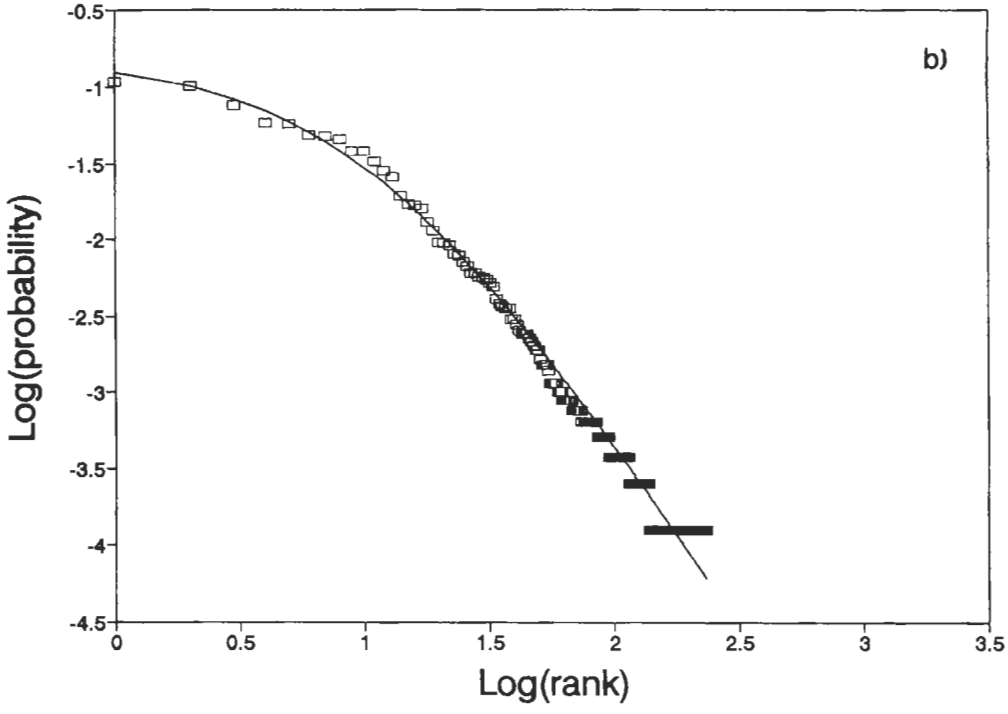
b)
Log(probability)
-0.5
-1
-1.5
-2
-2.5
-3
-3.5
-4
-4.5
0
0.5
1
1.5
2
2.5
3
3.5
Log(rank)

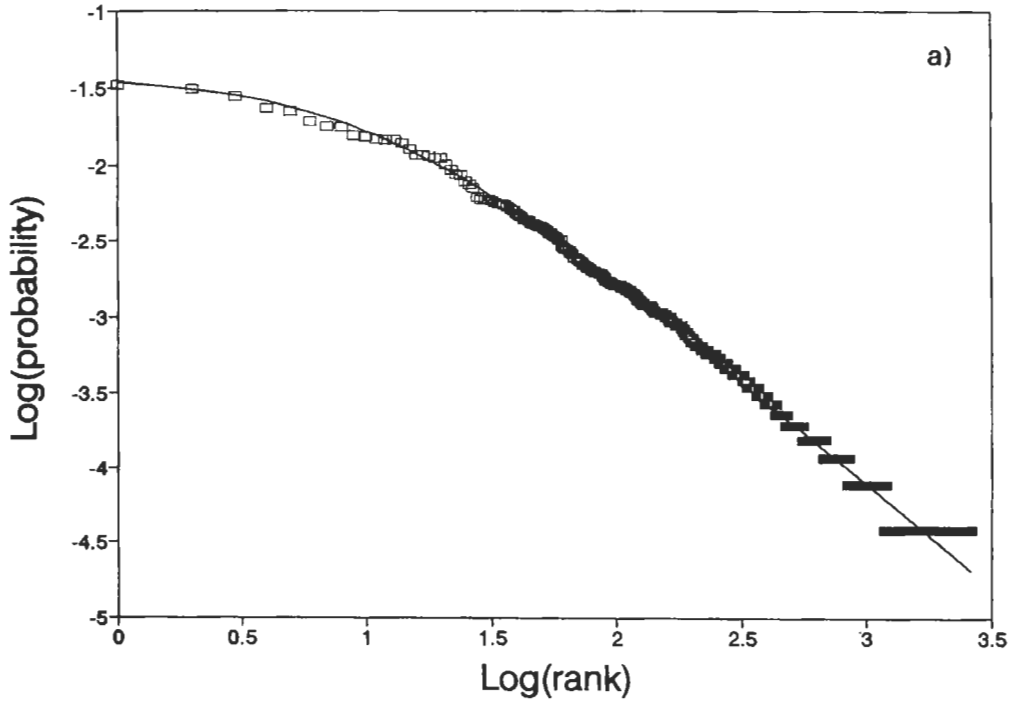
a)
Log(probability)
-1
-1.5
-2
-2.5
-3
-3.5
-4
-4.5
-5
0
0.5
1
1.5
2
2.5
3
3.5
Log(rank)

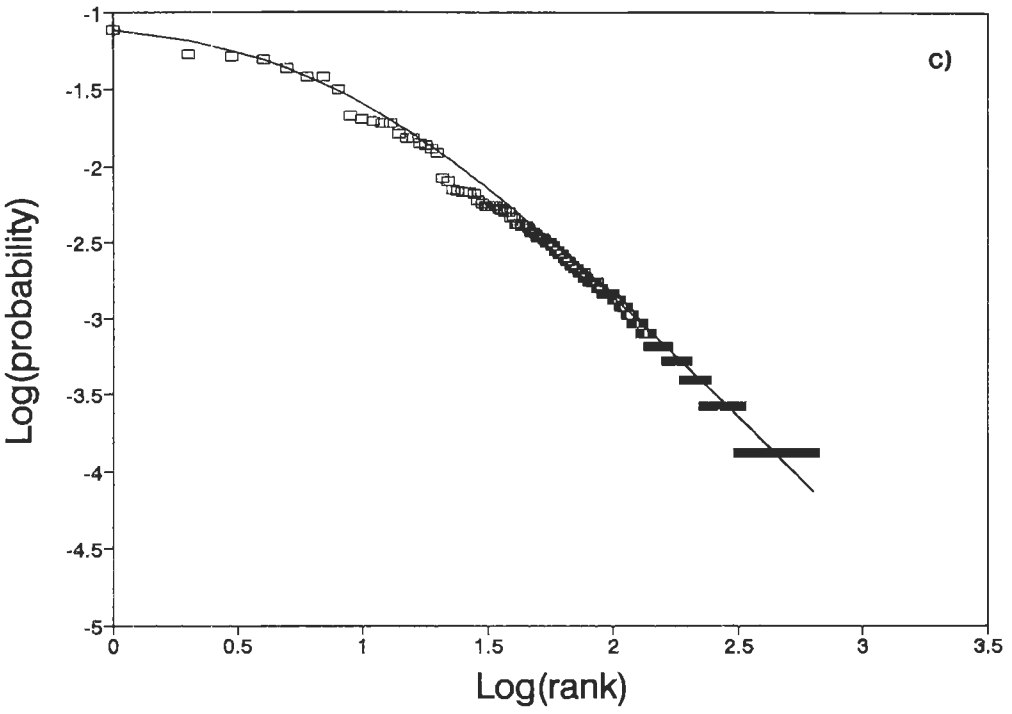

Fig. 47c. Distribution of the intermetallic phases among the structural types. In a double logarithmic diagram the phase numbers (expressed as ratios to the total number) are plotted versus the rank order of the structural type. The continuous line corresponds to the Mandelbrot's equation.
a) Number of phases belonging to the overall different structural types. (Compare with Table 6).
b) Number of phases belonging to the cubic structural types.
c) Number of phases belonging to the hexagonal structural types.

phases) has been reported by ELLNER and PREDEL [1994]. Some information about the computation of the enthalpy of formation of alloys according Miedema's model will be given in sec. 8.5. On this subject we may mention the peculiar properties of alloys of extraordinary stability formed by elements such as Al, Ti, Zr, Hf with the transition metals Re, Ru, Os, Rh, Ir, Pd, Pt, characterized by very high formation heats and discussed by BREWER [1973, 1990] as example of generalized Lewis acid–base interactions in metallic systems.

A general presentation and discussion of the origin of structure of crystalline solids and the structural stability of compounds and solid solutions have been given by Pettifor (see chapter 2 of this book).

In this section and in the following one a brief sampling of some *semiempirical* useful *correlations and, respecively, of methods of predicting phase* (and structure) *formation* will be summarized. The search for regularities and criteria for the synthesis of new representatives of particular structure types has been carried out by many authors. Several factors

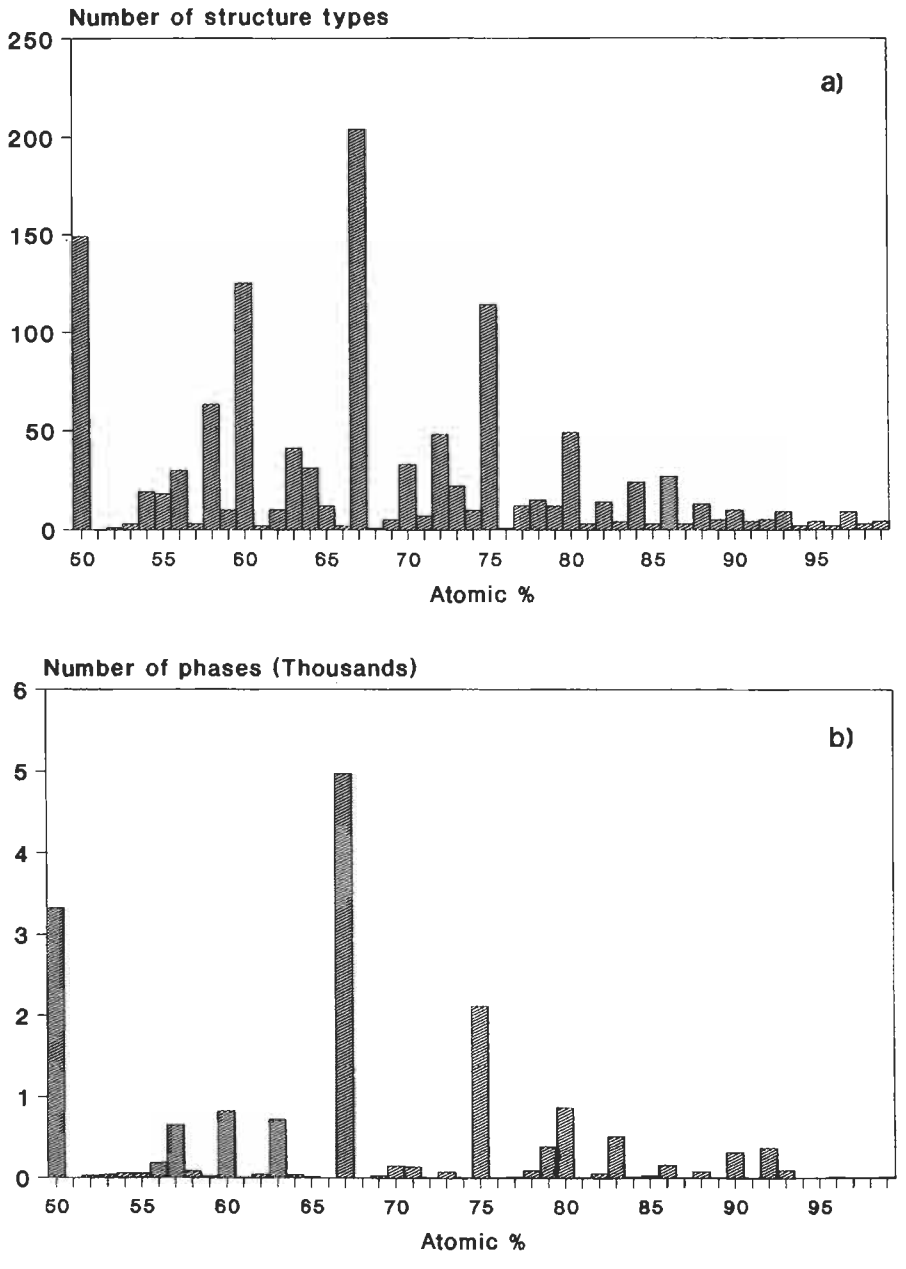

Fig. 48. Distribution of binary intermetallic phases and structural types, according to the stoichiometry.
a) Distribution of the structural types.
b) Distribution of the intermetallic phases.

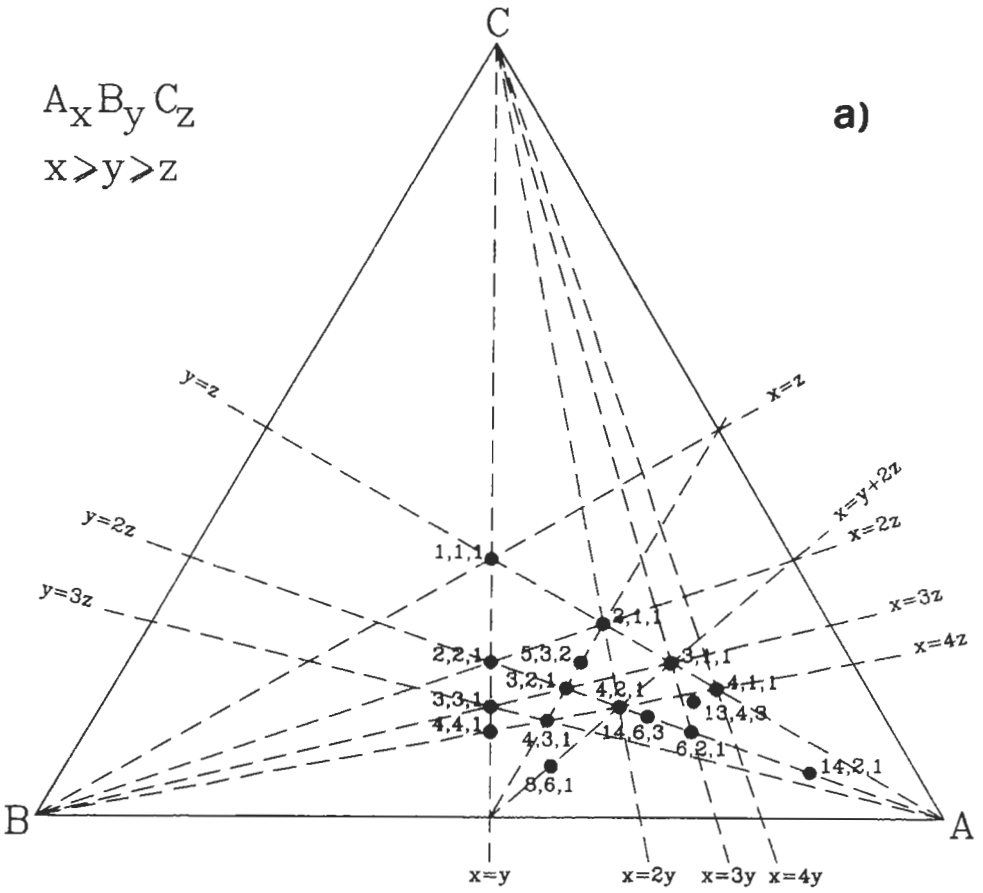

Fig. 49. Distribution of the known ternary intermetallic phases according to their stoichiometry.
a) In a representative portion of a general composition triangle, the more common stoichiometries are shown.

were recognized to be important in controlling the structural stability and some of them were used as coordinates for the preparation of "*classification and prediction maps*", in which various compounds can be plotted and separated into different structure domains.

Intermetallic phases, therefore, could be classified following the most important factor which controls their crystal structure (PEARSON [1972], WESTBROOK [1977], GIRGIS [1983], HAFNER [1989]).

According to PEARSON [1972], following factors may be evidenced:

— *Chemical bond factor,*
— *Electrochemical factor, (electronegativity difference)*
— *Energy band factor, electron concentration*
— *Geometrical factor*
— *Size factor*

References: p. 363.

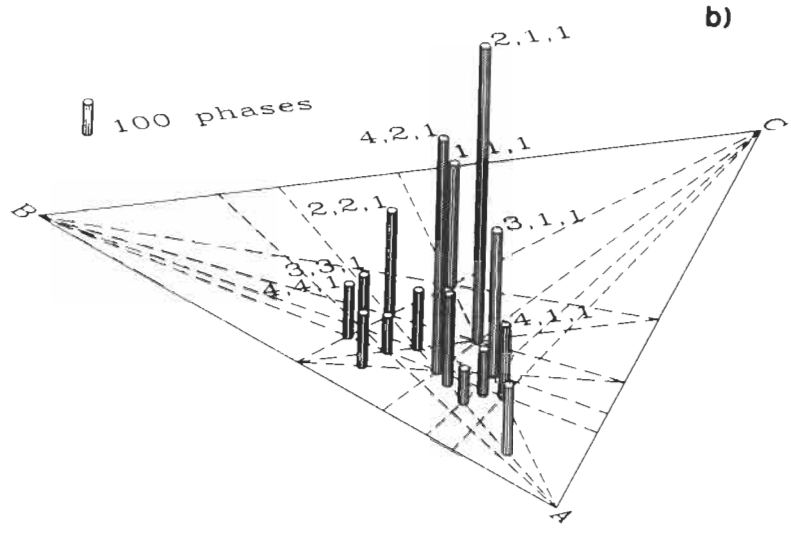

Fig. 49. Distribution of the known ternary intermetallic phases according to their stoichiometry.
b) For the same compositions shown in a), an indication is given of the number of phases.

In the following paragraphs a few comments will be reported on this matter. Emphasis, however, will be given only to those aspects which are more directly related to a description of the "geometrical" characteristics of the phases. For the other questions reference should be made to other parts of this volume.

For an introduction to the electronic structure of extended systems, see HOFFMANN [1987, 1988].

7.2.1. Chemical bond factor and electrochemical factor

A *chemical bond factor* can be said to control the structure when interatomic distances (and as a consequence unit cell dimensions) can be said to be determined by a particular set of chemical bonds. Two different situations can be considered: bonds having high *ionic characteristics* (largely non-directional, the larger anions tend to form symmetrical coordination polyhedra subjected to the limitation related to the anion/cation atomic size ratio) or bonds having *covalent character* (the directional characteristic of which tend to determine the structural arrangement in the phase).

To an increasing weight of the chemical bond factor (ionic and/or covalent bonding) will, of course, correspond, in the limit, the formation of *valence compounds*. According to PARTHE [1980b] a compound C_mA_n can be called a *normal valence compound* if the number of valence electrons of cations (e_C) and anions (e_A) correspond to the relation (normal valence compound rule):

$$m\,e_C = n(8 - e_A) \tag{2}$$

Table 7
Intermetallic phases: The most common structural types
(from the data reported in VILLARS and CALVERT [1991]).

Structural type	Number of phases belonging to each type			Relative Frequency		
	Total	Binary	Ternary	Specific	Cumulative	Rank order
cF8–NaCl	863	318	545	0.0332	0.0332	1
cF24–Cu_2Mg	806	243	563	0.0310	0.0642	2
tI10–$BaAl_4$	723	19	704	0.0278	0.0921	3
cF4–Cu	605	520	85	0.0233	0.1154	4
hP12–$MgZn_2$	580	148	432	0.0223	0.1377	5
oP12–Co_2Si	495	95	400	0.0191	0.1567	6
cP2–CsCl	461	307	154	0.0177	0.1745	7
cP4–$AuCu_3$	454	266	188	0.0175	0.1920	8
hP6–$CaCu_5$	405	106	299	0.0156	0.2076	9
hP2–Mg	393	362	31	0.0151	0.2227	10
cI2–W	382	309	73	0.0147	0.2374	11
cF16–BiF_3	379	39	340	0.0146	0.2520	12
hP9–Fe_2P	375	11	364	0.0144	0.2664	13
cI28–Th_3P_4	358	117	241	0.0138	0.2802	14
hP3–AlB_2	327	122	205	0.0126	0.2928	15
cF8–ZnS	302	40	262	0.0116	0.3044	16
cF56–$MgAl_2O_4$	301	11	290	0.0116	0.3160	17
tI26–$ThMn_{12}$	296	38	258	0.0114	0.3274	18
hP16–Mn_5Si_3	290	177	113	0.0112	0.3385	19
hP24–$Ce_6Al_3S_{14}$	288	0	288	0.0111	0.3496	20
cP8–Cr_3Si	260	82	178	0.0100	0.3596	21
hP4–NiAs	241	101	140	0.0093	0.3689	22
tP6–Cu_2Sb	227	74	153	0.0087	0.3777	23
cP5–$CaTiO_3$	225	3	222	0.0087	0.3863	24
cF116–Th_6Mn_{23}	202	49	153	0.0078	0.3941	25
oC8–CrB	193	120	73	0.0074	0.4015	26
tP68–$BFe_{14}Nd_2$	185	0	185	0.0071	0.4086	27
hR57–Th_2Zn_{17}	160	36	124	0.0062	0.4148	28
oP8–MnP	156	33	123	0.0060	0.4208	29
oP16–Fe_3C	155	101	54	0.0060	0.4268	30
hP6–Ni_2In	154	54	100	0.0059	0.4327	31
cP12–FeS_2	152	50	102	0.0059	0.4385	32
hP6–$CaIn_2$	149	11	138	0.0057	0.4443	33
hP38–$Ni_{17}Th_2$	145	62	83	0.0056	0.4499	34
oI12–$CeCu_2$	145	61	84	0.0056	0.4554	35
hR12–$NaCrS_2$	144	9	135	0.0055	0.4610	36
tI16–$FeCuS_2$	139	0	139	0.0053	0.4663	37
cF12–AlLiSi	135	1	134	0.0052	0.4715	38
cF12–CaF_2	133	87	46	0.0051	0.4767	39
cP40–$Pr_3Rh_4Sn_{13}$	126	0	126	0.0048	0.4815	40
hR36–Be_3Nb	122	49	73	0.0047	0.4862	41
oP8–FeB	121	73	48	0.0047	0.4909	42
hR45–Mo_6PbS_8	115	0	115	0.0044	0.4953	43
hP5–La_2O_3	115	22	93	0.0044	0.4997	44
tP2–AuCu	112	82	30	0.0043	0.5040	45

References: p. 363.

If we consider only the s and p block elements, the number of valence electrons of the elements correspond to their traditional group number) In this case (considering that no anions are formed from the elements of groups I, II and III) following formulae can be deduced for the *normal valence compounds* (formed in binary systems with large electronegativity difference between elements):

$-\ 1_4 4 - 2_2 4 - 3_4 4_3 - 1_3 5 - 2_3 5_2 - 35 - 4_3 5_4$
$-\ 1_2 6 - 26 - 3_2 6_3 - 46_2 - 5_2 6_3 - 17 - 27_2$
$-\ 37_3 - 47_4 - 57_5 - 67_6$

(in these formulae each element is indicated by a number corresponding to its number of valence electrons; for instance:
17 represent NaCl, KCl, etc, $3_2 6_3$ Al_2O_3, etc.)

In the more general case where some electrons are also considered to be used for bonds between cations and anions we have (general valence compound rule):

$$m(e_C - e_{CC}) = n(8 - e_A - e_{AA}) \tag{3}$$

In this formula, which can only be applied if all bonds are two-electron bonds and additional electrons remain inactive in non-bonding orbitals (or, in other words, if the compound is semiconductor and has not metallic properties) e_{CC} is the average number of valence electrons per cation which remain with the cation either in non-bonding orbitals or (in polycationic valence compounds) in cation–cation bonds; similarly e_{AA} can be assumed to be the average number of anion-anion electron pair bonds per anion (in polyanionic valence compounds).

In a more limited field than that of the previously considered general octet rule, it may be useful to mention the "*tetrahedral structures*" which form a subset of the general valence compounds. According to PARTHE [1963, 1964, 1991], if each atom in a structure is surrounded by 4 nearest neighbours at the corner of a tetrahedron, the structure is called "*normal tetrahedral structure*". The general formula of this structure, for the compound C_mA_n, is (*normal tetrahedral structure*):

$$(m\,e_C + n\,e_A) = 4(m + n) \tag{4}$$

(This may be considered a formulation of the so-called GRIMM–SOMMERFELD [1926] Rule).

For the same elements previously mentioned the possible combinations are:

$4_X 4_Y$ (all compositions, for instance, C, Ge, SiC)
35 (BP, AlSb, etc.), 26 (BeO, MgTe, ZnS), 17 (CuBr, AgI),
$3_2 6$, $3_3 7$, 25_2 (ZnP_2, $ZnAs_2$), $2_3 7_2$, 15_3 and $1_2 6_3$.
(ternary or more complex combinations may be obtained by a convenient addition of different binary formulae; for instance:
$14_2 5_3 = (15_3 + 44)$: for instance $CuGe_2P_3$
$136_2 = (1_2 6_3 + 3_2 6)/2$: $CuAlS_2$, $CuInTe_2$, etc.
$1_2 246_4 = (1_2 6_3 + 26 + 4)$: for instance Cu_2FeSnS_4 (Fe^{II}), etc.)

The aforementioned rule may be extended to include the "*defect tetrahedral structures*" where some atoms have less than four neighbours (*general tetrahedral structure*):

$$(m e_C + n e_A) = 4(m+n) + N_{NBO}(m+n) \tag{5}$$

In this formula N_{NBO} is the *average number of non-bonding orbitals* per atom.

By adding the *symbol 0* (zero) to the described notation, *vacant tetrahedral sites* can be represented. Examples of formulae of defect tetrahedral structures are:

40_37_4 (SiI_4, SnI_4); 406_2 (GeS_2); $3_605_46_3$ ($Ga_6As_4Se_3$), $1_25_206_4$ ($CuSbS_2$); etc.

Notice that the aforementioned compositional scheme is a *necessary condition* for building the tetrahedral structures, but *not* every compound that fulfills this condition is a tetrahedral compound. The influence of other parameters, such as the electronegativity difference, has been pointed out. By means of a diagram as shown in fig. 50, the separation of tetrahedral structures from other structures may be evidenced (MOOSER and PEARSON [1959]).

As a final comment to this point, we may mention that when one component in a binary alloy is very electropositive relative to the other, there is a strong tendency to form compounds of high stability in which valence rules are satisfied (PEARSON [1972]). Such alloys are considered to show a strong *electrochemical factor.*

7.2.2. Energy band factor, electron concentration

The properties of a solid on principle could be calculated on the basis of the states of the electrons in the crystal. The status of the understanding of the structures of the solids and indications on the technical and computational problems have been presented in other chapters.

We may mention here that if the stable crystal structure may be described as controlled by the number of electrons per atoms, the phase is called an "*electron compound*". An important class of electron compounds (generally showing rather wide homogeneity ranges) are the *Hume–Rothery phases.*

These include several groups of isostructural phases, each group corresponding to a given value of the so-called valence electron concentration (VEC). Three categories of Hume–Rothery phases are generally considered: those corresponding to VEC values of 3/2 (that is three valence electrons every two atoms), 21/13 and 7/4, respectively.

Representatives of the Hume–Rothery phases are the following:

VEC ≈ 3/2, body centered cubic, (cI2–W type): CuZn, ≈ Cu_3Al, ≈ Cu_5Sn, etc.
VEC ≈ 3/2, complex cubic, (cP20–β Mn type): Cu_5Si, Ag_3Al, Au_5Si, etc.
VEC ≈ 21/13, complex cubic, 52 atoms in the unit cell (or superstructures)
(cP52: ≈ Cu_9Al_4, ≈ Cu_9Ga_4, Ag_9In_4, ≈ Co_5Zn_{21}, etc.; cI52: ≈ Cu_5Zn_8, γ-brass, ≈ Ag_5Cd_8, Ag_5Zn_8, Ru_3Be_{10}, etc.; cF408: $Fe_{11}Zn_{39}$, etc.)
VEC ≈ 7/4, hexagonal close-packed, (hP2–Mg type or superstructures): ≈ $AgZn_3$, ≈ Au_3Ge, ≈ Ag_5Al_3, etc.

The VEC in all the aforementioned cases, for which approximate "ideal" formulae have been indicated, were calculated assuming the following "valence": transition elements with non-filled d-shells: 0; Cu,Ag,Au: 1; Mg and Zn,Cd,Hg: 2; Al,Ga,In: 3; Si,Ge,Sn: 4; Sb: 5.

The given ratios indicate ranges (which can even overlap). It has to be noted, moreover, that the number of electrons to be considered may be uncertain. The VEC

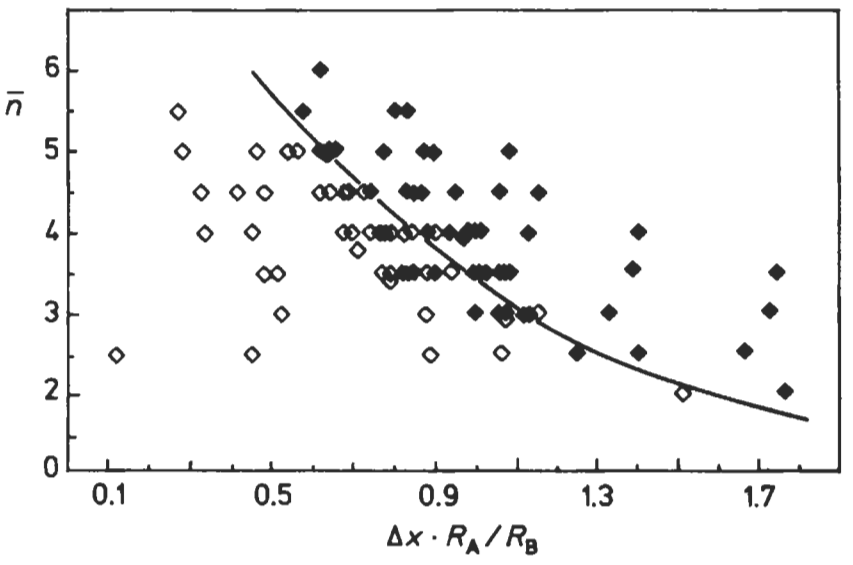

Fig. 50. Mooser–Pearson diagram separating AB compounds into covalent (◊) and ionic (♦) types after HUME–ROTHERY [1967]. The representative points of the different components are plotted in the map $\bar{n}$, average quantum number, versus the electronegativity difference multiplied by the radius ratio. (R_A and R_B radii of the anion and cation elements).

values, therefore, indicate only a composition range where one of the aforementioned structure types *may* occur.

According to GIRGIS [1983] the existence field of the electron phases may be especially related to the combinations of d elements with the elements of the Periodic Table columns from 11 to 14 (from Cu to Si groups).

7.2.3. Geometrical principles and factors, Laves' stability principles

LAVES [1956], when considering the factors which control the structures of the metallic elements, presented three principles that are interrelated and mainly geometric in character.

a) The principle of efficient (economical) use of space (*space-filling principle*).
b) The principle of *highest symmetry*.
c) The principle of the *greatest number of connections* (connection principle).

These principles may be considered to be valid to a certain extent for the intermetallic phase structures and not only for the metallic elements.

(See also some comments on this point as a result of the atomic-environment analysis of the structure types summarized in sec. 7.2.7.)

a) Space-filling principle

The *tendency to use the space economically* (to form structures with the best space-filling) which is especially exemplified by the closest-packing of spheres is considered to be the

result of a specific principle which operates in the metal structures (and also in ionic and, to a lesser degree, in van der Waals structures). This principle is less applicable to covalent crystals because the characteristic interbond angles are not necessarily compatible with an efficient use of the space. Among the metallic elements, 58 metals possess a close-packed arrangement (either cubic or hexagonal) which, in the assumption that the metal atoms are indeformable spheres having fixed diameters, corresponds to the best space-filling; 23 of the remaining metals crystallize in another highly symmetric structure, the body-centered cubic, which corresponds to a slightly less efficient space-filling.

(The space-filling concept has been analysed and discussed by several authors: we may mention LAVES [1956], PARTHE [1961], PEARSON [1972]. A short summary of this discussion will be reported in the following, together with some considerations on the atomic dimension concept itself).

b) The principle of highest symmetry (symmetry principle)

According to Laves a *tendency to build configurations with high symmetry* is evident and is called the symmetry principle. This tendency is particularly clear in metallic structures, especially in the simple ones.

However, according to HYDE and ANDERSSON [1989], for instance, the validity extension of this principle is difficult to evaluate. As time passes, crystallographers are able to solve more and more complex crystal structures and these tend to have low symmetry. The symmetry principle could perhaps be restated by observing that a crystal structure has the highest symmetry compatible with efficient use of space and the specific requirements of chemical bonding between nearest neighbours.

For a discussion on the "symmetry principles", its alternative formulations and the history of its development, papers by BRUNNER [1977] and by BÄRNIGHAUSEN [1980] may be consulted. In these papers a number of statements have been reported which perhaps may be considered equivalent. When considering close sphere packings, the following statements are especially worthy of mention.

a) A tendency to form arrangements of high symmetry is observable.
b) Points are disposed around each point in the same way as around every other.
c) Atoms of the same type tend to be in equivalent positions.

c) The principle of the greatest number of connections (connection principle)

To understand the meaning of this principle it may be at first necessary to define the *concept of connection*. To this end we may consider a certain crystal structure and imagine connecting each atom with the other atoms present in the structure by straight lines. There will be a *shortest segment* between any two atoms. We will then delete all links except the shortest ones. After this procedure, the atoms that are still connected constitute a "*connection*". The connection is *homogeneous* if it consists of structurally equivalent atoms, otherwise it is a *heterogeneous connection.*

Such connections may be finite or 1, 2, 3 dimensionally infinite and are respectively called *islands*, *chains*, *nets* or *lattices*. Symbols corresponding to the letters I, C, N, L (homogeneous connections) or i, c, n, l (heterogeneous connections) have been proposed. (see also the dimensionality indexes reported in sec. 3.5.1.).

As pointed out by Laves (for instance, LAVES [1967]) metallic elements and

intermetallic phases show a tendency to form multidimensional (possibly homogeneous) connections (*connection principle*).

7.2.4. Atomic dimensions and structural characteristics of the phases

a) Atomic radii and volumes

A few comments about the atomic dimension concept may be useful also in order to present a few characteristic parameters and diagrams (such as space-filling parameters, reduced strain parameters, near-neighbours diagrams, etc.).

Quoting from a comprehensive review on this subject (SIMON [1983]) we may remember that ever since it has been possible to determine atomic distances in molecules and crystals experimentally, efforts have been made to draw conclusions from such distances about the nature of the chemical bonding and to compare interatomic distances (dimensions) in the compounds with those in the chemical elements. Distances between atoms in an element can be measured with high precision. As such, however, they cannot be simply used in predicting interatomic distances in the compounds. In rational procedure, reference values (atomic radii) have to be "extracted" from the individual (interatomic distances) measured values. Various functions have been suggested for this purpose. In the specific case of the metals it has been pointed out that interatomic distances depend primarily on the number of ligands and on the number of valence electrons of the atoms (PEARSON [1972]).

Pauling's rule (PAULING [1947]):

$$R_n = R_1 - 30 \log n \,(pm) \tag{6}$$

relating radii for bond order (bond strength) n (number of valence electron per ligand) to that of strength 1, gives a means of correcting radii for coordination and/or for effective valencies. It has been shown (PEARSON [1972], SIMON [1983]) that, no matter what the limitations may be of any particular set of metallic radii (or valencies) that is adopted, the Pauling's relation appears to be reliable, giving a basis for comparing interatomic distances in metals. According to SIMON [1983] slightly better results could be obtained changing the Pauling's formula to:

$$R_n = R_1(1 - A \log n) \tag{7}$$

where A is not constant but can be represented as a function of the element valency.

The subsequent point is to select some system of (a set of) atomic radii which can be used when discussing interatomic distances.

The radii given by TEATUM *et al.* [1968] (and reported in table 8, together with the assumed "valencies") are probably the most useful for discussing metallic alloys. These radii have been reported for a coordination number of 12; they were taken from the observed interatomic distances in the fc cubic (cF4–Cu type) structure and in the hexagonal close-packed hP2–Mg type structure (averaging the distances of the first two groups of 6 neighbours, if the axial ratio has not the ideal 1.633.. value) or from the bc cI2–W type. Since the coordination is 8 in the cI2–W type structure, for the elements having this structure the observed radii were converted to coordination 12 by using a correction given by the formula:

Table 8
Radii (CN 12) of the Elements (from TEATUM *et al.* [1968])[a)]

Element	"Valence"	Radius (pm)	Element	"Valence"	Radius (pm)
H	−1	77.9	Sb	5	157.1
Li	1	156.2	Te	6	164.2
Be	2	112.8	Cs	1	273.1
B	3	92.0	Ba	2	223.6
C	4	87.6	La	3	187.7
N	−3	82.5	Ce	3	184.6
O	−2	89.7	Ce	4	167.2
Na	1	191.1	Pr	3	182.8
Mg	2	160.2	Nd	3	182.2
Al	3	143.2	Pm	3	180.9
Si	4	132.2	Sm	3	180.2
P	−3	124.1	Eu	2	204.1
S	−2	125.0	Eu	3	179.8
K	1	237.6	Gd	3	180.1
Ca	2	197.4	Tb	3	178.3
Sc	3	164.1	Dy	3	177.5
Ti	4	146.2	Ho	3	176.7
V	5	134.6	Er	3	175.8
Cr	6	128.2	Tm	3	174.7
Mn	5	130.7	Yb	2	193.9
Mn	7	125.4	Yb	3	174.1
Fe	8	127.4	Lu	3	173.5
Co	9	125.2	Hf	4	158.0
Ni	10	124.6	Ta	5	146.7
Cu	1	127.8	W	6	140.8
Zn	2	139.4	Re	7	137.5
Ga	3	135.3	Os	8	135.3
Ge	4	137.8	Ir	9	135.7
As	5	136.6	Pt	10	138.7
Se	6	141.2	Au	1	144.2
Rb	1	254.6	Hg	2	159.4
Sr	2	215.1	Tl	3	171.6
Y	3	177.3	Pb	4	175.0
Zr	4	160.2	Bi	5	168.9
Nb	5	146.8	Po	6	177.4
Mo	6	140.0	Fr	1	280
Tc	7	136.5	Ra	2	229.4
Ru	8	133.9	Ac	3	187.8
Rh	9	134.5	Th	4	179.8
Pd	10	137.6	Pa	5	162.6
Ag	1	144.5	U	6	154.3
Cd	2	156.8	Np	6	152.8
In	3	166.6	Pu	~4.8	164
Sn	2	163.1	Pu	5	159.2
Sn	4	158.0	Am	4	173.0

a) The elements are arranged according to their atomic number.
Noble gases and halogens are not included.

References: p. 363.

$$R_{CN\,12} = 1.0316\ R_{CN\,8} - 0.532\ \ (pm) \tag{8}$$

which was empirically obtained from the properties of elements having at least two allotropic modifications, cI2–W type and either cF4–Cu type or hP2–Mg type. The radii in the two structures (calculated at the same temperature by means of the known expansion coefficients) were compared and used to construct the reported equation. For the other metals (that is for the more general problem of the radius conversion from any coordination to coordination number 12) a percentage correction was applied (by using a curve which ranges from about +3% for the conversion from CN 8 to CN 12 to about +20% for the conversion from CN 3 to CN 12) as suggested by LAVES [1956] in a detailed paper dealing with several aspects of crystal structure and atomic sizes.

While dealing with atomic dimension concepts, *atomic volumes* may also be considered. A value of the volume per atom, V_{at} in a structure may be obtained from the room temperature lattice parameter data by calculating the volume of the unit cell and dividing by the number of atoms within the unit cell. See also the table reported by KING [1983].

An equivalent atomic radius could be obtained by computing, on the basis of the space-filling factor of the structure involved, the corresponding volume of a "spherical atom" using the relationship $V_{sph} = (4\ \pi\ R^3/3)$.

In the cP2–W type (CN 8) structure we have $V_{sph} \approx 0.68\ V_{at}$ (only a portion of the available space is occupied by the atomic "sphere", see the following paragraph b). In the cF4–Cu type, and in the "ideal" hP2–Mg type (CN 12) structures we have $V_{sph} \approx 0.74\ V_{at}$. Considering now the previously reported relationship between $R_{(CN\ 12)}$ and $R_{(CN\ 8)}$ we may compute for a given element, very little volume (V_{at}) changes in the allotropic transformation from a form with CN 12 to the form with CN 8. (The radius variation is nearly counterbalanced by the change in the space filling).

This generally is in agreement with the experimental observations (PEARSON [1972]).

We will see that on the basis of the atomic dimensions of the metals involved (expressed, for instance, as R_X–R_Y or R_X/R_Y) many characteristic structural properties of an X_nY_m phase may be conveniently discussed and/or predicted (*size factor effect*). As a further comment to this point we may mention here two "rules", the *Vegard's* and the *Biltz–Zen's rules*, which have been formulated for solid solutions and to a certain extent for ordered compounds. These rules, mutually incompatible, are very seldom obeyed; they may, however, be useful either as approximations or for defining reference behaviours. The first one, VEGARD's rule [1921], corresponds to an additivity rule for interatomic distances (or lattice parameters or "average" atomic diameters). For a solid solution A_xB_{1-x} (x = atomic fraction) between two components of similar structure it takes the form:

$$d_{AB} = x\,d_A + (1 - x)d_B \tag{9}$$

The BILTZ [1934], (or ZEN [1956]) rule has been formulated as a volume additivity rule:

$$V_{AB} = x\,V_A + (1 - x)V_B \tag{10}$$

These rules are only roughly verified in the general case (for the evaluation of interatomic distances weighted according to the composition and for a discussion on the calculation and prediction of the deviations from Vegard's rule see PEARSON [1972] and SIMON [1983]).

As contributions to the general question of an accurate prediction of the variation of the average atomic volume in alloying we may mention a few different approaches. MIEDEMA and NIESSEN [1982] calculated atomic volumes and volume contractions on the basis of the same model and parameters used for the evaluation of the formation enthalpy of the alloy (see sec. 8.5). In a simple model proposed by HAFNER [1985] no difference of electronegativity and no charge transfer were considered. Volume (and energy) changes in the alloy formation were essentially related to elastic effects. Good results have been obtained for alloys formed between s and p block-elements. An empirical approach has been suggested by MERLO [1988]. Deviations from Biltz–Zen trend have been discussed and represented as a function of a "charge transfer atomic parameter" which correlates with Pauling's electronegativity. This approach has been successfully employed for groups of binary alloys formed by the alkaline earths and the bivalent rare earth elements.

Negative experimental deviations from Vegard's rule (and values of the volume contractions) have been sometimes considered as an approximate indication of the formation of strong bonds and related to more or less negative enthalpies of formation (KUBASCHEWSKII [1967]). This indication is only very poor in the general case. For selected groups of alloys, however, the existence of a correlation between the formation volume and enthalpy ($\Delta_{form}V$ and $\Delta_{form}H$) has been pointed out (even if only as an evaluation of relative trends). This is the case of the rare earth (RE) alloys. As noticed by GSCHNEIDNER [1969] considering the trivalent members of the lanthanide series, we may compare the atomic volume decreasing observed in the metals (RE) (lanthanide contraction) with the decreasing of the average atomic volume measured in a series of $REMe_x$ compounds. If this diminution is more (less) severe in the compounds than in the RE metal series, this is considered an indication that the bonding strength in the $REMe_x$ compounds increases (decreases) as we proceed along the series from La to Lu; the heats of formation are expected to increase (decrease) in the same order. To make this comparison the unit cell volumes of the compounds are divided by the atomic volumes of the pure metals. The volume ratio for the series of compounds are then divided for that corresponding to a selected rare earth, this giving a relative scale. If the resultant values increase, with the atomic number of the rare earth, then the lanthanide contraction is less severe in the compounds (in comparison to the rare earth element) and a decrease of the heat of formation is expected (conversely if the relative volume ratio decreases, an increase of the heat of formation (more negative enthalpy of formation) is expected).

(Examples of this correspondence will be examined in sec. 8.6., see also fig. 59.)

b) Space-filling parameter (and curves)

The *space-filling parameter* introduced by LAVES [1956] and by PARTHE [1961] gives a means of studying the relationships between atomic dimensions and structure. For a compound, it is defined by the ratio between the volume of atoms in a unit cell and the volume of unit cell.

$$\varphi = \frac{(4\pi / 3)\left(\Sigma_i n_i R_i^3\right)}{V_{cell}} \tag{11}$$

(n_i, R_i number and radius of type i atoms).

References: p. 363.

To calculate the space filling value for a specific compound, one has to know the radii of the atoms and the lattice constant. Neither of these is needed for the construction of a *space filling curve* of a crystal *structure type*: it is sufficient to know the point positions of the atoms and the axial ratios. The curve is based on a *hard sphere model* of the atoms: the cell edges are expressed as functions of the atomic radii (R_X and R_Y for a binary system) for the special cases of X–X, X–Y and Y–Y contacts. The parameter can then be given (and plotted) as a function of the R_X/R_Y ratio.

Considering, for instance, the cF8–ZnS-sphalerite type structure (PARTHÉ [1964]) the space filling can be given by:

$$\phi = \left[4\pi/3\left(4R_X^3 + 4R_Y^3\right)\right]/a^3 \tag{12}$$

where a is the cubic cell edge and R_X and R_Y are the radii of the atoms in the a) and c) positions (4 Zn and 4 S, respectively) in the unit cell. (See the description of the structure in sec. 6.3.2.).

In the case that the two atoms (or, more accurately, the hard spheres) occupying the Zn and S sites are touching each other, then the sum of the two radii must be equal to one-quarter of the cubic cell diagonal.

$$R_X + R_Y = a\sqrt{3}/4 \tag{13}$$

By expressing the unit cell volume as a function of the sum of the radii we obtain:

$$\varphi = \frac{(4\pi/3)\left(4R_X^3 + 4R_Y^3\right)}{\left(4^3/3\sqrt{3}\right)\left(R_X + R_Y\right)^3} \tag{14}$$

Introducing the radius ratio $\varepsilon = R_X/R_Y$ one obtains:

$$\varphi = \left(\sqrt{3}\pi/4\right)\frac{\varepsilon^3 + 1}{(\varepsilon + 1)^3} \tag{15}$$

This equation describes the middle section ($0.225 < \varepsilon < 4.44$) of the space-filling curve for the sphalerite type structure plotted (with log scales) in fig. 51.

(The other sections, $0 < \varepsilon < 0.225$ and $4.44 < \varepsilon < \infty$ correspond to the cases in which Y–Y atoms or X–X atoms are touching.)

In the φ versus ε diagram every structure type is generally characterized by its own individually shaped *space-filling curve*. The space-filling curves, however, of all binary structures belonging to one *homeotect structure set* coincide with one curve (see sec. 4.3).

By assuming appropriate values for the radii R_X and R_Y it is possible to compare, with the specific curve of a given structure, the points representing actual compounds. Generally a good agreement is found for ionic structures (and/or compounds) while it is often observed that the φ versus ε points for particular metallic phases lie above the space-filling curves, indicating a denser packing and emphasizing the lack of unique radii associated with X–X, X–Y, etc. contacts (compressible atom model) (PEARSON [1972]).

In the specific case of unary structures (element structures), providing that there are no

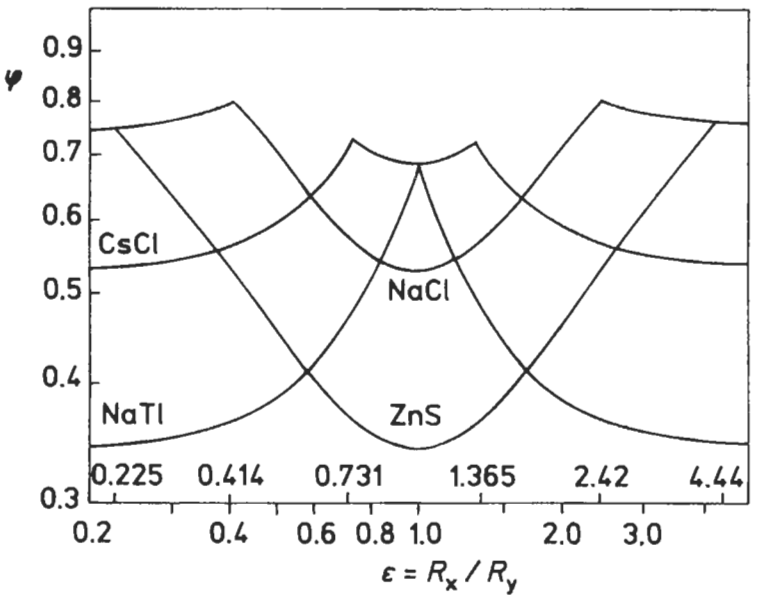

Fig. 51. Space filling diagram for the CsCl, NaCl and ZnS structures (from PARTHE [1961]).

variable atomic positional parameters or axial ratios, there is a unique space-filling parameter (independent of atomic size for every structure type). For the cF4–Cu type structure, for instance,

$$\varphi = (4\pi/3)(4R^3/a^3) \tag{16}$$

Assuming the atoms to be hard spheres $a = 2\sqrt{2}$ R, then $\varphi = 0.740$ (which is the highest value for an infinite collection of close-packed hard spheres of the same radius). Typical *space-filling parameters* of *elemental structures* are the following:

cF4–Cu type	0.740	
hP2–Mg type	0.740	(for the "ideal" value, c/a = 1.633.., of the axial ratio. It is $\varphi = 0.65$ in the case, for instance, of Zn, for which c/a = 1.86).
cI2–W type	0.680	
tI4–β-Sn type	0.535	
cP1–Po type	0.524	
cF8–Diamond	0.340	

Several other considerations and applications of the space filling concept may be found in PARTHE [1961], for instance: space-filling diagrams of ternary structures, applications of space-filling concept for discussing and predicting possible pressure structures, etc.

A similar treatment has been made by LIU and BASSETT [1986] defining a special "*volumetric index*" α, considering that the molar volume V of a crystal must be a linear function of the cube of the nearest neighbor interatomic distance d_{min}

References: p. 363.

$$V = \alpha d_{min}^3 \tag{17}$$

where α is a function of the axial ratio, axial angle(s) and positional parameters of a crystal structure.

Within a group of isostructural substances small variations are therefore generally observed in the α-value. If d_{min} is given in nm and V in cm^3/mol (moles of atoms or moles of formulae) the following α-values may be mentioned:

425.9 (cF4–Cu); 425.9 to 485.0 (hP2–Mg for $1.633 \leq c/a \leq 1.86$; 463.6 (cI2–W); 589.7 (tI4–βSn, $c/a = 0.5456$); 602.2 (cP1–Po); 927.2 (cF8–diamond); 927.1 (cP2–CsCl); 1204.4 (cF8–NaCl); $\approx$ 1843 (hP4–C graphite); etc.

The α-values are the slopes in the plots of the molar volume versus the cube of the interatomic distances for given types of structures such as those illustrated in fig. 52a. These indexes (as the space-filling parameters) may be useful, for instance, in a systematic description of the effect of pressure on the phase transformations which may be observed for a given compound. In a discussion of high-pressure phases (of elements, oxides and silicates) with implications for the Earth's interior, LIU and BASSETT [1986] presented data relevant to several families of compounds in a number of graphs such as those of fig. 52b. The transformations at increasing pressure from C graphite to diamond, from Si and Ge diamond type to βSn type, the modifications of a number of 1:1 compounds from NaCl to CsCl type structure and also for elements, such as Cd and Zn, the preservation of the same structure but with c/a approaching the "ideal" 1.633 value can all be effectively summarized in these type of graphs.

7.2.5. Reduced dimensional parameters

a) Reduced strain parameter and near-neighbours diagrams

By means of the comparison between the space-filling theoretical curves and the actual values of intermetallic phases it has been observed that an incompressible sphere model of the atom is unsuitable when discussing metallic structures.

PEARSON [1972] suggested the use of a model which allows the atoms of a binary X–Y alloy to be compressed until subsequently (and according to the structure geometry) X–X, X–Y, Y–Y contacts are established. The contacts are considered to occur when the X–X, X–Y and Y–Y interatomic distances in the compound structure, d_X, d_{XY} and d_Y are equal to 2 R_X ($=D_X$), $R_X + R_Y$ and 2 R_Y($=D_Y$) (R_X, R_Y, D_X, D_Y atomic radii and diameters, respectively). According to Pearson, the metallic radii choosen are those appropriate for the coordination of the atoms (compare with sec. 7.2.4.). The distances between all the close atoms in the structure may be expressed in terms of the cell (and atomic site) parameters. (As an example see, for instance, the phases XY_3, $AuCu_3$ type, described in sec. 3.5.5. and in figs. 12, 13, 14. In these phases around each X atom there are 6 X atoms at a distance equal to the unit cell edge $d_X = a$. Around the X atoms there are 12 Y atoms at a distance $d_{XY} = a\sqrt{2}/2$), and around the Y atoms at the same distance $d_Y = a\sqrt{2}/2$). All these distances may thence be expressed as a function of one of them, selected as a reference. (In the case of the $AuCu_3$ type phase, for instance:

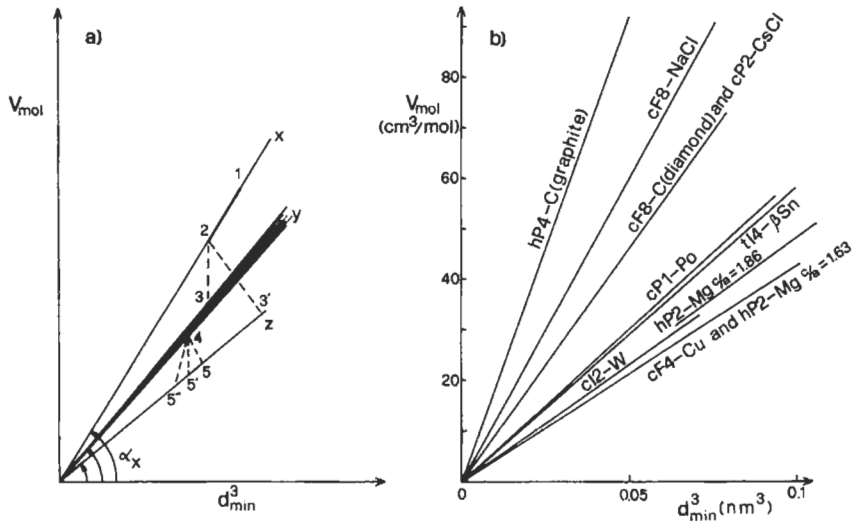

Fig. 52. Trends of the molar volumes of selected groups of phases as a function of the nearest neighbours interatomic distances.

a) Schematic trends for X, Y, Z, etc., structural types. (Y may represent a structure type for which, for instance, owing to different c/a ratios, several volume values may correspond to the same d_{min}). The hyphens 1 → 2, 2 → 3 (or 2 → 3'), etc. from 1 to 2 etc., represent different behaviours (and transformations) that may be observed by increasing pressure.

b) Actual trends for a group of common crystal structure types.

$$d_{XY} = d_X\sqrt{2}/2,\ d_Y = d_X\sqrt{2}/2 \tag{18}$$

A *reduced strain parameter* is then defined with reference to a arbitrarily selected set of contacts. With reference to the d_X distances the strain parameter may be defined as $S = (D_X - d_X)/D_Y$. This parameter gives an indication of the atomic dimension compression. It is computed, as a function of the ratio $\varepsilon = D_X/D_Y = R_X/R_Y$, for the different kinds of interatomic contacts.

In the aforementioned $AuCu_3$ type phases, we have 3 cases corresponding to X–X, X–Y and Y–Y contacts.

If X–X atoms are touching $d_X = D_X$, then the strain parameter S_{X-X} will be $(D_X - D_X)/D_Y = 0$ for all the ε-values.

If X–Y atoms are considered to be in contact $d_{XY} = d_X\sqrt{2}/2$ will be equal to $\frac{1}{2}(D_X + D_Y)$ so we will have:

$$S_{X-Y} = \frac{D_X}{D_Y} - \frac{d_X}{D_Y} = \frac{D_X}{D_Y} - \frac{d_{XY}\sqrt{2}}{D_Y} = \frac{D_X}{D_Y} - \frac{\frac{1}{2}\sqrt{2}D_X + \frac{1}{2}\sqrt{2}D_Y}{D_Y} \tag{19}$$

If, on the other hand, the Y–Y atoms are those which are considered to be in contact we will have:

References: p. 363.

$$d_Y = d_X\sqrt{2}/2 = D_Y; d_X = D_Y\sqrt{2} \text{ and} \tag{20a}$$

$$S_{Y-Y} = \frac{D_X}{D_Y} - \frac{\sqrt{2}D_Y}{D_Y} = \frac{D_X}{D_Y} - \sqrt{2} \tag{20b}$$

The values of the strain parameters are then plotted, according to PEARSON [1972], as a function of $\varepsilon = R_X/R_Y$. Several straight lines are obtained (see figs. 53, 54, 55) the lines corresponding to the reference contacts are horizontal and set at zero. What matters is only the *relative position* of the different straight lines (which does not change by taking another contact as the reference one: a rotation will only be obtained of the whole diagram). The diagram is called *Near-Neighbour Diagram*. In the diagram, points may also be plotted which represent actual phases. (To this end the experimental d_X, d_{XY}, etc., values will be used).

According to PEARSON [1972], when a point representing a specific phase has a larger value of the strain parameter than that of a particular contact line, then the contacts corresponding to that line are to be considered (on the basis of the D_X and D_Y assumed for the components) compressed. If, on the other hand, the experimental points lie below a line then those contacts have not been established.

Figs. 53 to 55 represent the data and the trend for a few structure types. For compounds having the cF8–ZnS sphalerite structure (see sec. 6.3.2.) it can be seen that the X–Y (Zn–S) bonds (corresponding to a tetrahedral coordination) are the most important in controlling the structural characteristics. The different points, representing actual compounds, are very close indeed, for a wide range of diameter ratio and of electronegativity differences to the line corresponding to the X–Y contacts. (The X–X and Y–Y contacts are not formed). The structure can, therefore, be considered as formed by a skeleton of presumably covalent (and directional in character) X–Y bonds. An X–Y chemical bond can similarly be recognized as important in several compounds having cF12–CaF_2 type (or antitype), cF16–Li_3Bi, hP3–CdI_2, hP8–Na_3As, etc., type structures. The different behaviours of more "metallic" phases can be seen in fig. 53 and fig. 55.

The $AuCu_3$ type near-neighbour diagram (fig. 53) shows the importance of contacts corresponding to high coordinations. A similar trend can be observed for the XY_2 Laves phases (see fig. 55 for the $MgCu_2$ type) for which, moreover, a certain compression of the X–X contacts generally results. (The X–X curve is, for $\varepsilon > 1.25$, far below the data points).

Many near-neighbour diagrams have been presented by PEARSON (1972) and systematically discussed for several structure types in order to show the importance of factors such as geometrical or chemical bond factors in controlling occurrence and structural characteristics of different phases.

For an analysis of the meaning and the applications of these diagrams see also SIMON [1983]. A representation, in generalized near neighbour diagrams, of structure families for alloy phases with given XY_n compositions has been presented and discussed.

b) Unit-cell dimension analysis

While discussing the interest in an analysis of the dimensional characteristics of phases with given structures and reconsidering advantages and limitations of the near-neighbour

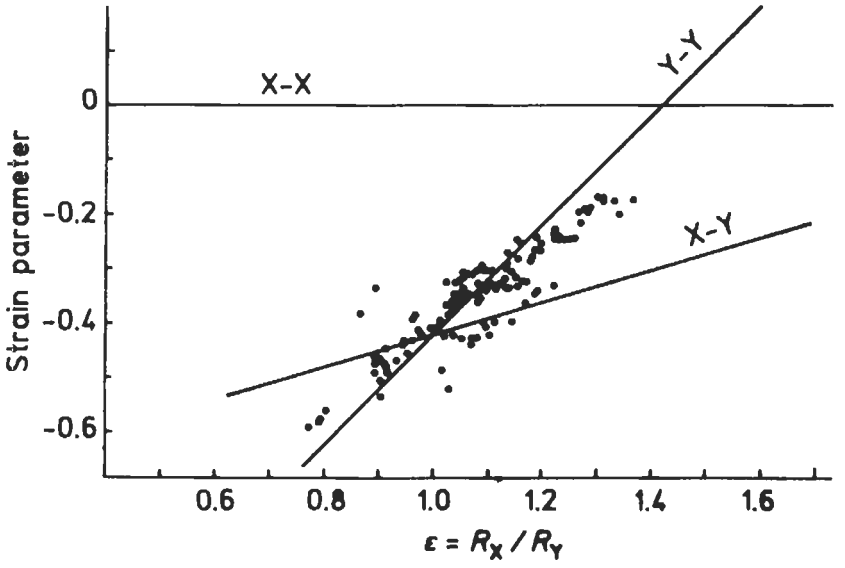

Fig. 53. Near neighbour diagram for binary phases with XY_3 formula belonging to the cP4–$AuCu_3$ structural type (according to PEARSON [1972]). The lines corresponding to the different contacts are shown.

diagrams, Pearson himself has proposed [1985a] a new analytical method based on plots as functions of the CN 12 atomic diameters determined from elemental structures and in which attention is paid to the group and period of the component elements in the selection of subsets of the data of phases to be considered together.

As an example of such an analysis we may consider the data reported in fig. 56. Phases are considered which pertain to the tI10–$ThCr_2Si_2$ type; the structure contains three different position sets, as described in sec. 6.5.9. It is one of the most populous of the different structure types. In particular, there are ten almost complete groups of data for RET_2X_2 phases given by rare earth metals (RE) with T = Mn, Fe, Co, Ni, Cu and X = Si or Ge. The data reported in fig. 56 are those concerning the $RENi_2Ge_2$ compounds. According to PEARSON [1985a] and PEARSON and VILLARS [1984] the contacts of interest between pairs (i,j) of the three components (RE, T, X) are defined by the relation:

$$\Delta_{ij} = \tfrac{1}{2}\left(D_i + D_j\right) - d_{ij} \tag{21}$$

where D_i, D_j are the atomic diameters and d_{ij} is the interatomic distance between i and j atoms (obtained from the experimental structure data). Generally it has been observed (see fig. 56) that Δ_{ij} varies linearly with D_{RE} (for series with different RE but the same T and X components).

A parameter f_{ij} may thus be defined by:

$$\Delta_{ij} = f_{ij} D_{RE} + k_{ij} \tag{22}$$

If a specific f_{ij} is of the order of zero (see, for instance, $\Delta_{RE\text{–}Ge}$ in fig. 56) this can be

References: p. 363.

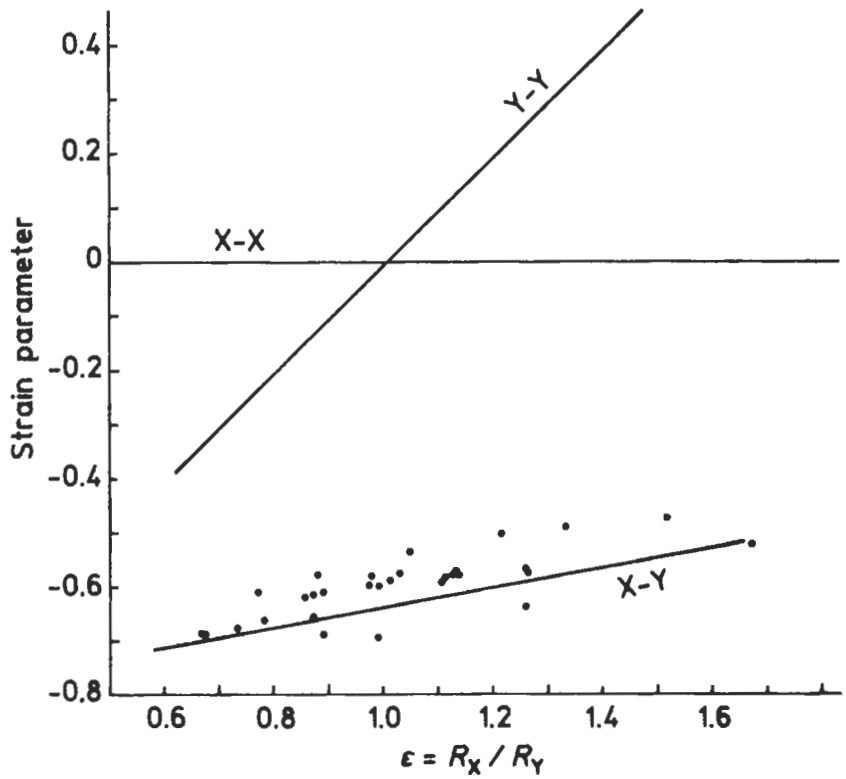

Fig. 54. Near neighbour diagram for binary phases with XY formula belonging to the cF8–ZnS structural type (according to PEARSON [1972]).

considered an indication that the particular ij contact is independent of change in D_{RE} and therefore it can be assumed to control the cell dimensions (as the size of RE changes in the series of phases having the same T and X components). For the different RET_2X_2 phases it was observed that $f_{RE-X} \approx 0$ for T = Fe, Co, Ni, Cu and X = Si, Ge, whereas $f_{RE-T} \approx 0$ for T = Mn.

Structural aspects of chemical bonding in another family of phases formed by similar groups, RE–T–X, of elements (1:1:1, RETX compounds) have been analysed by BAZELA [1987] using the same technique.

For a general discussion on the dimensional analysis of the structures of the metallic phases with special reference to the hR57–Th_2Zn_{17}, tI26–$ThMn_{12}$ and hP6–$CaCu_5$ type structures see also PEARSON [1980].

7.2.6. Alternative definitions of coordination numbers

We have seen in the previous sections that the determination of the coordination number of an atom in a structure is clearly recognized as an important point in the

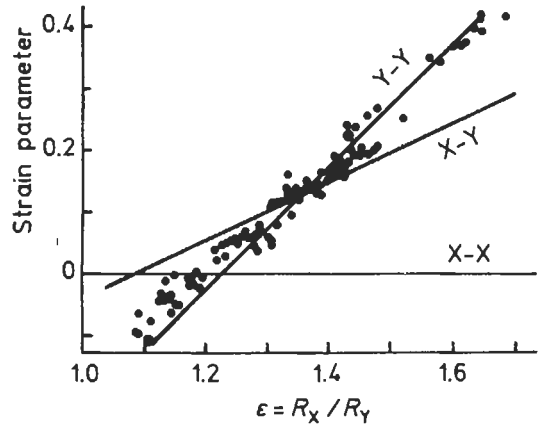

Fig. 55. Near neighbour diagram for binary phases with XY_2 formula belonging to the cF24–$MgCu_2$ structural type (according to PEARSON [1972]).

definition of that atom's contribution to the bulk material properties and in the characterization of the structure itself. Several properties (for instance, atomic size, atomic valence and magnetic properties and species stability and reactivity) are know to be coordination number dependent.

In many cases the coordination number (or ligancy) of a central atom is readily obtained by enumerating the number of neighbours; we have seen, however, that there are numerous cases where the criteria for the enumeration procedure may be ambiguous. As an introductory summary of this point see, for instance, CARTER [1978], O'KEEFFE [1979]).

As already pointed out by FRANK and KASPER [1958] the term "*coordination number*" *has been used in two ways* in crystallography. According to the first (more precisely defined, in principle) the coordination number, (CN), is the *number of the nearest neighbours* to an atom. According to this definition in the hexagonal close-packed hP2–Mg type structure CN is 6 unless the axial ratio c/a has exactly the "ideal" value $\sqrt{\frac{8}{3}}$ ($= 1.63299..$), in which case it is 12. (see fig. 26). In this structure the mentioned definition is seldom applied with rigour, that is, the CN in the hP2–Mg type structure is generally regarded as 12, even with c/a slightly different from the "ideal" value; that is not only the first group but also the very close second group of distances are considered together. More difficulties arise in less symmetrical structures and when there is a high coordination number. Near neighbours with slightly different interatomic distances are often found and it may be difficult to determine (and to state in an unambiguous way) how many should be considered as coordinating the central atom. Several schemes for the calculation of an "*effective*" *coordination* have been proposed.

According to FRANK and KASPER [1958] the computation of the coordination number may be based on the definition of the "*domain*" *of an atom* in a structure. This is the space in which all points are nearer to the centre of that atom than to any other. It is a polyhedron, (Voronoi polyhedron, Voronoi cell, Wigner–Seitz cell), each face of which

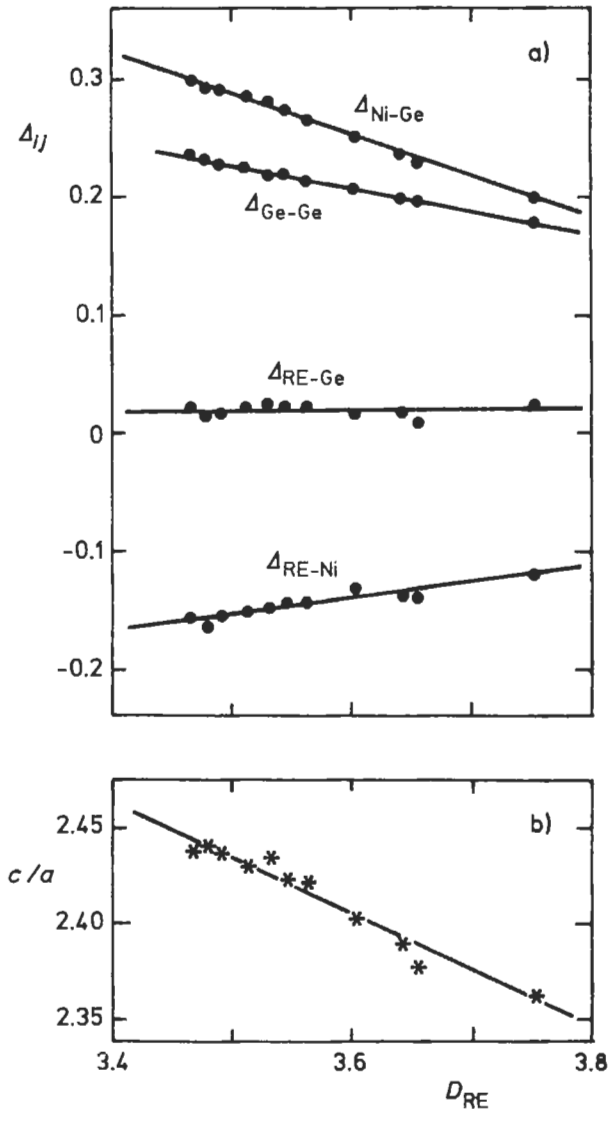

Fig. 56. $RENi_2Ge_2$ phases (RE=rare earth) with the tI10–$ThCr_2Si_2$ structure (from PEARSON [1985a]).
a) plot of Δ_{ij} ($= \frac{1}{2}(D_i + D_j) - d_{ij}$) versus D_{RE}.
b) plot of the c/a axial ratio of the cell versus D_{RE}.

is the plane equidistant between that atom and a neighbour. (Every atom whose domain has a face in common with the domain of the central atom is, by the Frank–Kasper definition, one of its neighbours). The counting of the faces of the *domain polyhedron* gives the number of neighbours: the set of neighbours is the "coordination shell". (The

coordination polyhedron, of course, is the polyhedron whose edges are the lines joining all the atoms in the coordination shell. The domain (Voronoi) polyhedron and the *coordination polyhedron*, therefore, stand in dual relationship, each having a vertex corresponding to each face of the other).

According to the Frank–Kasper definition the coordination number is unambiguously 12 in the hexagonal close-packed metals and assumes the value 14 in a body-centered cubic metal. Generally in several complex metallic structures this definition yields reasonable values such as 14, even when the nearest neighbour definition would give 1 or 2.

According, for instance, to O'Keeffe, however, this definition may lead to some difficulties (the value 14 for the bcc structure, higher than that of closest packing does not seem entirely reasonable, the difficulty becomes more acute in a structure as that of diamond for which a very high value, 16, is computed according to the mentioned definition).

For a better *quantification of the coordination number*, several alternative schemes have been proposed. For example, a simple procedure is based on the identification of a gap in the list of interatomic distances (and to add atoms up to this gap). A similar procedure (O'KEEFFE [1979]) may be to add atoms to the coordination polyhedron in order of increasing interatomic distances and to stop when the next addition would result in a non-convex polyhedron. BRUNNER and SCHWARZENBACH [1971] suggested *cutting off the coordinating atoms* at the *largest gap in the list of the interatomic distances* (see also sec. 7.2.7). According to BRUNNER [1977] the largest gap in the list of reciprocal interatomic distances is used to limit the coordination polyhedra. It has also been suggested to weight the contribution of the atoms according a weight that decreases with interatomic distances (BHANDARY and GIRGIS [1977]) or according to a bond strenghts of the Pauling type (BROWN and SHANNON [1973]). Non integral coordination numbers may of course be obtained.

In relation with the Frank–Kasper proposal, previously reported, O'KEEFFE [1979] suggested that coordinating atoms contribute faces to the Voronoi polyhedron around the central atom and their contributions are weighted in proportion to the solid angle subtended by that face at the center.

By using this definition increasing values of the (weighted) CN coordination number are obtained for the structures: diamond (4.54), simple cubic (6), body-centered cubic (10.16), face-centered cubic (12) (in agreement with the increasing packing density).

A more complex weighting scheme has been suggested by CARTER [1978] on the basis of the following assumptions:

The interactions of a central atom with its i^{th} neighbour is considered as being measured by a certain parameter A_i ($\Sigma A_i = A_{tot}$, finite).
The CN as a function of all the A_i should satisfy the following conditions:
— $CN(A_i)$ is dimensionless and ≥ 1 if any neighbours with non-zero A_i exists;
— $CN(A_i)$ is a continuous function of the A_i (its slope may not be);
— if N interactions exist such that $A_1 = A_2 = ... = A_N$, for all neighbours with non-zero A_i, then $CN(A_i) = N$;

References: p. 363.

— if some of the A_i are unequal, then $CN(A_i) < N$;
— if m of the A_i are equal and large and N-m equal are small, then $m < CN(A_i) < N$.

The formula proposed by Carter for the quantification is:

$$1 / CN = \Sigma_1^N \left(w_i A_i / \Sigma w_j A_j \right)^2 \tag{23}$$

(where w_i are finite weighting factors). Definitions and measures of A_i might include bond strenghts, bond energies, bond orders, etc.).

As an example, the structure of the CsCl type has been discussed by Carter using several criteria of evaluation of A_i. In a geometrical approach a weighted coordination number (varying from 8 to 14 to 6) as a function of atomic radii difference was described.

We may finally mention the so-called "effective coordination number" ECoN, proposed by HOPPE [1979] and HOPPE and MEYER [1980] computed by means of a rapidly converging function of the distances. According to Hoppe's scheme (which may be related to Brunner's suggestions previously mentioned), individual contributions $ECoN_j$, of all neighbours to the coordination number are summed together. Each contribution $ECoN_j$ quickly becomes vanishingly small with increasing atomic distances d_j according to an expression such as $ECoN_j = \exp(1-(d_j/d_m)^6)$, where d_m is a reference distance (the "mean fictive" atomic size) which has to be determined beforehand from the structure. The trend of the ECoN has, for instance, been discussed as a function of the axial ratio c/a for the hexagonal closest packing of spheres (hP2–Mg structure). Values of ECoN ranging from say 11.94 (for $c/a \approx 1.57$ as Ho or Er) to 12.02 (for the "ideal" c/a value, 1.633..,) and to 11.02 ($c/a = 1.856$, as for Zn) or to 10.74 ($c/a = 1.886$, as for Cd) have been computed. ECoN for different Laves phases have been presented. For a number of NaCl and CsCl type compounds, moreover, values have been given to show the dependence of ECoN as a function of varying ionic radii.

(For a discussion on the "effective coordination number" its relation with atomic size, bond-strength, Madelung constant, etc., see also SIMON [1983]. For a computation of the heats of formation based on the so-called effective coordination see a suggestion by KUBASCHEWSKI [1958], and for a discussion on the application and limits of this suggestion see BORZONE *et al.* [1993].).

7.2.7. Atomic-environment classification of the structure types

DAAMS *et al.* [1992] and DAAMS and VILLARS [1993, 1994] in a series of reviews have given an important contribution to the problem of the classification of intermetallic structural types, reporting a complete description of the *geometrical atomic environments* found in the structural types of cubic, rhombohedral and hexagonal intermetallic compounds, respectively. To *define* an *atomic environment* they used the maximum gap rule (see sec. 7.2.6.). The Brunner–Schwarzenbach method was considered, in which all interatomic distances between an atom and its neighbours are plotted in a histogram such as those shown in figs. 15, 23, 25, etc.. (The height of the bars is proportional to the number of neighbours, and all distances are expressed as reduced values relative to the shortest distance). In most cases a clear maximum gap is revealed (see, for instance, in

fig. 23 the gap between the second and the third bar). The atomic environment is then constructed with the atoms to the left of this gap (8+6 in the example of fig. 23). To avoid, in some particular cases, bad or ambiguous descriptions, however, a few additional rules have been considered. In those cases, for instances, where two (or more) nearly equal maximum gaps were observed, a selection was made in order to keep, in a given structure type, the number of different atomic environment types as small as possible. A convexity criterion for the environment polyhedron was also considered (the coordination polyhedron has to be defined as the maximum convex volume around only one central atom enclosed by convex faces with all coordinating atoms lying at the intersections of at least three faces). This rule was specially used where no clear maximum gap was detectable.

The different atomic environment types were characterized by a polyhedron code based on the number of triangles, squares, pentagons, hexagons, etc. that join each other in the different vertices (coordinating atoms). The *polyhedron code* gives the number of equivalent vertices with the number of faces in the above-mentioned sequence as an exponent. For example, a quadratic pyramid has four corners adjoining two triangles and one square (no pentagons or hexagons) and one corner adjoining four triangles: its code, therefore, is $4^{2.1.0.0}1^{4.0.0.0}$ (or briefly $4^{2.1}1^{4.0}$ with coordination number 5). The cube, 8 equivalent vertices, adjoining 3 squares, has the code $8^{0.3}$, the octahedron $6^{4.0}$ and the Frank–Kasper polyhedra have the codes $12^{5.0}$; $12^{5.0}2^{6.0}$; $12^{5.0}3^{6.0}$ and $12^{5.0}4^{6.0}$ (see sec. 6.6. and fig. 41).

DAAMS *et al.* [1992] have analysed all the *cubic structure types* reported in VILLARS and CALVERT [1985], after excluding all oxides and a few types with improbable interatomic distances, thus leaving 128 structure types representing 5521 compounds. Their analysis showed that these cubic structure types have 13917 atomic-environments (point sets). Of those environments 92% belong to one of the 21 most frequently occurring atomic-environment types, which are those reported in the following list:

$4^{3.0}$ (tetrahedron) – $4^{2.1}1^{4.0}$ – $6^{4.0}$ (octahedron) – $3^{5.0}3^{4.0}1^{3.0}$ – $8^{0.3}$ – $6^{5.0}3^{4.0}$ – $8^{5.0}2^{4.0}$ – $6^{6.0}4^{3.0}$ – $9^{2.2}2^{0.3}$ – $8^{5.0}2^{4.0}1^{6.0}$ – $12^{5.0}$ (icosahedron) – $12^{2.2}$ (cp. cubic) and $12^{2.2}$ (cp. hexagonal) (the same code describes the cubic as well as the hexagonal atomic environment of the ideal close-packing) – $10^{2.2}2^{5.0}$ – $10^{5.0}2^{6.0}1^{4.0}$ – $11^{2.2}2^{4.1}$ – $12^{5.0}2^{6.0}$ – $8^{0.3}6^{0.4}$ – $12^{5.0}3^{6.0}$ – $12^{5.0}4^{6.0}$ – $12^{6.0}6^{4.0}$.

Of the 5521 compounds crystallizing in the mentioned 128 structure types, 46% belong to a single-environment group (structures in which all atoms have the same type of environment), 37% have two environment types, 9% three and the rest four or more environments. (≈ 98% of the cubic compounds crystallize in structure types with 1, 2, 3 or 4 atomic environment types).

In a subsequent paper (DAAMS and VILLARS [1993]) the results of a similar classification of the rhombohedral intermetallic structure types were reported. The 195 *rhombohedral structure types* reported in VILLARS and CALVERT [1991] were analysed. 51 types have improbable interatomic distances or correspond to oxides with no intermetallic representatives and were excluded. The remaining 144 types (corresponding to 1324 compounds) were considered. It was observed that 14 atomic environment types are greatly preferred. Out of 6356 investigated point sets 71% belong to one of these 14 frequent atomic environment types which are those reported in the following list:

References: p. 363.

3 (loose triangle); $4^{3.0}$; $6^{4.0}$; $6^{1.2}$ (trigonal prism) $8^{0.3}$; $6^{5.0}3^{4.0}$; $6^{4.0}4^{3.0}$; $9^{2.2}2^{0.3}$; $12^{5.0}$; $12^{2.2}$ (cubic type); $10^{5.0}2^{6.0}1^{4.0}$; $12^{5.0}2^{6.0}$; $8^{0.3}6^{0.4}$; $12^{5.0}4^{6.0}$. (Compare this list with the previous one of the cubic compounds: notice that several atomic environment types are reported in both lists.)

Of the 1324 rhombohedral compounds crystallizing in one of the 144 types, 19% belong to a single-environment group, 15% combine two environment types, 25% three environments; 34% four and the rest , 7%, five or more environments ($\approx$ 94% of the rhombohedral compounds crystallize in structure types with 1, 2, 3 or 4 environment types).

The results of a similar analysis of the intermetallic *hexagonal structure types* have been reported by DAAMS and VILLARS [1994]. Of 442 structure types 315 (clearly intermetallic and correctly refined) were considered. In this case too it was observed that a small group of atomic environments is greatly preferred. The 23 atomic environment types most frequently occurring in the 315 hexagonal structure types are reported in the following list (to be compared with those previously reported for cubic and rhombohedral structure types):

3; $4^{3.0}$; 4; $6^{4.0}$; $6^{1.2}$; $3^{5.0}3^{4.0}1^{3.0}$; $8^{0.3}$; $6^{5.0}3^{4.0}$; $6^{4.0}4^{3.0}$; $6^{5.0}3^{4.0}1^{6.0}$; $9^{2.2}2^{0.3}$; $8^{5.0}2^{4.0}1^{5.0}$; $12^{5.0}$; $12^{2.2}$ (cubic); $12^{2.2}$ (hexagonal); $10^{5.0}2^{6.0}1^{4.0}$; $6^{4.1}3^{3.0}3^{2.2}1^{9.0}$; $12^{5.0}2^{6.0}$; $12^{2.2}2^{6.0}$; $6^{5.0}6^{3.0}2^{9.0}$; $12^{5.0}3^{6.0}$; $12^{5.0}4^{6.0}$; $12^{5.0}8^{6.0}$. (The 3 and 4 codes correspond to "irregular" atomic environment types. The reference atom is not included in the plane (volume) of the polygon (polyhedron) formed by the 3 (4) coordinating atoms.)

Out of 20131 poit sets investigated (belonging to 5646 compounds crystallizing in one of the aforementioned 315 hexagonal structure types), 81% (16392) belong to one of these 23 atomic environment types. Of the 5646 compounds, 14% belong to a single environment group; 35% combine two environment types; 32% three; 11% four and the rest (7%) five or more (93% of the hexagonal compounds crystallize in structure types with 1, 2, 3 or 4 atomic environment types).

As a result of these analysis several relations between structure types have been shown and discussed. Emphasis has been given to the fact that, in all the structure types considered (cubic, rhombohedral, hexagonal) it may be observed that: "Nature prefers one of the most symmetrical atomic environment types. Remarkably these atomic environment types (21 in the cubic structures, 14 in the rhombohedral and 23 in the hexagonal ones) are equally often found in single-environment up to poly-environment groups meaning that even in complex structures, symmetrical arrangements are preferred". The formation of the geometrically most simplest structure types containing a small number of different atomic environment types was also noticed.

As a comment, we may observe that the results of these analyses can be compared with the *"Stability Principles" stated by Laves* (see sec. 7.2.3.).

In conclusion to this section we may mention a paper by VILLARS and DAAMS [1993] concerning an atomic environment classification of the chemical elements. Critically evaluated crystallographic data for all element modifications (and recommended atomic volumes) have been reported. Special structural stability diagrams were used to separate atomic environment type stability domains and to predict the structure (in terms of

environment types) of hitherto unknown high pressure and high temperature modifications (see sec. 8.4.).

8. *Semi-empirical approaches to the prediction of (intermetallic) compound formation*

8.1. General remarks on procedures of prediction of compound and structure formation in alloy systems

In the previous sections a brief sampling of some correlations has been given which relate crystallochemical characteristics of the phase to the properties of the component elements. This group of correlations may be considered as a first reference point for a number of methods of predicting the formation, in a given system, of a compound and/or of a certain structure. It is well known that, in scientific literature, more and more space is dedicated to the question of the forecast of chemical equilibria in simple and complex systems. A clear indication of this interest, both from a general and a technological point of view, may be seen in the development and success of a number of monographs and periodic publications and proceedings on this subject. Several approaches to this problem have been considered: we may mention, with special attention to metal systems, the explicit over-all summary already presented by KAUFMAN *et al.* (see KAUFMAN and BERNSTEIN [1970]) and the more recent discussion by MASSALSKI [1989].

The role of a thermodynamic approach is well known: a thermodynamic control, optimization and prediction of the phase diagram may be carried out by using methods such as those envisaged by KUBASCHEWSKI and EVANS [1958], described by KAUFMAN and NESOR [1973], ANSARA *et al.* [1978], HILLERT [1981] and very successfully implemented by LUKAS *et al.* [1977, 1982], SUNDMAN *et al.* [1985]. The integration of phase diagram calculations into the design of multicomponent alloys, and performance prediction, has been discussed by MIODOWNIK [1993]. The knowledge (or the prediction) of the intermediate phases which are formed in a certain alloy system may be considered as a preliminary step in the more general, and complex, problem of assessment and prediction of all the features of phase equilibria and phase diagrams. (See also ALDINGER and SEIFERT [1993]).

Evidence has to be given to the phase stability problem (MASSALSKI [1989]). The significant progress and the limits, of the first principles calculations may be mentioned (HAFNER [1989], PETTIFOR, chapter 2), the usefulness, however, of a number of semiempirical approaches has to be pointed out. Several schemes and criteria have been suggested to forecast and/or optimize the data concerning certain properties. In the following a short outline will be reported on some prediction methods based on selected correlations between elemental properties and structure formation.

8.2. Stability diagrams, structure maps

Several authors have tried to classify and order the numerous data concerning the different intermetallic substances by using two (or three) dimensional structure maps (*stability, existence diagrams*).

References: p. 363.

These maps were prepared by selecting coordinates based on those parameters (generally properties of the component elements) which were considered to be determinant factors of the structural stability and phase formation control.

As an introductory example to this subject we may remember the well known diagrams developed by DARKEN and GURRY [1953] for *solid solution prediction*. In such diagrams (as shown in fig. 57) all elements may be included. The two coordinates represent the atomic size (generally the radius corresponding to CN 12) and the electronegativity of the elements. It is well known that the first table of electronegativity values was introduced by PAULING [1932]. Several alternative definitions have since been proposed. A reliable compilation extensively used in discussing the metallurgical behaviour is that by TEATUM *et al.* [1968]. References to other scales will be reported later.

To determine the solid solubility of the different elements in a given metal, in the Darken and Gurry map, the region with the selected metal (Mg, for instance, in fig. 57) in the center can be considered. Generally we observe that elements which have high solubility lie inside a small region around the selected metal. As a rule of thumb an ellipse may be drawn in the diagram (with the selected metal in the center), for instance, with ± 0.3 electronegativity unity difference in one axis and $\pm 15\%$ atomic radius difference on the other axis. For those elements for which there is a low (or a negligible) solubility a larger region has to be considered.

For a review of the application of the Darken and Gurry method to predict solid solubilities see GSCHNEIDNER [1980]. An improvement of the method by means of simultaneous use of rules based on the electronic and crystal structures of the metals involved, is also presented.

The diagrams reported in figs. 50 and 58 are examples of other structure stability maps which have been suggested and successfully used in order to obtain a good separation (classification) of typical alloying behaviours (compound formation, crystallization in a certain structure type, etc.).

As an outline of more general approaches along these lines we may mention a selection of a few methods proposed by several researchers.

8.3. Savitskii–Gribulya–Kiselyova method (cybernetic computer-learning prediction system)

Cybernetic computer-learning methods have been proposed by SAVITSKII *et al.* [1980] for predicting the existence of intermetallic phases with a given structure and/or with certain properties. The computer learning, in this case, is a process of collecting experimental evidence on the presence (or absence) of a property of interest in various physicochemical systems (defined by means of a convenient selection of the properties of the components).

As a result of machine learning a model is produced of characteristic exhibition of a property (for instance, the formation of a particular type of chemical compound) which corresponds to a distribution "pattern" of this property in the multidimensional representative space of the properties of the elements. The subsequent pattern recognition corresponds to a criterium for the classification of the known compounds and for the

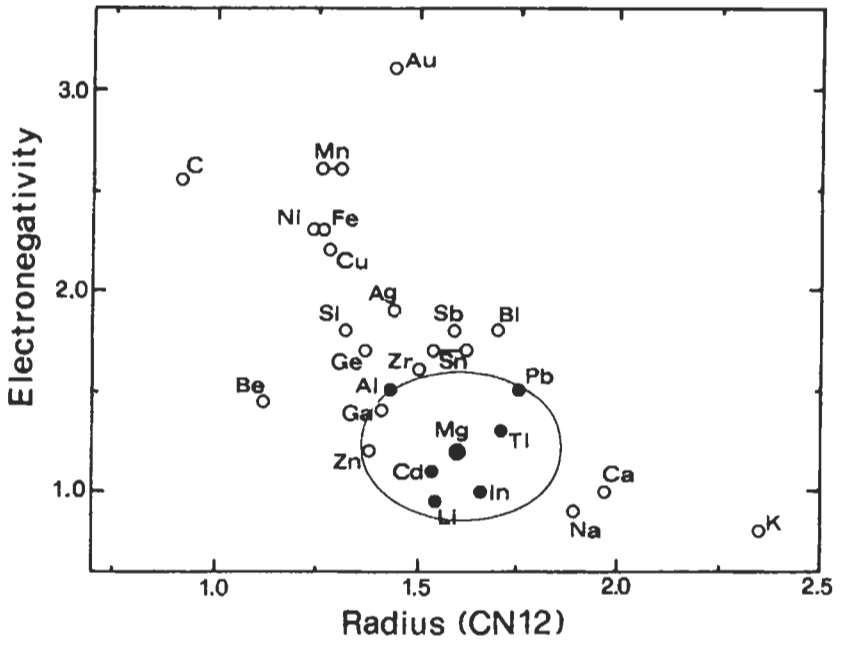

Fig. 57. Darken and Gurry diagram for the element Mg. (Solubility in Mg greater (•) or less (◦) than 5 atom % is indicated.)

prediction of those still unknown.

Examples of this approach reported by Savitskii are the prediction of the formation of Laves phases, of $CaCu_5$ type phases, of compounds XY_2Z_4 (X, Y any of the elements, Z = O, S, Se, Te), etc. (Data on the electronic structures of the components were selected as input).

The main principles and applications for the cybernetic prediction of inorganic substances which would have pre-defined properties have been summarized and discusssed by KISELYOVA [1993].

8.4. Villars, Villars and Girgis approaches (analysis of the dependence of the behaviour of alloy systems on the properties of the component elements)

In an examination of the binary structure types (containing more than five representatives, VILLARS and GIRGIS [1982] observed that 85% exihibited the following regularities:

a) linear dependence of interatomic distances on concentration weighted radii;
b) narrow ranges of the space-filling parameter and of the unit cell edge ratio c/a (and b/a) for the representatives of a given structure types;
c) dependence between the position of the elements in the Periodic Table (in the s, p, d, f blocks) and their equipoint occupation in the structure;

References: p. 363.

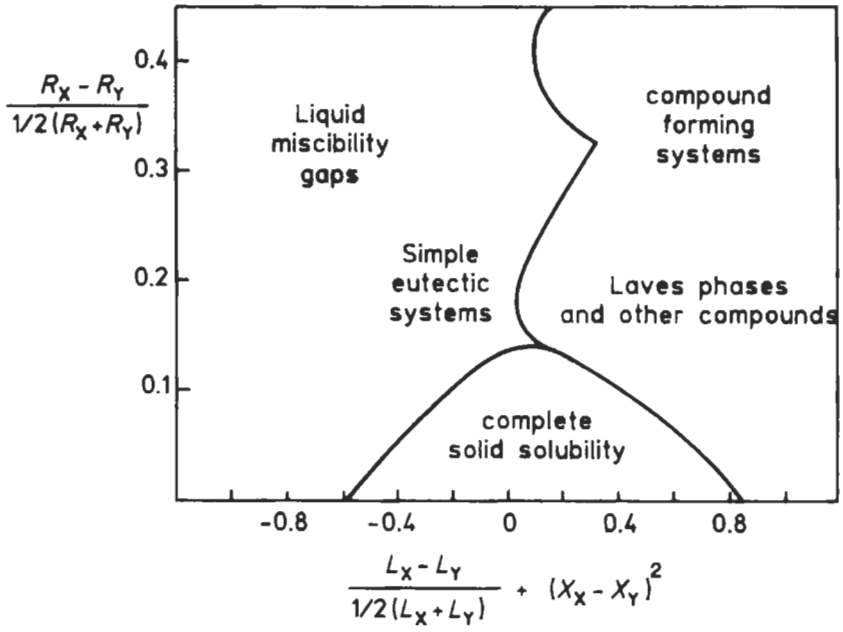

Fig. 58. Kubaschewski's plot of the regions of preference for formation of certain type of binary equilibrium diagrams (R_i, L_i and X_i are atomic radius, heat of sublimation and electronegativity of element i).

d) narrow grouping of the phases pertaining to a given structure type, in isostoichiometric diagrams based on the positions of the components in the Periodic Table.

These relationships have been used to predict the existence and/or the structure type (and the unit cell characteristics) of binary intermetallic compounds.

By using a systematic procedure to find the relevant element properties representing the alloying behaviour of binary systems VILLARS [1983, 1985] defined three expressions for atomic properties which enable systems that form compounds to be separated from those that do not.

A systematic elimination procedure was also used by VILLARS [1982] to find atomic property expressions which could be used to distinguish the crystal structures of intermetallic compounds. 182 sets of tabulated physical properties and calculated atomic properties were considered. These were combined, for binary phases, according to the modulus sums, differences and ratios. The best separations were obtained by using three-dimensional maps, which, for a binary A_xB_y, $x<y$ compound, were based on the following variables (VILLARS and HULLIGER [1987], VILLARS *et al.* [1989]):

ΣVE, averaged sum of the valence electrons of the elements A and B, defined by

$$\Sigma VE = \left(x\,VE_A + y\,VE_B\right)/\left(x + y\right), \tag{24}$$

ΔX, electronegativity difference, according to the MARTYNOV–BATSANOV [1980] scale defined by

$$\Delta X = \left[2x / (x + y)\right](X_A - X_B) \tag{25}$$

$\Delta (r_s + r_p)_Z$, difference of Zunger's pseudo-potential radii sum (ZUNGER [1981]), defined by

$$\Delta\left(r_s + r_p\right)_Z = \left[2x / (x + y)\right]\left[\left(r_s + r_p\right)_{Z,A} - \left(r_s + r_p\right)_{Z,B}\right] \tag{26}$$

The relevant data concerning the different elements have been reported in table 9 (from VILLARS [1983]).

Several structural types, corresponding to about 5500 binary compounds and alloys, were considered. 147 structure types were classified as 97 coordination types. The applications of these maps (which, in the most favorable cases, make it possible to predict not only the coordination number and polyhedron but also the structure type or a limited number of possibilities) were discussed. The possible extension to ternary and quaternary phases was also considered.

As an example of an investigation of a selected group of ternary alloys we may mention a paper by HOVESTREYDT [1988]. In analogy with the work of Villars a three-dimensional structure stability diagram was constructed. For the equiatomic RETX compounds formed by the rare earth metal (RE) with transition metal (T) and Ga, Si or Ge (X) the variables considered were: the difference in atomic radii $r_X - r_{RE}$, the Martynov–Batsanov electronegativity of the T metal and the expression $G_T + G_X + P_X$, related to the position in the Periodic Table of the T and X elements, where G is the group and P the period number. A good separation was obtained for the 8 structural types considered (corresponding to 202 compounds).

Special, modified, structure stability diagrams have been used for the elements by VILLARS and DAAMS [1993]. Maps were built by using the variables valence electron number and Zunger pseudopotential radius and reporting the atomic environment types (see sec. 7.2.7) found in the element structures. A simple separation into different stability domains was observed. By including the high temperature, high pressure crystal structure data, a prediction was made of the atomic environment modifications, hitherto unknown for several elements, to be found under high pressure, high temperature conditions. (See sec. 7.2.7.).

An empirical relation between band gap and Zunger's orbital electronegativity in sp-bonded compounds has been determined by MAKINO [1994a] using a formula derived from the bond orbital model. Based on the bond orbital model and Zunger's orbital electronegativity, new structural maps of AB, AB_2 and AB_3 compounds between transition metals have been successfully constructed (MAKINO [1994b]).

8.5. Miedema's theory and structural information

The model for energy effects in alloys suggested by Miedema and coworkers is well known. By assigning two coordinates (Φ and n_{WS}) to each transition element it was possible to separate all those binary alloys with positive heats of formation from those with negative values (MIEDEMA [1973]).

Successive steps in the formulation of the model have been described, for instance,

Table 9
Valence Electron Number (VE), Martynov–Batsanov electronegativity (X_{MB}) and Zunger's pseudo potential sum R_Z (from VILLARS [1983]).

H 1																
2.10																
1.25																
Li 1	Be 2					El	VE					B 3	C 4	N 5	O 6	F 7
0.90	1.45						X_{MB}					1.90	2.37	2.85	3.32	3.78
1.61	1.08						R_Z					0.795	0.64	0.54	0.465	0.405
Na 1	Mg 2											Al 3	Si 4	P 5	S 6	Cl 7
0.89	1.31											1.64	1.98	2.32	2.65	2.98
2.65	2.03											1.675	1.42	1.24	1.10	1.01
K 1	Ca 2	Sc 3	Ti 4	V 5	Cr 6	Mn 7	Fe 8	Co 9	Ni 10	Cu 11	Zn 12	Ga 3	Ge 4	As 5	Se 6	Br 7
0.80	1.17	1.50	1.86	2.22	2.00	2.04	1.67	1.72	1.76	1.08	1.44	1.70	1.99	2.27	2.54	2.83
3.69	3.00	2.75	2.58	2.43	2.44	2.22	2.11	2.02	2.18	2.04	1.88	1.695	1.56	1.415	1.285	1.20
Rb 1	Sr 2	Y 3	Zr 4	Nb 5	Mo 6	Tc 7	Ru 8	Rh 9	Pd 10	Ag 11	Cd 12	In 3	Sn 4	Sb 5	Te 6	I 7
0.80	1.13	1.41	1.70	2.03	1.94	2.18	1.97	1.99	2.08	1.07	1.40	1.63	1.88	2.14	2.38	2.76
4.10	3.21	2.94	2.825	2.76	2.72	2.65	2.605	2.52	2.45	2.375	2.215	2.05	1.88	1.765	1.67	1.585
Cs 1	Ba 2	La 3	Hf 4	Ta 5	W 6	Re 7	Os 8	Ir 9	Pt 10	Au 11	Hg 12	Tl 3	Pb 4	Bi 5	Po 6	At 7
0.77	1.08	1.35	1.73	1.94	1.79	2.06	1.85	1.87	1.91	1.19	1.49	1.69	1.92	2.14	2.40	2.64
4.31	3.402	3.08	2.91	2.79	2.735	2.68	2.65	2.628	2.70	2.66	2.41	2.235	2.09	1.997	1.90	1.83
Fr 1	Ra 2	Ac 3														
0.70	0.90	1.10														
4.37	3.53	3.12														
		Ce 3	Pr 3	Nd 3	Pm 3	Sm 3	Eu 3	Gd 3	Tb 3	Dy 3	Ho 3	Er 3	Tm 3	Yb 3	Lu 3	
		1.1	1.1	1.2	1.15	1.2	1.15	1.1	1.2	1.15	1.2	1.2	1.2	1.1	1.2	
		4.50	4.48	3.99	3.99	4.14	3.94	3.91	3.89	3.67	3.65	3.63	3.60	3.59	3.37	
		Th 3	Pa 3	U 3	Np 3	Pu 3	Am 3									
		1.3	1.5	1.7	1.3	1.3	1.3									
		4.98	4.96	4.72	4.93	4.91	4.89									

For a few elements, such as the rare earths, the Martynov–Batsanov electronegativity was not available, Pauling values were reported.

by NIESSEN *et al.* [1983] and by DE BOER *et al.* [1988].

The enthalpy of formation of solid and liquid binary alloys was described as proportional to the expression:

$$f\left[-P\left(\Delta\Phi^*\right)^2 + Q\left(\Delta n_{WS}^{1/3}\right)^2 - R\right] \tag{27}$$

where f is a concentration (and molar volumes) dependent function, $\Delta\Phi^* = \Phi_A^* - \Phi_B^*$ where $\Phi i*$ is the work function of each element, closely related to its electronegativity, (the values tabulated by Miedema, however, have been slightly readjusted by amounts comparable to the experimental uncertainty of work function values), n_{WS} is the electron density at the boundary of the Wigner–Seitz cell for each element. P, Q and R are constants for specific groups of elements (their values are related to the position in the Periodic Table of the elements involved). In the same model (MIEDEMA and NIESSEN [1982]) the volume variation in the formation of the intermetallic compound is evaluated as proportional to $(\Delta\Phi^*)[(\Delta(n_{WS})^{-1}])$.

Although the way to predict formation enthalpies of alloys was introduced as an empirical one it is important to observe that the model incorporates basic physics. A quantum-mechanical interpretation of Miedema's parameters has already been proposed by CHELIKOWSKY and PHILLIPS [1977, 1978].

Extensions of the model to complex alloy systems have been considered. As an interesting application we may mention the discussion on the stabilities of ternary compounds presented by DE BOER *et al.* [1988]. In the case of the Heusler type alloys XY_2Z, for instance, the stability conditions with respect to mechanical mixtures of the same nominal composition ($XY_2 + Z$, $X + Y_2Z$, $XY + YZ$, etc.) have been systematically examined and presented by means of diagrams.

The Miedema's parameters, $\Delta\Phi^*$, $\Delta n_{WS}^{1/3}$, moreover, have been used as variables for the construction of structural plots of intermetallic phases (ZUNGER [1981]), RAJASEKHARAN and GIRGIS [1983]). According to Rajasekharan and Girgis on a $\Delta\Phi^*$, $\Delta n_{WS}^{1/3}$ map, considerable resolution is obtained among the binary systems in which different structure types occur. The points corresponding to the systems in which the Laves phases (or the phases of types as Cr_3Si, $TiAl_3$, etc.) occur show linear relationships on the map. (The good separation, moreover, between the line connecting the Cr_3Si type phase points and that of the Laves phase points, can be related to the almost total exclusion of the Cr_3Si type phases from the 250 binary systems containing Laves phases and that of the Laves phases from the about 90 binary systems in which a Cr_3Si type phase occur). (See also ch. 2, § 7).

8.6. Prediction of the properties of selected families of alloys: Gschneidner's relations as an example

Stability maps and/or correlation diagrams may be especially simple and easy to handle for selected groups of similar alloys. (For instance, alloys of the elements of the same group of the Periodic Table).

As an example we may mention the alloys of the rare earth metals (especially the

"trivalent ones"). It is well known that, within this family of elements, several properties change according to well-recognized and systematic patterns. The atomic number itself can be used in this case as a simple and convenient chemical parameter). In several instances it has been pointed out that a systematic consideration of the crystal structures (and of the phase diagrams) of alloys formed by analogous elements (as those of the trivalent rare earth family) enables a number of empirical regularities to be deduced and theoretical statements to be made. (See a general discussion on this subject by GSCHNEIDNER [1969, 1971], the comments by YATSENKO *et al.* [1979, 1983], COLINET *et al.* [1984a, 1984b], VASSILIEV *et al.* [1993], FERRO *et al.* [1994] and SOMMER *et al.* [1995] on alloys thermodynamics, the papers by MASSALSKI [1989] on the applications of this behaviour to phase diagram assessment, by PARTHE and CHABOT [1984], ROGL [1984] and by IANDELLI and PALENZONA [1979] for a systematic crystallochemical description. See SERENI [1984] for examples and a discussion of the properties of the rare earth metals themselves. See also some comments of this point in sec. 7.2.4.a). Criteria based on the mentioned characteristics have been used in assessment procedures and in the prediction of phase diagrams and of phase (and structure type) formation. Fig. 59 may be considered as an example of such typical trends and of their correlations. Special applications (prediction of Pm-alloys) have been described by SACCONE *et al.* [1990] and (forecast of selected phase diagrams) by BORZONE *et al.* [1990], FERRO *et al.* [1993] and SACCONE *et al.* [1995]. The applicability of similar criteria to the assessment and prediction of phase equilibria in selected groups of ternary rare earth alloys (containing two different RE metals) has been exemplified by GIOVANNINI et al. [1994, 1995a, 1995b] in the description of complex Mg–RE alloy systems.

Considering other families of similar compounds we may mention as an other example of systematic descriptions of selected groups of phases and of the use of special interpolation and extrapolation procedures to predict specific properties, the contributions given by GUILLERMET *et al.* [1991, 1992] (cohesive and thermodynamic properties, atomic average volumes, etc. of nitrides, borides, etc. of transition metals).

8.7. Pettifor's chemical scale and structure maps

We have seen that in a phenomenological approach to the systematics of the crystal structures (and of other phase properties) several types of coordinates, derived from physical atomic properties, have been used for the preparation of (two, three-dimensional) stability maps. Differences, sums, ratios of properties such as electronegativities, atomic radii, valence electron numbers have been used. These variables, however, as stressed, for instance, by VILLARS *et al.* [1989] do not always clearly differentiate between chemically different atoms.

As already mentioned in sec. 1 of this chapter, PETTIFOR [1984, 1985a, 1986a] *created a chemical scale* (χ) which orders the elements along a single axis. This scale (and the progressive order number of the elements in this scale: the so-called *Mendeleev number*, M) starts with the least electronegativity element and ends with the most electronegative one (see table 1).

For binary compounds (and alloys) X_nY_m (with a given n:m ratio) two-dimensional

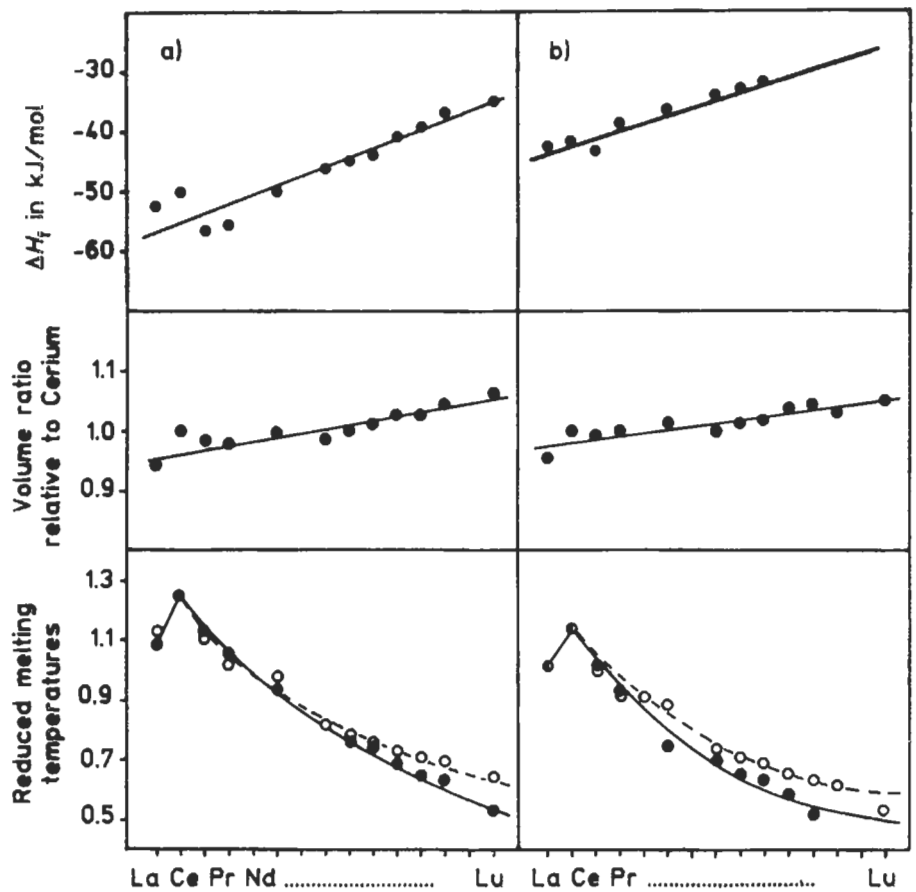

Fig. 59. Gschneidner's plots for some rare earth (RE) alloys.

a) $REIn_3$ compounds

b) $RETl_3$ compounds

Following data are reported as a function of RE atomic number: Formation enthalpy, volume ratio relative to cerium (see sec. 7.2.4.a) and reduced melting temperature T_R. This is the ratio (Kelvin/Kelvin) of the melting point of the phase and of the melting point of the involved earth metal. (•) experimental values; (°) hypothetical values (reference values) of T_R computed for compounds assumed to have a constant melting point. The difference between the experimental and computed slopes of T_R curves is considered to be an indication of the variation of the thermal stability of the phases along the series).

In these cases, all the diagrams show a decreasing phase stability for an increase of the atomic number.

χ_X, χ_Y (or M_X, M_Y) maps may be prepared. See chapter 2, § 6.2 and the simplified version reported in fig. 60 for the reader's convenience. It has been proved that by using this ordering of the elements an excellent structural separation may be obtained of the binary compounds of various stoichiometries (n:m = 1:1, 1:2, 1:3, 1:4, ..., 1:13, 2:3, 2:5, ..., 2:17, 3:4, ..., etc.) (PETTIFOR [1986a]). See also VILLARS *et al.* [1989] who have

References: p. 363.

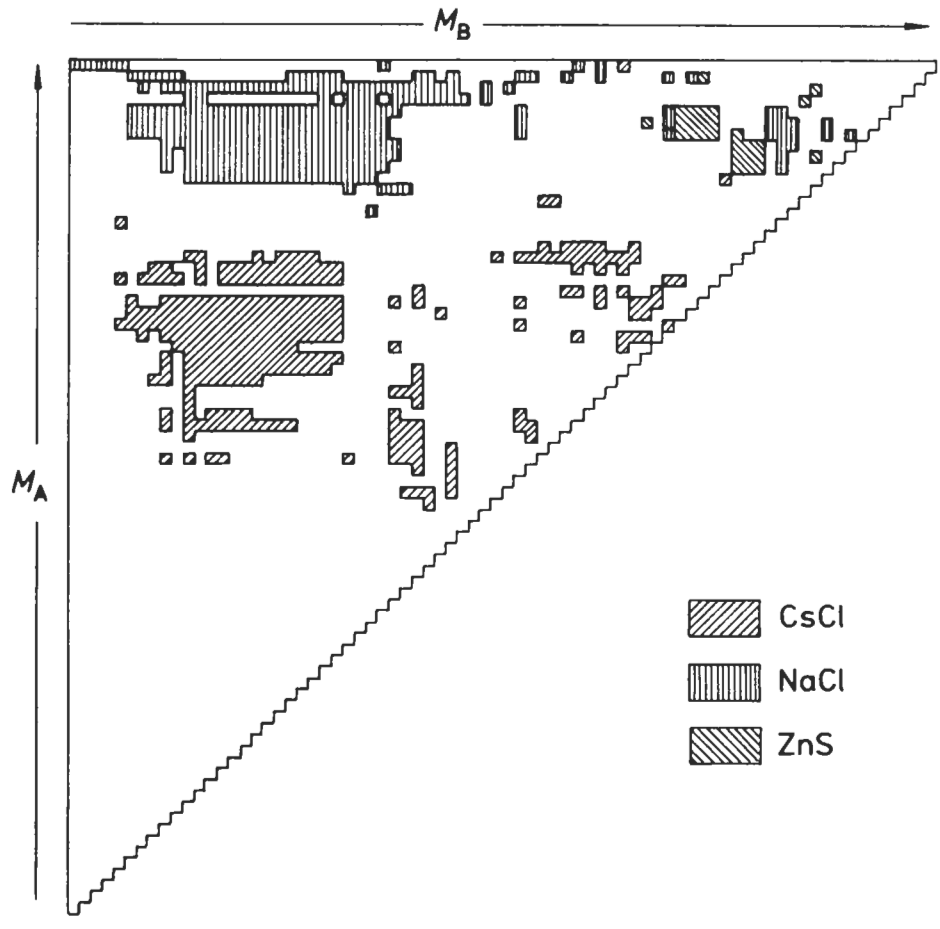

Fig. 60. Simplified version of the Pettifor's map for AB compounds. The elements are arranged along the axes according to their M_t, Mendeleev number. As an example the existence regions of the NaCl, CsCl and cubic ZnS type phases are evidenced. For more details see chapter 2, § 6.2.

updated the Pettifor maps for several stoichiometries.

An extension of the application of these maps to the systematic description of certain groups of ternary alloys has been presented also by PETTIFOR [1988a, 1988b]. Composition averaged Mendeleev numbers can be used, for instance, in the description of pseudobinary, ternary or quaternary alloys. All these maps show well defined domains of structural stability for a given stoichiometry, thus making the search easier for new ternary or quaternary alloys with a particular structure type and which, as a consequence, have the potential of interesting properties and applications (PETTIFOR [1988a, 1988b]; see also ch. 2, § 6.2).

9. *Acknowledgments*

This is a revised and somewhat extended version of a chapter by the same authors, published in 1993 in Volume 1, edited by V. Gerold, of the *Materials Science and Technology* series. We, and the Editors of *Physical Metallurgy*, are grateful to VCH Publishers, Weinheim, for permission to use this material.

Appendix 1. Gazetteer, in alphabetic order, of intermetallic phases cited in this chapter.

(In the formulae of the phases in the 1st column the element symbols are in alphabetical order, in the prototype formulae they are in the Pettifor's order (see sec. 2). Heavy-faced characters have been used for the phases corresponding to the prototypes)

Phase and Prototype	Corresponding Prototype	Section of this chapter
A1, A_2,...B_1, B_2,..., etc.:	Strukturberichte Symbols	3.4
Ag	cF4–Cu	6.2.1
Ag_3Al	cP20–Mn	7.2.2
Ag_5Al_3	hP2–Mg	7.2.2
AgAsBa	hP6–Ni_2In	6.5.3
AgAsMg	**cF12–AgMgAs**	6.4.3
Ag_5Cd_8	cI52–Cu_5Zn_8	6.1.5, 7.2.2
AgI	hP4–ZnO	6.3.3
Ag_9In_4	cP52–Cu_9Al_4	6.1.5, 7.2.2
Ag_5Li_7	cI52–Cu_5Zn_8	6.1.5, 7.2.2
AgSe	cF8–ZnS (sphalerite)	6.3.3
$AgTe_2Tl$	**tI8–$AgTlTe_2$**	6.5.9
$AgZn_3$	hP2–Mg	7.2.2
Ag_5Zn_8	cI52–Cu_5Zn_8	6.1.5, 7.2.2
Al	cF4–Cu	6.2.1
AlAs	cF8–ZnS (sphalerite)	6.3.3
Al_2Au	cF12–CaF_2	6.4.2
AlB_2	**hP3–AlB_2**	6.5.6, 6.5.10
Al_4Ba	**tI10–$BaAl_4$**	6.5.9
$Al_{1-x}Co_x$	cP2–CsCl	6.1.2
$AlCr_6Si$	cP8–Cr_3Si	6.6.2
β-Al-Cu	cI2–W	6.1.1
$AlCu_3$	cI2–W	7.2.2
Al_2Cu	**tI12–$CuAl_2$**	**5**
Al_4Cu_9	**cP52–Cu_9Al_4**	6.1.5, 7.2.2
$AlCu_2Mn$	**cF16–$MnCu_2Al$**	3.4, 6.1.3
$Al_5(Cu,Ni)_3$		6.1.5
$Al_6(Cu,Ni)_4$		6.1.5
$Al_7(Cu,Ni)_5$		6.1.5
$Al_8(Cu,Ni)_6$		6.1.5
$Al_{11}(Cu,Ni)_6$		6.1.5
$Al_{13}(Cu,Ni)_8$		6.1.5

References: p. 363.

$Al_{15}(Cu,Ni)_{10}$		6.1.5
$Al_{17}(Cu,Ni)_{12}$		6.1.5
$AlCuS_2$	tI16–$CuFeS_2$	7.2.1, 6.3.3
Al_3Er	cP4–$AuCu_3$	6.2.7
AlFe	cP2–CsCl	6.1.2
$AlFe_3$	cF16–$BiLi_3$	4.1.1(a)
Al_3Gd	hP8–Ni_3Sn	6.2.7
$Al_{23}Gd_4Ni_6$		3.2.
Al_3La	hP8–Ni_3Sn	6.2.7
Al_3Mg_2	**cF1832–Mg_2Al_3**	6.6.5, 5
$Al_{12}Mg_{17}$	**cI58–$Mg_{17}Al_{12}$**	6.6.5
$AlMo_3$	cP8–Cr_3Si	6.6.2
AlN	hP4–ZnO	6.3.3
$AlNb_3$	cP8–Cr_3Si	6.6.2
$AlNi_3$	cP4–$AuCu_3$	3.5.5
$Al_{1-x}Ni_x$	cP2–CsCl	6.1.2
$Al_{23}Ni_6Y_4$		3.2.
Al_3OsU_2	**hP12–U_2OsAl_3**	6.6.4
AlP	cF8–ZnS (sphalerite)	6.3.3
$AlPd_2$	oP12–Co_2Si	6.5.4
$AlPt_3$	cP4–$AuCu_3$	3.5.5
Al_2Pt	cF12–CaF_2	6.4.2
AlSb	cF8–ZnS (sphalerite)	6.3.3, 7.2.1
Al_3Sc	cP4–$AuCu_3$	6.2.7
$AlSnV_6$	cP8–Cr_3Si	6.6.2
Al_3Th	hP8–Ni_3Sn	6.2.7
$AlTi_3$	hP8–Ni_3Sn	6.2.7
Al_3Ti	**tI8–$TiAl_3$**	4.1.1(a)
Al_3Tm	cP4–$AuCu_3$	6.2.7
AlV_3	cP8–Cr_3Si	6.6.2
Al_8V_5	cI52–Cu_5Zn_8	6.1.5, 7.2.2
AlY_3	cP4–$AuCu_3$	3.5.5
Al_3Y	hP8–Ni_3Sn	6.2.7
Al_3Y	cP4–$AuCu_3$	3.5.5
Al_3Yb	cP4–$AuCu_3$	6.2.7
$AlZr_2$	hP6–Ni_2In	6.5.3
Al_2Zr	hP12–$MgZn_2$	6.6.4
Al_3Zr	**tI16–Al_3Zr**	4.1.1(a)
Al_3Zr_4	**hP7–Zr_4Al_3**	Table 6
Ar	cF4–Cu	6.2.1
AsB	cF8–ZnS (sphalerite)	6.3.3
AsCaCu	hP6–Ni_2In	6.5.3
AsCuS	**oP12–CuAsS**	5
AsGa	cF8–ZnS (sphalerite)	6.3.3
AsIn	cF8–ZnS (sphalerite)	6.3.3
$AsNa_3$	**hP8–$NaAs_3$**	3.4.
AsNb	**tI8–NbAs**	6.5.9
AsNi	**hP4–NiAs**	4.1, 6.5.1
As_2Zn	mP24–ZnP_2	7.2.1
Au	cF4–Cu	6.2.1
$AuBe_5$	**cF24–$AuBe_5$**	6.6.4
Au_5Cd_8	cI52–Cu_5Zn_8	6.1.5, 7.2.2
AuCu (I)	**tP2–AuCu**	4.1.1,.6.2.4

AuCu (II)	**oI40–AuCu**	4.1.1, 4.2, 6.2.4
$AuCu_3$	**cP4–$AuCu_3$**	3.5.5, 4.1, 4,1,1, 6.2.3.
Au_3Ge	hP2–Mg	7.2.2
Au_5Hg_8	cI52–Cu_5Zn_8	6.1.5, 7.2.2
Au_9In_4	cP52–Cu_9Al_4	6.1.5, 7.2.2
Au_5K	hP6–$CaCu_5$	6.2.8
$AuNb_3$	cP8–Cr_3Si	6.6.2
AuSiTh	hP3–BaPtSi	6.5.6
$AuSn_2$	**oP24–$AuSn_2$**	5
$AuTa_3$	cP8–Cr_3Si	6.6.2
$AuTi_3$	cP8–Cr_3Si	6.6.2
$B_3C_xPd_5Y$		6.6.2
$BCeCo_4$	**hP12–$CeCo_4B$**	4.5
B_2CeCo_3	**hP6–$CeCo_3B_2$**	4.5, 6.2.8
$B_3Ce_2Co_7$	**hP24–$Ce_2Co_7B_3$**	4.5
$B_4Ce_3Co_{11}$	**hP18–$Ce_3Co_{11}B_4$**	4.5
B_2CoW_2	**oI10–W_2CoB_2**	4.5
B_3CoW_3	**oC28–W_3CoB_3**	4.5
BCr	**oC8–CrB**	4.5
B_3Cr_5	**tI32–Cr_5B_3**	3.4
BIr	hP2–WC	6.5.5
$B_6Lu_5Ni_{19}$	**hP30–$Lu_5Ni_{19}B_6$**	4.5
B_4LuRh_4		6.6.2
$B_2Nd_3Ni_{13}$	**hP18–$Nd_3Ni_{13}B_2$**	4.5
BNi	oC8–BCr	3.2
BOs	hP2–WC	6.5.5
BRu	hP2–WC	6.5.5
Ba	cI2–W	6.1.1
$BaCd_{11}$	**tI48–$BaCd_{11}$**	5
$Ba_2Cu_3O_{7-x}Y$		6.6.2
BaH_2(h)	oP12–Co_2Si	6.5.4
$BaHg_{11}$	**cP36–$BaHg_{11}$**	5
$BaPb_3$	**hR36–$BaPb_3$**	6.2.3
BaPtSb	**hP3–BaPtSb**	6.5.6
α-Be	hP2–Mg	6.2.6
Be	cI2–W	6.1.1
$Be_{1-x}Co_x$	cP2–CsCl	6.1.2
$Be_{1-x}Cu_x$	cP2–CsCl	6.1.2
BeN_2Si	**oP16–$BeSiN_2$**	6.3.3
$Be_{1-x}Ni_x$	cP2–CsCl	6.1.2
BeO	hP4–ZnO	6.3.3
BePd	cP2–CsCl	6.1.2
BePo	cF8–ZnS (sphalerite)	6.3.3
BeS	cF8–ZnS (sphalerite)	6.3.3
BeSe	cF8–ZnS (sphalerite)	6.3.3
BeTe	cF8–ZnS (sphalerite)	6.3.3
$Bi_2(Ca,Sr)_3Cu_2O_{9-x}$		6.6.2
BiF_3	**cF16–BiF_3**	3.5.1, 6.1.4
$BiLi_3$	**cF16–Li_3Bi**	4.1.1, 6.1.4, 6.2.2
BrCs	cP2–CsCl	6.1.2
BrCu	hP4–ZnO	6.3.3, 7.2.1
BrTl	cP2–CsCl	6.1.2
C(diamond)	**cF8–C**	6.3.1

References: p. 363.

C(graphite)	**hP4–C**	6.3.4
C(lonsdaleite)	**hP4–C**	6.3.3
C_2Ca	tI6–CaC_2	3.2
$C_{1-x}Hf$	cF8–NaCl	6.4.1
CMo	hP2–WC	6.5.5
$C_{1-x}Nb$	cF8–NaCl	6.4.1
C_5Nb_6	mC22–Nb_6C_5	6.4.1
CSi polytypes		4.3, 6.3.3, 7.2.1
$C_{1-x}Th$	cF8–NaCl	6.4.1
$C_{1-x}Ti$	cF8–NaCl	6.4.1
$C_{1-x}V$	cF8–NaCl	6.4.1
C_5V_6	m??44–V_6C_5	6.4.1
C_7V_8	cP60–V_8C_7	6.4.1
CW	**hP2–WC**	6.4.1, 6.5.5, 5
$C_{1-x}W$	cF8–NaCl	6.4.1
$C_{1-x}Zr$	cF8–NaCl	6.4.1
α-Ca	cF4–Cu	6.2.1
β-Ca	cI2–W	6.1.1
$CaCu_5$	**hP6–$CaCu_5$**	4.5, 6.2.8
CaF_2	**cF12–CaF_2**	3.2, 6.2.2, 6.4.2
$CaIn_2$	**hP6–$CaIn_2$**	6.4.3, 6.5.7
Ca_2Pb	oP12–Co_2Si	6.5.4
$CaSi_2$	**hR18–$CaSi_2$**	3.4
Ca_2Si	oP12–Co_2Si	6.5.4
$Ca_{31}Sn_{20}$	tI204–$Pu_{31}Rh_{20}$	3.2
Cd	hP2–Mg	6.2.6
Cd_3Cu_4	**cF1124–Cu_4Cd_3**	5, 6.6.5
CdI_2	**hP3–CdI_2**	3.2, 4.1, 6.5.2
Cd_2Na	**cF1192–$NaCd_2$**	5, 6.6.5
$Cd_{43}Pd_8$	cP52–Cu_9Al_4	6.1, 7.2.2
CdPo	cF8–ZnS (sphalerite)	6.3.3
CdS	cF8–ZnS (sphalerite)	6.3.3
CdS	hP4–ZnO	6.3.3
CdSe	cF8–ZnS (sphalerite)	6.3.3
CdSe	hP4–ZnO	6.3.3
CdTe	cF8–ZnS (sphalerite)	6.3.3
α-Ce	cF4–Cu	6.2.1
γ-Ce	cF4–Cu	6.2.1
Ce_5Mg_{41}	**tI92–Ce_5Mg_{41}**	5
Ce_2Ni_{17}	**hP36–Ce_2Ni_{17}**	4.5
$\approx Ce_2NiSi_3$	hP3–AlB_2	6.5.6, Table 3
$Ce_6Ni_2Si_3$	**hP22–$Ce_6Ni_2Si_3$**	4.1, 6.5.6
$Ce_5Ni_2Si_3$	**hP40–$Ce_5Ni_2Si_3$**	4.1, 6.5.6
CeO_2	cF12–CaF_2	6.4.2
ClCu	hP4–ZnO	6.3.3
ClNa	**cF8–NaCl**	6.2,2, 6.4.1
Cl_2Pb	**oP12–$PbCl_2$**	3.4, 6.5.4
ClCs	**cP2–CsCl**	4.1.1, 6.1.2, Table 3
ClTl	cP2–CsCl	6.1.2
Co	hP2–Mg	6.2.6
α-Co	cF4–Cu	6.2.1
Co–Cr–Mo (R phases)	3.4	
Co_2EuP_2	tI10–$ThCr_2Si_2$	4.4, 6.5.9

CoFeSn	hP6–Ni_2In	6.5.3
Co_3GaY_3	oC28–W_3CoB_3	4.5
Co_4GaY_4	**mC18–Y_4Co_4Ga**	4.5
Co_5GaY_5	**oC44–Y_5Co_5Ga**	4.5
Co_2Ge	hP6–Ni_2In	6.5.3
Co_2Ge_2RE	tI10–$ThCr_2Si_2$	6.5.9
Co_5La	hP6–$CaCu_5$	6.2.8
CoO	**tI4–CoO**	6.1.5
Co_2RESi_2	tI10–$ThCr_2Si_2$	6.5.9
Co_2Si	**oP12–Co_2Si**	6.5.4
Co_5Sm	hP6–$CaCu_5$	6.2.8
$CoTe_2$	hP3–CdI_2	6.5.2
Co_3V	**hP24–VCo_3**	6.2.3
Co_5Zn_{21}	cP52–Cu_9Al_4	6.1.5
Cr	cI2–W	6.1.1
σCr–Fe	**tP30–σCr–Fe**	6.6.3, Table 6
Cr–Mo-Ni (P phases)		3.4, Table 6
Cr_3Os	cP8–Cr_3Si	6.6.2
$Cr_{12}P_7$	hP19–26–$Cr_{12}P_7$	Table 3
Cr_3Si	cP8–Cr_3Si	6.6.2, Table 6
Cr_2Si_2Th	**tI10–$ThCr_2Si_2$**	6.5.9
Cr_3Pt	cP8–Cr_3Si	6.6.2
ω-Cr–Ti phase	**hP3–Cr–Ti**	6.5.6
α-Cr_2Ti	cF24–Cu_2Mg	6.6.4
β-Cr_2Ti	hP12–$MgZn_2$	6.6.4
γ-Cr_2Ti	hP12–Ni_2Mg	6.6.4
Cu	**cF4–Cu**	6.2.1
$CuFeS_2$	**tI16–$FeCuS_2$**	5, 6.3.1, 6.3.3
Cu_9Ga_4	**cP52–Cu_9Al_4**	6.1.5
Cu_2Ge_2RE	tI10–$ThCr_2Si_2$	6.5.9
CuI	hP4–ZnO	6.3.3
Cu_5La	hP6–$CaCu_5$	6.2.8
CuLaSi	hP6–Ni_2In	6.5.3
Cu_2Mg	**cF24–Cu_2Mg**	3.4, 4.3, 6.6.4, Table 6
$Cu_{16}Mg_6Si_7$	cF116–Th_6Mn_{23}	3.4
Cu_4MgSn	**cF24–Cu_4MgSn**	6.6.4
CuPt(I)	**hR96–CuPt(I)**	4.1.1a
Cu_2RESi_2	tI10–$ThCr_2Si_2$	6.5.9
CuS_2Sb	**oP16–$CuSbS_2$**	5
Cu_5Si	t**	7.2.2
Cu_5Sn		7.2.2
$CuTi_3$	**tP4–Ti_3Cu**	4,1,1 a, 6.2.5
(β-)Cu–Zn	cI2–W	4.1.1, 6.1.1, 7.2.2
(β'-)Cu–Zn	cP2–CsCl	4.1.1, 6.1.2
Cu_5Zn_8	**cI52–Cu_5Zn_8**	6.1.5
Diamond: see C (diamond)		
α-Dy	hP2–Mg	6.2.6
E phases: see oP12–TiNiSi		
Er	hP2–Mg	6.2.6
Er_2RhSi_3	**hP24–Er_2RhSi_3**	6.5.6
Eu	cI2–W	6.1.1
α-Fe (δ)	cI2–W	6.1.1
γ-Fe	cF4–Cu	6.2.1

References: p. 363.

Fe_3Ga	hP8–Ni_3Sn	6.2.7
Fe_3Ge	hP8–Ni_3Sn	6.2.7
Fe_2Ge_2RE	tI10–$ThCr_2Si_2$	6.5.9
Fe_4N	**cP5–Fe_4N**	4.1, 4.1.1 b
Fe_8N	**tI8–Fe_8N**	4.1.1 b
FeNNi	**tP3–FeNiN**	4.1.1 b
Fe_2P	**hP9–Fe_2P**	6.5.8
Fe_2RESi_2	tI10–$ThCr_2Si_2$	6.5.9
FeS_2 (pyrite)	**cP12–FeS_2**	4.1
FeSbV	hP6–Ni_2In	6.5.3
Fe_3Sn	hP8–Ni_3Sn	6.2.7
Fe_7W_6	**hR39–W_6Fe_7**	3.4,5, 6.6.3, Table 6
Fe_3Zn_{10}	cI52–Cu_5Zn_8	6.1.5
Frank–Kasper phases		3.4, 6.6
G phases: see cF116–$Mn_{23}Th_6$		
$GaGeNb_6$	cP8–Cr_3Si	6.6.2
Ga_5Ir_3	**tP32–Ir_3Ga_5**	4.4
GaN	hP4–ZnO	6.3.3
$GaNb_3$	cP8–Cr_3Si	6.6.2
Ga_4Ni	cI52–Cu_5Zn_8	6.1.5
GaV_3	cP8–Cr_3Si	6.6.2
Ga_7V_6	cI52–Cu_5Zn_8	6.1.5
GdNi	oC8–CrB	3.2.
$GdSe_2$	oP12–Co_2Si	6.5.4
Ge	cF8–C (diamond)	6.3.1
Ge_5Ir_4	**tP36–Ir_4Ge_5**	4.4
$GeMg_2$	cF12–CaF_2	6.4.2, Table 3
Ge_2Mn_2RE	tI10–$ThCr_2Si_2$	6.5.9
GeNa	**mP32–NaGe**	3.4
$GeNb_3$	cP8–Cr_3Si	6.6.2
Ge_2Ni_2RE	tI10–$ThCr_2Si_2$	6.5.9, 7.2.5 b
$GeRh_2$	oP12–Co_2Si	6.5.4
$Ge_{31}V_{17}$	**tP192–$V_{17}Ge_{31}$**	4.4
Graphite: see C (graphite)		
Hägg phases		3.4
Heusler phases		3.4, 6.1.3
HfS_2	hP3–CdI_2	6.5.2
HgS	cF8–ZnS (sphalerite)	6.3.3
HgSe	cF8–ZnS (sphalerite)	6.3.3
HgTe	cF8–ZnS (sphalerite)	6.3.3
$HgTi_3$	cP4–$AuCu_3$	3.5.5
$HfPt_3$	cP4–$AuCu_3$	3.5.5
Ho	hP2–Mg	6.2.6
Hume–Rothery phases		3.4, 6.1.5, 7.2.2
$InLa_2$	hP6–Ni_2In	6.5.3
$InLa_3$	cP4–$AuCu_3$	3.5.5
In_3La	cP4–$AuCu_3$	3.5.5
InN	hP4–ZnO	6.3.3
$InNi_2$	**hP6–Ni_2In**	6.5.3
ITl	cP2–CsCl	6.1.2
Ir	cF4–Cu	6.2.1
$IrMo_3$	cP8–Cr_3Si	6.6.2
K	cI2–W	6.1.1

K_2O	cF12–CaF_2	6.4.2
Kr	cF4–Cu	6.2.1
K_2S	cF12–CaF_2	6.4.2
KSbZn	hP6–Ni_2In	6.5.3
K_2Se	cF12–CaF_2	6.4.2
K_2Te	cF12–CaF_2	6.4.2
α-La	**hP4–La**	6.2.6
β-La	cF4–Cu	6.2.1
$LaNi_5$	hP6–$CaCu_5$	6.2.8
$LaPt_5$	hP6–$CaCu_5$	6.2.8
LaPtSi	**tI12–LaPtSi**	6.5.10
Laves phases		3.4, 4.3, 6.6.4, Table 6
$LaZn_5$	hP6–$CaCu_5$	6.2.8
Li	cI2–W	6.1.1
Li–Mg–Zn Laves polytypes		6.6.4
Li_2O	cF12–CaF_2	6.4.2
Li_2O_3Si		3.2.
LiN_3Si_2		3.2.
$Li_{10}Pb_3$	cP52–Cu_9Al_4	6.1.5
Li_2S	cF12–CaF_2	6.4.2
Li_2Se	cF12–CaF_2	6.4.2
Li_2Te	cF12–CaF_2	6.4.2
Lonsdaleite: see C (lonsdaleite)		
Lu	hP2–Mg	6.2.6
M phases		Table 6
Martensite (Fe/C)		6.1.5
Mg	**hP2–Mg**	6.2.6
$MgNi_2$	**hP24–Ni_2Mg**	3.4, 6.6.4, 4.3, Table 6
Mg_2Pb	cF12–CaF_2	6.4.2
Mg_2Si	cF12–CaF_2	6.4.2
Mg_2Sn	cF12–CaF_2	3.4, 6.4.2
$MgZn_2$	**hP12–$MgZn_2$**	3.4, 6.6.4, 4.3, Table 6
α-Mn	**cI58 α-Mn**	6.6.5
Mn_2RESi_2	tI10–$ThCr_2Si_2$	6.5.9
MnS	hP4–ZnO	6.3.3
MnSe	hP4–ZnO	6.3.3
Mn_2Sn	hP6–Ni_2In	6.5.3
MnTe	hP4–ZnO	6.3.3
$Mn_{12}Th$	**tI26–$ThMn_{12}$**	6.2.8
$Mn_{23}Th_6$	**cF116–Th_6Mn_{23}**	3.4
$MnZn_3$	cP4–$AuCu_3$	3.5.5
Mo	cI2–W	6.1.1
$MoNi_4$	**tI10–$MoNi_4$**	4.1.1a
MoP	hP2–WC	6.5.5
$MoPt_2$	**oI6–$MoPt_2$**	4.1.1a
$MoSi_2$	**tI6–$MoSi_2$**	3.2, Table 3
NNb	hP4–ZnO	6.3.3
NNb	hP2–WC	6.5.5
$N_{1-x}V$	cF8–NaCl	6.4.1
$N_{1-x}W$	cF8–NaCl	6.4.1
NW	hP2–WC	6.4.1, 6.5.5
Na	cI2–W	6.1.1
Na_2O	cF12–CaF_2	6.4.2

References: p. 363.

Na_2S	cF12–CaF_2	6.4.2
Na_2Se	cF12–CaF_2	6.4.2
NaSi	**mC32–NaSi**	3.4
Na_2Te	cF12–CaF_2	6.4.2
NaTl	**cF16–NaTl**	3.4, 6.1.4
$NaZn_{13}$	**cF112–$NaZn_{13}$**	5
Nb_3Sn	cP8–Cr_3Si	6.6.2
Nb_3Pt	cP8–Cr_3Si	6.6.2
Ne	cF4–Cu	6.2.1
$Ni_7Pr_{15}Si_{10}$	**hP64–$Pr_{15}Ni_7Si_{10}$**	4.1,6.5.6
Ni_2Si_2RE	tI10–$ThCr_2Si_2$	6.5.9
NiSiTi	**oP12–TiNiSi**	6.5.4
Ni_3Sn	**hP8–Ni_3Sn**	6.2.7, 4.1.1a
$Ni_{17}Th_2$	**hP38–Th_2Ni_{17}**	6.2.8
Ni_3Ti	**hP16–$TiNi_3$**	6.2.3
Ni_2Zn_{11}	cI52–Cu_5Zn_8	6.1.5, 7.2.2
Ni_3Zr	hP8–Ni_3Sn	6.2.7
Nowotny phases		4.4
Os	hP2–Mg	6.2.6
OTa_4	**oP5–Ta_4O**	4.1.1b
O_2Th	cF12–CaF_2	6.4.2
$O_{1\pm x}Ti$	cF8–NaCl	6.4.1
OTi_2	hP3–CdI_2	6.5.2
O_2U	cF12–CaF_2	6.4.2
$O_{1\pm x}V$	cF8–NaCl	6.4.1
OW_3	cP8–Cr_3Si	6.6.2
OZn	**hP4–ZnO**	6.3.2
P phases	oP56–(Cr-Mo-Ni)	Table 6
Pb	cF4–Cu	6.2.1
Pb_3U	cP4–$AuCu_3$	3.5.5
Pd	cF4–Cu	6.2.1
Pd_2Sn	oP12–Co_2Si	6.5.4
$Pd_{1-x}Ti_x$ (r)	oP4–AuCd	6.1.2
$Pd_{1-x}Ti_x$ (h)	cP2–CsCl	6.1.2
α-Po	cP1–Po	3.5.2
Pt	cF4–Cu	6.2.1
$PtMn_3$	cP4–$AuCu_3$	3.5.5
PtS_2	hP3–CdI_2	6.5.2
Pt_2RESn_2	tI10–$ThCr_2Si_2$	6.5.9
$Pt_{1-x}Ti_x$ (r)	oP4–AuCd	6.1.2
$Pt_{1-x}Ti_x$ (h)	cP2–CsCl	6.1.2
Pt_2U	**oC12–UPt_2**	4.5
$Pu_{31}Rh_{20}$	**tI204–$Pu_{31}Rh_{20}$**	3.2.
Pyrite: see FeS_2		
$\mathfrak{R}$ phases	hR159 Co-Cr-Mo	Table 6
RE (rare earth) alloys		8.6
RE (metals)		6.1.1, 6.2.6
Rb	cI2–W	6.1.1
Re	hP2–Mg	6.2.6
$Re_{24}Ti_5$(χ-phase)	**cI58–Ti_5Re_{24}**	6.6.5
Rh	cF4–Cu	6.2.1
Rh_2Sn	oP12–Co_2Si	6.5.4
Ru	hP2–Mg	6.2.6

Ru_2Sn_3	**tP20–Ru_2Sn_3**	4.4
Samson phases		6.6.5
SZn(sphalerite)	**cF8–ZnS**	6.3.1, 6.3.2
SZn(wurtzite)	**hP4–ZnO**	6.3.2
S_2Th	oP12–Co_2Si	6.5.4
SeZn	hP4–ZnO	6.3.3
Si	cF8–C (diamond)	6.3.1
α-Si_2Th	**tI12–α-$ThSi_2$**	6.5.10
β-Si_2Th	hP3–AlB_2	6.5.10
$\approx Si_5Th_3$	hP3–AlB_2	6.5.10
Si_2Ti	**oF24–$TiSi_2$**	4.4
Si_2U_3	**tP10–U_3Si_2**	5
SiV_3	cP8–Cr_3Si	6.6.2
Si_3W_5	**tI32–W_5Si_3**	3.4
Sm	**hR9–Sm**	6.2.6
α-Sn	cF8–C (diamond)	6.3.1
β-Sn	**tI4–β-Sn**	6.3.1
$SnTi_2$	hP6–Ni_2In	6.5.3
α-Sr	cF4–Cu	6.2.1
Sr	cI2–W	6.1.1
T_1 phases: see Si_3W_5		
T_2 phases: see B_3Cr_5		
Ta	cI2–W	6.1.1
Tc	hP2–Mg	6.2.6
TeTh	cP2–CsCl	6.1.2
TeZn	hP4–ZnO	6.3.3
α-Th	cF4–Cu	6.2.1
Th	cI2–W	6.1.1
Th_2Zn_{17}	**hR57–Th_2Zn_{17}**	6.2.8
$TiZn_3$	cP4–$AuCu_3$	3.5.5
V	cI2–W	6.1.1
W	**cI2–W**	4.1.1, 6.1.1
Wurtzite: see SZn (wurtzite)		
Xe	cF4–Cu	6.2.1
α-Y	hP2–Mg	6.2.6
Zintl phases		3.4, 6.1.4
Zn	hP2–Mg	6.2.6
β-(Cu–Zn)		4.1.1
β'-(Cu–Zn)		4.1.1
ε-Mg type		
γ-(Cu_5Zn_8)		6.1.5
μ-(Fe_7W_6)		5.3.4, Table 6
σ-phases (see (σ) Cr–Fe)	3.4	Table 6
χ-phase:see $Re_{24}Ti_5$		6.6.5
ω-phase : see ω-Cr–Ti		Table 6

References

ALBERING, J. H., Pöttgen, R., Jeitschko, W., Hoffmann, R-D., Chevalier, B., Etourneau, J., 1994, J. Alloys and Compounds, **206**, 133.

ALDINGER, F., SEIFERT, H. J., 1993, Z. Metallkd., **84**, 2.

ANDERSSON, S., HYDE, B. G., 1982, Z. Kristallogr., **158**, 119.

ANSARA, I., BERNARD, C., KAUFMAN, L., SPENCER, P., 1978, Calphad, **2**, 1.

ASM INTERNATIONAL, Monograph Series on Alloy Phase Diagrams. "Phase Diagrams of Binary Gold Alloys", 1987, H. Okamoto and T. B. Massalski (Eds.); "Phase Diagrams of Binary Berillium Alloys", 1987, H. Okamoto and L. Tanner (Eds.); "Phase Diagrams of Binary Titanium Alloys", 1987, J. L. Murray (Ed.); "Phase Diagrams of Binary Magnesium Alloys", 1988, A. A. Nayeb-Hashemi and J. B. Clark (Eds.); "Phase Diagrams of Binary Vanadium Alloys", 1989, J. F. Smith (Ed.); "Phase Diagrams of Binary Indium Alloys", 1992, C. E. T. White and H. Okamoto (Eds.).

BÄRNIGHAUSEN, H., 1980, Match (Comm. Mathematical Chemistry), **9**, 139.

BARRETT, C. S., MASSALSKI, T. B., 1966, "Structure of Metals", III Ed., (McGraw Hill Book Company, New-York).

BAUGHMAN, R. H., GALVAO, D. S., 1993, Nature, **365**, 735.

BAZELA, W, 1987, J. Less-Common Metals, **133**, 193.

BHANDARY, K. K., GIRGIS, K., 1977, Acta Crystallogr., **A33**, 903.

BILTZ, W., 1934, "Raumchemie der Festen Stoffe", (Voss-Verlag, Leipzig).

BOKII, G. B., LAPTEV, V. I., 1994, Crystallography Reports, **39**, 409; translated from Kristallografiya, 1994, **39**, 464.

BORZONE, G., CACCIAMANI, G., FERRO, R., 1990, Calphad, **14**, 139.

BORZONE, G., PARODI, N., FERRO, R., 1993, J. Phase Equilibria, **14**, 485.

BREWER, L., 1990, J. Phys. Chem., **94**, 1196.

BREWER, L., WENGERT, P. R., 1973, Metall. Trans. **4**, 83.

BROWN, I. D., SHANNON, R. D., 1973, Acta Cryst., **A29**, 266.

BRUNNER, G. O., 1977, Acta Crystallogr., **A33**, 226.

BRUNNER, G. O., SCHWARZENBACH, D., 1971, Z. Kristallogr., **133**, 127.

CAHN, R. W., 1987, "Antiphase Domains, Disordered Films and the Ductility of Ordered Alloys Based on Ni_3Al", in Stoloff, N. S., Koch, C. C., Liu, C. T. and Izumi, O. (Eds.), High-Temperature Ordered Intermetallic Alloys II, MRS, Pittsburgh, vol. 81, p. 27.

CAHN, R. W., 1990 in: "Recovery, Strain-age-hardening and Recrystallization in Deformed Intermetallics", Whang, S. H., Liu, C. T., Pope, D., and Stiegler, J. O., (Eds.), High Temperature Aluminides and Intermetallics, TSM, Warrendale, p. 245.

CARTER, F. L., 1978, Acta Cryst. **B34**, 2962.

CAVA, R. J., TAKAGI, H., BATLOGG, B., ZANDBERGEN, H. W., KRAJEWSKI, J. J., Peck, W. F. Jr., VAN DOVER, R. B., FELDER, R. J., SIEGRIST, T., MIZUHASHI, K., LEE, J. O., EISAKI, H., CARTER, S. A., UCHIDA, S., 1994a, Nature, **367**, 146.

CAVA, R. J., ZANDBERGEN, H. W., BATLOGG, B., EISAKI, H., TAKAGI, H., KRAJEWSKI, J. J., PECK, W. F. Jr., GYORGY, E. M., UCHIDA, S., 1994b, Nature, **372**, 245.

CHELIKOWSKY, R., PHILLIPS, J. C., 1977, Phys. Rev. Lett., **39**, 1687.

CHELIKOWSKY, R., PHILLIPS, J. C., 1978, Phys. Rev. B, **17**, 2453.

COLINET, C., PASTUREL, A., PERCHERON-GUEGAN, A., ACHARD, J. C., 1984a, J. Less-Common Metals, **102**, 167.

COLINET, C., PASTUREL, A., PERCHERON-GUEGAN, A., ACHARD, J. C., 1984b, J. Less-Common Metals, **102**, 239.

CORBETT, J. D., 1985, Chem. Rev., **85**, 383.

DAAMS, J. L. C., VILLARS, P., VAN VUCHT, J. H. N., 1991, "Atlas of Crystal Structure Types for Intermetallic Phases", Vol. 1–4, (Materials Park, Oh 44073: American Society for Metals).

DAAMS, J. L. C., VAN VUCHT, J. H. N., VILLARS, P., 1992, J. Alloys and Compounds, **182**, 1.

DAAMS, J. L. C., VILLARS, P., 1993, J. Alloys and Compounds, **197**, 243.

DAAMS, J. L. C., VILLARS, P., 1994, J. Alloys and Compounds, **215**, 1.

DARKEN, L. S., GURRY, R. W., 1953, "Physical Chemistry of Metals", (McGraw-Hill, New York).

DE BOER, F. R., BOOM, R., MATTENS, W. C. M., MIEDEMA, A. R., NIESSEN, A. K., 1988, "Cohesion in Metals, Transition Metal Alloys", (North Holland, Amsterdam).

DONNAY, J. D. H., HELLNER, E., NIGGLI, A., 1964, Z. Krist., **120**, 364.

DWIGHT, A. E., 1974, in: Proc. 11th Rare Earth Res. Conf., Oct. 9–10, Traverse City, Michigan, USA, p. 642.

ELLIOTT, R. P., 1965, "Constitution of Binary Alloys", First Supplement, (McGraw-Hill Book Company, New York).
ELLNER, M., PREDEL, B., 1994, in: "Intermetallic Compounds", Vol. 1, Principles, Westbrook, J. H., Fleischer, R. L., (Eds.), p. 91 (John Wiley and Sons Ltd.).
FERRO, R., DELFINO, S., BORZONE, G., SACCONE, A., CACCIAMANI, G., 1993, J. Phase Equilibria, **14,** 273.
FERRO, R., BORZONE, G., PARODI, N., CACCIAMANI, G., 1994, J. Phase Equilibria, **15,** 317.
FERRO, R., CACCIAMANI, G., SACCONE, A., 1995 to be submitted.
FERRO, R., GIRGIS, K., 1990, J. Less-Common Metals, **158,** L41.
FLIEHER, G., VÖLLENKLE, H., NOWOTNY, H., 1968a, Monatsh. Chemie, **99,** 877.
FLIEHER, G., VÖLLENKLE, H., NOWOTNY, H., 1968b, Monatsh. Chemie, **99,** 2408.
FRANK, F. C., KASPER, J. S., 1958, Acta Cryst., **11,** 184.
FRANK, F. C., KASPER, J. S., 1959, Acta Cryst., **12,** 483.
FRANZEN, H. F., 1986, "Physical Chemistry of Inorganic Crystalline Solids", (Springer-Verlag, Berlin).
FREVEL, L. K., 1985, Acta Cryst., **B41,** 304.
GIALANELLA, S., CAHN, R. W., 1993, Materials Engineering **4,** 407.
GIOVANNINI, M., SACCONE, A., FERRO, R., ROGL, P., FLANDORFER, H., EFFENBERG, G., 1994, in "Perspectives in Inorganic Chemistry", DAOLIO, S., TONDELLO, E., VIGATO, P. A., Eds. (La Photograph Publishing, Padova), p. 230.
GIOVANNINI, M., SACCONE, A., MARAZZA, R., FERRO, R., 1995a, Metall. Trans. A, **26A,** 5.
GIOVANNINI, M., SACCONE, A., FERRO, R., 1995b, J. Alloys and Compounds, **220,** 167.
GIRGIS, K., 1983, in: "Physical Metallurgy", Cahn, R. W., Haasen, P., Eds., p. 219, (North-Holland Physics Publishing, Amsterdam).
GIRGIS K., VILLARS, P., 1985, Monatsh. Chemie, **116,** 417.
GLADYSHEVSKII, R.E., CENZUAL, K., PARTHÉ, E., 1992, J. Alloys and Compounds, **189,** 221.
GRIMM, H. G., SOMMERFELD, A., 1926, Z. Physik, **36,** 36.
GRIN', Yu. N., YARMOLYUK, Ya. P., GLADYSHEVSKII, E. I., 1982, Sov. Phys. Crystallogr., **27,** 413.
GRIN', Yu. N., AKSELRUD, L. G., 1990, Acta Crystallogr., **A46** Suppl. C 338.
GRIN' Yu. N., 1992, in :"Modern Perspectives in Inorganic Crystal Chemistry", A NATO Advanced Study Institute, Director Erwin Parthe', Lecture Notes of 19th Course, Ettore Majorana Centre for Scientific Culture, Erice (Trapani), (Italy).
GSCHNEIDNER, K. A., Jr., 1969, J. Less-Common Metals, **17,** 1.
GSCHNEIDNER, K. A., Jr., 1980, in: "Theory of Alloy Phase Formation", Bennett, L. H. Ed., Proceedings 108th AIME Annual Meeting, New Orleans, USA, February 19–20, 1979, p. 1.
GSCHNEIDNER, K. A., Jr., MCMASTERS, O. D., 1971, Monatsh. Chemie, **102,** 1499.
GUILLERMET, A. F., GRIMVALL, G., 1991, J. Less-Common Metals, **169,** 257.
GUILLERMET, A. F., FRISK, K., 1992, Calphad **16,** 341.
GUINIER, A., BOKIJ, G. B., BOLL-DORNBERGER, K., COWLEY, J. M., DUROVIC, S., JAGODZINSKI, H., KRISHNA, P., DE WOLFF, P. M., ZVYAGIN, B. B., COX, D. E., GOODMAN, P., HAHN, Th., KUCHITSU, K., ABRAHAMS, S. C., 1984, Acta Cryst., **A40,** 399.
HAFNER, J., 1985, J. Phys. F., **15,** L43.
HAFNER, J., 1989, in: "The Structures of Binary Compounds. Cohesion and Structure", Vol. 2: de Boer, F. R., Pettifor, D. G. (Eds.), (North-Holland, Amsterdam), p. 147.
HÄGG, G., 1931, Z. Phys., Chem., **B12,** 33.
HAHN, T., (Ed.), 1989, "International Tables for Crystallography", (Kluwer Academic Publishers, Dordrecht).
HANSEN, M., 1936, "Der Aufbau der Zweistofflegierungen", (Springer-Verlag, Berlin).
HANSEN, M., ANDERKO, K., 1958, "Constitution of Binary Alloys", (McGraw-Hill Book Company, New York).
HAWTHORNE, F. C., 1983, Acta Cryst., **A39,** 724.
HELLNER, E. E., 1979, in: "The Frameworks (Bauverbände) of the Cubic Structure Types", Structure and Bonding, Vol. 37, (Springer-Verlag, Berlin), p. 61.
HILLERT, M., 1981, Physica B, **103,** 30.
HOCH, M., ARPSHOFEN, I., PREDEL, B., 1984, Z. Metallkd., **75,** 30.
HOFFMANN, R., 1987, Angew. Chem. Int. Ed. Engl. **26,** 846.
HOFFMANN, R., 1988, "Solids and Surfaces", (VCH Publishers, New York).

HOPPE, R., 1979, Z. Kristallogr., **150**, 23.
HOPPE, R., MEYER, G., 1980, Z. Metallkd., **71**, 347.
HYDE, B. G., ANDERSSON, S., 1989, "Inorganic Crystal Structures", (J. Wiley & Sons, New-York).
HOVESTREYDT, E., 1988, J. Less-Common Metals, **143**, 25.
HUME-ROTHERY, J., 1926, J. Inst. Metals, **35**, 295.
HUME-ROTHERY, J., MABBOT, G. W., CHANNEL EVANS, K. M., 1934, Phil. Trans. Roy. Soc., **A 233**, 1.
HUME-ROTHERY, J., 1967, in: "Phase Stability in Metals and Alloys", Rudman, P. S., Stringer, J., Jaffee, R. I. Eds., (McGraw-Hill Book Company, New-York), p. 3.
IANDELLI, A., PALENZONA, A., 1979: in "Handbook on the Physics and Chemistry of Rare Earths", Vol. 2: Gschneidner, K. A., Jr., Eyring L. (Eds.), (North-Holland, Amsterdam), p. 1.
JAGODZINSKI, H., 1954, Acta Cryst., **7**, 17.
JEITSCHKO, W., PARTHÉ, E., 1967, Acta Cryst., **22**, 417.
JENSEN, W. B., 1984, in: "Communicating Solid-State Structures to the Uninitiated", Rochester, Institute of Technology, Rochester.
JENSEN, W. B., 1989, in: "The Structures of Binary Compounds. Cohesion and Structure", Vol. 2: de Boer, F. R., Pettifor, D. G. (Eds.), (North-Holland, Amsterdam), p. 105.
KAO, C. R., PIKE, L. M., CHEN, S. -L., CHANG, Y. A., 1994, Intermetallics, **2**, 235.
KAUFMAN, L., BERNSTEIN, H., 1970, "Computer Calculation of Phase Diagrams", Vol. 4, "Refractory Materials", (Academic Press, New-York).
KAUFMAN, L., NESOR, H., 1973, Ann. Rev. Mater. Sci., R. Huggins Ed., vol. 3. p. 1.
KHACHATURYAN, A. G., 1983, "Theory of Structural Transformations in Solids", (John Wiley & Sons, New York).
KING, H. W., 1983, in: "Physical Metallurgy", Cahn, R. W., Haasen, P., Eds., (North-Holland Physics Publishing, Amsterdam), p. 37.
KISELYOVA, N. N., 1993, J. Alloys and Compounds, **197**, 159.
KLEE, H., WITTE, H., 1954, Z. Phys. Chem., **202**, p. 352.
KRIPYAKEVICH, P. I., 1963, "A Systematic Classification of Types of Intermetallic Structures", from J. Structural Chemistry, vol. 4.
KRIPYAKEVICH, P. I., 1976, Sov. Phys. Crystallogr., **21**, 273.
KRIPYAKEVICH, P. I., GLADYSHEVSKII, E. I., 1972, Acta Cryst., **A28**, Suppl.,S97.
KRIPYAKEVICH, P. I., GRIN´, Yu. N., 1979, Sov. Phys. Crystallogr., **24**, 41.
KUBASCHEWSKI, O., EVANS, E. LL., 1958, "Metallurgical Thermochemistry", (Pergamon Press, London).
KUBASCHEWSKI, O., 1967, in: "Phase Stability in Metals and Alloys", Rudman, P. S., Stringer, J., Jaffee, R. I. Eds., (McGraw-Hill Book Company, New-York), p. 63.
LAMPARTER, P., STEEB, S., 1993 in: "Structure of Amorphous and Molten Alloys", Materials Science and Technology, Cahn, R. W., Haasen, P., Kramer, E. J., (Eds.), Vol. 1, (VCH, Weinheim).
LANDOLT-BÖRNSTEIN TABLES, 1971, "Structure Data of Elements and Intermetallic Phases", Vol. 6, Hellwege, K.-H., Hellwege, A. M. (Eds.); 1991, "Phasengleichgewichte, Kristallographische und Thermodynamische Daten Binaren Legierungen", MADELUNG, O., Ed. Vol. 5a, Predel, B., (Springer-Verlag, Berlin).
LATROCHE, M., SELSANE, M., GODART, C., SCHIFFMACHER, G., THOMPSON, J. D., BEYERMANN, W. P., 1992, J. Alloys and Compounds, **178**, 223.
LAVES, F., 1930, Z. Krist., **73**, 303.
LAVES, F., 1956, in: "Theory of Alloy Phases", (Amer. Soc. Met., Cleveland (Ohio)), p. 124.
LAVES, F., 1967, in: "Phase Stability in Metals and Alloys", Rudman, P. S., Stringer, J., Jaffee, R. I. Eds., (McGraw-Hill Book Company, New-York), p. 85.
LAVES, F., WITTE, H., 1936, Metallwirtschaft, **15**, 840.
LEIGH G. J. (Ed.), 1990, "Nomenclature of Inorganic Chemistry. Recommendations 1990", Issued by the Commission on the Nomenclature of Inorganic Chemistry, (Blackwell Scientific Publications, Oxford).
LIMA-DE-FARIA, J., FIGUEIREDO, M. O., 1976, J. Solid State Chem., **16**, 7.
LIMA-DE-FARIA, J., FIGUEIREDO, M. O., 1978, Garcia de Orto, Ser. Geol. **2**, 69.
LIMA-DE-FARIA, J., HELLNER, E., LIEBAU, F., MAKOVICKY, E., PARTHÉ, E., 1990, Acta Cryst., **A46**, 1.

LIU L. -G., BASSETT, W. A., 1986, "Elements, Oxides, and Silicates - High Pressure Phases with Implications for the Earth's Interior", Oxford Monographs on Geology and Geophysics, N. 4, (Oxford University Press, New York).
LU, S. S., CHANG, T., 1957a, Sci. Rec. Peking, **1**, 41.
LU, S. S., CHANG, T., 1957b, Acta. Phys. Sinica, **13**, 150.
LUKAS, H. L., HENIG, E-Th., ZIMMERMANN, B., 1977, CALPHAD, **1**, 225.
LUKAS, H. L., WEISS, J., HENIG, E.-Th., 1982, CALPHAD, **6**, 229.
MACHATSCHKI, F., 1938, Naturwissenschaften, **26**, 67.
MACHATSCHKI, F., 1947, Monatsh. Chemie, **77**, 333.
MACHATSCHKI, F., 1953, "Spezielle Mineralogie auf Geochemischer Grundlage", (Springer, Wien), p. 1 and p. 298.
MAKINO, Y., 1994a, Intermetallics, **2**, 55.
MAKINO, Y., 1994b, Intermetallics, **2**, 67.
MALLIK, A. K., 1987, J. Alloy Phase Diagrams (Indian Institute of Metals), **3**, 12.
MANDELBROT, B., 1951, C. R. Acad. Sc., Paris, **232**, p. 1638.
MARAZZA, R., ROSSI, D., FERRO, R., 1980, J. Less-Common Metals, **75**, P25.
MARAZZA, R., ROSSI, D., FERRO, R., 1988, J. Less-Common Metals, **138**, 189.
MARTYNOV, A. I., BATSANOV, S. S., 1980, Russian J. Inorg. Chem., **25**, 1737.
MASSALSKI, T. B. (Editor in Chief), 1990, "Binary Alloy Phase Diagrams", Vol. 1–3, Second edition: Okamoto, H., Subramanian, P. R., Kacprzak, L. (Eds.), (ASM International, USA).
MASSALSKI, T. B., 1989, Metall. Trans., **20A**, 1295.
MELNIK, E. V., KRIPYAKEVICH, P. I., 1974, Kristallografiya, **19**, 645.
MERLO, F., 1988, J. Phys. F: Met. Phys., **18**, 1905.
MIEDEMA, A. R., 1973, J. Less-Common, Metals, **32**, 117.
MIEDEMA, A. R., NIESSEN, A. K., 1982, Physica **114B**, 367.
MIODOWNIK, A. P., 1993, in "Computer Aided Innovation of New Materials", M. DOYAMA *et al.* Eds., (Elsevier), p. 689.
MOFFATT, W. G., 1986, "The Handbook of Binary Phase Diagrams", Vol. 1–5, (Genium Publishing Corporation, Schenectady, New York).
MOORE, J. S., 1993, Nature, **365**, 690.
MOOSER, E., PEARSON, W. B., 1959, Acta Cryst., **12**, 1015.
MORRIS, D. G., 1992, in: "Ordered Intermetallics - Physical Metallurgy and Mechanical Behaviour", Liu, C. T., Cahn, R. W. and Sauthoff, G., (Eds.), (Kluwer Academic Publishers, Dordrecht).
NIESSEN, A. K., DE BOER, F. R., BOOM, R., DE CHATEL, P. F., MATTENS, W. C. M., MIEDEMA, A. R., 1983, CALPHAD, **7**, 51.
NIGGLI, P., 1945, Grundlagen der Stereochemie, (Birkhäuser, Basel), p. 125.
NIGGLI, P., 1948, Gesteine und Minerallagerstätten, Vol. 1, (Birkhäuser, Basel), p. 42.
OCHIAI, S., OYA, Y., SUZUKI, T., 1984, Acta Metall., **32**, 289.
OKAMOTO, H., MASSALSKI, T. B., CHAKRABARTI, D. J., LAUGHLIN, D. E., 1987 in: "Phase Diagrams of Binary Gold Alloys", Monograph Series on Alloy Phase Diagrams, Okamoto, H. and Massalski, T. B., (Eds.), (ASM International, USA), p. 76.
O'KEEFFE, M. O., 1979, Acta Cryst., **A35**, 772.
PANI, M., FORNASINI, M. L., 1990, Z. Kristallogr., **190**, 127.
PARTHÉ, E., 1961, Z. Krystallogr., **115**, 52.
PARTHÉ, E., 1963, Z. Krystallogr., **119**, 204.
PARTHÉ, E., 1964, "Crystal Chemistry of Tetrahedral Structures", (Gordon and Breach Publishers, New-York).
PARTHE, E., 1969 in: "Developments in the Structural Chemistry of Alloy Phases", Giessen, B. C. (Ed.), (Plenum Press, New York), p. 49.
PARTHÉ, E., 1980a, Acta Crystallogr., **B 36**, 1.
PARTHÉ, E., 1980b, "Valence and Tetrahedral Structure Compounds", in: Summer School on Inorganic Crystal Chemistry, Geneva, ed. E. Parthé (Parthé, Geneva).
PARTHÉ, E., 1991, J. Phase Equilibria, **12**, 404.

PARTHÉ, E., CHABOT, B., 1984 in : "Handbook on the Physics and Chemistry of Rare Earths", Vol. 6: Gschneidner, K. A., Jr., Eyring L. (Eds.), (North-Holland, Amsterdam), p. 113.
PARTHÉ, E., GELATO, L. M., 1984, Acta Cryst., **A40**, 169.
PARTHÉ, E., CENZUAL, K., GLADYSHEVSKII, R. E., 1993, J. Alloys and Compounds, **197**, 291.
PARTHÉ, E. Chabot, B. A., CENZUAL, K., 1985, Chimia, **39**, 164.
PAULING, L., 1932, J. Amer. Chem. Soc., **54**, 988.
PAULING, L., 1947, J. Amer. Chem. Soc., **69**, 542.
PEARSON, W. B., 1967, "A Handbook of Lattice Spacings and Structures of Metals and Alloys", Vol. 2, (Pergamon Press, Oxford).
PEARSON, W. B., 1972, "The Crystal Chemistry and Physics of Metals and Alloys", (Wiley-Interscience, New-York).
PEARSON, W. B., 1980, Z. Kristallogr. **151**, 301.
PEARSON, W. B., 1985a, J. Less-Common Metals, **114**, 17.
PEARSON, W. B., 1985b, J. Less-Common Metals, **109**, L3.
PEARSON, W. B., VILLARS, P., 1984, J. Less-Common Metals, **97**, 119.
PETTIFOR, D. G., 1984, Solid State Communications, **51**, 31.
PETTIFOR, D. G., 1985, J. Less-Common Metals, **114**, 7.
PETTIFOR, D. G., 1986a, J. Phys. C.: Solid State Phys., **19**, 285.
PETTIFOR, D. G., 1986b, New Scientist, May **29**, 48.
PETTIFOR, D. G., 1988a, Physica B, **149**, 3.
PETTIFOR, D. G., 1988b, Materials Science and Technology, **4**, 675.
PETZOW, G., EFFENBERG, G. (Editors), 1988 *et seq.*, "Ternary Alloys. A Comprehensive Compendium of Evaluated Constitutional Data and Phase Diagrams", (VCH, Weinheim-Germany).
PRINCE, A., 1991, "Aluminium-Copper-Nickel" in: "Ternary Alloys. A Comprehensive Compendium of Evaluated Constitutional Data and Phase Diagrams", Vol. 4, G. Petzow and G. Effenberg (Eds), (VCH, Weinheim-Germany).
RAGHAVAN, V., ANTIA, D. P., 1994, J. Phase Equilibria, **15**, 42.
RAJASEKHARAN, T., GIRGIS, K., 1983, Physical Review B, **27**, 910.
REEHUIS, M., JEITSCHKO, W., MÖLLER, M. H., BROWN, P. J., 1992, J. Phys. Chem. Solids, **53**, 687.
REIJERS, H. T. J., SABOUNGI, M. -L., PRICE, D. L., VAN DER LUGT, W., 1990, Phys. Rev., **B41**, 5661. J.
RODGERS, J. R., VILLARS, P., 1993, J. Alloys and Compounds, **197**, 167.
ROGL, P., 1984, in : "Handbook on the Physics and Chemistry of Rare Earths", Vol. 6: Gschneidner, K. A., Jr., Eyring L. (Eds.), (North-Holland, Amsterdam), p. 335.
ROGL, P., 1985, J. Less-Common Metals, **110**, 283.
ROGL, P., 1991, in: "Inorganic Reactions and Methods", A. Hagen, Ed., Vol. 13, (VCH-Publishers, New-York), p. 85.
ROSSI, D., MARAZZA, R., FERRO, R., 1979, J. Less-Common Metals, **66**, P17.
SACCONE, A., DELFINO, S., FERRO, R., 1990, CALPHAD, **14**, 151.
SACCONE, A., MACCIÓ, D., DELFINO, S., FERRO, R., 1995, J. Alloys and Compounds, **220**, 161.
SAMSON, S., 1967, Acta Cryst., **23**, 586.
SAMSON, S., 1969, in: "Development in the Structural Chemistry of Alloy Phases": Giessen, B. C. (ed.), (Plenum Press, New York), p. 65.
SAVITSKII, E. M., GRIBULYA, V. B., KISELYOVA, N. N., 1980, J. Less-Common Metals, **72**, 307.
SCHUBERT, K., 1964, "Kristallstrukturen zweikomponentiger Phasen", (Springer-Verlag, Berlin).
SCHWOMMA, O., NOWOTNY, H., WITTMANN, A., 1964a, Monatsh. Chemie, **95**, 1538.
SCHWOMMA, O., PREISINGER, A., NOWOTNY, H., WITTMANN, A., 1964b, Monatsh. Chemie, **95**, 1527.
SERENI, J. G., 1984, J. Phys. Chem. Solids, **45**, 1219.
SHOEMAKER, C. B., SHOEMAKER, D. P., 1969, in: "Development in the Structural Chemistry of Alloy Phases": Giessen, B. C. (ed.), (Plenum Press, New York), p. 107.
SHUNK, F. A., 1969, "Constitution of Binary Alloys", Second Supplement, (McGraw-Hill Book Company, New York).
SIMON, A., 1983, Angew. Chem. Int. Ed. Engl., **22**, 95.
SINGH, R. N., SOMMER, F., 1992, Z. Metallkd., **83**, 533.

SOMMER, F., 1982, Z. Metallkd., **73**, 77.
SOMMER, F., PREDEL, B., BORZONE, G., PARODI, N., FERRO, R., 1995, Intermetallics, **3**, 15.
SUNDMAN, B., JANSSON, B., ANDERSSON, J. -O., 1985, CALPHAD, **9**, 153.
SZYTULA, A., 1992, J. Alloys and Compounds, **178**, 1.
TEATUM, E. T., GSCHNEIDNER, K. A., Jr., WABER, J. T., 1968, "Compilation of Calculated Data Useful in Predicting Metallurgical Behavior of the Elements in Binary Alloy Systems", Report LA-4003, UC-25, Metals, Ceramics and Materials, TID-4500, Los Alamos Scientific Laboratory.
VAN DER LUGT, W., GEERTSMA, W., 1984, Proc. LAM V, 187.
VAN VUCHT, J. H. N., BUSCHOW, K. H. J., 1965, J. Less-Common Metals, **10**, 98.
VASSILIEV, V., GAMBINO, M., BROS, J.P., BORZONE, G., CACCIAMANI, G., FERRO, R., 1993, J. Phase Equilibria, **14**, 142.
VEGARD, L., 1921, Z. Phys., **5**, 17.
VILLARS, P., 1983, J. Less-Common Metals, **92**, 215.
VILLARS, P., 1985, J. Less-Common Metals, **109**, 93.
VILLARS, P., CALVERT, L. D., 1985, "Pearson's Handbook of Crystallographic Data for Intermetallic Phases", Vol 1–3, 1st Edition, (Materials Park, Oh 44073: American Society for Metals).
VILLARS, P., CALVERT, L. D., 1991, "Pearson's Handbook of Crystallographic Data for Intermetallic Phases", Vol. 1–4, 2nd Edition, (Materials Park, Oh 44073: American Society for Metals).
VILLARS, P., DAAMS, J. L. C., 1993, J. Alloys and Compounds, **197**, 177.
VILLARS, P., GIRGIS, K., 1982, Z. Metallkd., **73**, 455.
VILLARS, P., HULLIGER, F., 1987, J. Less-Common Metals, **132**, 289.
VILLARS, P., MATHIS, K., HULLIGER, F., 1989 in: "The Structures of Binary Compounds. Cohesion and Structure", Vol. 2: de Boer, F. R., Pettifor, D. G. (Eds.), (North-Holland, Amsterdam), p. 1.
WELLS, A. F., 1970, "Models in Structural Inorganic Chemistry", (Oxford University Press, London).
WENSKI, G., MEWIS, A., 1986, Z. Anorg. Allg. Chem., **543**, 49.
WESTBROOK, J. H., 1977, Metall. Trans., **8A**, 1327.
WESTGREN, A. F., PHRAGMEN, G., 1926, Z. Metallkd., **18**, 279.
WONDRATSCHEK, H., JEITSCHKO, W, 1976, Acta Crystallogr. **32A**, 664.
YATSENKO, S. P., SEMYANNIKOV, A. A., SEMENOV, B. G., CHUNTONOV, K. A., 1979, J. Less-Common Metals, **64**, 185.
YATSENKO, S. P., SEMYANNIKOV, A. A., SHAKAROV, H. O., FEDOROVA, E. G., 1983, J. Less-Common Metals, **90**, 95.
ZEN, E-an, 1956, Amer. Min., **41**, 523.
ZHDANOV, G. S., 1945, C. R. Acad. Sc., USSR, **48**, 39.
ZINTL, E., WOLTERSDORF, G., 1935, Z. Elektrochem., **41**, 876.
ZIPF, G. K., 1949, "Human Behavior and the Principle of Least Effort", Addison-Wesley Press.
ZUNGER, A., 1981, in: "Structure and Bonding in Crystals", Vol. I: O'Keeffe, M. and Navrotski, A. (Eds.), Academic Press, New-York), p. 73.
ZVYAGIN, B. B., 1987, Sov. Phys. Crystallogr., **32(3)**, 394.
ZVYAGIN, B. B., 1993, Sov. Phys. Crystallogr. Rep., **38**, 54.

Note: A very recent publication (Intermetallic Compounds — Principles and Practice, eds. J. H. Westbrook and R. L. Fleischer, Wiley, Chichester, 1995) includes a group of ten substantial chapters devoted to the crystal structures and crystal chemistry of intermetallic compounds and phases (Vol. 1, pages 225–491). A large collection of data has been reported in the "Handbook of Ternary Alloy Phase Diagrams", by P. Villars, A. Prince and H. Okamoto (Ten-Volume Set, ASM International, 1995): binary and ternary crystallographic data are included with ternary diagrams.

APPENDIX TO CHAPTER 4

THE STRUCTURE OF QUASICRYSTALS

WALTER STEURER

Institute of Crystallography
ETH-Zentrum, CH-8092 Zürich
Switzerland

R. W. Cahn and P. Haasen†, eds.
Physical Metallurgy; fourth, revised and enhanced edition

1. Introduction

The first years of quasicrystal structure analysis were marked by the investigation of badly characterized samples with non-crystallographic diffraction symmetry, called "quasicrystals" for short, with spectroscopic and powder diffraction techniques. It was

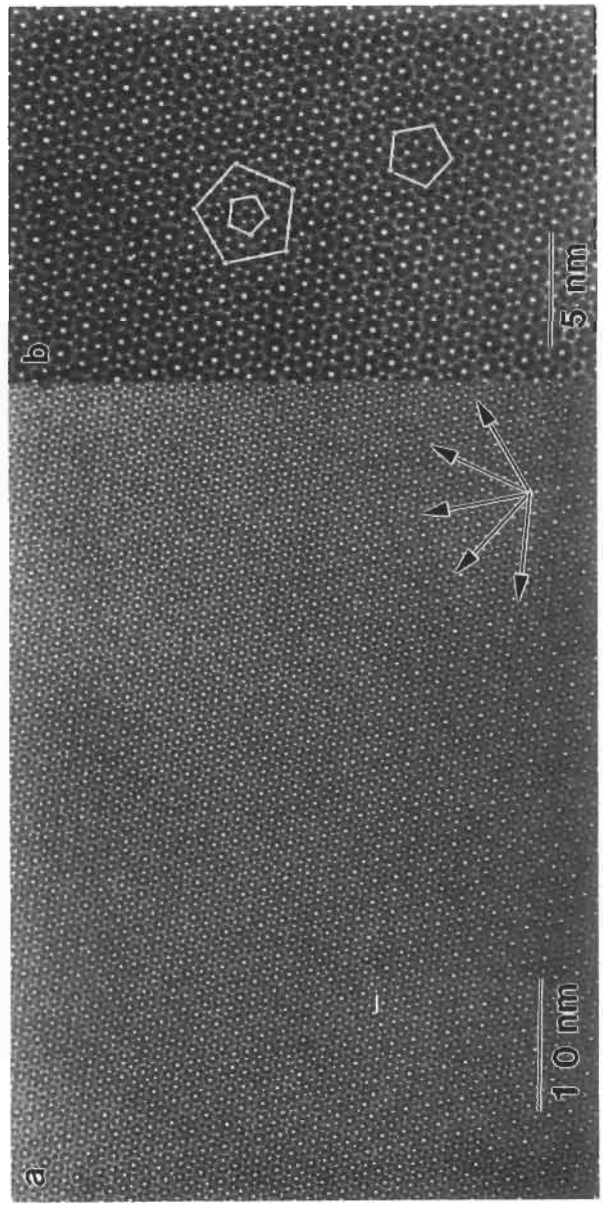

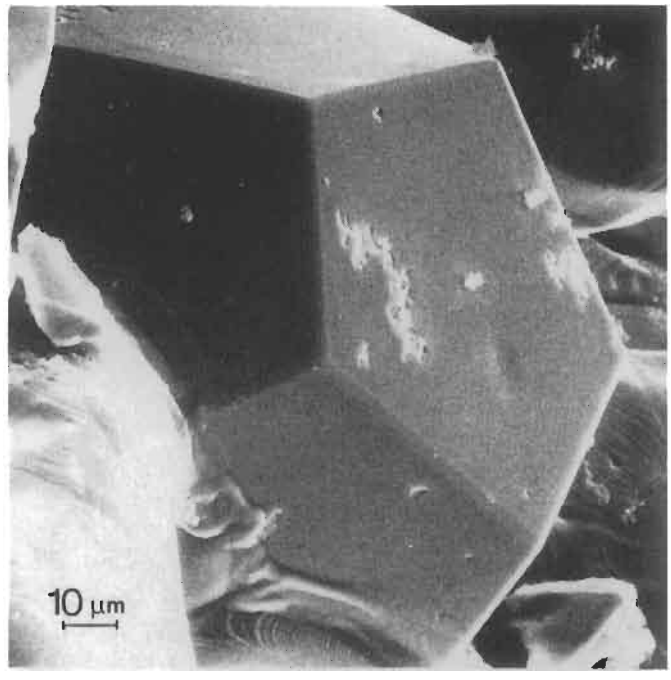

(c)

Fig. A1. (a) HRTEM image of perfectly ordered icosahedral $Al_{65}Cu_{20}Fe_{15}$ with enlarged part in (b) (from HIRAGA, ZHANG, HIRABAYASHI, INOUE and MASUMOTO [1988], and (c) REM photograph of a single crystal with pentagon-dodecahedral morphology (from TSAI, INOUE and MASUMOTO [1987].

not at all clear whether these samples were homogenous and quasiperiodically ordered (fig. A1), whether they were twinned approximants (fig. A2), i.e. closely related structures with huge unit cells, or had rather a kind of complicated crystalline nano-domain structure. The generalization of models based on single experimental results caused confusion in many cases until investigation learnt that the experimental findings were strongly dependent on chemical composition, thermal history and growth conditions of the samples. It turned out that most stable quasicrystals transform to crystalline phases at lower temperature or higher pressure running through intermediate states with sometimes complicated modulated and/or nanodomain structures. Some structural principles of quasicrystals and their relationships to approximants are now fairly well understood: both the quasiperiodic and periodic related structures are built from the same clusters. Whether the structural units order periodically or quasiperiodically can be influenced by slight changes in composition for stable samples and also by the annealing conditions for metastable ones.

References: p. 408.

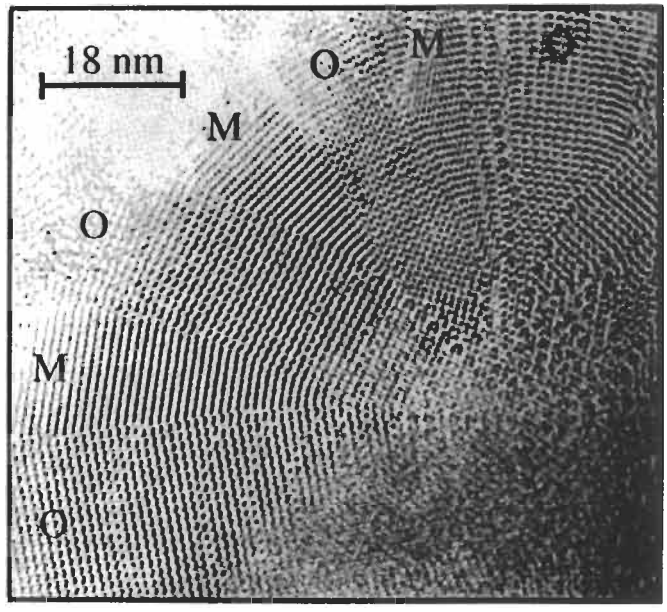

Fig. A2. Twinned $Al_{11}Mn_4$–Pd approximant with pseudo-tenfold diffraction symmetry. O and M mark the orthorhombic, and monoclinic phases, respectively (from DAULTON and KELTON [1993]).

2. *Description of quasiperiodic structures*

Regular crystal structures can be characterized by the dimensions of the unit cell, the space group, and the information what atoms occupy which Wyckoff position (cf. chapter 1 of this volume). The space group includes the information about the crystal system, the Bravais lattice type, atomic coordinates and site symmetries. A comparable description for quasiperiodic structures is possible in terms of the higher-dimensional approach (JANSSEN [1986]). Another way is the structure description by a quasilattice (quasiperiodic tiling) with two or more different unit cells, its symmetry and decoration with atomic clusters.

2.1. Decoration of quasiperiodic tilings

The classical example of a quasiperiodic tiling with five-fold orientational symmetry is the Penrose tiling (PT) (fig. A3). It can be constructed by two types of unit cells, a fat rhomb (72° and 108° angles) and a skinny rhomb (36° and 144° angles) with edge lengths all equal to a_r, and areas in the ratio τ:1, like their frequencies in the tiling. The irrational number τ, related to the golden mean, is the solution of the algebraic equation $\tau^2-\tau-1=0$, and has the value $\tau=\frac{1+\sqrt{5}}{2}=2\cos 36°=1.6180\ldots$. Since the unit tiles can also be arranged periodically or randomly, local matching rules are necessary to obtain a quasiperiodic tiling. The PT has the following characteristic properties (PAVLOVITCH and KLEMAN [1987]; LEVINE and STEINHARDT [1986]):

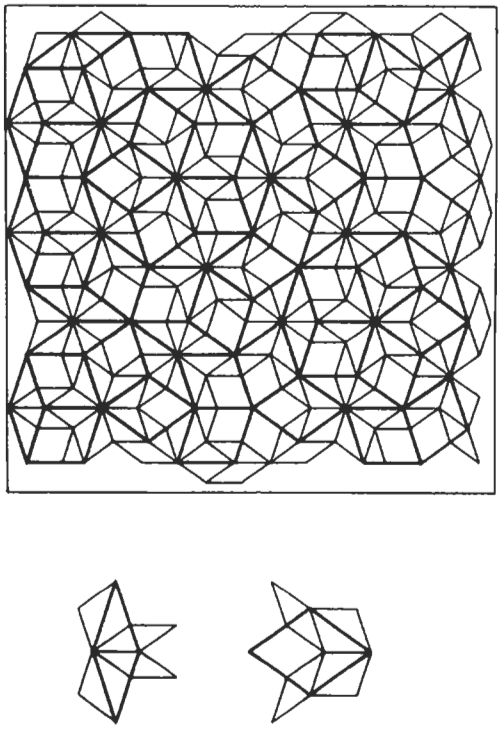

Fig. A3. Penrose tiling (bold lines) with deflated tiling drawn in (light lines). The deflation rules for the fat, and skinny rhombs are also shown in the lower part of the drawing. The edge lengths of the deflated tiles are smaller by a factor τ than the original ones (from SOCOLAR and STEINHARDT [1986]).

Quasiperiodic translational order: there is no nontrivial translation leaving the tiling invariant. The mass density function is quasiperiodic, i.e. it can be expressed as a finite sum of periodic functions with periods incommensurate to each other. For example, the function is quasiperiodic $f(x) = \cos x + \cos ax$ if a is an irrational algebraic number (i.e., an irrational solution of an equation of the type $a_n x^n + a_{n-1} x^{n-1} + ... a_0 = 0$).

Orientational order: each edge of each unit tile is oriented along one of the set of orientational star axes. Except in singular cases, there is no rotational or mirror symmetry in a quasiperiodic tiling.

Indeterminacy of the construction process: the infinite pattern is not determined by a finite region. Starting from a finite region allows an uncountable infinity of ways to continue the construction. All resulting tilings belong to the same local isomorphism class and are homometric structures (i.e., have the same diffraction patterns).

Local isomorphism: any region, however large it might be, belonging to a given infinite tiling, can be found in any other different (i.e., non superposable) tiling.

References: p. 408.

Self-similarity: to any PT a different PT can be associated, whose tiles are smaller by a factor τ and which includes all the vertices of the former tiling (this operation is termed *deflation*). The local matching rules can be obtained from the deflation operation.

The Penrose tiling may serve as quasilattice for structures with two-dimensional quasiperiodicity and five-fold orientational order (decagonal phases). A three-dimensional variation of the PT, with prolate and oblate rhombohedra for unit cells (their volumes in the ratio τ:1 like their frequencies) may represent a quasilattice for the icosahedral quasicrystals (fig. A4).

In the course of a normal crystal structure analysis, the determination of the correct crystal lattice, which has to be one of the 14 Bravais lattices, never poses any problems. In the case of quasicrystal structure analysis, however, for a given diffraction symmetry an infinite number of different quasilattices are possible. Thus, the selection of the quasilattice cannot be separated from the determination of the quasicrystal structure itself. Helpful as the tiling approach may be for the understanding of the geometrical principles of a quasicrystal structure, it is not suited for performing *ab initio* structure analyses of quasicrystals. This has to be done by means of the higher-dimensional approach.

2.2. Higher-dimensional approach

Quasiperiodic structures can always be decribed as sections of higher-dimensional periodic structures (JANSSEN [1986]). Five-fold rotational symmetry, for instance, which is incompatible with three-dimensional translational order, can be a symmetry operation of a four-dimensional lattice. Thus, non-crystallographic symmetries in the three-dimensional space $\mathbb{R}^3$ can become crystallographic in $\mathbb{R}^n$ space. It is quite natural, consequently, to describe quasiperiodic structures with their non-crystallographic symmetries as periodic structures in the $\mathbb{R}^n$. For the axial quasicrystals, which are quasiperiodic in two dimensions and periodic in the third one, the five-dimensional embedding space $\mathbb{R}^5$ is necessary. The icosahedral phases can be embedded in the $\mathbb{R}^6$, and one-dimensional quasicrystals in the $\mathbb{R}^4$.

The principles of the higher-dimensional embedding method are demonstrated on the

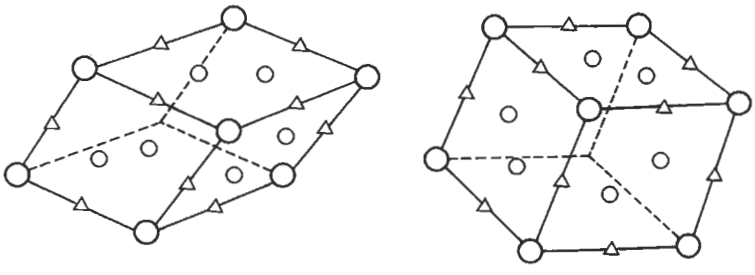

Fig. A4. Prolate (left), and oblate (right) rhombohedron, the unit tiles of the three-dimensional Penrose tiling, with special sites marked.

simple example of the one-dimensional quasiperiodic Fibonacci sequence, which can be described as a quasiperiodic section of a two-dimensional periodic lattice (fig. A5).

The Fibonacci sequence may be obtained from the substitution rule

$$\begin{pmatrix} L \\ S \end{pmatrix} \rightarrow \begin{pmatrix} 1 & 1 \\ 1 & 0 \end{pmatrix} \begin{pmatrix} L \\ S \end{pmatrix} = \begin{pmatrix} L+S \\ L \end{pmatrix},$$

where L denote 'long' and S denotes 'short'. Starting with L one obtains the sequences

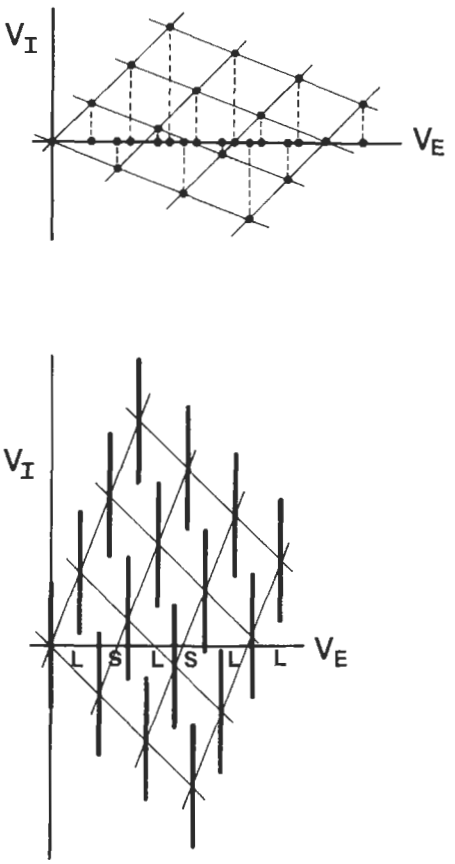

Fig. A5. Embedding of a one-dimensional quasicrystal with point atoms in the $\mathbb{R}^2$. The observed diffraction pattern of the Fibonacci sequence in the physical (external, parallel) space $\mathbf{V}_E$ corresponds to a projection of an appropriate two-dimensional reciprocal lattice down the complementary (external, perpendicular) space $\mathbf{V}_I$ (upper drawing). The quasiperiodic structure, connected via Fourier transform with reciprocal space, consequently results from a section of $\mathbf{V}_E$ with the two-dimensional hypercrystal. Since the slope of $\mathbf{V}_E$ is irrational with regard to the lattice vectors, the hyperatoms have to be extended (line-shaped) to get a non-empty intersection (lower drawing).

References: p. 408.

sequence	number of L	S
L	1	0
LS	1	1
LSL	2	1
LSLLS	3	2
LSLLSLSL	5	3
LSLLSLSLLSLLS	8	5
LSLLSLSLLSLLSLSLLSLSL	13	8
.	.	.
.	.	.
.	.	.
.	F_{n+1}	F_n

where $F_n = F_{n-1} + F_{n-2}$ are the Fibonacci numbers with $\lim_{n\to\infty} \frac{F_{n+1}}{F_n} = \tau$.

One finds that the substitution rule always leaves the existing sequence invariant. Thus, it corresponds to a self-similarity operation in the case of an infinite Fibonacci sequence. Replacing the letters L and S by intervals of length τ and 1 one gets, because of the relation

$$\frac{L}{S} = \frac{L+S}{L} = \tau$$

a structure invariant under scaling by a factor τ^n, n being an integer.

In fig. A6 the correlation between hyperatoms in the five-dimensional description and the actual quasiperiodic structure is illustrated on the example of decagonal $Al_{70}Co_{15}Ni_{15}$ (cf. section 3.2.2).

One big advantage of the higher-dimensional approach is that the structural information can be given in closed form. It is mainly contained in the position and shape of the hyperatoms. In terms of the tiling-decoration method, it would not be sufficient to define the type of tiling (what needs not always be possible in closed form) and the decoration of the unit tiles since, generally, the decoration can be context dependent.

2.3. Symmetry of quasicrystals

A first classification of quasicrystals, without knowing anything about their structure, can be performed by means of their diffraction symmetry. As for regular crystals, the diffraction symmetry is equivalent to the centrosymmetric point group related to the space group of the crystal structure. Experimentally observed have been phases with diffraction symmetries 8/mmm, 10/mmm, 12/mmm, and $m\bar{3}\bar{5}$ so far, called *octagonal, decagonal, dodecagonal* and *icosahedral* phases, respectively. Systematically absent reflections in the diffraction patterns (fig. A7) allow the assignment of centered lattices and symmetry elements with translation components in the higher-dimensional description.

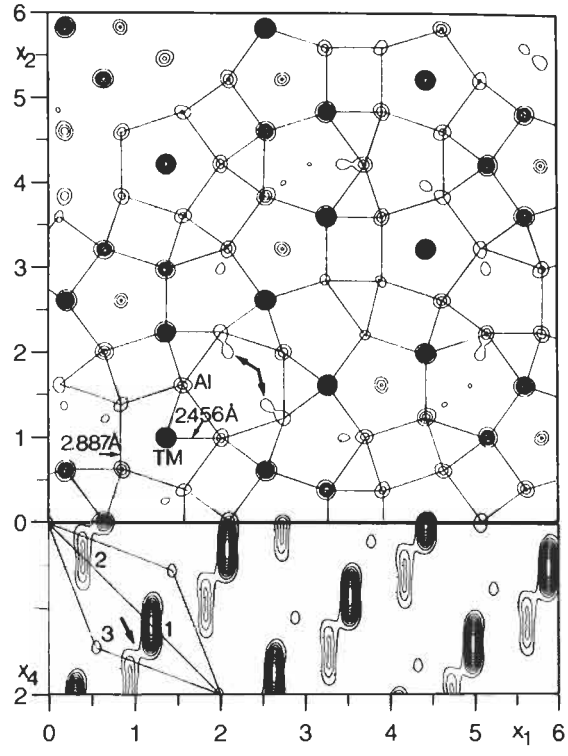

Fig. A6. Physical space electron density map (atomic structure in the (x_1, x_2)-plane) of decagonal $Al_{70}Co_{15}Ni_{15}$ with aluminum, and transition metal atoms, bond lengths, and pentagon-rectangle structure motifs marked (upper part of the drawing). In the lower part of the drawing, a section containing the perpendicular-space direction x_4 is shown to visualize the generation of real atoms from the hyperatoms marked 1, 2, and 3. The outline of one unit cell is also drawn in.

Fortunately, the number of possible superspace groups is very limited owing to the restriction that the corresponding point group has always to leave invariant the point group of the physical subspace. Thus, for the icosahedral phase, the combination of the three Bravais groups, generating the primitive (P), the body-centered (I) and the face-centered (F) hypercubic lattice, with the point groups 235 and $m\bar{3}\bar{5}$, produces only six symmorphous and five non-symmorphous superspace groups: P235, $P235_1$, I235, $I235_1$, F235, $F235_1$, $P2/m\bar{3}\bar{5}$, $P2/q\bar{3}\bar{5}$, $I2/m\bar{3}\bar{5}$, $F2/m\bar{3}\bar{5}$, $F2/q\bar{3}\bar{5}$.

3. *The structure of quasicrystals and approximants*

Depending on the preliminary character of our present knowledge of the real structure of quasicrystals, the following classification and description of quasicrystal structures may be revised in future. The fundamental relationships between quasicrystals and

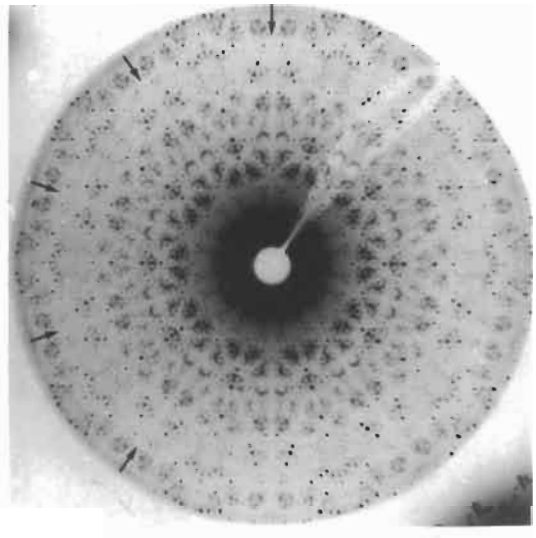

Fig. A7. First-layer X-ray precession photograph of decagonal $Al_{70.5}Mn_{16.5}Pd_{13}$ with symmetry 10/mmm. The zonal systematic extinctions (marked by arrows) obey tenfold symmetry.

*approximants** seem to be fairly reliable, however. The metastable quasicrystals mentioned in the following have all been prepared by rapid solidification methods (melt-spinning or splat-cooling); stable quasicrystals have been grown from the melt in the same way as any other metal crystals.

3.1. One-dimensional quasicrystals

There are only a few, mostly metastable phases known which are periodic in two dimensions and quasiperiodic in the third one (table A1). The structural units in these phases are ordered along one direction similarly to a Fibonacci sequence (*Fibonacci phases*). Well-studied examples are Al–Pd, Al–Cu and Al–Cu–Ni phases with basic cP2–CsCl type structure and vacancies ordered quasiperiodically along the [111] direction (CHATTOPADHYAY, LELE, THANGARAJ and RANGANATHAN [1987]). Fibonacci phases also often occur as intermediate states during the transition icosahedral ↔ crystalline or decagonal ↔ crystalline phase. Examples of the latter case were found in the systems Al–Ni–Si, Al–Co–Cu and Al–Cu–Mn (HE, LI, ZHANG and KUO [1988]; LI and KUO [1993]).

A stable one-dimensional quasicrystal as transformation product from the decagonal phase was found in a fully annealed $Al_{65}Cu_{20}Fe_{10}Mn_5$ sample. It has six-layer periodicity

* A crystalline phase with a structure closely related to that of a quasicrystal is called an *approximant*. If both structures can be transformed into each other by a rotation in superspace the crystalline phase is called a *rational approximant*.

Table A1
Systems with one-dimensional quasiperiodic (Fibonacci) phases (approximate compositions given). Stable decagonal phases are marked by a star.

GaAs–AlAs	artificial	TODD, MERLIN, CLARKE, MOHANTY and AXE [1986]
Mo–V	artificial	KARKUT, TRISCONE, ARIOSA and FISCHER [1986]
Al–Pd, Al–Cu–(Ni)		CHATTOPADHYAY, LELE, THANGARAJ and RANGANATHAN [1987]
$Al_{80}Ni_{14}Si_6$ $Al_{65}Cu_{20}Mn_{15}$ $Al_{65}Cu_{20}Co_{15}$		HE, LI, ZHANG and KUO [1988]
$*Al_{65}Cu_{20}Fe_{10}Mn_5$		TSAI, INOUE, MASUMOTO, SATO and YAMAMOTO [1992]
$*Al_{75}Fe_{10}Pd_{15}$		TSAI, MASUMOTO and YAMAMOTO [1992]

along the original tenfold axis and eight-layer periodicity perpendicular to it (TSAI, INOUE, MASUMOTO, SATO and YAMAMOTO [1992]). Another one was prepared from slowly cooled $Al_{75}Pd_{15}Fe_{10}$ (TSAI, MATSUMOTO and YAMAMOTO [1992]). Its structure can be derived from a decagonal quasicrystal by introducing a finite linear phason strain.*

By means of molecular beam epitaxy, Fibonacci phases were constructed from GaAs and AlAs layers (TODD, MERLIN, CLARKE, MOHANTY and AXE [1986]), as well as from Mo and V layers (KARKUT, TRISCONE, ARIOSA and FISCHER [1986]), in order to study their physical properties.

3.2. Two-dimensional quasicrystals

Two-dimensional quasicrystals consist of quasiperiodically ordered atomic layers which are stacked periodically. They combine the structural characteristics of both quasicrystals and regular crystals in one and the same sample. According to their diffraction symmetry octagonal, decagonal and dodecagonal quasicrystals are known so far.

3.2.1. Octagonal phases

The known octagonal phases (table A2) are all metastable and closely related to the cP20–βMn type, whose lattice parameter, $a = 6.315$ Å, is preserved along the translationally periodic direction of the quasiperiodic phases (fig. A8).

* A strain field introduced parallel to the perpendicular space is called a *phason-strain field.* In the case of a uniform shift of the hyperatoms along the perpendicular space coordinates one gets a *linear phason-strain field.* This is equivalent to rotating the hypercrystal relative to to the parallel space, producing a rational approximant.

Table A2
Systems with octagonal phases (approximate compositions given). In the second column the translation period along the eight-fold axis is given.

$Ni_{10}SiV_{15}$	6.3Å	WANG, CHEN and KUO [1987]
$Cr_5Ni_3Si_2$	6.3Å	
Mn_4Si	6.2Å	CAO, YE and KUO [1988]
$Al_3Mn_{82}Si_{15}$	6.2Å	WANG, FUNG and KUO [1988]
Fe–Mn–Si		WANG and KUO [1988]

3.2.2. Decagonal phases

Decagonal phases (table A3) are built in many cases from quasiperiodically packed columnar clusters with eigensymmetry $10_5/mmc$ or 10_5mc. The clusters are periodic along their tenfold axes, their translation periods can be ~4 Å, ~8 Å, ~12 Å, ~16 Å, ~24 Å and ~36 Å corresponding to stackings of 2, 4, 6, 8, 12 and 18 flat or puckered atomic layers. All decagonal phases have needle-like decaprismatic crystal morphology, indicating preferred crystal growth along the periodic direction (fig. A9).

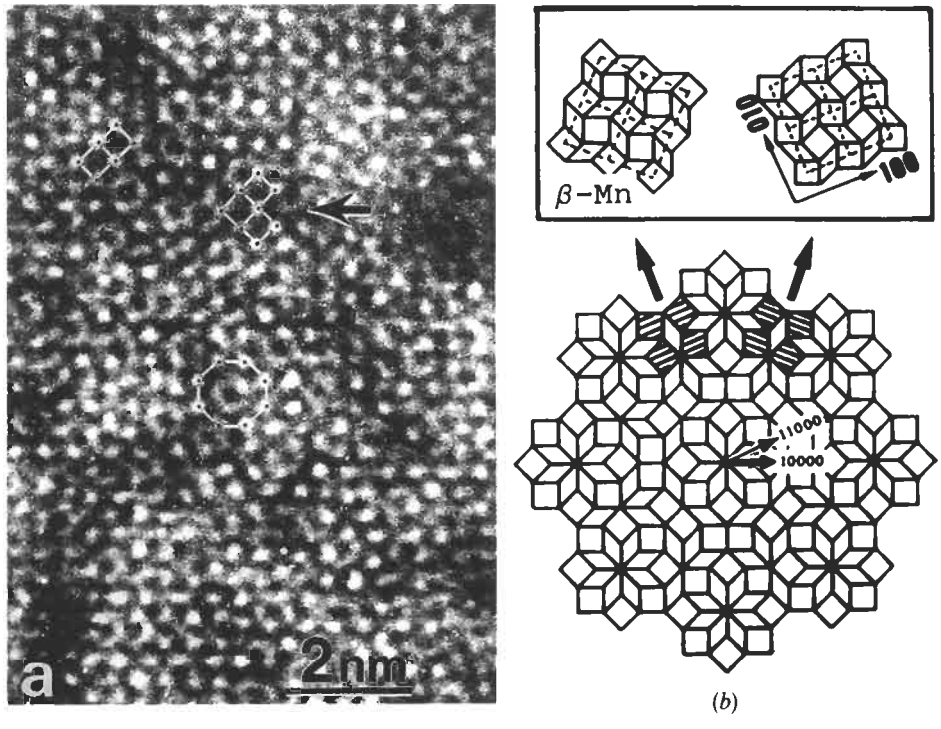

Fig. A8. (a) HRTEM image taken from octagonal Cr–Ni–Si. Nuclei of the β-Mn structure are marked by an arrow. (b) A tiling model of the octagonal phase with β-Mn structure units (hatched) indicated (from WANG and KUO [1990]).

Table A3

Systems with decagonal phases (approximate compositions given). In the second column the translation period along the tenfold axis is given. In the third column the closely related crystalline phase (approximant) is listed. Stable decagonal phases are marked by stars.

*$Al_{65}Co_{15}Cu_{20}$	4 Å	$Al_{13}Co_4$	STEURER and KUO [1990]
*$Al_{70}Co_{15}Ni_{15}$	4 Å	$Al_{13}Co_4$	STEURER, HAIBACH, ZHANG, KEK and LÜCK [1993]
*$Al_{70}Ni_{15}Rh_{15}$	4 Å	$Al_{13}Co_4$	TSAI, INOUE and MASUMTO [1989]
*$Al_{65}Cu_{15}Rh_{20}$	4 Å	$Al_{13}Co_4$	
*$Al_{71}Fe_5Ni_{24}$	4 Å	$Al_{13}Co_4$	LEMMERZ, GRUSHKO, FREIBURG and JANSEN [1994]
$Al_{75}Cu_{10}Ni_{15}$	4 Å		ZHANG and KUO [1989]
Al_4Ni	4 Å		LI and KUO [1988]
$Fe_{52}Nb_{18}$	4 Å	Zr_4Al_3	HE, YANG and YE [1990]
*$Al_{10}Co_4$	8Å	$Al_{13}Co_4$	MA and KUO [1994]
Al_4Mn	12 Å	μ-Al_4Mn	STEURER [1991]
$Al_{79}Fe_{2.6}Mn_{19.4}$	12 Å		MA and STERN [1987]
*$Al_{70.5}Mn_{16.5}Pd_{13.5}$	12 Å	μ-Al_4Mn	STEURER, HAIBACH, ZHANG, BEELI and NISSEN [1994]
Al–Cr(Si)	12 Å	$Al_{45}Cr_7$	KUO [1987]
$Al_{65}Cu_{20}Mn_{15}$	12 Å	$Al_{11}Mn_4$	HE, WU and KUO [1988]
$Al_{65}Cu_{20}Fe_{15}$	12 Å	$Al_{13}Fe_4$	
$Al_{65}Cr_7Cu_{20}Fe_8$	12 Å	$Al_{13}Fe_4$	LIU, KÖSTER, MÜLLER and ROSENBERG [1992]
Al_5Ir	16 Å	Al_3Ir	MA, WANG and KUO [1988]
Al_5Pd	16 Å	Al_3Pd	
Al_5Pt	16 Å	Al_3Pt	
Al_5Os	16 Å	$Al_{13}Os_4$	KUO [1987]
Al_5Ru	16 Å	$Al_{13}Ru_4$	BANCEL, HEINEY, STEPHENS, GOLDMAN and HORN [1985]
Al_5Rh	16 Å	Al_9Rh_2	WANG and KUO [1988]
Al_4Fe	16 Å	$Al_{13}Fe_4$	FUNG, YANG, ZHOU, ZHAO, ZHAN and SHEN [1986]
$Al_{74}Mg_5Pd_{21}$	16 Å	Al_3Pd	KOSHIKAWA, EDAGAWA, HONDA and TAKEUCHI [1993]
*$Al_{80}Fe_{10}Pd_{10}$	16 Å	$Al_{13}Fe_4$	TSAI, INOUE and MASUMOTO [1991]
*$Al_{80}Ru_{10}Pd_{10}$	16 Å	$Al_{13}Fe_4$	
*$Al_{80}Os_{10}Pd_{10}$	16 Å	$Al_{13}Fe_4$	
$Al_6Ni(Si)$	16 Å	$Al_9(Ni, Si)_2$	LI and KUO [1988, 1993]
$Al_{72}Cr_{16}Cu_{12}$	36 Å		OKABE, FURIHATA, MORISHITA and FUJIMORI [1992]

References: p. 408.

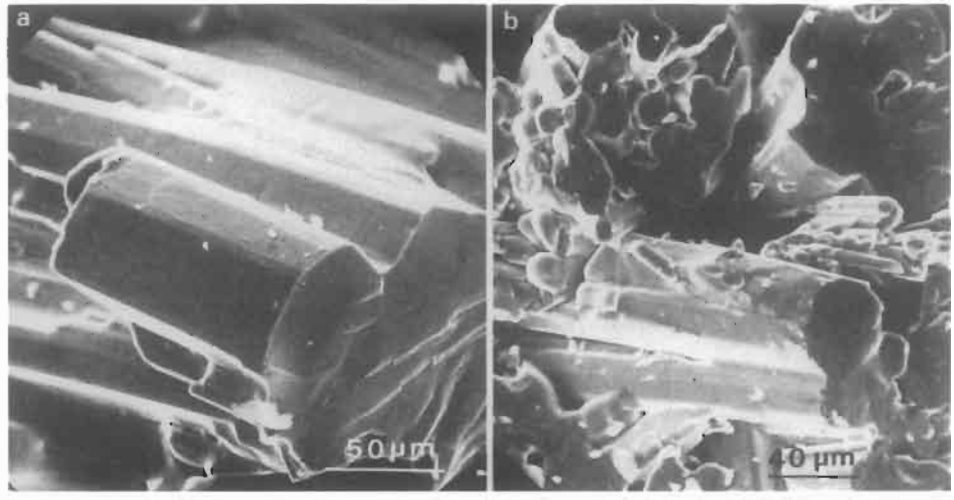

Fig. A9. Single crystals with decaprismatic growth morphology of decagonal (a) $Al_{70}Co_{15}Ni_{15}$, and (b) $Al_{65}Co_{20}Cu_{15}$ (from TSAI, INOUE and MASUMOTO [1989]).

Crystals of the decagonal phase epitaxially grown on icosahedral quasicrystals exhibit a defined orientation relationship: the tenfold axis of the decagonal phase is parallel to one of the fivefold axes of the icosahedral phase. Thus, in many cases decagonal phases can be considered as approximants of icosahedral quasicrystals. Stable decagonal phases were observed so far in the systems Al–Co–Cu (HE, ZHANG, WU and KUO [1988]), Al–Co–Ni, Al–Cu–Rh, Al–Ni–Rh (TSAI, INOUE and MASUMOTO [1989]) and Al–Me–Pd with Me=Mn, Fe, Ru, Os (BEELI, NISSEN and ROBADEY [1991]; TSAI, INOUE and MASUMOTO [1991]). The Al–Mn–Pd system is the only one for which both stable icosahedral and decagonal phases are known.

Three different basic decagonal structure types were identified hitherto: $Al_{65}Co_{15}Cu_{20}$ and $Al_{70}Co_{15}Ni_{15}$ belong to the deca-Al–Co–Cu type, $Al_{78}Mn_{22}$, $Al_{70.5}Mn_{16.5}Pd_{13}$ and $Al_{65}Cu_{20}Cr_7Fe_8$ to the deca-Al–Mn type, $Al_{80}Fe_{10}Pd_{10}$, $Al_{80}Ru_{10}Pd_{10}$, $Al_{80}Os_{10}Pd_{10}$ and $Al_{75}Mn_5Pd_{20}$ to the deca-Al–Fe–Pd type. In all cases the most probable superspace group of the average structures is $P10_5/mmc$ (table A4).

It is remarkable that all three decagonal structure types result from different stacking sequences of only three types of layers: *A*, *B* and *C*. In all cases, similar columnar clusters are formed with interplanar bonds stronger than intraplanar ones. It is also noteworthy that the electron density maps, projected along the tenfold axis, show the respective hyperatoms all centered at the same special positions on the [11110] diagonal of the five-dimensional unit cell, as is the case for a general Penrose tiling. This means that at least a substructure of any decagonal phase shows close resemblance to a decorated Penrose tiling. For the description of the full structure, however, only a context dependent decoration is adequate.

Table A4
Selected symmetry information on the five-dimensional superspace group $P10_5/mmc$. p is an integer with $0 \le p \le 4$. Reflection condition: $h_1h_2\bar{h}_2\bar{h}_1h_5=2n$.

Multiplicity	Wyckoff position	site symmetry	coordinates
4	c	5m	$\pm$(p/5 p/5 p/5 p/5 x_5) $\pm$(p/5 p/5 p/5 p/5 $\frac{1}{2}$-x_5)
2	b	$\bar{1}0$m2	$\pm$(p/5 p/5 p/5 p/5 $\frac{1}{4}$)
2	a	$\bar{5}$m2	(0 0 0 0 0), (0 0 0 0 $\frac{1}{2}$)

Deca-Al–Co–Cu type:
For Al–Co–Cu, there exist studies on phase equilibria and transformation properties (GRUSHKO [1993]; DAULTON, KELTON, SONG and RYBA [1992]; DONG, DUBOIS, DEBOISSIEU and JANOT [1991]), on structural relationships to approximants (LIAO, KUO, ZHANG and URBAN [1992]; DONG, DUBOIS, KANG and AUDIER [1992]; DAULTON and KELTON [1992]; SONG and RYBA [1992]; KUO [1993]), on twinning and microdomain structures (SONG, WANG and RYBA [1991]; LAUNOIS, AUDIER, DENOYER, DONG, DUBOIS and LAMBERT [1990]), as well as investigations using high-resolution transmission electron microscopy (HRTEM) (REYES-GASGA, LARA, RIVEROS and JOSE-YACAMAN [1992]; HIRAGA, SUN and LINCOLN [1991]), the extended X-ray absorption fine structure (EXAFS) technique (DONG, LU, YANG and SHAN [1991]), scanning tunneling microscopy (KORTAN, BECKER, THIEL and CHEN [1990]), or fast-ion channeling (PLACHKE, KUPKE, CARSTANJEN and EMRICK [1993]). For Al–Co–Ni the stability range between 500° C and the melting point was investigated (KEK [1991]), and a wealth of HRTEM and electron diffraction studies of the decagonal phase in comparison with its approximant phases was performed (e.g., HIRAGA, LINCOLN and SUN [1991]; EDAGAWA, ICHIHARA, SUZUKI and TAKEUCHI [1992]). Also a large number of theoretical studies have been published dealing with structure modelling or tiling decoration to understand the rules governing the formation of quasiperiodic phases (HENLEY [1993]; ROMEU [1993]; WIDOM and PHILLIPS [1993]; KANG and DUBOIS [1992]; BURKOV [1991]; BURKOV [1992]).

From the results of the five-dimensional single crystal X-ray structure analyses of decagonal $Al_{65}Co_{15}Cu_{20}$ (STEURER and KUO [1990]) and $Al_{70}Co_{15}Ni_{15}$ (STEURER, HAIBACH, ZHANG, KEK and LÜCK [1993]), the following characteristics of the deca-Al-Co–Cu structure type can be derived:

(1) Two-layer structure with approximate translation period 4 Å. There are two planar layers stacked with sequence *Aa* (*a* means *A* rotated around 36° under the action of the 10_5–screw axis). At lower temperature a disordered superstructure doubling the translation period is observed.
(2) There are two hyperatoms per asymmetric unit on the special Wyckoff position (b): one with p = 2 consisting mainly of transition metal (marked 1), and one with p = 4 (marked 2) consisting of Al atoms (fig. A10).

References: p. 408.

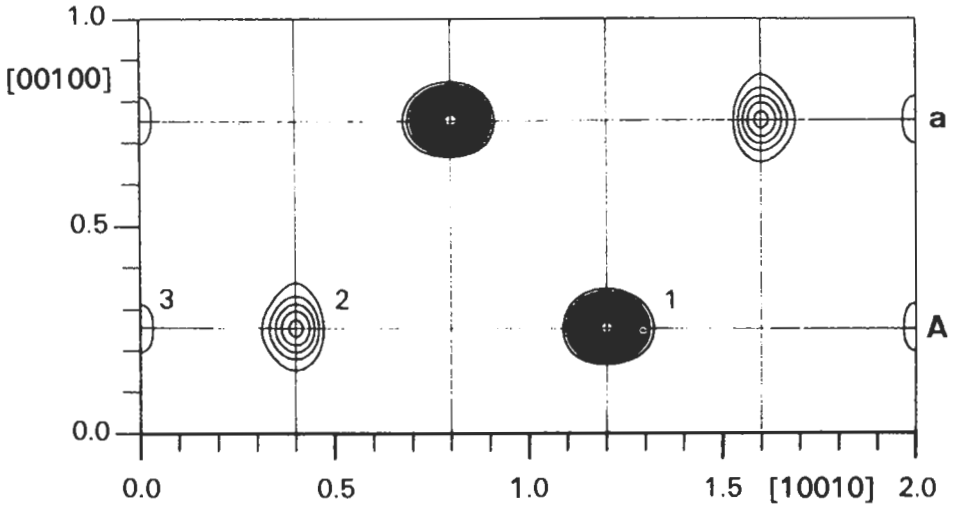

Fig. A10. Characteristic (10110) section of the five-dimensional electron density of decagonal $Al_{70}Co_{15}Ni_{15}$. The hyperatoms 1, and 2 generate an atomic layer A separated by ≈2 Å from the symmetrically equivalent layer a generated by the 10_5–screw axis which is parallel to [00100].

(3) Shape and chemical composition of the hyperatoms are roughly compatible with tiling models like the binary tiling model (BURKOV [1991]), for instance.

(4) Columnar clusters (Ø ≈ 20 Å) with eigensymmetry 10_5/mmc can be identified as basic structural units (fig. A11). Their cross sections can be described as parts of a Penrose tiling with edge lengths $a_r \approx 2.5$ Å. The unit rhombs are decorated by atoms on the vertices and in some cases on the diagonals.

(5) The global structure can be described as a rhombic tiling with unit tiles of edge length $a_r \approx 20$ Å (equivalent to the distance between two ≈ 20 Å columnar clusters), decorated by the columnar clusters at the vertices and at one position on the long diagonal of the fat rhomb (fig. A12).

(6) The formation of a network of icosagonal rings of pentagonal and rectangular structure motifs may act as weak matching rule stabilizing quasiperiodic tilings (fig. A13).

(7) A closely related approximant structure is that of monoclinic $Al_{13}Co_4$ (HUDD and TAYLOR [1962]; BARBIER, TAMURA and VERGER-GAUGRY [1993]). It contains locally similar structure motifs (pentagon-rectangle strips) which are arranged in a different way (wavy bands instead of icosagons), however (fig. A14).

Deca-Al–Mn type:

Decagonal $Al_{78}Mn_{22}$, $Al_{70.5}Mn_{16.5}Pd_{13}$ and $Al_{65}Cu_{20}Cr_7Fe_8$ are representatives of the deca-Al–Mn type with ~ 12 Å translational period. Stable decagonal $Al_{70.5}Mn_{16.5}Pd_{13}$, may be considered as Pd-stabilized $Al_{78}Mn_{22}$. There exist several HRTEM (BEELI, NISSEN and ROBADEY [1991]; HIRAGA, SUN, LINCOLN, KANEKO and MATSUO [1991]; HIRAGA and

SUN [1993]; BEELI and NISSEN [1993]) and X-ray diffraction investigations (FREY and STEURER [1993]; STEURER, HAIBACH, ZHANG, BEELI and NISSEN [1994]) and also structure determinations of the approximants Al_3Mn (HIRAGA, KANEKO, MATSUO and HASHIMOTO [1993]) and μ-$Al_{4.12}Mn$ (SHOEMAKER [1993]). Stable decagonal $Al_{65}Cu_{20}Cr_7Fe_8$, i.e., Fe-stabilized metastable (?) $Al_{65}Cu_{20}Cr_{15}$, and its approximants were studied by (LIU, KÖSTER,

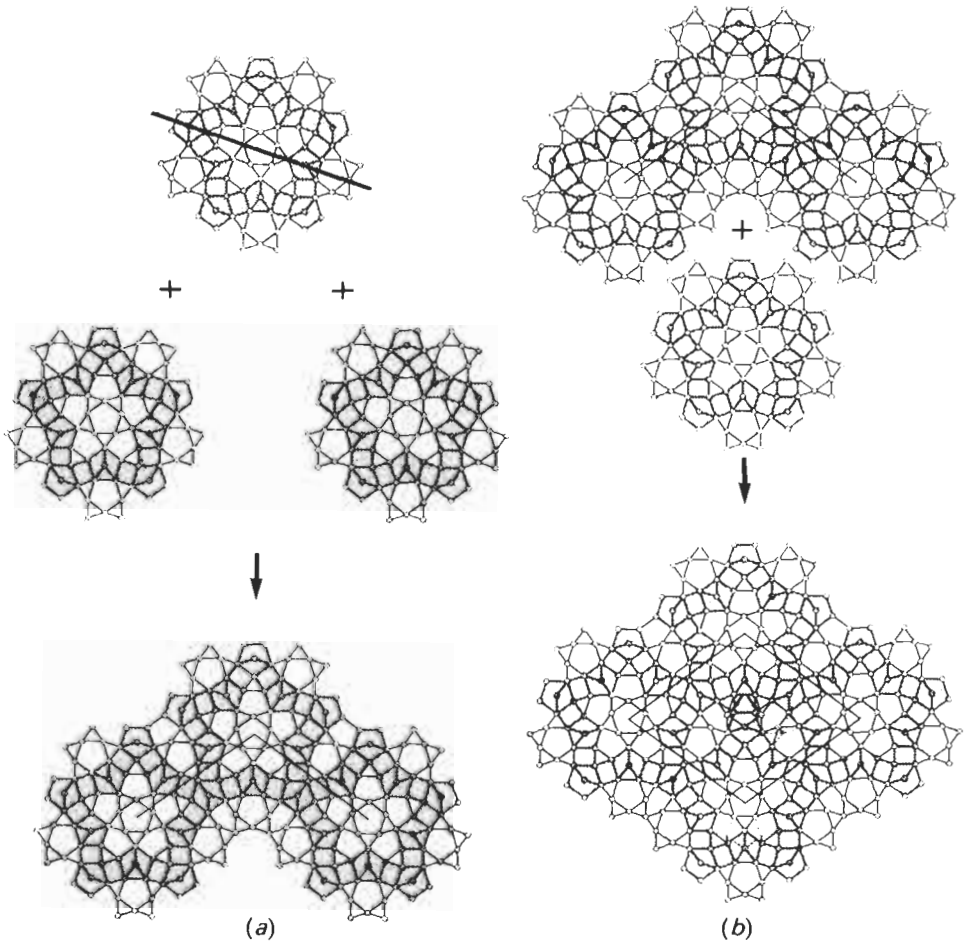

(*a*) (*b*)

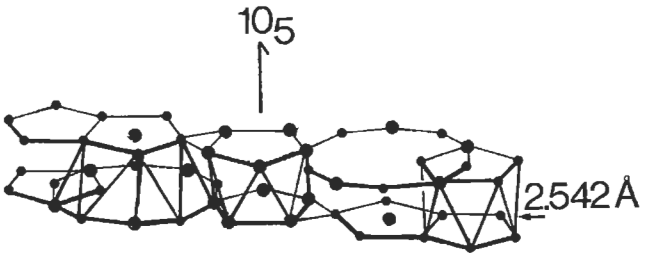

Fig. A11. (a), and (b): Schematic drawings illustrating how the ≈ 20 Å columnar clusters (shown in sections) agglomerate to a fat decorated Penrose unit rhomb. (c) Stacking principle of the layers *A* and *a* along the line drawn in the uppermost section of (a).

MÜLLER and ROSENBERG [1992]; KANG, DUBOIS, MALAMAN and VENTURINI [1992]).

The X-ray single-crystal structure analyses of $Al_{78}Mn_{22}$ (STEURER [1991]) and $Al_{70.5}Mn_{16.5}Pd_{13}$ (STEURER, HAIBACH, ZHANG, BEELI and NISSEN [1994]) allow the characterization of the deca-Al–Mn type in the following way:

(1) Six-layer structure with approximate translation period 12 Å. One puckered (±0.3 Å) layer *A* (related to the layer *a* of the deca-Al–Co–Cu type) and one planar layer *B* are stacked with sequence *ABAaba*.

(2) Four hyperatoms per asymmetric unit: two on the Wyckoff position (c); one with $p=1$, $x_5=0.063$ (marked 1), consisting in its core region of transition metal (TM) and in its remaining part of Al, and one with $p=3$, $x_5=0.113$ (marked 2), consisting of Al. Two further hyperatoms are located on Wyckoff position (b), one with $p=0$ (marked 4), consisting mainly of Al, and one with $p=3$ (marked 5), of similar chemical composition as hyperatom 1 (fig. A15).

(3) Shape and chemical composition of the hyperatoms are roughly compatible with tiling models such as the triangular tiling model (BURKOV [1992]; WELBERRY [1989]), for instance.

(4) Columnar clusters (diameter ≈ 20 Å) with point symmetry 10_5/mmc can be identified as basic structural units. Their cross sections can be described as sections of a Penrose tiling with edge lengths $a_r \approx 2.5$ Å of the unit rhombs (fig. A16).

(5) The global structure can be described as a random Robinson-triangle tiling with unit tiles of edge lengths $S \approx 20$ Å, and $L = \tau S$, decorated by the columnar clusters on the vertices (fig. A17).

(6) The decagonal phase shows close resemblance to the respective icosahedral phase, orthorhombic Al_3Mn (HIRAGA, KANEKO, MATSUO and HASHIMOTO [1993]), and hexagonal μ-$Al_{4.12}Mn$ (SHOEMAKER [1993]), which has nearly all Mn atoms icosahedrally coordinated.

(7) Contrary to the phases with deca-Al–Co–Cu type, those with deca-Al–Mn type show icosahedral pseudosymmetry and can be considered as rational approximants of icosahedral quasicrystals. There is also a larger amount of Mackay icosahedra (MI) or fragments of MI present in this structure type than in the other decagonal ones.

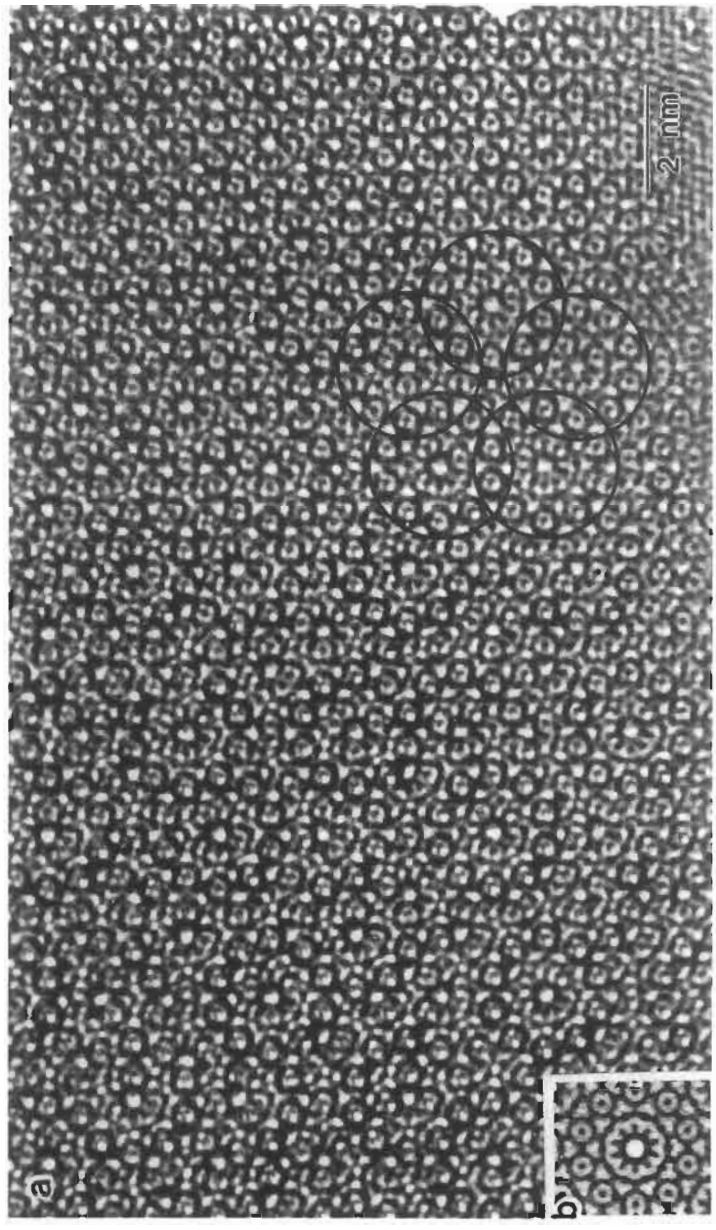

Fig. A12. (a) HRTEM image of decagonal $Al_{70}Co_{15}Ni_{15}$ (b) simulation image calculated from the 20 Å columnar cluster (from HIRAGA [1992]).

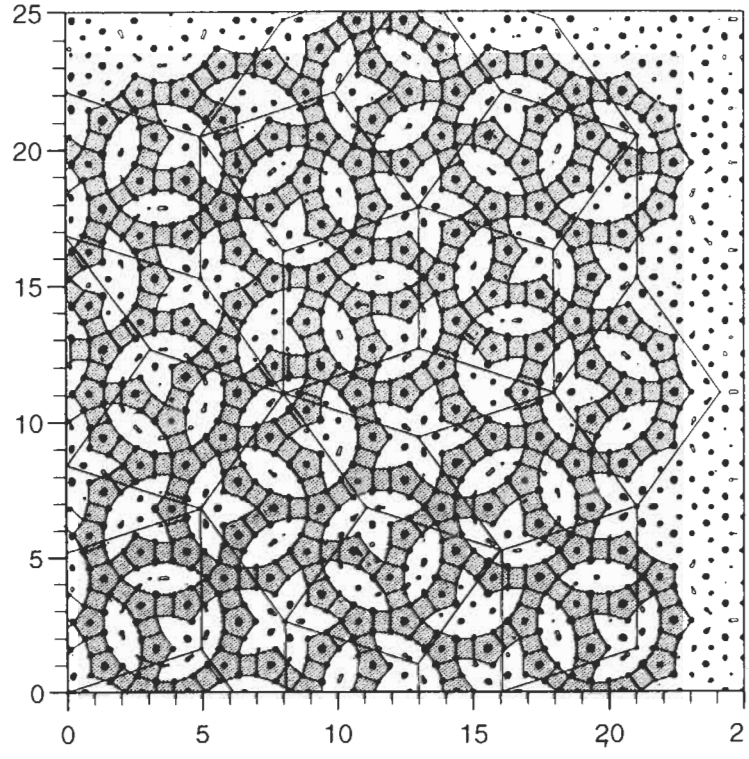

Fig. A13. Parallel space section with Penrose tiling from the type of $a_r \approx 20$ Å rhombs shown in fig. A11 indicated. The pentagonal and rectangular structure motifs form a network of interconnected icosagons.

Deca-Al–Fe–Pd type:

The stable decagonal phases $Al_{80}Fe_{10}Pd_{10}$, $Al_{80}Ru_{10}Pd_{10}$, $Al_{80}Os_{10}Pd_{10}$ (TSAI, INOUE and MASUMOTO [1991]) and $Al_{75}Mn_5Pd_{20}$ (TSAI, YOKOYAMA, INOUE and MASUMOTO [1991]) belong to the deca-Al–Fe–Pd type with 16 Å translational periodicity. $Al_{80}Fe_{10}Pd_{10}$ is the only one of this group studied so far by X-ray single-crystal diffraction (HAIBACH, ZHANG and STEURER [1994]), electron diffraction and HRTEM (TSAI, INOUE and MASUMOTO [1993]), and also by Mössbauer spectroscopy (LAWTHER and DUNLAP [1993]). A stable one-dimensional quasiperiodic phase, a rational approximant of the decagonal phase, was also identified in the system Al–Fe–Pd (TSAI, MASUMOTO and YAMAMOTO [1992]). On the basis of early results, the deca-Al–Fe–Pd type may be characterized in the following way:

(1) Eight-layer structure with approximate translation period 16 Å. Two puckered (± 0.3 Å) layers *A* and *C*, and one planar layer *B* are stacked with sequence *CABACaba*, with *C* identical to *c*.

(2) Four hyperatoms per asymmetric unit: one on the Wyckoff position (a), one on the Wyckoff position (c) with $p = 1$, $x_5 = 0.125$, and two with $p = 0$ and 2 on (b).

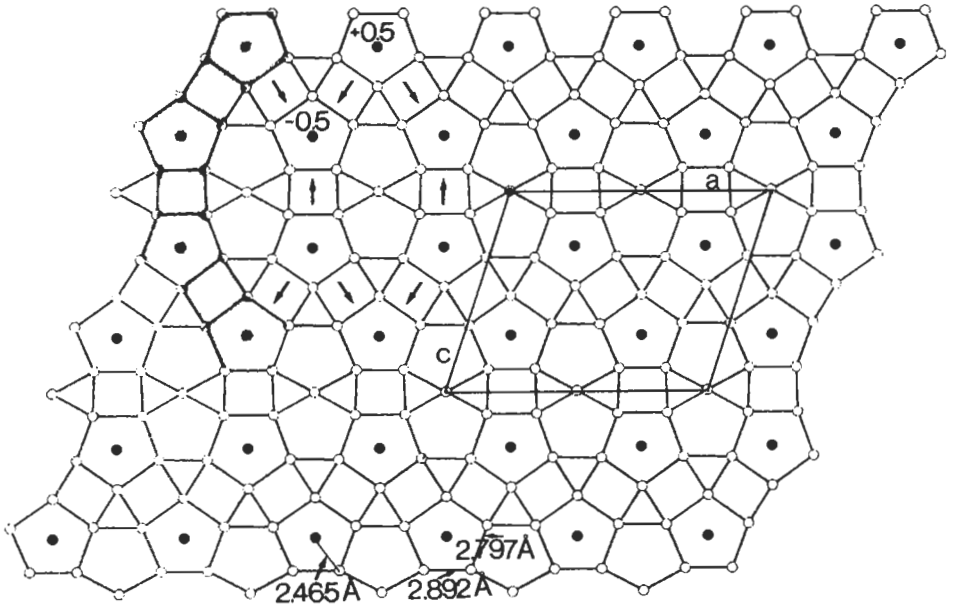

Fig. A14. Schematic drawing of the puckered atomic layer of the monoclinic approximant $Al_{13}Co_4$ with the same pentagon-rectangle strips as found in the decagonal phase. One unit cell is also drawn in.

(3) Shape and chemical composition of the hyperatoms are roughly compatible with tiling models like the binary tiling model (BURKOV [1991]), for instance.
(4) Columnar clusters ($Ø \approx 20$ Å) with point symmetry $10_5/mmc$ can be identified as basic structural units. Their cross sections can be described as section of a Penrose tiling with edge lengths $a_r \approx 2.5$ Å of the unit rhombs.
(4) The global structure can be described as a rhombic tiling with unit tiles of edge lengths $a_r \approx 20$ Å decorated by the columnar clusters at the vertices and at one site on the long diagonal of the fat rhombs.

3.2.3. Dodecagonal phases

Beside one, probably stable, dodecagonal Ta_xTe phase (KRUMEICH, CONRAD and HARBRECHT [1994]), only metastable dodecagonal phases are known so far (table A5). These phases are closely related to the tP30–σCrFe type phases, which are built up from hexagon-triangle and triangle-square layers (fig. A18). The c lattice parameter of the σ-phase corresponds with 4.544 Å to the translation period of the dodecagonal phases.

3.3. Icosahedral phases

The icosahedral phases discovered so far (table 6) can be grouped into two main classes (HENLEY and ELSER [1986]): the ico-Al–Mn structure type (A) with quasilattice constant $a_r \sim 4.6$ Å and free electron per atom ratio of ~ 1.75, and the ico-Al–Mg–Zn

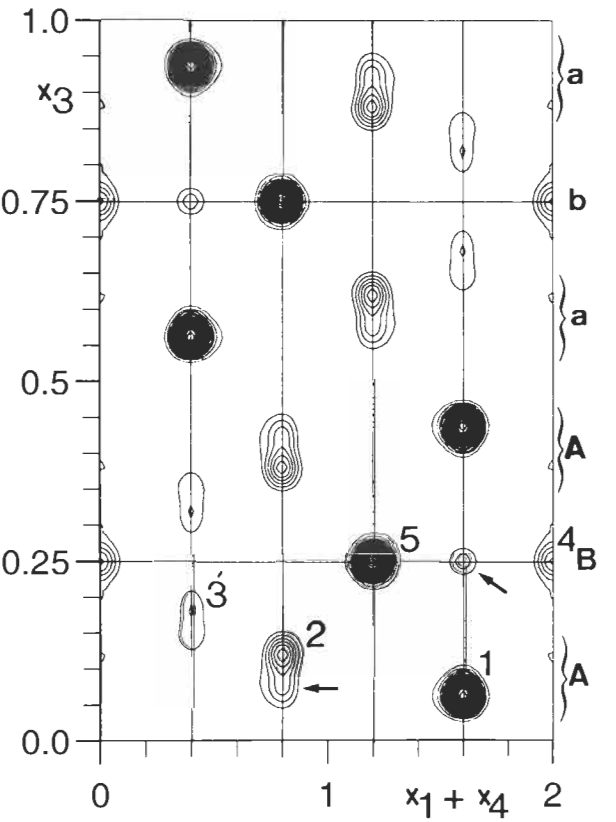

Fig. A15. Characteristic (10110) section of the five-dimensional electron density of decagonal $Al_{70.5}Mn_{16.5}Pd_{13}$. The hyperatoms create a six-layer structure *ABAaba*.

structure type (B) with $a_r \sim 5.2$ Å and free electron per atom ratio of ~ 2.1. The A type phases contain 54–atom Mackay icosahedra as structural building elements which also occur in the approximant α-Al–Mn–Si, while the B type consists of 137–atom Bergmann rhombic triacontahedra which are also typical for Frank–Kasper phases like

Table A5
Systems with dodecagonal phases (approximate compositions given). In the second column the translation period along the twelve-fold axis is given. Stable dodecagonal phases are marked by a star.

$Cr_{70.6}Ni_{29.4}$		Ishimasa, Nissen and Fukano [1985]
Ni_2V_3	4.5 Å	Chen, Li and Kuo [1988]
$Ni_{10}SiV_{15}$	4.5 Å	
*Ta_xTe	20.7 Å	Krumeich, Conrad and Harbrecht [1994]

$Mg_{32}(Al,Zn)_{42}$, for instance. The A-type icosahedral phases are mostly aluminum-transition metal compunds contrary to the B-type phases which rarely contain transition metals.

The first quasicrystal structure ever studied was that of metastable ico-Al–Mn and

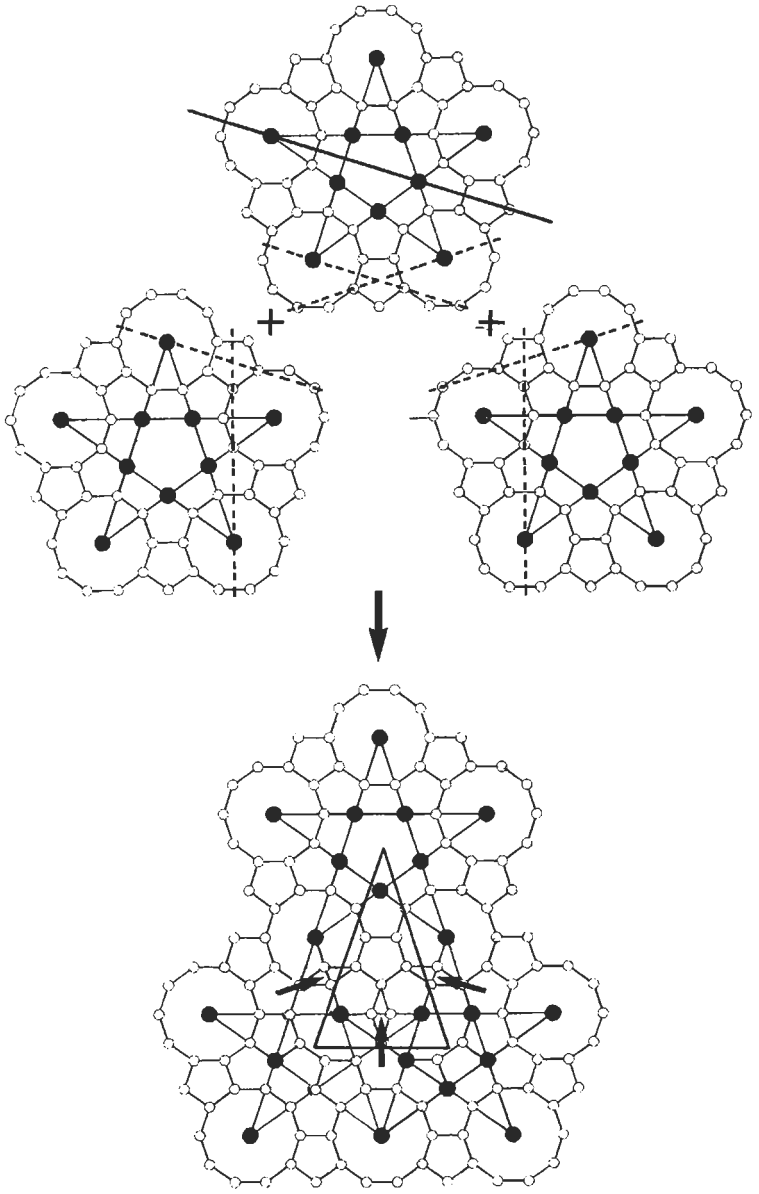

(a)

Figure continued on p. 394

isotypic, higher-quality ico-Al–Mn–Si, respectively (CAHN, GRATIAS and MOZER [1988]). Single-crystal X-ray and neutron diffraction methods became possible with the discovery of stable ico-Al–Cu–Li (DE BOISSIEU, JANOT, DUBOIS, AUDIER and DUBOST [1991]; VAN SMAALEN, DE BOER and SHEN [1991]; YAMAMOTO [1992]; QIU and JARIC [1993]) also allowing for a further developement of six-dimensional structure analytical techniques. The existence of closely related cubic α-$Al_{73}Mn_{16}Si_{11}$ (COOPER and ROBINSON [1966]) and R–Al_5CuLi_3 (AUDIER, PANNETIER, LEBLANC, JANOT, LANG and DUBOST [1988]), both rational (1,1)-approximants of the respective icosahedral phases, was very helpful for their structure analyses.

Ico-Al–Cu–Li and shortly later found stable ico-Ga–Mg–Zn (OHASHI and SPAEPEN [1987]) could both be prepared only with poor quality setting a limit for the achievable

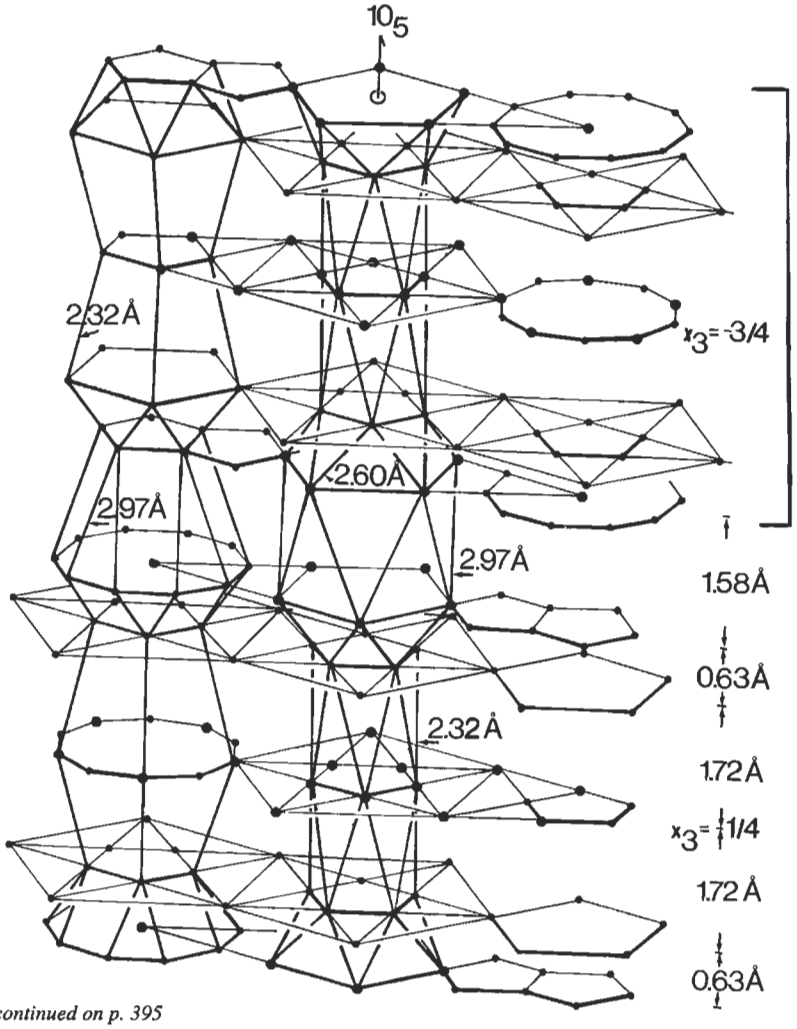

(b)

Figure continued on p. 395

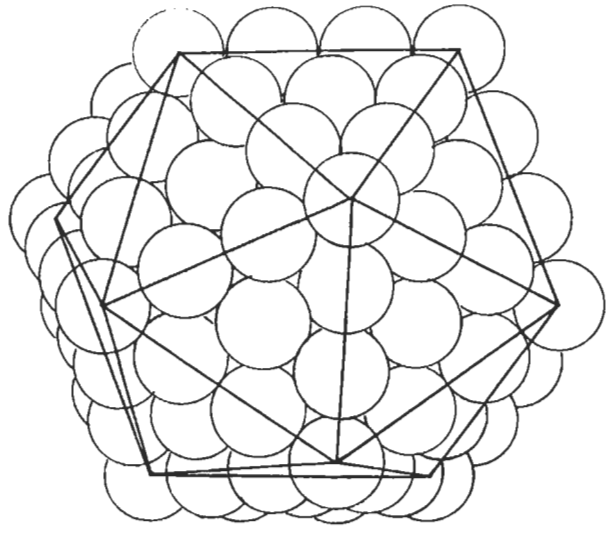

(c)

Fig. A16. (a) Schematical drawings illustrating how the ≈20 Å columnar clusters (shown in sections) agglomerate to a Robinson triangle (coincidence lines are dotted). (b) Stacking principle along the full line drawn in the uppermost section of (a). The pentagons and decagons in the right upper part marked by a bracket form one half of a 54-atom Mackay icosahedron illustrated in (c).

structural resolution. The discovery of very well ordered icosahedral quasicrystals in the systems Al–Cu–Me, with Me = Fe, Ru, Os (TSAI, INOUE and MASUMOTO [1987]; TSAI, INOUE and MASUMOTO [1988]b) and Al–Me–Pd, with Me = Mg, Mn, Re (TSAI, INOUE, YOKOYAMA and MASUMOTO [1990]; KOSHIKAWA, SAKAMOTO, EDAGAWA and TAKEUCHI [1992]) brought the turning point. During the last years, structure analyses focused on ico-Al–Cu–Fe (CORNIER-QUIQUANDON, QUIVY, LEFEBVRE, ELKAIM, HEGER, KATZ and GRATIAS [1991]; CORNIER-QUIQUANDON, BELLISENT, CALVAYRAC, CAHN, GRATIAS and MOZER [1993]) and ico-Al–Mn–Pd (BOUDARD, DEBOISSIEU, AUDIER, JANOT, HEGER, BEELI, NISSEN, VINCENT, IBBERSON and DUBOIS [1992]). In both cases, the ternary phase diagrams have been intensively investigated and the phase transitions studied (AUDIER, DURAND-CHARRE and DE BOISSIEU [1993]).

3.3.1. Primitive hypercubic icosahedral phases

Representatives of stable quasicrystals with superspace group $Pm\bar{3}\bar{5}$ are ico-$Al_{73}Mn_{21}Si_6$ (JANOT, DEBOISSIEU, DUBOIS, and PANNETIER [1989]), ico-Al_6CuLi_3 (DEBOISSIEU, JANOT, DUBOIS, AUDIER and DUBOST [1991]; YAMAMOTO [1992]), ico-$Ga_{20.4}Mg_{36.7}Zn_{42.9}$ (OHASHI and SPAEPEN [1987]) and ico-$Al_{38}Mg_{47}Pd_{15}$ (KOSHIKAWA, SAKAMOTO, EDAGAWA and TAKEUCHI [1992]). The structures of ico-$Al_{73}Mn_{21}Si_6$ and ico-Al_6CuLi_3 (fig. A19) were analysed using X-ray powder diffraction and neutron scattering techniques. Of the large number of papers dealing with other structure sensitive methods, only two HRTEM studies will be quoted (HIRAGA [1991]; NISSEN and BEELI [1993]). The results are shortly summarized as follows:

References: p. 408.

Table A6

Systems with icosahedral phases (approximate compositions given). The quasilattice constant $a_t = 1/a^*_{100000}$ is listed in the second column. The structures with face-centered hypercubic unit cells are marked by F, the ico-Al–Mn–Si structure type is labeled by A, and that of ico-(Al, Zn)–Mg by B. Stable quasicrystals are marked by asterisks.

$Al_{85}Cr_{15}$	4.65 Å		A	Zhang, Wang and Kuo [1988]
$Al_{86}Fe_{14}$			A	Bancel, Heiney, Stephens, Goldman and Horn [1985]
$Al_{86}Mn_{14}$	4.60 Å		A	Shechtman, Blech, Gratias and Cahn [1984]
Al–Mo			A	Chen, Phillips, Villars, Kortan and Inoue [1987]
$Al_{78}Re_{22}$			A	Bancel and Heiney [1986]
Al_4Ru			A	Anlage, Fultz and Krishnan [1988]
Al_4V	4.75 Å		A	Chen, Phillips, Villars, Kortan and Inoue [1987]
Al–W			A	
$Al(Cr_{1-x}Fex)$			A	Schurer, Koopmans and van der Woude [1988]
$Al(Mn_{1-x}Fe_x)$			A	
$Al_{62}Cr_{19}Si_{19}$	4.60 Å		A	Inoue, Kimura, Masumoto, Tsai and Bizen [1987]
$Al_{65}Cr_{20-x}Fe_xGe_{15}$			A	Srinivas, Dunlap, Bahadur and Dunlap [1990]
Al–Cr–Ru			A	Bancel and Heiney [1986]
$*Al_{65}Cu_{20}Cr_{15}$			A	Tsai, Inoue and Masumoto [1988a]
$*Al_{65}Cu_{20}Fe_{15}$	4.45 Å	F	A	Ebalard and Spaepen [1989]; Tsai, Inoue and Masumoto [1988d]
$Al_{65}Cu_{20}Mn_{15}$		F	A	He, Wu and Kuo [1988]
$*Al_{65}Cu_{20}Os_{15}$	4.51 Å	F	A	Tsai, Inoue and Masumoto [1988b]
$*Al_{65}Cu_{20}Ru_{15}$	4.53 Å	F	A	
$Al_{65}Cu_{20}V_{15}$	4.59 Å		A	Tsai, Inoue and Masumoto [1988a]
$Al_{70}Fe_{20}Ta_{10}$	4.55 Å		A	Tsai, Inoue and Masumoto [1988c]
$Al_{73}Mn_{21}Si_6$	4.60 Å		A	Gratias, Cahn and Mozer [1988]
$Al_{60}Mn_{20}Ge_{20}$			A	Tsai, Inoue and Masumoto [1988d]
$Al_{75.5}Mn_{17.5}Ru_4Si_3$			A	Heiney, Bancel, Goldman and Stephens [1986]
$Al_{74}Mn_{17.6}Fe_{2.4}Si_6$	4.59 Å		A	Ma and Stern [1988]
$Al_{75}Mn_{15}Cr_5Si_5$			A	Nanao, Dmowski, Egami, Richardson and Jorgensen [1987]
$*Al_{70.5}Mn_{8.5}Pd_{21}$	4.56 Å	F	A	Tsai, Inoue, Yokoyama and Masumoto [1990]
$*Al_{70.5}Pd_{20.5}Re_9$	4.60 Å	F	A	
*Al–Mn–Pd–B	4.55 Å	F	A	Yokoyama, Inoue and Masumoto [1992]
*Al–Cu–Mn–B	4.51 Å	F	A	

Table A6–*Continued*

$Al_{72}Pd_{25}V_3$		F	A	TSAI, YOKOYAMA, INOUE and MASUMOTO [1990]
$Al_{70}Fe_{13}Pd_{17}$		F	A	
$Al_{72}Cr_8Pd_{20}$		F	A	
$Al_{75}Co_{10}Pd_{15}$		F	A	
*Al–Pd–Cr–Fe		F	A	YOKOYAMA, TSAI, INOUE, MASUMOTO and CHEN [1991]
*Al–Pd–Co–V		F	A	
*Al–Pd–Mo–Ru		F	A	
*Al–Pd–W–Os		F	A	
$Al_{52}Mg_{17}Pd_{31}$	4.63 Å	F	A	KOSHIKAWA, EDAGAWA, HONDA and TAKEUCHI [1993]
$Al_{70}Mg_8Rh_{22}$		F	A	
Ti_2Fe	4.72 Å	F	A	KELTON, GIBBONS and SABES [1988]
Ti_2Mn	4.79 Å	F	A	
Ti_2Co	4.82 Å	F	A	
$Ti_2(Ni,V)$		F	A	ZHANG, YE and KUO [1985]
$Ti_{56}Ni_{28}Si_{16}$		F	A	CHATTERJEE and O'HANDLEY [1989]
$V_{41}Ni_{36}Si_{23}$			A	KUO, ZHOU and LI [1987]
$Pd_{58.8}U_{20.6}Si_{20.6}$	5.14 Å		A	POON, DREHMANN and LAWLESS [1985]
*$Al_{43}Mg_{44}Pd_{13}$	5.13 Å		B	KOSHIKAWA, SAKAMOTO, EDAGAWA and TAKEUCHI [1992]
*Al_6CuLi_3	5.04 Å		B	SAINTFORT and DUBOST [1986]
Al_6CuMg_4	5.21 Å		B	SASTRY, RAO, RAMACHANDRARAO and ANANTHARAMAN [1986]
$Al_{51}Cu_{12.5}$–$(Li_xMg_{36.5-x})$	5.05 Å		B	SHEN, SHIFLET and POON [1988]
$Al_{50}Li_{25}Mg_{25}$	5.17 Å	F	B	NIIKURA, TSAI, INOUE, MASUMOTO and YAMAMOTO [1993]
Al_6AuLi_3	5.11 Å		B	CHEN, PHILLIPS, VILLARS, KORTAN and INOUE [1987]
$Al_{51}Zn_{17}Li_{32}$	5.11 Å		B	
$Al_{50}Mg_{35}Ag_{15}$	5.23 Å		B	MUKHOPADHYAY, CHATTOPADHYAY, and RAGANATHAN [1988]
Al–Ni–Nb			B	
$(Al,Zn)_{49}Mg_{32}$	5.15 Å		B	HENLEY and ELSER [1986]
$(Al,Zn,Cu)_{49}Mg_{32}$	5.15 Å		B	MUKHOPADHYAY, THANGARAJ, CHATTOPADHYAY and RANGANATHAN [1987]
*$Ga_{16}Mg_{32}Zn_{52}$	5.09 Å		B	OHASHI and SPAEPEN [1987]
*Mg–Y–Zn			B	LUO, ZHANG, TANG and ZHAO [1993]
*Mg–Y–Zn–Zr			B	TANG, ZHAO, LUO, SHENG and ZHANG [1993]
Nb–Fe			B	KUO [1987]

References: p. 408.

Table A7
Selected symmetry information on the six-dimensional superspace group $Pm\bar{3}\bar{5}$.

Multiplicity	Wyckoff position	site symmetry	coordinates
6	c	$m\bar{5}$	$\frac{1}{2}$(1 0 0 0 0 0)
1	b	$m\bar{3}\bar{5}$	$\frac{1}{2}$(1 1 1 1 1 1)
1	a	$m\bar{3}\bar{5}$	(0 0 0 0 0 0)

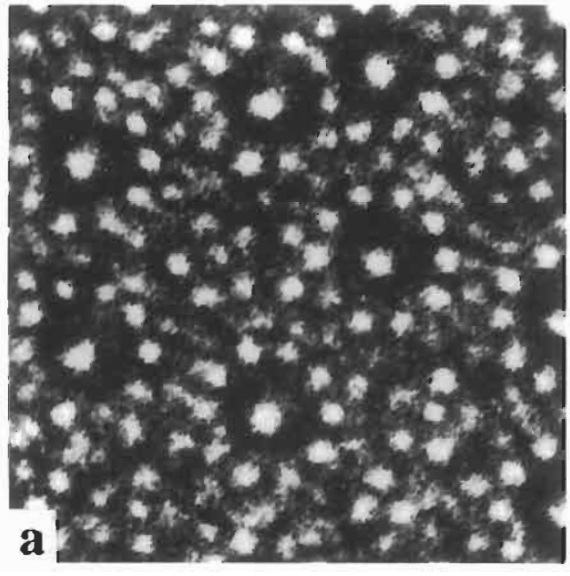

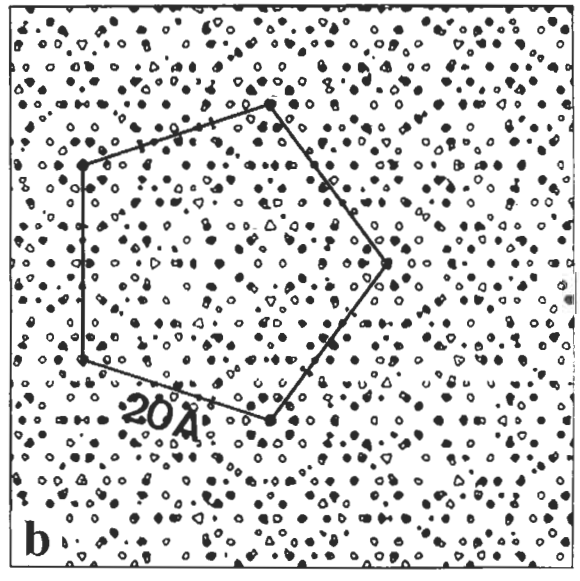

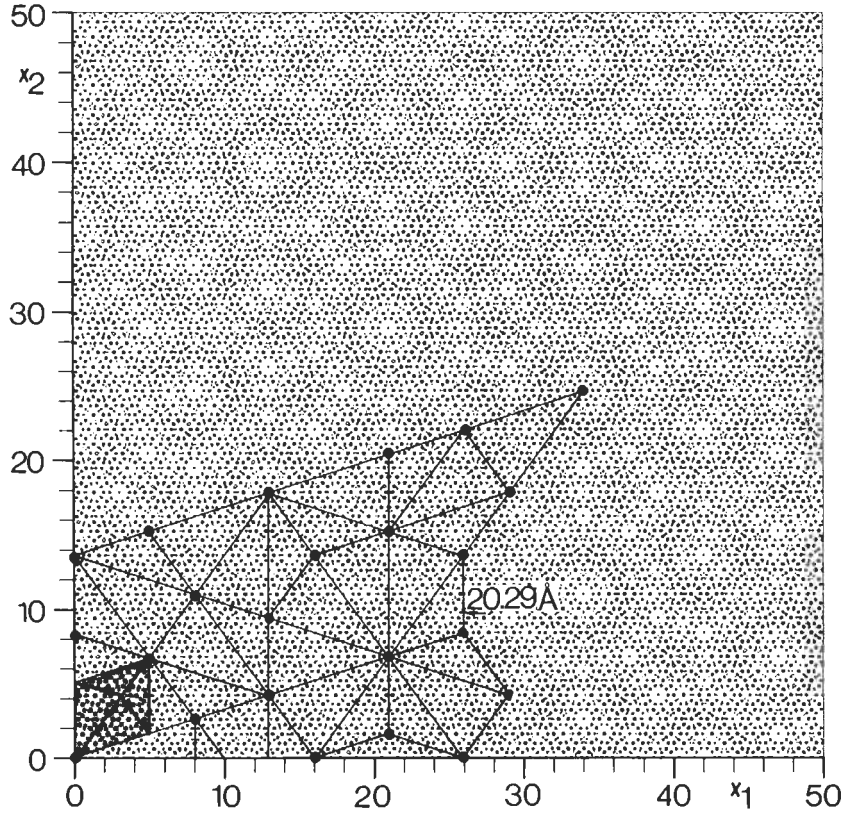

Fig. A17. (a) HRTEM image of decagonal $Al_{70.5}Mn_{16.5}Pd_{13}$ with a point to point resolution of 2 Å, and (b) comparison with the projected decagonal Al–Mn structure (from BEELI and NISSEN [1993]). (c) Physical space projection of the electron density of decagonal $Al_{70.5}Mn_{16.5}Pd_{13}$ with large, and small ROBINSON triangles drawn in.

(1) The hyperatoms occupy the Wyckoff positions (a), (b) and (c) (table A7), i.e., the vertices, the body center and the mid-edge positions of the six-dimensional hypercubic unit cell. In the case of ico-$Al_{73}Mn_{21}Si_6$, one hyperatom is centered at (a), its core consisting of Mn and the surrounding part of Al/Si. The second hyperatom is located at the body center (b), (c) remains unoccupied. Ico-Al_6CuLi_3 has Al/Cu-hyperatoms at (a) and (c), and one Li-hyperatom at (b) (figs. A20 and A21).

(2) The structures of ico-$Al_{73}Mn_{21}Si_6$, ico-Al_6CuLi_3 and their related crystalline phases show close resemblance in the six-dimensional description. This confirms the assumption that cubic α-$Al_{73}Mn_{16}Si_{11}$ and R–Al_5CuLi_3 are (1,1)-approximants related to the icosahedral phases merely by a hyperspace rotation.

(3) There exist orientation relationships for epitaxially grown α-$Al_{73}Mn_{16}Si_{11}$ on icosahedral $Al_{73}Mn_{21}Si_6$: [100] of the cubic phase is parallel to a twofold direction of the icosahedral phase, and [111] is parallel to a threefold one.

References: p. 408.

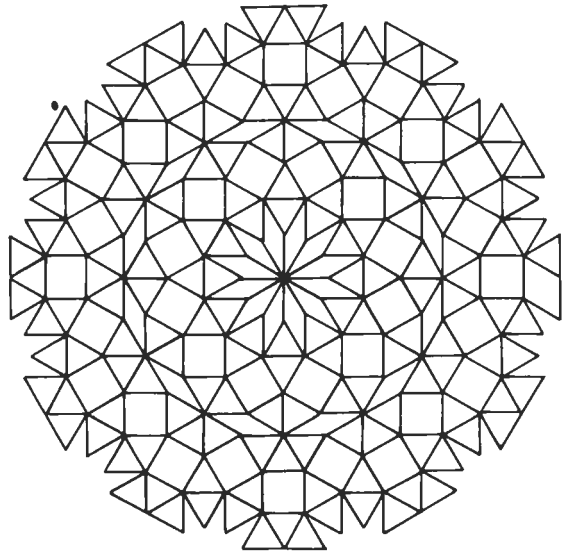

Fig. A18. Dodecagonal tiling as example for a quasilattice with twelve-fold symmetry.

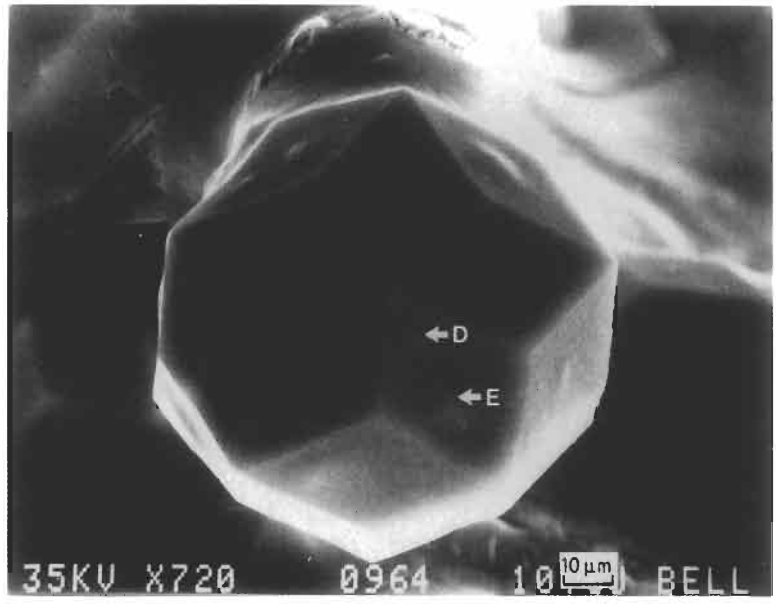

Fig. A19. Single crystal of ico-$Al_{5.1}CuLi_3$ with triacontahedral shape (from KORTAN, CHEN, PARSEY and KIMERLING [1989]).

(4) α-$Al_{73}Mn_{16}Si_{11}$ contains a high percentage of atoms forming slightly distorted Mackay icosahedra (78.3%), and its structure can be described by a near-bcc packing of these 54–atom polyhedra. Ico-$Al_{73}Mn_{21}Si_6$, on the other hand, contains 66.6% of atoms in regular but often fragmented Mackay icosahedra.

(5) R–Al_5CuLi_3 can be described as bcc packing of distorted Pauling triacontahedra or 104–atoms Samson complexes (fig. A22). These structure motifs are also locally present in ico-Al_6CuLi_3. In the Penrose tiling description, there are icosahedral clusters placed on the twelvefold vertices.

3.3.2. Face-centered hypercubic icosahedral phases

The face-centering of the six-dimensional hypercubic unit cell results from chemical

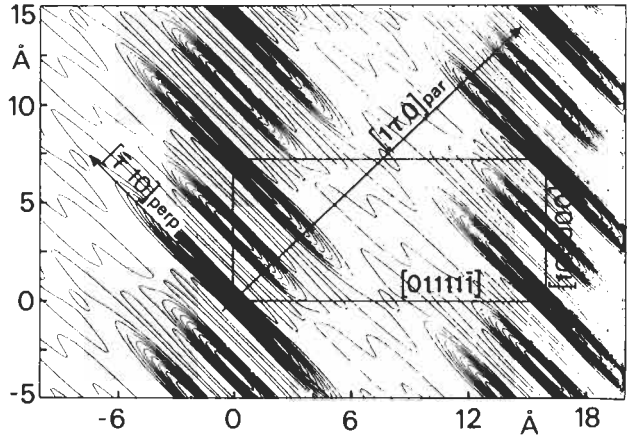

(a)

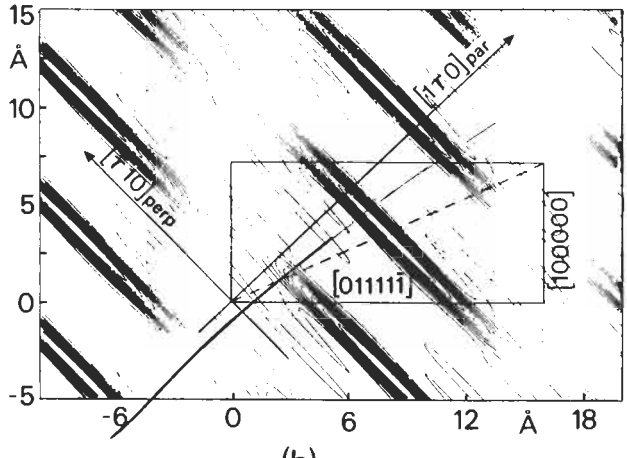

(b)

References: p. 408.

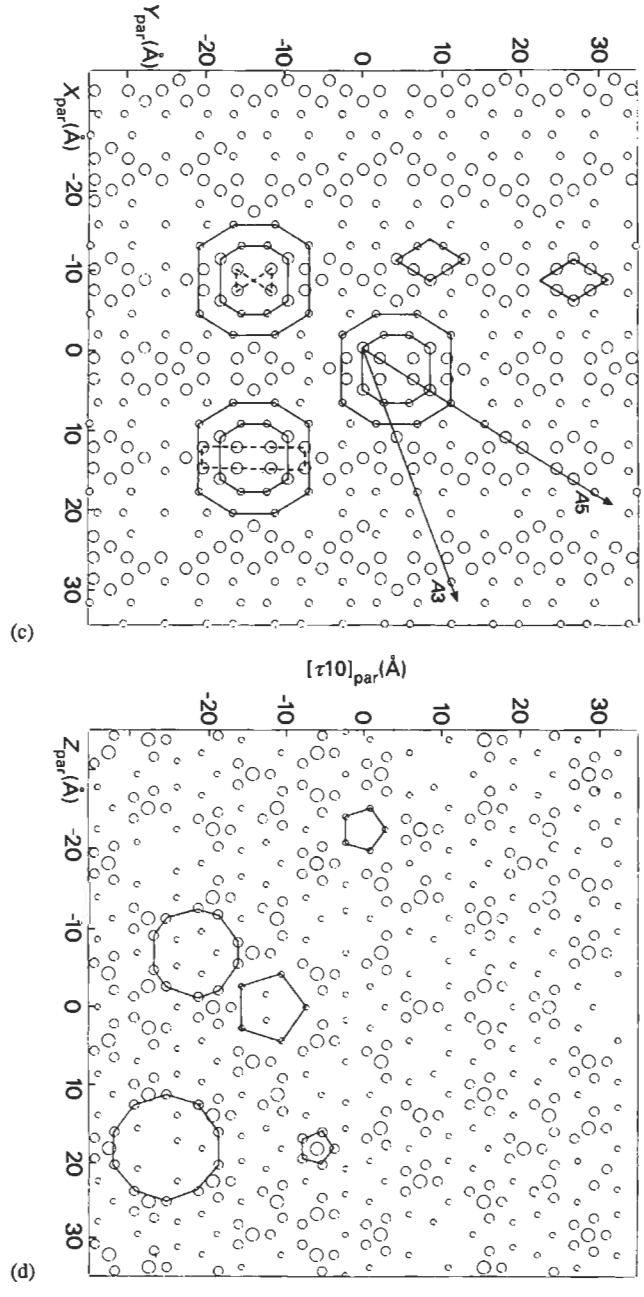

Fig. A20. Cuts of six-dimensional partial hyperatomic density of ico-Al_6CuLi_3. (a) Al/Cu hyperatoms at the vertices, and mid-edge positions, (b) Li at the body center. Parallel-space atomic planes as obtained by a cut of the six-dimensional model; layer with twofold symmetry in (c), with fivefold symmetry in (d) (from JANOT [1992]).

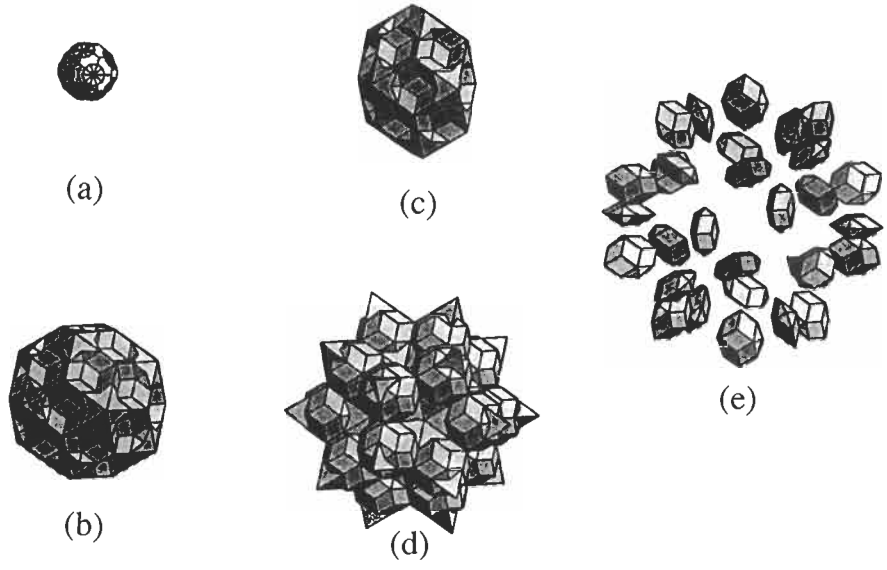

Fig. A21. Hyperatoms of the ideal ico-Al_6CuLi_3 structure derived from the R-Al_5CuLi_3 structure: (a) vacant twelve-fold, (b) vertex Al/Cu, (c) mid-edge Al/Cu, (d) body-center Li surrounded by (e) Al/Cu hyperatoms. The domain (a) has to be subtracted from (b) to remove unoccupied twelve-fold vertices (from YAMAMOTO [1992]).

ordering of the atoms. Therefore, the resulting structure may also be described as a superstructure, with twice the lattice parameters of the primitive hypercubic unit cell used in the preceding paragraph: the Wyckoff positions occupied are often named $n_1 = (0\ 0\ 0\ 0\ 0\ 0)$, $n_2 = \frac{1}{2}(1\ 0\ 0\ 0\ 0\ 0)$, $bc_1 = \frac{1}{4}(1\ 1\ 1\ 1\ 1\ 1)$ and $bc_2 = \frac{1}{4}(1\ 1\ 1\ 1\ 1\ \bar{1})$.

Representatives of stable quasicrystals with superspace group $Fm\bar{3}\bar{5}$ are ico-Al–Cu–Me, with Me=Fe, Ru, Os (TSAI, INOUE and MASUMOTO, 1989; TSAI, INOUE and MASUMOTO [1988b]) and ico-Al–Me–Pd, with Me=Mn, Re (TSAI, INOUE, YOKOYAMA and MASUMOTO [1990]). Ico-$Al_{63}Cu_{25}Fe_{12}$ (CORNIER-QUIQUANDON, QUIVY, LEFEBVRE, ELKAIM, HEGER, KATZ and GRATIAS [1991]; CORNIER-QUIQUANDON, BELLISENT, CALVAYRAC, CAHN, GRATIAS and MOZER [1993]) and ico-$Al_{70.5}Mn_{8.5}Pd_{21}$ (BOUDARD, DEBOISSIEU, AUDIER, JANOT, HEGER, BEELI, NISSEN, VINCENT, IBBERSON and DUBOIS [1992]) were analysed using X-ray diffraction and neutron scattering techniques on single- and polycrystalline samples, and by HRTEM (BEELI, NISSEN and ROBADEY [1991]; HIRAGA [1991]; KRAKOW, DI VINCENZO, BANCEL, COCKAYNE and ELSER [1993]). Ico-$Al_{65}Cu_{20}Ru_{15}$ was investigated by anomalous X-ray diffraction on polycristalline samples (HU, EGAMI, TSAI, INOUE and MASUMOTO [1992]). The results of the structure analyses can be summarized briefly:

(1) The hyperatoms occupy the positions n_1, n_2, bc_1 and bc_2, i.e. the vertices, mid-edge positions, and body centers of the subhypercubes of the six-dimensional face-centered hypercubic unit cell. In the case of ico-$Al_{63}Cu_{25}Fe_{12}$, Fe is concentrated at

References: p. 408.

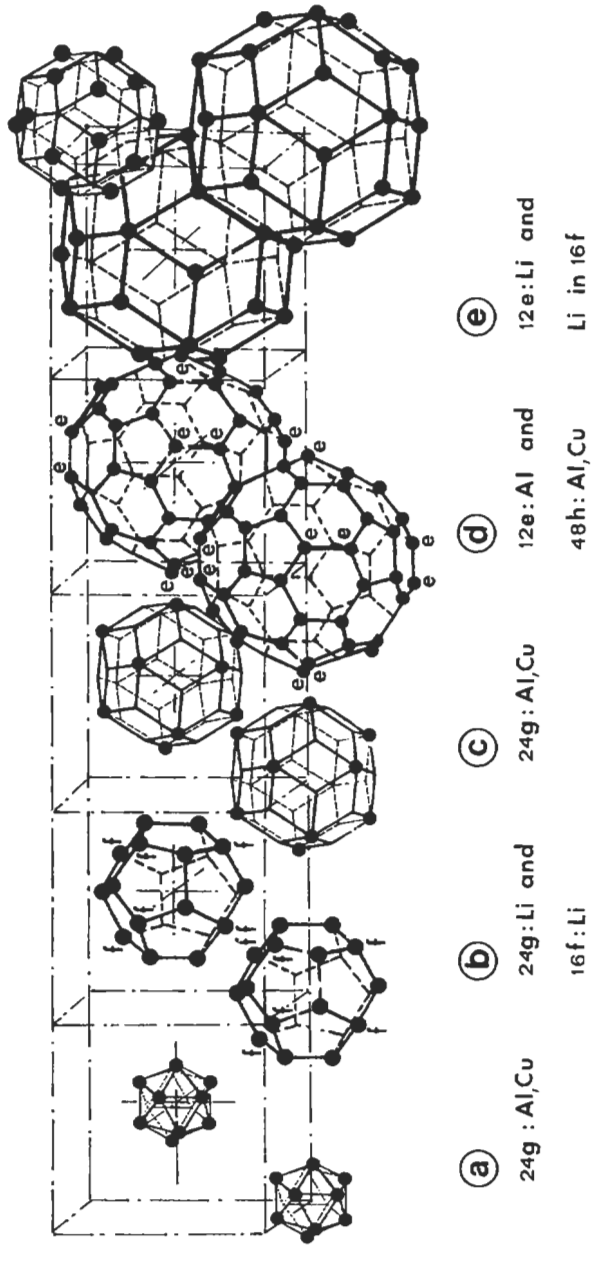

Fig. A22. Schematical illustration of the structure, and bcc packing of Pauling triacontahedra in R-Al_5CuLi_3 (from AUDIER, PANNETIER, LEBLANC, JANOT, LANG and DUBOST [1988]).

the core of hyperatoms centered on n_1 and n_2 and surrounded by successive shells of Cu and Al. Cu also occupies the body center bc_1, while bc_2 remains unoccupied. For ico-$Al_{70.5}Mn_{8.5}Pd_{21}$ (fig. A23) was found that Mn occupies the core of the

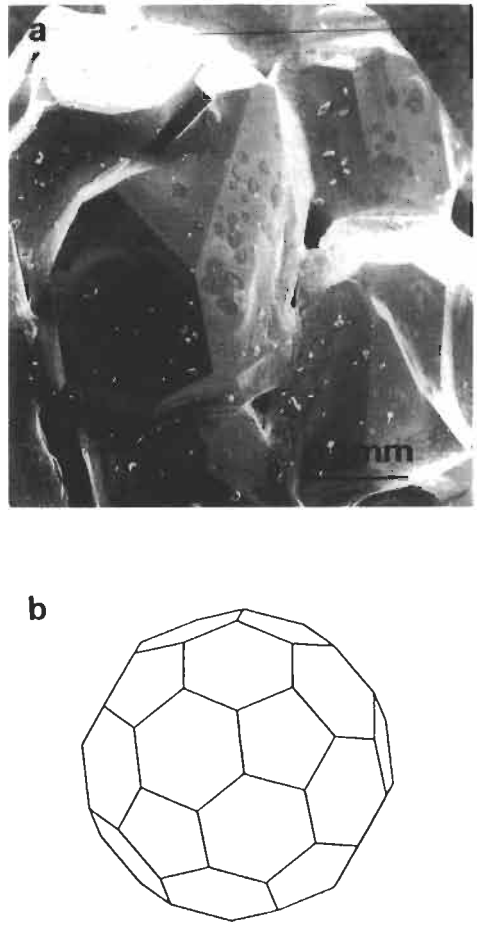

Fig. A23. (a) Single crystal of ico-$Al_{70}Mn_{20}Pd_{10}$ with shape like an (b) icosidodecahedron (from TSAI, INOUE, YOKOYAMA and MASUMOTO [1990]).

hyperatom on n_1 surrounded by an intermediate Pd and one outer Al shell, the hyperatom at n_2 consists of Mn surrounded by Al; at bc_2 a small Pd and at bc_1 possibly a small Al hyperatom may be located (fig. A24).

(2) The shapes of the hyperatoms for $Al_{63}Cu_{25}Fe_{12}$ were assumed as a large triacontahedron at n_1, a truncated triacontahedron of the same size at n_2 and a small polyhedron bounded by twofold planes at bc_1 (fig. A25). For $Al_{70.5}Mn_{8.5}Pd_{21}$ only spherical hyperatomic shapes were used in the refinements.

(3) Since the hyperatoms at the lattice nodes have a subset in common with the triacontahedra generating a canonical Penrose rhombohedra tiling, also a subset of the atoms in the three-dimensional quasicrystal structure is located on the vertices

of a Penrose tiling. The location of the other atoms, however cannot be described by a simple decoration of the unit tiles, a context dependent decoration would be necessary.

(4) In the three-dimensional structure of ico-$Al_{70.5}Mn_{8.5}Pd_{21}$ two types of pseudo-Mackay cluster are present: type 1 refers to a large icosahedron of Mn/Al and a icosidodecahedron of Pd/Al, type 2 to a large icosahedron of Mn/Pd and a icosidodecahedron of Al. The small icosahedron core of MI is absent.

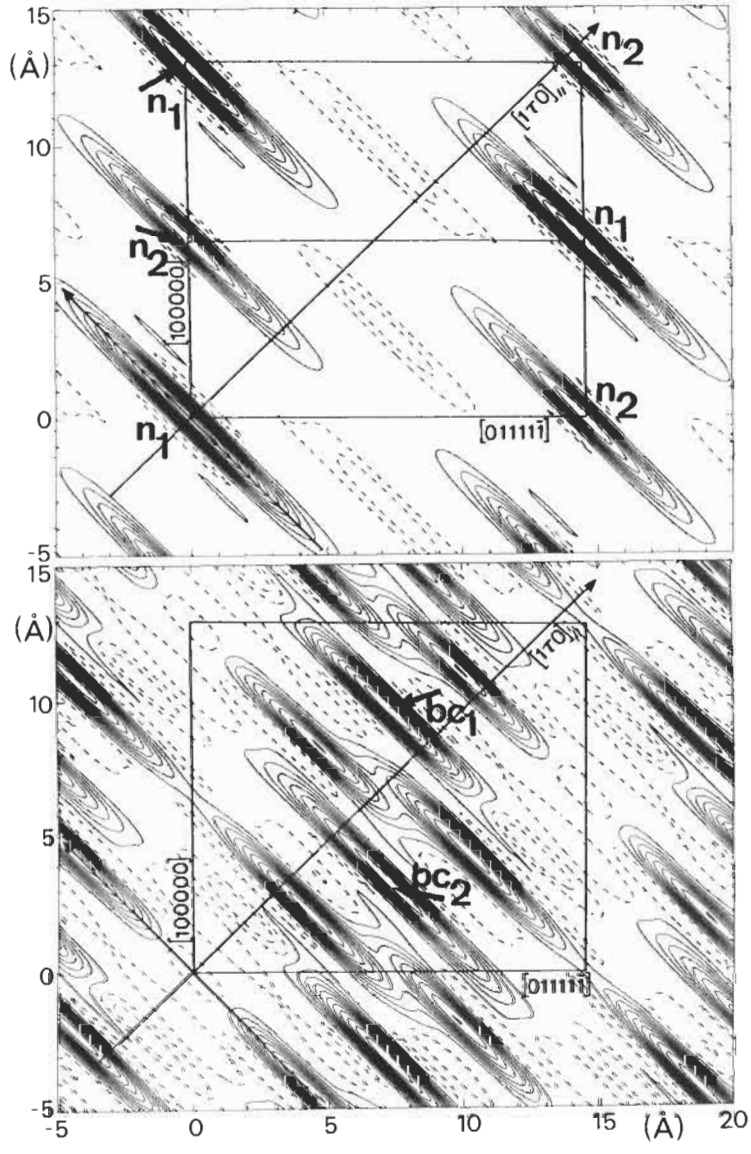

(a)

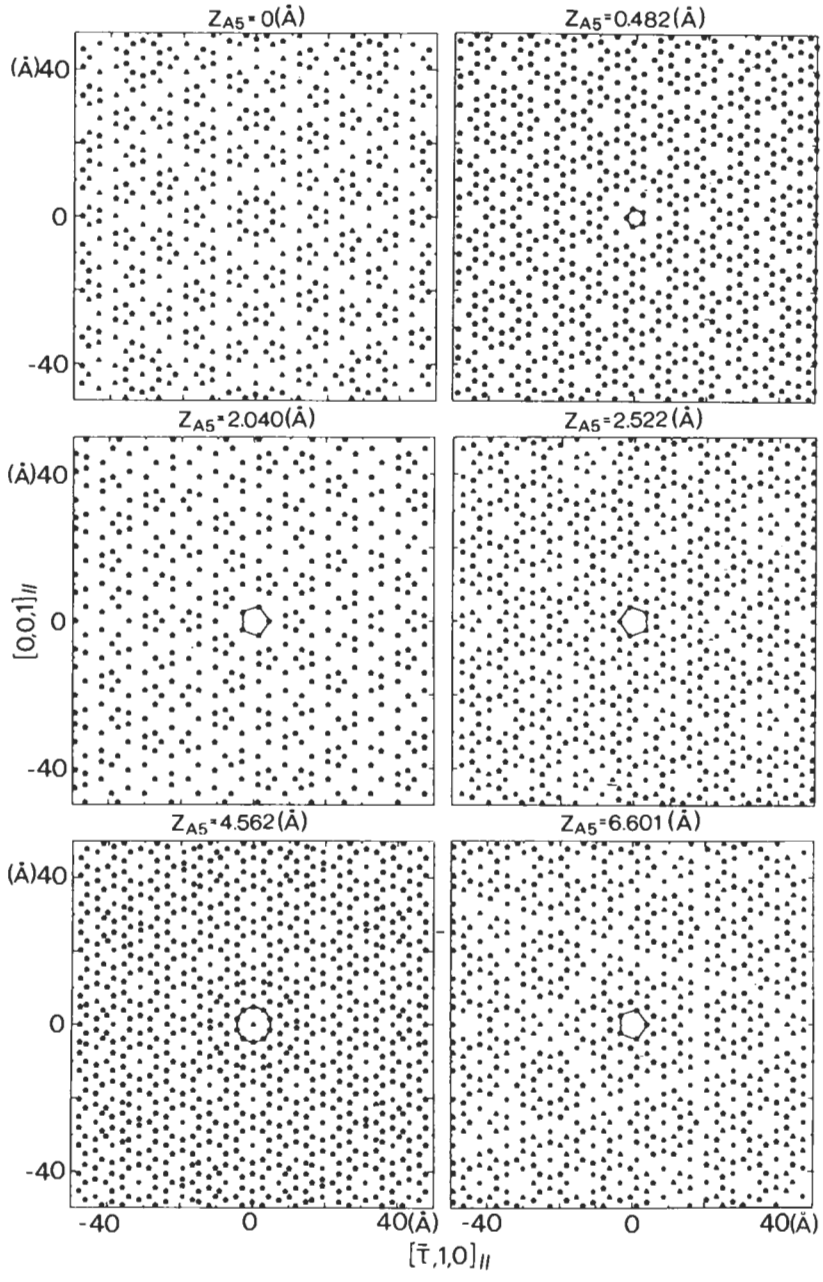

(b)

Fig. A24. (a) Cuts of six-dimensional partial hyperatomic density of ico-$Al_{70.5}Mn_{8.5}Pd_{21}$ for lattice nodes n_1, and mid-edge positions n_2 (upper drawing), and the body centers bc_1 of the subhypercubes of the F-hypercell (lower drawing). (b) Parallel-space atomic planes as obtained by cuts of the six-dimensional model (from BOUDARD, DEBOISSIEU, JANOT, DUBOIS and DONG [1991]).

References: p. 408.

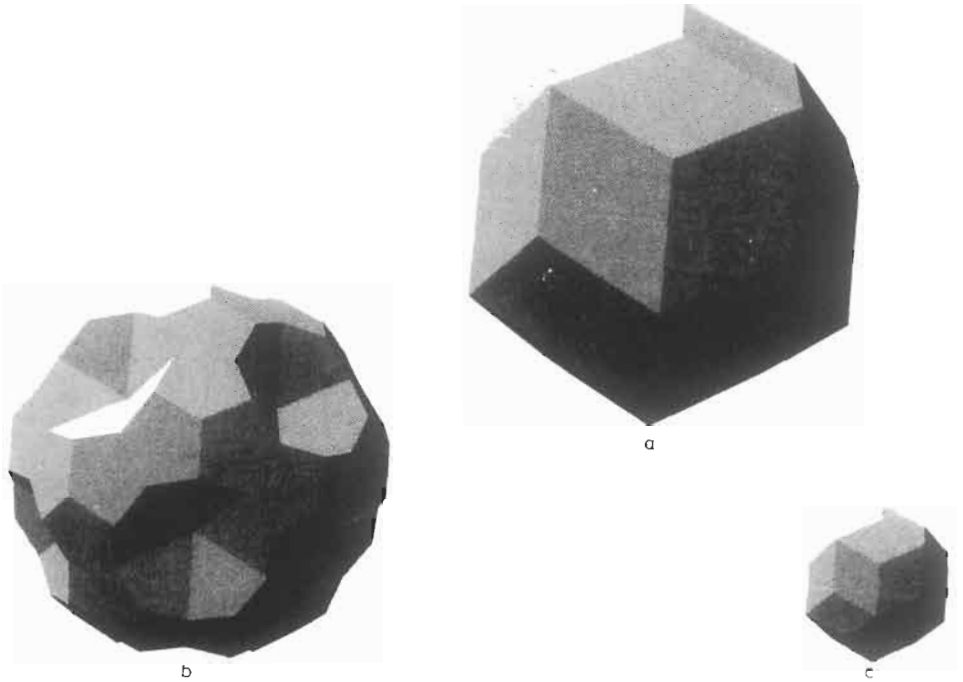

Fig. A25. The shapes of the hyperatoms in ico-$Al_{63}Cu_{25}Fe_{12}$. (a) Fe/Cu/Al triacontahedral hyperatom in the origin n_1, (b) mid-edge (n_2) Fe/Cu/Al hyperatom, and (c) Cu/Al hyperatom at bc_1 (from CORNIER–QUIQUANDON, QUIVY, LEFEBVRE, ELKAIM, HEGER, KATZ and GRATIAS [1991]).

References

ANLAGE, S.M., B. FULTZ and K.M. KRISHNAN, 1988, J. Mater. Res. **3,** 421–5.
AUDIER, M., M. DURAND-CHARRE and M. DEBOISSIEU, 1993, Phil. Mag. **B68**, 607–18.
AUDIER, M., J. PANNETIER, M. LEBLANC, C. JANOT, J.M. LANG and B. DUBOST, 1988 Physica **B153**, 136–42.
BANCEL, P.A., and P.A. HEINEY, 1986, Phys. Rev. **B33**, 7917–22.
BANCEL, P.A., P.A. HEINEY, P.W. STEPHENS, A.I. GOLDMAN and P.M. HORN, 1985, Phys. Rev. Lett. **54**, 2422–5.
BARBIER, J.-N., N. TAMURA and J.-L. VERGER-GAUGRY, 1993, J. Non-Crystall. Solids **153, 154**, 126–31.
BEELI, C., and H.-U. NISSEN, 1993, J. Non-Crystall. Solids **153, 154**, 463–7.
BEELI, C., H.-U. NISSEN and J. ROBADEY, 1991, Phil. Mag. Lett. **63**, 87–95.
BOUDARD, M., M. DEBOISSIEU, C. JANOT, J.M. DUBOIS and C. DONG, 1991, Phil. Mag. Lett. **64**, 197–206.
BOUDARD, M., M. DEBOISSIEU, M. AUDIER, C. JANOT, G. HEGER, C. BEELI, H.-U. NISSEN, H. VINCENT, R. IBBERSON and J.M. DUBOIS, 1992, J. Phys.: Condens. Matt. **4**, 10149– 68.
BURKOV, S.E., 1991, Phys. Rev. Lett. **67**, 614–7.
BURKOV, S.E., 1992, Phys. Rev. **B47**, 12325–8.
CAHN, J.W., D. GRATIAS and B. MOZER, 1988, J. Phys. France **49,** 1225–33.
CAO, W., H.Q. YE and K.H. KUO, 1988, Phys. Status Solidi (a) **107**, 511–9.

CHATTERJEE, R., and R.C. O'HANDLEY, 1989, Phys. Rev. **B39**, 8128–31.
CHATTOPADHYAY, K., S. LELE, N. THANGARAJ and S. RANGANATHAN, 1987, Acta Metall. **35**, 727–33.
CHEN, H., D.X. LI and K.H. KUO, 1988, Phys. Rev. Lett. **60**, 1645–8.
CHEN, H.S., J.C. PHILLIPS, P. VILLARS, A.R. KORTAN and A. INOUE, 1987, Phys. Rev. **B35**, 9326–9.
COOPER, M., and K. ROBINSON, 1966, Acta Crystallogr. **20**, 614–17.
CORNIER-QUIQUANDON, M., R. BELLISENT, Y. CALVAYRAC, J.W. CAHN, D. GRATIAS and B. MOZER, 1993, J. Non-Crystall. Solids **153, 154**, 10–4.
CORNIER-QUIQUANDON, M., A. QUIVY, S. LEFEBVRE, E. ELKAIM, G. HEGER, A. KATZ and D. GRATIAS, 1991, Phys. Rev. **B44**, 2071–84.
DAULTON, T.L., and K.F. KELTON, 1992, Phil. Mag. **B66**, 37–61.
DAULTON, T.L., and K.F. KELTON, 1993, Phil. Mag. **B68**, 697–711. .
DAULTON, T.L., K.F. KELTON, S. SONG and E.R. RYBA, 1992, Phil. Mag. Lett. **65**, 55–65.
DEBOISSIEU, M., C. JANOT, J.M. DUBOIS, M. AUDIER and B. DUBOST, 1991,
J. Phys.: Condens. Matt. **3**, 1–25.
DONG, C., J.M. DUBOIS, M. DEBOISSIEU and C. JANOT, 1991, J. Phys.: Cond. Matt. **3**, 1665–73.
DONG, C., J.M. DUBOIS, S.S. KANG and M. AUDIER, 1992, Phil. Mag. **B65**, 107–26.
DONG, J., K. LU, H. YANG and Q. SHAN, 1991, Phil. Mag. **B64**, 599–609.
EBALARD, S., F. SPAEPEN, 1989, J. Mater. Res. **4**, 39–43.
EDAGAWA, K., M. ICHIHARA, K. SUZUKI and S. TAKEUCHI, 1992, Phil. Mag. Lett. **66**, 19–25.
FREY, F., and W. STEURER, 1993, J. Non-Crystall. Solids **153, 154**, 600–5.
FUNG, K.K., C.Y. YANG, Y.Q. ZHOU, J.G. ZHAO, W.S. ZHAN and B.G. SHEN, 1986, Phys. Rev. Lett. **56**, 2060–3.
GRATIAS, D., J.W. CAHN, B. MOZER, 1988, Phys. Rev. **B38**, 1643–6.
GRUSHKO, B., 1993, Mater. Trans. JIM **34**, 116–21.
HAIBACH, T., B. ZHANG and W. STEURER, 1994, in preparation.
HE, L.X., X.Z. LI, Z. ZHANG and K.H. KUO, 1988, Phys. Rev. Lett. **61**, 1116–8.
HE, L.X., Y.K. WU, K.H. KUO, 1988, J. Mater. Sci. **7**, 1284–6.
HE, A.Q., Q.B. YANG and H.Q. YE, 1990, **61**, 69–75.
HE, L. X, Z. ZHANG, Y.K. WU and K.H. KUO, 1988, Inst. Phys. Conf. Ser. No. 93, **2**, 501–2.
HEINEY, P.A., P.A. BANCEL, A.I. GOLDMAN and P.W. STEPHENS, 1986, Phys. Rev. **B34**, 6746–51.
HENLEY, C.L., 1993, J. Non-Crystall. Solids **153, 154**, 172–6.
HENLEY, C.L., and V. ELSER, 1986, Phil. Mag. **B53**, L59–66.
HIRAGA, K., 1991, J. Electron Microsc. **40**, 81–91.
HIRAGA, K., 1992, Electron Microscopy **2**, EUREM 92, Granada, Spain.
HIRAGA, K., M. KANEKO, Y. MATSUO and S. HASHIMOTO, 1993, Phil. Mag. **B67**, 193–205.
HIRAGA, K., F.J. LINCOLN and W. SUN, 1991, Mater. Trans. **32**, 308–14.
HIRAGA, K., and W. SUN, 1993, Phil. Mag. Lett. **67**, 117–23.
HIRAGA, K., W. SUN and F.J. LINCOLN, 1991, Jap. J. Appl. Phys. **30**, L302–5.
HIRAGA, K., W. SUN, F.J. LINCOLN, M. KANEKO and Y. MATSUO, 1991, Jap. J. Appl. Phys. **30**, 2028–34.
HIRAGA, K., B.P. ZHANG, M. HIRABAYASHI, A. INOUE and T. MASUMOTO, 1988, Jpn. J. Appl. Phys. **27**, L951–3.
HU, R., T. EGAMI, A.P. TSAI, A. INOUE and T. MASUMOTO, 1992, Phys. Rev. **B46**, 6105–14.
HUDD, R.C., and W.H. TAYLOR, 1962, Acta Crystallogr. **15**, 441–2.
INOUE, A., H.M. KIMURA, T. MASUMOTO, A.P. TSAI and Y. BIZEN, 1987, J. Mater. Sci. Lett. **67**, 771–4.
ISHIMASA, T., H.-U. NISSEN and Y. FUKANO, 1985, Phys. Rev. Lett. **85**, 511–3.
JANOT, C., 1992, Quasicrystals. A Primer (Clarendon Press, Oxford).
JANOT, C., M. DEBOISSIEU, J.M. DUBOIS and J. PANNETIER, 1989, J. Phys.: Condens. Matt. **1**, 1029–48.
JANSSEN, T., 1986, Acta Crystallogr. **A42**, 261–71.
KANG, S., and J.M. DUBOIS, 1992, J. Phys.: Condens. Matt. **4**, 10169–98.
KANG, S.S., J.M. DUBOIS, B. MALAMAN and G. VENTURINI, 1992, Acta Crystallogr. **B48**, 770–6.
KARKUT, M.G., J.M. TRISCONE, D. ARIOSA and Ø. FISCHER, 1986, Phys. Rev. **B34**, 4390–3.
KEK, S., 1991, Thesis, Univ. Stuttgart, FRG.
KELTON, K.F., P.C. GIBBONS and P.N. SABES, 1988, Phys. Rev. **B38**, 7810–3.

KORTAN, A.R., R.S. BECKER, F.A. THIEL and H.S. CHEN, 1990, Phys. Rev. Lett. **64**, 200–3.
KORTAN, A.R., H.S. CHEN, J.M. PARSEY and L.C. KIMERLING, 1989, J. Mater. Sci. **24**, 1999–2005.
KOSHIKAWA, N., K. EDAGAWA, Y. HONDA and S. TAKEUCHI, 1993, Phil. Mag. Lett. **68**, 123–9.
KOSHIKAWA, N., S. SAKAMOTO, K. EDAGAWA and S. TAKEUCHI, 1992, Jpn. J. Appl. Phys. **31**, 966–9.
KRAKOW, W., D.P. DIVINCENZO, P.A. BANCEL, E. COCKAYNE and V. ELSER, 1993, J. Mater. Res. **8**, 24–7.
KRUMEICH, F., M. CONRAD and B. HARBRECHT, 1994, 13th International Congress on Electron Microscopy, ICEM, Paris.
KUO, K.H., 1987, Mater. Sci. Forum **22–24**, 131–40.
KUO, K.H., 1993, J. Non-Crystall. Solids **153, 154**, 40–4.
KUO, K.H., D.S. ZHOU and D.X. LI, 1987, Phil. Mag. Lett. **B55**, 33–7.
LAUNOIS, P., M. AUDIER, F. DENOYER, C. DONG, J.M. DUBOIS and M. LAMBERT, Europhys. Lett. **13**, 629–34.
LAWTHER, D.W., and R.A. DUNLAP, 1993, J. Non-Crystall. Solids **153, 154**, 611–4.
LEMMERZ, U., B. GRUSHKO, C. FREIBURG and M. JANSEN, 1994, Phil. Mag. Lett. **69**, 141–6.
LEVINE, D., and P.J. STEINHARDT, 1986, Phys. Rev. **B34**, 596–616.
LI, X.Z., and K.H. KUO, 1988, Phil. Mag. Lett. **58**, 167–71.
LI, X.Z., and K.H. KUO, 1993, J. Mater. Res. **8**, 2499–503.
LIAO, X.Z., K.H. KUO, H. ZHANG and K. URBAN, 1992, Phil. Mag. **B66**, 549–58.
LIU, W., U. KÖSTER, F. MÜLLER and M. ROSENBERG, 1992, Phys. Stat. Sol. (a) **132**, 17–34.
LUO, Z., S. ZHANG, Y. TANG and D. ZHAO, 1993, Scr. Metall. and Mater. **28**, 1513–8.
MA, X.L., and K.H. KUO, 1994, Met. and Mater. Trans. **25A**, 47–56.
MA, Y., and E.A. STERN, 1987, Phys. Rev. **B35**, 2678–81.
MA, Y., and E.A. . STERN, 1988, Phys. Rev. **B38**, 3754–65.
MA, L., R. WANG and K.H. KUO, 1988, Scr. Metall. **22**, 1791–6.
MUKHOPADHYAY, N.K., K. CHATTOPADHYAY and S. RANGANATHAN, 1988, Met. Trans. **A20**, 805–12.
MUKHOPADHYAY, N.K., N. THANGARAJ, K. CHATTOPADHYAY and S. RANGANATHAN, 1987, J. Mater. Res. **2**, 299–304.
NANAO, S., W. DMOWSKI, T. EGAMI, J.W. RICHARDSON and J.D. JORGENSEN, 1987, Phys. Rev. **B35**, 435–40.
NIIKURA, A., A.P. TSAI, A. INOUE, T. MASUMOTO and A. YAMAMOTO, 1993, Jpn. J. Appl. Phys. **32**, L1160–3.
NISSEN, H.-U., and C. BEELI, 1993, J. Non-Crystall. Solids **153, 154**, 68–71.
OHASHI, W., and F. SPAEPEN, 1987, Nature **330**, 555–6.
OKABE, T., J.I. FURIHATA, K. MORISHITA and H. FUJIMORI, 1992, Phil. Mag. Lett. **66**, 259–64.
PAVLOVITCH, A., and M KLEMAN, 1987, J. Phys. A: Math. Gen. **20**, 687–702.
PLACHKE, D., T. KUPKE, H.D. CARSTANJEN and R.M. EMRICK, 1993, J. Non-Crystall. Solids **153, 154**, 72–6.
POON, S.J., A.J. DREHMANN and K.R. LAWLESS, 1985, Phys. Rev. Lett. **55**, 2324–7.
QIU, S.-Y., and M.V. JARIC, 1993, J. Non-Crystall. Solids **153, 154**, 221–6.
REYES-GASGA, J., A. LARA, H. RIVEROS and M. JOSE-YACAMAN, 1992, Mater. Sci. Eng. **A150**, 87–99.
ROMEU, D., 1993, Phil. Mag. **B67**, 77–96.
SAINTFORT, P., and B. DUBOST, 1986, J. Phys. France **47**, C3-321–30.
SASTRY, G.V.S., V.V. RAO, P. RAMACHANDRARAO and T.R. ANANTHARAMAN, 1986, Scr. metall. **20**, 191–3.
SCHURER, P.J., B. KOOPMANS, F. VAN DER WOUDE, 1988, Phys. Rev. **B37**, 507–10.
SHECHTMAN, D., I. BLECH, D. GRATIAS and J.W. CAHN, 1984, Phys. Rev. Lett. **53**, 1951–3.
SHEN, Y., G.J. SHIFLET and S.J. POON, 1988, Phys. Rev. **B38**, 5332–7.
SHOEMAKER, C.B., 1993, Phil. Mag. **B67**, 869–81.
VAN SMAALEN, S., J.L. DE BOER and Y. SHEN, 1991, Phys. Rev. **B43**, 929–37.
SOCOLAR, J.E.S., and P.J. STEINHARDT, 1986, Phys. Rev. **B34**, 617–47.
SONG, S., and E.R. RYBA, 1992, Phil. Mag. Lett. **65**, 85–93.
SONG, S., L. WANG and E.R. RYBA, 1991, Phil. Mag. Lett. **63**, 335–44.
SRINIVAS, V., R.A. DUNLAP, D. BAHADUR and E. DUNLAP, 1990, Phil. Mag. **B61**, 177–88.
STEURER, W., 1991, J. Phys.: Condens. Matter **3**, 3397–410.
STEURER, W., T. HAIBACH, B. ZHANG, C. BEELI and H.-U. NISSEN, 1994, J. Phys.: Condens. Matter **6**, 613–32.
STEURER, W., T. HAIBACH, B. ZHANG, S. KEK and R. LÜCK, 1993, Acta Crystallogr. **B49**, 661–75.
STEURER, W., and K.H. KUO, 1990, Acta Crystallogr. **B46**, 703–12.

TANG, Y., D. ZHAO, Z. LUO, N. SHENG and S. ZHANG, 1993, Mater. Lett. **18**, 148–50.
TODD, J., R. MERLIN, R. CLARKE, K.M. MOHANTY and J.D. AXE, 1986, Phys. Rev. Lett. **57**, 1157–60.
TSAI, A.P., A. INOUE and T. MASUMOTO, 1987, Jpn. J. Appl. Phys. **26**, L1505–7.
TSAI, A.P., A. INOUE and T. MASUMOTO, 1988a, Trans. JIM **29**, 521–4.
TSAI, A.P., A. INOUE and T. MASUMOTO, 1988b, J.J. Appl. Phys. **27**, L1587–90
TSAI, A.P., A. INOUE and T. MASUMOTO, 1988c, J.J. Appl. Phys. **27**, L5–8.
TSAI, A.P., A. INOUE and T. MASUMOTO, 1988d, J. Mater. Sci. Lett. **7**, 322–6.
TSAI, A.P., A. INOUE and T. MASUMOTO, 1989, Mater. Trans. JIM **30**, 463–73.
TSAI, A.P., A. INOUE and T. MASUMOTO, 1991, Phil. Mag. Lett. **64**, 163–7.
TSAI, A.P., A. INOUE and T. MASUMOTO, 1993, Mater. Trans. JIM **34**, 155–61.
TSAI, A.P., A. INOUE, T. MASUMOTO, A. SATO and A. YAMAMOTO, 1992, Jpn. J. Appl. Phys. **31**, 970–3.
TSAI, A.P., A. INOUE, Y. YOKOYAMA and T. MASUMOTO, 1990, Mater. Trans. JIM **31**, 98–103.
TSAI, A.P., T. MASUMOTO and A. YAMAMOTO, 1992, Phil. Mag. Lett. **66**, 203–8.
TSAI, A.-P., Y. YOKOYAMA, A. INOUE and T. MASUMOTO, 1990, Jpn. J. Appl. Phys. **29**, L1161–4.
TSAI, A.-P., Y. YOKOYAMA, A. INOUE and T. MASUMOTO, 1991, J. Mater. Res. **6**, 2646–52.
WANG, N., H. CHEN and K.H. KUO, 1987, Phys. Rev. Lett. **59**, 1010–13.
WANG, N., K.K. FUNG and K.H. KUO, 1988, Appl. Phys. Lett. **52**, 2120–22.
WANG, N., and K.H. KUO, 1988, Acta Crystallogr. **A44**, 857–63.
WANG, N., and K.H. KUO, 1990, Phil. Mag. Lett. **61**, 63–8.
WELBERRY, T.R., 1989, J. Appl. Cryst. **22**, 308–14.
WIDOM, M., and R. PHILLIPS, 1993, J. Non-Crystall. Solids **153, 154**, 282–7.
YAMAMOTO, A., 1992, Phys. Rev. **B45**, 5217–27.
YOKOYAMA, Y., A. INOUE and T. MASUMOTO, 1992, Mater. Trans. JIM **33**, 1012–9.
YOKOYAMA, Y., A.P. TSAI, A. INOUE, T. MASUMOTO and H.S. CHEN, 1991, Mater. Trans. JIM **32**, 421–8.
ZHANG, H., and K.H. KUO, 1989, Scr. Metall. **23**, 355–8.
ZHANG, H., D.H. WANG and K.H. KUO, 1988, Phys. Rev. **B37**, 6220–5.
ZHANG, Z., H.Q. YE and K.H. KUO, 1985, Phil. Mag. **A52**, L49–52.

Further reading

FUJIWARA, T., and T. OGAWA, (eds.) 1990, Quasicrystals, Springer Series in Solid State Science **93**.
GOLDMAN, A.I., and K.F. KELTON, 1993, Rev. Mod. Phys. **65**, 213–30.
KELTON, K.F., 1995, in: Intermetallic Compounds — Principles and Practice, eds. J.H. Westbrook and R.L. Fleischer (Wiley, Chichester), Vol. 1, pp. 453–491.
JANOT, C., 1992, Quasicrystals. A Primer (Clarendon Press, Oxford).
JANSSEN, T., 1988, Phys. Rep. **168**, 55–113.
STEURER, W., 1990, Z. Kristallogr. **190**, 179–234.

CHAPTER 5

METALLURGICAL THERMODYNAMICS

D.R. GASKELL

School of Materials Engineering
Purdue University
West Lafayette, IN 47907, USA

R. W. Cahn and P. Haasen†, eds.
Physical Metallurgy; fourth, revised and enhanced edition

1. Introduction

Metallurgical thermodynamics is concerned with the equilibrium states of existence available to systems, and with the effects of external influences on the equilibrium state. The thermodynamic state of a system is defined in terms of state variables (or *state functions*) and the state variables occur in two categories; *intensive* variables such as pressure, P, and temperature, T, the values of which are independent of the size of the system, and *extensive* variables such as internal energy, U, and volume, V, the values of which are dependent on the size of the system. The simplest equation of state is the ideal gas law,

$$PV = nRT \tag{1}$$

where n is the number of moles of the gas and R is the universal gas constant. In considering a fixed quantity of ideal gas, only two of the state functions in eq. (1) are independent and the other is dependent. Thus, in a three-dimensional diagram employing P, V and T as ordinates, the equilibrium states of existence of the fixed quantity of gas lie on a definite surface. In any *reversible* change of state of the gas the path of the process lies on this equilibrium surface, such that, in moving from the initial to the final state, the gas passes through a continuum of equilibrium states. Under such conditions the *work*, w, done on or by the gas during the process is given by:

$$w = \int_{V_{initial}}^{V_{final}} P dV, \tag{2}$$

and thus the magnitude of w is dependent on the actual process path taken over the equilibrium surface between the final and initial states. In an *irreversible* process the state of the gas momentarily leaves the equilibrium surface while moving between the initial and final states.

1.1. The First and Second Laws of Thermodynamics

When a system undergoes a process in which it moves from one state to another, the change in the internal energy of the system, ΔU, is given by:

$$\Delta U = U_2 - U_1 = q - w, \tag{3}$$

where q is the heat entering or leaving the system and w is the work done on or by the system during the change of state. For an increment of the process the change is:

$$dU = dq - dw. \tag{4}$$

Equations (3) and (4) are statements of the *First Law of Thermodynamics*. By convention, heat entering the system and work done *by* the system are positive quantities. Equation (3) is remarkable in that, although the individual values of q and w are dependent on the path taken by the system between the initial and final states, their algebraic sum (which is the difference between U_2 and U_1) is independent of the process path. Thus integration of eq. (4) to obtain eq. (3) requires that the process path be known and that the process

be conducted reversibly.

The *Second Law of Thermodynamics* states that, for a reversible change of state, the integral of dq/T is independent of the process path. As one of the properties of a state function is that the difference between the values of the function in any two thermodynamic states is independent of the process path taken by the system in moving between the two states, the term dq/T is the differential of a state function. The state function *entropy*, S, is thus defined as:

$$dS = dq_{rev} / T. \tag{5}$$

If change in volume against an external pressure is the only form of work performed during a reversible change of state of a closed system, the work performed is given by eq. (2), and substitution of eqs. (2) and (5) into eq. (4) gives:

$$dU = TdS - PdV. \tag{6}$$

Equation (6), which is a combination of the First and Second Laws of Thermodynamics, gives the variation of U (as the dependent variable) with S and V (as the independent variables).

From consideration of the difference between reversible and irreversible processes and the Second Law, eq. (6) gives the following criteria for thermodynamic equilibrium in a closed system of fixed composition:

(i) S is a maximum at constant U and V;

(ii) U is a minimum at constant S and V.

Equation (6) involves the extensive thermodynamic properties S and U as independent variables. Although it is possible to measure and, with sufficient ingenuity on the part of the experimenter, to control the volume of a system, experimental control of the entropy of a system is virtually impossible, and consequently the criteria for equilibrium obtained from eq. (6) are not of practical use. From the practical point of view it would be desirable to have an equation as simple in form as eq. (6) but in which the independent variables are the intensive properties P and T, both of which are amenable to experimental measurement and control. Such an equation would also provide a criterion for equilibrium in a constant pressure–constant temperature system.

1.2. Auxiliary thermodynamic functions

The required auxiliary state functions are generated by Legendre transformations of U. For example, in eq. (6), written as

$$U = U(S, V),$$

a Legendre transform, H, of U is obtained using:

$$-P = \left(\frac{\partial U}{\partial V}\right)_S = \frac{U - H}{V - 0}. \tag{7}$$

At constant S, the tangent to the variation of U with V passes through the points $U = U$, $V = V$ and $U = H$, $V = 0$. Rearrangement of eq. (7) gives:

$$H = U + PV,$$

which, on differentiation, gives:

$$dH = dU + PdV + VdP. \tag{8}$$

Substitution of eq. (6) into eq. (8) gives:

$$dH = TdS + VdP, \tag{9}$$

in which the extensive variable V has been replaced by the intensive variable P. The transform H is called the *enthalpy*.

Writing eq. (9) as

$$H = H(S, P),$$

a Legendre transform, G, of H is obtained as:

$$T = \left(\frac{\partial H}{\partial S}\right)_P = \frac{H - G}{S - 0} \tag{10}$$

or: $G = H - TS,$

which, on differentiation, gives:

$$dG = dH - TdS - SdT = -SdT + VdP, \tag{11}$$

in which the extensive variable S has been replaced by the intensive variable T. This transform, G, is called the *Gibbs free energy*. Being dependent on the independent variables T and P, the Gibbs free energy is the most useful of thermodynamic functions and provides the practical criterion that, at constant T and P, thermodynamic equilibrium is established when the Gibbs free energy is minimized.

A third Legendre transform yields the *Helmholtz free energy*, or work function A, defined as

$$A = U - TS.$$

In a multicomponent system containing n_1 moles of component 1, n_2 moles of component 2, n_i moles of component i, etc.:

$$G = G(T, P, n_1, n_2, ..., n_i)$$

and thus,

$$dG = \left(\frac{\partial G}{\partial T}\right)dT + \left(\frac{\partial G}{\partial P}\right)dP + \left(\frac{\partial G}{\partial n_1}\right)dn_1 + \ldots \left(\frac{\partial G}{\partial n_i}\right)dn_i \tag{12}$$

The derivative

$$\left(\frac{\partial G}{\partial n_i}\right)_{T, P, n_j}$$

is of particular significance and is called the *chemical potential*, μ_i, or the partial molar free energy, $\overline{G_i}$, of the component i. Thus, in view of eq. (11), eq. (12) can be written as

$$dG = -SdT + VdP + \sum \bar{G}_i dn_i, \tag{13}$$

and the equilibrium state of any system undergoing any type of reaction at constant temperature and pressure can be determined by application of this equation.

2. *Metallurgical thermochemistry*

2.1. The measurement of changes in enthalpy

In order to distinguish between the value of an extensive property of a system containing n moles and the molar value of the property, the former will be identified by the use of a prime ('), e.g., with respect to enthalpy, $H' = nH$.

From eqs. (5) and (9), for a process occurring reversibly at constant pressure P:

$$dH' = dq_P,$$

which, on integration, gives:

$$\Delta H' = q_P.$$

Thus, in a system undergoing a process in which the only work performed is the work of expansion or contraction against the constant pressure P, the change in enthalpy, $\Delta H'$, can be measured as the heat q_P entering or leaving the system during the constant pressure process. In the case of heat entering the system the process involves an increase in the temperature of the system and the *constant pressure molar heat capacity*, c_P, is defined as:

$$c_p = \frac{dq_p}{dT} = \left(\frac{\partial H}{\partial T}\right)_p. \tag{14}$$

The constant pressure molar heat capacity of a system can be measured by the methods of calorimetry. In metallurgical applications the measured values are fitted to an equation of the form

$$c_p = a + bT + cT^{-2}.$$

For example, the constant pressure molar heat capacity of solid silver varies with temperature in the range 298–1234 K as:

$$c_{p,Ag(s)} = 21.3 + 8.54 \times 10^{-3} T + 1.51 \times 10^{5} T^{-2} \text{ J/K mole}$$

and hence, from eq. (14), the difference between the molar enthalpy of solid Ag at a temperature T and the molar enthalpy at 298 K is

References: p. 469.

$$\Delta H = \int_{298}^{T} c_{P,Ag} \mathrm{d}T$$
$$= 21.3(T - 298) + 4.27 \times 10^{-3}\left(T^2 - 298^2\right)$$
$$- 1.51 \times 10^{5}\left(\frac{1}{T} - \frac{1}{298}\right) \mathrm{J/mole},$$

which is thus the quantity of heat required to raise the temperature of one mole of solid Ag from 298 K to T.

Transformation of a low-temperature phase to a high-temperature phase involves the absorption of the latent heat of the phase change, e.g., the transformation of one mole of silver from the solid to the liquid state at the normal melting temperature of 1234 K requires a heat input of 11.09 kJ. Thus at 1234 K the molar enthalpy of melting of Ag, ΔH_m, is

$$\Delta H_{m,Ag.1234\mathrm{K}} = H_{Ag(l),1234\mathrm{K}} - H_{Ag(s),1234\mathrm{K}} = 11.09\mathrm{kJ}.$$

The molar heat capacity of liquid Ag is independent of temperature, $c_{P,\mathrm{Ag(l)}} = 30.5$ J/K mole, and the difference between the molar enthalpy of liquid Ag at a temperature T and the molar enthalpy of solid Ag at 298 K is

$$H_{Ag(l),T} - H_{Ag(s),298\mathrm{K}} = \int_{298}^{1234} c_{p,Ag(s)} \mathrm{d}T + \Delta H_{m,Ag.1234\mathrm{K}} + \int_{1234}^{T} c_{p,Ag(l)} \mathrm{d}T.$$

As chemical reactions involve the absorption or evolution of heat, they also necessarily involve changes in enthalpy. For example, when conducted at *298* K, the oxidation reaction

$$2\mathrm{Ag}_{(s)} + \tfrac{1}{2}\mathrm{O}_{2(g)} = \mathrm{Ag_2O}_{(s)}$$

is accompanied by the evolution of 30.5 kJ of heat per mole of Ag_2O produced. Thus,

$$q = \Delta H = -30.5k\mathrm{J},$$

or the system existing as one mole of Ag_2O has an enthalpy of 30.5 kJ less than the system existing as two moles of Ag and half a mole of oxygen gas at 298 K.

As the enthalpies of substances are not measurable quantities, i.e., only changes in enthalpy can be measured (as the evolution or absorption of heat), it is conventional to designate a reference state in which the relative enthalpy is zero. This reference state is the elemental substance existing in its stable form at 298 K and $P = 1$ atm. In practice the designation of $P = 1$ atm is relatively unimportant as the enthalpies of condensed phases are not significantly dependent on pressure and the enthalpy of an ideal gas is independent of pressure. Thus, in the above example:

$$\Delta H_{298} = H_{\mathrm{Ag_2O(s),298}} - 2H_{\mathrm{Ag(s),298}} - \tfrac{1}{2} H_{\mathrm{O_2(g),298}}.$$

As $H_{Ag(s),298}$ and $H_{O_2(g),298}$ are arbitrarily assigned values of zero, the relative molar enthalpy of Ag_2O at 298 K is simply equal to the experimentally-measured molar heat of formation of Ag_2O at 298 K. At any other temperature T:

$$\begin{aligned}\Delta H_T &= H_{Ag_2O,T} - 2H_{Ag,T} - \tfrac{1}{2} H_{O_2,T} \\ &= H_{Ag_2O,298} + \int_{298}^{T} c_{p,Ag_2O} dT - 2H_{Ag,298} - 2\int_{298}^{T} c_{p,Ag} dT \\ &\quad - \tfrac{1}{2} H_{O_2,298} - \tfrac{1}{2}\int_{298}^{T} c_{p,Ag} dT \\ &= \Delta H_{298} + \int_{298}^{T} \Delta c_p dT,\end{aligned}$$

where

$$\Delta c_p = c_{p,Ag_2O} - 2c_{p,Ag} - \tfrac{1}{2} c_{p,O_2}.$$

The enthalpy–temperature diagram for the oxidation of silver is shown in fig. 1.

2.2. The measurement of entropy

From eqs. (5) and (14), we find:

$$dS = \frac{dq_p}{T} = \frac{c_p dT}{T}.$$

Thus, the variation of entropy with temperature at constant pressure is obtained from measured heat capacities as

$$S_T = S_0 + \int_0^T \frac{c_p}{T} dT.$$

Nernst's heat theorem, which is also known as the *Third Law of Thermodynamics*, states that all substances at complete internal equilibrium have zero entropy at 0 K, i.e., $S_0 = 0$. Thus, in contrast to enthalpies, the entropies of substances have absolute values.

According to Gibbs, entropy is a measure of the degree of disorder in a system. Thus the entropy of the gaseous state is greater than that of the liquid state, which, in turn, is greater than that of the solid state. The transformation of a solid to a liquid at the normal melting temperature, T_m, involves the absorption of ΔH_m per mole. Thus, at T_m, the molar entropy of the liquid exceeds that of the solid by the molar entropy of fusion, ΔS_m, given by eq. (5) as:

$$\Delta S_m = \Delta H_m / T_m.$$

This corresponds with the fact that the liquid state is more disordered than the solid state, and ΔS_m is a measure of the difference in degree of order. For simple metals, with similar crystal structures and similar liquid structures, ΔS_m lies in the range 8–16 J/K. This correlation is known as *Richard's rule*. Similarly, at the normal boiling temperature, T_b, the molar entropy of boiling, ΔS_b, is obtained from the molar heat of boiling as:

References: p. 469.

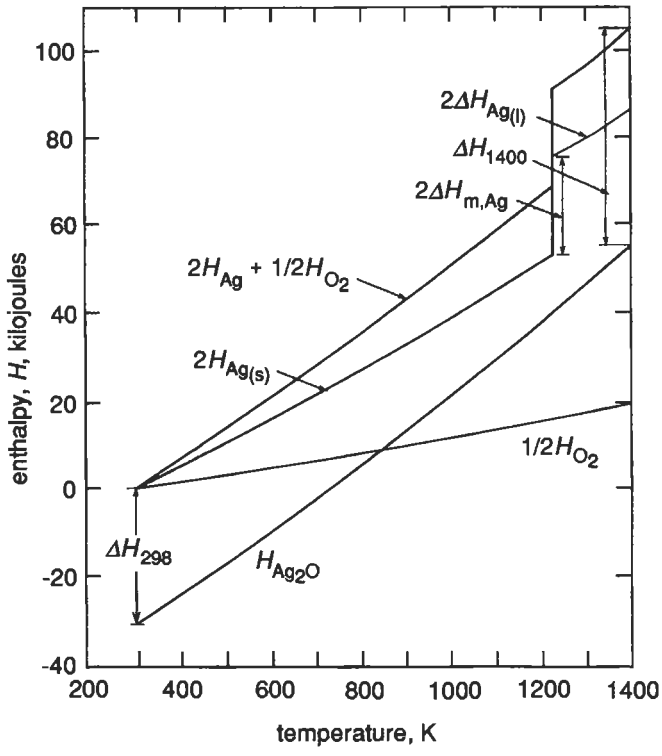

Fig. 1. The enthalpy–temperature diagram for the reaction $2Ag + \frac{1}{2}O_2 = Ag_2O$.

$$\Delta S_b = \Delta H_b / T_b.$$

For simple metals $\Delta S_b \approx 88$ J/K, which indicates that the difference in disorder between the gaseous state at 1 atm pressure and the liquid state significantly exceeds the corresponding difference between the liquid and solid states. The correlation $\Delta H_b = 88 T_b$ is known as *Trouton's rule*.

Although the degrees of disorder, and hence the entropies of condensed states, are not noticeably dependent on pressure, the entropy of a gas is a significant function of pressure. As the internal energy, U', of an ideal gas is dependent only on T, an isothermal compression of an ideal gas from P_1 to P_2 does not involve a change in U'. Thus, from eq. (3), the work of compression, w, equals the heat transferred from the gas to the isothermal surroundings at the temperature T. This transfer of heat from the gas decreases its entropy by the amount

$$\Delta S' = \frac{q}{T} = \frac{w}{T} = \int_1^2 \frac{P \mathrm{d}V'}{T},$$

which, from eq. (1), gives:

$$\Delta S' = \int_1^2 \frac{nR\,dV}{V} = -\int_1^2 nR\,d\ln P.$$

Thus

$$S_2' - S_1' = nR\ln(P_1/P_2),$$

which corresponds with the fact that a gas at high pressure is a less disordered state than a gas at low pressure.

As changes in entropy are caused by the transfer of heat, chemical reactions involving heat changes necessarily involve changes in entropy. At 298 K and 1 atm pressure, the molar entropies of $Ag_{(s)}$, $O_{2(g)}$ and $Ag_2O_{(s)}$ are 42.7, 205 and 122 J/K, respectively. Thus the entropy change for the oxidation

$$2Ag_{(s)} + \tfrac{1}{2}O_{2(g)} = Ag_2O_{(s)}$$

at 298 is:

$$\Delta S = 122 - (2 \times 42.7) - (0.5 \times 205) = -65.9\ \text{J/K mole}.$$

This can be viewed in two ways: (i) the entropy decrease is due to the loss of the heat of oxidation from the reacting system, or (ii) the degree of disorder in the system existing as one mole of Ag_2O is less than that when the system exists as two moles of Ag and half a mole of oxygen gas at 1 atm pressure.

The variation, with temperature, of the entropy change for the reaction is determined by the heat capacities of the reactants and products as:

$$\Delta S_T = \Delta S_{298} + \int_{298}^{T} (\Delta c_p/T)dT$$

The entropy–temperature diagram corresponding to fig. 1 is shown in fig. 2.

From the definition of Gibbs free energy, eq. (10), the change in Gibbs free energy due to a chemical reaction occurring at a temperature T, ΔG_T, is

$$\begin{aligned}\Delta G_T &= \Delta H_T - T\Delta S_T \\ &= \Delta H_{298} + \int_{298}^{T} \Delta c_p dT - T\Delta S_{298} - T\int_{298}^{T} (\Delta c_p/T)dT.\end{aligned} \tag{15}$$

Thus, the variation of the change in Gibbs free energy with temperature can be determined from measurement of the variation, with temperature, of the constant pressure molar heat capacities of the reactants and products and measurement of the enthalpy change of the reaction at one temperature. For the oxidation of solid silver, such data give

$$\begin{aligned}\Delta G_T = &-34200 + 87.9T - 1.76T\ln T - 10.8 \times 10^{-3}T^2 \\ &+ 3.2 \times 10^5 T^{-1}\ \text{J/mole}\ Ag_2O.\end{aligned} \tag{16}$$

References: p. 469.

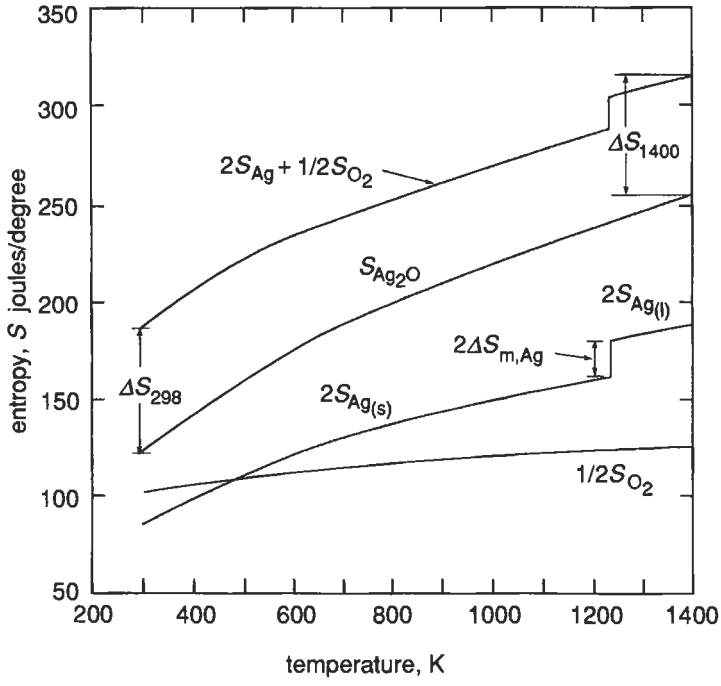

Fig. 2. The entropy–temperature diagram for the reaction $2Ag + \frac{1}{2}O_2 = Ag_2O$.

3. *Phase equilibrium in a one-component system*

At constant T and P the equilibrium state is that in which the Gibbs free energy has its minimum possible value. In a one-component system the states of existence available are the gaseous and liquid states and the various allotropic or polymorphic forms of the solid state. At any T and P the state with the lowest Gibbs free energy is the stable state. For the transformation

solid $\rightarrow$ liquid:

$$\Delta G_m(P,T) = G_{(l)}(P,T) - G_{(s)}(P,T) = \Delta H_m(P,T) - T\Delta S_m(P,T). \tag{17}$$

If ΔG_m is negative, the transformation decreases the Gibbs free energy of the system and hence the liquid is stable relative to the solid. Conversely, if ΔG_m is positive the solid is stable relative to the liquid. As absolute values of enthalpy cannot be measured it follows that absolute values of Gibbs free energy cannot be measured. Thus only changes in G can be measured.

The solid and liquid phases coexist in equilibrium with one another in that state at which $\Delta G_m = 0$, i.e., where $G_{(l)} = G_{(s)}$. From eq. (15), at any pressure P this equilibrium occurs at the temperature T_m given by

$$T_m = \Delta H_m / \Delta S_m,$$

and hence T_m is the equilibrium melting temperature of the solid at the pressure P. From eq. (10), G is decreased by decreasing H and increasing S and hence nature prefers states of low enthalpy and high entropy. As $H_{(l)} > H_{(s)}$ and $S_{(l)} > S_{(s)}$ the enthalpy contribution to G favors the solid as the stable state and the entropy contribution favors the liquid as the stable state. In eq. (17) the entropy contribution to ΔG is temperature–dependent and the enthalpy contribution is not. Thus, at high temperatures the former contribution dominates, at low temperatures the latter contribution dominates, and at a unique temperature T_m the two contributions cancel to make $\Delta G = 0$.

For the two-phase equilibrium to exist,

$$G_{(l)} = G_{(s)},$$

and maintenance of the two-phase equilibrium with variation in T and P requires that T and P be varied in such a manner that

$$dG_{(l)} = dG_{(s)}$$

or, from eq. (11), such that

$$-S_{(l)}dT + V_{(l)}dP = -S_{(s)}dT + V_{(s)}dP,$$

i.e.,

$$(dP / dT)_{eq} = \left(S_{(l)} - S_{(s)}\right) / \left(V_{(l)} - V_{(s)}\right) = \Delta S_m / \Delta V_m$$

As equilibrium between the two phases is maintained, $\Delta H_m = T\Delta S_m$:

$$\left(dP/dT\right)_{eq} = \Delta H_m / T\Delta V_m. \tag{18}$$

Equation (18) is the *Clapeyron equation*, which, on integration, gives the variation of T and P required for maintenance of the two-phase equilibrium. Strictly, integration requires knowledge of the pressure and temperature dependences of ΔH_m and ΔV_m. However, for relatively small departures from the state $P = 1$ atm, T_m, ΔH_m and ΔV_m can be taken as constants, in which case:

$$P_2 - P_1 = \frac{\Delta H_m}{\Delta V_m} \ln\left(\frac{T_2}{T_1}\right).$$

Equation (18) can be applied to condensed phase–vapor phase equilibria by making the approximation $\Delta V = V_{(v)} - V_{(\text{condensed phase})} \approx V_{(v)}$ and assuming ideal behavior of the vapor phase, i.e., $V_{(v)} = RT/P$, i.e.,

$$\left(dP/dT\right)_{eq} = \frac{P\Delta H_b}{RT^2}. \tag{19}$$

Equation (19) is the *Clausius–Clapeyron equation.*

References: p. 469.

If ΔH_b (the molar enthalpy of boiling) is not a function of temperature (which requires $c_{p(v)} = c_{p(l)}$), integration of eq. (19) gives

$$\ln P = -\frac{\Delta H_b}{RT} + \text{const.},$$

and if ΔH_b is a linear function of T (which requires that Δc_p be independent of temperature) given by $\Delta H_{b,T} = \Delta H_0 + \Delta c_p T$, integration gives

$$\ln P = -\frac{\Delta H_0}{RT} + \frac{\Delta c_p}{R} \ln T + \text{const.}$$

as either (i) the variation of the saturated vapor pressure with temperature or (ii) the variation of the equilibrium boiling temperature with pressure. Experimentally measured vapor pressures are normally fitted by an equation of the type

$$\ln P = -A/T + B \ln T + C.$$

The solid, liquid and vapor states exist on surfaces in G–T–P space. The solid- and liquid-surfaces intersect at a line (along which $G_{(l)} = G_{(s)}$) and projection of this line onto the basal P–T plane of the G–T–P diagram gives the pressure dependence of T_m. Similarly the vapor- and liquid-surfaces intersect at a line, projection of which onto the basal P–T plane gives the variation, with temperature, of the saturated vapor pressure of the liquid. Similar projection of the line of intersection of the surfaces for the solid and vapor states gives the variation, with temperature, of the saturated vapor pressure of the solid. The three lines of two-phase equilibrium in G–T–P space intersect at a point, called the *triple point*, at which all three phases are in equilibrium with one another. Consideration of the geometry of the intersections of the surfaces in G–T–P space shows that, in a one-component system, a maximum of three phases can exist in equilibrium. Alternatively, as the three phases co-exist in equilibrium at fixed values of T and P the equilibrium is invariant, i.e., has no degrees of freedom. The phase diagram for H_2O is shown in fig. 3 and a schematic representation of the section of G–T–P space at 1 atm pressure is shown in fig. 4. In fig. 4, the slope of any line at any point is $-S$ for that state and hence the "steepness" of the lines increases in the order solid, liquid, vapor. Also the curvatures of the lines are $(\partial^2 G/\partial T^2)_p = -(\partial S/\partial T)_p = -c_p/T$.

4. *Chemical reaction equilibrium*

From eq. (13), at constant T and P, the Gibbs free energy varies with composition in a chemically reacting system as

$$dG' = \sum \overline{G}_i \, dn_i.$$

The reaction proceeds spontaneously in that direction which involves a decrease in Gibbs free energy, and reaction equilibrium is attained when, thereby, the Gibbs free energy is minimized, i.e., when $dG' = 0$.

Consider the water–gas reaction

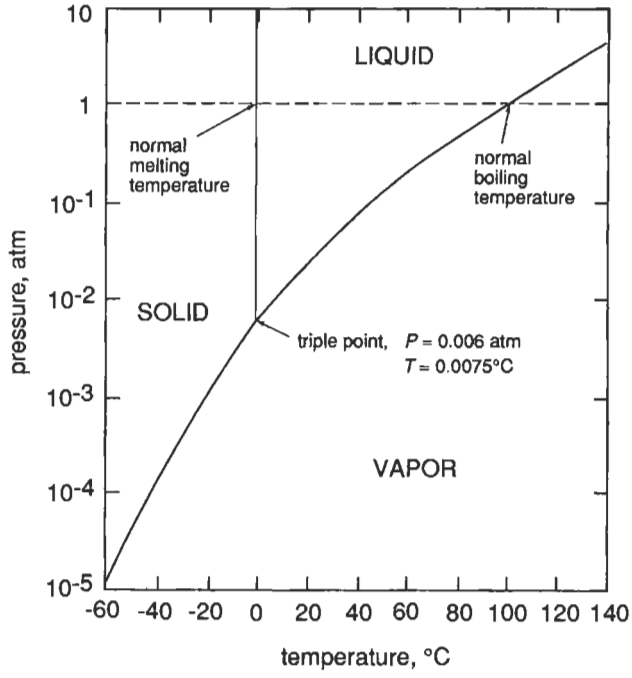

Fig. 3. The phase diagram for H_2O.

$$H_2O_{(g)} + CO_{(g)} = H_{2(g)} + CO_2.$$

At equilibrium:

$$dG = \overline{G}_{H_2} dn_{H_2} + \overline{G}_{CO_2} dn_{CO_2} - \overline{G}_{H_2O} dn_{H_2O} - \overline{G}_{CO} dn_{CO} = 0$$

or, in view of the stoichiometry requirement

$$-dn_{H_2O} = -dn_{CO} = dn_{H_2} = dn_{CO_2}:$$

$$dG = \left(\overline{G}_{H_2} + \overline{G}_{CO_2} - \overline{G}_{H_2O} - \overline{G}_{CO}\right) dn_{H_2} = 0$$

Thus, at equilibrium:

$$\left(\overline{G}_{H_2} + \overline{G}_{CO_2}\right) = \left(\overline{G}_{H_2O} + \overline{G}_{CO}\right). \tag{20}$$

The isothermal transfer of a mole of ideal gas i from the pure state at the pressure P_i and temperature T to an ideal gas mixture at the *partial pressure* p_i involves a change in Gibbs free energy:

$$\Delta G = \overline{G}_i - G_i = RT \ln\left(p_i / P_i\right). \tag{21}$$

References: p. 469.

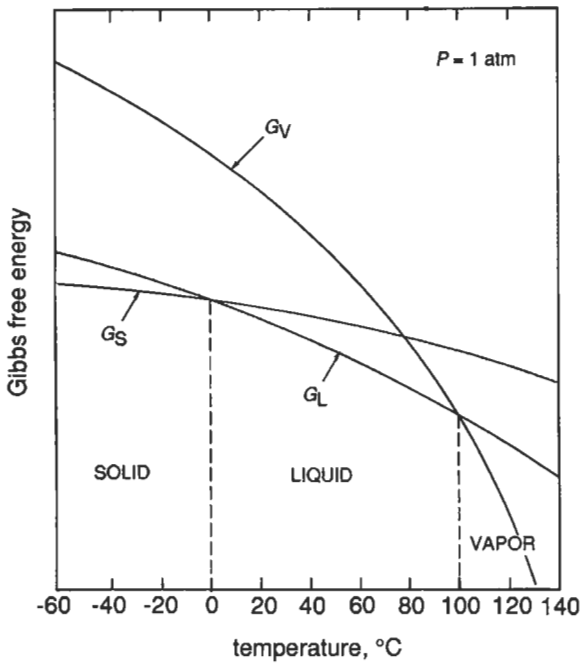

Fig. 4. Schematic representation of the variations of $G_{(s)}$, $G_{(l)}$ and $G_{(v)}$ with temperature at $P = 1$ atm for H_2O.

Again, as only changes in Gibbs free energy can be measured, it is convenient to select a standard state for the gas and consider the Gibbs free energy of the gas in any other state in terms of the difference between the free energy of the gas in this state and the free energy of the gas in the standard state. The standard state for an ideal gas at the temperature T is the pure gas at 1 atm pressure and in this state the Gibbs free energy is the standard free energy, designated G^0. Thus eq. (21) can be written as:

$$\overline{G}_i = G_i^0 + RT \ln p_i. \tag{22}$$

Substitution of eq. (22) into eq. (20) and rearrangement gives:

$$\left(G^0_{H_2} + G^0_{CO_2} - G^0_{H_2O} - G^0_{CO}\right) = -RT \ln \frac{p_{H_2} p_{CO_2}}{p_{H_2O} p_{CO}}. \tag{23}$$

Being the difference between the standard free energies of the products and the standard free energies of the reactants, the left-hand side of eq. (23) is termed the *standard free energy* for the reaction at the temperature T, ΔG_T^0, and, being dependent only on T, it has a definite fixed value at any T. Consequently the quotient of the partial pressures of the reactants and products occurring in the logarithm term on the right-hand side of eq. (23) has a fixed value at any T. This term is called the *equilibrium constant*, K_p, and hence the equilibrium state in any reacting system is such that

$$\Delta G_T^0 = -RT \ln K_p. \tag{24}$$

For the general reaction

$$aA + bB = cC + dD: \quad K_p = \frac{p_C^c p_D^d}{p_A^a p_B^b}.$$

Dalton's law of partial pressures in an ideal gas mixture gives

$$p_i = X_i P,$$

where X_i, being the ratio of the number of moles of i in the gas to the total number of moles of all species, is the *mole fraction* of i in the gas and P is the total pressure of the gas. Thus

$$K_p = \frac{X_C^c X_D^d}{X_A^a X_B^b} P^{c+d-a-b} = K_X P^{c+d-a-b}, \tag{25}$$

where K_X is the equilibrium constant expressed in terms of the mole fractions of the reactants and products occurring at reaction equilibrium. From the definition of ΔG_T^0, K_p is independent of pressure and hence, from eq. (25), K_X is only independent of pressure if $c+d-a-b=0$.

From eqs. (24) and (15):

$$\Delta G_T^0 = -RT \ln K_p = \Delta H_T^0 - T\Delta S_T^0.$$

Thus

$$\ln K_p = -\frac{\Delta H_T^0}{RT} + \frac{\Delta S_T^0}{R},$$

$$\text{or} \quad \frac{\partial \ln K_p}{\partial T} = \frac{\Delta H_T^0}{RT^2}.$$

For the water–gas reaction:

$$CO + H_2O = CO_2 + H_2;$$

$$\Delta G_T^0 = -36400 + 32.0T \text{ J/mole};$$

thus

$$K_p = \exp\left(\frac{36400}{8.3144T}\right)\exp\left(\frac{-32.0}{8.3144}\right).$$

The reaction of a moles of CO with b moles of H_2O produces x moles of each CO_2 and H_2 and leaves $(a - x)$ moles of CO and $(b - x)$ moles of H_2. Thus at any point along the reaction coordinate in a reacting mixture at the constant pressure P:

References: p. 469.

$$p_{CO} = \frac{a-x}{a+b}P, \qquad p_{H_2O} = \frac{b-x}{a+b}P, \qquad \text{and} \qquad p_{CO_2} = p_{H_2} = \frac{x}{a+b}P,$$

and at reaction equilibrium:

$$\frac{p_{CO_2}p_{H_2}}{p_{CO}p_{H_2O}} = \frac{x^2}{(a-x)(b-x)} = K_p = \exp\left(\frac{36400}{8.3144T}\right)\exp\left(\frac{-32.0}{8.3144}\right)$$

If one or more of the reactants and/or products occurs in a condensed state the attainment of equilibrium involves both phase and reaction equilibrium. For example, at a temperature T the equilibrium

$$2Ag_{(s)} + \tfrac{1}{2}O_{2(g)} = Ag_2O_{(s)} \tag{26}$$

requires the establishment of the phase equilibria

$$Ag_{(s)} = Ag_{(v)} \quad \text{and} \quad Ag_2O_{(s)} = Ag_2O_{(v)},$$

and, in the vapor or gas phase, requires establishment of the reaction equilibrium

$$2Ag_{(v)} + \tfrac{1}{2}O_{2(g)} = Ag_2O_{(v)}. \tag{27}$$

Conditions for the phase equilibria are $p_{Ag} = p^0_{Ag}$ (the saturated vapor pressure of solid silver at temperature T) and $p_{Ag_2O} = p^0_{Ag_2O}$ (the saturated vapor pressure of solid Ag_2O at temperature T), and thus, as the equilibrium constant K for the vapor phase reaction, given by eq. (27), has a fixed value at temperature T, the equilibrium oxygen pressure, p_{O_2}, is uniquely fixed by:

$$K = \frac{p^0_{Ag_2O}}{\left(p^0_{Ag}\right)^2 p^{1/2}_{O_2}}.$$

Alternatively, reaction equilibrium in the vapor phase requires that:

$$2\overline{G}_{Ag(v)} + \tfrac{1}{2}\overline{G}_{O_{2(g)}} = \overline{G}_{Ag_2O(v)}, \tag{28}$$

and the two-phase equilibria require that:

$$\overline{G}_{Ag(v)} = \overline{G}_{Ag(s)} \tag{29}$$

and

$$\overline{G}_{Ag_2O(v)} = \overline{G}_{Ag_2O(s)}. \tag{30}$$

From eq. (11), at constant T, $dG = VdP$, and hence eq. (29) can be written as:

$$G^0_{Ag(v)} + RT\ln p^0_{Ag} = G^0_{Ag(s)} + \int_1^{p^0_{Ag}} V_{Ag(s)}dP, \tag{31}$$

where $G^0_{Ag(s)}$ is the standard molar free energy of solid Ag at temperature T. The integral

on the right-hand side of eq. (31) is negligibly small and hence eq. (31) can be written as:

$$G^0_{Ag(v)} + RT \ln p^0_{Ag} = G^0_{Ag(s)}. \tag{32}$$

Similarly, eq. (30) can be written as:

$$G^0_{Ag_2O(v)} + RT \ln p^0_{Ag_2O} = G^0_{Ag_2O(s)}. \tag{33}$$

Substitution of eqs. (32) and (33) into eq. (28) gives:

$$2G^0_{Ag(s)} + \tfrac{1}{2} G^0_{O_2(g)} + RT \ln p^{1/2}_{O_2} = G^0_{Ag_2O(s)}.$$

$$\text{or} \quad \Delta G^0_T = -RT \ln \frac{1}{p^{1/2}_{O_2(eq.T)}}, \tag{34}$$

where ΔG^0_T is the standard free energy change for the reaction given by eq. (26) and $p_{O_2(eq,T)}$ is the value of p_{O_2} required for equilibrium between $Ag_{(s)}$, $Ag_2O_{(s)}$ and oxygen gas at temperature T. The variations of ΔH^0_T, $-T\Delta S^0_T$ and ΔG^0_T [given by eq. (16)] are shown in fig. 5. Thus, from eq. (34), $p_{O_2(eq.\,485\,K)} = 1$ atm, at which temperature $\Delta G^0 = 0$. At $T < 485$ K, ΔG^0_T is a negative quantity and hence $p_{O_2(eq,T)} < 1$ atm. At $T > 485$ K, ΔG^0_T is a positive quantity and hence $p_{O_2(eq.T)} > 1$ atm.

5. *Ellingham diagrams*

In 1944 ELLINGHAM published diagrams showing the variation, with temperature, of the standard free energies of formation of a number of oxides and sulfides, and pointed out that these diagrams "would show at a glance the relative stabilities of the various substances within a given class at any temperature, and would thus indicate, in a direct fashion, the range of conditions required for their reduction to the corresponding elements. It would provide, in fact, what might be described as a ground plan of metallurgical possibilities with respect to the reduction of compounds of the specified class". Such diagrams, which are now available for a wide range of classes of compounds, are known as *Ellingham diagrams*, and the Ellingham diagram for oxides is shown in fig. 6. (See also ch. 14, § 2.1).

In order to facilitate comparison of the stabilities of the various oxides, the standard free energies are for the reaction

$$(2x/y)M + O_2 = (2/y)M_xO_y,$$

i.e., for reactions involving the consumption of one mole of O_2. By choosing this basis:

$$\Delta G^0_T = RT \ln p_{O_2(eq.T)},$$

and hence, in addition to being a plot of ΔG^0_T versus temperature, the Ellingham diagram is a plot of the variation, with temperature, of the oxygen pressure, $p_{O_2(eq,T)}$, required for equilibrium between the metal and its oxide. The free energy change for the change of state $O_2(T, P = 1\text{ atm}) \rightarrow O_2(T, P = p_{O_2})$ is:

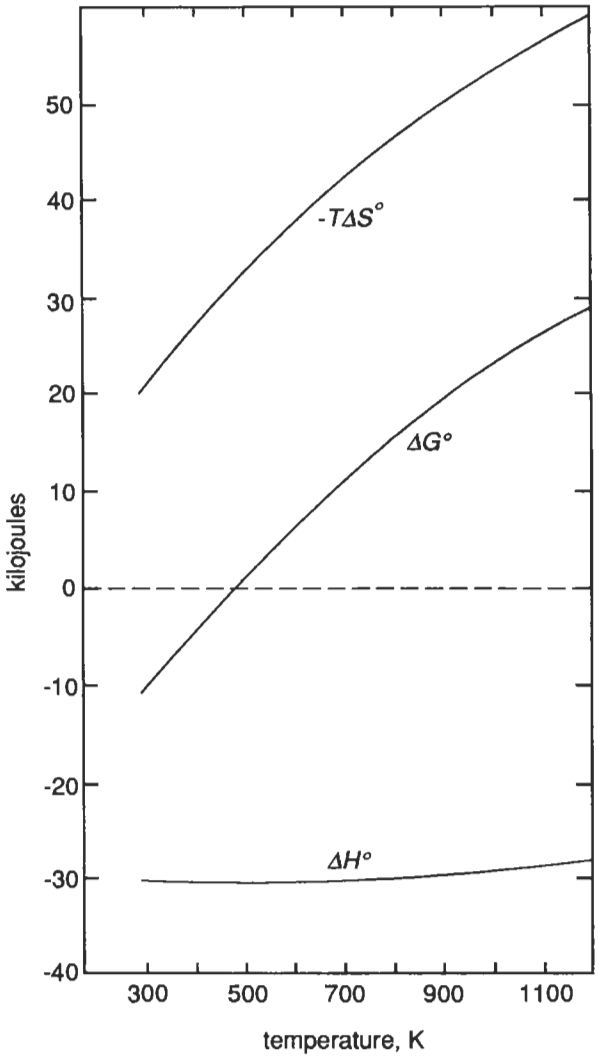

Fig. 5. The variations of ΔH_T^0, $-T\Delta S_T^0$ and ΔG_T^0 with temperature for the reaction $2Ag + \frac{1}{2}O_2 = Ag_2O$.

$$\Delta G_T = RT \ln p_{O_2},$$

and thus, in the Ellingham diagram, lines of constant p_{O_2} radiate from the origin, $\Delta G^0 = 0$, $T = 0$ K, with slopes of $R \ln p_{O_2}$. Consequently, a nomographic scale of p_{O_2} can be placed on the edges of the diagram and $p_{O_2(eq)}$ at any point on an Ellingham line is obtained as the reading on the nomographic scale which is collinear with the given point and the origin of the diagram. The Ellingham diagram is thus a stability diagram, in that any point in the diagram lying **above** the Ellingham line for a given oxide is a state in which $p_{O_2(T)} > p_{O_2(eq.\ T)}$

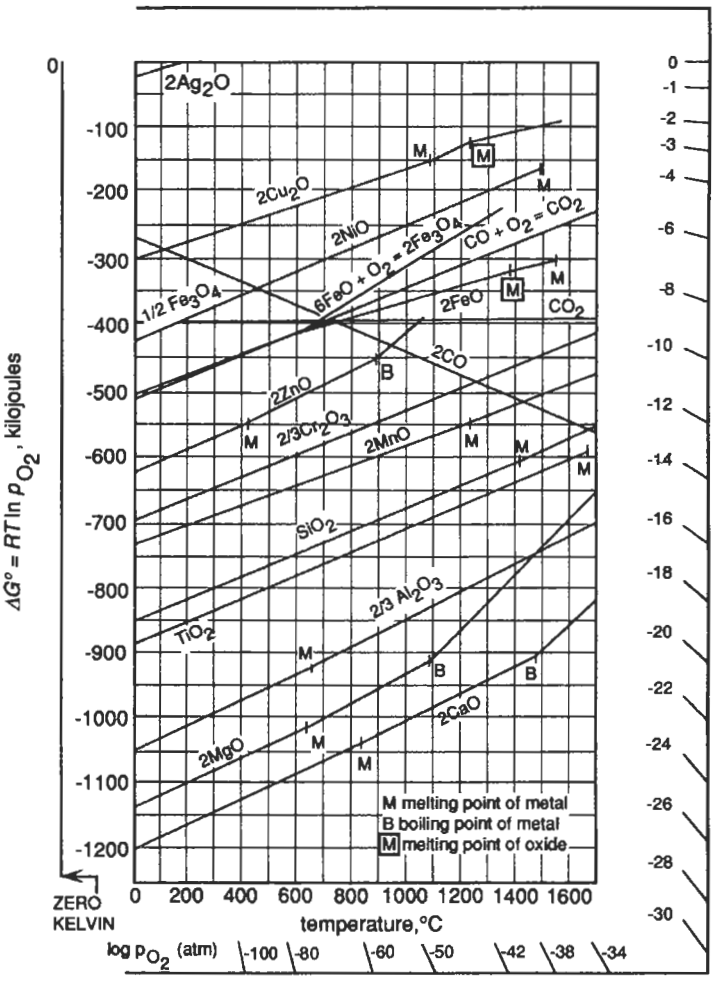

Fig. 6. The Ellingham diagram for several oxides.

and hence, in all states above the line the oxide is stable relative to the metal. Conversely, any point lying **below** the Ellingham line for the given oxide is a state in which $p_{O_2(T)} < p_{O_2(eq.\ T)}$ and hence, below the line, the metal is stable relative to the oxide. The Ellingham line thus divides the diagram into stability fields and, if it is required that a given oxide be reduced, the thermodynamic state must be moved from a point above the Ellingham line for the oxide to a point below the line, i.e., must be moved from a position within the oxide stability field to a position within the metal stability field.

The magnitude of ΔG_T^0 is a measure of the relative stability of the oxide and hence, with increasing stability, the Ellingham lines occur progressively lower in the diagram. Consequently, in principle, the element A can reduce the oxide B_xO_y, if, in the diagram,

References: p. 469.

the Ellingham line for A_xO_y, lies below that for B_xO_y.

Over the ranges of temperature in which no phase transitions occur the Ellingham lines are virtually linear, being given by

$$\Delta G_T^0 = A + BT.$$

In this expression A, the intercept of the line with the $T=0$ K axis, is identified with ΔH^0, the standard enthalpy change for the oxidation, and B, the slope of the line, is identified with $-\Delta S^0$, the standard entropy change for the reaction. The Ellingham lines for the oxidation of solid and liquid metals are more or less parallel with one another, with slopes corresponding to the disappearance of one mole of oxygen gas in the standard oxidation equation. Consequently, the stabilities of these oxides are determined primarily by the magnitudes of their enthalpies of formation.

At the temperature of a phase change the slope of the Ellingham line changes by an amount equal to the entropy change for the phase transition. The slope increases at the transition temperatures of the metal and decreases at the transition temperatures of the oxide. These changes in slope are most noticeable at normal boiling temperatures, e.g., at 1090°C the slope of the Ellingham line for MgO increases by 190.3 J/K, which is the entropy of boiling of 2Mg, and at 1484°C the slope of the Ellingham line for CaO increases by 174.2 J/K, the entropy of boiling of 2Ca.

Carbon is unique in that it forms two gaseous oxides, CO and CO_2, and the positions of the Ellingham lines for these oxides are of particular significance in extraction metallurgy. The Ellingham line for CO has a negative slope due to the fact that the oxidation

$$2C + O_2 = 2CO$$

involves the net production of one mole of gas, and, because the oxidation

$$C + O_2 = CO_2$$

does not involve a change in the number of moles of gas, the Ellingham line for CO_2 is virtually horizontal. The enthalpy change for the oxidation of C to form CO as $C + \frac{1}{2}O_2 = CO$ is −111 700 J and the enthalpy change for the oxidation of CO to CO_2 as $CO + \frac{1}{2}O_2 = CO_2$ is −282 400 J. Thus the standard enthalpy change for the Ellingham line for CO is $2 \times (-111700) = -223400$ J and the standard enthalpy change for the Ellingham line for CO_2 is $(-111700) + (-282400) = -394100$ J. Thus, on the basis that the stability of an oxide is determined primarily by the magnitude of ΔH^0, it would appear that CO_2 should be more stable than CO. However, as the Ellingham line for CO has a negative slope, which means that the stability of CO increases with increasing temperature, the Ellingham lines for the two oxides intersect. Consequently, although CO_2 is more stable than CO at lower temperature, the reverse is the case at higher temperatures. The gaseous phase in equilibrium with solid carbon is a CO–CO_2 mixture in which the ratio p_{CO}/p_{CO_2} increases with increasing temperature. For a total pressure of 1 atm, the equilibrium gas contains less than 1% CO at temperatures less than 400°C, contains less than 1% CO_2 at temperatures greater than 980°C, and is an equimolar mixture at 674°C. The "carbon

line" in the diagram, which is the continuum of states in which carbon is in equilibrium with a CO–CO_2 mixture at 1 atm pressure, follows the CO_2 Ellingham line up to about 400°C and then curves down gently to tangentially meet and join the Ellingham line for CO at about 1000°C. Along the carbon line the ratio p_{CO}/p_{CO_2} is fixed by the equilibrium

$$C + CO_2 = 2CO,$$

and, by virtue of the equilibrium

$$CO + \tfrac{1}{2}O_2 = CO_2$$

the oxygen pressure is also fixed. Thus the carbon line divides the other oxides into two classes, those with Ellingham lines which lie above the carbon line, and those with Ellingham lines which lie below the carbon line. With respect to the former class, the carbon line lies in the stability field of the metal and hence carbon is a potential reducing agent for these oxides, whereas, with respect to the latter class, the carbon line lies in the oxide stability field and hence carbon cannot reduce the oxide. Furthermore, if the Ellingham line for a metal oxide intersects the carbon line, the temperature of intersection is the minimum temperature at which the oxide may be reduced by carbon. Thus, for example, FeO cannot be reduced by carbon at temperatures less than 675°C.

Whether or not carbon can be used as a reducing agent is determined by the stability of any carbide phase which may form, i.e., by the sign of the standard free energy for formation of the carbide from metal and carbon. For example, in the Ellingham diagram the carbon line intersects with the Ellingham line for SiO_2 at 1676°C, and hence above this temperature liquid Si is stable relative to SiO_2 in the presence of C and its equilibrium CO–CO_2 gas mixture at 1 atm pressure. However, for the reaction

$$Si_{(l)} + C = SiC,$$

the standard free energy change is $\Delta G_T^0 = -122600 + 37.0T$ J and hence SiC is stable relative to liquid Si in the presence of carbon at 1676°C and $P = 1$ atm.

The stability fields in the system Si–O–C at 1676°C are shown in fig. 7 as functions of $\log p_{CO}$ and $\log p_{CO_2}$. Line A is the variation of p_{CO} and p_{CO_2} required for the equilibrium

$$Si_{(l)} + 2CO_2 = SiO_2 + 2CO.$$

Line B is the corresponding variation required for the equilibrium

$$Si_{(l)} + 2CO = SiC + CO_2,$$

and line C is the variation for the equilibrium

$$SiC + 3CO_2 = SiO_2 + 4CO.$$

These lines divide the diagram into stability fields for Si, SiC and SiO_2 and meet at the values of p_{CO} and p_{CO_2} required for the four-phase equilibrium involving the three condensed phases Si, SiC and SiO_2 and the CO–CO_2 gas phase. Line D is the variation of p_{CO} and p_{CO_2} required for the equilibrium between carbon and the gas phase at 1676°C

References: p. 469.

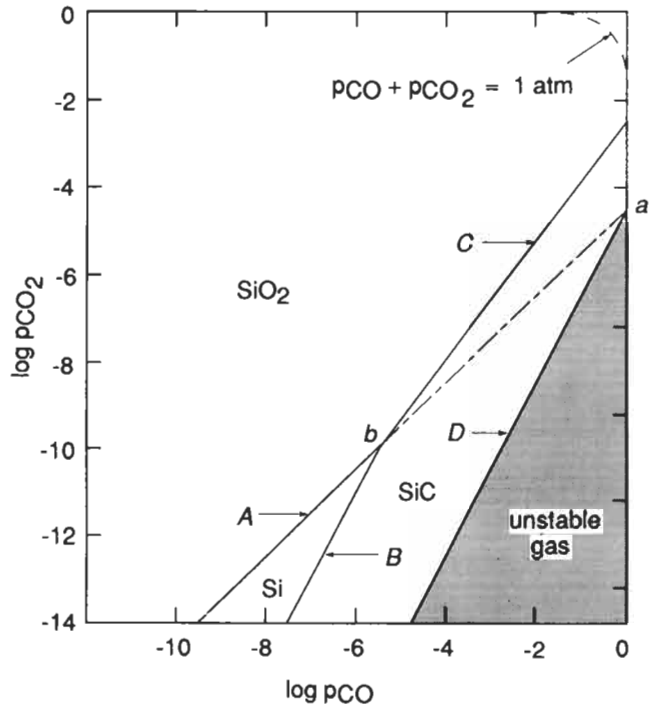

Fig. 7. The stability diagram for the system Si–O–C at 1949 K.

and, as such, represents the compositions of CO–CO_2 gas mixtures which are saturated with carbon. The field below line D is designated "unstable" gas, as any gas mixture in this field is supersaturated with carbon and hence will spontaneously undergo the carbon deposition reaction

$$2CO \rightarrow C_{(graphite)} + CO_2,$$

until, thereby, the composition of the gas lies on line D. The dashed line is the $(p_{CO} + p_{CO_2}) = 1$ atm isobar. Consequently, the system containing solid carbon and a gas phase at 1 atm pressure exists at the state **a**, and as this state is in the field of stability of SiC, SiO_2 is not reduced to Si by carbon at 1676°C. However, if the standard free energy for formation of SiC had been positive, lines B and C would have occurred below line D in the diagram and, as shown by the dashed–dotted extension of line A, the equilibrium Si–SiO_2–C would occur at the state **a**, which is the state of intersection of the carbon line with the Ellingham line for SiO_2 in the Ellingham diagram.

6. *The thermodynamic properties of solutions*

6.1. Mixing processes

The relationship between entropy and the "degree of mixed-up-ness" is quantified by Boltzmann's expression as:

$$S' = k \ln W,$$

where S' is the entropy of the system and W is the number of microstates available to the system*. In the simplest of mixing processes, W is the number of distinguishable arrangements of the constituent atoms on the sites available to them. Consider the mixing of N_A atoms of solid A and N_B atoms of solid B as the process:

state 1 → state 2,

i.e., unmixed A and B → mixed A and B.

In state 1, interchange of the positions of A atoms in the crystal of pure A and/or interchange of the positions of B atoms in the crystal of pure B does not produce a distinguishably different arrangement and hence W sub1 = 1. However, the N_A atoms of A and N_B atoms of B can be placed on the $N_A + N_B$ lattice sites of the mixed crystal (state 2) in $(N_A + N_B)!$ ways, of which $(N_A + N_B)!/N_A!N_B!$ are distinguishable. Thus

$$W_2 = \frac{(N_A + N_B)!}{N_A!\,N_B!}.$$

Thus, for the process:

$$\Delta S' = S'_2 - S'_1 = k \ln W_2 - k \ln W_1 = k \ln \frac{(N_A + N_B)!}{N_A!\,N_B!}. \tag{35}$$

If N_A and N_B are sufficiently large numbers, *Stirling's theorem* can be applied as

$$\ln \frac{(N_A + N_B)!}{N_A!\,N_B!} = (N_A + N_B)\ln(N_A + N_B) - N_A \ln N_A - N_B \ln N_B$$

$$= -N_A \ln X_A - N_B \ln X_B,$$

where, respectively, X_A and X_B are the mole fractions of A and B in the mixed crystal.

Thus, the change in entropy, $\Delta S'^M$, due to mixing, is

$$\Delta S'^M = k \ln(N_A \ln X_A + N_B \ln X_B),$$

and, if $N_A + N_B = N_0$ (Avogadro's number) then the molar entropy of mixing is

* The equivalence between this definition of entropy and the definition in terms of heat flow (§1.1) is demonstrated in general terms in many texts; a particularly clear treatment is provided in ch. 2 of FAST's book (see bibliography).

References: p. 469.

$$\Delta S^M = -R\left(X_A \ln X_A + X_B \ln X_B\right). \tag{36}$$

This increase in entropy is caused by the increase in the number of spatial configurations made available to the system as a result of the mixing process and, hence, is *configurational* in origin. If there is no change in enthalpy on mixing, the Gibbs free energy change due to the mixing process is given by

$$\Delta G^M = -T\Delta S^M = RT\left(X_A \ln X_A + X_B \ln X_B\right). \tag{37}$$

Alternatively, consider the following. Consider that p_A^0 and p_B^0 are the saturated vapor pressures of pure A and pure B at temperature T and that p_A and p_B are the partial pressures of A and B exerted by the mixed crystal (or solid solution) of composition X_A at temperature T. Consider that one mole of A is isothermally evaporated from pure solid A to form A vapor at the pressure p_A^0, that the mole of A vapor is isothermally expanded to the pressure p_A and is then isothermally condensed into a large quantity of the solid solution. As the evaporation and condensation processes are conducted at equilibrium, they do not involve any change in Gibbs free energy and hence the change in Gibbs free energy for the three-step process is simply that caused by the change in pressure from p_A^0 to p_A, i.e.,

$$\Delta G = \overline{G}_{A(\text{in the solution})} - G^0_{A(\text{pure})} = RT \ln\left(p_A / p_A^0\right).$$

Similarly, for the corresponding three-step process for B,

$$\Delta G = \overline{G}_{B(\text{in the solution})} - G^0_{B(\text{pure})} = RT \ln\left(p_B / p_B^0\right). \tag{38}$$

Thus, for the mixing of n_A moles of A and n_B moles of B:

$$\begin{aligned}\Delta G' &= G'(\text{solution}) - G'(\text{unmixed A and B}) \\ &= \left(n_A \overline{G}_A + n_B \overline{G}_B\right) - \left(n_A G_A^0 + n_B G_B^0\right) \\ &= n_A\left(\overline{G}_A - G_A^0\right) + n_B\left(\overline{G}_B - G_B^0\right),\end{aligned}$$

which, from eqs. (37) and (38), can be written for one mole of solution as

$$\Delta G^M = RT\left[X_A \ln\left(p_A / p_A^0\right) + X_B \ln\left(p_B / p_B^0\right)\right]. \tag{39}$$

Comparison of eqs. (37) and (39) indicates that, if the mixing process does not involve a change in enthalpy,

$$p_A = X_A p_A^0 \quad \textit{and} \quad p_B = X_B p_B^0. \tag{40}$$

Equation (40) is an expression of *Raoult's Law* and a solution conforming with this behavior is said to exhibit Raoultian ideal behavior. If the energies of the pure states and the solution are considered to be the sums of the pair-wise bond energies between neighboring atoms, Raoultian ideal mixing requires that:

$$E_{AB} = (E_{AA} + E_{BB})/2, \tag{41}$$

where E_{AB}, E_{AA} and E_{BB} are the pair-wise bond energies of A–B, A–A and B–B pairs, respectively. If the condition given by eq. (41) is not met, the isothermal mixing process is accompanied by the evolution or absorption of heat, which, for mixing at constant pressure, represents a change in the enthalpy of the system. In such a situation random mixing of A and B atoms does not occur and hence the entropy of mixing is no longer given by eq. (36).

Any change in the enthalpy on mixing arises from a redistribution of the atoms among their quantized energy levels and this gives rise to a change in the *thermal* (as distinct from the configurational) component of the entropy of the system. Boltzmann's equation can be written as

$$S'_{total} = S'_{conf} + S'_{thermal} = k \ln (W_{conf} W_{thermal}),$$

where W_{conf} is the number of distinguishable ways in which the atoms can be distributed on the available sites and $W_{thermal}$ is the number of ways in which the energy of the system can be distributed among the particles. Thus, for the mixing process,

$$\Delta S' = k \ln \frac{W_{conf(2)} W_{thermal(2)}}{W_{conf(1)} W_{thermal(1)}},$$

and hence $\Delta S'$ is only given by eq. (35) if $W_{thermal(1)} = W_{thermal(2)}$, i.e., if no redistribution of the energy occurs, and hence no change in enthalpy occurs. This condition is required for Raoultian ideal mixing. If

$$|E_{AB}| > |(E_{AA} + E_{BB})/2|,$$

the solution exhibits a tendency towards *ordering*, i.e., towards maximizing the number of A–B contacts, and if

$$|E_{AB}| < |(E_{AA} + E_{BB})/2|,$$

the solution exhibits a tendency towards *clustering* or phase separation, i.e., towards minimizing the number of A–B contacts.

Configurational entropy is responsible for the occurrence of vacancies in metals. Consider a perfect single crystal containing N atoms on N lattice sites. If a single atom is removed from a lattice position within the crystal and is placed on the surface of the crystal, random placement of the vacancy on $N+1$ sites gives rise to a configurational entropy of

$$S = k \ln \frac{(N+1)!}{N!}.$$

This process involves an enthalpy change ΔH_v and, as the vibration frequencies of the nearest-neighbor atoms to the vacancy are altered, a change occurs in the thermal entropy, ΔS_{th}. Thus, for the formation of N_v vacancies,

$$\Delta G' = \Delta H' - T\Delta S'$$

$$= N_v \Delta H_v - N_v \Delta S_{th} T + kT \ln \frac{(N + N_v)!}{N! N_v!}$$

$$= N_v (\Delta H_v - N_v \Delta S_{th}) + kT \left[N \ln \frac{N}{N + N_v} + N_v \ln \frac{N_v}{N + N_v} \right]. \quad (42)$$

The formation of vacancies in an initially perfect crystal is thus a spontaneous process which proceeds until, thereby, the Gibbs free energy of the crystal is minimized, in which state

$$\frac{\partial \Delta G'}{\partial N_v} = 0.$$

From eq. (42), this condition occurs when

$$\frac{N_v}{N + N_v} = \exp\left(\frac{-\Delta H_v}{kT}\right) \exp\left(\frac{\Delta S_{th}}{k}\right).$$

The fraction of vacant sites in a crystal can be determined from simultaneous measurement of the thermal expansion of a sample, $\Delta l/l$, and the change in the lattice parameter, $\Delta a_0/a_0$, as measured by X-ray diffraction (see ch. 18, §2.2.2.2). As the former is influenced by both the increase in the average spacing between lattice planes and the creation of vacancies, and the latter is a measure only of the average spacing between planes, the increase in the fraction of vacant lattice sites is proportional to the difference between $\Delta l/l$ and $\Delta a_0/a_0$. Measurements of this type on aluminum give:

$$\frac{N_v}{N + N_v} = 11 \exp\left(\frac{-8820}{T}\right),$$

from which $\Delta H_v = 73.3$ kJ/mole and $\Delta S_v = 20$ J/K mole. At the melting temperature of 660°C this gives the fraction of vacant sites as 9×10^{-4}.

The thermodynamic properties of solutions which do not exhibit Raoultian ideal behavior are dealt with by introducing the concept of activity. The *activity*, a_i, of the component i in a solution is defined as:

$$a_i = p_i / p_i^0 \quad (43)$$

and, from eq. (40), is equal to the mole fraction, X_i, in a Raoultian ideal solution. Thus, the molar free energy of formation of a binary A–B solution, ΔG^M, is given by

$$\Delta G^M = RT(X_A \ln a_A + X_B \ln a_B). \quad (44)$$

The free energy of formation of n moles of a solution, $\Delta G'^M$, can be written in terms of the partial molar free energies of mixing of the components as:

$$\Delta G'^{M} = n_A \Delta \overline{G}_A^M + n_B \Delta \overline{G}_B^M$$

or, the molar free energy, ΔG^M, as:

$$\Delta G^M = X_A \Delta \overline{G}_A^M + X_B \Delta \overline{G}_B^M, \tag{45}$$

where $\Delta G_i^M = \overline{G}_i - G_i^0$ (the difference between the molar free energy of i in the solution and the molar free energy of pure i) is termed the *partial molar free energy of mixing* of i. The partial molar free energy of mixing of i and the molar free energy of formation of the solution are related as:

$$\Delta \overline{G}_i^M = \Delta G^M + (1 - X_i)\left(\frac{\partial \Delta G^M}{\partial X_i}\right)_{T,P}. \tag{46}$$

Comparison of eqs. (39) and (45) shows that in a Raoultian ideal solution

$$\Delta \overline{G}_i^M = RT \ln X_i,$$

and comparison of eqs. (39) and (44) shows that, generally,

$$\Delta \overline{G}_i^M = RT \ln a_i. \tag{47}$$

A typical ideal variation of ΔG^M with composition is shown in fig. 8. In this figure the tangent drawn to the free energy curve at any composition intercepts the $X_A = 1$ axis at $\Delta \overline{G}_A^M$ and intercepts the $X_B = 1$ axis at $\Delta \overline{G}_B^M$. This construction is a geometric representation of eq. (46). Also, as $X_i \to 0$, $a_i \to 0$ and hence, from eq. (47), $\Delta \overline{G}_i^M \to -\infty$, i.e., the vertical axes are tangents to the curve at its extremities. The relationship between the variations of the tangential intercepts with composition is given by the *Gibbs–Duhem equation*:

$$X_A \mathrm{d} \ln a_A + X_B \mathrm{d} \ln a_B = 0. \tag{48}$$

Usually, the activity of only one component of a solution is amenable to experimental measurement, and the activity of the other component, and hence ΔG^M, are obtained from integration of the Gibbs–Duhem equation.

The *activity coefficient*, γ_i, is defined as $\gamma_i = a_i / X_i$ and hence eq. (44) can be written as:

$$\Delta G^M = RT(X_A \ln X_A + X_B \ln X_B) + RT(X_A \ln \gamma_A + X_B \ln \gamma_B). \tag{49}$$

The first term on the right-hand side of eq. (49) is the molar free energy of formation of a Raoultian ideal solution, $\Delta G^{M,id}$, and the second term, being the difference between the actual molar free energy of solution and the ideal value, is called the *excess molar free energy of mixing*, G^{xs}.

6.2. Regular solution behavior

A *regular solution* is one which has an ideal entropy of mixing and a nonzero enthalpy of mixing. The properties of such a solution are best examined by means of a

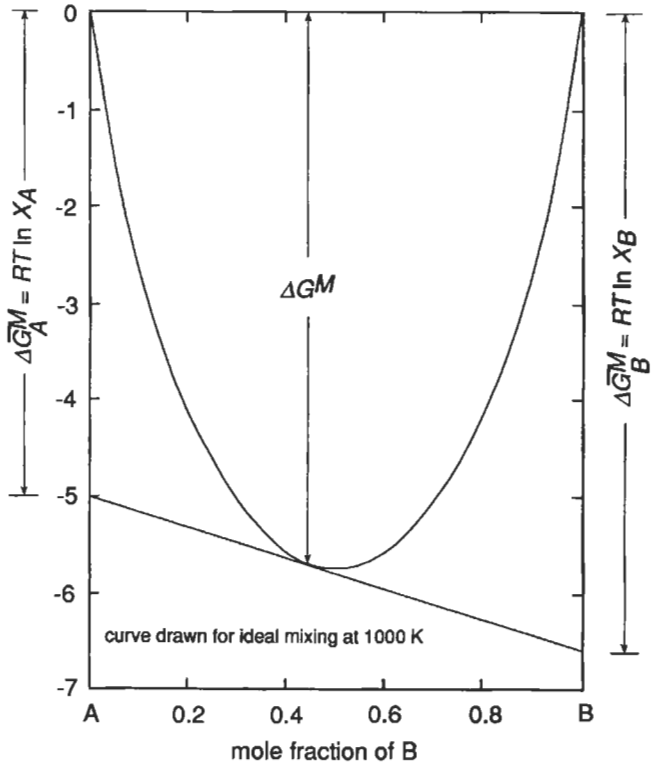

Fig. 8. The variation of ΔG^M with composition in an ideal system at 1000 K.

simple statistical model of the mixing of N_A atoms of A and N_B atoms of B. If the internal energy, U', of the solution can be taken as the sum of the pair-wise bond energies then

$$U' = P_{AB}E_{AB} + P_{AA}E_{AA} + P_{BB}E_{BB}, \tag{50}$$

where P_{ij} is the number of i–j pairwise bonds and E_{ij} is the energy of the bond relative to i and j at infinite separation. If the coordination number of an atom is z, the number of bonds involving A atoms, $N_A z$, is given by $2P_{AA} + P_{AB}$ and, similarly, the number of bonds involving B atoms, $N_B z$, is given by $2P_{BB} + P_{AB}$. Thus:

$$P_{AA} = \tfrac{1}{2} N_A z - \tfrac{1}{2} P_{AB} \text{ and } P_{BB} = \tfrac{1}{2} N_B z - \tfrac{1}{2} P_{AB},$$

substitution of which into eq. (50) gives:

$$U' = \tfrac{1}{2} N_A z E_{AA} + \tfrac{1}{2} N_B z E_{BB} + P_{AB}\left[E_{AB} - \left(E_{AA} + E_{BB}\right)/2\right].$$

The first two terms on the right-hand side represent the internal energies of N_A atoms of A and N_B atoms of B before mixing and hence, for the mixing process:

$$\Delta U' = P_{AB}\left[E_{AB} - \left(E_{AA} + E_{BB}\right)/2\right]. \tag{51}$$

If the mixing process, conducted at constant pressure, does not involve a change in volume, then, as $P\Delta V' = 0$, $\Delta H' = \Delta U'$ and eq. (51) is the expression for the enthalpy of mixing. As random mixing of the atoms is assumed, the number of A–B bonds is calculated as the product of the probability of occurrence of an A–B pair and the number of pairs of atoms. The former is given by:

$$2\frac{N_A}{N_A + N_B}\frac{N_B}{N_A + N_B},$$

and the latter is $\frac{1}{2}(N_A + N_B)z$, and hence:

$$\Delta H' = \frac{N_A N_B}{N_A + N_B} z\left[E_{AB} - \left(E_{AA} + E_{BB}\right)/2\right]. \tag{52}$$

For the mixing of n_A moles of A ($= n_A N_0$ atoms of A) and n_B moles of B ($= n_B N_0$ atoms of B), eq. (52) becomes:

$$\Delta H' = \frac{n_A n_B}{n_A + n_B} N_0 z\left[E_{AB} - \left(E_{AA} + E_{BB}\right)/2\right].$$

or, per mole of solution:

$$\Delta H^M = X_A X_B N_0 z\left[E_{AB} - \left(E_{AA} + E_{BB}\right)/2\right].$$

If $|E_{AA}| > |(E_{AA} + E_{BB}/2|$, ΔH^M is negative, which leads to exothermic mixing, and if $|E_{AA}| < |(E_{AA} + E_{BB}/2|$, ΔH^M is positive, which leads to endothermic mixing. On the other hand, if E_{AB} is the average of E_{AA} and E_{BB}, ΔH^M is zero and Raoultian ideal mixing occurs. For any given system,

$$\Omega = N_0 z\left[E_{AB} - \left(E_{AA} + E_{BB}\right)/2\right]$$

is a constant, and hence, in a regular solution, ΔH^M is a parabolic function of composition, given by:

$$\Delta H^M = \Omega X_A X_B, \tag{53}$$

and $$\Delta S^M = -R\left(X_A \ln X_A + X_B \ln X_B\right). \tag{36}$$

For any extensive thermodynamic property Q, the relationship between $\Delta\overline{Q}_i^M$ and ΔQ^M in a binary system is given by:

$$\Delta\overline{Q}_i^M = \Delta Q^M + \left(1 - X_i\right)\left(\frac{\partial \Delta Q^M}{\partial X_i}\right),$$

and thus, in a regular solution, from eq. (53):

$$\Delta\overline{H}_i^M = \Omega(1 - X_i)^2,$$

and from eq. (36):

$$\Delta\overline{S}_i^M = -R \ln X_i.$$

The partial molar free energy of mixing of i can be expressed variously as

$$\Delta\overline{G}_i^M = \Delta\overline{H}_i^M - T\Delta\overline{S}_i^M = \Delta\overline{G}_i^{M,\text{id}} + \overline{G}_i^{\text{xs}} = RT \ln X_i + RT \ln \gamma_i,$$

and hence, in a regular solution:

$$\overline{G}_i^{\text{xs}} = \Delta\overline{H}_i^M = RT \ln \gamma_i = \Omega(1 - X_i)^2.$$

Consequently, the limiting values of γ_i as $X_i \to 1$ and $X_i \to 0$ are unity and $\exp(\Omega/RT)$, respectively; i.e., with increasing dilution, the solvent approaches Raoultian ideal behavior and the activity coefficient of the solute approaches a constant value designated γ_i^0. The tendency of γ_i towards a constant value as $X_i \to 0$ is expressed as *Henry's Law*, i.e.:

$$\gamma_i \to \gamma_i^0 \text{ as } X_i \to 0,$$

and if γ_i is constant over some finite range of composition of dilute solution of i, component i is said to exhibit ideal Henrian behavior in this range, its activity being given by:

$$a_i = \gamma_i^0 X_i.$$

Application of the Gibbs–Duhem relation, eq. (48), shows that, over the composition range in which the solute B exhibits ideal Henrian behavior, the solvent A exhibits ideal Raoultian behavior.

The occurrence of Henrian ideal behavior gives rise to the concept of the Henrian standard state, illustrated in fig. 9 which shows the activity of B as a function of composition in the system A–B. The Raoultian standard state is pure B, located at the point R where $a_B = 1$. If, however, pure B behaved as it does in dilute solution in A, extrapolation of its activity along the Henry's Law line would give an activity of γ_B^0 in the hypothetical pure state at $X_B = 1$, relative to the Raoultian standard state. This hypothetical pure state is the Henrian standard state, located at the point H in fig. 9, and, relative to this standard state, the activity of B in any solution, h_B, is

$$h_B = f_B X_B,$$

where f_B is the *Henrian activity coefficient*. In the range of dilute solutions over which B exhibits Henrian ideal behavior, $f_B = 1$ and hence:

$$h_B = X_B.$$

If the vapor pressure of B in the Raoultian standard state is p_B^0, then the vapor pressure of B in the Henrian standard state is $\gamma_B^0 p_B^0$, and hence the change of standard state,

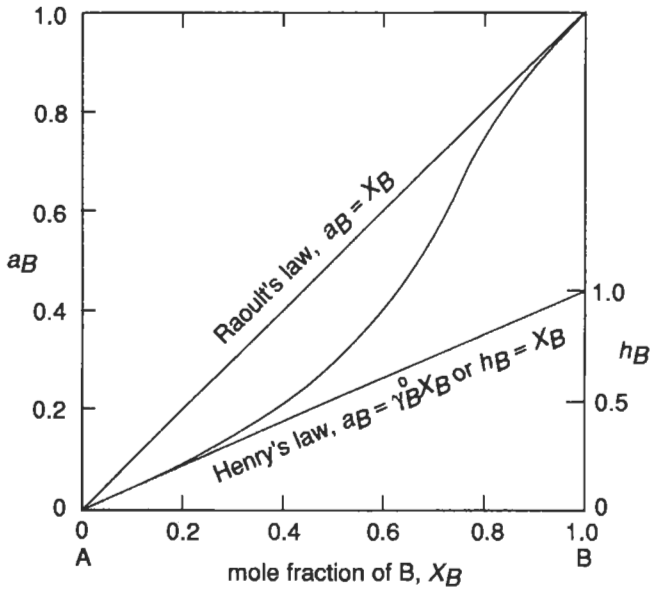

Fig. 9. Illustration of the Raoultian and Henrian standard states.

$$B_{(\text{Raoultian standard state})} \rightarrow B_{(\text{Henrian standard state})},$$

corresponds to

$$B_{\left(\text{vapor at pressure } p_B^0\right)} \rightarrow B_{\left(\text{vapor at pressure } \gamma_B^0 p_B^0\right)},$$

with a free energy change of

$$\Delta G_B(R \rightarrow H) = RT \ln \gamma_B^0.$$

7. *The thermodynamic origin of phase diagrams*

In the definition of activity, given by eq. (43), p_i^0 is the vapor pressure of pure i at the temperature of interest. However, depending on the convenience of the situation, either pure solid i or pure liquid i can be chosen as the standard state. At temperatures below the triple point, $p_{i(\text{solid})}^0 < p_{i(\text{liquid})}^0$, and so the activity of i in a solution, relative to pure solid i as the standard state, is larger than the activity relative to pure liquid i as the standard state. Conversely, at temperatures higher than the triple point temperature the reverse is the case. The activities on the two activity scales are related as

$$\frac{a_{i(\text{relative to solid standard state})}}{a_{i(\text{relative to liquid standard state})}} = \frac{p_{i(\text{liquid})}^0}{p_{i(\text{solid})}^0} = \exp\left(\Delta G_{m,i}^0 / RT\right).$$

References: p. 469.

Consider the molar free energies of mixing in the system A–B, the phase diagram for which is shown in fig. 10a. For simplicity of discussion it will be assumed that both the solid and liquid solutions exhibit ideal Raoultian behavior. The molar free energies, at temperature T, are shown in fig. 10b. Pure liquid A and pure solid B are chosen as the reference states and are located at points **a** and **b** respectively. $G^0_{A(s)}$ is located at **c**, where $G^0_{A(s)} - G^0_{A(l)} = -\Delta G^0_{m,A}$ at temperature T, and $G^0_{B(l)}$ is located at **d** where $G^0_{B(l)} - G^0_{B(s)} = \Delta G^0_{m,B}$ at temperature T. Thus, relative to unmixed pure liquid A and pure solid B as the reference state, the molar free energy of the unmixed pure liquids (given by line **ad**) is $X_B \Delta G^0_{m,B}$ and the corresponding free energy of the unmixed pure solids (given by line **cb**) is $-X_A \Delta G^0_{m,A}$. Upon mixing to form Raoultian ideal solutions, the molar free energies decrease by $|RT(X_A \ln X_A + X_B \ln X_B|$ and hence, relative to the chosen reference state:

$$\Delta G^M(\text{solid solutions}) = -X_A \Delta G^0_{m,A} + RT\left(X_A \ln X_A + X_B \ln X_B\right),$$

and

$$\Delta G^M(\text{liquid solutions}) = X_B \Delta G^0_{m,B} + RT\left(X_A \ln X_A + X_B \ln X_B\right).$$

The double tangent drawn to the two free energy curves touches the curve for the solid solutions at **g** and the curve for the liquid solutions at **f**, with the intercepts at $X_A = 1$ and $X_B = 1$ being **e** and **h** respectively. As the equilibrium state is that of minimum free energy, points **f** and **g** divide the composition range into three regions. At compositions between **a** and **f** the homogeneous liquid solution has the lowest possible free energy and at compositions between **g** and **b** the homogeneous solid solution has the lowest possible free energy. However, at compositions between **f** and **g**, a two-phase mixture of liquid solution of composition **f** and solid solution of composition **g**, the free energy of which lies on line **fg**, has a lower free energy than both the homogeneous solid solution and the homogeneous liquid solution. Thus point **f** is the limit of solution of B in liquid A and **g** is the limit of solution of A in solid B, and so points **f** and **g** are, respectively, the liquidus and solidus compositions at temperature T.

Furthermore, for phase equilibrium:

$$\overline{G}_A(\text{in liquid solution } \mathbf{f}) = \overline{G}_A(\text{in solid solution } \mathbf{g}),$$

and:

$$\overline{G}_B(\text{in liquid solution } \mathbf{f}) = \overline{G}_B(\text{in solid solution } \mathbf{g})$$

or $$\Delta\overline{G}^M_A(\text{in liquid } \mathbf{f}) = \Delta\overline{G}^M_A(\text{in solid } \mathbf{g}),$$

and:

$$\Delta\overline{G}^M_B(\text{in liquid } \mathbf{f}) = \Delta\overline{G}^M_B(\text{in solid } \mathbf{g}).$$

These requirements state that, for phase equilibrium, the tangent to the molar free energy curve for the liquid solutions at the liquidus composition **f** is also the tangent to the molar free energy curve for the solid solutions at the solidus composition **g**. Geometrically, this condition is such that, simultaneously,

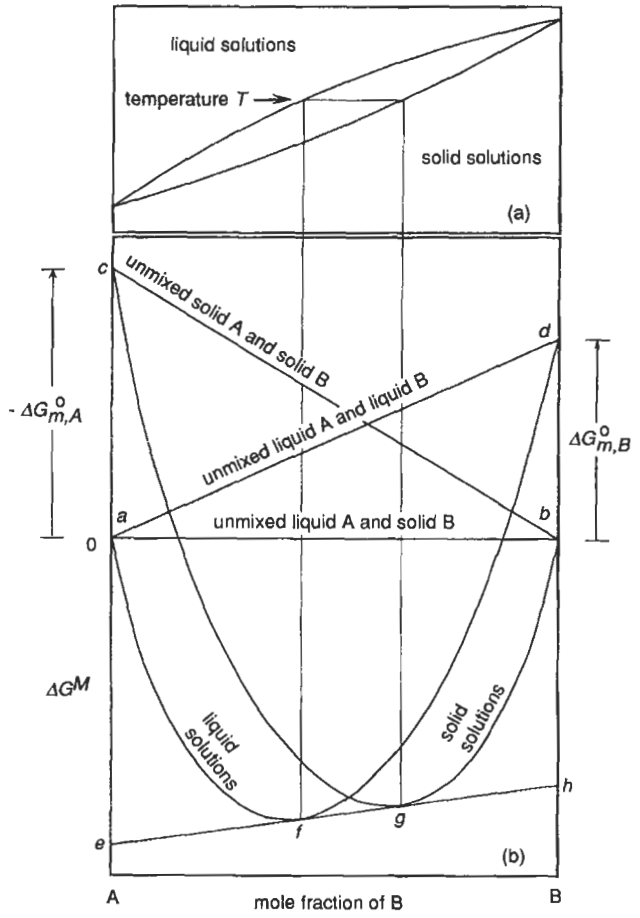

Fig. 10. (a) The phase diagram for the system A–B. (b) The ideal free energy of mixing curves for the system A–B at temperature T.

$$\mathbf{ca} + \mathbf{ae} = \mathbf{ce} \text{ and } \mathbf{db} + \mathbf{bh} = \mathbf{dh}, \tag{54}$$

where: $\mathbf{ce} = \Delta\overline{G}^{M}_{A}$ (relative to solid A as the standard state)
$= RT \ln X_A$ (at the composition **g**),
$\mathbf{ae} = \Delta\overline{G}^{M}_{A}$ (relative to liquid A as the standard state)
$= RT \ln X_A$ (at the composition **f**),
$\mathbf{dh} = \Delta\overline{G}^{M}_{B}$ (relative to liquid B as the standard state)
$= RT \ln X_B$ (at the composition **f**),
and $\mathbf{bh} = \Delta\overline{G}^{M}_{B}$ (relative to solid B as the standard state)
$= RT \ln X_B$ (at the composition **g**).

References: p. 469.

Thus eqs. (54) become:

$$\Delta G^0_{m,A} + RT \ln X_A(\text{liquidus}) = RT \ln X_A(\text{solidus}),$$

and

$$-\Delta G^0_{m,B} + RT \ln X_B(\text{solidus}) = RT \ln X_B(\text{liquidus}).$$

As $X_A(\text{liquidus}) + X_B(\text{liquidus}) = 1$ and $X_A(\text{solidus}) + X_B(\text{solidus}) = 1$, the solidus and liquidus compositions (in a Raoultian system) are thus uniquely determined by the values of $\Delta G^0_{m,A}$ and $\Delta G^0_{m,B}$ as:

$$X_{A(\text{liquidus})} = \frac{1 - \exp\left(-\Delta G^0_{m,B}/RT\right)}{1 - \left[\exp\left(-\Delta G^0_{m,B}/RT\right)\right]\left[\exp\left(\Delta G^0_{m,A}/RT\right)\right]} \tag{55}$$

and

$$X_{A(\text{solidus})} = \frac{\exp\left(\Delta G^0_{m,A}/RT\right)\left[1 - \exp\left(-\Delta G^0_{m,B}/RT\right)\right]}{1 - \left[\exp\left(-\Delta G^0_{m,B}/RT\right)\right]\left[\exp\left(\Delta G^0_{m,A}/RT\right)\right]}. \tag{56}$$

The phase diagram for the system Si–Ge, calculated from eqs. (55) and (56) and the known variations of $\Delta G^0_{m,Si}$ and $\Delta G^0_{m,Ge}$ with temperature, is compared, in fig. 11, with the liquidus and solidus lines determined experimentally by thermal and X-ray analysis. As is seen, the behavior in the system is very close to Raoultian.

Raoultian behavior is very much the exception rather than the rule, and even complete mutual solid solubility between A and B requires that A and B have the same crystal structure, similar atomic sizes, similar electronegativities, and similar valences. The requirement of similar atomic size arises from the introduction of a strain energy into the lattice when the solvent and substitutional solute atoms are of differing size. This strain energy always increases the Gibbs free energy and, hence, can significantly influence the phase relationships in the system. It is found that terminal solid solutions extend only a few atomic percent into a binary system if the atomic diameters differ by more than 14%. Significant differences in electronegativity cause the formation of intermetallic compounds such as Mg_2Si, Mg_2Sn and Mg_2Pb, and differences in valences can cause the formation of electron compounds such as occur in the systems Cu–Zn and Cu–Sn.

Although Cu and Ag are chemically similar, the atomic radius of Ag is 13% larger than that of Cu and hence, as shown in fig. 12a, Cu and Ag form a simple eutectic system. In this system it is presumed that Ag exhibits Raoultian ideal behavior in the Ag-rich α-solid solution and that Cu exhibits Raoultian ideal behavior in the Cu-rich β-solid solution. Consequently Cu in α and Ag in β exhibit Henrian ideal behavior and, at 1000 K, the activities of the components, relative to the pure solids as standard states, are as shown in fig. 12b. At 1000 K, saturation of the α-phase with Cu occurs at $X_{Ag} = 0.9$, and hence, as Ag obeys Raoult's law in the α-phase, $a_{Ag} = 0.9$ at this composition. Phase equilibrium between α saturated with Cu and β saturated with Ag requires that the

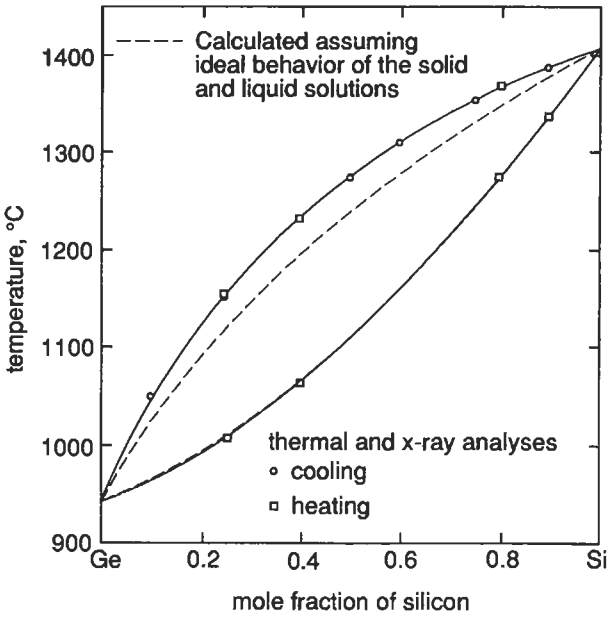

Fig. 11. Comparison of the phase diagram for the system Si–Ge as determined experimentally by X-ray and thermal analysis, with that calculated assuming Raoultian ideal behavior in both the solid and liquid solutions.

activities of both Ag and Cu be the same in both phases, and hence $a_{Ag} = 0.9$ in the Ag-saturated β-phase of composition $X_{Ag} = 0.04$. Similarly, $a_{Cu} = 0.96$ in the Ag-saturated β (at $X_{Cu} = 0.96$) and in the Cu-saturated α (at $X_{Ag} = 0.9$). Thus, in the α-phase, Henrian behavior of Cu is given by:

$$a_{Cu} = 9.6X_{Cu}, \tag{57}$$

and in the β-phase, Henrian behavior of Ag is given by:

$$a_{Ag} = 22.5X_{Ag}.$$

8. *Reaction equilibrium involving solutions and the Gibbs phase rule*

8.1. The dependence of the equilibrium state on activity

In §4 it was shown that, at constant temperature and pressure, equilibrium is established in the reaction

$$aA + bB = cC + dD,$$

when

$$a\overline{G}_A + b\overline{G}_B = c\overline{G}_C + d\overline{G}_D. \tag{58}$$

References: p. 469.

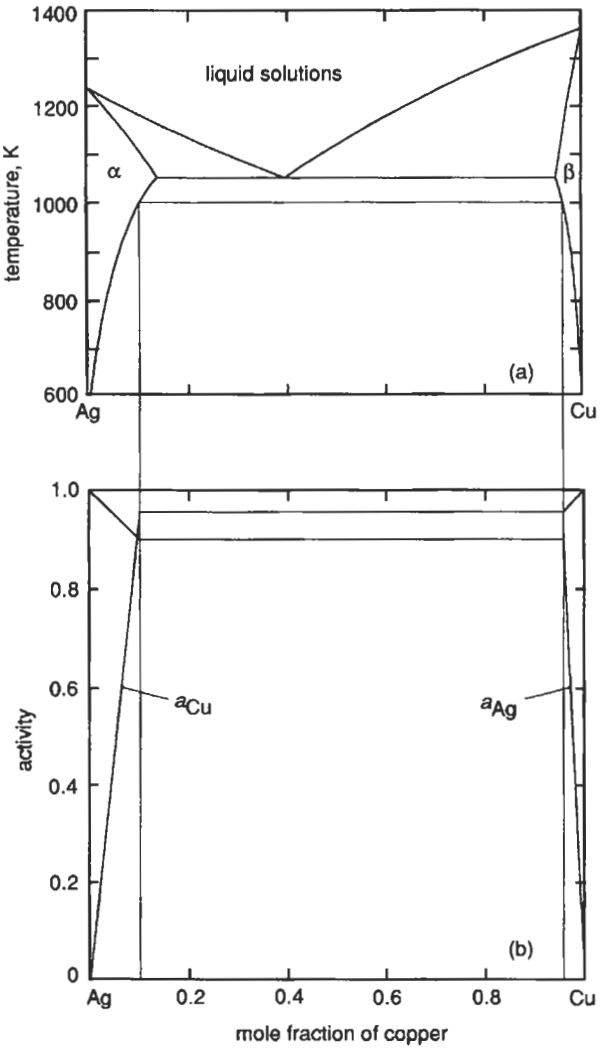

Fig. 12. (a) The phase diagram for the system Ag–Cu. (b) The activities of Ag and Cu in the system Ag–Cu at 1000 K.

As:

$$\overline{G}_i = G_i^0 + RT \ln a_i,$$

eq. (58) can be written as:

$$\Delta G_T^0 = -RT \ln \frac{a_C^c a_D^d}{a_A^a a_B^b},$$

where the quotient in the logarithm term is K_T the equilibrium constant for the reaction.

Consider the oxidation, at 1000 K, of Cu from an Ag–Cu alloy of $X_{Cu} = 0.08$. From eq. (57), the activity of Cu in this alloy, relative to pure solid Cu as the standard state, is

$$a_{Cu} = 9.6X_{Cu} = 9.6 \times 0.08 = 0.768.$$

For the reaction:

$$4Cu_{(s)} + O_{2(g)} = 2Cu_2O_{(s)}$$

$$\Delta G_T^0 = -336810 + 142.5T \text{ J}.$$

Thus, $\Delta G_{1000}^0 = -194300 \text{ J} = -8.3144 \times 1000 \ln K_{1000}$ and so:

$$K_{1000} = 1.41 \times 10^{10} = \frac{a_{Cu_2O}^2}{a_{Cu}^4 p_{O_2}}. \tag{59}$$

Oxidation of the Cu occurs when the oxygen pressure in the system has been increased to the level at which $a_{Cu_2O} = 1$. From eq. (59) this oxygen pressure is:

$$p_{O_2} = \frac{1}{(0.768)^4 \times 1.41 \times 10^{10}} = 2.04 \times 10^{-10} \text{atm}.$$

From eq. (16), ΔG_{1000}^0 for the reaction

$$2Ag_{(s)} + \tfrac{1}{2} O_{2(g)} = Ag_2O_{(s)}$$

has the value 31 062 J. Thus:

$$K_{1000} = \frac{a_{Ag_2O}}{a_{Ag}^2 p_{O_2}^{1/2}} = 0.024.$$

Thus, with $a_{Ag} = 0.92$ (Raoultian behavior in the α-solid solution) and $p_{O_2} = 2.04 \times 10^{-10}$ atm:

$$a_{Ag_2O} = 2.9 \times 10^{-7},$$

which shows that the equilibrium oxide is virtually pure Cu_2O. As the oxygen pressure in the system is further increased, the Cu content in the alloy decreases in accordance with eq. (59). Thus the alloy in equilibrium with virtually pure Cu_2O and air (oxygen fraction 0.21) at 1000 K is that in which

$$a_{Cu} = \left[\frac{1}{1.41 \times 10^{10} \times 0.21}\right]^{1/4} = 0.0043,$$

or $X_{Cu} = a_{Cu}/9.6 = 4.5 \times 10^{-4}$.

At this oxygen pressure the activity of Ag_2O in the equilibrium oxide phase, with $a_{Ag} \approx 1$, is:

References: p. 469.

$$a_{Ag_2O} = 0.024 \times 1 \times 0.21^{1/2} = 0.011,$$

and so the equilibrium oxide phase is still essentially pure Cu_2O.

8.2. The Gibbs phase rule

The complete description of a thermodynamic system containing C components existing in P phases requires specification of the temperatures, pressures and compositions of each of the P phases. As the composition of each phase is defined when the concentrations of $C-1$ of its components are known, the total number of variables in the description is P pressures + P temperatures + $P(C-1)$ concentrations $= P(C+1)$. For thermodynamic equilibrium in the system, each of the P phases must be at the same temperature and same pressure and the activity (or partial molar free energy) of each of the individual components must be the same in each of the P phases. Thus, for equilibrium, there are $(P-1)$ equalities of temperature, $(P-1)$ equalities of pressure and $(P-1)C$ equalities of activity, and hence the total number of equilibrium conditions, given as the number of equations among the variables of the system, is $(P-1)(C+2)$. The number of *degrees of freedom*, F, which the equilibrium system may have, is defined as the maximum number of variables which may be independently altered in value without disturbing the equilibrium in the system. This number is obtained as the difference between the total number of variables available to the system and the minimum number of equations among these variables that is required for maintenance of the equilibrium, i.e.:

$$\begin{aligned} F &= P(C+1) - (P-1)(C+2) \\ &= C + 2 - P. \end{aligned} \tag{60}$$

Equation (60) is the *Gibbs phase rule* and is a powerful tool in the determination of possible equilibria which may occur in multicomponent, multiphase systems.

In the simplest of applications, i.e., in a one-component system, $F = 3 - P$. Thus, with reference to the phase diagram for H_2O, shown in fig. 3, for the existence of a single phase $F = 2$ and so the pressure and temperature can be varied independently without disturbing the equilibrium, i.e., with $F = 2$ the state of the system can be moved about within the area of stability of the single phase in the pressure–temperature diagram. However, for a two-phase equilibrium the state of the system must lie on one of the lines in fig. 3 and thus only the pressure or the temperature can be varied independently. From the phase rule, $F = 1$ and hence the two-phase equilibrium is univariant. The triple point, where the three phases are in equilibrium, occurs at fixed values of temperature and pressure, in accordance with $F = 0$ from the phase rule. The three-phase equilibrium is thus invariant and three is the maximum number of phases which can be in equilibrium with one another in a one-component system.

In a binary system, the inclusion of a second component adds an extra degree of freedom to each equilibrium and hence the maximum number of phases which can be in equilibrium with one another in a two-component system is four. However, phase diagrams for binary systems of metallurgical interest are normally presented for a

pressure of 1 atm, i.e., they are the 1 atm isobaric sections of the phase equilibria occurring in pressure–temperature–composition space, and hence one of the degrees of freedom is used in specifying the pressure. Thus, at an arbitrarily selected pressure such as 1 atm, the maximum number of phases which can exist in equilibrium with one another in a binary system is three (unless, by chance, the arbitrarily selected pressure happens to be that at which an invariant four-phase equilibrium occurs). In the binary system A–B, considered at constant pressure, the available variables are T, a_A and a_B. For the existence of a single phase, such as α, β or liquid in fig. 12a, the phase rule gives $F=2$, and hence any two of T, a_A and a_B may be varied independently. For any two-phase equilibrium, $F=1$ and hence the specification of any one of the three variables fixes the state of the system. For example, specification of the temperature at which the two-phase equilibrium exists fixes the compositions of the equilibrated phases on the appropriate liquidus, solidus or solvus lines; and specification of the composition of one of the equilibrated phases fixes the temperature at which the chosen composition lies on the appropriate liquidus, solidus or solves line and fixes the composition of the second phase at the other end of the tie-line between the two equilibrated phases. The three-phase equilibrium with $F=0$ is invariant, and, in fig. 12a, the eutectic equilibrium occurs at a fixed temperature at which the compositions of the α, β and liquid phases are also fixed.

If some, or all, of the components of a system can react chemically with one another to produce new chemical species, a distinction must be drawn between the terms component and species. For example the *components* silver and oxygen in the binary system Ag–O are capable of reacting to form the new *species* Ag_2O, and hence an equilibrium among the three species Ag, Ag_2O and O_2 can occur in the two-component system. The equilibrium among Ag, Ag_2O and O_2 is called an *independent reaction equilibrium*. In a system containing N species and existing in P phases among which there are R independent reaction equilibria, the number of variables is $P(N+1)$, i.e., P pressures + P temperatures + $P(N-1)$ concentrations. However, if the species i and j react to form the species k, reaction equilibrium requires that

$$\overline{G}_i + \overline{G}_j = \overline{G}_k,$$

and this is an additional equation required among the variables. Thus, if R independent reaction equilibria occur, the number of equations among the $P(N+1)$ variables, required for equilibrium is $(P-1)$ equalities of temperature $+(P-1)$ equalities of pressure $+(P-1)N$ equalities of activity $+R=(P-1)(N+2)+R$, and hence the number of degrees of freedom, F, is

$$\begin{aligned} F &= P(N+1) - (P-1)(N+2) - R \\ &= (N-R) + 2 - P. \end{aligned}$$

Comparison with eq. (60) indicates that

$$C = N - R, \tag{61}$$

References: p. 469.

i.e., the number of components in a system equals the number of species present minus the number of reaction equilibria. Equation (61) is normally used to calculate the number of independent reaction equilibria from knowledge of the number of components and the number of species. For example, in the two-component system Ag–O, the independent reaction equilibrium among the three species is

$$2Ag + \tfrac{1}{2}O_2 = Ag_2O.$$

For equilibrium among the phases metal, metal oxide and oxygen gas in the two-component system, $F=1$ and thus only T or p_{O_2} can be selected as the single degree of freedom. Selection of T fixes ΔG_T^0 and hence, via eq. (34), fixes p_{O_2}, and vice versa.

Consider the various equilibria which can occur in the ternary system Si–C–O, for which a stability diagram is shown in fig. 7. It can be considered that this system contains the six species Si, SiO_2, SiC, C, CO and CO_2, and hence $R=6-3$, i.e., there are three independent reaction equilibria. These are derived as follows. The chemical reaction for formation of each compound from its elements is written:

$$Si + O_2 = SiO_2,$$
$$Si + C = SiC,$$
$$C + O_2 = CO_2,$$
$$C + \tfrac{1}{2}O_2 = CO.$$

These equations are then combined in such a way as to eliminate any elements which are not considered as species in the system, and the minimum number of equations so obtained, is the number of independent reaction equilibria, R. In this case oxygen is not considered as species, and elimination of O_2 gives:

$$C + CO_2 = 2CO, \tag{i}$$

$$Si + C = SiC, \tag{ii}$$

and

$$Si + 2CO_2 = SiO_2 + 2CO \tag{iii}$$

as the independent equilibria. From the phase rule, the maximum number of phases which can coexist in equilibrium is five (the condensed phases Si, SiO_2, SiC, C and the gas phase CO–CO_2). This equilibrium is invariant and occurs at the temperature T_{eq} at which $\Delta G_{(ii)}^0 = 0$ and at the pressure $P = p_{CO} + p_{CO_2}$ at which $K_{(i),T_{eq}} = p_{CO}/p_{CO_2}$ and $K_{(iii),T_{eq}} = (p_{CO}/p_{CO_2})^2$ are simultaneously satisfied. If the temperature is arbitrarily fixed, as is the case in fig. 7, the maximum number of phases which can coexist in equilibrium is four (three condensed phases and a gas phase). One such equilibrium occurs in fig. 7 at point **b**. For the coexistence of two condensed phases and a gas phase at the arbitrarily selected temperature, $F=1$, and such equilibria lie on the univariant lines A, B, C and D in fig. 7, and for equilibrium between a single condensed phase and a gas phase, $F=2$, corresponding to areas of single condensed phase stability in fig. 7.

Occasionally situations are found in which it might appear, at first sight, that the

phase rule is not obeyed, and usually, in such situations a degree of freedom is used by a condition of stoichiometry in the system. For example, in the reduction of ZnO by graphite to produce Zn vapor, CO and CO_2, it might appear that the three-phase equilibrium (ZnO, C and the gas phase) in the three-component system (Zn–O–C) has $F = 5 - 3 = 2$ degrees of freedom, and that, with the five species ZnO, C, $Zn_{(v)}$, CO and CO_2, two independent reaction equilibria occur, which can be selected as

$$ZnO_{(s)} + C_{(gr)} = Zn_{(v)} + CO_{(g)} \tag{iv}$$

and

$$2ZnO_{(s)} + C_{(gr)} = 2Zn_{(v)} + CO_{2(g)}, \tag{v}$$

for which

$$K_{(iv)} = p_{CO} p_{Zn}, \tag{vi}$$

and

$$K_{(v)} = p_{Zn}^2 p_{CO_2}. \tag{vii}$$

However, selecting T, which fixes the values of $K_{(iv)}$ and $K_{(v)}$ and any one of p_{Zn}, p_{CO} or p_{CO_2} as the two apparent degrees of freedom does not fix the state of the system, i.e., does not allow simultaneous solution of eqs. (vi) and (vii). This difficulty arises because the stoichiometry requirement has not been taken into consideration, i.e. that, as all the Zn and O occurring in the gas phase originates from the stoichiometric ZnO, the condition

$$\frac{n_O}{n_{Zn}} = 1 = \frac{n_{CO} + 2n_{CO_2}}{n_{Zn}} = \frac{p_{CO} + 2p_{CO_2}}{p_{Zn}} \tag{viii}$$

must also be satisfied. This stoichiometric requirement decreases F to unity and hence selecting T as the single degree of freedom fixes the partial pressures of Zn, CO and CO_2 as the values required for simultaneous solution of eqs. (vi), (vii) and (viii).

9. *The thermodynamics of surfaces and interfaces*

9.1. The Gibbs adsorption isotherm

In passing from one phase to another in a heterogeneous system, some of the properties undergo significant changes as the boundary between the two phases is traversed. The thin region over which these changes occur is called the *interface*, and a complete thermodynamic analysis of the system requires consideration of the thermodynamic properties of the interface.

Consider fig. 13 which shows the variation of the concentration, c_1, of the component 1 across the interface region in a system comprising equilibrated α and β phases. Calculation of the total number of moles of component 1 in the system as the sum $c_1^\alpha V^\alpha + c_1^\beta V^\beta$, where V^α and V^β are the volumes of the phases, involves the assumption

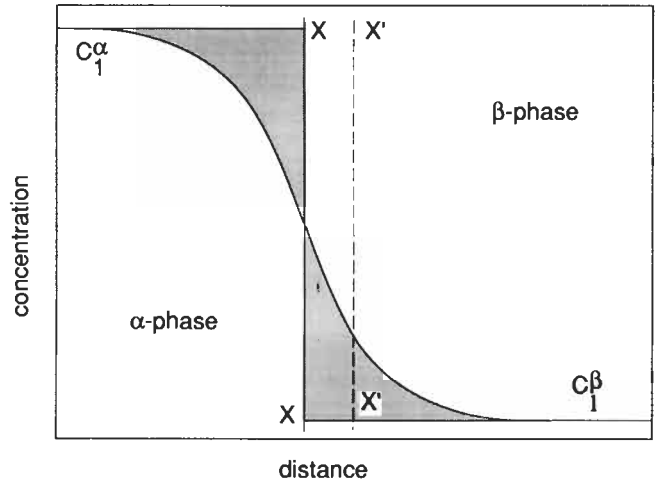

Fig. 13. The variation, with distance, of concentration on passing through the interface between two phases.

that the values c_1^{α} and c_1^{β} occur up to some plane in the interface region, and evaluation of $c_1^{\alpha}V^{\alpha} + c_1^{\beta}V^{\beta}$ requires that a mathematical plane be located somewhere in the interface region. In fig. 13 it is seen that the number of moles of component 1 in the system, calculated as $c_1^{\alpha}V^{\alpha} + c_1^{\beta}V^{\beta}$, is only equal to the actual number of moles of 1 in the system, n_1 when the boundary plane X–X is located such that the shaded areas in fig. 13 are equal. If the boundary plane is located to the right of X–X, say at X′–X′, then:

$$n_1 < c_1^{\alpha}V^{\alpha} + c_1^{\beta}V^{\beta}$$

or, if the boundary plane is located to the left of X–X:

$$n_1 > c_1^{\alpha}V^{\alpha} + c_1^{\beta}V^{\beta}.$$

The difference between n_1 and $c_1^{\alpha}V^{\alpha} + c_1^{\beta}V^{\beta}$ defines the *surface concentration of component 1*, Γ_1, (moles/cm^2), as:

$$\Gamma_1 A_s = n_1 - (c_1^{\alpha}V^{\alpha} + c_1^{\beta}V^{\beta}),$$

where A_s is the area of surface between the two phases. Thus, with the boundary located to the left of X–X, Γ_1 is a positive quantity and with the boundary located to the right of X–X, Γ_1 is a negative quantity. In a single-component system where the boundary is between a condensed phase and a vapor phase, it is logical to locate the boundary at X–X so that the surface concentration is zero. However, with two or more components in the system it is not generally possible to locate the interface at a position at which more than one of the surface concentrations are zero. In such a case X–X is located such that the surface concentration of the solvent, Γ_1, is zero and the surface concentration of the solute, Γ_2, is not zero. This is illustrated in fig. 14.

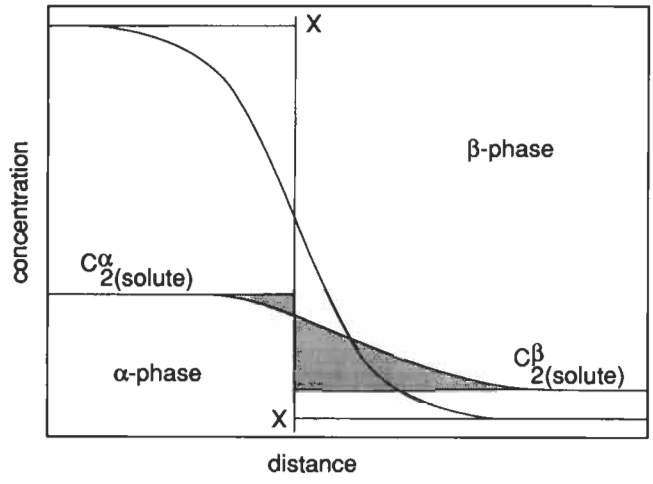

Fig. 14. The variations, with distance, of the concentrations of solvent and solute on passing through an interface, and illustration of the origin of surface concentration of the solute.

The definition of *surface free energy per unit area*, G_s, is analogous to that for the surface concentration, i.e.:

$$G_s A_s = G' - \sum \overline{G}_i^{\alpha} n_i^{\alpha} - \sum \overline{G}_i^{\beta} n_i^{\beta}, \tag{62}$$

where G' is the total free energy of the system.

The *surface tension*, σ, is defined as:

$$\sigma = \left(\frac{\partial G'}{\partial A_s} \right)_{T,P,n_i},$$

and hence, when surfaces are included in the discussion, eq. (13) is written as:

$$dG' = -S'dT + V'dP + \sigma dA_s + \sum \overline{G}_i dn_i \tag{63}$$

If the surface area is increased by dA_s at constant T, P, and n_i, combination of eqs. (62) and (63) gives:

$$G_s dA_s = \sigma dA_s + \left(\sum \overline{G}_i^{\alpha} n_i^{\alpha} + \sum \overline{G}_i^{\beta} n_i^{\beta} \right). \tag{64}$$

As phase equilibrium is maintained, $\overline{G}_i^{\alpha} = \overline{G}_i^{\beta}$; mass balance requires that:

$$dn_i^{\alpha} + dn_i^{\beta} = -\Gamma_i dA_s,$$

in which case eq. (64) can be written as:

$$G_s dA_s = \sigma dA_s + \sum \overline{G}_i \Gamma_i dA_s$$

or:

$$G_s = \sigma + \sum \overline{G}_i \Gamma_i, \tag{65}$$

i.e., the surface free energy is the surface tension plus the free energy due to the surface concentrations of the components.

Complete differentiation of eq. (65) gives:

$$dG_s = d\sigma + \sum \overline{G}_i d\Gamma_i + \sum \Gamma_i d\overline{G}_i, \tag{66}$$

and the differential of G_s for conditions of fixed surface area and fixed P gives:

$$dG_s = -S_s dT + \sum \overline{G}_i d\Gamma_i. \tag{67}$$

Combination of eqs. (66) and (67) gives:

$$d\sigma = -S_s dT - \sum \Gamma_i dG_i, \tag{68}$$

which is *Gibbs' equation for surface tension*. At constant T, eq. (68) gives, for the binary system A–B in which $\Gamma_A = 0$:

$$\begin{aligned} \Gamma_B &= -\left(\frac{\partial \sigma}{\partial \overline{G}_B}\right)_T = -\left(\frac{\partial \sigma}{RT \partial \ln a_B}\right)_T \\ &= -\frac{1}{RT}\left(\frac{d\sigma}{d \ln a_B}\right). \end{aligned} \tag{69}$$

Equation (69), which is known as the *Gibbs adsorption isotherm*, indicates that any solute which lowers the surface tension has a positive value of Γ and hence is concentrated in the surface, and, conversely, any solute which raises the surface tension has a lower concentration in the surface than in the bulk phase.

The influence of dissolved oxygen on the surface tension of liquid iron at 1550°C is shown in fig. 15 as the variation of σ with the activity of oxygen relative to the 1 weight percent standard state. The surface concentration of oxygen at any concentration of oxygen in the bulk phase is obtained from the slope of the line and the Gibbs adsorption isotherm. At high oxygen contents the slope of the line approaches the constant value of −240 dyne/cm, which corresponds to saturation coverage of the surface by adsorbed oxygen. From the Gibbs adsorption isotherm this saturation coverage is calculated as

$$\Gamma_0 = 6.023 \times 10^{23} \times \frac{240}{8.3144 \times 10^7 \times 1823} = 9.5 \times 10^{14} \text{ atoms/cm}^2 .$$

9.2. The Langmuir adsorption isotherm

Consider the equilibrium between the component i in a vapor phase and i adsorbed on the surface of a condensed phase. If is is considered that the atoms of i are adsorbed on specific adsorption sites on the surface of the condensed phase, the limit of adsorption

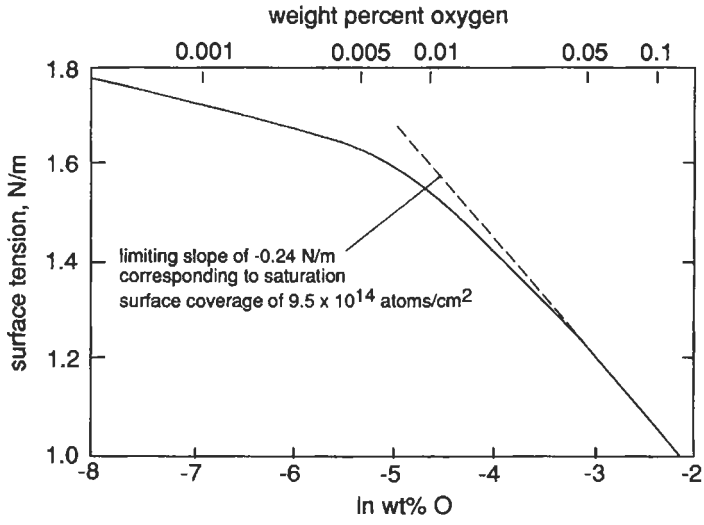

Fig. 15. The variation of the surface tension of Fe–O melts with activity of oxygen at 1550°C.

occurs when all of the available sites are occupied by adsorbed atoms. This limit corresponds to the surface being covered by a monolayer of adsorbed atoms at the surface concentration Γ_i^0. At surface concentrations, Γ_i, less than that corresponding to monolayer coverage, the fraction of surface sites occupied, θ_i (or the fractional saturation of the surface) is defined as:

$$\theta_i = \frac{\Gamma_i}{\Gamma_i^0}. \tag{70}$$

At equilibrium, the rates of adsorption and desorption of i are equal, the former being proportional to the pressure of i in the vapor phase, p_i, and the fraction of unoccupied surface sites, $(1-\theta_i)$, and the latter being proportional to the fraction of surface sites occupied by i, i.e.:

$$k_a p_i(1-\theta_i) = k_d \theta_i,$$

where k_a and k_d are the rate constants for the adsorption and desorption reactions, respectively. Thus:

$$p_i = K_i \frac{\theta_i}{1-\theta_i}, \tag{71}$$

where

$$K_i = k_d/k_a = \exp\left(-\Delta G_i^0/RT\right),$$

References: p. 469.

and ΔG_i^0 is the change in molar free energy accompanying the transfer of one mole of i from the vapor state at 1 atm pressure to the adsorbed layer on the surface at the surface concentration Γ_i^0. Equation (71), which is *Langmuir's adsorption isotherm*, shows that θ_i is proportional to p_i at small θ_i and $(1 - \theta_i)$ is inversely proportional to p_i at large θ_i.

Alternatively, eq. (71) can be written as:

$$a_i = K_i' \frac{\theta_i}{1 - \theta_i}. \tag{72}$$

BELTON has combined the Gibbs and Langmuir adsorption isotherms by substitution of eqs. (70) and (72) into eq. (69) to give:

$$\frac{d\sigma}{d \ln a_i} = -RT\, \Gamma_i = -RT\theta_i\Gamma_i^0 = -RT\, \Gamma_i^0 \frac{K_i'a_i}{1 + K_i'a_i},$$

which, on integration between the composition limits X_i' and X_i'', becomes:

$$\sigma'' - \sigma' = -RT\, \Gamma_i^0 \ln \frac{1 + K'a_i''}{1 + K'a_i'}. \tag{73}$$

If Langmuir's isotherm holds at all compositions, one limit can be taken as the pure solvent, in which case eq. (73) becomes

$$\sigma^P - \sigma = -RT\, \Gamma_i^0 \ln(1 + K'a_i). \tag{74}$$

where σ^P refers to the surface tension of the pure solvent. Curve-fitting of eq. (74) with the experimental data shown in fig. 16 and $\sigma^P = 1788$ dyne/cm, $\Gamma_O^0 = 240$ dyne/cm, gives $K' = 220$. Thus, if oxygen adsorbed on liquid iron exhibits ideal Langmuir behavior:

$$\theta_\sigma = \frac{220 \cdot [\text{wt\%O}]}{1 + 220 \cdot [\text{wt\%O}]}. \tag{75}$$

Equation (75) is shown in fig. 16 in comparison with the variation of θ_O obtained from the slopes in fig. 15 as $\theta_O = \Gamma_O / \Gamma_O^0$.

A number of applications of the Gibbs and Langmuir absorption isotherms will be found in ch. 13, §§2 and 4.

9.3. Curved interfaces

The existence of surface tension gives rise to the interesting phenomenon that the equilibrium vapor pressure exerted by a spherical droplet is a function of the radius of curvature of the droplet. This phenomenon, which was first discussed by Kelvin in 1871, is of importance with respect to the dependence of the limit of solid solution of one component in another on the particle size of the second phase.

The general equation

$$dG' = -S'dT + V'dP + \sigma dA_s + \sum \overline{G}_i dn_i \tag{63}$$

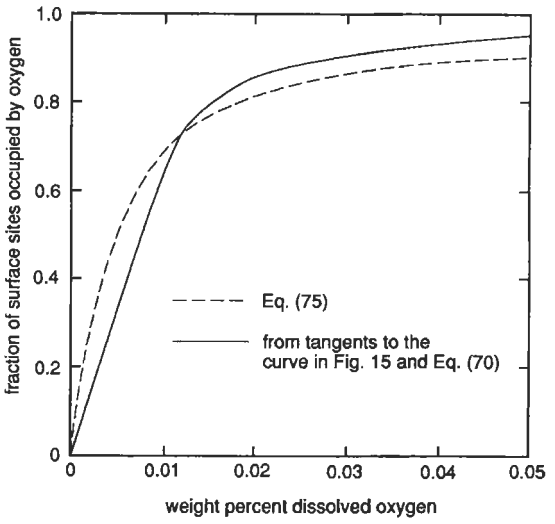

Fig. 16. The variation, at 1550°C, of the fractional coverage of the surface of liquid iron by adsorbed oxygen with concentration of oxygen in the melt.

was tacitly applied to systems containing flat interfaces. However, provided that σ is not a function of the radius of curvature of the interface, and that the interface within the system does not influence the exterior pressure, eq. (63) can be applied to the transfer of matter across curved interfaces. The *partial molar free energy*, $\overline{G}_i^*$, defined from eq. (63) as:

$$\overline{G}_i^* = \left(\frac{\partial G'}{\partial n_i}\right)_{T,P,A_s,n_j},$$

pertains to the addition of i to the system in such a manner that A_s remains constant. However, in a process involving the transfer of matter to a small spherical droplet, A_s, being dependent on the volume, and hence on the amount of matter in the droplet, is not an independent variable. The incremental increase in volume of a droplet caused by the addition of dn_i moles of the various components is:

$$dV' = \sum \overline{V}_i dn_i,$$

where $\overline{V}_i$ is the partial molar volume of i in the system. From the relationship between the surface area and the volume of a sphere,

$$dA_s = \frac{2dV'}{r} = \sum \frac{2\overline{V}_i}{r} dn_i,$$

substitution of which into eq. (63) gives:

$$dG' = -S'dT + V'dP + \sum\left(\overline{G}_i^* + \frac{2\overline{V}_i\sigma}{r}\right)dn_i.$$

Comparison with eq. (63) gives the identity

$$\overline{G}_i = G_i^* + \frac{2\overline{V}_i\sigma}{r} \tag{76}$$

as the variation of partial molar free energy with spherical particle size. From the relationship between partial molar free energy and activity, eq. (76) can be written as

$$\ln a_i = \ln a_i^* + \frac{2\overline{V}_i\sigma}{RT_r}. \tag{77}$$

In a limited terminal solid solution of B in A, in which B obeys Henry's Law, the activity of B at the limit of solubility is:

$$a_B = \gamma_B^0 X_{B(sat)},$$

and hence, from eq. (77), the solubility limit varies with particle size of the second phase as

$$\ln \frac{X_{B(sat,r)}}{X_{B(sat)}^*} = \frac{2\sigma\overline{V}_B}{RT_r}, \tag{78}$$

where $X_{B(sat,r)}$ is the solubility limit when the second phase occurs as a dispersion of spherical particles of radius r and $X_{B(sat)}^*$ is the solubility limit when the second phase is massive. Equation (78), which is known as the *Thomson–Freundlich equation*, provides a thermodynamical explanation of the phenomenon of *Ostwald ripening* (see ch. 9, § 3.2.2). When the second phase, precipitating from a primary solid solution, occurs in a range of particle sizes, it is observed that the particles of radius greater than some average value grow and that the smaller particles redissolve in the matrix. As the concentration of solute in the matrix at the interface between the matrix and a small precipitate is greater than that at the interface between the matrix and a large precipitate, a concentration, and hence activity, gradient exists between the two interfaces. This, in turn, provides the driving force for the diffusion of dissolved solute from one interface to the other, with the overall result that the larger particle grows and the smaller particle dissolves. Equation (78) is also of interest in that it indicates that no such quantity as "maximum solubility" exists.

10. The measurement of thermodynamic activity

Although activities are thermodynamic functions of state, their magnitudes and variations are determined by the interactions among the constituent particles of the system, which, in turn, determine bond energies and influence the spatial configurations assumed by the particles. Thus measurement of activities within a class of similar simple

systems can be expected to provide, at best, some fundamental understanding of the natures of these interactions or, at least, a basis for correlation of the behavior, which can then be used for extrapolation of the behavior of more complex systems.

The molar free energy of formation of a solution or compound from its pure components is obtained from the activities via eq. (44) and as the various phase equilibria occurring in a materials system are determined by the variations, with composition, temperature and pressure, of the relative free energies of the various phases, such equilibria can be most precisely determined by accurate measurement of activity. Also, the activity of a component in a solution is a measure of the minimum free energy required to convert the component from its state in solution to the pure state in any proposed extraction or refining process.

In the majority of the experimental methods the activity of only one component is measured. In such cases the activities of the other components can be obtained by integration of the Gibbs–Duhem equation. For constant temperature and total pressure this expression is $\Sigma X_i \mathrm{d} \ln a_i = 0$ or, in a more convenient form, $\Sigma X_i \mathrm{d} \ln \gamma_i = 0$ where $\gamma_i = a_i / X_i$ is the activity coefficient of i. Applied to the binary system A–B in which the variation of γ_A is known across the entire range of composition:

$$\ln \gamma_B (\text{at } X_B) = -\int_{X_B=1}^{X_B} \frac{X_A}{X_B} \mathrm{d} \ln \gamma_A . \tag{79}$$

10.1. Determination of activity by experimental measurement of vapor pressure

The experimental technique for the measurement of vapor pressure is determined by the magnitude of the pressure to be measured, and the various techniques which have been developed can be classified as *absolute methods* (direct and indirect static methods) and *indirect methods* (effusion and transpiration methods).

The earliest activity measurements were made on binary alloys of Hg with Zn, Au, Ag and Tl at temperatures near the boiling point of Hg. The partial pressure of Hg exerted by an amalgam is so much greater than the partial pressure of the other component that the former can be equated with the total vapor pressure of the amalgam. In the first studies the alloy was used as the sealing liquid in a U-tube null-point manometer. The vapor in equilibrium with the alloy is contained in the closed arm of the manometer, and hydrogen, the pressure of which is measured at a second manometer, is introduced to the other arm until the meniscuses in both arms are at the same level. The vapor pressures of amalgams at lower temperatures have been measured using various devices such as membrane manometers, quartz spiral manometers and ionization gages.

The partial pressures of Zn and Cd over α-Ag–Zn–Cd alloys and of Zn over α-brasses have been measured by resonance absorption spectroscopy. In studying the Zn alloys, light produced by a spark between Zn electrodes, is passed through a sample of vapor in equilibrium with the alloy, and the absorption of the 3076 Å resonance line is measured. As absorption of the 3035 Å resonance line does not occur, it is used as an internal standard and the vapor pressure, p, of Zn is obtained from Beer's Law as $-\ln(I_{3076}/I_{3035}) = Kpd/T$ where I is the intensity of the transmitted light, K is the absorp-

tion coefficient, T is the absolute temperature and d is the distance travelled by the light through the sample of vapor.

The *dew point method* is well-suited to systems containing a distinctly volatile component and has been applied to measurement of the activity of Zn in binary alloys containing Cu, Al, Ag, Au, Zr, Th, U, and Y, and the activity of Cd in Ag–Cd alloys. Experimentally, the alloy is placed at one end of a long initially evacuated tube which is heated to the desired temperature T_1. The temperature of the other end of the tube is lowered until condensation of the volatile component is observed at the temperature T_2. As the pressure within the tube is uniform, the partial pressure of the volatile component exerted by the alloy at T_1 equals the saturated vapor pressure of the pure volatile component at T_2. The use of fused silica tubes, which permits visual observation of condensation at the cooler end, has limited the temperature to less than 1100°C and, generally, measurements have been made in the range 400–900°C. In a similar *isopiestic technique*, the pure volatile component is placed in the cool end of an initially evacuated tube maintained in a known temperature gradient, and weighed quantities of the pure second component are placed at intervals along the temperature gradient. The volatile component is transferred from the vapor phase to the specimens of nonvolatile component until the alloys in equilibrium with the prevailing pressure of the volatile component are formed. In this technique, which has been applied to measurement of the activities of Al in solid Al–Fe and Al–Ni alloys, the compositions of the equilibrated alloys are determined gravimetrically.

Application of the dew point and isopiestic techniques to measurement of activity requires knowledge of the temperature dependence of the saturated vapor pressure of the volatile component.

In the *transpiration technique*, an inert carrier gas is passed over a sample at a flow rate which permits evaporation of the alloy to occur to the extent necessary to saturate the carrier gas. This technique has been used to measure the activities in liquid Fe–Cu and Fe–Ni alloys. The material evaporated from the sample is condensed downstream and is chemically analyzed. The total amount of evaporation into unit volume of the carrier gas at the total pressure P is determined by measuring the weight loss of the sample or by quantitative analysis of the amount of condensate recovered from a known volume of gas. If n_{Fe}, n_{Cu} and n_{He} are the numbers of moles of Fe, Cu and He carrier gas in the sampled volume, the partial pressure of Fe is calculated, from the ideal gas law, as $p_{Fe} = Pn_{Fe}/(n_{Fe} + n_{Cu} + n_{He})$. An advantage of this technique is that the activities of both components are measured and hence internal consistency of the results can be checked using the Gibbs–Duhem equation. However, in order that surface depletion of the more volatile component be avoided, the rates of diffusion in the alloy must be faster than the rates of evaporation.

In the *effusion technique* the alloy to be studied is placed in a *Knudsen cell* (a sealed crucible containing a small orifice in its lid) and the crucible is heated in vacuum to the desired temperature. Phase equilibrium is established between the vapor phase and the condensed phase in the cell and, if the dimensions of the orifice are small in comparison with the mean free path of the vapor species, the passage of vapor species through the orifice is not disturbed by collisions. Thus the rates of effusion of the vapor species are

proportional to their vapor pressures within the cell. From gas kinetic theory, the number of particles in a vapor phase striking unit area of the containing wall in unit time is $0.25n\bar{c}$, where n is the density of vapor species and $\bar{c} = (8RT/\Pi M)^{1/2}$ is the average speed of the particles. Consequently, the *weight loss*, W, due to effusion through an orifice of area A in time t is $pAt/(2\Pi MRT)^{1/2}$ and hence the pressure, p, of the species in the cell is $p = (W/At)(2\Pi RT/M)^{1/2}$. If a radioactive tracer is added to the alloy, very small amounts of effusing substance can be detected. For example, gamma-ray spectrometry of neutron-irradiated Au–Cu alloys has facilitated estimation of quantities as small as 10^{-10} g.

The transpiration and effusion techniques require that the molecular weights of the vapor species be known and hence they can only be used to study systems in which no complex vapor molecules are formed.

The problems caused by complex molecule formation can be eliminated by mass-spectrometric analysis of the vapor effusing from the Knudsen cell. In the *Knudsen cell-time of flight mass-spectrometer* combination, the beam of particles effusing from the cell is introduced to the ionization chamber of the mass-spectrometer through a slit. Ionization is produced by a pulsing electron beam and after each pulse the ionization chamber is cleared of ions by a pulse of small negative potential. The ions are then subjected to a continuously maintained high negative potential which accelerates them into a field-free drift tube, and the time required for a given ion to traverse the drift tube and be detected is proportional to $(m/e)^{1/2}$. The ion current, I_i^+, measured for the species i is related to the vapor pressure of i as:

$$p_i = KI_i^+T, \tag{80}$$

where the constant K is determined by the ionization cross-section of the ion, the detector sensitivity and the geometry of the Knudsen cell-ion source. The application of the technique to measurement of activities in binary systems was greatly facilitated by a manipulation of the Gibbs–Duhem equation which allows the variations, with composition, of the activity coefficients of the individual components to be obtained from the corresponding measured ratio of the activity coefficients as:

$$\ln \gamma_B(\text{at } X_B) = -\int_1^{X_B} X_A \, d \ln \frac{\gamma_A}{\gamma_B}. \tag{81}$$

From eq. (80):

$$\frac{I_A^+}{I_B^+} \propto \frac{p_A}{p_B} \propto \frac{a_A}{a_B} \frac{\gamma_A X_A}{\gamma_B X_B},$$

substitution of which into eq. (81) gives:

$$\ln \gamma_B(\text{at } X_B) = -\int_1^{X_B} X_A \, d\left(\ln \frac{I_A^+}{I_B^+} - \frac{X_A}{X_B} \right).$$

Use of a mass-spectrometer requires that a pressure of less than 10^{-8} atm be maintained in the areas of the ion source, analyzer and detector. This technique has been applied to

References: p. 469.

measurement of activities in a large number of binary and ternary systems containing V, Cr, Fe, Co, Ni, Cu, Ag, Au, Al, Tl, Pb, Sn, Bi, Sb, and In.

10.2. Determination of activity by establishing heterogeneous equilibrium

Heterogeneous equilibrium at constant temperature and pressure requires that the partial molar free energy, and hence activity, of each component of the system be the same in each of the phases present, i.e., a_i (in phase I) $= a_i$ (in phase II) $= a_i$ (in phase III) $= \ldots$. Thus, if the activity of a component can be fixed at a known value in any one of the phases, its value in every other phase is known.

One of the more simple heterogeneous equilibria involves a binary liquid, saturated with one of its components. In a simple binary eutectic system exhibiting virtually complete mutual immiscibility in the solid state, the saturated liquids on the liquidus lines are in equilibrium with virtually pure solids. Thus, in the melt of A-liquidus composition at the liquidus temperature T, the activity of A relative to pure liquid A as the standard state equals the activity of pure solid A relative to liquid A as the standard state, both being given by $a_A = \exp(-\Delta G^0_{m,A}/RT)$ where $\Delta G^0_{m,A}$ is the molar free energy of melting of A at temperature T. Activities have been calculated in this manner along liquidus lines in such systems as Ag–Si and Ag–Pb.

Fe and Ag are virtually immiscible in the liquid state, and when Si is added as a solute to coexisting liquid Fe and Ag it is distributed between the two liquids such that its activity is the same in both phases. The activities of Si in liquid Fe and liquid Fe–C alloys have been determined by chemical analysis of equilibrated Fe and Ag liquids containing Si, and knowledge of the activity of Si in Ag–Si alloys. In a similar manner the activity of Ag in Al–Ag alloys has been determined from measurement of the equilibrium partitioning of Ag between the virtually immiscible liquids Al and Pb, and the activity of Al in Al–Co alloys has been determined by partitioning Al between the virtually immiscible liquids Ag and Co.

The respective equilibrium constants for the reactions $CO_2 + C_{(graphite)} = 2CO$ and $CO + \frac{1}{2}O_2 = CO_2$ are:

$$K_4 = \frac{p^2_{CO}}{p_{CO_2} a_C} \tag{82}$$

and

$$K_5 = \frac{p_{CO_2}}{p_{CO} p^{1/2}_{O_2}}. \tag{83}$$

Thus, at a fixed temperature, which determines the values of K_4 and K_5, a CO–CO_2 gas mixture of known p_{CO} and p_{CO_2} has an activity of carbon given by eq. (82) and a partial pressure of oxygen given by eq. (83). Similarly, by virtue of the equilibrium $H_2 + \frac{1}{2}O_2 = H_2O$, an H_2–H_2O mixture of known p_{H_2} and p_{H_2O} exerts a unique partial pressure of oxygen at any temperature; by virtue of the equilibrium $H_2 + \frac{1}{2}S_2 = H_2S$, an H_2–H_2S mixture of known p_{H_2} and p_{H_2S} exerts a unique partial pressure of sulfur at any temperat-